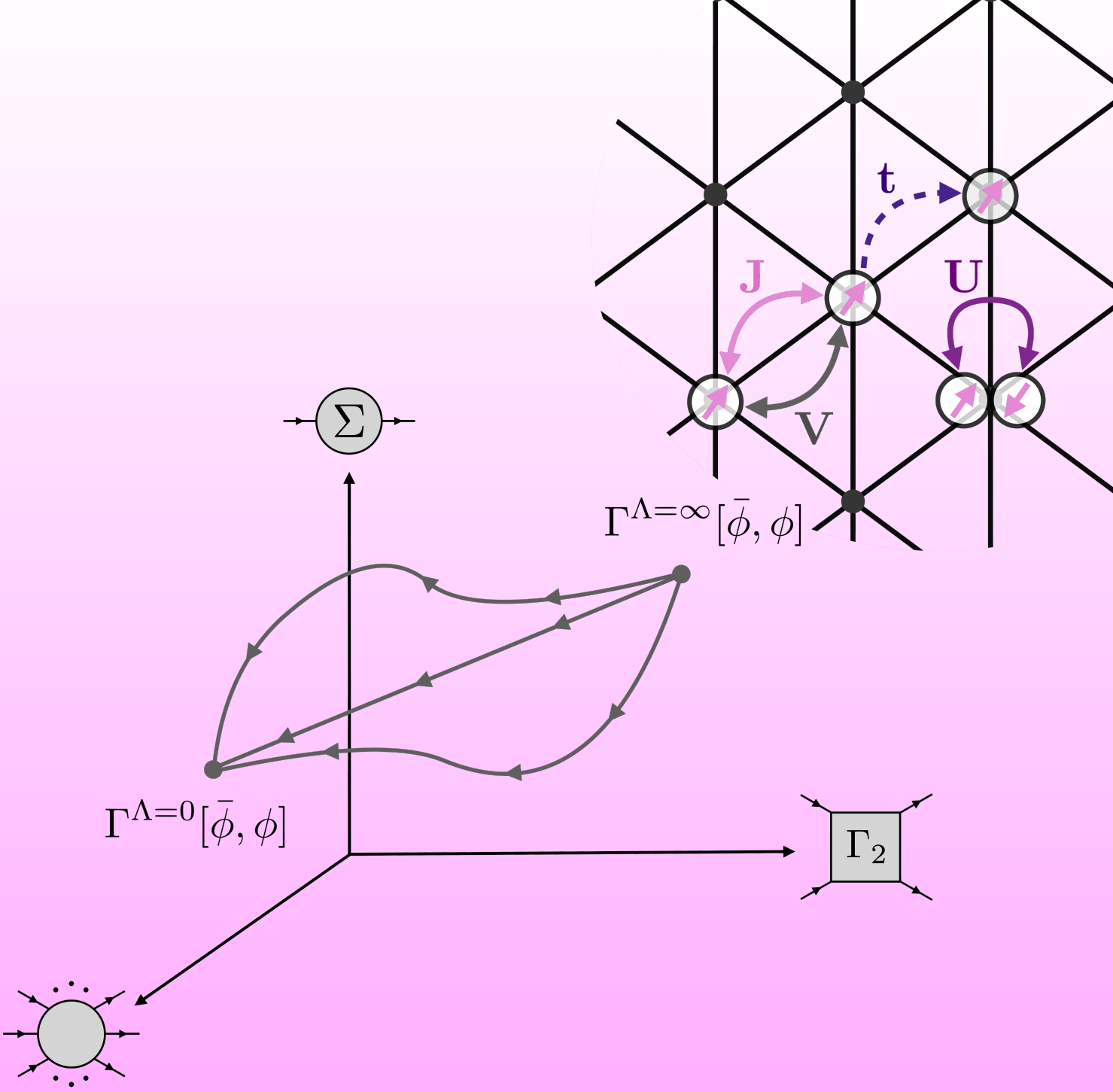

Effective field theories for strongly correlated fermions

Insights from the functional renormalization group

Dominik Kiese

Dissertation

Effective field theories for strongly correlated fermions

Insights from the functional renormalization group

Inaugural dissertation presented for the degree of

DOCTOR RERUM NATURALIUM

by

Dominik Kiese

from Leverkusen

Institute for Theoretical Physics
University of Cologne

June 3, 2022

First referee: Prof. Dr. Simon Trebst
Second referee: Prof. Dr. Achim Rosch
Third referee: Prof. Dr. Carsten Honerkamp
Day of submission: June 3, 2022
Day of the oral examination: August 5, 2022

Dissertation accepted by the mathematics science faculty of the University of Cologne in 2022.

Abstract

'There are very few things that can be proved rigorously in condensed matter physics.'

These famous words, brought to us by Nobel laureate Anthony James Leggett in 2003, summarize very well the challenging nature of problems researchers find themselves confronted with when entering the fascinating field of condensed matter physics. The former roots in the inherent many-body character of several quantum mechanical particles with modest to strong interactions between them: their individual properties might be easy to understand, while their collective behavior can be utterly complex. Strongly correlated electron systems, for example, exhibit several captivating phenomena such as superconductivity or spin-charge separation at temperatures far below the energy scale set by their mutual couplings. Moreover, the dimension of the respective Hilbert space grows exponentially, which impedes the exact diagonalization of their Hamiltonians in the thermodynamic limit. For this reason, renormalization group (RG) methods have become one of the most powerful tools of condensed matter research - scales are separated and dealt with iteratively by advancing an RG flow from the microscopic theory into the low-energy regime.

In this thesis, we report on two complementary implementations of the functional renormalization group (fRG) for strongly correlated electrons. Functional RG is based on an exact hierarchy of coupled differential equations, which describe the evolution of one-particle irreducible vertices in terms of an infrared cutoff Λ. To become amenable to numerical solutions, however, this hierarchy needs to be truncated. For sufficiently weak interactions, three-particle and higher-order vertices are irrelevant at the infrared fixed point, justifying their neglect. This one-loop approximation lays the foundation for the N-patch fRG scheme employed within the scope of this work. As an example, we study competing orders of spinless fermions on the triangular lattice, mapping out a rich phase diagram with several charge and pairing instabilities. In the strong-coupling limit, a cutting-edge implementation of the multiloop pseudofermion functional renormalization group (pffRG) for quantum spin systems at zero temperature is presented. Despite the lack of a kinetic term in the microscopic theory, we provide evidence for self-consistency of the method by demonstrating loop convergence of pseudofermion vertices, as well as robustness of susceptibility flows with respect to occupation number fluctuations around half-filling. Finally, an extension of pffRG to Hamiltonians with coupled spin and orbital degrees of freedom is discussed and results for exemplary model studies on strongly correlated electron systems are presented.

Kurzzusammenfassung

'There are very few things that can be proved rigorously in condensed matter physics.'

Diese berühmten Worte des Nobelpreisträgers Anthony James Leggett aus dem Jahr 2003, fassen die herausfordernde Natur der Probleme, mit denen Wissenschaftler im faszinierenden Gebiet der Physik kondensierter Materie konfrontiert werden, sehr gut zusammen. Diese resultieren aus dem inhärenten Vielteilchen-Charakter von mehreren quantenmechanischen Teilchen mit mässigen bis starken Wechselwirkungen: ihre individuellen Eigenschaften mögen einfach zu verstehen sein, ihr kollektives Verhalten aber ist äusserst komplex. In Systemen bestehend aus stark korrelierten Elektronen beispielsweise, treten spannende Phänomene wie Supraleitung oder die Trennung von Spin- und Ladungsfreiheitsgraden erst bei Temperaturen auf, die weitaus niedriger sind als die Energieskala ihrer wechselseitigen Kopplungen. Zudem verhindert das exponentielle Wachstum der Dimension des zugehörigen Hilbert-Raums die exakte Diagonalisierung ihrer Hamiltonoperatoren im thermodynamischen Limes. Renormierungsgruppen (RG) Methoden gehören aus diesem Grund zu den mächtigsten Werkzeugen der Forschung an kondensierter Materie, da Skalen voneinader separiert und iterativ abgehandelt werden indem ein RG Fluss von der mikroskopischen Theorie bis hin zum Niedrigenergiebereich fortgesetzt wird.

In dieser Arbeit diskutieren wir zwei komplementäre Implementierungen der funktionalen Renormierungsgruppe (fRG) für stark korrelierte Elektronen. Funktionale RG basiert auf einer exakten Hierarchie von gekoppelten Differentialgleichungen, welche die Entwicklung Einteilchen-irreduzibler Vertizes anhand eines Infrarot *cutoff* Λ beschreiben. Damit sie numerisch lösbar wird, muss diese Hierarchie jedoch trunkiert werden. Für hinreichend schwache Wechselwirkungen sind Dreiteilchen-Vertizes und solche noch höherer Ordnung am Infrarotfixpunkt irrelevant und können daher vernachlässigt werden. Diese *one-loop* Näherung bildet im Rahmen dieser Arbeit die Grundlage für das angewandte N-Patch fRG Schema. Als Beispiel betrachten wir konkurrierende Ordnungen spinloser Fermionen auf dem Dreiecksgitter, für welche wir ein ergiebiges Phasendiagramm mit mehreren Ladungs- und Paarungsinstabilitäten berechnen. Für den Fall starker Wechselwirkungen stellen wir eine Spitzenimplementierung der *multiloop* Pseudo-Fermion funktionalen Renormierungsgruppe (pffRG) zur Anwendung auf quantenmechanische Spinsysteme am absoluten Nullpunkt vor. Darüber hinaus zeigen wir, dass die Methode, trotz des Fehlens eines kinetischen Terms in der mikroskopischen Theorie, selbstkonsistent ist, indem wir sowohl die *loop*-Konvergenz der Pseudo-Fermion Vertizes demonstrieren, als auch die Stabilität von Suszeptibilitätsflüssen gegenüber Teilchenzahlfluktuationen nahe halber Füllung. Schliesslich diskutieren wir die Anwendung der pffRG Methode auf Hamiltonoperatoren mit gekoppelten Spin- und Orbitalfreiheitsgraden und stellen die Ergebnisse von Modellstudien an stark korrelierten Elektronensystemen vor.

Erklärung zur Dissertation

Hiermit versichere ich an Eides statt, dass ich die vorliegende Dissertation selbstständig und ohne die Benutzung anderer als der angegebenen Hilfsmittel und Literatur angefertigt habe. Alle Stellen, die wörtlich oder sinngemäß aus veröffentlichten und nicht veröffentlichten Werken dem Wortlaut oder dem Sinn nach entnommen wurden, sind als solche kenntlich gemacht. Ich versichere an Eides statt, dass diese Dissertation noch keiner anderen Fakultät oder Universität zur Prüfung vorgelegen hat; dass sie - abgesehen von unten angegebenen Teilpublikationen und eingebundenen Artikeln und Manuskripten - noch nicht veröffentlicht worden ist sowie, dass ich eine Veröffentlichung der Dissertation vor Abschluss der Promotion nicht ohne Genehmigung des Promotionsausschusses vornehmen werde. Die Bestimmungen dieser Ordnung sind mir bekannt. Darüber hinaus erkläre ich hiermit, dass ich die Ordnung zur Sicherung guter wissenschaftlicher Praxis und zum Umgang mit wissenschaftlichem Fehlverhalten der Universität zu Köln gelesen und sie bei der Durchführung der Dissertation zugrundeliegenden Arbeiten und der schriftlich verfassten Dissertation beachtet habe und verpflichte mich hiermit, die dort genannten Vorgaben bei allen wissenschaftlichen Tätigkeiten zu beachten und umzusetzen. Ich versichere, dass die eingereichte elektronische Fassung der eingereichten Druckfassung vollständig entspricht.

8 August 2022, Dominik Kiese

Publications

This work is based on the following articles, ordered by appearance in this thesis.

[P1] *Multiloop functional renormalization group approach to quantum spin systems*
D. Kiese, T. Mueller, Y. Iqbal, R. Thomale, and S. Trebst
Physical Review Research 4, 023185 (2022)

[P2] *Benchmark Calculations of Multiloop Pseudofermion fRG*
M. K. Ritter, **D. Kiese**, T. Müller, F. B. Kugler, R. Thomale, S. Trebst, and J. v. Delft
The European Physical Journal B 95, 102 (2022)

[P3] *Moments and multiplets in moiré materials:*
A pseudo-fermion functional renormalization group for spin-valley models
L. Gresista, **D. Kiese**, and S. Trebst
The European Physical Journal B 95, 119 (2022)

[P4] *Functional renormalization of spinless triangular-lattice fermions:*
N-patch vs. truncated-unity scheme
N. Gneist, **D. Kiese**, R. Henkel, L. Classen, and M. M. Scherer
arXiv:2205.12547

[P5] *Pinch-points to half-moons and up in the stars: the kagome skymap*
D. Kiese, F. Ferrari, N. Astrakhantsev, N. Niggemann, P. Ghosh, T. Müller, R. Thomale, T. Neupert, J. Reuther, M. J. P. Gingras, S. Trebst, and Y. Iqbal
arXiv:2206.00264

[P6] *TMDs as a platform for spin liquid physics: A strong coupling study of twisted bilayer WSe_2*
D. Kiese, Y. He, C. Hickey, A. Rubio, and D. M. Kennes
APL Materials 10, 031113 (2022)

[P7] *Emergence and stability of spin-valley entangled quantum liquids in moiré heterostructures*
D. Kiese, F. L. Buessen, C. Hickey, S. Trebst, and M. M. Scherer
Physical Review Research 2, 013370 (2020)

[P8] *Realization of Nearly Dispersionless Bands with Strong Orbital Anisotropy*
from Destructive Interference in Twisted Bilayer MoS_2
L. Xian, M. Claassen, **D. Kiese**, M. M. Scherer, S. Trebst, D. M. Kennes and A. Rubio
Nature Communications 12, 5644 (2021)

[P9] *Cavity-induced quantum spin liquids*
A. Chiocchetta, **D. Kiese**, C. P. Zelle, F. Piazza and S. Diehl
Nature Communications 12, 5901 (2021)

Acknowledgements

First and foremost, I would like to express my deepest gratitude to my PhD supervisor Simon Trebst for his continuous support and invaluable advice without which this work would not have been possible. Despite all obstacles owed to the Corona pandemic, I still feel like I received the best possible mentorship I could have hoped for.

Second, I sincerely thank Achim Rosch for acting as co-examiner of this thesis. His indespensable ability to open up alternative perspectives on any physics related problem has been an genuine inspiration for me.

I very much appreciate to have had the opportunity to collaborate with many great people over the years. In particular, I truly enjoyed discussions with Michael Scherer, Laura Classen, Dante Kennes, Yasir Iqbal, Johannes Reuther and Ronny Thomale on fRG related topics and beyond. I am especially grateful to Michael for hosting me as his teaching assistant for lecturing quantum mechanics at AIMS Ghana in the beginning of 2020. Moreover, I am thankful to Julian Thoenniss, Marc Ritter, Matthias Punk and Jan von Delft for their pioneering contributions to the development of multiloop pffRG. I am indepted to Fabian Kugler for sharing his expertise on mfRG in countless encouraging debates. My cordial thanks goes to Francesco Ferrari, Nikita Astrakhantsev, Nils Niggemann and Pratyay Ghosh for joining me in the quest for the kagome skymap. Moreover, it has been a pleasure to engineer cavity spin liquids together with Alessio Chiocchetta, Carl Philip Zelle, Franceso Piazza and Sebastian Diehl. In addition, I would like to express my appreciation for fruitful discussions with Finn Lasse Buessen, Ciarán Hickey, Björn Sbierksi, Martin Claassen and Lede Xian.

Tobias Müller and Lasse Gresista deserve special credit for the tremendous effort they put into development of the `PFFRGSolver` software. The package could not have advanced thus far without their priceless contributions. I thank Tobias for numerous day and night time discussions during the months we implemented the relevant numerics from scratch and for his lasting enthusiasm despite the obstacles we were facing along the way. Lasse, on the other hand, has been the central figure in extending spin-valley pffRG to models without residual SU(2) symmetries.

My obligation is due to the Simons foundation for having me as a virtual Research Scholar at the Flatiron Institute in the summer of 2021. I am grateful to Angel Rubio for supervising my work during this exciting time and for on-going collaborations on twisted transition metal dichalcogenides.

Being part of the Institute for Theoretical Physics at the University of Cologne has been a thrilling experience for me. I would like to extend my thanks to all the great colleagues I was allowed to meet, in particular Oriana Diessel, Jan Attig and Nico Gneist for stimulating discussions on physics and beyond. Moreover, I want to express my appreciation for the administrative staff of the University of Cologne and the Bonn-Cologne Graduate School of Physics and Astronomy, especially Andreas Sindermann, Petra Neubauer-Guenther, Claudia Herrmann and Ute Graffenberger for backing up every student without ever taking credit for it.

Furthermore, I would like to thank the organziation of the supercomputing centers at the University of Cologne and the Forschungzentrum Jülich, in particular Stefan Borowski and Daniel Rohe, for ensuring smooth workflows on the Cheops, JURECA and JUWELS cluster, on which the numerical calculations in this thesis have been performed.

I thank Ciarán, Tobias, Lasse, Nico, Laura and Michael for proofreading this thesis.

Finally, I am deeply indepted to Charlotte, my family, and my friends for their everlasting support and encouragement. I cannot express how much you mean to me.

Contents

1 Introduction

Strongly correlated electron systems haven proven themselves fertile ground for the discovery of novel and intriguing physical phenomena, such as high-temperature superconductivity, frustrated magnetism or the fractionalization of quantum numbers. The common motif shared by materials exhibiting these strong correlations is the absence of a coherent *single-particle picture* - interactions between them are often on a par with their kinetic energy, which calls for a *many-body perspective*.

To develop the latter, the consultancy of theoretical models is of paramount importance. Ideally, these should be simple enough to distill the essential properties of an interacting electron system, while being of relevance for actual materials. A prototypical Hamiltonian for strongly correlated electrons is the Hubbard model [1, 2], which describes fermions within a single band subject to Coulomb repulsion. Their movement is thereby restricted to hopping processes between nearest neighbor sites of the crystal lattice, characterized by some rate t, whereas their interactions are assumed to be screened, such that only an on-site term of magnitude U remains.

In the weak-coupling limit, that is $U/t \ll 1$, one may view the interacting system as a perturbed version of the Fermi gas in which the constituents acquire an effective or *renormalized* mass and magnetic moment [3]. Excitations of such a Fermi liquid (FL), its so-called quasiparticles, are thus qualitatively equivalent to those of the non-interacting system. In general, their lifetime is finite due to scattering processes close the Fermi level. Importantly, one should not labor the misapprehension that the Fermi liquid state is stable just because U is sufficiently small. An infinitesimal attractive interaction, for example, could cause an unbounded growth of scattering amplitudes with vanishing total spin and momentum and ultimately lead to a breakdown of FL theory [4, 5]. Such a *pairing instability* marks the onset of a superconducting phase in which electron pairs obey Bose-Einstein statistics and are thus capable of condensing into a coherent ground state. Yet, the bare Coulomb interaction is repulsive, which should impede the formation of bound electron states all together. This raises the question how an *effective interaction* capable of glueing one electron to another can be generated. A famous paper by Bardeen, Cooper and Schrieffer (BCS) [6] provides one possible explanation by attributing the adhesion to electron-phonon coupling: one electron perturbs its surrounding crystal structure and indirectly attracts another electron nearby. For some materials, such as iron-pnictides, however, phonon mediated pairing is too weak to explain their ability to conduct electrical currents without resistivity. A general explanation for the pairing mechanism in superconducting materials has, despite all efforts, remained obscure up to the present day.

According to conventional wisdom, partially filled valence bands make for archetypal electrical conductors. For sufficiently strong interactions $U/t \gtrsim 1$ though, metals may undergo a Mott transition and become insulators, which sharply contrasts this single-particle picture. In the strong-coupling limit $U/t \to \infty$, electrons localize and one expects some sort of magnetic ground state driven by residual interactions between their spin degrees of freedom. In the presence of strong quantum fluctuations, however, such spin models can harbor quantum spin liquids (QSLs), massively entangled states of matter which host *fractionalized* spinon excitations and refuse to order even at lowest temperatures. Apart from few exceptions, such as the honeycomb Kitaev model [7] and the observation of a half-integer thermal quantum hall response in α-$RuCl_3$ [8], their pivotal property, namely the absence of a magnetic order parameter, complicates the unambiguous identification of QSLs in experiments as well as numerical simulations. Moreover, despite ambitions to characterize them in terms of their underlying *gauge structure* [9], physicists have hitherto struggled to come up with a complete classification of elusive quantum spin liquids [10].

Capturing the multitude of *collective phenomena* inherent to strongly correlated electron systems is particularly challenging due to their *scale-dependent* nature. In cuprate superconductors, for example, one traverses three orders of magnitude in energy starting from the Coulomb repulsion, over magnetic exchange couplings, down to the superconducting transition temperature [11]. The renormalization group (RG) framework is particularly powerful for bridging between microscopic models and their effective low-energy description. Over the years, various implementations of the RG idea have come forth, many of which can only be pursued numerically. Wilson's numerical renormalization group (NRG), for example, is an excellent tool for solving impurity models in an accurate and non-perturbative way. In conjunction with dynamical mean-field theory (DMFT) it can also be extended to lattice systems at the cost of neglecting non-local correlations and yields valuable insights into the metal-insulator transition exhibited by the Hubbard model [12]. In one dimension, the density matrix renormalization

group (DMRG) is probably the single most potent method for determining properties of strongly correlated quantum models, since one is able to calculate static, as well as dynamic quantities up to machine precision while invoking only moderate computational resources [13]. The generalization of DMRG to higher spatial dimensions in the form of tensor network methods [14] is currently one of the most vibrant fields in computational condensed matter physics.

The RG flavor laying the foundation for this thesis is the functional renormalization group (fRG) [15], which will be formally introduced in Chapter 1. In particular, we discuss the derivation of the differential equation for the effective action at heart of the fRG approach, as well as important approximations required to render its solution feasible. Chapters 2 and 3 are devoted to two complementary incarnations of functional RG: one for weakly-coupled itinerant electrons and the other one capable of dissecting magnetic instabilities in quantum spin models. Special emphasis is payed to their numerical implementation - we will detail each and every algorithm and point out mayor improvements regarding the accuracy of the so-obtained results when compared to existing literature. Both chapters are closed with two examples each, giving insight into the outputs produced by the different fRG solvers and simultaneously highlighting the flexibility of the method. Chapter 5 summarizes methodological developments pursued within the scope of this thesis: the implementation of multiloop flow equations for quantum spin systems and the extension of the fRG formalism to spin-valley coupled Hamiltonians, relevant for moiré heterostructures such as TLG/h-BN [16]. Applications of functional RG to various model systems are discussed in Chapter 6. Chapter 7 is concerned with side projects disconnected from the fRG aspect of this work. We present two novel platforms for engineering exotic quantum states, multi-layer compositions of transition metal dichalcogenides (TMDs), in which the twist angle between adjacent TMD sheets provides another tuning parameter for controlling properties of the band structure, and magnetic materials coupled to an optical cavity. The latter hold promise for the realization of robust QSL states, which we decipher via a Schwinger-Boson analysis. Chapter 8 provides a summary of the insights gained in this work and speculates about future methodological directions for the fRG approach.

2 Functional renormalization group

In this chapter, the functional renormalization group (fRG) approach to correlated fermionic systems is introduced on a general level, closely following the derivations presented in Refs. [17, 18]. After its inception in high-energy physics [19, 20], fRG calculations are, nowadays, also employed in the context of condensed matter systems, ranging from applications to variants of the Hubbard model [11, 21], over strongly-coupled spin Hamiltonians [22, 23] to impurity models [24, 25].

The general idea behind fRG is the successive inclusion of fermionic fluctuations during a renormalization group flow, which evolves the many-body interactions of a microscopic theory in terms of an infrared cutoff Λ. The outcome of an fRG calculation are fully renormalized, one-particle irreducible vertices, which characterize the effective interactions of the system at low energies. From these, useful physical quantities such as magnetic response functions or superconducting gaps can be obtained.

While the fRG description of a given fermionic model is in principle exact, appropriate truncation schemes are essential for facilitating numerical solutions of the flow equations. Most implementations of fRG concern themselves with the self-energy and two-particle vertex, while neglecting higher-order terms. Although many physical phenomena can already be captured by this seemingly simple approach, functional RG calculations have often been lacking quantitative accuracy. In recent years, however, multiple attempts for improving the predictive power of fRG have been made [26, 27]. The multiloop scheme by Kugler and von Delft [28] is the latest iteration in that series, allowing to efficiently incorporate all diagrams of parquet type, that is, diagrams which can be evaluated at the numerical cost of the conventional one-loop flow.

In the following, we first present the derivation of fRG flow equations from general principles. We continue by discussing different truncation schemes and how they can be motivated from the parquet formalism, which offers an alternative field-theoretical description of the many-body problem up to the two-particle level. Given the vast amount of literature that exists on the matter, some of our considerations are kept short and the reader is encouraged to follow the given references, which provide excellent discussions beyond the scope of this work.

2.1 Generating functionals

We consider Hamiltonians of the form $\mathcal{H} = \mathcal{H}_0 + \mathcal{H}_{\text{int}}$, featuring a quadratic part

$$\mathcal{H}_0 = \sum_{x_1', x_1} \xi_{x_1'|x_1} c^\dagger_{x_1'} c_{x_1} \,, \tag{2.1}$$

and a two-particle interaction

$$\mathcal{H}_{\text{int}} = \sum_{x_1', x_2', x_1, x_2} V_{x_1' x_2'|x_1 x_2} c^\dagger_{x_1'} c^\dagger_{x_2'} c_{x_2} c_{x_1} \,. \tag{2.2}$$

Here, $c^\dagger_x$ (c_x) creates (annihilates) a fermion with quantum numbers encoded in the multi-index x. According to the algebra of fermionic operators, the matrix elements $V_{x_1' x_2'|x_1 x_2}$ must be antisymmetric with respect to permutations $(x_1' \leftrightarrow x_2')$ and $(x_1 \leftrightarrow x_2)$, as indicated by a vertical line separating the respective index sets.

Since fRG is formulated in the path-integral formalism, we introduce the action of our Hamiltonian in terms of Grassmann fields $\bar{\psi}, \psi$ as

$$S[\bar{\psi}, \psi] = -(\bar{\psi}, G_0^{-1} \psi) + \sum_{x_1', x_2', x_1, x_2} V_{x_1' x_2'|x_1 x_2} \bar{\psi}_{x_1'} \bar{\psi}_{x_2'} \psi_{x_2} \psi_{x_1} \,, \tag{2.3}$$

where we defined $(\bar{\psi}, G_0^{-1}\psi) \equiv \sum_{x_1', x_1} \bar{\psi}_{x_1'} [G_0^{-1}]_{x_1' x_1} \psi_{x_1}$. The bare propagator G_0 can be determined from $\mathcal{H}_0$ and we write out its algebraic expression explicitly once we settle on a particular model. For now, however, G_0 is left unspecified. The partition function Z for the action in Eq. (2.3) can be expressed as

$$Z = \frac{1}{Z_0} \int D[\bar{\psi}, \psi] e^{-S[\bar{\psi}, \psi]} \,, \tag{2.4}$$

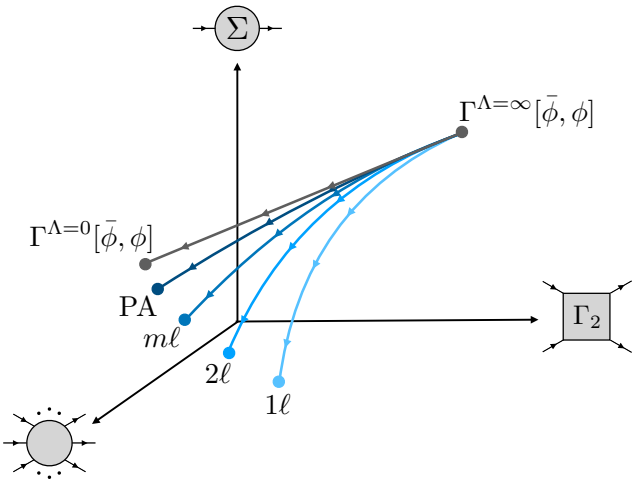

Figure 2.1: Schematic illustration of the functional renormalization group. The effective action $\Gamma[\phi,\phi]$ lives in a high-dimensional parameter space spanned by the self-energy Σ, the two-particle vertex Γ_2 and higher-order vertex functions. Under the RG flow, the couplings are evolved from the ultraviolet (UV) to the infrared (IR) limit as a function of some cutoff scale Λ. In practical applications, however, approximations are unavoidable, such that one computes effective low-energy theories only in proximity to the exact solution (grey). The multiloop ($m\ell$) truncation, for example, successively incorporates more complex diagrams, until one recovers a solution to the parquet approximation (PA) for $m \to \infty$.

where we normalize with its non-interacting counterpart Z_0.

The sought-after quantities for a given action are correlations between its fermionic constituents, which can be computed as Taylor coefficients of properly defined generating functionals. The generator of disconnected n-particle Green's functions $W[\bar{\eta},\eta]$, for example, is obtained by adding source fields $\bar{\eta},\eta$ to the partition function, yielding

$$W[\bar{\eta},\eta] = \frac{1}{Z_0}\int D[\bar{\psi},\psi]e^{-S[\bar{\psi},\psi]-(\bar{\psi},\eta)-(\bar{\eta},\psi)}\,. \tag{2.5}$$

Disconnected correlation functions can subsequently be calculated as

$$G_n(x_1',...,x_n'|x_1,...,x_n) = \frac{\delta^n}{\delta\bar{\eta}_{x_1}...\delta\bar{\eta}_{x_n}}\frac{\delta^n}{\delta\eta_{x_n'}...\delta\eta_{x_1'}}W[\bar{\eta},\eta]\Big|_{\bar{\eta}=\eta=0}\,. \tag{2.6}$$

The G_n are fully determined by their connected components as spawned by the Schwinger functional $W_c[\bar{\eta},\eta] = \ln(W[\bar{\eta},\eta])$, whose Legendre transform

$$\Gamma[\bar{\phi},\phi] = -W_c[\bar{\eta},\eta] - (\bar{\phi},\eta) - (\bar{\eta},\phi) + (\bar{\phi},G_0^{-1}\phi)\,, \tag{2.7}$$

is the generator for one-particle irreducible (1PI) vertex functions [15]. Here, $\phi = -\frac{\delta W_c[\bar{\eta},\eta]}{\delta\bar{\eta}}$ and $\bar{\phi} = \frac{\delta W_c[\bar{\eta},\eta]}{\delta\eta}$ denote conjugate source fields. The 1PI vertices cannot be decomposed any further by cutting single propagator lines and thus constitute the elementary building blocks for computing connected correlation functions via the so-called tree expansion [15]. To clarify their physical meaning, let us consider the matrix identity

$$R \equiv \begin{pmatrix} \frac{\delta^2 W_c[\bar{\eta},\eta]}{\delta\bar{\eta}\delta\eta} & -\frac{\delta^2 W_c[\bar{\eta},\eta]}{\delta\bar{\eta}\delta\bar{\eta}} \\ -\frac{\delta^2 W_c[\bar{\eta},\eta]}{\delta\eta\delta\eta} & \frac{\delta^2 W_c[\bar{\eta},\eta]}{\delta\eta\delta\bar{\eta}} \end{pmatrix} = \begin{pmatrix} \frac{\delta^2\Gamma[\bar{\phi},\phi]}{\delta\phi\delta\bar{\phi}} + G_0^{-1} & \frac{\delta^2\Gamma[\bar{\phi},\phi]}{\delta\phi\delta\phi} \\ \frac{\delta^2\Gamma[\bar{\phi},\phi]}{\delta\bar{\phi}\delta\bar{\phi}} & \frac{\delta^2\Gamma[\bar{\phi},\phi]}{\delta\bar{\phi}\delta\phi} - (G_0^{-1})^T \end{pmatrix}^{-1}\,, \tag{2.8}$$

which can be derived from Eq. (2.7). Focusing on the matrix element to the upper left for vanishing source fields and pairing terms[1], we find the identity

$$G = \left(G_0^{-1} + \Gamma_1\right)^{-1}\,, \tag{2.9}$$

[1] With *pairing terms*, we refer to derivatives $\frac{\delta^2 F}{\delta\psi\delta\psi}$ and the likes of them. F denotes some generic functional of Grassmann fields.

where we defined the dressed or full propagator

$$G \equiv \left.\frac{\delta W_c[\bar{\eta},\eta]}{\delta\bar{\eta}\delta\eta}\right|_{\bar{\eta}=\eta=0}, \tag{2.10}$$

and the one-particle vertex

$$\Gamma_1 \equiv \left.\frac{\delta\Gamma[\bar{\phi},\phi]}{\delta\bar{\phi}\delta\phi}\right|_{\bar{\phi}=\phi=0}. \tag{2.11}$$

Equation (2.9) resembles the form of Dyson's identity $G = (G_0^{-1} - \Sigma)^{-1}$, which defines the self-energy as the interaction correction to the bare propagator. Consequently, $\Gamma_1 = -\Sigma$. This sheds light on the interpretation of 1PI vertices: they capture *effective* many-body interactions and their generating functional $\Gamma[\bar{\phi},\phi]$ is therefore commonly referred to as *effective action* [11, 15].

2.2 Exact flow equations

The central step for setting up the fRG approach amounts to implementing a cutoff Λ into the bare propagator, such that it vanishes in the ultraviolet limit, $G_0^{\Lambda\to\infty} = 0$, and coalesces with G_0 when approaching the infrared, $G_0^{\Lambda\to 0} = G_0$. By construction, all other Green's functions become cutoff dependent, too, since they depend on G_0 through their respective generating functional. In order to capture the variation of 1PI vertices under incremental changes of the cutoff parameter, one rephrases Eq. (2.7) as a differential equation. For this sake, we need the cutoff-derivative of $W_c[\bar{\eta},\eta]$, which reads

$$\frac{d}{d\Lambda}W_c^\Lambda[\bar{\eta},\eta] = -\operatorname{Tr}\left(Q^\Lambda G_0^\Lambda\right) + \operatorname{Tr}\left(Q^\Lambda \frac{\delta^2 W_c^\Lambda[\bar{\eta},\eta]}{\delta\bar{\eta}\delta\eta}\right) - \left(\frac{\delta W_c^\Lambda[\bar{\eta},\eta]}{\delta\eta}, Q^\Lambda \frac{\delta W_c^\Lambda[\bar{\eta},\eta]}{\delta\bar{\eta}}\right), \tag{2.12}$$

with $Q^\Lambda \equiv \frac{d}{d\Lambda}(G_0^\Lambda)^{-1}$. The cutoff-derivative of the effective action evaluates to

$$\frac{d}{d\Lambda}\Gamma^\Lambda[\bar{\phi},\phi] = -\frac{d}{d\Lambda}W_c^\Lambda[\bar{\eta}^\Lambda,\eta^\Lambda] - \left(\bar{\phi},\frac{d}{d\Lambda}\eta^\Lambda\right) - \left(\frac{d}{d\Lambda}\bar{\eta}^\Lambda,\phi\right) + \left(\bar{\phi},Q^\Lambda\phi\right), \tag{2.13}$$

where a Λ-dependence needs to be added to the $\bar{\eta},\eta$ source fields to make up for the change of variables in the Legendre transformation. Plugging Eq. (2.12) into Eq. (2.13) one finds

$$\frac{d}{d\Lambda}\Gamma^\Lambda[\bar{\phi},\phi] = \operatorname{Tr}\left(Q^\Lambda G_0^\Lambda\right) - \operatorname{Tr}\left(Q^\Lambda R_{11}^\Lambda\right), \tag{2.14}$$

where we made use of Eq. (2.8). Eliminating G_0^{-1} in R using Dyson's equation, this expression can be rephrased as

$$\frac{d}{d\Lambda}\Gamma^\Lambda[\bar{\phi},\phi] = \operatorname{Tr}\left(Q^\Lambda G_0^\Lambda\right) - \operatorname{Tr}\left(G^\Lambda Q^\Lambda \tilde{R}_{11}^\Lambda\right), \tag{2.15}$$

where $\tilde{R}_{11}^\Lambda$ denotes the upper left element of

$$\tilde{R}^\Lambda = \left[\mathbb{1} - \begin{pmatrix} -G^\Lambda & 0 \\ 0 & (G^\Lambda)^T \end{pmatrix}\begin{pmatrix} U^\Lambda & \frac{\delta^2\Gamma^\Lambda[\bar{\phi},\phi]}{\delta\bar{\phi}\delta\bar{\phi}} \\ \frac{\delta^2\Gamma^\Lambda[\bar{\phi},\phi]}{\delta\phi\delta\phi} & -(U^\Lambda)^T \end{pmatrix}\right]^{-1}, \tag{2.16}$$

with $U^\Lambda = \frac{\delta^2\Gamma^\Lambda[\bar{\phi},\phi]}{\delta\bar{\phi}\delta\phi} - \Gamma_1^\Lambda$. $\tilde{R}^\Lambda$ resembles a geometric series, which is particularly useful for the derivation of vertex flow equations discussed below.

Starting from Eq. (2.15), we expand $\Gamma^\Lambda[\bar{\phi},\phi]$ in powers of the conjugate source fields

$$\Gamma^\Lambda[\bar{\phi},\phi] = \sum_{n=0}^{\infty}\frac{(-1)^n}{(n!)^2}\sum_{\substack{x_1',\dots,x_n' \\ x_1,\dots,x_n}}\Gamma_n^\Lambda(x_1',\dots,x_n'|x_1,\dots,x_n)\bar{\phi}_{x_1'}\dots\bar{\phi}_{x_n'}\phi_{x_n}\dots\phi_{x_1}, \tag{2.17}$$

in order to obtain flow equations for the Taylor coefficients of the effective action (see Fig. 2.1). Limiting ourselves to terms of first and second order in the fields, we arrive at the self-energy flow

$$\frac{d}{d\Lambda}\Sigma^\Lambda(x_1'|x_1) = -[\Gamma^\Lambda \circ S^\Lambda]_\Sigma \equiv -\sum_{x_2',x_2}\Gamma^\Lambda(x_1',x_2'|x_1,x_2)S^\Lambda(x_2|x_2'). \tag{2.18}$$

Here, $S^\Lambda \equiv G^\Lambda Q^\Lambda G^\Lambda = -\frac{d}{d\Lambda} G^\Lambda|_{\Sigma^\Lambda}$[2] denotes the single-scale propagator. The corresponding flow equation for the two-particle vertex reads

$$\begin{aligned}\frac{d}{d\Lambda}\Gamma^\Lambda(x_1', x_2'|x_1, x_2) = &\sum_{x_3', x_3} \zeta^\Lambda(x_1', x_2', x_3'|x_1, x_2, x_3) S^\Lambda(x_3|x_3') \\ &+ \sum_{x_3', x_4', x_3, x_4} [\Gamma^\Lambda(x_3', x_4'|x_1, x_2)\Gamma^\Lambda(x_1', x_2'|x_3, x_4) \\ &- \Gamma^\Lambda(x_1', x_4'|x_1, x_3)\Gamma^\Lambda(x_3', x_2'|x_4, x_2) - (x_3' \leftrightarrow x_4', x_3 \leftrightarrow x_4) \\ &+ \Gamma^\Lambda(x_2', x_4'|x_1, x_3)\Gamma^\Lambda(x_3', x_1'|x_4, x_2) + (x_3' \leftrightarrow x_4', x_3 \leftrightarrow x_4)] \\ &\times G^\Lambda(x_3|x_3') S^\Lambda(x_4|x_4') \,, \end{aligned} \tag{2.19}$$

where we employed the abbreviations

$$\begin{aligned}\Gamma^\Lambda(x_1', x_2'|x_1, x_2) &\equiv \Gamma_2^\Lambda(x_1', x_2'|x_1, x_2) \\ \zeta^\Lambda(x_1', x_2', x_3'|x_1, x_2, x_3) &\equiv \Gamma_3^\Lambda(x_1', x_2', x_3'|x_1, x_2, x_3) \,. \end{aligned} \tag{2.20}$$

For $\Lambda \to \infty$, the effective action reduces to the *bare* many-body interactions [15], which constitute the initial condition for the RG flow. Here, we have focused on two-particle interactions and as such only Γ survives in the UV limit

$$\Gamma^{\Lambda\to\infty}(x_1', x_2'|x_1, x_2) = \Gamma_0(x_1', x_2'|x_1, x_2) = V_{x_1' x_2'|x_1 x_2} \,. \tag{2.21}$$

To simplify the following discussions, contributions to $\frac{d}{d\Lambda}\Gamma^\Lambda$ are grouped into three channels: the particle-particle (s) channel, the direct particle-hole (t) channel and the crossed particle-hole (u) channel, corresponding to the first/second/third diagram depicted in Fig. 2.2, respectively. A diagram is referred to as two-particle reducible (2PR) in the s channel if it can be decomposed by cutting two parallel propagator lines. Diagrams which can be split up by cutting two antiparallel lines, on the other hand, are dubbed particle-hole reducible and therefore belong either to the t or u channel, depending on whether the disconnected parts carry external indices $(x_1', x_1)/(x_2', x_2)$ or $(x_2', x_1)/(x_1', x_2)$. Note that two-particle diagrams are either $s/t/u$-reducible or fully two-particle irreducible (2PI). With each channel c, we associate a bubble function $B_c = [\Gamma \circ (G \times G') \circ \Gamma']_c$ defined for generic two-particle vertices Γ, Γ' and propagators G, G', namely

$$\begin{aligned} B_s(x_1', x_2'|x_1, x_2) &\equiv -\frac{1}{2} \sum_{x_3', x_4', x_3, x_4} \Gamma(x_3', x_4'|x_1, x_2) G(x_3|x_3') G'(x_4|x_4') \Gamma'(x_1', x_2'|x_3, x_4) \\ B_t(x_1', x_2'|x_1, x_2) &\equiv + \sum_{x_3', x_4', x_3, x_4} \Gamma(x_1', x_4'|x_1, x_3) G(x_3|x_3') G'(x_4|x_4') \Gamma'(x_3', x_2'|x_4, x_2) \\ B_u(x_1', x_2'|x_1, x_2) &\equiv - \sum_{x_3', x_4', x_3, x_4} \Gamma(x_2', x_4'|x_1, x_3) G(x_3|x_3') G'(x_4|x_4') \Gamma'(x_3', x_1'|x_4, x_2) \,. \end{aligned} \tag{2.22}$$

Hence, the flow of the two-particle vertex can be compactly written as

$$\frac{d}{d\Lambda}\Gamma^\Lambda(x_1', x_2'|x_1, x_2) = \sum_{x_3', x_3} \zeta^\Lambda(x_1', x_2', x_3'|x_1, x_2, x_3) S^\Lambda(x_3|x_3') + \sum_c \tilde{B}_c^\Lambda(x_1', x_2'|x_1, x_2) \,, \tag{2.23}$$

with $\tilde{B}_c^\Lambda = [\Gamma^\Lambda \circ \frac{d}{d\Lambda}(G^\Lambda \times G^\Lambda)\big|_{\Sigma^\Lambda} \circ \Gamma^\Lambda]_c$. Note that the particle-hole bubbles fulfill

$$\begin{aligned} B_t(x_1', x_2'|x_1, x_2) &= -B_u(x_2', x_1'|x_1, x_2) = -B_u(x_1', x_2'|x_2, x_1) \\ B_u(x_1', x_2'|x_1, x_2) &= -B_t(x_2', x_1'|x_1, x_2) \ = -B_t(x_1', x_2'|x_2, x_1) \,, \end{aligned} \tag{2.24}$$

which follows from antisymmetry of the two-particle vertex under commutations of incoming or outgoing legs (crossing symmetry).

The biggest obstacle in solving the flow equations is the appearance of the three-particle vertex ζ in Eq. (2.19). Generally speaking, the flow for any 1PI vertex Γ_n depends on all Γ_m with $m \leq n+1$, such that a closed set of fRG equations necessitates a truncation. In the next section, we discuss three different truncation schemes of increasing diagrammatic complexity and how they can be derived from the parquet formalism.

[2] $\frac{d}{d\Lambda} G^\Lambda|_{\Sigma^\Lambda}$ is a shorthand notation for $\frac{d}{d\Lambda} G^\Lambda|_{\Sigma^\Lambda = \text{const.}}$.

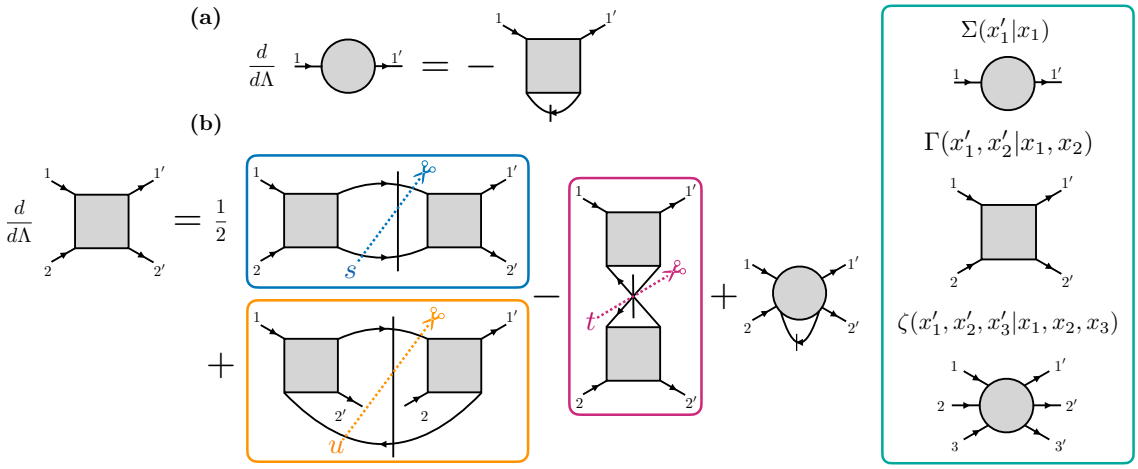

Figure 2.2: fRG equations for the self-energy (a) and two-particle vertex (b). The slashed line in the Σ-flow denotes a single-scale propagator S^Λ, while pairs of slashed lines correspond to cutoff-derivatives of the form $\frac{d}{d\Lambda}(G^\Lambda \times G^\Lambda)|_{\Sigma^\Lambda}$ (see text). The first three diagrams appearing in the Γ-flow differ in their two-particle reducibility: they can either be split into disconnected parts by cutting parallel (for the s channel) or antiparallel lines (for the t and u channel). The three-particle vertex ζ cannot be computed exactly and in general requires some approximation. Note that we have exchanged the outgoing lines for both two-particle vertices in the u channel compared to Eq. (2.19).

2.3 Systematic truncation via parquet approximation

In the last section, we derived flow equations for the self-energy and two-particle vertex, concluding that some approximation for the three-particle vertex is vital for closing the infinite hierarchy of fRG equations. Here, we switch gears and tackle the problem of computing fermionic vertices in the parquet formalism [29], which provides a different, yet concomitant perspective on our previous considerations. In doing so, we refrain from deriving the parquet equations explicitly, referring the reader to the excellent discussion given in Ref. [30] instead.

Within the parquet formalism, the two-particle vertex is decomposed into two distinct classes of diagrams, those which are 2PI and those reducible in one of the three channels introduced in Sec. 2.2. Schematically, we may thus write

$$\Gamma = I_{\mathrm{2PI}} + \gamma_s + \gamma_t + \gamma_u \,, \tag{2.25}$$

or, alternatively,

$$\Gamma = I_c + \gamma_c \,, \tag{2.26}$$

where $I_c = I_{\mathrm{2PI}} + \sum_{\bar{c}} \gamma_{\bar{c}}$[3] denotes diagrams irreducible in channel c. For each channel, one formulates a self-consistent Bethe-Salpeter equation (BSE)

$$\gamma_c = [I_c \circ (G \times G) \circ \Gamma]_c = [\Gamma \circ (G \times G) \circ I_c]_c \,, \tag{2.27}$$

which requires full propagators G as input [28, 29]. To dress them with self-energies, one determines Σ likewise self-consistently via the Schwinger-Dyson equation (SDE), which, using the compact notation introduced in the previous section, reads

$$\Sigma = [\Gamma_0 \circ G]_\Sigma + [[\Gamma_0 \circ (G \times G) \circ \Gamma]_s \circ G]_\Sigma = [\Gamma_0 \circ G]_\Sigma + \frac{1}{2}\,[[\Gamma_0 \circ (G \times G) \circ \Gamma]_u \circ G]_\Sigma \,. \tag{2.28}$$

While solving the parquet equations for an action as in Eq. (2.3) amounts to finding an exact solution for effective interactions up to the two-particle level [29, 30], one needs to determine I_{2PI} before all other vertices follow self-consistently from the SDE and BSEs. Away from weak-coupling, however, this becomes a formidable challenge, since more complicated diagrams start to contribute. Henceforth, we work in the famous parquet approximation (PA) [29], which replaces the fully irreducible vertex by its first-order contribution $I_{\mathrm{2PI}} = \Gamma_0$ (see Fig. 2.3). Although the PA corresponds to the most

[3] With $\bar{c}$ we refer to all $c' \neq c$.

simple approximation for I_{2PI}, it retains a number of useful properties by (a) summing up the leading, logarithmically divergent diagrams from perturbation theory [29], (b) fulfilling the Mermin-Wagner theorem [31], (c) presenting a conserving approximation on the one-particle level [32], and (d) incorporating important diagrammatic identities [33].

In the following, we connect to our discussion of the fRG approach in Sec. 2.2 by using the parquet approximation as an alternative starting point to derive flow equations for the self-energy and two-particle vertex. Our motivation for doing so is twofold. On the one hand side, this allows us to replace the set of algebraic parquet equations by ordinary differential equations, for which efficient numerical solvers are readily available. On the other hand, different truncation schemes for approximating the three-particle vertex in fRG can be developed in a systematic manner.

We start by equipping the bare propagator with an infrared cutoff Λ, i.e. $G_0 \to G_0^\Lambda$. Consequently, Σ and Γ acquire a scale dependence through the SDE and BSEs, if we require the parquet equations to hold at any value of Λ for a given I_{2PI} [32]. Differentiating the c-channel with respect to the cutoff, we therefore arrive at the flowing BSE

$$\frac{d}{d\Lambda}\gamma_c = \left[\frac{d}{d\Lambda}I_c \circ (G\times G)\circ\Gamma\right]_c + \left[I_c \circ \frac{d}{d\Lambda}(G\times G)\circ\Gamma\right]_c + \left[I_c\circ(G\times G)\circ\frac{d}{d\Lambda}\Gamma\right]_c . \tag{2.29}$$

Note that we refrain from writing out Λ-superscripts for brevity, since all object are implicitly cutoff dependent. Using $\Gamma = I_c + \gamma_c$, the right hand side can be written as

$$\begin{aligned}\frac{d}{d\Lambda}\gamma_c = &\left[\Gamma\circ\frac{d}{d\Lambda}(G\times G)\circ\Gamma\right]_c \\ &+ \left[\frac{d}{d\Lambda}I_c\circ(G\times G)\circ\Gamma\right]_c + \left[\Gamma\circ(G\times G)\circ\frac{d}{d\Lambda}I_c\right]_c \\ &+ \left[\Gamma\circ(G\times G)\circ\frac{d}{d\Lambda}\gamma_c\right]_c - \left[\gamma_c\circ\frac{d}{d\Lambda}(G\times G)\circ\Gamma\right]_c - \left[\gamma_c\circ(G\times G)\circ\frac{d}{d\Lambda}\Gamma\right]_c .\end{aligned} \tag{2.30}$$

Finally, plugging [Eqs. (2.27) & (2.29)] into Eq. (2.30) yields

$$\begin{aligned}\frac{d}{d\Lambda}\gamma_c = &\left[\Gamma\circ\frac{d}{d\Lambda}(G\times G)\circ\Gamma\right]_c \\ &+ \left[\frac{d}{d\Lambda}I_c\circ(G\times G)\circ\Gamma\right]_c + \left[\Gamma\circ(G\times G)\circ\frac{d}{d\Lambda}I_c\right]_c \\ &+ \left[\Gamma\circ(G\times G)\circ\left[\frac{d}{d\Lambda}I_c\circ(G\times G)\circ\Gamma\right]_c\right]_c ,\end{aligned} \tag{2.31}$$

where we have ordered the contributions to the flow of γ_c according to the position of the cutoff-derivative in their respective bubble function. The first line in Eq. (2.31), which we dub one-loop part $\dot\gamma_c^{(1\ell)}$, resembles $\tilde B_c$, except that single-scale propagators are substituted by full Λ-derivatives of G. The three leftover terms are referred to as left, right and central part and denoted by $\dot\gamma_c^L, \dot\gamma_c^R$ and $\dot\gamma_c^C$, respectively. In consequence, we can recast Eq. (2.31) in the compact form

$$\frac{d}{d\Lambda}\gamma_c = \dot\gamma_c^{(1\ell)} + \dot\gamma_c^L + \dot\gamma_c^C + \dot\gamma_c^R , \tag{2.32}$$

from which the flow of the full two-particle vertex follows as $\frac{d}{d\Lambda}\Gamma = \sum_c \frac{d}{d\Lambda}\gamma_c$. Remarkably, the inner bubble of the central part can be substituted for the right vertex object (as in [Eq. (2.31)]) or, alternatively, for the left one. This can be seen, for example, by writing out the bubble functions explicitly and comparing the resulting expressions.

Although conceptually simple, deriving a flow equation for the self-energy from the SDE requires extensive algebraic modifications to rephrase all terms by known objects. Hence, we content ourselves with stating the final result

$$\begin{aligned}\frac{d}{d\Lambda}\Sigma &= -\left[\Gamma\circ S\right]_\Sigma + \dot\Sigma_1 + \dot\Sigma_2 \\ \dot\Sigma_1 &= \left[\dot\gamma_t^C\circ G\right]_\Sigma \\ \dot\Sigma_2 &= \left[\Gamma\circ(G\times\dot\Sigma_1\times G)\right]_\Sigma ,\end{aligned} \tag{2.33}$$

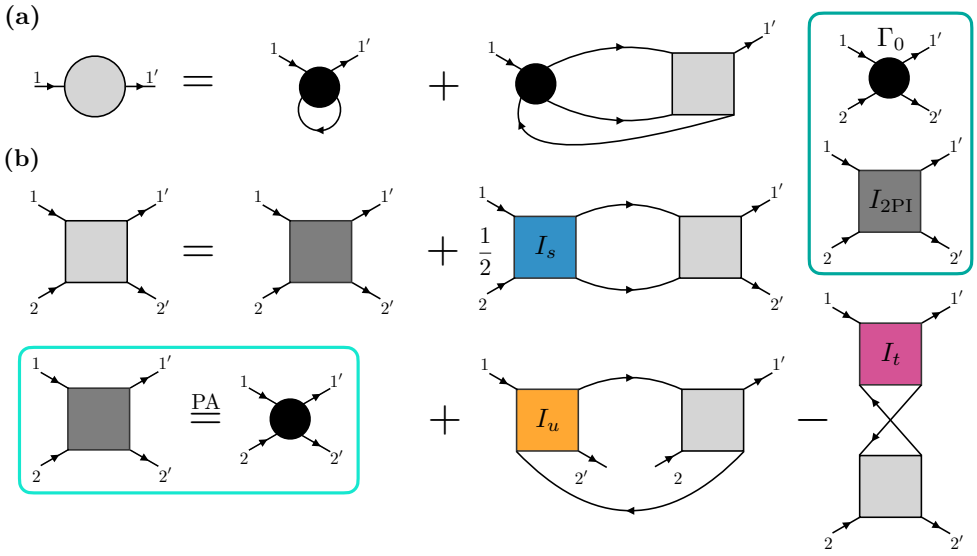

Figure 2.3: Diagrammatic representation of the parquet equations. (a) The self-energy is computed from the Schwinger-Dyson equation, such that the one and two-particle level are linked self-consistently. **(b)** Contributions to the two-particle vertex are segregated into a two-particle irreducible part $I_{2\mathrm{PI}}$ and three 2PR functions γ_c, each of which is determined by a Bethe-Salpeter equation. In the parquet approximation (cyan box), $I_{2\mathrm{PI}}$ is approximated by its lowest-order contribution Γ_0.

and refer the reader to Ref. [32] for further details. Note that the first contribution to the Σ-flow in the parquet approximation precisely coincides with the respective fRG flow derived in Sec. 2.2, while the other terms correspond to higher-order corrections.

Taken together, these equations track the evolution of the self-energy and reducible vertices along a self-consistent flow trajectory and their solution in the limit $\Lambda \to 0$ is equivalent to solving the parquet approximation. Nonetheless, the flowing SDE and BSEs resemble algebraic differential equations, which are generally hard to solve. For this reason, we proceed by approximating them via ordinary differential equations corresponding to resummation schemes of increasing diagrammatic complexity. This allows us to establish a stringent connection between common fRG truncations and simplified versions of the flowing PA.

2.3.1 Level-2 truncation

The simplest approximation for the flowing PA can be motivated from a perturbative point of view. To begin with, let us consider the flow of reducible vertices in Eq. (2.32), in which we substitute full vertices Γ by their lowest-order contribution Γ_0. It immediately follows that the one-loop contribution $\dot{\gamma}_c^{(1\ell)}$ is at least second order in Γ_0, while the left and right parts are $\mathcal{O}\left(\Gamma_0^3\right)$. Finally, contributions to the central part start at fourth power in Γ_0. Assuming the bare two-particle interactions to be weak, it thus makes sense to maintain only the leading term, given by $\dot{\gamma}_c^{(1\ell)}$, and discard the rest. Similarly, one finds that the leading contribution to the self-energy flow is given by the single-scale loop, whereas $\dot{\Sigma}_1$ and $\dot{\Sigma}_2$ are $\mathcal{O}\left(\Gamma_0^4\right)$ and $\mathcal{O}\left(\Gamma_0^5\right)$, respectively.

The simplified flow equations for the self-energy and reducible vertices thus read

$$\begin{aligned} \frac{d}{d\Lambda}\Sigma &= -[\Gamma \circ S]_\Sigma \\ \frac{d}{d\Lambda}\gamma_c &= \left[\Gamma \circ \frac{d}{d\Lambda}(G \times G) \circ \Gamma\right]_c . \end{aligned} \tag{2.34}$$

These particular equations, which will be discussed in greater detail in the next section, are known as Katanin flow equations in the fRG context [26]. Note that so far, the γ_c-flow implicitly depends on the flow of the self-energy due to the full Λ-derivative of G which appears in the bubble function. Therefore, it silently incorporates additional third order contributions. More explicitly, the cutoff-derivative of the (matrix valued) dressed propagator reads

$$\frac{d}{d\Lambda}G = \frac{d}{d\Lambda}\left(G_0^{-1} - \Sigma\right)^{-1} = -G\left[\frac{d}{d\Lambda}\left(G_0^{-1} - \Sigma\right)\right]G = -S + G\left(\frac{d}{d\Lambda}\Sigma\right)G\,. \tag{2.35}$$

Consequently, the flow of the vertices can be split into two parts

$$\frac{d}{d\Lambda}\gamma_c = -\left[\Gamma \circ (S \times G + G \times S) \circ \Gamma\right]_c + \left[\Gamma \circ \left(G\left(\frac{d}{d\Lambda}\Sigma\right) G \times G + G \times G\left(\frac{d}{d\Lambda}\Sigma\right) G\right) \circ \Gamma\right]_c , \quad (2.36)$$

where the second term summarizes precisely these higher-order terms. In order to eliminate the self-energy derivative from the vertex flows and thereby assemble flow equations which only contain the leading terms in the bare coupling, we simply drop the second term from Eq. (2.36), which yields

$$\begin{aligned} \frac{d}{d\Lambda}\Sigma &= -[\Gamma \circ S]_\Sigma \\ \frac{d}{d\Lambda}\gamma_c &= -\left[\Gamma \circ (S \times G + G \times S) \circ \Gamma\right]_c . \end{aligned} \quad (2.37)$$

Remarkably, we may now establish a stringent connection between the leading-order PA flows in Eq. (2.37) and the fRG equations (2.18) and (2.23): the former are recovered if one truncates all vertices beyond the two-particle level from the fRG hierarchy. Therefore, we call Eq. (2.37) level-2 (L2) truncation.

Importantly, our arguments to rationalize Eq. (2.37) were entirely based on the presence of a small bare interaction Γ_0. We are, however, interested in finding a suitable approximation to the PA, which is consistent for *all* RG scales Λ, not just in vicinity of the UV limit. To this end, we need to take the scaling behavior of different contributions to the effective action into account. On the crudest level of counting powers in Λ, one indeed finds that n-particle vertices with $n \geq 3$ are irrelevant in the RG sense [34], that is, they can be neglected at the infrared fixed point. For spatial dimensions $d > 1$ and curved Fermi surfaces, this holds true even if an improved power counting is applied [34]. Hence, the L2 equations should provide a *qualitatively* meaningful description of 1PI flows even upon lowering the cutoff.

The most noteworthy simplification over the full PA that we reached thus far, is the removal of differentiated vertices from the right hand side of the flow equations. In other words, we have successfully replaced the algebraic differential equations (2.32) and (2.33) by a set of ordinary differential equations, which can be solved numerically. Despite its simplicity (we merely distilled the leading-order terms in the bare interaction), this approximation already captures the non-trivial interplay of fluctuations in the 2PR channels and is therefore routinely employed to shed light on the pairing mechanism in prototypical model systems of high temperature superconductivity such as cuprates or iron-pnictides [11, 21, 35, 36]. More recently, it has also been applied to map out the phase diagrams of novel moiré heterostructures and eludicate the role of competing instabilities therein [37–40]. Note, however, that self-energy feedback is neglected in these works, i.e. the Σ-flow is set to zero and dressed propagators are replaced by bare ones. From a scaling point of view [15, 34], this approximation is inconsistent: the leading contribution $[\Gamma \circ S]_\Sigma$ to the self-energy flow is non-negligible on the bare level and Σ has marginal dependencies on Matsubara frequencies and momenta orthogonal to the Fermi surface. Yet, the inclusion of self-energy effects is in general quite complicated, which motivates their neglect for reasons of numerical simplicity if not for mathematical rigour.

2.3.2 Katanin's self-energy corrections

In hindsight of the simplified flow equations obtained in the previous section, we may ask whether there is any need to further improve them. After all, their validity could be justified on the bare level and more importantly even at the IR fixed point. One of the reasons to do so, is to remedy deficiencies related to the fulfillment of conservation laws. Recall that a solution of the full PA, which we would obtain if we could solve [Eqs. (2.32) & (2.33)] in the infrared limit $\Lambda \to 0$, is conserving on the one-particle level and thus fulfills certain Ward identities. In the derivation of Eq. (2.37), we have, however, discarded subclasses of parquet diagrams, which spoils the exact fulfillment of said conservation laws.

To lower the systematic error induced by the L2 truncation, the Katanin substitution

$$S \to -\frac{d}{d\Lambda}G \quad (2.38)$$

was proposed in Ref. [26]. It reinstantiates the full Λ-derivative of the propagator and allows for feedback of the self-energy flow into 2PR vertices (see [Fig. 2.4(a)]). One thus incorporates terms of the form indicated in Eq. (2.36) from the three-particle vertex. Notably, ladder summations in

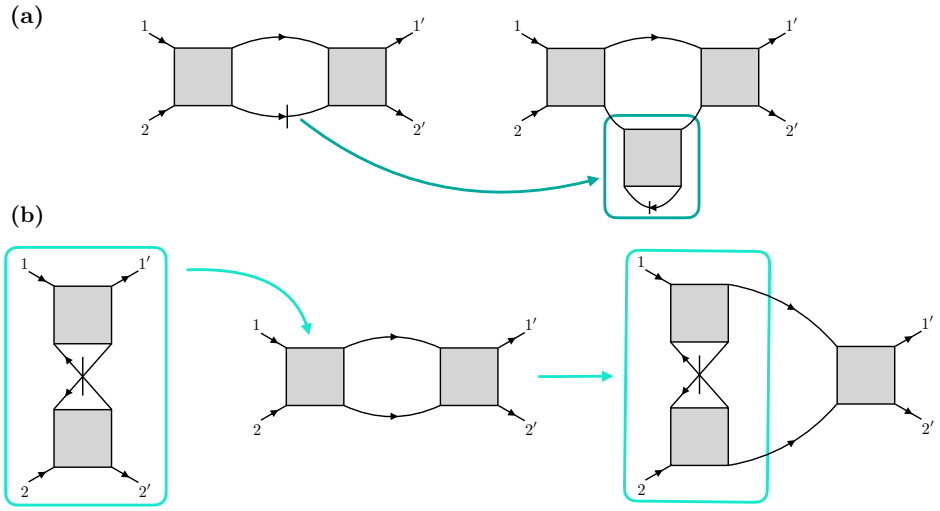

Figure 2.4: Katanin substitution and exemplary 2ℓ diagrams. (a) The Katanin substitution replaces single-scale propagators in the L2 flow equations by total Λ-derivatives of G. This way, the derivative of the self-energy (turquoise box) is fed back into the flow of the vertices, such that certain third order diagrams like the one on the right are generated. **(b)** Multiloop flows go beyond the Katanin substitution by incorporating parquet diagrams with overlapping loops. In 2ℓ flows, for example, one inserts 1ℓ diagrams into bubbles with complementary two-particle reducibility. Here, the 1ℓ flow in the t channel (cyan box) is plugged into the left vertex of the s bubble, giving rise to the $\dot{g}_s^{L(2\ell)}$ diagram on the right hand side.

the particle-hole channels with the Katanin substitution fulfill Ward identities exactly and recover standard mean-field results [26].

We have already seen that, from the perspective of the parquet approximation, the flow equations proposed by Katanin can be obtained by setting the left, right and central part in Eq. (2.32) to zero. Similar to the L2 equations, vertex derivatives are thus erased from the right hand side of the flow and we are again left with a coupled set of ordinary differential equations. The only exception is that the self-energy derivative is now required as additional input to compute the 2PR flows and therefore needs to be calculated beforehand.

2.3.3 Multiloop fRG

So far, we have discussed two approximations to the PA, which both discard differentiated vertices from the flow equations. The missing diagrams are, however, vital to achieve full consistency with the PA and instill confidence in the fulfillment of conservation laws. Yet, their appearance poses a numerical challenge, as the full set of flowing SDE and BSEs is algebraic, not ordinary. Fortunately, one can reconstruct the left, right and central part (and as such also the corrections to the self-energy) in an iterative manner, which results in the multiloop fRG (mfRG) scheme pioneered by Kugler and von Delft [28, 32].

The central idea to derive the multiloop flow equations has already been discussed: it is precisely the Γ power counting which we used to motivate the L2 and Katanin flow equations, that is, we start from the lowest-order contributions and iteratively generate higher-order diagrams. We start by considering the 1ℓ flows

$$\begin{aligned}\frac{d}{d\Lambda}\Sigma &\overset{(1\ell)}{=} -[\Gamma \circ S]_\Sigma \\ \frac{d}{d\Lambda}\gamma_c &\overset{(1\ell)}{=} \left[\Gamma \circ \frac{d}{d\Lambda}(G\times G)\circ\Gamma\right]_c .\end{aligned} \tag{2.39}$$

from which one constructs the lowest-order contributions to the left and right part as

$$\begin{aligned}\dot{\gamma}_c^{L(2\ell)} &= \left[\dot{\gamma}_{\bar{c}}^{(1\ell)} \circ (G\times G)\circ\Gamma\right]_c \\ \dot{\gamma}_c^{R(2\ell)} &= \left[\Gamma \circ (G\times G)\circ\dot{\gamma}_{\bar{c}}^{(1\ell)}\right]_c .\end{aligned} \tag{2.40}$$

Hence, the *two-loop flow* [27] computes to

$$\frac{d}{d\Lambda}\gamma_c \overset{(2\ell)}{=} \dot{\gamma}_c^{(2\ell)} = \dot{\gamma}_c^{(1\ell)} + \dot{\gamma}_c^{L(2\ell)} + \dot{\gamma}_c^{R(2\ell)} \,. \tag{2.41}$$

At the three-loop level and beyond, consecutive loop orders are constructed in similar fashion. The multiloop $(m\ell)$ flow for the two-particle vertex with $m \geq 3$ reads

$$\frac{d}{d\Lambda}\gamma_c \overset{(m\ell)}{=} \dot{\gamma}_c^{(1\ell)} + \sum_{n=2}^{m} \dot{\gamma}_c^{L(n\ell)} + \sum_{n=3}^{m} \dot{\gamma}_c^{C(n\ell)} + \sum_{n=2}^{m} \dot{\gamma}_c^{R(n\ell)} \,, \tag{2.42}$$

with

$$\begin{aligned} \dot{\gamma}_c^{L(m\ell)} &= \left[\dot{\gamma}_{\bar{c}}^{([m-1]\ell)} \circ (G \times G) \circ \Gamma\right]_c \\ \dot{\gamma}_c^{C(m\ell)} &= \left[\Gamma \circ (G \times G) \circ \dot{\gamma}_c^{L([m-1]\ell)}\right]_c \\ \dot{\gamma}_c^{R(m\ell)} &= \left[\Gamma \circ (G \times G) \circ \dot{\gamma}_{\bar{c}}^{([m-1]\ell)}\right]_c \,. \end{aligned} \tag{2.43}$$

For $m \to \infty$, Eq. (2.42) incorporates all parquet diagrams, which can be computed with the same cost as the one-loop flow. Hence, the calculation of vertex corrections with overlapping loops scales only linear in ℓ and is therefore well-suited for numerical simulations [28].

Finally, we need to discuss how to reinstantiate self-energy corrections. Before we proceed, however, let us remind ourselves why these corrections are necessary. From the perspective of the PA, the terms $\dot{\Sigma}_{1(2)}$ naturally appeared when computing the cutoff-derivative of the Schwinger-Dyson equation. In the fomally exact fRG, on the other hand, $\frac{d}{d\Lambda}\Sigma$ is given solely by the single-scale loop. However, the flow equations are truncated and the vertex which enters the single-scale loop is therefore only determined approximately. Hence, the additional corrections ensure self-consistency between the one and two-particle level by virtue of the PA. The only input required to explicitly compute them are t-irreducible contributions to the central part

$$\dot{\gamma}_{\bar{t}}^{C} \overset{(m\ell)}{=} \sum_{n\geq 3}^{m} \dot{\gamma}_{\bar{t}}^{C(n\ell)} \,. \tag{2.44}$$

which are needed anyways to account for vertex corrections. On the other hand, $\dot{\gamma}_{\bar{t}}^{C}$ depends on $\frac{d}{d\Lambda}\Sigma$ via Katanin diagrams and restoring the self-energy corrections in full glory would therefore already require the exact solution. This means that a *one-shot* calculation of $\dot{\Sigma}_{1(2)}$ from $\dot{\gamma}_{\bar{t}}^{C}$ does not necessarily suffice to reach self-consistency and the refined self-energy should, in turn, be used to recompute vertex corrections until convergence is reached. The importance of such self-energy cycles can, for example, be seen in fRG calculations for the two-dimensional Hubbard model, where they are essential to achieve quantitative agreement with other numerical approaches [41].

2.4 Final remarks

In this chapter, we have introduced the fRG approach to fermionic many-body systems and discussed three different truncation schemes to close the hierarch of flow equations: level-2 truncation, Katanin scheme and mfRG. The Katanin scheme extended the diagrams of the L2 truncation by replacing single-scale propagators S with full cutoff-derivatives $\frac{d}{d\Lambda}G$. This way, certain contributions from the three-particle vertex could be included. The multiloop fRG developed this approach even further, adding parquet diagrams with overlapping loops to the flow of 2PR vertices and accounting for additional self-energy diagrams. Both, vertex and self-energy corrections are essential to establish consistency with the parquet approximation, from which these different truncation schemes could be motivated, and guarantee the fulfillment of conservation laws on the one-particle level. Here, we add some further comments on different aspects of (multiloop) fRG.

Hitherto, the only requirements for the regularization $G_0 \to G_0^\Lambda$ were that $G_0^{\Lambda\to\infty} = 0$ and $G_0^{\Lambda\to 0} = G_0$, but otherwise Λ could have been implemented arbitrarily. For this reason, however, fRG results obtained within the L2 or Katanin scheme depend on the actual choice of regulator, even if it acts on the same physical quantity, such as momentum [11] or frequency [24, 42]. The quantitative accuracy of such a renormalization group flow is therefore difficult to assess. Remarkably, regulator independence is

restored in mfRG calculations, since the couplings flow towards a solution of the parquet approximation. The latter, as a general many-body relation, has cutoff independent solutions. Numerical evidence for this property of mfRG is, for example, provided in Ref. [43].

Although the multiloop flow has a number of beneficial properties, namely those incorporated by the PA, it cannot go beyond the parquet approximation. Outside the weak-coupling regime, the neglect of diagrams beyond the bare vertex Γ_0 could therefore be insufficient to characterize two-particle irreducible contributions to the vertex. Any deficiency embodied by the PA would thus carry over to mfRG and render its outcome self-consistent, but only qualitative. One can come up with different strategies to extend the multiloop flow even beyond the PA, some of which are reported in Ref. [28].

Up to now, we have not addressed the role of symmetries, which play a vital role in reducing the numerical effort for computing 1PI functions. Usually, they are incorporated via efficient vertex parametrizations, which reduce, for example, the number of flow equations in the fRG formalism. These symmetries are model specific after all, and their discussion has therefore been postponed to later sections of this thesis.

3 Weak-coupling fRG for itinerant fermions

In this chapter, we consider the application of the functional renormalization group framework presented in Ch. 2 to itinerant electron systems. Our focus lies on spin-polarized or spinless fermions, throughout. This allows us, on the one hand, to study toy models for the single band physics in so-called *moiré* systems, specifically transition metal dichalcogenides (TMDs). On the other hand, the capabilities of the fRG approach can be presented without complicating the matter by additional spin or orbital degrees of freedom. Furthermore, we exclusively consider level-2 truncated flow equations, which incorporate the lowest-order contributions to the parquet approximation. This is justified insofar that we assume only moderately strong interactions (see Sec. 2.3.1). Self-energy feedback and frequency dependencies of the two-particle vertex are neglected. Yet, monitoring the full momentum dependence of the 2PR channels remains numerically challenging.

Nonetheless, some implementations [37, 38, 44] successfully managed to integrate the vertex flow[1] on a dense grid with up to 24×24 momenta in the first Brillouin zone by exploiting the sheer power of large scale computing architectures. While this approach offers a lot of flexibility and allows to tackle, for example, few-band models with ease, its scalability is severely limited by the cubic growth of the required memory resources with the number of momenta. Furthermore, subtle incommensurate effects, which require even more fine grained grids, are difficult to capture. This circumstance calls for more efficient ways to store the vertex.

Traditionally, N-patch schemes[2] have been employed to study competing orders in two-dimensional Hubbard models [21, 35, 36, 40]. Within this approach, scattering processes perpendicular to the Fermi surface (FS) are not accounted for due to their negative scaling dimension [15] and the vertex is consequently approximated by its values along the FS. For illustrative purposes and due to its comparably simple numerical implementation, N-patch fRG is our method of choice in the following. There are, however, more advanced techniques, such as truncated-unity (TU) approximations [45, 46], which deserve to be mentioned. Within TU schemes, computing times grow only linear in the number of momenta, such that further methodological improvements like those presented in Refs. [41, 47, 48] can be considered.

This chapter is structured as follows. First, some basic aspects of superconductivity, such as its mean-field description or its classification in term of irreducible representations of the lattice point group are recapped. We proceed by presenting our numerical implementation of N-patch fRG and the analysis of results obtained therein. Lastly, exemplary results for spinless fermion models on the triangular lattice are discussed.

3.1 A prelude on superconductivity

More than a century after its discovery by Kamerlingh Onnes in 1911 [49], the phenomenon of superconductivity - vanishing electral resistivity and the sudden expulsion of magnetic fields at low temperatures known as Meissner-Ochsenfeld effect [50] - has remained one of the most intensely studied subjects in condensed matter physics. Its first theoretical characterization was due to Bardeen, Cooper and Schrieffer (BCS) in 1957 [6]. Their celebrated BCS theory attributes superconductivity to an attractive electron-electron interaction mediated by phonon modes which cause them to bind as *Cooper pairs*. In their most symmetric form, the s-wave state, these pairs form a spin singlet without relative angular momentum. Such superconductors are nowadays dubbed *conventional*.

Unconventional superconductors, in contrast, exhibit different kinds of pairing mechanisms which disfavor the conventional s-wave state. After the discovery of superfluidity in liquid ^{3}He, highly sought-after unconventional pairing in a solid state platform was reported in multiple heavy fermion materials, although the nature of the superconducting state in, for example, $CeCu_2Si_2$ is still under debate [51]. In 1987, Bednorz and Müller received the noble prize for uncovering superconductivity in $LaBaCu_4$ with a transition temperature $T_c \approx 35K$, higher than the critical temperatures measured so far. Materials with similar or even higher T_c were consequently dubbed *high-T_c* superconductors. Note that unconventional does not imply high-T_c. Strontium ruthenate (Sr_2RuO_4), for example, exhibits unconventional pairing analogous to ^{3}He but only at temperatures as low as $0.93K$ [52].

[1] Since $\Sigma = 0$, we occasionally refer to the two-particle vertex simply as *the vertex*.

[2] A review on N-patch fRG can be found in Ref. [11].

Recently, superconductivity with a transition temperature $T_c \approx 1.7K$ has also been reported in twisted bilayer graphene (tBG) [53]. The latter, as its name suggests, consists of two stacked graphene sheets which are rotated with respect to each other, giving rise to nearly flat bands for certain *magic-angles* [54]. In consequence, the strength of electronic interactions relative to the bandwidth is strongly enhanced, resulting in a plethora of fascinating low-temperature phases [55]. Since then, many more twisted van der Waals heterostructures have received prominent attention in the search for exotic states of matter. The most remarkable property of such materials is the degree of experimental tunability they offer. The ability to change, for example, the carrier concentration by electrostatic gating has therefore assigned moiré materials a prominent role in the search for robust condensed matter quantum simulators [56].

In addition to moiré heterostructures, kagome metals such as CsV_3Sb_5 [57] have been put forward as another exciting platform for realizing novel superconducting states. Their special appeal arises from the intricate three-orbital geometry of the kagome network [58], which, already by itself, gives rise to an enriched single-particle dispersion featuring flat bands, Dirac cones and Van Hove points. The discovery of all these new platforms for unconventional superconductivity brings tremendous progress to the field. Further, it lays the foundation for new theoretical concepts and numerical tools for deciphering the nature of the pairing mechanism in condensed matter systems.

3.1.1 Mean-field theory

The BCS Hamiltonian for spin-polarized fermions reads

$$\mathcal{H} = \sum_{\boldsymbol{k}} \xi(\boldsymbol{k}) c^\dagger_{\boldsymbol{k}} c_{\boldsymbol{k}} + \frac{1}{2N} \sum_{\boldsymbol{k},\boldsymbol{k}'} V_{\mathrm{BCS}}(\boldsymbol{k},\boldsymbol{k}') c^\dagger_{\boldsymbol{k}} c^\dagger_{-\boldsymbol{k}} c_{-\boldsymbol{k}'} c_{\boldsymbol{k}'} \,, \tag{3.1}$$

where $\xi(\boldsymbol{k}) = \epsilon(\boldsymbol{k}) - \mu$ is the single-particle dispersion relative to the chemical potential μ and $V_{\mathrm{BCS}}(\boldsymbol{k},\boldsymbol{k}') = V_{\boldsymbol{k}-\boldsymbol{k}|\boldsymbol{k}'-\boldsymbol{k}'}$ denotes the hermitian pairing potential[3]. We assume that V_{BCS} is attractive in a thin shell around the Fermi level $\xi(\boldsymbol{k}) = 0$ without specifying its origin for now. To simplify the interaction, we resort to the mean-field decouplings

$$\begin{aligned} c^\dagger_{\boldsymbol{k}} c^\dagger_{-\boldsymbol{k}} &= \langle c^\dagger_{\boldsymbol{k}} c^\dagger_{-\boldsymbol{k}} \rangle + \left(c^\dagger_{\boldsymbol{k}} c^\dagger_{-\boldsymbol{k}} - \langle c^\dagger_{\boldsymbol{k}} c^\dagger_{-\boldsymbol{k}} \rangle \right) \\ c_{-\boldsymbol{k}'} c_{\boldsymbol{k}'} &= \langle c_{-\boldsymbol{k}'} c_{\boldsymbol{k}'} \rangle + \left(c_{-\boldsymbol{k}'} c_{\boldsymbol{k}'} - \langle c_{-\boldsymbol{k}'} c_{\boldsymbol{k}'} \rangle \right) \,, \end{aligned} \tag{3.2}$$

and discard terms of second order in the fluctuations (the terms in rounded brackets). Up to a constant, the Hamiltonian now reads

$$\mathcal{H}_{\mathrm{MF}} = \sum_{\boldsymbol{k}} \xi(\boldsymbol{k}) c^\dagger_{\boldsymbol{k}} c_{\boldsymbol{k}} - \frac{1}{2} \sum_{\boldsymbol{k}} \left[\bar{\Delta}(\boldsymbol{k}) c_{-\boldsymbol{k}} c_{\boldsymbol{k}} + \Delta(\boldsymbol{k}) c^\dagger_{\boldsymbol{k}} c^\dagger_{-\boldsymbol{k}} \right] \,, \tag{3.3}$$

where we defined the pairing fields

$$\begin{aligned} \Delta(\boldsymbol{k}) &= -\frac{1}{N} \sum_{\boldsymbol{k}'} V_{\mathrm{BCS}}(\boldsymbol{k},\boldsymbol{k}') \langle c_{-\boldsymbol{k}'} c_{\boldsymbol{k}'} \rangle \\ \bar{\Delta}(\boldsymbol{k}) &= -\frac{1}{N} \sum_{\boldsymbol{k}'} V_{\mathrm{BCS}}(\boldsymbol{k}',\boldsymbol{k}) \langle c^\dagger_{\boldsymbol{k}'} c^\dagger_{-\boldsymbol{k}'} \rangle \,. \end{aligned} \tag{3.4}$$

Introducing the *spinor* $\boldsymbol{\Psi}_{\boldsymbol{k}} = (c_{\boldsymbol{k}}, c^\dagger_{-\boldsymbol{k}})^T$, $\mathcal{H}_{\mathrm{MF}}$ assumes the quadratic form

$$\mathcal{H}_{\mathrm{MF}} = \sum_{\boldsymbol{k}} \boldsymbol{\Psi}^\dagger_{\boldsymbol{k}} \boldsymbol{Q}(\boldsymbol{k}) \boldsymbol{\Psi}_{\boldsymbol{k}} \text{ with } \boldsymbol{Q}(\boldsymbol{k}) = \frac{1}{2} \begin{pmatrix} \xi(\boldsymbol{k}) & -\Delta(\boldsymbol{k}) \\ -\bar{\Delta}(\boldsymbol{k}) & -\xi(\boldsymbol{k}) \end{pmatrix} \,. \tag{3.5}$$

In order to solve the mean-field theory, the decoupled Hamiltonian needs to be diagonalized. To this end, one performs the Bogoliubov-Valatin transformation

$$\boldsymbol{\Phi}_{\boldsymbol{k}} = \begin{pmatrix} b_{\boldsymbol{k}} \\ b^\dagger_{-\boldsymbol{k}} \end{pmatrix} = \boldsymbol{U}(\boldsymbol{k}) \boldsymbol{\Psi}_{\boldsymbol{k}} \text{ with } \boldsymbol{U}(\boldsymbol{k}) = \begin{pmatrix} \bar{u}(\boldsymbol{k}) & -v(\boldsymbol{k}) \\ \bar{v}(\boldsymbol{k}) & u(\boldsymbol{k}) \end{pmatrix} \,, \tag{3.6}$$

[3] That is, it obeys $V_{\mathrm{BCS}}(\boldsymbol{k},\boldsymbol{k}') = \bar{V}_{\mathrm{BCS}}(\boldsymbol{k}',\boldsymbol{k})$, where the bar denotes complex conjugation.

and subsequently eliminates all non-diagonal terms, which results in the condition

$$2\xi(\boldsymbol{k})\bar{u}(\boldsymbol{k})v(\boldsymbol{k}) + \bar{\Delta}(\boldsymbol{k})[v(\boldsymbol{k})]^2 - \Delta(\boldsymbol{k})[\bar{u}(\boldsymbol{k})]^2 = 0\,. \tag{3.7}$$

In general, Δ, u and v are complex valued, such that we can express them via Euler's identity

$$\begin{aligned}\Delta(\boldsymbol{k}) &= |\Delta(\boldsymbol{k})|e^{i\alpha(\boldsymbol{k})}\\ u(\boldsymbol{k}) &= |u(\boldsymbol{k})|e^{i\beta(\boldsymbol{k})}\\ v(\boldsymbol{k}) &= |v(\boldsymbol{k})|e^{i\gamma(\boldsymbol{k})}\,.\end{aligned} \tag{3.8}$$

Plugging into Eq. (3.7), one possible choice that diagonalizes the mean-field Hamiltonian is

$$|u(\boldsymbol{k})|^2 - |v(\boldsymbol{k})|^2 = \frac{\xi(\boldsymbol{k})}{E(\boldsymbol{k})}\,, \tag{3.9}$$

for $\beta(\boldsymbol{k}) = 0$ and $\alpha(\boldsymbol{k}) = \gamma(\boldsymbol{k})$. Here, $E(\boldsymbol{k}) = \sqrt{[\xi(\boldsymbol{k})]^2 + |\Delta(\boldsymbol{k})|^2}$. Requiring that the Bogoliubov quasiparticles $b_{\boldsymbol{k}}^{(\dagger)}$ obey fermionic commutation relations[4], we obtain our central result

$$\mathcal{H}_{\mathrm{MF}} = \sum_{\boldsymbol{k}} E(\boldsymbol{k}) b_{\boldsymbol{k}}^\dagger b_{\boldsymbol{k}}\,. \tag{3.10}$$

Note that in order to derive Eq. (3.10), we assumed inversion symmetry, that is, $\xi(\boldsymbol{k}) = \xi(-\boldsymbol{k})$ and $|\Delta(\boldsymbol{k})| = |\Delta(-\boldsymbol{k})|$.

Remarkably, the quasiparticles $b_{\boldsymbol{k}}^{(\dagger)}$ have a largely gapped excitation spectrum with $|\Delta(\boldsymbol{k})|$ characterizing magnitude and symmetry of the gap[5]. Consequently, $\Delta(\boldsymbol{k})$ is dubbed *gap function*. The gap can be determined self-consistently by applying $[\boldsymbol{U}(\boldsymbol{k})]^{-1}$ to the pairing terms in Eqs. (3.4) and utilizing Fermi-Dirac statistics to compute the remaining quasiparticle expectation values. This procedure yields the self-consistent gap equation at temperature T

$$\Delta(\boldsymbol{k}) = -\frac{1}{N}\sum_{\boldsymbol{k}'} V_{\mathrm{BCS}}(\boldsymbol{k},\boldsymbol{k}')\frac{\Delta(\boldsymbol{k}')}{2E(\boldsymbol{k}')}\tanh\left(\frac{E(\boldsymbol{k}')}{2T}\right)\,. \tag{3.11}$$

Let us consider the form of this algebraic equation close to the critical temperature T_c, where the gap opens (closes). In that case, we may assume that $E(\boldsymbol{k}) \approx \xi(\boldsymbol{k})$ and, thus, contributions away from the Fermi level $\xi(\boldsymbol{k}) = 0$ are strongly suppressed[6]. The dominant terms in the momentum sum therefore cover only a thin energy shell $-\epsilon_c \leq \xi_{\boldsymbol{k}} \leq \epsilon_c \ll \epsilon_{\mathrm{FS}}$ around the Fermi surface and, consequently, we can approximate the right-hand side of the gap equation by

$$\Delta(\boldsymbol{k}) \approx -\frac{1}{N}\left[\int_{-\epsilon_c}^{\epsilon_c} d\xi\ \frac{1}{2\xi}\tanh\left(\frac{\xi}{2T_c}\right)\right]\sum_{\boldsymbol{k}'\in\mathrm{FS}} V_{\mathrm{BCS}}(\boldsymbol{k},\boldsymbol{k}')\Delta(\boldsymbol{k}')\,, \tag{3.12}$$

where the integral evaluates to

$$\int_{-\epsilon_c}^{\epsilon_c} d\xi\ \frac{1}{2\xi}\tanh\left(\frac{\xi}{2T_c}\right) \approx \ln\left(1.13\frac{\epsilon_c}{T_c}\right)\,. \tag{3.13}$$

The *linearized* gap equation (3.12) has the form of an eigenvalue problem. The eigenvalues of V_{BCS},

$$\lambda = -\frac{N}{\ln\left(1.13\frac{\epsilon_c}{T_c}\right)}\,, \tag{3.14}$$

characterize different mean-field critical temperatures $T_c = 1.13\epsilon_c e^{\frac{N}{\lambda}}$, respectively. The dominant pairing fields are thus obtained as the eigenvectors with the largest, negative λ [59].

[4] This implies that U is unitary.

[5] In general, $|\Delta(\boldsymbol{k})|$ vanishes only at special values of $\boldsymbol{k}$.

[6] This can be seen by expanding $\frac{1}{\xi}\tanh(\frac{\xi}{2T})$ around $\xi = 0$.

C_{6v}	E	C_2	$2C_3$	$2C_6$	$3\sigma_\nu$	$3\sigma_d$
$\mathcal{A}_1$	1	1	1	1	1	1
$\mathcal{A}_2$	1	1	1	1	-1	-1
$\mathcal{B}_1$	1	-1	1	-1	1	-1
$\mathcal{B}_2$	1	-1	1	-1	-1	1
$\mathcal{E}_1$	2	-2	-1	1	0	0
$\mathcal{E}_2$	2	2	-1	-1	0	0

Table 3.1: Character table for the point group C_{6v}. The columns denote the six different classes of the group: identity map, two-fold, three-fold and six-fold rotations as well as two kinds of reflections, respectively. The rows, on the other hand, denote the different irreps. Note that the characters of the identity map E, i.e. the first column of the table, characterize the dimensions of the different irreducible representations.

3.1.2 Classification via representation theory

In the last section, we derived an eigenvalue equation for the hermitian pairing potential $\boldsymbol{V}_{\mathrm{BCS}}$, whose eigenvectors with the largest negative eigenvalue, $\boldsymbol{\Delta}$, correspond to the superconducting gap functions with the highest critical temperature. Note that we have switched to a matrix-vector notation $(\boldsymbol{V}_{\mathrm{BCS}})_{\boldsymbol{k}\boldsymbol{k}'} \equiv V_{\mathrm{BCS}}(\boldsymbol{k},\boldsymbol{k}')$ and $\boldsymbol{\Delta}_{\boldsymbol{k}} \equiv \Delta(\boldsymbol{k})$, respectively. Now, unitary transformations $\boldsymbol{U}$ from the symmetry group G of the Hamiltonian should leave the pairing potential invariant, thus $\boldsymbol{U}^\dagger \boldsymbol{V}_{\mathrm{BCS}} \boldsymbol{U} = \boldsymbol{V}_{\mathrm{BCS}}$ for all $\boldsymbol{U} \in G$. Consequently, $\lambda(\boldsymbol{U}\boldsymbol{\Delta}) = \boldsymbol{V}_{\mathrm{BCS}}(\boldsymbol{U}\boldsymbol{\Delta})$ or in other words, the eigenspace $\mathrm{span}(\{\boldsymbol{\Delta}^i\}_\lambda)$ corresponding to the eigenvalue λ is also invariant under G. In that case, we can expand $\boldsymbol{U}\boldsymbol{\Delta}^i$ as a linear combination of the other eigenvectors as

$$\boldsymbol{U}\boldsymbol{\Delta}^i = \sum_{j=1}^{n} \mathcal{R}^G_{ij}(\boldsymbol{U})\boldsymbol{\Delta}^j \,, \tag{3.15}$$

that is, the gaps transform in an n-dimensional representation $\mathcal{R}^G$ of the symmetry group G, where $n = \dim(\{\boldsymbol{\Delta}^i\}_\lambda)$ is the dimension of the eigenspace. Conversely, it should be possible to represent to the gap by characteristic *basis functions* which likewise transform in this representation.

To formalize this discussion, let us recap some basic mathematical aspects of representation theory. We focus on concepts which are elementary for the renormalized mean-field analysis that is carried out on the basis of the fRG formalism presented in Ch. 2. For an in-depth presentation of these concepts, we refer the reader to Ref. [60]. To start with, recall that any group G can be separated into different classes of conjugate group elements. Two elements x and y are called conjugate, if there exists another element, say u, such that $y = u^{-1} \circ x \circ u$, where $\circ$ denotes the group operation. Computing all ensembles of conjugate elements, the classes of G, is surprisingly simple and can be done by brute force. One simply calculates $y = u^{-1} \circ x \circ u$ for all $u \in G$ and for a fixed $x \in G$ and thereby determines all conjugate elements y of x. Iterating this procedure over all x then allows one to sort conjugate elements into the respective class.

Secondly, recall that a representation $\mathcal{R}^G : G \to \mathrm{GL}(W)$ is a group homomorphism that maps the elements of G into the general linear group $\mathrm{GL}(W)$ of some vector space W. As such, the algebraic structure of the group operation is preserved, that is, $\mathcal{R}^G(x \circ y) = \mathcal{R}^G(x) \times \mathcal{R}^G(x)$ ($\times$ is the group operation in $\mathrm{GL}(W)$). W is dubbed representation space of $\mathcal{R}^G$ and $\dim(W)$ is called the dimension of the representation. For finite dimensional representations in particular, one can choose a basis in W and identify the images of the group elements $\mathcal{R}^G(x)$ with invertible matrices, such that $\times$ becomes the usual matrix product. Group representations are extremely useful for practical purposes, since the abstract elements of G can be identified with familiar algebraic objects (matrices). In other words, the representation of a group G basically defines its action on the vector space W. Our discussion from this point on always assumes finite dimensional representations. Moreover, we consider Hilbert spaces W and require that the matrices $\mathcal{R}^G(x)$ are unitary. $\mathcal{R}^G$ is thus called unitary representation.

A representation $\mathcal{R}^G$ of G is called irreducible, if it has no invariant subspaces $S \subset W$, that is $\mathcal{R}^G(x)s \in S$ for $s \in S$ and $x \in G$, except the zero element $\{0\}$ and W itself. If this is not the case, $\mathcal{R}^G$ is coined reducible. Every matrix in a unitary representation of a Hilbert space can be written as

a direct sum of the respective *irreps*[7]. Hence, the latter are sufficient to fully characterize possible representations of G. A powerful concept to determine irreducible representations or finding out whether a particular representation is reducible are the characters $\chi^G(x)$ of the group elements in a representation $\mathcal{R}^G$, which are defined as

$$\chi^G(x) = \mathrm{Tr}[\mathcal{R}^G(x)]\,. \tag{3.16}$$

The character of the identity element $e \in G$, for example, corresponds to the dimension of $\mathcal{R}^G$. In general, the characters of group elements in the same class are equal. Moreover, the number of classes in G corresponds to the number of its irreducible representations. For this reason, we may sort all characters in an $n_G \times n_G$ tableau, the character table of G, where n_G is the number of classes. The character table for the group C_{6v}, for example, is given in Tab. 3.1. Deciding, whether or not a representation $\mathcal{R}^G$ is irreducible thus boils down to computing its characters and comparing the result with the rows of the character table.

We can use the concepts outlined above to characterize superconducting gaps in terms of irreducible representations of the Hamiltonian's point group. From the action of unitary transformations on the eigenspaces of the gap equation (see [Eq. (3.15)]) it became apparent that the gaps transform in some representation of the symmetry group. In principle, that respective representation might be reducible or irreducible, in most cases, however, it is irreducible [59, 60]. We can therefore reconstruct the gaps in terms of basis functions or lattice harmonics of a suitable irrep. To accomplish this goal, we utilize the projection

$$\mathcal{P}(\mathcal{R}^G) = \sum_{x\in G} \bar{\chi}^G(x) x\,, \tag{3.17}$$

which singles out those contributions that transform in the irrep $\mathcal{R}^G$ [60]. Given some trial function $f(\boldsymbol{r}_i, \boldsymbol{r}_j)$ on lattice sites $\boldsymbol{r}_i$ and $\boldsymbol{r}_j$, we compute $\mathcal{P}(\mathcal{R}^G)f$ and transform to momentum space to allow for comparison with $\Delta(\boldsymbol{k})$. Consider, for example, $f(\boldsymbol{r}_i, \boldsymbol{r}_j) = \delta_{\boldsymbol{r}_i, \boldsymbol{r}_j = \boldsymbol{r}_i + \boldsymbol{a}_1}$, where $\boldsymbol{a}_1 = (1,0)^T$ is the nearest-neighbor bond of the triangular lattice with point group C_{6v}. Operating upon f with the projection operator for the $\mathcal{E}_1$ irrep yields

$$[\mathcal{P}(\mathcal{E}_1)f](\boldsymbol{r}_i, \boldsymbol{r}_j) = 2(\delta_{\boldsymbol{r}_i, \boldsymbol{r}_i+\boldsymbol{a}_1} - \delta_{\boldsymbol{r}_i, \boldsymbol{r}_i-\boldsymbol{a}_1}) + \delta_{\boldsymbol{r}_i, \boldsymbol{r}_i+\boldsymbol{a}_2} - \delta_{\boldsymbol{r}_i, \boldsymbol{r}_i-\boldsymbol{a}_2} - \delta_{\boldsymbol{r}_i, \boldsymbol{r}_i+\boldsymbol{a}_3} + \delta_{\boldsymbol{r}_i, \boldsymbol{r}_i-\boldsymbol{a}_3}\,, \tag{3.18}$$

with $\boldsymbol{a}_2 = \left(\frac{1}{2}, \frac{\sqrt{3}}{2}\right)^T$ and $\boldsymbol{a}_3 = \left(-\frac{1}{2}, \frac{\sqrt{3}}{2}\right)^T$. In momentum space, we therefore obtain

$$[\mathcal{P}(\mathcal{E}_1)f](\boldsymbol{k}, \boldsymbol{k'}) = i\delta_{\boldsymbol{k},\boldsymbol{k'}} \left[4\sin\left(\boldsymbol{k}_x\right) + 2\sin\left(\frac{\boldsymbol{k}_x}{2} + \frac{\sqrt{3}\boldsymbol{k}_y}{2}\right) - 2\sin\left(-\frac{\boldsymbol{k}_x}{2} + \frac{\sqrt{3}\boldsymbol{k}_y}{2}\right)\right]\,, \tag{3.19}$$

which can now be compared to the momentum dependence of the gap function. In similar fashion, basis functions for the other irreps and beyond the nearest-neighbor level can be computed. Note that $\mathcal{E}_1$ is two-dimensional, and as such, one needs at least two lattice harmonics to characterize functions transforming in $\mathcal{E}_1$ for each nearest-neighbor shell, as demonstrated in Fig. 3.1. To find an additional basis function, one can simply repeat the calculation above, but for a linearly independent bond.

3.1.3 Topological superconductivity

On the mean-field level (see Sec. 3.1.1), superconductors can be described in terms of Bogoliubons, that is, quasiparticles with energy spectrum $E(\boldsymbol{k}) = \sqrt{[\xi(\boldsymbol{k})]^2 + |\Delta(\boldsymbol{k})|^2}$[8]. On the Fermi line, the energy is entirely determined by the gap function, since $E(\boldsymbol{k}) = |\Delta(\boldsymbol{k})|$. A conventional s-wave superconductor with $\Delta(\boldsymbol{k}) = \Delta$ therefore opens a finite energy gap of magnitude $|\Delta|$. Generally speaking, however, there might be zero-crossings, so-called nodes, at which $\Delta(\boldsymbol{k})$ becomes gapless. In many cases, these nodes are energetically unfavorable since excited states could be occupied without any penalty.

Imaginary contributions to the gap function, on the other hand, can reinstate a finite energy gap at the Fermi level and render superconducting states with extended symmetries, such as $d + id$, competitive [61]. A complex order parameter $\Delta(\boldsymbol{k})$ is not invariant under the anti-unitary time-reversal operation

[7] Note that each group has a trivial irrep which assigns $\mathcal{R}^G(x) = 1$ to any $x \in G$.

[8] We still focus on spinless fermions for which $\Delta(\boldsymbol{k})$ has no spin dependence.

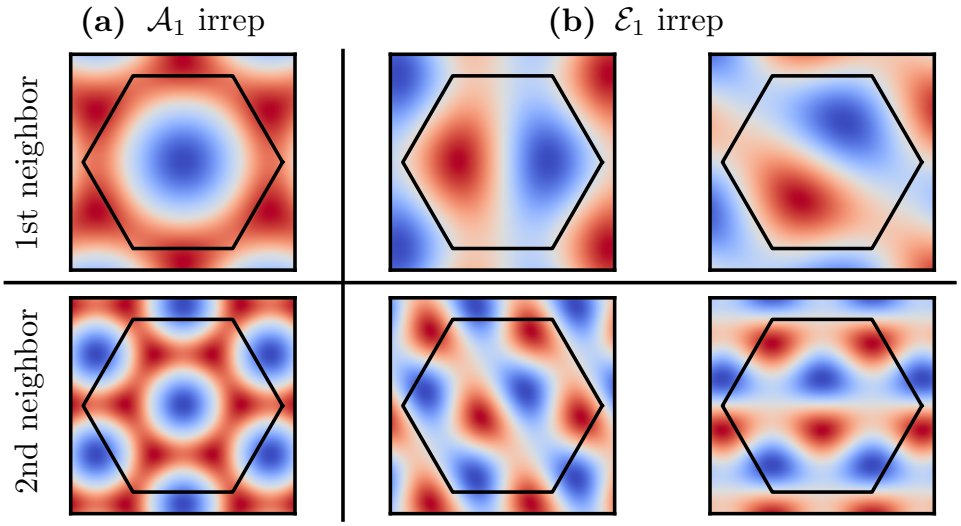

Figure 3.1: Basis functions of C_{6v} irreps on the triangular lattice. **(a)** The $\mathcal{A}_1$ irrep (s-wave) is one-dimensional and thus a single basis function suffices on both the first and second neighbor level. The p-wave irrep $\mathcal{E}_1$ shown in **(b)** is, on the other hand, two-dimensional and another linearly independent lattice harmonic needs to be computed. The black hexagon denotes the boundary of the first Brillouin zone.

$\Delta(\boldsymbol{k}) \to \bar{\Delta}(-\boldsymbol{k})$[9], since the latter involves complex conjugation. For spinful systems with SU(2) symmetry, such states would thus belong to class C in the Altland-Zirnbauer tenfold-way [61, 62] and can exhibit non-trivial topology. To unravel the latter, we can resort to an integer-valued topological invariant, the Chern number $\mathcal{C}$, which can be computed from the winding of the pseudospin $\boldsymbol{m}(\boldsymbol{k})$ along the contour lines of $\xi(\boldsymbol{k})$ resulting in the skyrmion number formula [61, 63] [10]

$$\mathcal{C} = \frac{1}{4\pi}\int_{\mathrm{BZ}} d\boldsymbol{k}\, \left\langle \boldsymbol{m}(\boldsymbol{k}) \middle| \frac{\partial \boldsymbol{m}(\boldsymbol{k})}{\partial k_x} \times \frac{\partial \boldsymbol{m}(\boldsymbol{k})}{\partial k_y} \right\rangle \text{ with } \boldsymbol{m}(\boldsymbol{k}) = \frac{1}{E(\boldsymbol{k})} \begin{pmatrix} \mathrm{Re}[\Delta(\boldsymbol{k})] \\ \mathrm{Im}[\Delta(\boldsymbol{k})] \\ \xi(\boldsymbol{k}) \end{pmatrix} . \tag{3.20}$$

Finite $|\mathcal{C}| > 0$ indicate non-trivial topology and imply, for example, quantized spin Hall conductances proportional to the Chern number in spinful systems [64] as well as the existence of gapless edge modes by virtue of the bulk-boundary correspondence [65]. For vanishing $\mathrm{Re}[\Delta(\boldsymbol{k})]$ or $\mathrm{Im}[\Delta(\boldsymbol{k})]$, the Chern number evaluates to $\mathcal{C} = 0$ and the superconducting state is thus topologically trivial. The sign of $\mathcal{C}$ is related to the handedness of the Skyrmion winding. In consequence, superconductors with $\mathcal{C} \neq 0$ are commonly referred to as chiral superconductors. Notably, any chiral superconductor breaks time-reversal, otherwise $\mathcal{C} = 0$ as discussed above. Conversely, superconductors breaking time-reversal do not generically qualify as chiral (see Ref. [61] and references therein).

3.2 Level-2 fRG for spin-polarized fermions

In Ch. 2, the fRG formalism was introduced on a general level and flow equations for the self-energy and two-particle vertex were derived. Here, we work in the L2 truncation and simplify these equations for spin-polarized fermions. Much in the spirit of related weak-coupling fRG implementations [11, 21, 39, 40, 66, 67], self-energy feedback is neglected such that we content ourselves with the flow of the two-particle vertex Eq. (2.37), which reads

$$\begin{aligned} \frac{d}{d\Lambda}\Gamma(x_1', x_2'|x_1, x_2) = \frac{1}{2}\sum_{x_3,x_4} \Gamma(x_3,x_4|x_1,x_2)\Gamma(x_1',x_2'|x_3,x_4)P(x_3,x_4) \\ - \sum_{x_3,x_4} \Gamma(x_1',x_4|x_1,x_3)\Gamma(x_3,x_2'|x_4,x_2)P(x_3,x_4) \\ + \sum_{x_3,x_4} \Gamma(x_2',x_4|x_1,x_3)\Gamma(x_3,x_1'|x_4,x_2)P(x_3,x_4)\,, \end{aligned} \tag{3.21}$$

with $P(x_3,x_4) \equiv S(x_3)G(x_4) + G(x_3)S(x_4)$. Note that we dispense with symbolically indicating the Λ-dependence of the vertices and, instead, assume it implicitly. We consider an action of spin-polarized

[9] In spinful systems, time-reversal would additionally flip the spin.

[10] $\langle .|. \rangle$ denotes the inner product of Euclidean space.

fermions in imaginary time, such that $x_i = (\omega_i, \boldsymbol{k}_i)$ with Matsubara frequency ω_i and momentum $\boldsymbol{k}_i$[11]. For translation invariant systems, the propagators are diagonal and conserve energy and momentum [11, 15]. In addition, the vertex obeys

$$\Gamma(x_1', x_2'|x_1, x_2) = V(x_1', x_2', x_1) \times \beta\delta_{\omega_1'+\omega_2',\omega_1+\omega_2} \times A_{\mathrm{BZ}}\delta_{\boldsymbol{k}_1'+\boldsymbol{k}_2',\boldsymbol{k}_1+\boldsymbol{k}_2}\,, \tag{3.22}$$

that is, the fourth frequency (momentum) in Γ can be computed from the other three and does not need to be written out explicitly. Here, A_{BZ} denotes the volume of the first Brillouin zone and $\beta = 1/T$ is the inverse temperature.

3.2.1 Temperature flow scheme

The cutoff scale Λ can be implemented differently, as long as the boundary conditions $G_0^{\Lambda\to\infty} = 0$ and $G_0^{\Lambda\to 0} = G_0$ are fulfilled. This implies, however, that the results obtained with a truncated fRG flow are affected by the choice of regulator (see Sec. 2.4). Moreover, depending on the type of regulator that is selected, e.g., momentum or frequency, fluctuations in some channels may be artificially enhanced or suppressed, leading to an inherent bias towards specific phases. A momentum-shell RG flow, for example, underestimates fluctuations with small total momenta in the particle-hole channels above scales set by the temperature and, thus, long-range antiferromagnetic correlations may overhaul putative ferromagnetic ordering tendencies [67]. Choosing an appropriate regulator is, therefore, of uttermost importance to make robust predictions.

Here, we adopt the temperature flow scheme pioneered by Honerkamp and Salmhofer [67], which directly associates Λ with the physical temperature T and allows to track small momentum transfers on equal footing in all interaction channels. The central step to implement the T-flow, amounts to removing all temperature dependencies in the quartic part of the action, such that only the Gaussian part depends on T. This can be achieved, by rescaling the original fields by a factor $\beta^{3/4}$, which cancels the β^{-3} prefactor from the normalization of Matsubara sums [67]. The bare propagator then becomes

$$G_0(\omega_n, \boldsymbol{k}) \to G_0^T(\omega_n, \boldsymbol{k}) = \frac{T^{1/2}}{i\omega_n - \xi(\boldsymbol{k})}\,, \tag{3.23}$$

where $\xi(\boldsymbol{k}) = \epsilon(\boldsymbol{k}) - \mu$ is the single-particle dispersion for chemical potential μ. Using $\omega_n = (2n+1)\pi T$, we now observe that G_0^T scales like $T^{-1/2}$ for large T and therefore $G_0^{T\to\infty} = 0$. The second boundary condition, which qualifies Eq. (3.23) as a suitable cutoff implementation, is fulfilled by construction, since G_0^T presents the usual bare propagator for the rescaled field theory. Therefore, we can straightforwardly use the flow equation (3.21), substituting $\Lambda \to T$ and dropping the temperature normalization of the Matsubara sums. Without self-energy feedback, the propagator bubble in the vertex flow then evaluates to

$$P(\omega_n\boldsymbol{k}, \omega_{n'}\boldsymbol{k'}) = -\frac{d}{dT}\left[G_0(\omega_n, \boldsymbol{k})G_0(\omega_{n'}, \boldsymbol{k'})\right] = -\frac{d}{dT}\left[\frac{T}{(\omega_n - \xi(\boldsymbol{k}))(\omega_{n'} - \xi(\boldsymbol{k'}))}\right]\,, \tag{3.24}$$

where we again suppress temperature dependencies to keep the notation convenient.

3.2.2 Patching approximation

Following the RG flow in Eq. (3.21), corresponds to integrating the right-hand side of the vertex flow from the UV to the IR limit. The vertex itself is, even after utilizing translation invariance, a high-dimensional object with three momentum and three frequency arguments and as such scales as $N_\omega^3 N_{\boldsymbol{k}}^3$. Its most singular contributions, however, are located at zero frequency and along the Fermi surface [11]. The momentum dependence orthogonal to the FS is, in contrast, less important.

As a first simplification, we therefore set external frequencies in the flow equation (3.21) to zero and neglect the frequency dependence of vertices. Using Eq. (3.22), the vertex flow then computes to

$$\begin{aligned}\frac{d}{dT}V(\boldsymbol{k}_1', \boldsymbol{k}_2', \boldsymbol{k}_1) = &\frac{1}{2A_{\mathrm{BZ}}}\int_{\mathrm{BZ}} d\boldsymbol{k}\; V(\boldsymbol{k}, \boldsymbol{q}_s - \boldsymbol{k}, \boldsymbol{k}_1)V(\boldsymbol{k}_1', \boldsymbol{k}_2', \boldsymbol{k})\mathcal{L}_s(\boldsymbol{k}, \boldsymbol{q}_s)\\ &- \frac{1}{A_{\mathrm{BZ}}}\int_{\mathrm{BZ}} d\boldsymbol{k}\; V(\boldsymbol{k}_1', \boldsymbol{k}, \boldsymbol{k}_1)V(\boldsymbol{q}_t + \boldsymbol{k}, \boldsymbol{k}_2', \boldsymbol{k})\mathcal{L}_t(\boldsymbol{k}, \boldsymbol{q}_t)\\ &+ \frac{1}{A_{\mathrm{BZ}}}\int_{\mathrm{BZ}} d\boldsymbol{k}\; V(\boldsymbol{k}_2', \boldsymbol{q}_u + \boldsymbol{k}, \boldsymbol{k}_1)V(\boldsymbol{k}, \boldsymbol{k}_1', \boldsymbol{q}_u + \boldsymbol{k})\mathcal{L}_u(\boldsymbol{k}, \boldsymbol{q}_u)\,,\end{aligned} \tag{3.25}$$

[11] Sums $\sum_{x_i}$ therefore have to be interpreted as $\frac{1}{\beta}\sum_{\omega_i}\frac{1}{A_{\mathrm{BZ}}}\int d\boldsymbol{k}_i$.

where we introduced the particle-particle and particle-hole loop functions

$$\begin{aligned}\mathcal{L}_s(\boldsymbol{k},\boldsymbol{q}) &= \frac{\lambda_f(\xi(\boldsymbol{k}))+\lambda_f(\xi(\boldsymbol{q}-\boldsymbol{k}))}{\xi(\boldsymbol{k})+\xi(\boldsymbol{q}-\boldsymbol{k})}\\ \mathcal{L}_t(\boldsymbol{k},\boldsymbol{q}) &= -\frac{\lambda_f(\xi(\boldsymbol{k}))-\lambda_f(\xi(\boldsymbol{q}+\boldsymbol{k}))}{\xi(\boldsymbol{k})-\xi(\boldsymbol{q}+\boldsymbol{k})} = \mathcal{L}_u(\boldsymbol{k},\boldsymbol{q})\,,\end{aligned} \tag{3.26}$$

with $\lambda_F(x) = \frac{d}{dT}\eta_F(x)$ and Fermi function $\eta_F(x) = (e^{x/T}+1)^{-1}$. The expressions for the loop functions result from carrying out Matsubara sums over (3.24) analytically using

$$\sum_{\omega_n} \frac{T}{(i\omega_n-\zeta_1)(i\omega_n-\zeta_2)} = \frac{\eta_F(\zeta_1)-\eta_F(\zeta_2)}{\zeta_1-\zeta_2}\,. \tag{3.27}$$

Here, the *transfer momenta* $\boldsymbol{q}_c$ are given by the Mandelstam variables

$$\begin{aligned}\boldsymbol{q}_s &\equiv \boldsymbol{k}_1'+\boldsymbol{k}_2'\\ \boldsymbol{q}_t &\equiv \boldsymbol{k}_1'-\boldsymbol{k}_1\\ \boldsymbol{q}_u &\equiv \boldsymbol{k}_1'-\boldsymbol{k}_2\,.\end{aligned} \tag{3.28}$$

In a second step, we define the projection $\pi : \mathrm{BZ} \to \mathbb{Z}_{\mathrm{FS}}^N$, mapping any momentum $\boldsymbol{k}$ in the first Brillouin zone to its nearest-neighbor $\pi(\boldsymbol{k})$ within an angular discretization $\mathbb{Z}_{\mathrm{FS}}^N$ of the Fermi surface consisting of N points. The set of all points closer to one discretization point then to any other point is called a *patch*, which lends the approximation its name: N-patch fRG [11]. In this manuscript, we consider $\mathbb{Z}_{\mathrm{FS}}^N = \{\phi_i = \frac{2\pi}{N}i \mid i = 1,...,N\}$, but the generalization of our results to non-uniform grids is straightforward. Applying this projection to the momentum dependence of the vertex, we obtain the flow equation

$$\begin{aligned}\frac{d}{dT}V(\phi_1',\phi_2',\phi_1) = &\frac{1}{2A_{\mathrm{BZ}}}\int_{\mathrm{BZ}} d\boldsymbol{k}\; V(\pi(\boldsymbol{k}),\pi(\boldsymbol{q}_s-\boldsymbol{k}),\phi_1)V(\phi_1',\phi_2',\pi(\boldsymbol{k}))\mathcal{L}_s(\boldsymbol{k},\boldsymbol{q}_s)\\ &-\frac{1}{A_{\mathrm{BZ}}}\int_{\mathrm{BZ}} d\boldsymbol{k}\; V(\phi_1',\pi(\boldsymbol{k}),\phi_1)V(\pi(\boldsymbol{q}_t+\boldsymbol{k}),\phi_2',\pi(\boldsymbol{k}))\mathcal{L}_t(\boldsymbol{k},\boldsymbol{q}_t)\\ &+\frac{1}{A_{\mathrm{BZ}}}\int_{\mathrm{BZ}} d\boldsymbol{k}\; V(\phi_2',\pi(\boldsymbol{q}_u+\boldsymbol{k}),\phi_1)V(\pi(\boldsymbol{k}),\phi_1',\pi(\boldsymbol{q}_u+\boldsymbol{k}))\mathcal{L}_u(\boldsymbol{k},\boldsymbol{q}_u)\,,\end{aligned} \tag{3.29}$$

where we replaced all arguments which coincide with a patching point $\boldsymbol{k}_i$ by the respective angle ϕ_i. Note that the patching approximation spoils momentum conservation: the momentum $\boldsymbol{k}_2 = \pi(\boldsymbol{k}_1')+\pi(\boldsymbol{k}_2')-\pi(\boldsymbol{k}_1)$ for three projected momenta $\pi(\boldsymbol{k}_1'),\pi(\boldsymbol{k}_2'),\pi(\boldsymbol{k}_1)$ is usually offset from the Fermi surface and thus necessitates to be operated upon by an additional projection. Yet, the numerical effort and memory requirements for computing the two-particle vertex are greatly reduced. Instead of having to discretize momenta in the entire Brillouin zone, one only needs to account for patch points on the Fermi surface, that is, some lower dimensional manifold in momentum space. In most cases, fewer discretization points are thus sufficient for resolving the vertex.

3.3 Numerical implementation of N-patch fRG

Having simplified the flow equations as much as possible, we now want solve Eq. (3.29) numerically. This requires two ingredients: (a) some *quadrature* to compute the two-dimensional momentum integrals and (b) an ordinary differential equation (ODE) solver to lower the temperature (see Fig. 3.2). It turns out beneficial to change the basis and formulate the momentum integrals in polar coordinates. Without loss of generality, let us focus on the particle-particle channel (the first line in [Eq. 3.29]), which, after performing the basis change, reads

$$\frac{d}{dT}\gamma_{\mathrm{s}}(\phi_1',\phi_2',\phi_1) = \frac{1}{2A_{\mathrm{BZ}}}\int_0^{2\pi} d\theta \int_0^{R_\theta} dk\; k\times V(\pi(\boldsymbol{k}_\theta),\pi(\boldsymbol{q}_s-\boldsymbol{k}_\theta),\phi_1)V(\phi_1',\phi_2',\pi(\boldsymbol{k}_\theta))\mathcal{L}_s(\boldsymbol{k}_\theta,\boldsymbol{q}_s)\,. \tag{3.30}$$

Recall that the vertices possess no radial dependence on momentum due to the projection onto patch points and we can thus write

$$\frac{d}{dT}\gamma_{\mathrm{s}}(\phi_1',\phi_2',\phi_1) = \frac{1}{2A_{\mathrm{BZ}}}\int_0^{2\pi} d\theta\; V(\pi(\boldsymbol{k}_\theta),\pi(\boldsymbol{q}_s-\boldsymbol{k}_\theta),\phi_1)V(\phi_1',\phi_2',\pi(\boldsymbol{k}_\theta))\Pi_s(\theta,\boldsymbol{q}_s)\,, \tag{3.31}$$

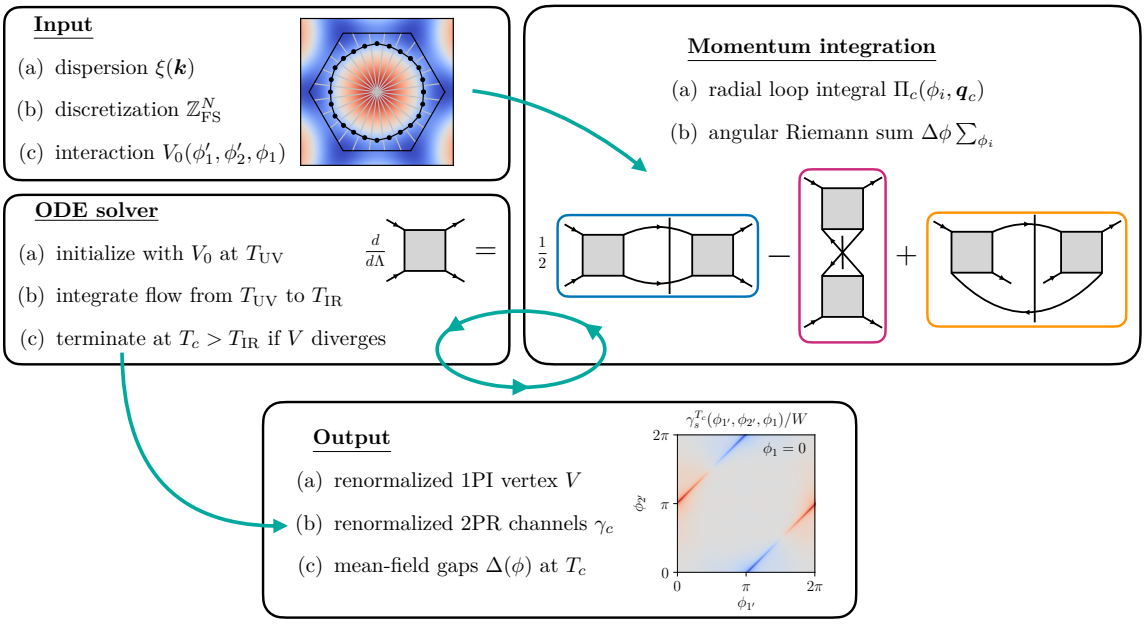

Figure 3.2: Numerical implementation of N-patch fRG for spinless fermions. For a given single-particle dispersion $\xi(\boldsymbol{k})$ one computes the renormalized interactions V from the bare interaction V_0 by integrating the renormalization group flow from some initial temperature T_{UV} to some final scale T_{IR} using an ODE solver. The latter step involves the computation of two-dimensional momentum integrals, which can efficiently be evaluated in polar coordinates. The renormalized 2PR channels, obtained at T_{IR} or at $T_c > T_{\mathrm{IR}}$ where one of them eventually diverges, characterize the effective low-energy theory and can be used to extract symmetries of the associated mean-field gaps. For more details on the individual algorithms, see text.

where $\Pi_s(\theta, \boldsymbol{q}_s)$ is the radial integral over the loop function

$$\Pi_s(\theta, \boldsymbol{q}_s) = \int_0^{R_\theta} dk\ k \times \mathcal{L}_s(\boldsymbol{k}_\theta, \boldsymbol{q}_s)\,. \tag{3.32}$$

Usually, the k-integral needs to be computed with high-accuracy to obtain a stable and qualitatively correct fRG flow as will be demonstrated in the next section. The θ-integral, on the other hand, causes mostly quantitative changes, but leaves the important physics, regarding, for example, which couplings become relevant in the low-temperature regime, unchanged. We therefore approximate the latter by a simple Riemann sum over the patch points, such that our exemplary flow in the s channel becomes

$$\frac{d}{dT}\gamma_s(\phi_1', \phi_2', \phi_1) \approx \frac{\Delta\phi}{2A_{\mathrm{BZ}}} \sum_{i=1}^{N} V(\phi_i, \pi(\boldsymbol{q}_s - \boldsymbol{k}_{\phi_i}), \phi_1) V(\phi_1', \phi_2', \phi_i) \Pi_s(\phi_i, \boldsymbol{q}_s) + \mathcal{O}((\Delta\phi)^2)\,, \tag{3.33}$$

with $\Delta\phi = \frac{2\pi}{N}$. Hence, higher resolution on the Fermi surface, which is desirable anyways, simultaneously reduces the error for the θ-integration (see Fig. 3.4).

3.3.1 Radial integration of the loop function

As we have seen in the last section, the only input required to evaluate the right-hand side of the flow equation are the radially-integrated loop functions Π_c. In order to choose an appropriate quadrature from the large pool of numerical algorithms which exist for that matter, a meticulous study of the target function is required to make a well-informed decision.

To do so, we compute the loop function as well at its k-integral taking the dispersion

$$\epsilon(\boldsymbol{k}) = -2t \times \left[\cos(k_x) + \cos\left(\frac{k_x}{2} + \frac{\sqrt{3}k_y}{2}\right) + \cos\left(\frac{k_x}{2} - \frac{\sqrt{3}k_y}{2}\right)\right], \tag{3.34}$$

of the single-band Hubbard model on the triangular lattice as an example. In [Figs. 3.3(c) & (d)], we show the loop function along the same two representative momentum space cuts, but at

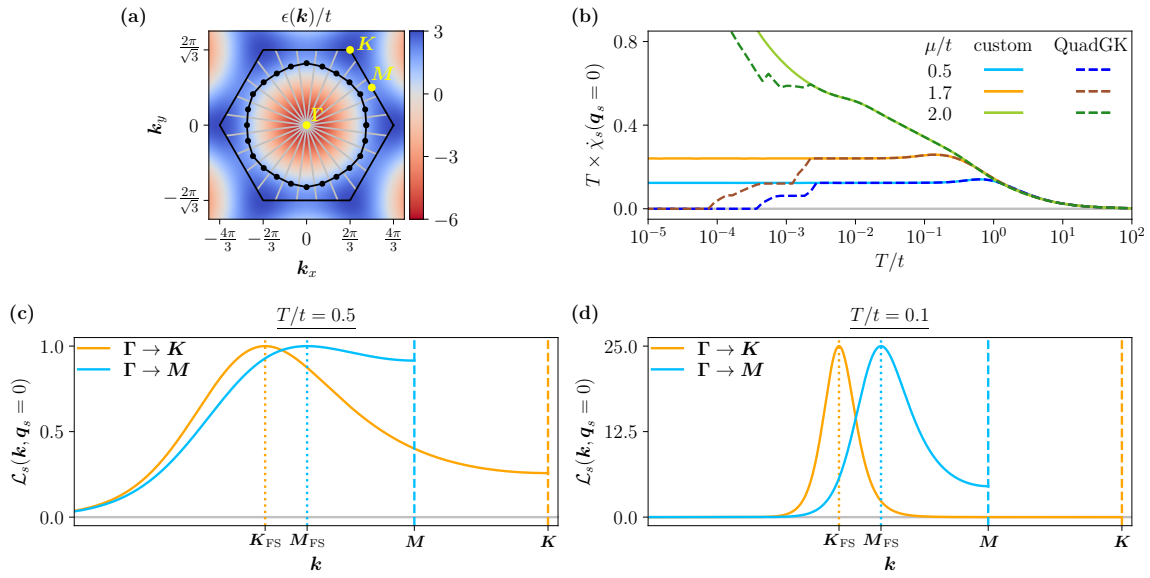

Figure 3.3: Radial integration of the loop function. **(a)** Schematic illustration of the N-patch fRG scheme for the single-band triangular lattice Hubbard model with $N = 24$. Silver lines mark the boundaries of the individual patches and black dots denote their respective patch points on the Fermi surface. **(b)** Temperature flow of the scale-derivative of the pairing susceptibility $\dot{\chi}_s(\boldsymbol{q}_s = 0)$. Standard integration schemes such as Gauss-Kronrod quadrature (dashed lines) fail to faithfully compute the radial component of the necessary momentum integral, resulting in non-analytic results for $T/t < 10^{-2}$. In contrast, a temperature adaptive routine (dubbed *custom* for brevity), yields stable results for temperatures as low as $T/t = 10^{-5}$ (full lines). The origin for this behavior roots in the progressive sharpening of the loop function around the Fermi level, as displayed in **(c)** and **(d)**. Here, we plot $\mathcal{L}_s(\boldsymbol{k}, \boldsymbol{q}_s = 0)$ for $\mu/t = 1.7$ along two high-symmetry directions of the triangular lattice. The respective intersection points $\boldsymbol{K}_{\mathrm{FS}}$ and $\boldsymbol{M}_{\mathrm{FS}}$ with the circularly shaped Fermi surface are marked by dotted vertical lines.

different temperatures. In both cases, the largest value is assumed at the Fermi level. The width of the corresponding peak, however, is strongly modulated upon lowering T. An efficient quadrature should take this effect into account and successively increase the radial resolution upon lowering the temperature.

Here, we adress this issue in three consecutive steps. We firstly subdivide the integral into two parts, one ranging from the origin $\boldsymbol{k} = 0$ to the Fermi surface and a second one ranging from the Fermi surface to the boundary of the Brillouin zone. We thus have

$$\Pi_c(\theta, \boldsymbol{q}_c) = \int_0^{F_\theta} dk\ k \times \mathcal{L}_c(\boldsymbol{k}_\theta, \boldsymbol{q}_c) + \int_{F_\theta}^{R_\theta} dk\ k \times \mathcal{L}_c(\boldsymbol{k}_\theta, \boldsymbol{q}_c)\,, \tag{3.35}$$

where the radius F_θ corresponds to the Fermi level at angle θ. This way, we can rest assured that the most dominant contribution is always accounted for. In a second step, we further subdivide both integrals into n_T uniform domains, that is

$$\Pi_c(\theta, \boldsymbol{q}_c) = \sum_{i=0}^{n_T-1} \left[\int_{\frac{F_\theta}{n_T} i}^{\frac{F_\theta}{n_T}(i+1)} dk\ k \times \mathcal{L}_c(\boldsymbol{k}_\theta, \boldsymbol{q}_c) + \int_{F_\theta + \frac{R_\theta - F_\theta}{n_T} i}^{F_\theta + \frac{R_\theta - F_\theta}{n_T}(i+1)} dk\ k \times \mathcal{L}_c(\boldsymbol{k}_\theta, \boldsymbol{q}_c) \right], \tag{3.36}$$

where we scale the number of subdomains according to

$$n_T = \min\left(\max\left(\frac{n_{T_{\mathrm{UV}}}}{\sqrt{T}}, n_{T_{\mathrm{UV}}} \right), n_{T_{\mathrm{IR}}} \right). \tag{3.37}$$

This procedure ensures stability of the routine also at small temperatures by successively increasing the number of integration nodes. Lastly, each integral is solved by an adaptive routine to obtain error-controlled results. We opt for Simpson's rule as a compromise between numerical efficiency and accuracy. The number of function evaluations is thereby doubled until we either meet the error tolerance or surpass the maximum number of function evaluations. Unless stated otherwise, we use an absolute tolerance $a_{\mathrm{tol}} = 10^{-8}$ and a relative tolerance $r_{\mathrm{tol}} = 10^{-4}$. The integration is terminated

preemptively if the number of function evaluations exceeds 2^{20}. Additionally, we fix $n_{T_{\mathrm{UV}}} = 10$ and $n_{T_{\mathrm{IR}}} = 10^3$. Note that in order to estimate the integration error, a single Richardson extrapolation between two consecutive steps, as well as on the final result, is performed.

To demonstrate the superiority of our implementation, we compute the scale-derivative of the pairing susceptibility, i.e. the momentum integral

$$\dot{\chi}_s(\boldsymbol{q_s} = 0) = \frac{1}{A_{\mathrm{BZ}}} \int_{\mathrm{BZ}} d\boldsymbol{k}\ \mathcal{L}_s(\boldsymbol{k}, \boldsymbol{q}_s = 0)\,, \tag{3.38}$$

as a function of temperature. In Fig. 3.3(b), we have contrasted our radial quadrature with an adaptive Gauss-Kronrod rule as exported by the `QuadGK` library in the Julia programming language. In all cases, we employ a $N = 192$ Riemann sum for the angular integration. For temperatures $T/t > 10^{-2}$ both methods are in perfect agreement. Below this scale, however, one observes non-analytic jumps in the results obtained with the Gauss-Kronrod rule, whereas the implementation described here yields accurate results for temperatures as low as $T/t = 10^{-5}$ - an appreciable boost by more than two orders of magnitude. On the triangular lattice, such temperature scales can in fact become relevant due to the collective interplay between fluctuations and geometric frustration [39, 40].

3.3.2 Differential equation solver

Knowing how to compute the right-hand side of Eq.(3.29), one can evolve the vertex V given at some initial temperature scale T_i to some lower temperature $T_f < T_i$ by integrating the flow equations. More specifically, these are of the form

$$\frac{d}{dT} V = f(T, V) \tag{3.39}$$

where f schematically represents the sum of channel derivatives, which makes up the right-hand side of the flow. This equation amounts to a set of ordinary differential equations for which numerous solvers are available. Ideally, one would like to use that algorithm which produces V^{T_f} with the highest possible accuracy but the least number of evaluations of f. Indeed, as recent efforts have demonstrated [44], an optimal solver for a specific incarnation of the flow equations may exist. Although the ideal choice may be model dependent after all, there are some generic traits shared by well-performing ODE solvers for fRG flow equations. A qualified ODE solver should

(a) adjust its step size dynamically to account for sudden changes such as the rapid growth of certain couplings when approaching the infrared regime.

(b) account for the change of difficulty upon lowering the temperature. A maximum step width that one deems appropriate for large T might be a bad choice close to the infrared, where the vertex has been subject to strong renormalization effects. Conversely, if the couplings change only weakly with T, small step sizes are inefficient and should be circumvented to safe computation time.

(c) optimize both efficiency and numerical accuracy. Multiple evaluations of f should be avoided if the hypothetical gain in accuracy is in an imbalance with the actual change of the results. For example, if one is only interested in qualitative results simple methods such as single-step Euler solvers might suffice already.

To respect these conditions, we integrate the flow equations using the Bogacki-Shampine [RK3(2)] method [68] from the Runge-Kutta family and implement the step-size adjustment (a) according to the proposal in Ref. [69]. We set an absolute (relative) error tolerance of 10^{-8} (10^{-2}), unless stated otherwise. In order to factor in (b), the maximum step size of the solver is chosen relative to the current temperature, $\max(\Delta T) = T/10$. The minimum step size, on the other hand, is fixed to $\min(\Delta T) = 10^{-7}$ (T is given in units of the hopping). Most notably, this algorithm possesses the First-Same-As-Last (FSAL) property, allowing one to recycle the function evaluation for the error estimate in the subsequent ODE step, which helps to pay heed to (c).

3.3.3 Linearized gap equations and calculation of Chern numbers

In Sec. 3.1.1, we linearized the mean-field equation for the superconducting gap $\Delta(\boldsymbol{k})$ around the Fermi surface. The resulting gap equation then assumed the form

$$\lambda \Delta(\boldsymbol{k}) = \sum_{\boldsymbol{k}' \in \mathrm{FS}} V_{\mathrm{BCS}}(\boldsymbol{k}, \boldsymbol{k}') \Delta(\boldsymbol{k}')\,, \tag{3.40}$$

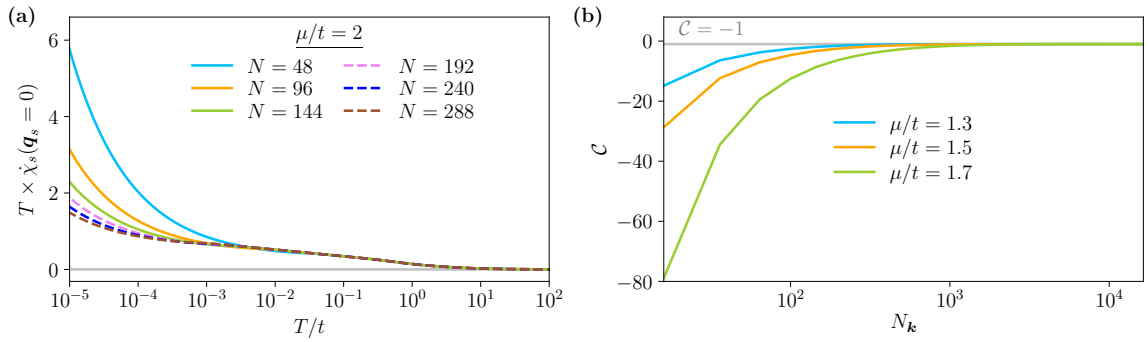

Figure 3.4: Numerical convergence checks in N-patch fRG. In **(a)** we plot temperature flows of the scale-derivative of the pairing susceptibility $\dot{\chi}_s(\boldsymbol{q}_s = 0)$ at van Hove filling for various angular resolutions N. In the high temperature regime $T/t \gtrsim 10^{-2}$ all curves agree sufficiently well, while at low temperatures significant deviations are visible. In our fRG calculations we typically use $N = 192$ as a compromise between accuracy and computing time. Note that below van Hove filling convergence is typically reached much faster. The scaling of the Chern number calculation with the Brillouin zone resolution for the $\mathcal{E}_1$ irrep is shown in **(b)**. The convergence behavior generally depends on the filling (close to nesting, convergence is typically slower), yet, $N_{\boldsymbol{k}} \approx 10^3$ momenta are usually sufficient to obtain the correct result.

that is, an eigenvalue equation for the pairing potential V_{BCS}, whose solutions (eigenvectors) are superconducting gaps with associated eigenvalue λ, which sets the corresponding mean-field critical temperature. Our analysis further revealed that the largest, negative eigenvalue represents the dominant pairing tendency.

At that point, however, the precise form and origin of the pairing potential remained obscure. Fortunately, it can be explicitly computed from the fRG approach. When one integrates the flow, some contributions to the vertex usually become singular, indicating spontaneous symmetry breaking and the onset of an ordered phase [11, 15, 70]. At this point, the fRG flow has to be stopped. Now, consider an effective interaction of the form $V_{\mathrm{BCS}}(\boldsymbol{k}, \boldsymbol{k}') = V(\boldsymbol{k}, -\boldsymbol{k}|\boldsymbol{k}', -\boldsymbol{k}')$, which has a transfer momentum $\boldsymbol{q}_s = 0$ and should thus be dominated by fluctuations in the particle-particle channel. If it occurs that the latter diverges during the fRG flow[12], this means that the fermions become strongly-interacting and the Fermi liquid state thus exhibits a *pairing instability*. The pairing potential at the critical scale T_c[13] can then be extracted as

$$V_{\mathrm{BCS}}(\boldsymbol{k}, \boldsymbol{k}') \approx \gamma_s(\boldsymbol{k}, -\boldsymbol{k}|\boldsymbol{k}', -\boldsymbol{k}') \,. \tag{3.41}$$

Consequently, any numerical eigenvalue solver can be applied in order to calculate the leading superconducting gap from Eq. (3.40). More generally speaking, an instability in *any* channel can be associated with a linearized gap equation for the respective scattering potential [71]. A mean-field decoupling $\langle \bar{\psi}_{\boldsymbol{k}+\boldsymbol{q}_t} \psi_{\boldsymbol{k}} \rangle$, for example, corresponds to an effective interaction $\gamma_t(\boldsymbol{k} + \boldsymbol{q}_t, \boldsymbol{k}'|\boldsymbol{k}, \boldsymbol{k}' + \boldsymbol{q}_t)$ in the t channel with transfer momentum $\boldsymbol{q}_t$ and the eigenvectors would therefore characterize a density wave. Note, however, that the gap is computed from a singular vertex γ_c at $T = T_c$ and as such, there is no real meaning in its size, but only in its symmetry.

Having obtained the pairing field from the renormalized vertex, the symmetry based classification discussed in Sec. 3.1.2 can be applied. In particular, one can find an optimal fit of lattice harmonics by comparing the agreement of different irreps with the dominant eigenvectors of the scattering potential. Recall that in the case of degenerate pairing solutions, corresponding to multi-dimensional representations, complex superpositions of lattice harmonics would open a gap at the Fermi surface and are thus preferable from an energetic point of view. Superconducting gaps of this form could exhibit non-trivial topology, that is, they could have a finite Chern number $\mathcal{C}$. For a complex superposition of two such fits, the latter can be determined from the winding of the pseudospin $\boldsymbol{m}(\boldsymbol{k})$ around the Fermi surface (see Sec. 3.1.3) using

$$\mathcal{C} = \frac{1}{4\pi} \int_{\mathrm{BZ}} d\boldsymbol{k} \, \left\langle \boldsymbol{m}(\boldsymbol{k}) \middle| \frac{\partial \boldsymbol{m}(\boldsymbol{k})}{\partial k_x} \times \frac{\partial \boldsymbol{m}(\boldsymbol{k})}{\partial k_y} \right\rangle \,. \tag{3.42}$$

[12] Numerically, a divergence can, for example, be characterized by the channel maximum growing larger than some multiple of the electronic bandwidth.

[13] In this context, T_c corresponds to the temperature at which the fRG flow breaks down.

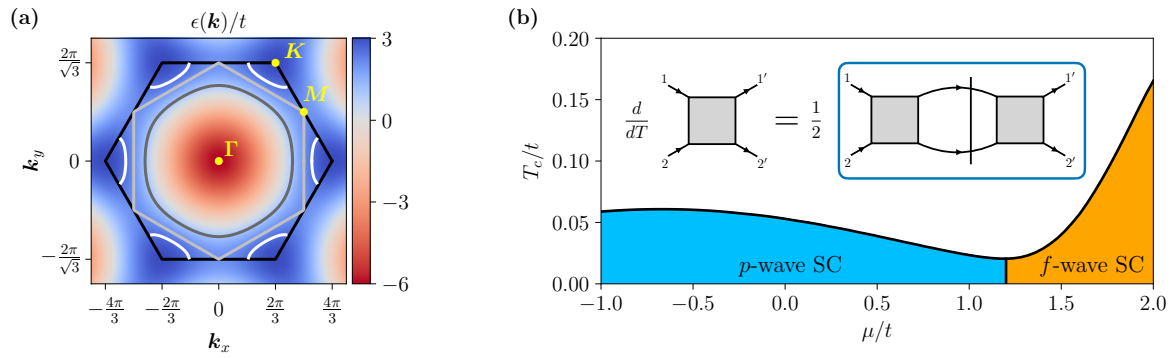

Figure 3.5: Spinless N-patch fRG in the pairing channel for $V/t = -1$. (a) For low densities $\mu/t < 2$, the Fermi surface (dark grey line) resembles a circular shape. Beyond Van Hove filling $\mu/t = 2$, where nesting (silver line) occurs, the Fermi surface intersects with the boundary of the Brillouin zone (black line) and forms pockets around the $\boldsymbol{K}$ points (white lines). **(b)** Critical fRG scale T_c/t as a function of the chemical potential μ/t. At $\mu/t \approx 1.2$ one finds a transition from p-wave to f-wave superconductivity. The p-wave instability could be chiral with Chern number $\mathcal{C} = -1$.

Computing $\mathcal{C}$ boils down to calculating a two-dimensional momentum integral. The difficulty in solving the latter for arbitrary $\boldsymbol{m}$ evolves around developing a stable algorithm, which is able to cope with repeated evaluations of the product of partial derivatives. Here, we proceed in two steps. First, the integral is replaced by a two-dimensional Riemann sum

$$\mathcal{C} = \frac{\Delta A_{\mathrm{BZ}}}{4\pi} \sum_{i=1}^{N} \left\langle \boldsymbol{m}(\boldsymbol{k}_i) \middle| \frac{\partial \boldsymbol{m}(\boldsymbol{k})}{\partial k_x}\bigg|_{\boldsymbol{k}=\boldsymbol{k}_i} \times \frac{\partial \boldsymbol{m}(\boldsymbol{k})}{\partial k_y}\bigg|_{\boldsymbol{k}=\boldsymbol{k}_i} \right\rangle , \tag{3.43}$$

where the $\boldsymbol{k}_i$ form a uniform discretization of the Brillouin zone, that is, the Wigner-Seitz cell for each point encloses the same volume $\Delta A_{\mathrm{BZ}} = \frac{A_{\mathrm{BZ}}}{N}$. To compute the sum, we evaluate the partial derivatives via forward mode automatic differentiation (AD), as exported by the `ForwardDiff` Julia module. Compared to finite-difference methods, AD has turned out to be more stable in the present context. We find the interval to converge already with a modest momentum resolution $N_{\boldsymbol{k}} \approx 10^3$, as exemplified in Fig. 3.4(b).

3.4 Examples

In the last decades, the Hubbard model on the square lattice has attracted tremendous attention as *the* prototypical Hamiltonian of strong correlations in high-T_c candidate materials, such as cuprates or iron-pnictides [1, 2]. Moreover, it has served as a valuable environment for benchmarking novel numerical approaches and exploring their performance for disentangling the non-trivial interplay between thermal and quantum fluctuations [41, 72].

The advent of twisted bilayer graphene [53, 73] as one of the first moiré materials for which a plethora of correlated many-body states could be observed, however, renewed the conceptual interest in effective Hamiltonians on hexagonal geometries, such as the honeycomb, kagome or triangular lattice. Remarkably, the phase diagram of tBG [53, 55, 73], resembles that of the high-T_c cuprate materials: superconducting domes are separated by insulating regions as a function of doping. Moreover, a comparison of the superconducting transition temperature T_c relative to the Fermi temperature T_{F} [53] shows that T_c/T_{F} for twisted bilayer graphene lies somewhere between the iron-pnictides and cuprates, indicating tBG as a potential platform for the study of unconventional superconductivity.

Recently, multilayer transition metal dichalcogenides (TMDs) have been put forward as another highly-tunable platform for the simulation of exotic many-body states [40, 74–81]. The effective models considered for TMDs usually involve a couple of spin-split bands that arise from broken SU(2) symmetry due to strong spin-orbit coupling in the monolayer system [78, 82, 83]. To capture the elementary physics of interacting fermions on a lattice relevant to the field of TMDs and, more importantly, to exemplify the capabilities of the functional renormalization group approach, we consider a toy model of spinless fermions on the triangular lattice with real-space Hamiltonian

$$\mathcal{H} = -t \sum_{\langle ij \rangle} c_i^\dagger c_j - \mu \sum_i c_i^\dagger c_i + V \sum_{\langle ij \rangle} c_i^\dagger c_j^\dagger c_j c_i \, , \tag{3.44}$$

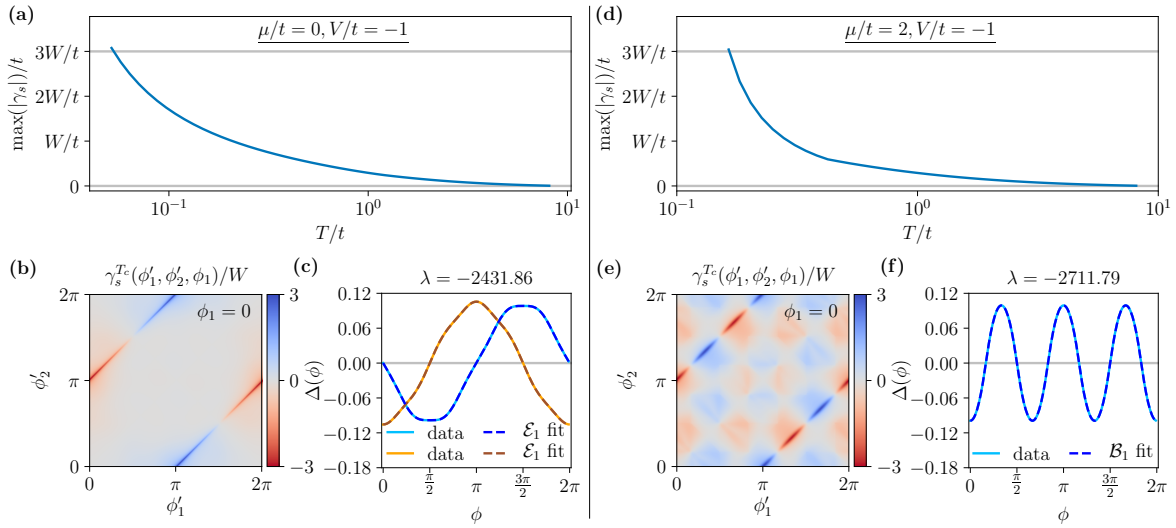

Figure 3.6: Characterization of pairing instabilities in the Cooper channel. **(a)** Temperature flow of the maximum of γ_s for $\mu/t = 0$. The calculation is terminated preemptively, once an upper bound of $3W/t$ (upper silver line) is surpassed. **(b)** Renormalized 2PR vertex γ_s at the critical scale T_c. Singular couplings appear as two parallel lines, whose momenta add up to $\boldsymbol{q}_s = 0$. **(c)** p-wave gap function extracted from the vertex in **(b)**. The leading eigenvalue is doubly degenerate and can be accurately described by the nearest-neighbor harmonics of the $\mathcal{E}_1$ irrep (dashed lines). **(d)** & **(e)** same as **(a)** & **(b)** but at Van Hove filling. **(f)** Gap function for the f-wave instability. Here, only a single eigenvector, which transforms in the $\mathcal{B}_1$ irrep, is competitive.

which could perhaps be realized by coupling an external magnetic field to spins in the moiré valence band and driving the system into a polarized state. Note that in the absence of a spin degree of freedom, the nearest-neighbor density interaction V presents the simplest conceivable interaction term. Here, our sign convention is chosen such that $V < 0$ (> 0) denotes an attractive (repulsive) interaction. In momentum space Eq. (3.44) becomes

$$\mathcal{H} = \sum_{\boldsymbol{k}} \xi(\boldsymbol{k}) c_{\boldsymbol{k}}^\dagger c_{\boldsymbol{k}} + \sum_{\boldsymbol{k}_1', \boldsymbol{k}_2', \boldsymbol{k}_1, \boldsymbol{k}_2} V \mathcal{F}(\boldsymbol{k}_2', \boldsymbol{k}_2) \times \delta(\boldsymbol{k}_1' + \boldsymbol{k}_2' - \boldsymbol{k}_1 - \boldsymbol{k}_2) c_{\boldsymbol{k}_1'}^\dagger c_{\boldsymbol{k}_2'}^\dagger c_{\boldsymbol{k}_2} c_{\boldsymbol{k}_1} \,, \tag{3.45}$$

where $\mathcal{F}(\boldsymbol{k}, \boldsymbol{k'}) = \sum_{\{\boldsymbol{\delta}\}} e^{i(\boldsymbol{k}-\boldsymbol{k'})\boldsymbol{\delta}}$ corresponds to the nearest-neighbor form factor with triangular displacement vectors $\boldsymbol{\delta}$. The single-particle dispersion

$$\xi(\boldsymbol{k}) = -2t \left[\cos(k_x) + \cos\left(\frac{k_x}{2} + \frac{\sqrt{3} k_y}{2} \right) + \cos\left(\frac{k_x}{2} - \frac{\sqrt{3} k_y}{2} \right) \right] - \mu \,, \tag{3.46}$$

is computed for Bravais lattice vectors $\boldsymbol{a}_1 = (1, 0)^T$ and $\boldsymbol{a}_2 = (1/2, \sqrt{3}/2)^T$.

To shed light on the ground state instabilities of this toy model, we employ the N-patch fRG scheme from Sec. 3.2.2 combined with the renormalized mean-field analysis discussed in Sec. 3.3.3. The properly antisymmetrized initial condition for the two-particle vertex is given by

$$V_0(\boldsymbol{k}_1', \boldsymbol{k}_2', \boldsymbol{k}_1) = V \left[\mathcal{F}(\boldsymbol{k}_1, \boldsymbol{k}_1') - \mathcal{F}(\boldsymbol{k}_2', \boldsymbol{k}_1) \right] \,, \tag{3.47}$$

where we utilized inversion symmetry of the triangular lattice. We set the initial scale T_{UV} to the bandwidth $W = 9t$ and terminate the flow for temperatures $T \leq T_{\mathrm{IR}} = 10^{-5} t$ or if the maximum of one channels exceeds $3W$, in which case we declare to have reached the strong-coupling regime. The flow of the vertex is tracked on $N = 192$ patches, for which our susceptibility results in Fig. 3.4 seemed reasonably well converged. In total, this corresponds to a set of roughly seven million differential equations in every channel, which goes significantly beyond previously used patching resolutions.

In the following, numerical results for the phase diagram of Eq. (3.44) are presented. We proceed in two steps. Firstly, our approach is benchmarked against mean-field results from Ref. [84] by exclusively considering the s channel and setting all other 2PR diagrams to zero. In this case, the fRG flow resembles a ladder summation of particle-particle diagrams. Secondly, we perform full patching calculations and map out the phase diagram for both attractive and repulsive four-fermion interactions V.

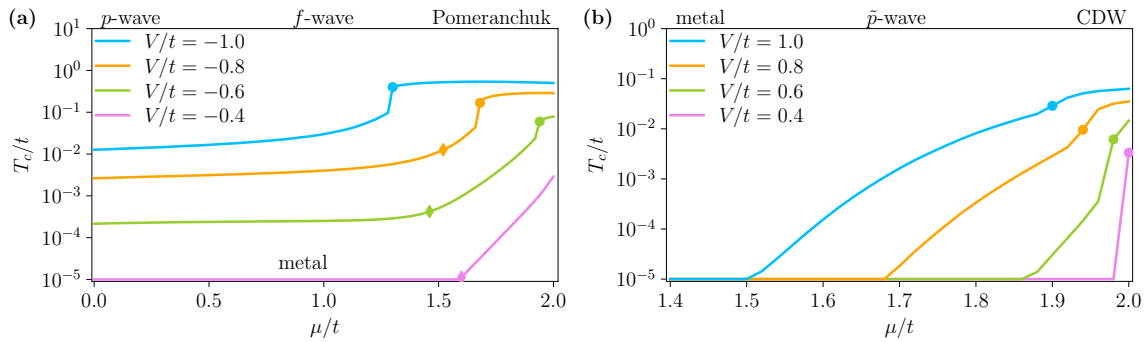

Figure 3.7: Phase diagrams for spinless fermions on the triangular lattice. (a) Close to Van Hove filling and for sizable attractive interactions $V/t < 0$, one finds a Pomeranchuk instability, whose onset is marked by a colored dot for the respective T_c line. Below $\mu/t = 2$, however, two pairing instabilities can occur: p-wave at low densities and an f-wave superconductor at intermediate fillings, for which we indicate the respective transition by diamond markers. Note that for $V/t = -1.0$ (blue line) no f-wave instability is found in the fRG calculation. For weak interactions $V/t = -0.4$ there additionally exists a metallic regime. **(b)** Same as **(a)**, but for repulsive density interactions $V/t > 0$. Instead of a Pomeranchuk instability, one finds a charge density wave with a finite pitch vector $\boldsymbol{q}_t = \boldsymbol{M}$ that breaks translation invariance. If the filling is reduced, the particle-hole instability is overhauled by a divergence in the s channel. The respective gap has $\tilde{p}$-wave symmetry, i.e. it transforms in the $\mathcal{E}_1$ irrep, but further neighbor contributions need to be accounted for. At low densities we find a metallic phase, in which singular couplings are absent.

3.4.1 Example 1: Channel truncated N-patch fRG

For the mean-field scenario, we study the Hamiltonian presented in Eq. (3.44) with attractive interactions $V/t = -1$ and for fillings $\mu/t \in [-1, 2]$. For $\mu/t = 2$, the dispersion Eq. (3.46) exhibits a Van Hove singularity at $\boldsymbol{k} = \boldsymbol{M}$ due to saddle points in the dispersion. Moreover, the Fermi surface is perfectly nested (see [Fig. 3.5(a)]) and touches the Brillouin zone at the Van Hove points. For larger chemical potentials, the $\xi(\boldsymbol{k}) = 0$ line intersects with the boundary of the Brillouin zone, giving rise to Fermi pockets around the $\boldsymbol{K}$-points. This opens up the possibility for superconducting states with extended symmetries (such as f-wave) if their respective nodes lie in the regions between the pockets. Below Van Hove filling, nesting is absent and the Fermi surface assumes a circular shape, which progressively shrinks around the $\boldsymbol{\Gamma}$-point when μ/t is decreased. One could therefore expect a competition between two superconducting instabilities in the chosen range of fillings: one with extended symmetry in vicinity of Van Hove filling, and one with a lesser number of nodes for $\mu/t < 2$.

Indeed, as depicted Fig. 3.5(b) and in agreement with Ref. [84], we find a transition between a p-wave instability at low fillings and an f-wave superconductor for $\mu/t \gtrsim 1.2$, signified by a local minimum in the critical temperature. The p-wave instability features two nodes on the Fermi surface and its gap, which is best described by the nearest-neighbor basis functions δ_1, δ_2 of the two-dimensional $\mathcal{E}_1$ irrep, is doubly degenerate (see [Fig. 3.6(a) - (c)]). Its Chern number for a mean-field constructed as $\Delta(\boldsymbol{k}) = \delta_1(\boldsymbol{k}) \pm i\delta_2(\boldsymbol{k})$ evaluates to $\mathcal{C} = -1$, that is, the respective $p_x + ip_y$ state is topologically non-trivial, which agrees with the findings of Ref. [84]. The f-wave state (see [Fig. 3.6(d) - (f)]), on the other hand, transforms in the one-dimensional $\mathcal{B}_1$ irrep and is therefore topologically trivial. Consequently, there must be a quantum phase transition in between, which according to Ref. [84] is likely first order.

3.4.2 Example 2: N-patch fRG for spinless triangular-lattice fermions

Having instilled some confidence in the correctness of our implementation, we now turn to the discussion of the fRG results with competing channels. To generalize the results from the ladder resummation, we begin by presenting the phase diagram for various attractive interactions $V/t < 0$, plotted in Fig. 3.7(a).

In total, we find three different ground state instabilities. Starting from a p-wave instability at low densities, the symmetry of the gap changes from p- to f-wave for interactions $-0.4 < V/t < -1$, followed by a plateau of particle-hole instabilities. For smaller $|V|/t$, the critical temperature of the p-wave instability is suppressed below $T_{\mathrm{IR}} = 10^{-5}$ and thus becomes elusive. The respective region in the phase diagram is therefore coined *metal*. For larger $|V|/t$, on the other hand, the region of f-wave superconductivity diminishes.

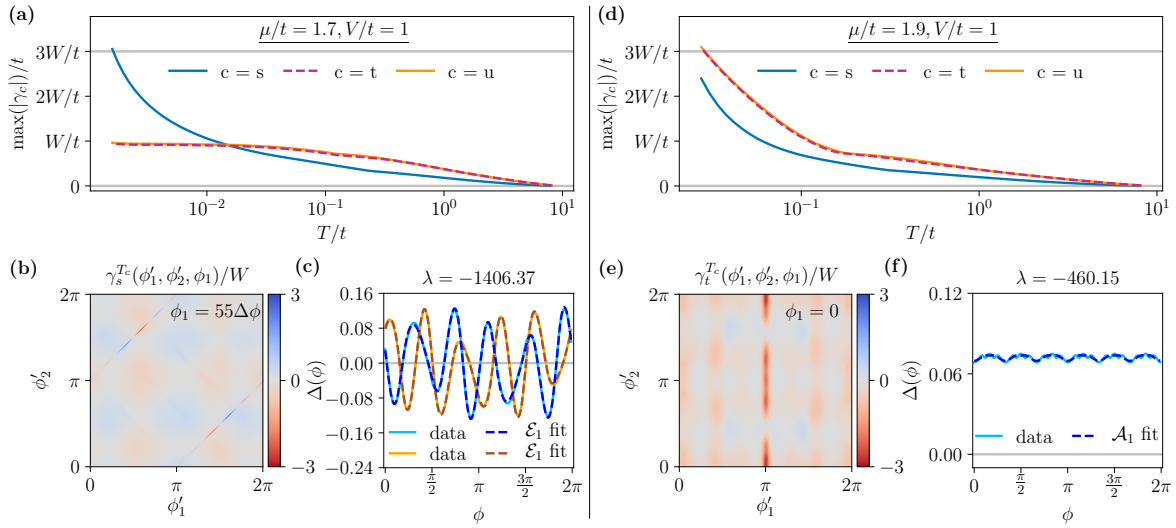

Figure 3.8: Competing instabilities for repulsive interactions close to Van Hove filling. (a) Flow of the maxima in the 2PR channels, signifying an instability in the pairing channel. **(b)** Renormalized pairing vertex at the critical scale T_c. **(c)** Superconducting gap function computed from **(b)**. The solution is doubly degenerate and hast extended $\tilde{p}$-wave symmetry, as indicated by multiple nodes on the Fermi surface. A fit of $\mathcal{E}_1$ basis functions is plotted as dashed lines. **(d)** Same as **(a)**, but with an instability in the particle-hole channels. **(e)** Direct particle-hole channel at the critical temperature. The respective order parameter is plotted in **(f)**, with a fit of $\mathcal{A}_1$ (s-wave) lattice harmonics (dashed blue line).

Close to Van Hove filling, one finds a simultaneous divergence of the two particle-hole channels (see Fig. 3.8). Due to crossing symmetry, which relates the respective bubble functions ([Eq. 2.24]), the flows closely align and we can reduce our discussion to γ_t for brevity. The direct particle-hole channel becomes singular for transfer momenta $\boldsymbol{q}_t = 0$, that is, a *Pomeranchuk* instability occurs. Since the respective gap equation possesses a large negative eigenvalue, it seems that the system develops a tendency towards Fermi surface deformation [35]. This result, however, has to be taken with a grain of salt, since the respective mean-field $\langle \bar{\psi}_{\boldsymbol{k}} \psi_{\boldsymbol{k}} \rangle$, corresponding to the fermion density, does not break any symmetries. Therefore, we cannot associate the singularity with any order. One possible reason for the divergence of the flow could be the neglect of self-energy effects in N-patch fRG. The latter could, in principle, acquire a non-trivial momentum dependence and counteract the divergence, but in the absence of numerical results, this remains speculation.

On a qualitative level, our results obtained with additional fluctuations in the particle-hole channels are consistent with those obtained in the previous section, since the gaps for both the p and f-wave instabilities transform in the same irreps of C_{6v}. Moreover, the sequence of their appearance as a function of doping remains identical. The Pomeranchuk instability, on the other hand, could not be obtained from exclusively considering fluctuations in γ_s.

Let us now consider repulsive interactions $V/t > 0$. Similar to the attractive case, we again find an instability of the particle-hole channels for chemical potentials $\mu/t \approx 2$. This time, however, finite momenta $\boldsymbol{q}_t = \boldsymbol{M}$ are transferred through the internal bubble, signaling the emergence of a charge density wave (CDW), which breaks translation invariance. Since $\boldsymbol{q}_t$ coincides with the nesting vector, this instability can be considered a two-dimensional analogue of a Peierl's instability. The dominant eigenvector of the associated scattering potential is found to transform in the $\mathcal{A}_1$ irrep and has s-wave symmetry.

Below Van Hove filling nesting is lost, but fluctuations in the particle-hole channels remain sizable. Nonetheless, one finds an instability in γ_s if μ/t is decreased far enough. This is remarkable, since the nearest-neighbor interaction is repulsive, $V/t > 0$, and an attractive interaction in the Cooper channel must be caused by inter-channel feedback during the RG flow, similar to the generation of d-wave superconductivity from antiferromagnetic fluctuations in the square lattice Hubbard model [21, 36]. The flows of the 2PR channels plotted in Fig. 3.8(a), for sufficiently strong V/t mimic this behavior. At large temperatures, the vertex is dominated by the particle-hole channels. When the temperature is decreased, however, both γ_t and γ_u freeze out and flow to a constant value. The particle-particle channel, which is subdominant in the ultraviolet, then displays a strong increase in the low-temperature regime and its maximum ultimately surpasses the upper numerical bound $3W$. The corresponding gap function features an unusual large number of ten nodes on the Fermi surface and has higher-order

$\tilde{p}$-wave symmetry, that is it transforms in the $\mathcal{E}_1$ irrep but its momentum dependence needs to be modeled with both first and second neighbor harmonics. From an experimental point of view this is interesting insofar that a superposition of nearest and next-nearest-neighbor functions of the $\mathcal{E}_1$ irrep can boost the Chern number to values $\mathcal{C} > 1$ (see Ch. 6.1), which would result in a strongly enhanced quantum Hall response.

Let us summarize the main achievements of this section. We have presented an accurate, yet numerically efficient implementation of N-patch fRG, which facilitated calculations with Fermi surface resolutions well beyond the scope of other studies. Motivated by twisted transition metal dichalcogenides with hexagonal superlattices, we considered a toy model of spinless fermions on the triangular lattice, for which a plethora of charge and pairing instabilities could be uncovered. Moreover, our results have been carefully benchmarked with a truncated-unity fRG solver (see Ch. 6.1). Therefore, our work can be readily generalized to more realistic models for moiré materials with additional spin and/or orbital degrees of freedom.

4 Pseudofermion fRG for quantum spin systems

In this chapter, we concern ourselves with another flavor of the fRG approach: the pseudofermion functional renormalization group (pffRG) and its application to quantum spin systems. The method was pioneered by Reuther and Wölfle in Ref. [22] and, as its name suggests, is based on a representation of spin operators in terms of Abrikosov fermions. In sharp contrast to itinerant electron models, where the Hamiltonian typically contains both, a kinetic part characterized by some hopping amplitude t and interaction terms identified with some energy scale U, the pseudofermion Hamiltonian resembles the $t/U \to 0$ limit, where only quartic terms remain. Since the approximations presented in Sec. 2.3 were derived assuming weak coupling, the question arises to which extent a truncated and thus formally uncontrolled pffRG flow is able to capture the low-energy physics of strongly interacting spin models.

First insight into this issue can be gained from a closer inspection of the 1ℓ flow. The Katanin truncated pffRG equations boil down to a resummation of ladder diagrams both in the large-S (spin length) and large-N (as in in SU(N)) limit [70, 85], the former boosting classical order, whereas the latter promotes quantum fluctuations. In both cases the exact mean-field results are recovered. This indicates that, even for $S = 1/2$ and $N = 2$, some competition between magnetic instabilities and paramagnetic fluctuations, which hamper the spread of long-range correlations, is built into the pffRG flow. Note that feedback of the self-energy derivative into the flow of 2PR vertices is crucial for establishing this delicate balance, since flows without the Katanin truncation appear to be heavily biased towards magnetic instabilities [22].

Throughout the past decade 1ℓ-pffRG has, due to its versatility, been picked up by quite a number of research groups, which uttered in a surge of papers that concern themselves with a plethora of (frustrated) spin models in different spatial dimensions [22, 86–114]. Apart from the addition of 2ℓ corrections by Rück and Reuther [115], the assessment of systematic errors induced by truncating the pffRG flow, has, until recently [P1, 116], attracted much less attention. This is surprising insofar that $1/S$ ($1/N$) is usually not a small parameter such that the neglect of higher-order contributions is unjustified. Therefore, assuring self-consistency of the method becomes a mandatory task. As outlined in Sec. 2.3.3, the addition of multiloop corrections restores the equivalence between fRG and solutions of the self-consistent parquet approximation. For this reason, mfRG can be deemed a valid starting point for gauging the importance of higher-order corrections. The loop order hereby serves as a control parameter: convergence of the pseudofermion vertices with increasing ℓ instills confidence in the respective level of truncation and ensures that mutual screening effects between the 2PR channels are fully accounted for.

The remainder of this chapter is structured as follows. In Sec. 4.1 we provide a brief introduction to the intricate physics of frustrated quantum spins systems and the appearance of exotic spin liquid states therein. We proceed by reviewing the pseudofermion representation of spin operators in Sec. 4.2 and, following Refs. [117, 118], present an efficient parametrization of the vertices with regard to their real space, spin and frequency structure. At last, the numerical implementation of pffRG is extensively discussed and rounded off with a few computational examples in Sec. 4.5.

4.1 Frustrated magnetism and quantum spin liquids

Quantum spin models are Hamiltonians which describe interactions between the magnetic moments of firmly localized, yet strongly correlated electrons. At high temperatures, spins usually exhibit paramagnetic behavior, that is, the contributions from individual moments to the macroscopic magnetization cancel out. Upon cooling, however, they can behave cooperatively and give rise to long-range magnetic order. Frustrated quantum magnets, on the other hand, provide prominent exceptions to this rule. Here, the proliferation of magnetic correlations is impeded by strong fluctuations and the presence of competing ground states.

One recurring motif in frustrated magnets is the formation of so-called quantum spin liquids (QSLs), exotic states of matter in which the spins remain disordered even at the lowest temperature scales. A positive definition of QSLs goes to back to the resonating valence bond (RVB) state proposed by Anderson as an alternative ground state of spin-1/2 antiferromagnets [119]. In an RVB, the ground state wave function is composed of a massive superposition of singlet coverings of the lattice, so-called valence bond states, and thus shows an anomalously large degree of quantum entanglement. Moreover,

the RVB state features spin-1/2 quasiparticles called *spinons*, which can be generated by fractionalizing one of the singlets into two deconfined magnetic charges. These excitations can be gapped or gapless depending on the spatial extent of singlet bonds.

Over the years, the theory of quantum spin liquids has rapidly evolved, resulting in many excellent review papers such as Refs. [10, 120, 121]. However, the key ingredients of QSL states, namely competing interactions, frustration and strong quantum fluctuations, have impeded the development of a complete classification scheme [10]. In this vacuum, the consultancy of realistic models which are exactly solvable and thus provide invaluable insights into the physics of spin liquids are of paramount importance. A famous example of a Hamiltonian which precisely fits these criteria is Kitaev's honeycomb model [7], which, despite its simplicity, harbors both gapped and gapless QSL states. Here, spins fractionalize into Majorana fermions and a static $\mathbb{Z}_2$ gauge field. Their respective fate in the presence of tilted magnetic fields has recently been investigated in breakthrough experiments by Kasahara [8] and, concomitantly, by numerical calculations with different many-body techniques [122–125].

The revelation that the Kitaev model could be realized in Mott insulators with partially filled t_{2g} shells and strong spin-orbit coupling [126] has ignited a lasting interest in the quest for palpable spin liquid materials. This search is, of course, not strictly limited to pristine Kitaev materials, but includes triangular and kagome systems such as $EtMe_3Sb[Pd(dmit)_2]_2$ [127] and Herbertsmithite ($ZnCu_3(OH)_6Cl_2$) [128] besides three-dimensional spin-ice materials like $Ho_2Ti_2O_7$ and $Dy_2Ti_2O_7$ [129]. Despite the steady stream of additions to the family of QSL candidates, tackling the multifaceted spin Hamiltonians encountered therein has remained challenging, although many established numerical methods have become very sophisticated. The exponential growth of the Hilbert space dimension with system size has, so far, prohibited the study of large systems with exact diagonalization or DMRG, while the infamous sign problem restricts quantum Monte Carlo (QMC) simulations to relatively high temperatures. This calls for the development of novel theoretical tools to unravel the low-temperature phase diagrams of frustrated quantum magnets.

4.2 Abrikosov fermion representation of spin operators

We consider general spin-1/2 Hamiltonians of the form

$$\mathcal{H} = \frac{1}{2}\sum_{ij} J_{ij}^{\mu\nu} S_i^\mu S_j^\nu \,, \tag{4.1}$$

where S_i^μ denotes the $\mu \in \{x, y, z\}$ component of the $\mathfrak{su}(2)$[1] spin operator on lattice site i. The prefactor $1/2$ ensures that each bond (i, j) contributes to the total energy only once. We assume that the couplings $J_{ij}^{\mu\nu}$ (usually $J_{ii}^{\mu\nu} = 0$) between sites i and j are real, such that the spin Hamiltonian is hermitian and time-reversal symmetric [117]. Moreover, we impose

$$J_{ij}^{\mu\nu} = \xi J_{ji}^{\mu\nu} = \xi J_{ij}^{\nu\mu} \,. \tag{4.2}$$

Here, $\xi \in \{\pm 1\}$ is a $\mathbb{Z}_2$ variable such that $J_{ij}^{\mu\nu}$ can be symmetric or antisymmetric in spin space and either break or preserve inversion symmetry on individual bonds. This Hamiltonian already captures a plethora of different spin models including, for example, SU(2) symmetric Heisenberg interactions for which $J_{ij}^{\mu\nu}$ evaluates to $J_{ij}^{\mu\nu} = J_{ij}\delta^{\mu\nu}$.

In order to apply the fRG framework developed in Ch. 2, the spin operators are expressed in terms of complex pseudofermions [130] as

$$S_i^\mu = \frac{1}{2} c_{i\alpha}^\dagger \sigma_{\alpha\beta}^\mu c_{i\beta} \,, \tag{4.3}$$

where equal spin indices $\alpha \in \{\uparrow, \downarrow\}$ are summed over. Here, $\sigma_{\alpha\beta}^\mu$ are the elements of the Pauli matrix $\boldsymbol{\sigma}^\mu$. Introducing the matrix operator

$$\boldsymbol{F}_i = \begin{pmatrix} c_{i\uparrow} & -c_{i\downarrow}^\dagger \\ c_{i\downarrow} & c_{i\uparrow}^\dagger \end{pmatrix} , \tag{4.4}$$

S_i^μ can alternatively be represented as

$$S_i^\mu = \frac{1}{2}\mathrm{Tr}[\boldsymbol{F}_i^\dagger \boldsymbol{\sigma}^\mu \boldsymbol{F}_i \,] \,. \tag{4.5}$$

[1] $\mathfrak{su}(2)$ denotes the spin algebra.

Importantly, S_i^μ is invariant under $\boldsymbol{F}_i \to \boldsymbol{F}_i \boldsymbol{T}_i$, where $\boldsymbol{T}_i \in \mathrm{SU}(2)$ is a local *gauge transformation*. Note that in contrast to a physical symmetry, which would be implemented by left multiplication with some unitary matrix $\boldsymbol{U}^\dagger$, the gauge transformation is defined by right multiplication, instead. A general symmetry, in the sense that it leaves the Hamiltonian unchanged, can therefore act both globally as well as in the gauge sector: $\boldsymbol{F}_i \to \boldsymbol{U}^\dagger \boldsymbol{F}_i \boldsymbol{T}_i$. Guided the pioneering work of Wen [9], this observation has led to the notion of projective symmetry groups (PSGs)[2] and *quantum order*, which can be used to classify mean-field ansätze for spin liquid phases.

Although the Pauli matrices $\boldsymbol{\sigma}^\mu$ ensure that the $\mathfrak{su}(2)$ commutator stays intact, Eq. (4.5) does not yet suffice to faithfully reproduce the original spin model. This is because the dimension $d = 2 \times 2 = 4$ of the local pseudofermion Hilbert space is larger than that of the spin-1/2 representation ($d = 2$). Two of these states, namely $|n_\uparrow, n_\downarrow\rangle = |0, 0\rangle$ and $|n_\uparrow, n_\downarrow\rangle = |1, 1\rangle$, where n_α denotes the spin up (down) occupation are unphysical, since they corresponds to magnetic vacancies which are absent in Eq. (4.1). Their existence requires an additional half-filling constraint

$$c_{i\alpha}^\dagger c_{i\alpha} = 1\,, \tag{4.6}$$

to be fulfilled on every lattice site in order to render the pseudofermion model isomorphic to the spin-1/2 Hamiltonian. In the context of pffRG, several ways to cope with this local constraint have been suggested:

(a) An exact fulfillment in a field-theoretical setup such as fRG could, for example, be accomplished by introducing a functional δ-distribution on the level of the fermionic action [131]. In consequence, one would need to keep track of an additional flowing constraint field, which complicates the fRG analysis tremendously. For this reason, we refrain from employing this approach.

(b) At *finite temperatures*, unphysical contributions to the partition function can be projected out by means of an imaginary valued chemical potential $\mu = i\frac{\pi T}{2}$ as suggested by Popov and Fedotov [132]. For $T \to 0$ the chemical potential vanishes, which motivates its neglect at zero temperature. Indeed, as has been demonstrated in Ref. [133], pseudofermion fRG results obtained with and without the Popov-Fedotov constraint coincide in the low temperature regime. Unfortunately, μ breaks the hermitian symmetry of the Hamiltonian, which makes its implementation comparably expensive [22].

(c) At *zero temperature*, the constraint is usually not exactly enforced, but holds on average due to local particle-hole symmetry of the pseudofermion Hamiltonian [P1, 117]. As will be exemplified in Sec. 4.5.2, the magnitude of fluctuations around the average $\langle c_{i\alpha}^\dagger c_{i\alpha}\rangle = 1$ can be further reduced by means of local level repulsion terms $A S_i^\mu S_i^\mu$ which, for $A < 0$, swell the gap between physical and unphysical states proportional to $|A|$ [85, 116]. In principle, one could achieve the same by employing a Lagrange multiplier $\lambda(n_i - 1)^2$ on every site, where n_i denotes the local pseudofermion density. Yet, this approach manifestly breaks particle-hole symmetry and is therefore numerically inefficient (see Sec. 4.3.4).

In the following, our focus lies on the implementation of local half-filling as outlined in (c), which restricts us to quantum spin models in the zero temperature limit.

4.3 Parametrization of pseudofermion vertices

In its pseudofermion representation, the general spin Hamiltonian Eq. (4.1) computes to

$$\mathcal{H} = \frac{1}{8}\sum_{ij} J_{ij}^{\mu\nu}\sigma_{\alpha\beta}^\mu \sigma_{\gamma\delta}^\nu c_{i\alpha}^\dagger c_{j\gamma}^\dagger c_{j\delta} c_{i\beta}\,, \tag{4.7}$$

that is, it does not comprise a kinetic part and assumes a purely quartic form instead. The bare propagator G_0 is therefore particularly simple and reads

$$G_0(x_1'|x_1) = \frac{1}{i\omega_1} \times \beta\delta_{i_1' i_1}\delta_{\alpha_1'\alpha_1}\delta_{\omega_1'\omega_1} \equiv G_0(\omega_1) \times \beta\delta_{i_1' i_1}\delta_{\alpha_1'\alpha_1}\delta_{\omega_1'\omega_1}\,, \tag{4.8}$$

i.e., G_0 is diagonal in all fermionic indices $x_1 = (i_1, \alpha_1, \omega_1)$, where lattice sites are denoted by i_1, spin indices by α_1 and Matsubara frequencies by ω_1, respectively. Following the initial proposal

[2] A PSG combines the symmetry group of a QSL with its invariant gauge group, i.e. the set of pure gauge transformations which leave a given pseudfermion mean-field ansatz unchanged.

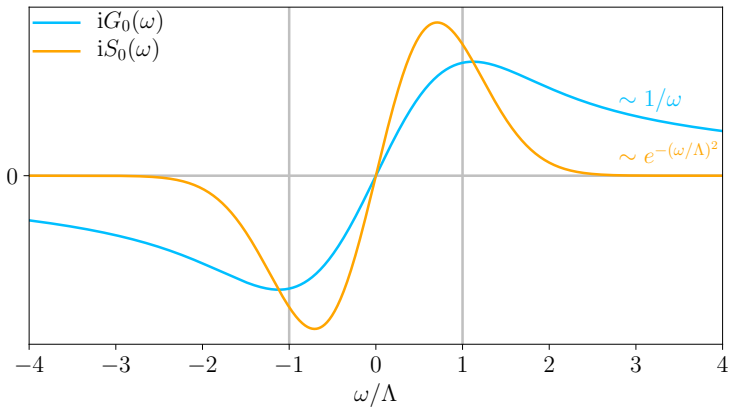

Figure 4.1: Sketch of scale-dependent bare propagators. The regularized bare propagator $G_0(\omega)$ (blue line) peaks for frequencies close to the RG scale Λ and decays algebraically for $|\omega| \gg \Lambda$. The bare single-scale propagator $S_0(\omega) = -\frac{d}{d\Lambda} G_0(\omega)$ displays even sharper features close to $|\omega| = \Lambda$ and falls off exponentially for large $|\omega|/\Lambda$. Both propagators are antisymmetric with respect to the origin.

by Reuther [22], the pffRG cutoff has commonly been implemented via a Heavyside θ-function: $G_0^\Lambda(\omega) = \theta(|\omega| - \Lambda) G_0(\omega)$. This way, fluctuations with $|\omega| < \Lambda$ are sharply suppressed. Although the sharp cutoff helps to facilitate analytical calculations [70, 85], θ is not a smooth function, which has prohibited the usage of higher-order numerical integration methods. To circumvent this issue, we employ a Gaussian regulator

$$G_0^\Lambda(\omega) = \left(1 - e^{-\omega^2/\Lambda^2}\right) G_0(\omega)\,, \tag{4.9}$$

as shown in Fig. 4.1. Notably, $G_0^\Lambda(\omega)$ exhibits an algebraic fall-off with $1/\omega$ for frequencies $|\omega| \gg \Lambda$.

Our parametrization of pseudofermion vertices is largely based on the thorough symmetry analysis performed in Ref. [117]. The general strategy unfolds in two steps: First, symmetry transformations are verified on the level of the action and their validity is subsequently imposed on the level of 1PI/2PR vertices. In a second step, one derives a set of constraints that they ought to obey. Equipped with these prerequisites, the general expressions for the self-energy loop and channel specific bubble functions from Sec. 2.2 can be drastically simplified.

4.3.1 Local flow equations

The first invariance we concern ourselves with, is the local U(1) gauge redundancy of the pseudofermion action, i.e. Grassmann fields are assigned a local phase ϕ_j as

$$\begin{aligned} \psi_{j\alpha} &\to e^{i\phi_j} \psi_{j\alpha} \\ \bar{\psi}_{j\alpha} &\to e^{-i\phi_j} \bar{\psi}_{j\alpha}\,, \end{aligned} \tag{4.10}$$

which leaves single spin operators S_j^μ unchanged. Due to the absence of any kinetic term in Eq. (4.7), this implies conservation of the particle number per site and thus demands (bi-)locality of the propagators and 1PI vertices [117]. In other words, Σ (as well as G) is diagonal in site indices

$$\Sigma(x_1'|x_1) = \Sigma_{i_1}(\tilde{x}_1'|\tilde{x}_1) \times \delta_{i_1' i_1}\,, \tag{4.11}$$

whereas Γ (as well as γ_c) is subject to the condition

$$\Gamma(x_1', x_2'|x_1, x_2) = \Gamma^{=}_{i_1 i_2}(\tilde{x}_1', \tilde{x}_2'|\tilde{x}_1, \tilde{x}_2) \times \delta_{i_1' i_1} \delta_{i_2' i_2} + \Gamma^{\times}_{i_1 i_2}(\tilde{x}_1', \tilde{x}_2'|\tilde{x}_1, \tilde{x}_2) \times \delta_{i_1' i_2} \delta_{i_2' i_1}\,. \tag{4.12}$$

On the right-hand side of these equations, dependencies on the lattice sites have been made explicit such that $\tilde{x}_i$ solely comprises frequency and spin indices. In pffRG, one usually assumes that all sites are symmetry equivalents of one another and, consequently, the self-energy and propagators are spatially uniform $\Sigma_{i_1}(\tilde{x}_1'|\tilde{x}_1) = \Sigma(\tilde{x}_1'|\tilde{x}_1)$. For the models considered in this work, this conjecture is indeed fulfilled. The components $\Gamma^{=}$ and $\Gamma^{\times}$ correspond to the two possibilities of connecting incoming and outgoing fermions at a generic two-particle vertex: lattice indices are either preserved along two parallel ($=$) or two crossing lines ($\times$) (see Fig. 4.2). Notably, crossing symmetry implies that

$$\Gamma^{\times}_{i_1 i_2}(\tilde{x}_1', \tilde{x}_2'|\tilde{x}_1, \tilde{x}_2) = -\Gamma^{=}_{i_1 i_2}(\tilde{x}_2', \tilde{x}_1'|\tilde{x}_1, \tilde{x}_2) = -\Gamma^{=}_{i_2 i_1}(\tilde{x}_1', \tilde{x}_2'|\tilde{x}_2, \tilde{x}_1)\,, \tag{4.13}$$

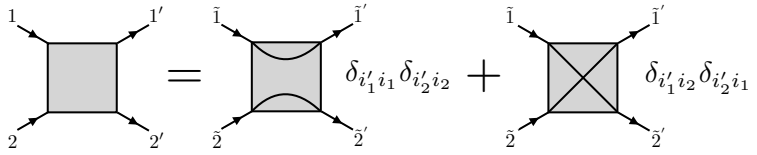

Figure 4.2: Bilocal parametrization of the two-particle vertex. Due to local U(1) symmetry, Γ decomposes into a parallel ($\Gamma^{=}$) and a crossed component ($\Gamma^{\times}$), corresponding to the two possibilities to connect in and outgoing legs. Here, lattice indices are preserved along single fermion lines. The two vertices $\Gamma^{=}$ and $\Gamma^{\times}$ are related to one another by crossing symmetry.

which allows us to formulate the flow equations entirely in terms of $\Gamma^{=}$ or $\Gamma^{\times}$[3]. Applying this parametrization to the self-energy loop we find

$$\begin{aligned}
[\Gamma \circ G]_\Sigma &= \sum_{x_2', x_2} \left[\Gamma^{=}_{i_1 i_2}(\tilde{x}_1', \tilde{x}_2'|\tilde{x}_1, \tilde{x}_2)\delta_{i_1' i_1}\delta_{i_2' i_2} - \tilde{\Gamma}^{=}_{i_1 i_2}(\tilde{x}_2', \tilde{x}_1'|\tilde{x}_1, \tilde{x}_2)\delta_{i_1' i_2}\delta_{i_2' i_1}\right] G(\tilde{x}_2|\tilde{x}_2')\delta_{i_2' i_2} \\
&= \sum_{\tilde{x}_2', \tilde{x}_2} \sum_{i_2} \left[\Gamma^{=}_{i_1 i_2}(\tilde{x}_1', \tilde{x}_2'|\tilde{x}_1, \tilde{x}_2)\delta_{i_1' i_1}\delta_{i_2 i_2} - \tilde{\Gamma}^{=}_{i_1 i_2}(\tilde{x}_2', \tilde{x}_1'|\tilde{x}_1, \tilde{x}_2)\delta_{i_1' i_2}\delta_{i_2 i_1}\right] G(\tilde{x}_2|\tilde{x}_2') \\
&= \sum_{\tilde{x}_2', \tilde{x}_2} \left[\sum_j \Gamma^{=}_{i_1 j}(\tilde{x}_1', \tilde{x}_2'|\tilde{x}_1, \tilde{x}_2) - \tilde{\Gamma}^{=}_{i_1 i_1}(\tilde{x}_2', \tilde{x}_1'|\tilde{x}_1, \tilde{x}_2)\right] G(\tilde{x}_2|\tilde{x}_2') \times \delta_{i_1' i_1} \,. \qquad (4.14)
\end{aligned}$$

Note that we have highlighted vertex components $\Gamma^{=}$ which have been obtained through Eq. (4.13) as $\tilde{\Gamma}^{=}$. This level of book keeping becomes essential for the formulation of the multiloop pffRG flow, where Γ is occasionally substituted with 2PR contributions γ_c. To compute the mfRG flow for the self-energy, for example, t-irreducible vertex contributions need to be inserted into the self-energy loop in order to compute $\dot{\Sigma}_1$. This is important insofar that γ_t and γ_u are exchanged by crossing symmetry, giving rise to the identities

$$\begin{aligned}
\gamma^{\times}_{t,i_1 i_2}(\tilde{x}_1', \tilde{x}_2'|\tilde{x}_1, \tilde{x}_2) &= -\gamma^{=}_{u,i_1 i_2}(\tilde{x}_2', \tilde{x}_1'|\tilde{x}_1, \tilde{x}_2) = -\gamma^{=}_{u,i_2 i_1}(\tilde{x}_1', \tilde{x}_2'|\tilde{x}_2, \tilde{x}_1) \\
\gamma^{\times}_{u,i_1 i_2}(\tilde{x}_1', \tilde{x}_2'|\tilde{x}_1, \tilde{x}_2) &= -\gamma^{=}_{t,i_1 i_2}(\tilde{x}_2', \tilde{x}_1'|\tilde{x}_1, \tilde{x}_2) = -\gamma^{=}_{t,i_2 i_1}(\tilde{x}_1', \tilde{x}_2'|\tilde{x}_2, \tilde{x}_1) \,. \qquad (4.15)
\end{aligned}$$

In similar fashion, one can bring the general bubble functions B_c into their bilocal form, which likewise decomposes into a parallel and a crossed component. Here, we present results for the former and dispense with presenting the explicit calculation. The s bubble only operates on crossing symmetric objects like Γ, γ_s or $\gamma_{\bar{s}}$ and projections between the parallel and crossed components thus do not need to be especially accounted for, resulting in the compact expression

$$B^{=}_{s,i_1 i_2}(\tilde{x}_1', \tilde{x}_2'|\tilde{x}_1, \tilde{x}_2) = -\sum_{\tilde{x}_3', \tilde{x}_4', \tilde{x}_3, \tilde{x}_4} \Gamma^{=}_{i_1 i_2}(\tilde{x}_3', \tilde{x}_4'|\tilde{x}_1, \tilde{x}_2) G(\tilde{x}_3|\tilde{x}_3') G(\tilde{x}_4|\tilde{x}_4') \Gamma^{=}_{i_1 i_2}(\tilde{x}_1', \tilde{x}_2'|\tilde{x}_3, \tilde{x}_4) \,. \qquad (4.16)$$

The bubble function for the direct particle-hole channel, in contrast, contains contributions affected by [Eqs. (4.15)], such that further book keeping is required. Using the $\tilde{\Gamma}^{=}$ notation introduced for the self-energy loop, $B^{=}_{t,i_1 i_2}$ computes to

$$\begin{aligned}
B^{=}_{t,i_1 i_2}(\tilde{x}_1', \tilde{x}_2'|\tilde{x}_1, \tilde{x}_2) = &+ \sum_{\tilde{x}_3', \tilde{x}_4', \tilde{x}_3, \tilde{x}_4} \sum_j \Gamma^{=}_{i_1 j}(\tilde{x}_1', \tilde{x}_4'|\tilde{x}_1, \tilde{x}_3) G(\tilde{x}_3|\tilde{x}_3') G(\tilde{x}_4|\tilde{x}_4') \Gamma^{=}_{j i_2}(\tilde{x}_3', \tilde{x}_2'|\tilde{x}_4, \tilde{x}_2) \\
&- \sum_{\tilde{x}_3', \tilde{x}_4', \tilde{x}_3, \tilde{x}_4} \Gamma^{=}_{i_1 i_2}(\tilde{x}_1', \tilde{x}_4'|\tilde{x}_1, \tilde{x}_3) G(\tilde{x}_3|\tilde{x}_3') G(\tilde{x}_4|\tilde{x}_4') \tilde{\Gamma}^{=}_{i_2 i_2}(\tilde{x}_3', \tilde{x}_2'|\tilde{x}_2, \tilde{x}_4) \\
&- \sum_{\tilde{x}_3', \tilde{x}_4', \tilde{x}_3, \tilde{x}_4} \tilde{\Gamma}^{=}_{i_1 i_1}(\tilde{x}_1', \tilde{x}_4'|\tilde{x}_3, \tilde{x}_1) G(\tilde{x}_3|\tilde{x}_3') G(\tilde{x}_4|\tilde{x}_4') \Gamma^{=}_{i_1 i_2}(\tilde{x}_3', \tilde{x}_2'|\tilde{x}_4, \tilde{x}_2) \,. \qquad (4.17)
\end{aligned}$$

For the calculation of the u bubble, only parallel components need to be invoked and we can straightforwardly calculate $B^{=}_{u,i_1 i_2}$, which yields

$$B^{=}_{u,i_1 i_2}(\tilde{x}_1', \tilde{x}_2'|\tilde{x}_1, \tilde{x}_2) = -\sum_{\tilde{x}_3', \tilde{x}_4', \tilde{x}_3, \tilde{x}_4} \Gamma^{=}_{i_1 i_2}(\tilde{x}_3', \tilde{x}_2'|\tilde{x}_1, \tilde{x}_4) G(\tilde{x}_3|\tilde{x}_3') G(\tilde{x}_4|\tilde{x}_4') \Gamma^{=}_{i_1 i_2}(\tilde{x}_1', \tilde{x}_4'|\tilde{x}_3, \tilde{x}_2) \,. \qquad (4.18)$$

[3] We choose $\Gamma^{=}$.

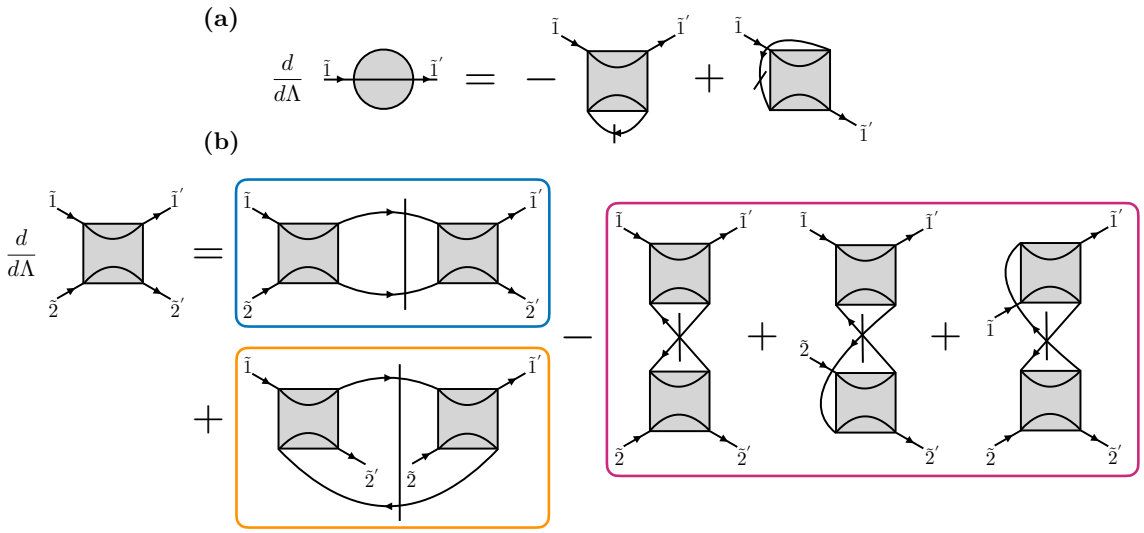

Figure 4.3: (Bi-)local pffRG flow equations in 1ℓ truncation. (a) The self-energy flow decomposes into a non-local Fock and a local Hartree term (the first and second diagram, respectively). Slashed lines denote single-scale propagators. **(b)** The flow of the two-particle vertex can be entirely expressed in terms of its parallel component. Notably, t-reducible contributions to Γ (magenta box) fall apart into three terms, the first of which is the RPA diagram, responsible for the proliferation of magnetic correlations over the lattice. Here, a pair of slashed fermion lines corresponds to $\frac{d}{d\Lambda}(G \times G)$.

Having parametrized the bubble functions, one can formulate the pffRG flow equations in terms of bilocal vertices, as diagrammatically shown in Fig. 4.3 for $\ell = 1$. Remarkably, only the first term in the t bubble, the RPA diagram, contains a lattice summation and is therefore responsible for the proliferation of (magnetic) correlations. This argument is further supported by the large-S generalization of pffRG, wherein the RPA loop receives an additional sum over fermion flavors [85] and thus a prefactor proportional to S. Other contributions to the flow are on the order of unity, instead. Instabilities in the t channel are therefore prominently associated with long-range magnetic order.

4.3.2 Efficient evaluation of spin sums

We now turn to the simplification of the spin dependence of the vertices. To keep the notation concise, we refrain from writing out superscripts for the parallel vertex component and, instead, assume $\Gamma_{i_1 i_2} = \Gamma^{=}_{i_1 i_2}$ from now on. In agreement with Ref. [117], we expand the vertices in terms of the basis elements of the $\mathfrak{su}(2)$ spin-1/2 representation, i.e. in Pauli matrices, and add 2×2 unities, which cover density fluctuations. The self-energy (and propagators) then assume the general form

$$\Sigma(\tilde{x}_1'|\tilde{x}_1) = \sum_{\mu} \Sigma^{\mu}(\omega_1'|\omega_1)\sigma^{\mu}_{\alpha_1'\alpha_1}\,, \tag{4.19}$$

with $\mu \in \{d, x, y, z\}$, whereas bilocal two-particle vertices decompose into

$$\Gamma_{i_1 i_2}(\tilde{x}_1', \tilde{x}_2'|\tilde{x}_1, \tilde{x}_2) = \sum_{\mu,\nu} \Gamma^{\mu\nu}_{i_1 i_2}(\omega_1', \omega_2'|\omega_1, \omega_2)\sigma^{\mu}_{\alpha_1'\alpha_1}\sigma^{\nu}_{\alpha_2'\alpha_2}\,. \tag{4.20}$$

Here, $\boldsymbol{\sigma}^d = \mathbb{1}$. For highly symmetric spin models, such as spin-rotation invariant Heisenberg Hamiltonians, some functions $\Gamma^{\mu\nu}_{i_1 i_2}$ remain identical to zero and can thus be neglected. Here, however, we keep them for the sake of generality. At this point, we can make use of the hermiticity and time-reversal symmetry of the general spin Hamiltonian in Eq. (4.1), which impose that single-particle objects are diagonal in spin space [117]. In the expansion of the self-energy, we therefore only need to consider density contributions.

Plugging the spin parametrization into the local self-energy loop Eq. (4.11) therefore yields

$$[\Gamma \circ G]_{\Sigma} = \frac{1}{\beta^2} \sum_{\omega_2', \omega_2} \left[2 \sum_{j} \Gamma^{dd}_{i_1 j}(\omega_1', \omega_2'|\omega_1, \omega_2) - \sum_{\mu} \tilde{\Gamma}^{\mu\mu}_{i_1 i_1}(\omega_2', \omega_1'|\omega_1, \omega_2) \right] G(\omega_2|\omega_2') \times \delta_{i_1' i_1}\delta_{\alpha_1'\alpha_1}\,, \tag{4.21}$$

that is, only vertex functions with equal spin directions $\mu = \nu$ contribute. Note that we have dropped the d superscript over the propagator G for brevity. To compress the respective algebraic expression for the 2PR bubbles, we introduce the rank-4 doublet and rank-5 triplet tensors, denoted by Π_2 and Π_3 respectively, and defined as

$$\begin{aligned}\Pi^{\mu\nu}_{2,\alpha'_1\alpha_1} &\equiv \sum_{\alpha_2} \sigma^{\mu}_{\alpha'_1\alpha_2}\sigma^{\nu}_{\alpha_2\alpha_1} \\ \Pi^{\mu\nu\tau}_{3,\alpha'_1\alpha_1} &\equiv \sum_{\alpha'_2,\alpha_2} \sigma^{\mu}_{\alpha'_1\alpha'_2}\sigma^{\nu}_{\alpha'_2\alpha_2}\sigma^{\tau}_{\alpha_2\alpha_1}\,.\end{aligned} \tag{4.22}$$

The spin-parametrized bubble functions then read

$$\begin{aligned}B_{s,i_1i_2}(\tilde{x}'_1,\tilde{x}'_2|\tilde{x}_1,\tilde{x}_2) =& -\frac{1}{\beta^4}\sum_{\omega'_3,\omega'_4,\omega_3,\omega_4}\sum_{\mu,\nu,\tau,\kappa}\Pi^{\tau\mu}_{2,\alpha'_1\alpha_1}\Pi^{\kappa\nu}_{2,\alpha'_2\alpha_2} \\ &\times \Gamma^{\mu\nu}_{i_1i_2}(\omega'_3,\omega'_4|\omega_1,\omega_2)G(\omega_3|\omega'_3)G(\omega_4|\omega'_4)\Gamma^{\tau\kappa}_{i_1i_2}(\omega'_1,\omega'_2|\omega_3,\omega_4) \\ B_{t,i_1i_2}(\tilde{x}'_1,\tilde{x}'_2|\tilde{x}_1,\tilde{x}_2) =& +\frac{2}{\beta^4}\sum_{\omega'_3,\omega'_4,\omega_3,\omega_4}\sum_{\mu,\nu,\kappa}\sum_{j}\sigma^{\mu}_{\alpha'_1\alpha_1}\sigma^{\kappa}_{\alpha'_2\alpha_2} \\ &\times \Gamma^{\mu\nu}_{i_1j}(\omega'_1,\omega'_4|\omega_1,\omega_3)G(\omega_3|\omega'_3)G(\omega_4|\omega'_4)\Gamma^{\nu\kappa}_{ji_2}(\omega'_3,\omega'_2|\omega_4,\omega_2) \\ &-\frac{1}{\beta^4}\sum_{\omega'_3,\omega'_4,\omega_3,\omega_4}\sum_{\mu,\nu,\tau,\kappa}\sigma^{\mu}_{\alpha'_1\alpha_1}\Pi^{\kappa\nu\tau}_{3,\alpha'_2\alpha_2} \\ &\times \Gamma^{\mu\nu}_{i_1i_2}(\omega'_1,\omega'_4|\omega_1,\omega_3)G(\omega_3|\omega'_3)G(\omega_4|\omega'_4)\tilde{\Gamma}^{\tau\kappa}_{i_2i_2}(\omega'_3,\omega'_2|\omega_2,\omega_4) \\ &-\frac{1}{\beta^4}\sum_{\omega'_3,\omega'_4,\omega_3,\omega_4}\sum_{\mu,\nu,\tau,\kappa}\Pi^{\mu\tau\nu}_{3,\alpha'_1\alpha_1}\sigma^{\kappa}_{\alpha'_2\alpha_2} \\ &\times \tilde{\Gamma}^{\mu\nu}_{i_1i_1}(\omega'_1,\omega'_4|\omega_3,\omega_1)G(\omega_3|\omega'_3)G(\omega_4|\omega'_4)\Gamma^{\tau\kappa}_{i_1i_2}(\omega'_3,\omega'_2|\omega_4,\omega_2) \\ B_{u,i_1i_2}(\tilde{x}'_1,\tilde{x}'_2|\tilde{x}_1,\tilde{x}_2) =& -\frac{1}{\beta^4}\sum_{\omega'_3,\omega'_4,\omega_3,\omega_4}\sum_{\mu,\nu,\tau,\kappa}\Pi^{\tau\mu}_{2,\alpha'_1\alpha_1}\Pi^{\nu\kappa}_{2,\alpha'_2\alpha_2} \\ &\times \Gamma^{\mu\nu}_{i_1i_2}(\omega'_3,\omega'_2|\omega_1,\omega_4)G(\omega_3|\omega'_3)G(\omega_4|\omega'_4)\tilde{\Gamma}^{\tau\kappa}_{i_1i_2}(\omega'_1,\omega'_4|\omega_3,\omega_2)\,.\end{aligned} \tag{4.23}$$

To obtain a specific $B^{\mu\nu}_{c,i_1i_2}$, one can yet again expand the doublet and triplet tensors in $\boldsymbol{\sigma}^{\mu}$ and exploit that the Pauli matrices, in contrast to the Kronecker delta, are traceless, i.e. $\mathrm{Tr}(\boldsymbol{\sigma}^{\mu}) = 0$ for $\mu \neq d$. Without loss of generality (for Π_3 one proceeds analogously), consider $\Pi^{\mu\nu}_2 = \sum_\tau a_\tau \boldsymbol{\sigma}^{\tau}$, which implies

$$a_d = \frac{1}{2}\mathrm{Tr}(\Pi^{\mu\nu}_2)\,. \tag{4.24}$$

Moreover, we have the identity $\boldsymbol{\sigma}^{\mu}\boldsymbol{\sigma}^{\nu} = \delta^{\mu\nu}\mathbb{1} + i\epsilon_{\mu\nu\tau}\boldsymbol{\sigma}^{\tau}$, where ϵ is the Levi-Civita symbol. From this equation, we are able to obtain the coefficient a_τ (with $\tau \neq d$) as simple as

$$a_\tau = \frac{1}{2}\mathrm{Tr}\left[(\Pi^{\mu\nu}_2 - a_d\mathbb{1})\boldsymbol{\sigma}^{\tau}\right]\,, \tag{4.25}$$

such that the right-hand side of each bubble function can ultimately be decomposed into contributions to specific components $B^{\mu\nu}_{c,i_1i_2}$. Using a computer algebra program to perform these algebraic manipulations for a given model, one can straightforwardly derive efficient, spin-parametrized pffRG flow equations for the general Hamiltonian in Eq. (4.1).

4.3.3 Asymptotic frequency parametrization

The last step in reducing the complexity of the flow equations amounts to exploiting frequency (energy) conservation by virtue of time translation invariance [117], that is, we impose

$$\Sigma(\omega'_1|\omega_1) = \Sigma(\omega_1) \times \beta\delta_{\omega'_1,\omega_1} \tag{4.26}$$

on the self-energy and propagators and

$$\Gamma^{\mu\nu}_{i_1i_2}(\omega'_1,\omega'_2|\omega_1,\omega_2) = \Gamma^{\mu\nu}_{i_1i_2}(\omega_s,\omega_t,\omega_u) \times \beta\delta_{\omega'_1+\omega'_2,\omega_1+\omega_2} \tag{4.27}$$

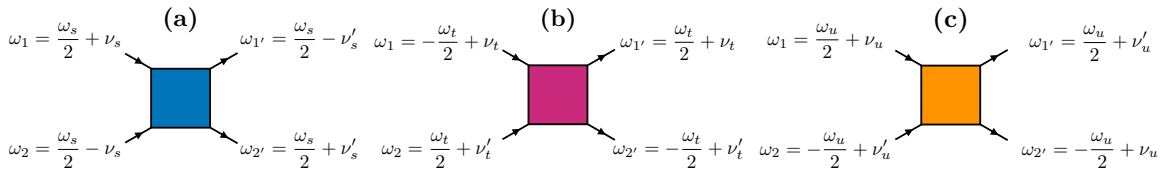

Figure 4.4: Natural frequency parametrization of 2PR vertices. Each channel γ_c is associated with one bosonic transfer frequency ω_c and two fermionic frequencies ν_c and ν'_c. Our convention is chosen such that ν_c (ν'_c) exclusively appears as an argument of the left (right) vertex object in the respective bubble function B_c. Moreover, the general vertex symmetries Eq. (4.36) assume a particularly convenient form when projected into γ_c.

on two-particle vertices, where we introduced the *transfer frequencies*

$$\begin{aligned}\omega_s &= \omega'_1 + \omega'_2\\ \omega_t &= \omega'_1 - \omega_1\\ \omega_u &= \omega'_1 - \omega_2\,.\end{aligned} \tag{4.28}$$

This way, only one instead of two frequency arguments for one-particle objects and three instead of four frequencies for two-particle objects need to be accounted for. So far, we kept our derivations applicable also to finite temperatures for the sake of generality. When approaching $T = 0$, however, the spectrum of Matsubara frequencies becomes continuous and, consequently, Matsubara sums are promoted to integrals over the imaginary axis. Since zero temperature is the preferred regime of operation for pffRG because thermal fluctuations which could boost the occupation of unphysical states are frozen out, we switch to the integral notation from now on. The self-energy loop thus simplifies to

$$[\Gamma \circ G]_\Sigma = \int dv \left[2\sum_j \Gamma^{dd}_{i_1 j}(\omega_1 + v, 0, \omega_1 - v) - \sum_\mu \tilde{\Gamma}^{\mu\mu}_{i_1 i_1}(\omega_1 + v, v - \omega_1, 0) \right] G(v)\delta_{i'_1 i_1}\delta_{\alpha'_1\alpha_1}\delta_{\omega'_1,\omega_1}\,. \tag{4.29}$$

Note that using the simplified self-energy loop (or 2PR bubbles) to derive flow equations for 1PI vertices requires to parametrize the respective left-hand side of the equation in similar terms. This procedure cancels not only the leftover Kronecker deltas or Pauli matrices, but also produces a prefactor 2π, which needs to be included in an explicit implementation. Using energy conservation, the spin parametrized bubbles Eq. (4.23) evaluate to

$$\begin{aligned}
B_{s,i_1 i_2}(\tilde{x}'_1, \tilde{x}'_2|\tilde{x}_1, \tilde{x}_2) = &-\int dv \sum_{\mu,\nu,\tau,\kappa} \Pi^{\tau\mu}_{2,\alpha'_1\alpha_1}\Pi^{\kappa\nu}_{2,\alpha'_2\alpha_2}\delta_{\omega'_1+\omega'_2,\omega_1+\omega_2}\\
&\times \Gamma^{\mu\nu}_{i_1 i_2}(\omega_s, v-\omega_1, v-\omega_2)G(v)G(\omega_s - v)\Gamma^{\tau\kappa}_{i_1 i_2}(\omega_s, \omega'_1 - v, \omega'_1 - s + v)\\
B_{t,i_1 i_2}(\tilde{x}'_1, \tilde{x}'_2|\tilde{x}_1, \tilde{x}_2) = &+2\int dv \sum_{\mu,\nu,\kappa}\sum_j \sigma^{\mu}_{\alpha'_1\alpha_1}\sigma^{\kappa}_{\alpha'_2\alpha_2}\delta_{\omega'_1+\omega'_2,\omega_1+\omega_2}\\
&\times \Gamma^{\mu\nu}_{i_1 j}(\omega'_1 - \omega_t + v, \omega_t, \omega'_1 - v)G(v)G(v-\omega_t)\Gamma^{\nu\kappa}_{j i_2}(\omega'_2 + v, \omega_t, v - \omega_2)\\
&-\int dv \sum_{\mu,\nu,\tau,\kappa} \sigma^{\mu}_{\alpha'_1\alpha_1}\Pi^{\kappa\nu\tau}_{3,\alpha'_2\alpha_2}\delta_{\omega'_1+\omega'_2,\omega_1+\omega_2}\\
&\times \Gamma^{\mu\nu}_{i_1 i_2}(\omega'_1 - \omega_t + v, \omega_t, \omega'_1 - v)G(v)G(v-\omega_t)\tilde{\Gamma}^{\tau\kappa}_{i_2 i_2}(\omega'_2 + v, v - \omega_2, \omega_t)\\
&-\int dv \sum_{\mu,\nu,\tau,\kappa} \Pi^{\mu\tau\nu}_{3,\alpha'_1\alpha_1}\sigma^{\kappa}_{\alpha'_2\alpha_2}\delta_{\omega'_1+\omega'_2,\omega_1+\omega_2}\\
&\times \tilde{\Gamma}^{\mu\nu}_{i_1 i_1}(\omega'_1 - \omega_t + v, \omega'_1 - v, \omega_t)G(v)G(v-\omega_t)\Gamma^{\tau\kappa}_{i_1 i_2}(\omega'_2 + v, \omega_t, v - \omega_2)\\
B_{u,i_1 i_2}(\tilde{x}'_1, \tilde{x}'_2|\tilde{x}_1, \tilde{x}_2) = &-\int dv \sum_{\mu,\nu,\tau,\kappa} \Pi^{\tau\mu}_{2,\alpha'_1\alpha_1}\Pi^{\nu\kappa}_{2,\alpha'_2\alpha_2}\delta_{\omega'_1+\omega'_2,\omega_1+\omega_2}\\
&\times \Gamma^{\mu\nu}_{i_1 i_2}(\omega'_2 + v, v-\omega_1, \omega_u)G(v)G(v-\omega_u)\tilde{\Gamma}^{\tau\kappa}_{i_1 i_2}(\omega'_1 - \omega_u + v, \omega'_1 - v, \omega_u)\,.
\end{aligned} \tag{4.30}$$

Remarkably, every transfer frequency ω_c is intimately tied to one of the 2PR bubbles and describes the energy transmitted through the internal loop. The frequency ω_s, for example, only appears in the

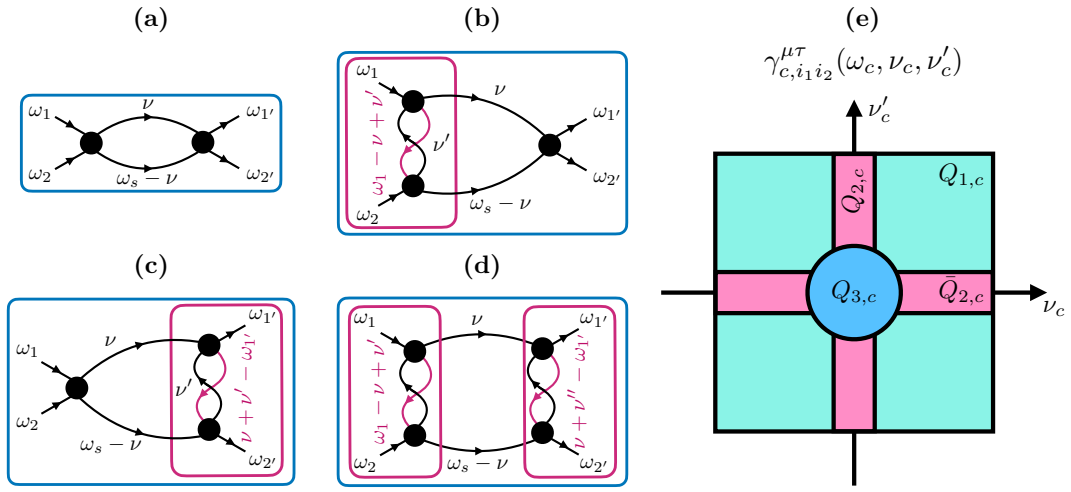

Figure 4.5: Decomposition of reducible vertices into asymptotic classes. In panels **(a)** - **(d)**, examples for s-reducible diagrams with different high-frequency behavior are shown. If both incoming and both outgoing legs are attached to the same bare vertex as in **(a)**, the vertex function only depends on the transfer frequency ω_s. By replacing either the left or right bare vertex by a diagram reducible in the t channel [see **(b)** & **(c)**], one feeds an external frequency and thereby ν_s or ν'_s into the loops. In case both bare vertices are substituted this way [see **(d)**], one recovers the full frequency dependence on $(\omega_s, \nu_s, \nu'_s)$. In **(e)**, we show a sketch of the asymptotic behavior of 2PR vertices in their respective natural parametrization. Their main features for fixed ω_c are a localized structure around the origin, described by $Q_{3,c}$, two stripes along the ν_c and ν'_c axis, determined by $\bar{Q}_{2,c}$ or $Q_{2,c}$ and, lastly, a constant background for large $|\nu_c|$ and $|\nu'_c|$ given by $Q_{1,c}$ (see Fig. A.1 for explicit numerical data).

corresponding s bubble. This motivates us to parametrize each channel γ_c in terms of the respective bosonic frequency and two additional fermionic arguments, i.e. we write

$$\Gamma^{\mu\tau}_{i_1i_2}(s,t,u) = \Gamma^{\mu\tau}_{0,i_1i_2} + \sum_c \gamma^{\mu\tau}_{c,i_1i_2}(\omega_c,\nu_c,\nu'_c)\,, \tag{4.31}$$

where $\Gamma^{\mu\tau}_{0,i_1i_2} = \frac{1}{4}J^{\mu\tau}_{i_1i_2}$ are the components of the frequency independent bare pseudofermion vertex. Our convention for projecting the Mandelstam variables $(\omega_s, \omega_t, \omega_u)$ of the full vertex into the *natural frequency arguments* $(\omega_c, \nu_c, \nu'_c)$ of its 2PR contributions is shown in Fig. 4.4. This specific choice ensures that frequencies ν_c (ν'_c) exclusively appear in the left (right) vertex of B_c. On the other hand, it simplifies the implementation of frequency symmetries, which will be further discussed in the next section. The sum of all 2PR diagrams in a specific channel is characterized by a total of three frequencies and the numerical effort to compute it thus grows as $N_\omega \times N_\nu^2$ where N_ω (N_ν) is the number of bosonic (fermionic) discretization points. Certain contributions to γ_c depend, however, on a lesser number of arguments and can be classified according to their high-frequency behavior [118, 134]. This asymptotic parametrization of the 2PR vertices roots in the frequency independence of the bare two-particle vertex. Whenever both external legs associated with frequencies ν_c (ν'_c) are attached to the same Γ_0, information about them cannot be fed into the internal loop. The dependence on these arguments is therefore eradicated. For the transfer frequencies ω_c, in contrast, this is not possible due to their appearance in the propagators. This motivates the following decomposition of γ_c: Diagrams which solely depend on the transfer frequency are summarized as K^1_c. Those contributions where information about one of the two fermionic frequencies is deleted by a bare vertex are coined K^2_c or $\bar{K}^2_c$ depending on whether the diagram depends on ν_c (for K^2_c) or ν'_c (for $\bar{K}^2_c$). Lastly, diagrams where each external leg connects to a different bare vertex depend on all three frequencies $(\omega_c, \nu_c, \nu'_c)$ and belong to K^3_c. Examples for each asymptotic class are presented in Fig. 4.5. In total, we thus have

$$\gamma^{\mu\tau}_{c,i_1i_2}(\omega_c,\nu_c,\nu'_c) = K^{1,\mu\tau}_{c,i_1i_2}(\omega_c) + K^{2,\mu\tau}_{c,i_1i_2}(\omega_c,\nu_c) + \bar{K}^{2,\mu\tau}_{c,i_1i_2}(\omega_c,\nu'_c) + K^{3,\mu\tau}_{c,i_1i_2}(\omega_c,\nu_c,\nu'_c)\,. \tag{4.32}$$

From our convention in Fig. 4.4 it is apparent that two external legs which are assigned the same fermionic frequency can only connect to different bare vertices in a c-reducible diagram if they are attached to some building block which is is c-irreducible. In that case, one external frequency ν_c or $\nu_{c'}$ is processed in the propagators of the internal $\bar{c}$-loop. Since $G_0(\omega) \sim (i\omega)^{-1}$, the latter vanish, if the respective external frequency is taken to infinity. One can therefore project out contributions from a

specific K_c^n to γ_c considering an appropriate high-frequency limit, namely

$$\begin{aligned}\lim_{|\nu_c|\to\infty}\lim_{|\nu_c'|\to\infty}\gamma^{\mu\tau}_{c,i_1i_2}(\omega_c,\nu_c,\nu_c') &= K^{1,\mu\tau}_{c,i_1i_2}(\omega_c)\\ \lim_{|\nu_c'|\to\infty}\gamma^{\mu\tau}_{c,i_1i_2}(\omega_c,\nu_c,\nu_c') &= K^{1,\mu\tau}_{c,i_1i_2}(\omega_c)+K^{2,\mu\tau}_{c,i_1i_2}(\omega_c,\nu_c)\\ \lim_{|\nu_c|\to\infty}\gamma^{\mu\tau}_{c,i_1i_2}(\omega_c,\nu_c,\nu_c') &= K^{1,\mu\tau}_{c,i_1i_2}(\omega_c)+\bar{K}^{2,\mu\tau}_{c,i_1i_2}(\omega_c,\nu_c')\,.\end{aligned} \tag{4.33}$$

Finally, K_c^3 can be computed by calculating the other classes beforehand and subtracting them from the full 2PR channel. The decay of K_c^3 in any frequency direction is the origin for the computational efficiency of the asymptotic classification scheme. Although γ_c is generally obtained by summing up diagrams from all classes, only some of them persist at larger frequencies. For large $|\nu_c'|$, for example, one just needs to compute K_c^1 and K_c^2. The more expensive K_c^3, on the other hand, solely needs to be monitored within a small, but three-dimensional domain around the origin.

For numerical purposes it is convenient to define the asymptotic classes in terms of new kernels Q_c^n, which are composed of sums of K_c^n functions. More precisely speaking, we define

$$\begin{aligned}Q^{1,\mu\tau}_{c,i_1i_2}(\omega_c)_c &\equiv K^{1,\mu\tau}_{c,i_1i_2}(\omega_c)\\ Q^{2,\mu\tau}_{c,i_1i_2}(\omega_c,\nu_c) &\equiv K^{1,\mu\tau}_{c,i_1i_2}(\omega_c)+K^{2,\mu\tau}_{c,i_1i_2}(\omega_c,\nu_c)\\ \bar{Q}^{2,\mu\tau}_{c,i_1i_2}(\omega_c,\nu_c) &\equiv K^{1,\mu\tau}_{c,i_1i_2}(\omega_c)+\bar{K}^{2,\mu\tau}_{c,i_1i_2}(\omega_c,\nu_c)\\ Q^{3,\mu\tau}_{c,i_1i_2}(\omega_c,\nu_c,\nu_c') &\equiv \gamma^{\mu\tau}_{c,i_1i_2}(\omega_c,\nu_c,\nu_c')\,.\end{aligned} \tag{4.34}$$

Since the K_c^n decay to zero if one of their arguments is taken to infinity, the Q_c^n are mapped to the respective class with lesser arguments, for example $Q^{3,\mu\tau}_{c,i_1i_2}(\omega_c,\nu_c,\nu_c')\to Q^{2,\mu\tau}_{c,i_1i_2}(\omega_c,\nu_c)$ for $|\nu_c'|\to\infty$. In principle, both the K_c^n formulation pioneered in Ref. [118] as well as the $\bar{Q}_c^n$ parametrization from Ref. [134] contain the same information about the asymptotic frequency structure of the 2PR vertex components and can be freely converted into one another using Eq. (4.34). For pffRG, this has been demonstrated in Ref. [P2]. The decisive difference between both approaches lies in their respective numerical performance. In terms of the K_c^n functions, one can more accurately model the channels choosing a tight mesh but with fewer frequencies to resolve K_c^3. To evoke a full 2PR vertex in the evaluation of bubble functions, however, one eventually needs to calculate the sum of all four K_c^n. In the Q_c^n formulation, only a single kernel needs to be computed to obtain γ_c, making this scheme more efficient for reassembling a 2PR vertex at the cost of having to use slightly more frequencies to resolve Q_c^3. Note that reading out a vertex from memory usually requires interpolations to handle the natural mismatch between discretization points and the frequency arguments in Eq. (4.30). We further discuss this aspect in Sec. 4.4.2.

4.3.4 Symmetries in Matsubara space

In Ref. [117] a comprehensive symmetry analysis of the pseudofermion action and the resulting constraints on the structure of 1PI vertices has been carried out. So far, we made use of local U(1) symmetry to simplify the spatial structure of the one and two-particle vertex functions, as well as time-reversal symmetry and hermiticity, which impose that one-particle vertices are diagonal in spin space. Moreover, we employed energy conservation to reduce the required number of frequency arguments. Combining these transformations with (local) particle-hole and crossing symmetry, further restrictions on the frequency structure can be derived, as shown in Ref. [117]. Most importantly, the self-energy (propagators) obeys

$$\begin{aligned}\Sigma(\omega) &= -\Sigma(-\omega)\\ \Sigma(\omega) &= -\bar{\Sigma}(\omega)\,.\end{aligned} \tag{4.35}$$

Hence, one-particle pseudofermion vertices are antisymmetric functions in frequency space and purely imaginary. Remarkably, this implies that the half-filling constraint is fulfilled on average [P1]. Two-

particle vertex functions $\Gamma^{\mu\nu}_{i_1 i_2}$, on the other hand, are subject to the conditions

$$\begin{aligned}
\Gamma^{\mu\nu}_{i_1 i_2}(\omega_s,\omega_t,\omega_u) &= \Gamma^{\nu\mu}_{i_2 i_1}(-\omega_s,\omega_t,\omega_u)\\
\Gamma^{\mu\nu}_{i_1 i_2}(\omega_s,\omega_t,\omega_u) &= \xi(\mu)\xi(\nu)\Gamma^{\mu\nu}_{i_1 i_2}(\omega_s,-\omega_t,\omega_u)\\
\Gamma^{\mu\nu}_{i_1 i_2}(\omega_s,\omega_t,\omega_u) &= \xi(\mu)\xi(\nu)\Gamma^{\nu\mu}_{i_2 i_1}(\omega_s,\omega_t,\omega_- u)\\
\Gamma^{\mu\nu}_{i_1 i_2}(\omega_s,\omega_t,\omega_u) &= -\xi(\nu)\Gamma^{\mu\nu}_{i_1 i_2}(\omega_u,\omega_t,\omega_s)\\
\Gamma^{\mu\nu}_{i_1 i_2}(\omega_s,\omega_t,\omega_u) &= \xi(\mu)\xi(\nu)\bar{\Gamma}^{\mu\nu}_{i_1 i_2}(\omega_s,\omega_t,\omega_u)\,,
\end{aligned} \tag{4.36}$$

where $\xi(d) = +1$ and $\xi(\mu) = -1$ for $\mu \neq d$. Consequently, $\Gamma^{\mu\nu}_{i_1 i_2}$ is imaginary if (μ,ν) mixes spin and density indices and real otherwise. Each of the first four identities in Eq. (4.36) translates into a respective equation for the 2PR vertices by converting $(\omega_s,\omega_t,\omega_u)$ into the corresponding natural parametrization. In summary, one finds

$$\begin{aligned}
\gamma^{\mu\nu}_{s,i_1 i_2}(\omega_s,\nu_s,\nu'_s) &= \gamma^{\nu\mu}_{s,i_2 i_1}(-\omega_s,\nu_s,\nu'_s)\\
\gamma^{\mu\nu}_{s,i_1 i_2}(\omega_s,\nu_s,\nu'_s) &= -\xi(\mu)\gamma^{\nu\mu}_{u,i_2 i_1}(\omega_s,-\nu_s,\nu'_s)\\
\gamma^{\mu\nu}_{s,i_1 i_2}(\omega_s,\nu_s,\nu'_s) &= -\xi(\nu)\gamma^{\mu\nu}_{u,i_1 i_2}(\omega_s,\nu_s,-\nu'_s)\\
\gamma^{\mu\nu}_{s,i_1 i_2}(\omega_s,\nu_s,\nu'_s) &= \xi(\mu)\xi(\nu)\gamma^{\nu\mu}_{s,i_2 i_1}(\omega_s,\nu'_s,\nu_s)\,,
\end{aligned} \tag{4.37}$$

for the s channel,

$$\begin{aligned}
\gamma^{\mu\nu}_{t,i_1 i_2}(\omega_t,\nu_t,\nu'_t) &= \xi(\mu)\xi(\nu)\gamma^{\mu\nu}_{t,i_1 i_2}(-\omega_t,\nu_t,\nu'_t)\\
\gamma^{\mu\nu}_{t,i_1 i_2}(\omega_t,\nu_t,\nu'_t) &= -\xi(\mu)\gamma^{\mu\nu}_{t,i_1 i_2}(\omega_t,-\nu_t,\nu'_t)\\
\gamma^{\mu\nu}_{t,i_1 i_2}(\omega_t,\nu_t,\nu'_t) &= -\xi(\nu)\gamma^{\mu\nu}_{t,i_1 i_2}(\omega_t,\nu_t,-\nu'_t)\\
\gamma^{\mu\nu}_{t,i_1 i_2}(\omega_t,\nu_t,\nu'_t) &= \xi(\mu)\xi(\nu)\gamma^{\nu\mu}_{t,i_2 i_1}(\omega_t,\nu'_t,\nu_t)\,,
\end{aligned} \tag{4.38}$$

for the t channel and finally

$$\begin{aligned}
\gamma^{\mu\nu}_{u,i_1 i_2}(\omega_u,\nu_u,\nu'_u) &= \xi(\mu)\xi(\nu)\gamma^{\nu\mu}_{u,i_2 i_1}(-\omega_u,\nu_u,\nu'_u)\\
\gamma^{\mu\nu}_{u,i_1 i_2}(\omega_u,\nu_u,\nu'_u) &= -\xi(\nu)\gamma^{\nu\mu}_{s,i_2 i_1}(\omega_u,-\nu_u,\nu'_u)\\
\gamma^{\mu\nu}_{u,i_1 i_2}(\omega_u,\nu_u,\nu'_u) &= -\xi(\nu)\gamma^{\mu\nu}_{s,i_1 i_2}(\omega_u,\nu_u,-\nu'_u)\\
\gamma^{\mu\nu}_{u,i_1 i_2}(\omega_u,\nu_u,\nu'_u) &= \xi(\mu)\xi(\nu)\gamma^{\mu\nu}_{u,i_1 i_2}(\omega_u,\nu'_u,\nu_u)\,,
\end{aligned} \tag{4.39}$$

for γ_u. In similar fashion, the symmetries of the kernel functions Q^n_c can be extracted from the symmetries of γ_c by considering the respective high-frequency limit. As can be seen from the conditions above, the numerical effort for computing the 2PR vertices can be drastically reduced. Most importantly, one can dispense with accounting for negative frequencies explicitly, since the latter can always be projected on the positive Matsubara axis. The exchange symmetry $\nu_c \leftrightarrow \nu'_c$, present in every channel, can be exploited to further restrict γ_c to a grid with $\nu_c \geq \nu'_c$, but it also comes with a caveat for multiloop pffRG flows. To compute the latter, one needs to calculate the left/right part $\gamma_c^{L/R}$ for every loop order $\ell \geq 2$. Since ν_c and ν'_c basically define how *left* and *right* is supposed to be understood for every bubble function, a swap of the two also induces a mapping $\gamma_c^L \leftrightarrow \gamma_c^R$. This can be used, for example, to obtain the entire γ_c^R solely from γ_c^L.

4.3.5 Observables

The central physical observable computed from the pseudofermion vertices is the spin-spin correlation function or magnetic susceptibility defined as

$$\chi^{\mu\nu}_{jk}(\omega) \equiv \int_0^\infty d\tau e^{i\omega\tau}\langle \hat{T}_\tau S^\mu_j(\tau) S^\nu_k(0)\rangle\,, \tag{4.40}$$

where $\hat{T}_\tau$ is the imaginary time-ordering operator. We are commonly interested in the elastic component $\chi^{\mu\nu}_{jk} = \chi^{\mu\nu}_{jk}(\omega = 0)$, from which one obtains the static structure factor

$$\chi^{\mu\nu}(\boldsymbol{k}) = \frac{1}{N}\sum_{j,k} e^{i\boldsymbol{k}(\boldsymbol{r}_i - \boldsymbol{r}_j)}\chi^{\mu\nu}_{jk}\,. \tag{4.41}$$

For magnetic materials, $\chi^{\mu\nu}(\boldsymbol{k})$ can be measured by neutron-scattering, which proliferates a direct comparison between the output produced by solving the pffRG flow equations and experimental results (see Ref. [114] for an instructive example). The most striking feature in the static structure factor are sharp Bragg peaks for long-range magnetic orders, whereas $\chi^{\mu\nu}(\boldsymbol{k})$ for paramagnetic states is more washed out.

In pseudofermion language, two-spin correlations translate into four-fermion disconnected Green's functions

$$\langle \hat{T}_\tau S_j^\mu(\tau) S_k^\nu(0)\rangle = \frac{1}{4}\sum_{\{\alpha_i\}} \sigma^\mu_{\alpha_1'\alpha_1}\sigma^\nu_{\alpha_2'\alpha_2}\langle \hat{T}_\tau \bar{\psi}_{j\alpha_1'}(\tau)\psi_{j\alpha_1}(\tau)\bar{\psi}_{k\alpha_2'}(0)\psi_{k\alpha_2}(0)\rangle\,. \tag{4.42}$$

By Fourier transforming the fields via $\psi_{j\alpha}(\tau) = \frac{1}{2\pi}\int d\omega\; e^{-i\omega\tau}\psi_{j\alpha}(\omega)$ one therefore obtains

$$\begin{aligned}\chi^{\mu\nu}_{jk}(\omega) &= \frac{1}{4}\sum_{\{\alpha_i\}} \sigma^\mu_{\alpha_1'\alpha_1}\sigma^\nu_{\alpha_2'\alpha_2}\int_0^\infty d\tau e^{i\omega\tau}\langle \hat{T}_\tau \bar{\psi}_{j\alpha_1'}(\tau)\psi_{j\alpha_1}(\tau)\bar{\psi}_{k\alpha_2'}(0)\psi_{k\alpha_2}(0)\rangle \\ &= \frac{1}{4(2\pi)^3}\sum_{\{\alpha_i\}} \sigma^\mu_{\alpha_1'\alpha_1}\sigma^\nu_{\alpha_2'\alpha_2}\int d\omega_2'\int d\omega_1\int d\omega_2\;\langle \bar{\psi}_{j\alpha_1'}(\omega_1-\omega)\psi_{j\alpha_1}(\omega_1)\bar{\psi}_{k\alpha_2'}(\omega_2')\psi_{k\alpha_2}(\omega_2)\rangle\,,\end{aligned} \tag{4.43}$$

where we used $\int d\tau e^{i(\omega+\omega_1'-\omega_1)\tau} = 2\pi\times\delta(\omega+\omega_1'-\omega_1)$ to derive the second from the first line. In order to express the disconnected correlator in term of 1PI vertices, one first uses the identity

$$G_4(x_1',x_2'|x_1,x_2) = G_{c,4}(x_1',x_2'|x_1,x_2) + G(x_1'|x_1)G(x_2'|x_2) - G(x_1'|x_2)G(x_2'|x_1) \tag{4.44}$$

which can straightforwardly be derived from the definition of the generating functional W_c from Sec. 2.1. It decomposes the disconnected four-particle Green's function into a connected part and disconnected products of propagators. Subsequently, one makes use of the tree expansion [15] to replace $G_{c,4}$ by a two-particle vertex. As a last step, one needs to plug in the site, spin and frequency parametrized form of the 1PI functions. We skip these somewhat lengthy derivations and directly state the final result, which reads

$$\begin{aligned}\chi^{\mu\nu}_{jk}(\omega) = &-\frac{1}{4\pi}\int dv\; G(v)G(\omega+v)\times\delta_{jk}\delta_{\mu\nu} \\ &-\frac{1}{16\pi^2}\int dv\int dv' G(v)G(\omega+v)G(v')G(\omega+v') \\ &\times\left[4\Gamma^{\mu\nu}_{jk}(\omega+v+v',\omega,v-v') - \sum_{\lambda,\kappa}\mathrm{Tr}\left(\Pi_2^{\mu\kappa}\Pi_2^{\nu\lambda}\right)\Gamma^{\lambda\kappa}_{jj}(\omega+v+v',v'-v,-\omega)\times\delta_{jk}\right].\end{aligned} \tag{4.45}$$

Here, Π_2 is the doublet spin tensor from Sec. 4.3.2.

One remarkable property of the spin-spin correlator is its intimate relation to the fulfillment of half-filling in the pseudofermion representation of spin Hamiltonians [116]. Consider the equal-time correlation function

$$\Upsilon^{\mu\nu}_{ij} = \frac{1}{2\pi}\langle S_i^\mu(t=0)S_j^\nu(0)\rangle = \int d\omega\;\chi^{\mu\nu}_{ij}(\omega)\,. \tag{4.46}$$

Replacing spin operators by pseudofermions, one verifies that

$$\sum_\mu \Upsilon^{\mu\mu}_{ii} = \frac{3}{2}\langle n_i\rangle - \frac{3}{4}\langle n_i^2\rangle \implies \langle n_i^2\rangle = 2\langle n_i\rangle - \frac{4}{3}\sum_\mu\Upsilon^{\mu\mu}_{ii}\,, \tag{4.47}$$

where $n_i = \sum_\alpha \bar{\psi}_{i\alpha}\psi_{i\alpha}$ is the particle number on site i. Since the pseudofermion self-energy is particle-hole symmetric, i.e., $\langle n_i\rangle = 1$ [P1], fluctuations around the mean evaluate to

$$\langle n_i^2\rangle - \langle n_i\rangle^2 = 1 - \frac{4}{3}\sum_\mu\Upsilon^{\mu\mu}_{ii}\,. \tag{4.48}$$

Consequently, $\sum_\mu \Upsilon^{\mu\mu}_{ii} = \frac{3}{4}$ implies exact fulfillment of the half-filling constraint. Since $\chi^{\mu\nu}_{ij}(\omega)$ can be computed from the renormalized propagators and two-particle vertex in pffRG, one can monitor the evolution of fluctuations under the RG flow (see Sec. 4.5.2) and thus gauge their impact within the formalism itself.

4.4 Numerical Implementation

In the last section, we presented an efficient parametrization of 2PR vertices and considered their symmetries in frequency space. Yet, we have to implement further approximations in order to obtain a finite set of flow equations that can be solved numerically. Importantly, the vertices need to be defined on a finite lattice graph and discrete frequency grid in such a way that the most relevant features with respect to, for example, the decay of correlation functions in real space or the extent of asymptotic kernels, are accounted for. In the following, we examine each and every aspect of the numerical implementation of pffRG and present a set of useful algorithms which we have learned to appreciate for their high-accuracy and computational efficiency. We also point out significant differences between our code and established pffRG implementations, with special emphasis devoted to the control over numerical errors therein.

4.4.1 Symmetry-reduced lattice representation

As discussed in Sec. 4.3.1, the pseudofermion self-energy and other one-particle vertices can be approximated as spatially uniform if one assumes that all lattice sites are symmetry equivalent to one another. Two-particle objects, on the other hand, depend on two site arguments. We can, however, employ symmetries to constrain Γ even further by imposing that

$$\Gamma^{\mu\nu}_{i_1 i_2} = \Gamma^{\mu\nu}_{Q(i_1)Q(i_2)}\,, \tag{4.49}$$

for any element Q of the lattice space group [117]. Note that we have dispensed with spelling out frequency dependencies for brevity.

Any lattice graph is characterized by a set of Bravais lattice vectors $\boldsymbol{a}_i$ with $i \in \{1, ..., d\}$ as well as a basis $\boldsymbol{b}_i$ with $i \in \{1, ..., N_b\}$, where we denote the spatial dimension by $d \leq 3$ and the number of basis sites by N_b. Consequently, one can characterize any lattice site with real space coordinates $\boldsymbol{r}$, by a set of $d+1$ indices $(\alpha_1, ..., \alpha_d, \beta)$ as

$$\boldsymbol{r} = \sum_{i=1}^{d} \alpha_i \boldsymbol{a}_i + \boldsymbol{b}_\beta\,, \tag{4.50}$$

where $\alpha_i \in \mathbb{Z}$ and $\beta \in \{1, ..., N_b\}$. In other words, one can obtain any site from shifting the unit cell containing the basis along integer multiples of the Bravais vectors. Since memory resources of computing machines are limited, one needs to decide on a finite set of indices $(\alpha_1, ..., \alpha_d, \beta)$ to perform the flow integration. In our code, we generate the lattice graph by computing all sites which can be reached from a reference site i_0, typically $(0, ..., 0, 1)$, by travelling at most L steps along the lattice bonds. This corresponds to building the lattice according to the *Manhattan* or $L1$ norm. Most importantly, this procedure preserves point group symmetries for any value of L.

To respect the space group, we proceed in three steps. At first, we compute transformations P, such as rotations and reflections, which leave i_0 unchanged. This is achieved by iterating over all pairs of non-collinear nearest-neighbor bonds and determining possible transformations between them using the *Rodrigues formula* [135]. In the next step, we group all sites which are mapped onto one another under P into classes of equivalent sites. Since all vertices $\Gamma^{\mu\nu}_{i_0 i_2^*}$ with i_2^* in such a class are equal by virtue of Eq. (4.49), this amounts to generating a reduced representation of the full lattice graph. At last, we compute mappings between sites in the unit cell by shifting basis elements $\boldsymbol{b}_i$ with $i \geq 2$ onto $\boldsymbol{b}_1$ and composing this translation with a point group symmetry that matches the respective nearest-neighbor bonds. This allows us to map any pair of indices (i_1, i_2) with bond distance $||i_1 - i_2||_b \leq L$ onto an equivalent pair (i_0, i_2^*) in the reduced lattice by first considering a translation $i_1 \to i_1'$, where i_1' lies in the unitcell of the reference site, and concomitantly applying a projection $i_1' \to i_0$ within the unitcell (if necessary). Here, $||i_1 - i_2||_b$ corresponds to the minimum number of bonds required to walk from i_1 to i_2 on the lattice graph. Since these mappings only need to be computed once, one effectively condenses the spatial dependence of the vertex into a single index, which tremendously reduces computation time and memory requirements (see Fig. 4.6).

We employ open boundary conditions and set $\Gamma^{\mu\nu}_{i_1 i_2} = 0$ if $||i_1 - i_2||_b$ exceeds the maximum bond distance L. Physically, this amounts to limiting the maximum length scale over which pseudofermions can be correlated. For this reason, L can be deemed a control parameter to check numerical convergence: it is large enough if the vertices have sufficiently decayed for large distances. This implementation bears the advantage that no artificial boundary is introduced such that lattice incommensurate phenomena can also be resolved.

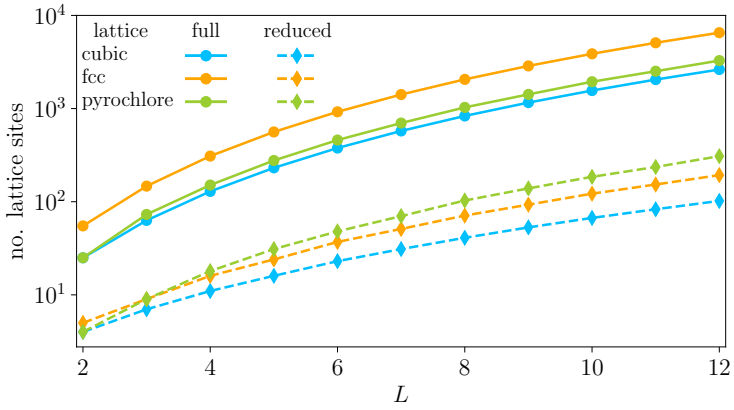

Figure 4.6: Comparison of lattices in full and symmetry-reduced representation. We plot the number of lattice sites for the cubic, fcc and pyrochlore lattice as a function of the maximum bond distance L using full lattices, denoted by straight lines and dots, and the decomposition into equivalence classes after employing point group symmetries with respect to the reference site (dashed lines and diamonds). Without the employment of lattice symmetries, the number of vertex components which need to be invoked during the pffRG flow scales quadratically in the number of sites. For the reduced representation, in contrast, the scaling is only linear and the numerical effort in computing Γ is, thus, reduced by several orders of magnitude.

4.4.2 Evaluation of Matsubara integrals

In Sec. 4.3, we derived concrete expressions for the $T = 0$ self-energy loop and 2PR bubble functions, which are essential to construct the flow of pseudofermion vertices. In this limit, the spectrum of Matsubara frequencies becomes continuous and frequency summations are promoted to integrals. The general motif that provides guidance for choosing an appropriate quadrature is the same as for the itinerant fermion case discussed in Sec. 4.4, that is, one needs to pay attention to the structure of the propagators and how it changes as a function of the RG scale Λ.

To begin with, consider the loop function $[\Gamma \circ G']_\Sigma$, which invokes a single propagator G'. The latter could be a single-scale propagator $G' = S$ as in the 1ℓ flow or a dressed propagator $G' = G$ as required by the multiloop corrections to $\frac{d}{d\Lambda}\Sigma$. As we have exemplified in Fig. 4.1, the overall shape of G and S is, neglecting self-energy corrections, quite similar: both propagators exhibit their maximum for frequencies close to Λ and asymptotically decay to zero for $|\omega| \gg \Lambda$. The peaks for the single-scale propagator are, however, more pronounced and its fall-off is much faster (exponential instead of algebraic). To cope with these characteristics, we employ adaptive Gauss-Kronrod (GK) quadrature as exported by the `QuadGK` Julia package. We divide the integration domain into three segments, $(-\infty, -2\Lambda)$, $(-2\Lambda, 2\Lambda)$ and $(2\Lambda, +\infty)$, which respect both the vivid frequency structure around the origin, as well as the asymptotic decay of the propagators. The $\pm\infty$-bounds are hereby implemented via a change of integration variables. In contrast to the itinerant case, where Gauss-Kronrod quadrature turned out to be inappropriate at low temperatures, the relevant energy scales in pffRG are somewhat larger, since Λ-values on the percent level relative to the spin coupling J[4] are often sufficient to resolve instabilities in the flow of pseudofermion vertices. Hence, `QuadGK` provides an accurate frequency integrator for evaluating self-energy loops. Note that this aspect is usually not discussed in the pffRG literature. This is because older works have primarily focussed on the sharp regulator, for which the single-scale propagator is proportional to a Dirac delta distribution such that the Matsubara integral boils down to an evaluation of the integrand at $\pm\Lambda$.

A crucial ingredient for the efficient integration of the bubble functions is the exploit of their real space and spin structure. To keep the discussion concise, consider, without loss of generality, the parametrized s bubble, which reads

$$B_{s,i_1i_2}(\tilde{x}_1', \tilde{x}_2'|\tilde{x}_1, \tilde{x}_2) = -\int dv \sum_{\mu,\nu,\tau,\kappa} \Pi^{\tau\mu}_{2,\alpha_1'\alpha_1} \Pi^{\kappa\nu}_{2,\alpha_2'\alpha_2} \delta_{\omega_1'+\omega_2',\omega_1+\omega_2} \times \Gamma^{\mu\nu}_{i_1i_2}(\omega_s, v-\omega_1, v-\omega_2) G(v) G(\omega_s - v) \Gamma^{\tau\kappa}_{i_1i_2}(\omega_s, \omega_1' - v, \omega_1' - s + v)\,. \quad (4.51)$$

Remarkably, all frequency dependent functions in B_{s,i_1i_2} preserve their arguments, independent of the respective index pairs (i_1, i_2) and superscripts μ, ν, τ, κ. However, there is no *a priori* guarantee that

[4] J denotes a heuristic measure for the magnitude of the exchange matrix $J^{\mu\nu}_{ij}$.

the frequency arguments of the vertices align with the numerical grid. For this reason, it has become common practice to obtain Σ by linear and Γ by trilinear interpolation [17, 18]. Here, we translate this principle to the 2PR vertices of which Γ is composed. For a given frequency triplet $(\omega_c, \nu_c, \nu'_c)$, we thus obtain $\gamma^{\mu\tau}_{c,i_1 i_2}$ as

$$\begin{aligned}\gamma^{\mu\tau}_{c,i_1 i_2}(\omega_c,\nu_c,\nu'_c) = \frac{1}{(\omega_{c,i_>}-\omega_{c,i_<})(\nu_{c,i_>}-\nu_{c,i_<})(\nu'_{c,i_>}-\nu'_{c,i_<})} \times \big[\\ \gamma^{\mu\tau}_{c,i_1 i_2}(\omega_{c,i_<},\nu_{c,i_<},\nu'_{c,i_<})(\omega_{c,i_>}-\omega_c)(\nu_{c,i_>}-\nu_c)(\nu'_{c,i_>}-\nu'_c) \\ +\gamma^{\mu\tau}_{c,i_1 i_2}(\omega_{c,i_<},\nu_{c,i_<},\nu'_{c,i_>})(\omega_{c,i_>}-\omega_c)(\nu_{c,i_>}-\nu_c)(\nu'_c-\nu'_{c,i_<}) \\ +\gamma^{\mu\tau}_{c,i_1 i_2}(\omega_{c,i_<},\nu_{c,i_>},\nu'_{c,i_<})(\omega_{c,i_>}-\omega_c)(\nu_c-\nu_{c,i_<})(\nu'_{c,i_>}-\nu'_c) \\ +\gamma^{\mu\tau}_{c,i_1 i_2}(\omega_{c,i_<},\nu_{c,i_>},\nu'_{c,i_>})(\omega_{c,i_>}-\omega_c)(\nu_c-\nu_{c,i_<})(\nu'_c-\nu'_{c,i_<}) \\ +\gamma^{\mu\tau}_{c,i_1 i_2}(\omega_{c,i_>},\nu_{c,i_<},\nu'_{c,i_<})(\omega_c-\omega_{c,i_<})(\nu_{c,i_>}-\nu_c)(\nu'_{c,i_>}-\nu'_c) \\ +\gamma^{\mu\tau}_{c,i_1 i_2}(\omega_{c,i_>},\nu_{c,i_<},\nu'_{c,i_>})(\omega_c-\omega_{c,i_<})(\nu_{c,i_>}-\nu_c)(\nu'_c-\nu'_{c,i_<}) \\ +\gamma^{\mu\tau}_{c,i_1 i_2}(\omega_{c,i_>},\nu_{c,i_>},\nu'_{c,i_<})(\omega_c-\omega_{c,i_<})(\nu_c-\nu_{c,i_<})(\nu'_{c,i_>}-\nu'_c) \\ +\gamma^{\mu\tau}_{c,i_1 i_2}(\omega_{c,i_>},\nu_{c,i_>},\nu'_{c,i_>})(\omega_c-\omega_{c,i_<})(\nu_c-\nu_{c,i_<})(\nu'_c-\nu'_{c,i_<})\big] , \end{aligned} \tag{4.52}$$

where subscripts $i_<(i_>)$ denote the nearest smaller (larger) grid point. Note that the frequency grid has been left general for now such that different discretizations for each channel and frequency axis are, in principle, accounted for. We elaborate on this aspect further in the next section. The kernel functions Q_c are obtained in similar fashion, using (bi-)linear interpolation if fewer than three arguments are required. For given external frequencies, it is thus computationally advantageous to perform the Matsubara integration for all combinations of lattice sites and spin components first, since both the interpolation nodes, i.e. the frequencies with $i_<(i_>)$ subscripts, as well as the respective weights only need to be computed once for any value of v invoked in the Matsubara integral. Moreover, the interpolation of the vertices as well as the contraction of vertex components in the bubble function can be very efficiently implemented using SIMD parallel processing. This is especially important for calculations on high-performance computing architectures where further hardware optimizations can be unlocked by utilizing advanced vector extensions (AVX).

Another important aspect for the calculation of bubble functions is the exploit of the high-frequency behavior of the vertex. The $T = 0$ Matsubara integral generally extends over the whole imaginary axis. Yet, some contributions to Γ have decayed at large v, justifying their neglect. For any bubble function, there, thus, exists some upper (lower) bound $\pm\tilde{v}_c$ beyond which the vertex effectively assumes a constant value. This implies that one can split the bubble integration into three parts: a costly bulk integral from $-\tilde{v}_c$ to $+\tilde{v}_c$ which evokes two interpolated vertices, and two boundary corrections from $-\infty$ to $-\tilde{v}_c$ and $+\tilde{v}_c$ to $+\infty$, respectively. Since the latter only involve the propagators, which themselves depend on a single frequency, they can be computed with lower computational costs. These considerations motivate the following integration strategy for the bubble functions:

(a) Precompute the boundary corrections for all ω_c using Gauss-Kronrod quadrature.

(b) Calculate the bulk integral for all pairs (i_0, i_2^*) and spin (density) components (μ, ν) in the symmetry-reduced lattice representation (see Sec. 4.4.1). GK quadrature requires the storage of intermediate results to perform the adaptive subdivision of the integration domain. In order to recycle interpolation parameters for the evaluation of the vertices though, we implement the integral over multiple pairs of real space indices and spin components by representing the integrand as an $N_\mu \times N_L$ array, where N_μ is the number of spin (density) components and N_L the number of symmetry-reduced lattice sites. Allocating multiple instances of these matrices, thus, comes with a large memory overhead. To circumvent this issue, we employ a matrix-valued version of the adaptive Simpson integration presented in Sec. 3.3.1 fixing the absolute error tolerance to $a_{\text{tol}} = 10^{-8}$ and relative tolerance to $r_{\text{tol}} = 10^{-4}$ if not stated otherwise. For further details see Fig. 4.7(a).

(c) Add the boundary corrections to the bulk integral by multiplying the results from (a) with the respective vertex values at $v = \pm\tilde{v}_c$.

This procedure offers a few advantages over older pffRG implementations [17, 18], where the quadrature was prevalently performed utilizing the trapezoidal rule with a fixed number of logarithmically spaced integration points. Most prominently, our results are error-controlled, which helps to instill confidence in the correctness of the obtained results. Moreover, it drastically improves the robustness of the

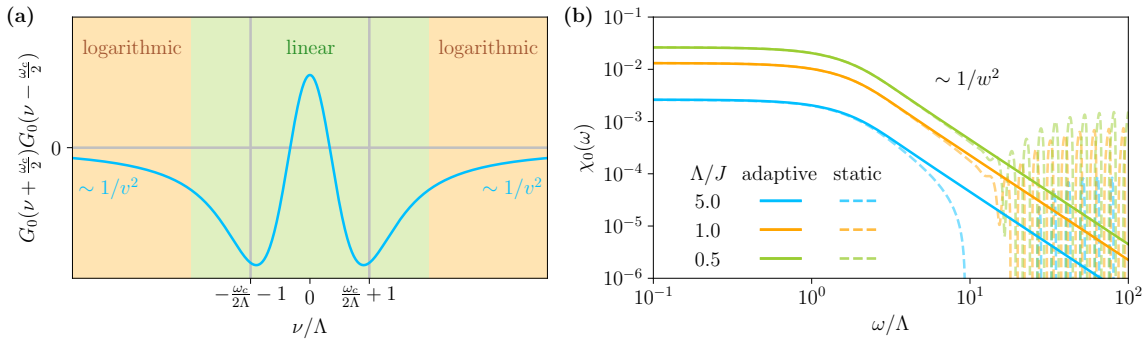

Figure 4.7: Numerical computation of Matsubara integrals. The bare propagator bubble is shown in **(a)**. Note that we have shifted ν by half a transfer frequency in order to center $G_0(\nu)G_0(\nu-\omega_c)$ at the origin. The bubble features two peaks whose position is determined by the transfer frequency ω_c and RG scale Λ and it decays algebraically for $|\nu|/\Lambda \gg 1$. To account for these characteristics when computing bubble functions in pffRG, we transcribe the quadrature presented in Sec. 3.3.1 to frequency space. The integration domain is consequently split into three segments, two of them exhibiting quadratic decay and one showing a more pronounced frequency structure. These are subsequently discretized into either logarithmically or linearly spaced intervals, where the number of intervals is increased proportional to $\Lambda^{-1/2}$. The integral for each of them is then computed with an adaptive Simpson rule. **(b)** Numerical results for the bare susceptibility χ_0. The required Matsubara integral is either computed adaptively (full lines) or with a non-adaptive trapezoidal rule (dashed lines) using 60 logarithmically spaced points between $\nu_{\text{min}} = 10^{-3}J$ and $\nu_{\text{max}} = 250J$, where J denotes the magnitude of the spin coupling.

Matsubara integration in the high-frequency regime. This is illustrated in Fig. 4.7(b), where we plot results for the bare susceptibility

$$\chi_0(\omega) = -\frac{1}{4\pi}\int d\nu\, G_0(\nu+\tfrac{\omega}{2})\, G_0(\nu-\tfrac{\omega}{2})\ , \tag{4.53}$$

for different values of the cutoff Λ obtained with the trapezoidal rule and our adaptive routine. For large ω/Λ, the non-adaptive quadrature is haunted by strong oscillations, indicating its insufficiency to resolve the asymptotic ω-regime. The results gathered with the adaptive algorithm, on the other hand, perfectly resemble the expected quadratic falloff. This, of course, raises the question to which extent non-adaptive quadrature is justified. The bare susceptibility computed here, constitutes the simplemost bubble-like integral in the pffRG flow, after all. Away from the UV limit, the propagators are additionally dressed with self-energy insertions and, in addition, two frequency dependent vertices enter the integral. Naively, one would therefore expect even larger numerical errors for the non-adaptive routine due to the enriched frequency structure. Note that this risk is greatly reduced for the adaptive routine. Although it might be more difficult to achieve convergence for small cutoffs, the algorithm does not terminate before the error bars on the results are sufficiently small, unless the number of function evaluations required to reach this goal becomes unusually large. The latter scenario would imply, however, that the integrand itself is numerically ill-behaved, in which case the continuation of the pffRG flow is anyways questionable.

4.4.3 Adaptive frequency discretization

Since the Matsubara frequencies become continuous in the zero temperature limit, any numerical implementation of pffRG needs to sample the vertices (and dynamical correlations) on a finite grid. As hinted at in the last section, there are several ways in which this could be achieved. One could imagine, for example, to have different meshes for every channel and frequency axis. Moreover, the spacing between adjacent grid points does not need to be uniform. Our choice for discretizing the self-energy, 2PR vertices and spin-spin correlations is based on several empirical observations, which, taken together, shall provide the reader with a few guidelines for setting up proper frequency grids for pffRG calculations.

Both, one-particle Green's functions, as well as two-particle objects decay for large frequencies. It is therefore sufficient to coarse-grain high-frequency tails and save the remaining grid points to resolve the more prosperous frequency structure around the origin. To reflect this behavior, we compose all our grids of a linear part, extending from $\omega = 0$ to $\omega_{\text{lin}} = \Delta\omega \times N_{\text{lin}}$, and a logarithmic tail from ω_{lin} to an upper bound ω_{max}. Here, $\Delta\omega$ denotes the linear grid spacing and N_{lin} the respective number of

equidistant points. The discrete frequencies of the logarithmic part are obtained as

$$\omega_i = \omega_{\text{lin}} \times \left(\frac{\omega_{\text{max}}}{\omega_{\text{lin}}} \right)^{i/N_{\text{log}}}, \tag{4.54}$$

with $N_{\text{log}} = N_\omega - N_{\text{lin}}$ and $i \in \{1, ..., N_{\text{log}}\}$. Here, N_ω denotes the total number of grid points, where, typically, $N_{\text{lin}} = 0.4 \times N_\omega$, if not stated otherwise. Note that we include only positive frequencies, since the vertices for negative arguments can be obtained by reflections at the origin (see Sec. 4.3.4).

Further criteria for an accurate discretization of 2PR vertices can be distilled from the symmetries in Sec. 4.3.4. All channels are, up to an eventual exchange of site indices and spin directions, invariant under $\omega_c \to -\omega_c$ and $\nu_c \leftrightarrow \nu_c'$. Moreover, the s and u-reducible contributions transform into one another under reflections of fermionic frequencies, whereas the t channel is either symmetric or antisymmetric for ν_c (ν_c') $\to -\nu_c$ ($-\nu_c'$). To cope with the different behavior of the channels, as well as the bosonic and fermionic frequency axis, we introduce a total of four grids for the 2PR vertices: the same set of discrete points for the transfer and fermionic frequency axis of the s and u channel and a separate pair of grids for the t channel. Choosing the grids equally for the particle-particle and crossed particle-hole diagrams improves the fulfillment of fermionic reflection symmetries on the level of the flow equations, while the different grids for t-reducible contributions help to resolve peculiarities tied specifically to the direct particle-hole channel. In principle, one could also separate the frequency grids in between different spin components of the vertex to account for exclusive features of certain $\gamma_c^{\mu\nu}$. This comes, however, with the great disadvantage that the external arguments entering the respective bubble functions would not be the same anymore, such that the interpolation parameters for evaluating the integrand cannot be recycled. To keep our code as efficient as possible, we therefore refrain from making use of this ansatz. Lastly, we implement two independent grids for the self-energy, as well as for the dynamic spin-spin correlations in addition to the discretization of the two-particle vertex.

One facet that sets our pffRG solver apart from other implementations, is the dynamical adjustment of the six different frequency grids throughout the flow. For large cutoffs, one would expect that the vertices are only weakly renormalized, such that all features in frequency space should scale roughly according to the features of the bare propagators, that is, with the RG scale Λ (see e.g. [Figs. 4.1 & 4.7(a)]). If Λ is, however, on the order of the spin coupling J, a more intricate frequency structure has been generated such that its precise extent may not be captured by simple Λ-scaling. This behavior is, for example, visible in Fig. 4.14 and has also been pointed out in Refs. [P1, 116, P2]. A static frequency grid, as, for example, used by the authors of Refs. [17, 18], consequently fails to accurately resolve the vertex. This has led to the appearance of strong numerical artifacts in the form of *wiggly* RG flows. In order to faithfully resolve the renormalized vertices over the entirety of the flow, we propose the following strategy. For Λ above some reference scale Λ_{ref}, the linear extent of the frequency grids is chosen proportional to Λ. Below Λ_{ref} we employ a sophisticated scanning routine to compute an appropriate ω_{lin} for every grid, which, for the 2PR vertices, operates as follows:

(a) Determine $\text{argmax}\{|\gamma^{\mu\tau}_{c,i_0 i_2^*}(\omega_c, \nu_c, \nu_c')|\}$ for each tuple (μ, τ).

(b) Sweep through γ_c along the bosonic and both fermionic axes, as well as along the diagonal $\nu_c = \nu_c'$ to extract one-dimensional snapshots of the data (see App. A.1 for further details). The respective other arguments are hereby fixed to the values determined in (a).

(c) For each cut, check if there exists a peak (at $\omega = \omega_{\text{peak}}$) somewhere close to the origin. Propose to set ω_{lin} to that value $\omega > \omega_{\text{peak}}$, where γ_c has decayed to 75 percent of the peak height, unless more than half of the equidistantly spaced grid points would be placed below ω_{peak}. In that case request $\omega_{\text{lin}} = \omega_{\text{peak}}/2$ in order to avoid excessive squeezing of the linear part of the mesh.

(d) If the value of γ_c at the origin of the respective cut is larger than one percent of the corresponding $\max\{|\gamma_c|\}$, propose ω_{lin}, such that the relative deviation between the vertex values at the origin and the first finite grid point, Δ, fulfills $p_1 < \Delta < p_2$, where p_1 and p_2 are free numerical parameters. This ensures that the grid is properly adjusted, even if there is no sharp peak at finite frequencies.

(e) Combine the heuristics (c) and (d), by setting ω_{lin} to the value from (d) if (c) does not apply, or to the minimum of their respective proposals. Assure that $p_3 < \omega_{\text{lin}} < p_4$, to prevent overambitious shrinking or expanding of the linear grid.

(f) For each tuple (μ, τ), (e) outputs four values: one ω_{lin} for the bosonic cut and three for the fermionic ones. The latter are fused to a single number by considering only their minimum value. Finally, the grids for all (μ, τ) components of γ_c are chosen according to the smallest ω_{lin} value

	Σ	ω_c	ν_c	χ
ω_{lin}	2Λ	6Λ	4Λ	4Λ
ω_{max}	50Λ	200Λ	150Λ	100Λ
p_1	/	0.02	0.02	0.02
p_2	/	0.05	0.05	0.05
p_3	/	$0.05\Lambda \times N_{\text{lin}}$	$0.03\Lambda \times N_{\text{lin}}$	$0.01\Lambda \times N_{\text{lin}}$
p_4	/	40Λ	30Λ	20Λ

Table 4.1: Summary of typical grid and scanning parameters. The linear extent ω_{lin} and upper bound ω_{max} are to be understood with respect to a reference scale $\Lambda_{\text{ref}}/J = 5$ and a stopping scale $\Lambda_{\text{stop}}/J = 0.5$. Some entries for the self-energy grid are left blank, since its frequency structure assumes a particularly simple form in pffRG. It consists of a single quasiparticle peak at $\omega = \omega_{\text{peak}}$ followed by a regime of linear decay (see Fig. 4.14). For this reason, we usually fix $\omega_{\text{lin}} = p_5 \times \omega_{\text{peak}}$ with $p_5 = 1 - 2$. The control parameters p_1 to p_4 are, in contrast, not relevant for the Σ-grid.

determined by scanning each component individually.

While we have only discussed the algorithm employed for the 2PR vertices, steps (c) - (e) can be applied to the spin-spin correlations, and, in principle, to the self-energy as well. In contrast to ω_{lin}, our routine to adjust the upper mesh bounds is much simpler. We scale ω_{max} proportional to Λ up to some Λ_{stop}, where ω_{max} remains fixed. This assures that the high-frequency tails of the vertices (and correlations) are sufficiently resolved. By determining ω_{lin} and ω_{max} according to these criteria after every RG step, we obtain a new set of frequency grids to which we transfer the vertices using the multilinear interpolation scheme from Sec. 4.4.2. The spin-spin correlations are, in contrast, post-processed from the vertices and can thus be directly evaluated on the new grid. A typical set of grid and scanning parameters is given in Tab. 4.1.

4.4.4 Parquet iterations

In the microscopic limit $\Lambda \to \infty$, the pseudofermion self-energy vanishes, while the vertex is characterized by the bare spin coupling. The pffRG flow has therefore traditionally been initialized with $\Gamma \sim J$ at some finite cutoff $\Lambda_i \gg J$. This does, however, introduce numerical artifacts the lower the value of Λ_i, since the vertices acquire non-trivial features beyond their frequency independent bare value. This problem can, of course, be mitigated by setting the initial scale to larger and larger values until one finds the numerical results to converge in the low-energy regime. An alternative approach makes use of the fact that the mfRG flow provides a solution to the parquet approximation at any Λ. This equivalence should, by construction, hold true also at $\Lambda = \Lambda_i$.

We thus determine the initial condition for the pffRG flow by computing an explicit solution of the regularized PA, which amounts to solving the algebraic set of equations given by the SDE and BSEs. To this end, we treat the parquet approximation as a fixed-point equation of the form $x = f(x)$ and try to find $x = (\Sigma, \Gamma)$ by self-consistent forward iterations, that is, we first converge $\Sigma = f_{\text{SDE}}(\Sigma, \Gamma)$ with $\Sigma = 0$ and the bare vertex $\Gamma = \Gamma_0$ as input (recall that $\Gamma = \Gamma_0 + \sum_c \gamma_c$). In a second step, this solution is used to update the 2PR vertices according to $\gamma_c = f_{\text{BSE}}(\Sigma, \Gamma)$ (see Fig. 4.8). We declare to have reached convergence once the absolute (relative) deviation between two updates is smaller than 10^{-8} (10^{-4}), if not stated otherwise. In practice, we find convergence already within a few iterations as long as $\Lambda \gg J$. If the cutoff is on the order of the bare interaction, however, the rate of convergence starts to drop, which eventually leads to divergent results. To improve on this front, we employ a mixing scheme between consecutive fixed-point iterations, such that the input x' for the next step is given by

$$x' = (1 - \eta) \times x + \eta \times f(x)\,, \tag{4.55}$$

where η denotes the *mixing factor*. For $\eta = 1$, one recovers the standard update scheme $x' = f(x)$. In our implementation, it has turned out beneficial to scale η roughly proportional to Λ as soon as $\Lambda \sim J$.

Having obtained a solution of the PA, the integration of the fRG flow of pseudofermion vertices corresponds, as usual, to the integration of an ODE. Here, we adhere to the general principles outlined in Sec. 3.3.2 and solve the flow equations using the adaptive Runge-Kutta solver described therein. The initial scale is typically chosen as $\Lambda_i/J = 5 - 10$ and we follow the flow down to the percent level

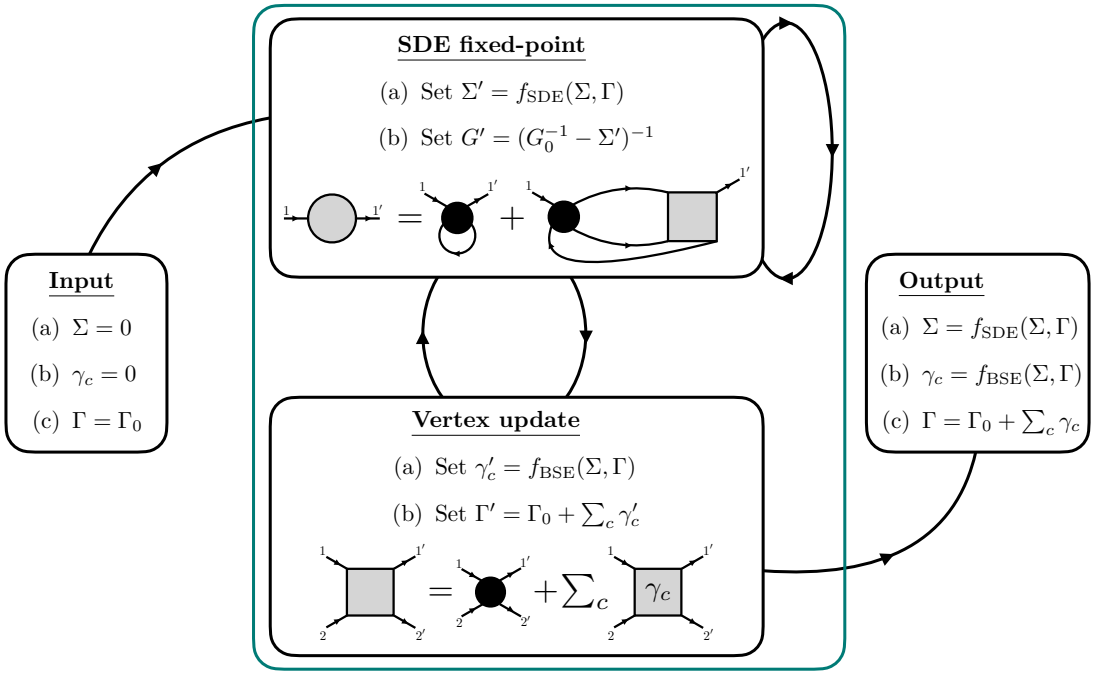

Figure 4.8: Numerical scheme for solving the parquet approximation. The central green box highlights the self-consistency cycle for determining the fixed-point, i.e. starting from the bare couplings, we first converge the self-energy via the SDE and subsequently update the vertex using the respective BSE for γ_c. The so-obtained two-particle vertex can, in turn, be used to start another set of SDE iterations until the fixed-point for both equations has been found. In this case the calculation is stopped.

relative to the spin coupling, which justifies a larger minimum step size $\min\{\Delta\Lambda\} = 10^{-4}J$.

4.4.5 Calculation of correlation functions

Computing the spin-spin correlation function $\chi_{ij}^{\mu\nu}(\omega)$ amounts to solving the Matsubara integrals in Eq. (4.45). The first term resembles the bare susceptibility from Sec. 4.4.2 and can thus be calculated with the techniques outlined therein. For the second part, we need to integrate vertices over the two-dimensional frequency domain. In principle, this could be achieved by computing two nested 1D integrals using a Gauss-Kronrod rule. For multidimensional integrals there exist, however, more efficient quadratures such as the Genz-Malik rule [136], which is implemented in the `Cubature` package of the Julia programming language. Since `Cubature` supports only finite rectangular domains, we employ the mapping

$$v \to \frac{2v-1}{1-(2v-1)^2}, \; dv \to \frac{1+(2v-1)^2}{(1-(2v-1)^2)^2}, \tag{4.56}$$

for both integration variables, such that the integral can be computed over $(0,1)^2 = (0,1) \times (0,1)$[5] instead of $(-\infty, \infty)^2$. In addition, we divide the rectangle $(0,1)^2$ into 9 smaller boxes, where the volume of the central box is scaled with Λ, to cope with the evolution of vertices and propagators under the RG flow.

4.5 Examples

In this section, we want to provide two examples for the application of pffRG and showcase the analysis of results obtained with the method. To begin with, we consider an effective spin model for twisted tungsten diselenide, which resembles a spinful version of the Hamiltonian from Sec. 3.4, but in the strong-coupling limit. Although the model itself is quite involved, featuring spatially anisotropic and off-diagonal nearest-neighbor couplings, we underline the simplicity with which it can be embedded into the general pffRG formalism (see Sec. 4.3). Here, our focus lies on arranging a closed discussion of the low-temperature phase diagram and its implications for experiments, rather than a conceptual debate, and we thus allow ourselves to truncate the flow equations at the 1ℓ level.

[5] Here, $\times$ denotes the cartesian product.

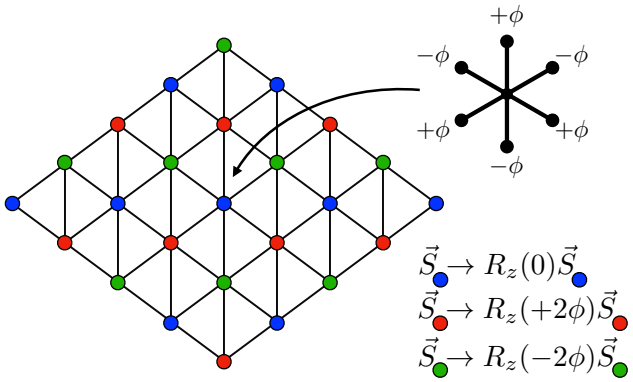

Figure 4.9: Three-sublattice transformation on the triangular lattice. As shown in the upper right, the phase factor ϕ inherited from the tight-binding model Eq. (4.57) changes sign on neighboring bonds of the triangular lattice and thus breaks inversion symmetry. By decomposing the lattice into three sublattices and transforming their respective spins according to the rules in the bottom right, SU(2) symmetry on the level of the strong-coupling Hamiltonian Eq. (4.58) can be restored if ϕ is an integer multiple of $\pi/3$.

To remedy this shortcoming, we study the implications of a multiloop truncated pffRG flow in our second example. For the sake of simplicity, we focus on the nearest-neighbor ferromagnet on the cubic lattice, for which the ground state is well known. Special emphasis is layed on self-consistency, that is, the question whether the pseudofermion vertices converge to a solution of the parquet approximation or not. We conclude by explicitly computing particle number fluctuations for different loop orders and gauging their influence on physical conclusions drawn from the fRG flow.

4.5.1 Example 1: Strong-coupling study of twisted WSe_2

Among the plethora of moiré heterostructures which have recently become of interest, twisted transition metal dichalcogenides are very much appreciated for their high degree of tunability and the variety of collective phases emerging therein [40, 74–81]. While tBG is based on graphene, an SU(2) symmetric semiconductor with gapless Dirac cones, tMDs are, as their name suggest, built from a transition metal like molybdenum (Mo) or tungsten (W) and two chalcogens like sulfur (S), selenium (Se) or tellurium (Te), which makes for vastly different physical properties: TMD monolayers usually feature a direct band gap, strong spin-orbit coupling and have no inversion symmetry. Similar to tBG, however, multilayer tTMD heterostructures can harbor superconducting [75] as well as correlated insulating states [74, 78] for different levels of carrier doping. To sharpen the discussion, we focus on the insulating phase reported for twisted tungsten diselenide at half-filling [74].

The effective lattice model proposed for $tWSe_2$ [82, 83] can be considered a spinful version of the Hamiltonian studied in Sec. 3.4 augmented by a transverse displacement field V_z corresponding to the potential difference between the gate voltages applied to the top and bottom TMD layer. On the level of the triangular moiré bandstructure, V_z generates a spin dependence of the single-particle dispersion: if $|V_z| > 0$, the emergent inversion symmetry of the bilayer system is broken and the bands are related to each other by threefold rotations, such that, due to strong spin-momentum locking in the monolayer system, the dispersion near the $\boldsymbol{K}$ ($\boldsymbol{K}'$) point is predominantly governed by spin up (down) states [82]. For $V_z = 0$ and sufficiently small twist angles, on the other hand, inversion symmetry is approximately restored [82]. These aspects can be summarized by a tight-binding Hamiltonian of the form

$$\mathcal{H}_{\mathrm{tb}} = \sum_{i,j} \sum_{\sigma\in\{\uparrow,\downarrow\}} t_{ij}^{\sigma} c_{i\sigma}^{\dagger} c_{j\sigma} \,. \tag{4.57}$$

The hopping parameters $t_{ij}^{\sigma} = |t_{ij}^{\sigma}| e^{i\phi_{ij}^{\sigma}}$ are parametrized by their respective magnitude $|t_{ij}^{\sigma}|$ and phase factor ϕ_{ij}^{σ}, where the aforementioned inversion symmetry breaking is implemented by imposing that $\phi_{ji}^{\sigma} = -\phi_{ij}^{\sigma}$ and $|t_{ji}^{\sigma}| = |t_{ij}^{\sigma}|$. Time-reversal symmetry then requires that the phase factors on the same bond have opposite sign for the two spin directions (see Fig. 4.9). Moreover, t_{ij}^{σ} should be invariant under $\mathcal{C}_3$ transformations. Due to these symmetry requirements, all hoppings in the n-th nearest-neighbor shell of the triangular lattice are fully determined by fixing $|t_n|$ and $\phi_n^{\uparrow(\downarrow)} = \phi_n$ for one representative bond [83]. An estimate of these parameters for a twist angle $\theta = 4°$ (see Fig. 4.10), reveals that nearest-neighbor hopping is predominant for displacement fields $|V_z| \leq 100\mathrm{meV}$ and we, thus, allow ourselves to truncate $\mathcal{H}_{\mathrm{tb}}$ beyond $n = 1$.

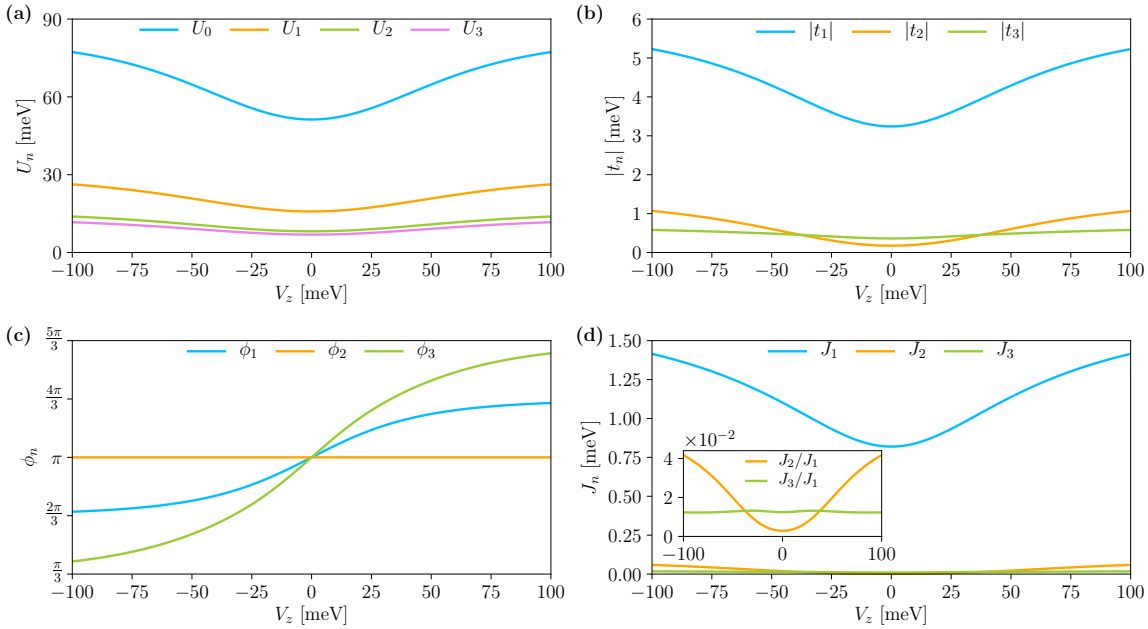

Figure 4.10: Hubbard model parameters for $tWSe_2$. The data in panels **(a)** - **(c)** was kindly provided by the authors of Ref. [83] for a twist angle $\theta = 4°$. In **(a)**, we plot the strength of n-th nearest-neighbor interactions up to $n = 3$. The most dominant contribution is given by an on-site Hubbard repulsion U_0. Panels **(b)** and **(c)** present the magnitude and phase factor of the hopping parameters for the n-th shell. Using $J_n = 4|t_n|^2/U_0$, one can estimate the magnitude of two-spin interactions in the strong-coupling limit, as shown in the inset of **(d)**. Remarkably, $\phi_2 = \pi$ is constant over the entire range of displacement fields, resulting in an SU(2) symmetric interaction characterized by J_2, which can reach values up to four percent relative to J_1.

The simplest conceivable interaction term is given by an on-site Hubbard repulsion U_0. Since U_0 is approximately one order of magnitude larger than $|t_1|$ (see Fig. 4.10), we consider the strong-coupling limit, in which case the Hamiltonian reads

$$\mathcal{H} = \frac{J_1}{2} \sum_{\langle ij \rangle} \left[\cos(2\phi_1)(S_i^x S_j^x + S_i^y S_j^y) + S_i^z S_j^z \right] + \frac{J_1}{2} \sum_{\langle ij \rangle} \sin(2\phi_1)(\boldsymbol{S}_i \times \boldsymbol{S}_j)^z \,, \tag{4.58}$$

that is, we obtain a model of interacting spins on the triangular lattice, featuring XXZ and Dzyaloshinski-Moriya (DM) exchange [82, 83]. With the estimates from Ref. [83], $J_1 = 4|t_1|^2/U_0$, lies in the range of 1meV and, thus, resembles the energy scales of typical Mott insulators such as α-$RuCl_3$ [137]. Note that in order to incorporate the symmetries of the tight-binding Hamiltonian, ϕ_1 has alternating signs on nearest-neighbor bonds (see Fig. 4.9). To shorten the notation, we use $J_1 = J$ and $\phi_1 = \phi$ from now on. Introducing the matrix

$$\boldsymbol{R}_z(-2\phi) = \begin{pmatrix} \cos(2\phi) & \sin(2\phi) & 0 \\ -\sin(2\phi) & \cos(2\phi) & 0 \\ 0 & 0 & 1 \end{pmatrix} , \tag{4.59}$$

corresponding to a rotation about the z-axis by an angle -2ϕ, Eq. (4.58) can alternatively be written as

$$\mathcal{H} = \frac{J}{2} \sum_{\langle ij \rangle} \boldsymbol{S}_i^T \boldsymbol{R}_z(-2\phi) \boldsymbol{S}_j \,. \tag{4.60}$$

In this form, it becomes apparent that the Hamiltonian possesses a hidden SU(2) symmetry for $|\phi| \in \mathbb{Z}\frac{\pi}{3}$. This can be seen by decomposing the triangular lattice into three sublattices as shown in Fig. 4.9 and subsequently transforming their spins according to $\boldsymbol{S}_i \to \boldsymbol{R}_z(\theta_i)\boldsymbol{S}_i$ with $\theta_i \in \{0, \pm 2|\phi|\}$, respectively. Along the same lines, one finds that the eigenvalues of the Hamiltonian for $|\phi|$, $|\phi| + \mathbb{Z}\frac{\pi}{3}$ and $\mathbb{Z}\frac{\pi}{3} - |\phi|$ are the same, although the corresponding eigenstates differ precisely by the sublattice transformation required to restore spin rotation invariance.

In order to study the ground state phase diagram of $tWSe_2$ using pffRG, we need to find a suitable parametrization of the vertex in spin space, that is, we must identify the minimal set of vertex

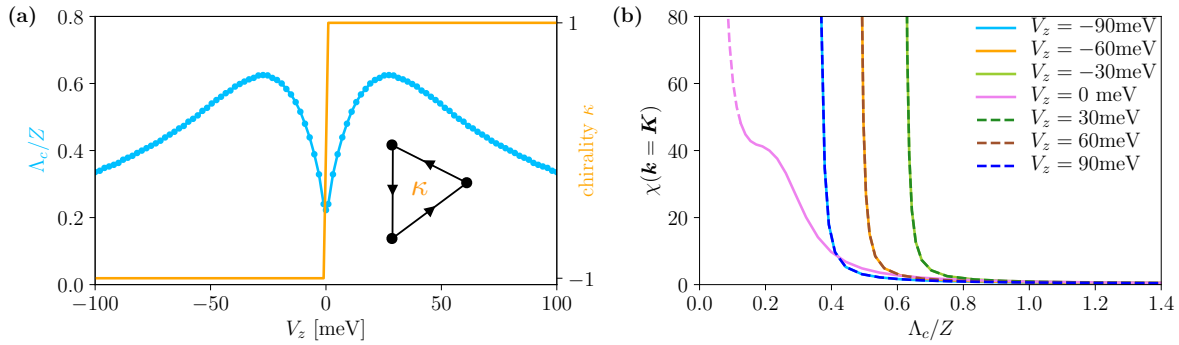

Figure 4.11: Phase diagram for tWSe$_2$ in the strong-coupling limit. The critical scale Λ_c and vector chirality κ as a function of the transversal displacement field V_z are plotted in **(a)**. Around the SU(2) symmetric point $V_z = 0$, κ changes sign, accompanied by a pronounced dip in the critical scale. The respective flow of the structure factor $\chi(\boldsymbol{k}) = \sum_\mu \chi^{\mu\mu}(\boldsymbol{k})$ indicated by a violet line in **(b)** for $\boldsymbol{k} = \boldsymbol{K}$ features a gentle shoulder, followed by a strong increase in the susceptibility. If SU(2) symmetry is broken by finite V_z, flow breakdowns become noticeable as sharp divergencies of $\chi(\boldsymbol{k})$. For symmetry reasons (see Fig. 4.9), the flows obtained for the same $|V_z|$ precisely match, although the respective instabilities have different chiralities.

components $\Gamma^{\mu\nu}_{i_1 i_2}$ that become finite throughout the flow. To this end, we exploit that $\mathcal{H}$ is U(1) symmetric, i.e. invariant for $\boldsymbol{S}_i \to \boldsymbol{R}_z(\theta)\boldsymbol{S}_i$[6]. Imposing this symmetry on the level of the vertex, we find the condition

$$\tilde{\boldsymbol{R}}_z(\theta)^T \boldsymbol{\Gamma}_{i_1 i_2} \tilde{\boldsymbol{R}}_z(\theta) = \boldsymbol{\Gamma}_{i_1 i_2} \,, \tag{4.61}$$

where $\boldsymbol{\Gamma}_{i_1 i_2}$ symbolically indicates the 4×4 matrix of vertex components (we suppress frequency arguments for brevity). Consequently, $\tilde{\boldsymbol{R}}_z(\theta)$ is defined as the direct sum $\boldsymbol{R}_z(\theta) \oplus 1$, generalizing the U(1) rotation to the combined space of spin and density indices. To fulfill Eq. (4.61), $\boldsymbol{\Gamma}_{i_1 i_2}$ needs to be of the form

$$\boldsymbol{\Gamma}_{i_1 i_2} = \begin{pmatrix} \Gamma^{xx}_{i_1 i_2} & \Gamma^{xy}_{i_1 i_2} & 0 & 0 \\ -\Gamma^{xy}_{i_1 i_2} & \Gamma^{xx}_{i_1 i_2} & 0 & 0 \\ 0 & 0 & \Gamma^{zz}_{i_1 i_2} & \Gamma^{zd}_{i_1 i_2} \\ 0 & 0 & \Gamma^{dz}_{i_1 i_2} & \Gamma^{dd}_{i_1 i_2} \end{pmatrix} , \tag{4.62}$$

and we, thus, need to monitor only six instead of 16 vertex components during RG flow. The respective initial conditions can be read off directly from Eq. (4.58): all components with a density subscript vanish, whereas

$$\begin{aligned} \Gamma^{xx}_{0,i_1 i_2}(\omega_s, \omega_t, \omega_u) &= \frac{J}{4}\cos(2\phi) \\ \Gamma^{zz}_{0,i_1 i_2}(\omega_s, \omega_t, \omega_u) &= \frac{J}{4} \\ \Gamma^{xy}_{0,i_1 i_2}(\omega_s, \omega_t, \omega_u) &= \frac{J}{4}\sin(2\phi) \,, \end{aligned} \tag{4.63}$$

if i_1 and i_2 are nearest-neighbors sites. With these prerequisites, closed expressions for the self-energy loop and bubble functions following the discussions in Sec. 4.3 can be derived and evaluated with the numerical algorithms outlined in Sec. 4.4. The two-particle vertex is hereby discretized on a dense $N_{\omega_c} \times N^2_{\nu_c} = 84 \times 72^2$ frequency grid and truncated beyond bond distances $L = 12$. For Σ, we choose $N_\Sigma = 200$ frequencies. Our main observables are the in-plane and out-of-plane correlation functions χ^{xx}_{ij} and χ^{zz}_{ij}, as well as χ^{xy}_{ij}.

To map out the ground state phase diagram as a function of the transverse displacement field, we utilize the microscopic coupling parameters given in Ref. [83], i.e. we consider $|V_z| \leq 100$meV and set $J > 0$ and ϕ accordingly. Our results for the characteristic RG scale Λ_c/Z[7], where the pffRG flow breaks down, is shown in Fig. 4.11(a). We find two reflection symmetric domes with $\Lambda_c > 0$, separated by a sharp minimum at $V_z = 0$. To identify the nature of the incipient magnetic orders, we probe the dominant structure factors in vicinity of Λ_c/Z. Both for $V_z > 0$ as well as $V_z < 0$, in-plane structure

[6] Note that in comparison to the sublattice transformation from before, θ now characterizes a global spin rotation.

[7] $Z = \sqrt{2}J$ defines the energy scale of the microscopic model as the Euclidean norm of $J \times (\cos(2\phi), 1, \sin(2\phi))^T$.

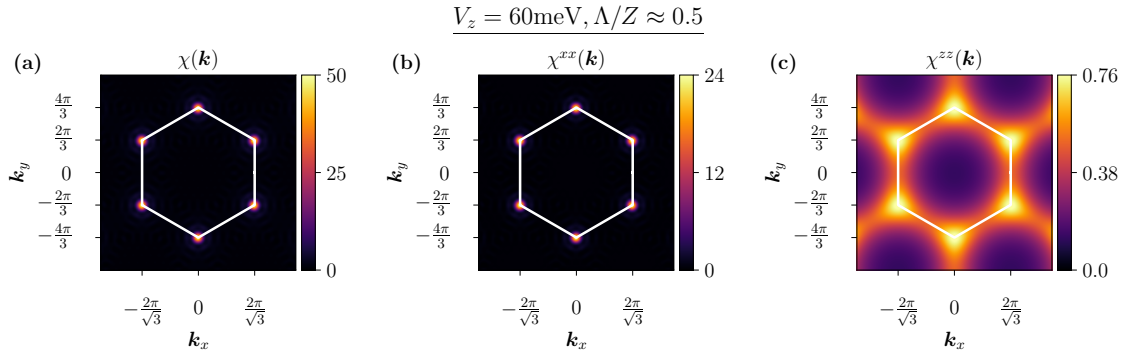

Figure 4.12: Characterization of in-plane 120° order. (a) We plot the full momentum-resolved structure factor $\chi(\boldsymbol{k})$, which features sharp incipient Bragg peaks at the $\boldsymbol{K}$ points, indicative of 120° order. It can subsequently be decomposed into in-plane components $\chi^{xx}(\boldsymbol{k})$ as plotted in **(b)** and an out-of-plane part described by $\chi^{zz}(\boldsymbol{k})$ and displayed in **(c)**. We find that $\chi^{xx}(\boldsymbol{k})$ is predominant for any value of V_z, signifying a strong tendency towards coplanar magnetic order in $tWSe_2$.

factors $\chi^{xx}(\boldsymbol{k})$ clearly dominate (see Fig. 4.12) and show pronounced Bragg peaks at the $\boldsymbol{K}$-points of the Brillouin zone, indicative of coplanar 120° spin order. The two 120° degree states differ, however, by their respective vector chirality

$$\kappa = \operatorname{sgn}\left(\frac{1}{2}\langle \boldsymbol{S}_{i_1} \times \boldsymbol{S}_{i_2} + \boldsymbol{S}_{i_2} \times \boldsymbol{S}_{i_3} + \boldsymbol{S}_{i_3} \times \boldsymbol{S}_{i_1}\rangle^z\right) = \operatorname{sgn}\left(\chi^{xy}_{i_1 i_2} + \chi^{xy}_{i_2 i_3} + \chi^{xy}_{i_3 i_2}\right) \tag{4.64}$$

which determines the sense of rotation for spins on a triangular plaquette spanned by sites i_1, i_2 and i_3. For the convention shown in the inset of Fig. 4.11(a), the chirality switches from $\kappa_- = -1$ for $V_z < 0$ to $\kappa_+ = +1$ for $V_z > 0$. For vanishing displacement field, SU(2) symmetry is fully recovered, which implies vanishing off-diagonal spin correlators and consequently $\kappa = 0$ in pffRG. The strong suppression of the critical scale observed for the Heisenberg antiferromagnet [86] may, therefore, be related to the κ_+ and κ_- state becoming degenerate for $V_z = 0$, which, apparently, hampers the growth of magnetic correlations during the RG flow.

At last, let us discuss possible corrections to the Hamiltonian in Eq. (4.58). As can be seen from Fig. 4.10, longer-ranged couplings J_2 and J_3 can assume values on the percent level relative to J_1. While third neighbor couplings J_3 are predominant for small $|V_z|$, their relevance falls off upon ramping up the displacement field and for $|V_z| \gtrsim 50\text{meV}$, second neighbor exchange J_2 presents the most important perturbation. This is interesting insofar that Ref. [83] predicts $\phi_2 = \pi$, such that the next-nearest-neighbor term would be SU(2) symmetric. For the triangular antiferromagnet, even small second-neighbor Heisenberg couplings tend to destabilize the 120° phase in favor of a paramagnetic state, widely believed to be a spin liquid [96, 138–140]. This raises the question, whether the same can happen in $tWSe_2$ where, for $|V_z| > 0$, SU(2) breaking interactions like XXZ anisotropy and DM exchange need to be accounted for. Indeed, as shown in Ch. 6.1, pffRG calculations for the J_2-augmented Hamiltonian predict extended regimes without a flow breakdown, indicative of spin liquid states lurking in the correlated insulating regime of twisted TMDs.

4.5.2 Example 2: Multiloop fRG for the cubic ferromagnet

In order to study the impact of multiloop corrections on 1ℓ-pffRG results, we consider the ferromagnet on the simple cubic lattice as characterized by the Hamiltonian

$$\mathcal{H} = \frac{J}{2}\sum_{\langle ij\rangle} S_i^\mu S_j^\mu\,, \tag{4.65}$$

with $J < 0$. The coupling matrix $\boldsymbol{J}_{ij}$ on nearest-neighbor sites $\langle ij\rangle$ assumes the particularly simple form $\boldsymbol{J}_{ij} = J \times \mathbb{1}$ and thus fulfills $\boldsymbol{U}^\dagger \boldsymbol{J}_{ij} \boldsymbol{U} = \boldsymbol{J}_{ij}$ for $\boldsymbol{U} \in \mathrm{SU}(2)$. Exploiting this symmetry on the vertex level, we obtain the decomposition

$$\boldsymbol{\Gamma}_{i_1 i_2} = \begin{pmatrix} \Gamma^s_{i_1 i_2} & 0 & 0 & 0 \\ 0 & \Gamma^s_{i_1 i_2} & 0 & 0 \\ 0 & 0 & \Gamma^s_{i_1 i_2} & 0 \\ 0 & 0 & 0 & \Gamma^d_{i_1 i_2} \end{pmatrix}, \tag{4.66}$$

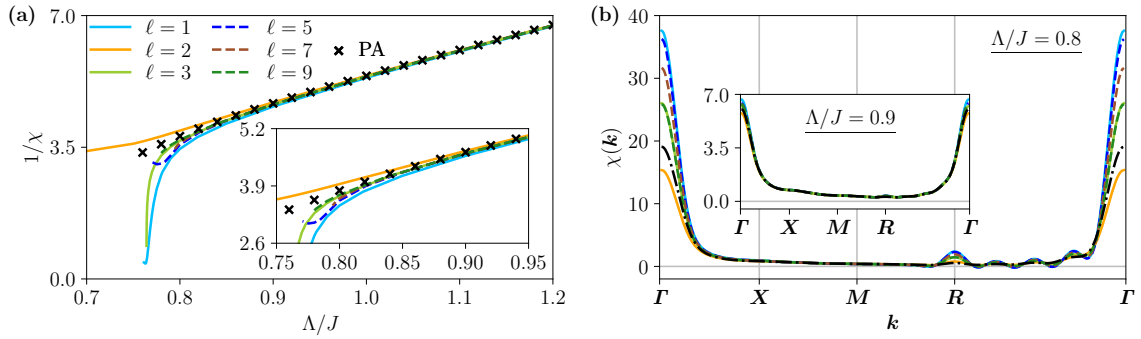

Figure 4.13: Ferromagnetic correlation functions from mfRG. In **(a)**, the flow of the inverse on-site correlator $1/\chi$ is plotted as a function of loop order ℓ and compared to results obtained with the parquet approximation (black crosses). The inset displays $1/\chi$ close to the critical scale $\Lambda_c^{(1\ell)}/J \approx 0.76$ at which a sharp downturn appears in the 1ℓ flow. For $\Lambda/J < 0.76$, the parquet equations could not be properly converged. Panel **(b)** shows the structure factor $\chi(\boldsymbol{k})$ in momentum space for two different cutoffs Λ: close to the ordering scale $\Lambda_c^{(1\ell)}$ (main plot) and for $\Lambda > \Lambda_c^{(1\ell)}$ (inset). Though the results are in good agreement among loop orders and with the PA for $\Lambda/J = 0.9$, featuring dominant peaks at the $\boldsymbol{\Gamma}$ point in all cases, convergence becomes harder to achieve for $\Lambda \to \Lambda_c^{(1\ell)}$.

that is, one only needs to consider a spin component Γ^s and a density contribution Γ^d. For our numerical calculations, we choose $L = 8$, $N_\Sigma = 200$ and $N_\omega \times N_\nu^2 = 84 \times 72^2$ for which our results seemed reasonably well converged.

Since our model is defined on a bipartite and non-frustrated lattice graph, we would expect to find a ferromagnetic instability at $\Lambda = \Lambda_c$ when approaching the infrared. The inverse spin-spin correlation function $1/\chi = 1/\chi_{ii}^{xx} = 1/\chi_{ii}^{yy} = 1/\chi_{ii}^{zz}$ for $\ell = 1$, plotted in Fig. 4.13(a), indeed features a sharp downturn away from its linear behavior at large cutoffs, indicative of an ordering transition. Moreover, the diagonal static structure factor $\chi(\boldsymbol{k}) = \sum_\mu \chi^{\mu\mu}(\boldsymbol{k})$ computed from $\chi_{ij}^{\mu\mu}$ in vicinity of $\Lambda_c^{(1\ell)}$ (see [Fig. 4.13(b)]), displays sharp peaks at $\boldsymbol{k} = \boldsymbol{\Gamma}$, which confirm that the correlations are ferromagnetic.

Comparing different loop orders, we observe a drastic change between $\ell = 1$ and $\ell = 2$. While the 1ℓ results clearly imply a diverging spin-spin correlation function at $\Lambda_c^{(1\ell)}/J \approx 0.76$, χ is suppressed in 2ℓ calculations and its flow remains regular. This discrepancy can be attributed to the construction of two loop contributions [141]: to compute $\gamma_c^{(2\ell)}$ in a specific 2PR channel, one solely considers 1ℓ diagrams from channels $\bar{c}$ complementary to c and thus accounts for screening effects [116, 141]. Since magnetic contributions primarily result from RPA diagrams in the t channel [85], the exclusive feedback of non-magnetic, i.e. s or u-reducible, diagrams apparently causes an underestimation of long-range order in the 2ℓ flow. For $\ell \geq 3$, this effect is partially remedied, since the central part allows for contractions of c-reducible diagrams. In consequence, we again observe a ferromagnetic instability in the 3ℓ flow (see Fig. 4.13). Resolving that divergence of χ at even higher loop orders, however, becomes increasingly difficult and for $\ell = 5, 7, 9$ (dashed lines in [Fig. 4.13(a)]) the mfRG flows have to be terminated prematurely, as the error of the numerical ODE solver grows unacceptably large. Yet, $\chi(\boldsymbol{k})$ shows a pronounced peak at $\boldsymbol{k} = \boldsymbol{\Gamma}$, consistent among loop orders. Note that self-energy corrections for loop orders $\ell \geq 3$ have been computed via *one-shot* iterations instead of self-consistency cycles.

To test for self-consistency of the pffRG truncation, we additionally computed solutions of the parquet approximation for various $\Lambda/J \in [0.76, 1.2]$. For $\Lambda/J < 0.76$, we were not able to converge the PA, even with finite damping factors. By construction, we would expect that Σ and γ_c calculated with mfRG should likewise solve the Schwinger-Dyson and Bethe-Salpeter equations for $\ell \to \infty$. Ideally, one would be able to obtain converged pseudofermion vertices and spin-spin correlations already for $\ell < \infty$, which, *a posteriori*, justifies the neglect of further corrections. For $\Lambda > \Lambda_c^{(1\ell)}$, the χ-flows for different loop orders certainly overlap with the PA results, which we have indicated with black crosses in Fig. 4.13(a). Remarkably, even $\ell = 1$ suffices to reproduce the parquet solution. Approaching $\Lambda_c^{(1\ell)}/J \approx 0.76$, deviations between the fRG and PA results are more visible and agreement among loop orders becomes harder to achieve. Furthermore, it seems that the convergence in ℓ is non-monotonous: for $\ell = 3$, we follow the PA solutions more closely than for $\ell = 5$ and $\ell = 7$, whereas the 9ℓ flow resembles the 3ℓ results. This behavior is also reflected in the momentum space profile of $\chi(\boldsymbol{k})$. For $\Lambda/J = 0.9$ (see the inset in [Fig. 4.13(b)]), the mfRG and parquet structure factors agree formidably

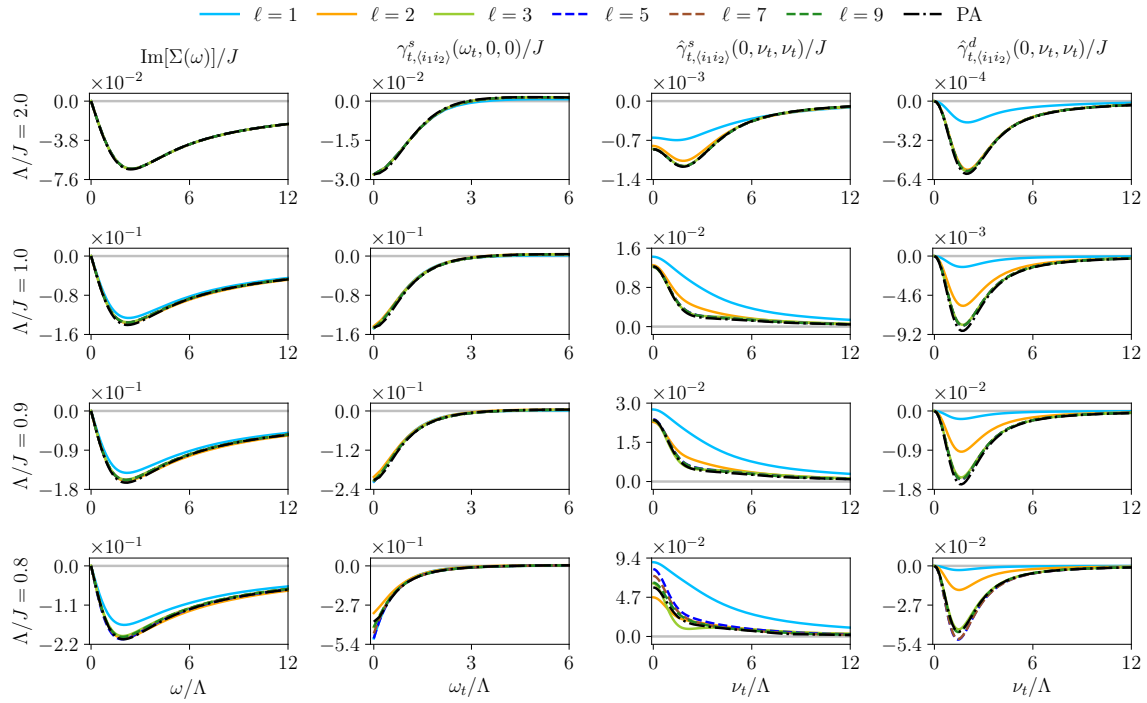

Figure 4.14: Comparison of mfRG and PA pseudofermion vertices. We plot the purely imaginary self-energy Σ (first column) and t-reducible contributions to the vertex (second to fourth column) at different scales Λ/J, corresponding to the individual rows. To display the reducible vertex γ_t, we focus on two representative cuts through frequency space: one along the bosonic ω_t-axis for fermionic frequencies $\nu_t = \nu_t' = 0$ and the other one along the $\nu_t' = \nu_t$ line with ω_t set to zero. For the ω_t-cut, we solely plot the spin contribution γ_t^s, since γ_t^d vanishes due to symmetries. Note that we have subtracted Q_1 from the vertices in the third and fourth column, as indicated by a hat over the respective labels. This is because Q_1 is independent of ν_t and therefore simply offsets γ_t by a constant value along this cut. Upon reducing Λ, the vertices grow in magnitude and their dominant features, such as the maximum at $\omega_t = 0$ in the second column, progressively sharpen. Though loop convergence and agreement with the parquet solution (black line) is quickly achieved for $\Lambda/J \gtrsim 0.9$, even $\ell = 9$ does not suffice to fully reproduce PA results for γ_t^s when Λ is further reduced (see the second and third column of the last row).

well, while at $\Lambda/J = 0.8$, somewhat closer to $\Lambda_c^{(1\ell)}$, larger discrepancies are visible.

Instead of comparing spin-spin correlations, which are, after all, obtained by integrating vertices over frequency space (see the discussion in Sec. 4.3.5), we can inspect Σ and γ_c directly. This additional step of numerical analysis is helpful in order to digest the influence of higher order corrections as well as to attest to the accuracy of the implementation[8]. In Fig. 4.14, we present results for the purely imaginary pseudofermion self-energy, as well as exemplary cuts through the t channel, which is responsible for proliferating magnetic correlations. Even above $\Lambda_c^{(1\ell)}/J \approx 0.76$, where the spin-spin correlations seem to converge already, pronounced deviations between the 1ℓ and higher loop results for γ_t can be observed. These are most prominently visible along the fermionic frequency axis, as shown in the third and fourth column of Fig. 4.14. At $\Lambda/J = 1$, for example, there is a pronounced peak in the density component γ_t^d, which gains in magnitude when higher loops are included. For $\ell \geq 3$, the mfRG vertices nonetheless converge and resemble the parquet solution. Close to the 1ℓ instability, however, 3ℓ calculations are not sufficient to reproduce the PA, which can be seen in the spin component γ_t^s at $\Lambda/J = 0.8$. For $\ell \geq 5$ one finds a cusp around the origin, followed by a rather rapid decay of the 2PR vertex along the fermionic $\nu_t = \nu_t'$ direction. In 3ℓ calculations, there is an additional change of curvature at $\nu_t/\Lambda \approx 2$, which is, however, absent in the PA solution. Remarkably, the self-energy seems well converged already for $\ell = 2$, indicating that self-energy corrections, which contribute only at the three loop level and beyond, are fairly small. This also implies that the neglect of expensive self-consistency loops between the Σ and Γ flows is indeed valid.

At last, we want to scrutinize the fulfillment of the pseudofermion constraint $n_i = 1$, where $n_i = \bar{\psi}_{i\alpha}\psi_{i\alpha}$ is the number of pseudofermions on site i. As shown in Ref. [P1], $\langle n_i \rangle = 1$ always holds if the self-energy

[8] To instill confidence in the mfRG and PA results, one needs to assure that discretization artifacts like sharp kinks or cusp are absent in the 1PI vertices.

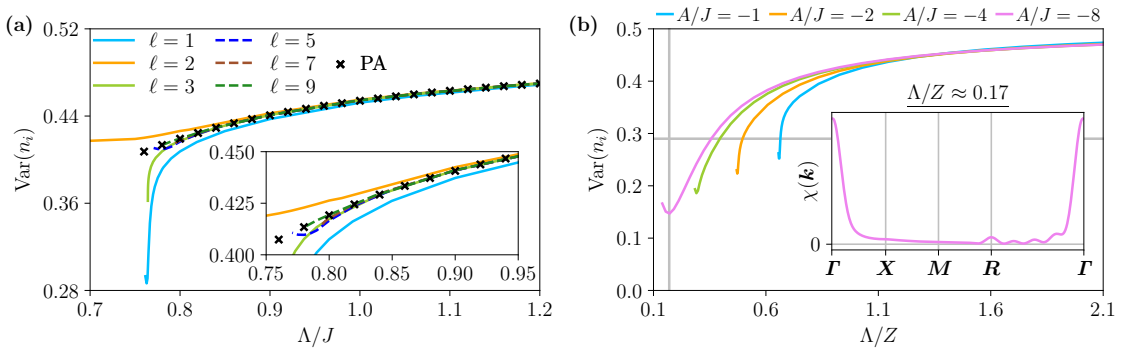

Figure 4.15: Pseudofermion occupation number fluctuations. (a) Flows of the variance $\mathrm{Var}(n_i)$ of the particle number $n_i = \bar{\psi}_{i\alpha}\psi_{i\alpha}$ at site i for different loop orders and the parquet approximation (see discussion in Sec. 4.3.5). Though fluctuations decrease with Λ, they remain fairly sizable even in vicinity of the ordering transition, where a sharp drop in the 1ℓ (3ℓ) flow occurs. **(b)** Same as **(a)** but for $\ell = 1$ and with finite level repulsion terms $A(\boldsymbol{S}_i)^2$ (for $A < 0$). Although fluctuations are suppressed in comparison to the $A = 0$ result (horizontal grey line), the structure factor profile, as shown in the inset for $A/J = -8$ at $\Lambda/Z \approx 0.17$ (vertical grey line), remains qualitatively unchanged and still suggests a ferromagnetic ground state. Here, $Z = \sqrt{A^2 + J^2}$.

is particle-hole symmetric. Nonetheless, there might be fluctuations around the mean, quantified by the variance $\mathrm{Var}(n_i) = \langle n_i^2 \rangle - \langle n_i \rangle^2$, which can be computed from equal-time spin-spin correlations (see Sec. 4.3.5). If every site was half-filled $\mathrm{Var}(n_i)$ vanishes, if not, $0 < \mathrm{Var}(n_i) \leq 1$[9], where $\mathrm{Var}(n_i) = 1/2$ indicates that all states, even the unphysical ones, occur with equal probabilities. As can be seen from the results in Fig. 4.15(a), the variance never vanishes and only mildly decreases below the infinite temperature limit $\mathrm{Var}(n_i) = 1/2$. In consequence, the pseudofermion constraint is not exactly fulfilled in pffRG. Close to the ordering transition $\Lambda_c^{(1\ell)}/J \approx 0.76$, $\mathrm{Var}(n_i)$ shows a strong downturn for $\ell = 1$ and $\ell = 3$, which remains obscure in the higher loop and parquet results. Recall, however, that we had to prematurely stop the calculation for those in order to maintain control over numerical errors, which explains the absence of such a feature in their respective flows.

In an attempt to manually impose half-filling, we repeated the 1ℓ calculations with finite level repulsion terms $A(\boldsymbol{S}_i)^2$ on every lattice site. To enforce $n_i = 1$, we initialize the flow with different $A < 0$, such that empty or doubly occupied states are energetically penalized. The respective results are shown in Fig. 4.15(b). There are three important observations to make: (a) The critical scale $\Lambda_c^{(1\ell)}$ is reduced for finite A. Since we have introduced an additional energy scale larger than the non-local spin coupling J and the cutoff is, therefore, given in units of $Z = \sqrt{A^2 + J^2}$, this is rather intuitive. Unfortunately, $A \to -\infty$, corresponding to the limit in which the constraint should be enforced exactly, simultaneously shifts $\Lambda_c \to 0$, that is, into the regime which is extremely challenging for numerics. (b) In line with our expectations, occupation number fluctuations are indeed reduced for finite A. For $A/J = -8$, for example, $\mathrm{Var}(n_i) \approx 0.15$ in vicinity of the ordering transition (vertical grey line in [Fig. 4.15(b)]), which is roughly half of the value it assumed for $A = 0$ (indicated by a horizontal grey line). (c) The nature of the incipient magnetic order is left unchanged, even if fluctuations are further reduced. As can be seen from the inset in Fig. 4.15(b), the structure factor still features dominant peaks at the Γ point and thus indicates ferromagnetic correlations. On a qualitative level, spin-spin correlations therefore seem remarkably robust to occupations of the spin zero states [85, 107, 116]: they suggest a ferromagnetically ordered ground state in any case.

Let us summarize the main results of this example section. We have compared multiloop pffRG results, that is, spin-spin correlations, pseudofermion vertices and occupation number fluctuations, among different loop orders ℓ and checked for their agreement with solutions of the parquet approximation. For our model system, the nearest-neighbor ferromagnet on the simple cubic lattice, a conclusive picture emerged: for cutoffs larger than the ordering scale $\Lambda_c^{(1\ell)}$, reaching convergence on the level of spin-spin correlations was fairly easy and already the 1ℓ calculations resembled the parquet results. For the pseudofermion vertices, further corrections up to $\ell = 3$ were necessary. Approaching $\Lambda_c^{(1\ell)}$, however, achieving convergence becomes progressively more difficult and even 9ℓ calculations showed slight deviations to the PA solution. Yet, all results consistently predict dominant ferromagnetic correlations, as expected. Regarding the pseudofermion constraint, we were able to show that fluctuations around

[9] $\mathrm{Var}(n_i) = 1$ signifies that only spin zero states contribute.

half-filling are indeed suppressed by local level repulsion terms, though their implementation does not affect the principal conclusion (emergence of long-range ferromagnetic order) drawn from the RG flow. We were thus able to provide evidence for the qualitative reliability of the pffRG approach by (a) demonstrating self-consistency of the employed truncation through loop convergence in regimes where the flow is well-behaved and (b) showing that particle number fluctuations do not seem to affect the principal interpretation of the results.

5 Methodological development of pseudofermion fRG

5.1 Overview

Quantum spin models continue to attract formidable research interest in condensed matter physics for harboring a plethora of interesting many-body states. Quantum fluctuations in frustrated magnets, for example, can become so violent as to impede the formation of magnetic order all together, even at temperatures down to absolute zero. These elusive quantum spin liquids present highly-entangled states of matter, featuring unusual properties such as fractionalized excitations and emergent gauge fields [9, 10, 120].

The accurate numerical treatment of generic spin Hamiltonians remains a daunting challenge, despite tremendous progress made with various techniques. Tensor network methods, for example, undoubtedly belong to the most powerful algorithms in condensed matter research, especially in one dimension. Although generalizations to higher dimension have been successfully developed [142, 143], their performance beyond $d = 1$ generally suffers from the area-law obedience of the entanglement entropy. Other sophisticated methods, such as quantum Monte Carlo simulations, face similar difficulties when applied to frustrated spin models. There, the infamous sign problem prohibits the study of the low-temperature regime. In the absence of any singular approach, which is able to resolve phase diagrams of arbitrary quantum magnets in an unbiased way, novel techniques are highly sought-after.

The pseudofermion functional renormalization group (pffRG) [22] is one of the few theoretical methods capable of treating spin models both in two and three spatial dimensions. This comes, however, at the cost of having to invoke an approximate treatment of the spin operators by decomposing them into fermionic partons. Nonetheless, pffRG has served as a valuable tool for providing insights into quantum phase diagrams of hitherto inaccessible Hamiltonians, such as Heisenberg models on extended cubic [105, 110, 111, P1], diamond [107], hyperkagome [98] and pyrochlore lattices [109, P1]. The quantitative accuracy of pffRG is, however, difficult to assess. This is because of the aforementioned pseudofermion representation as well as the truncation of three-particle vertex, which is inherent to any fRG approach. Both approximations are formally uncontrolled and their validity therefore needs to be tested *a posteriori*. An indication for the faithfulness of the method came from its generalization to arbitrary spin lengths S by Baez and Reuther in 2017 [85]. They were able to show, that for $S \to \infty$, pffRG results resemble those obtained by classical Luttinger-Tisza calculations. To establish this result, however, further parton flavors per lattice site had to be introduced and the question to which extent the pseudofermion representation is trustworthy thus became even more severe. Fortunately, qualitative conclusion regarding the nature of the magnetic ground state were robust with respect to suppressions of the unphysical states, which attested to the consistency of the method. Shortly afterwards, these observations were corroborated by an analogous treatment of the large-N limit [70, 131]. Hence, the diagrammatic resummations performed by pffRG resemble a simultaneous $1/S$ and $1/N$ expansion, which has been the standard justification for the employed truncation ever since. Yet, neither S nor N is typically small and as such, the challenge of evaluating the impact of higher order corrections is still pending.

The first two of the following papers document recent progress on that front. In Ref. [P1], we study three different Heisenberg models using multiloop pffRG. For the antiferromagnet on the pyrochlore lattice, corresponding to the Hamiltonian with the highest degree of frustration, a paramagnetic ground state is consistently predicted among loop orders. By a detailed inspection of susceptibility profiles at low energies, we provide evidence that mfRG corrections boost quantum fluctuations and thus substantiate more severe violations of the classical ice-rule. In a second step, we consider extended Heisenberg models on the simple and face-centered cubic lattice. Taking the cubic antiferromagnet as reference, we demonstrate that, in contrast to the pyrochlore Hamiltonian but in agreement with the results presented in Sec. 4.5.2, loop convergence becomes difficult to achieve once an ordering transition occurs. Principal results, such as critical scales and phase diagrams, are only moderately affected though, which supports the validity of 1ℓ results computed hitherto. In the second publication, Ref. [P2], our code is benchmarked against a complementary, but algorithmically distinct implementation developed by our colleagues at LMU Munich. Remarkably, the results produced with both solvers show a large degree of quantitative agreement, implying that pillar pffRG results are robust against numerical heuristics, such as the choice of frequency grids and their respective adaption during the flow.

Within the third article, Ref. [P3], an extension of pseudofermion fRG for spin-valley coupled Hamilto-

nians in the self-conjugate representation of $\mathfrak{su}(4)$ is developed. Such models have relevance for the study of the correlated insulating regimes in twisted bilayer graphene and related moiré materials, while being applicable to transition-metal oxides, where they are more prominently known as Kugel-Khomski Hamiltonians [144]. To facilitate computation, we perform a meticulous symmetry analysis to devise a set of constraints similar to those presented in Ref. [117]. Feasibility of the so-derived parametrization is exemplified by considering a toy model for trilayer graphene on hexagonal boron-nitride, for which we uncover a diverse phase diagram of spin and valley ordered states in vicinity of the SU(4) point.

Relevant publications:

[P1] *Multiloop functional renormalization group approach to quantum spin systems*
D. Kiese, T. Mueller, Y. Iqbal, R. Thomale, and S. Trebst
Physical Review Research 4, 023185 (2022)

[P2] *Benchmark Calculations of Multiloop Pseudofermion fRG*
M. K. Ritter, **D. Kiese**, T. Müller, F. B. Kugler, R. Thomale, S. Trebst, and J. v. Delft
The European Physical Journal B 95, 102 (2022)

[P3] *Moments and multiplets in moiré materials:*
A pseudo-fermion functional renormalization group for spin-valley models
L. Gresista, **D. Kiese**, and S. Trebst
The European Physical Journal B 95, 119 (2022)

Author contributions: *The author of this thesis is the principal developer for the code used to produce the results in Refs. [P1–P3]. He was the driving force for running the simulations in Refs. [P1, P2] and preparing the respective plots, if not indicated otherwise*[1]*. Furthermore, D. Kiese proposed the vertex parametrization in Ref. [P3] and supervised the derivation of symmetry constraints*[2]*. He contributed significantly to the writing of all manuscripts.*

[1] *Ref. [P2] relies on the Munich pffRG code to a similar extent. The corresponding results were produced by M. Ritter.*

[2] *The numerical calculations were carried out by L. Gresista, who implemented the necessary changes into the code of D. Kiese.*

Multiloop functional renormalization group approach to quantum spin systems

Dominik Kiese,[1,*,‡] Tobias Müller,[2,†,‡] Yasir Iqbal,[3] Ronny Thomale,[2,3] and Simon Trebst[1]

[1]*Institute for Theoretical Physics, University of Cologne, 50937 Cologne, Germany*

[2]*Institute for Theoretical Physics and Astrophysics, Julius-Maximilan's University of Würzburg, Am Hubland, 97074 Würzburg, Germany*

[3]*Department of Physics and Quantum Centers in Diamond and Emerging Materials (QuCenDiEM) Group, Indian Institute of Technology Madras, Chennai 600036, India*

(Received 11 June 2021; revised 6 April 2022; accepted 7 April 2022; published 6 June 2022)

Renormalization group methods are well-established tools for the (numerical) investigation of the low-energy properties of correlated quantum many-body systems, allowing us to capture their scale-dependent nature. The functional renormalization group (FRG) allows us to continuously evolve a microscopic model action to an effective low-energy action as a function of decreasing energy scales via an exact functional flow equation, which is then approximated by some truncation scheme to facilitate computation. Here, we report on our implementation of multiloop FRG, an extended truncation scheme recently developed for electronic FRG calculations, within the pseudofermion functional renormalization group (pf-FRG) framework for interacting quantum spin systems. We discuss in detail the conceptual intricacies of the flow equations generated by the multiloop truncation, as well as essential refinements to the integration scheme for the resulting integrodifferential equations. To benchmark our approach, we analyze antiferromagnetic Heisenberg models on the pyrochlore, simple cubic, and face-centered cubic lattice, discussing the convergence of physical observables for higher-loop calculations and comparing with existing results where available. Combined, these methodological refinements systematically improve the pf-FRG approach to one of the numerical tools of choice when exploring frustrated quantum magnetism in higher spatial dimensions.

DOI: 10.1103/PhysRevResearch.4.023185

I. INTRODUCTION

The intriguing physics of quantum many-body systems often plays out on a multitude of scales. Archetypal examples include the spread of correlations on diverging length scales at phase transitions, the formation of coherent states of matter such as superconductivity at low temperatures, or the emergence of macroscopic entanglement in topological quantum liquids.

Capturing such diverse physics starting from simple microscopic models is a notoriously hard problem, since the most interesting phenomena manifest themselves solely at low temperatures and large system sizes. To establish a stringent connection between microscopic models and their effective low-energy, i.e., long-range physics, one often turns to renormalization group (RG) techniques that, by design, treat different scales iteratively rather than simultaneously, and thereby allow us to evolve the original high-energy model description in an RG flow to an effective low-energy action [1,2].

*dkiese@thp.uni-koeln.de

†tobias.mueller@physik.uni-wuerzburg.de

‡These authors equally contributed to this work.

While the RG concept was originally developed in high-energy particle physics [3], its quick adaptation in the context of condensed matter physics and statistical physics has not only provided deeper understanding but also a multitude of applications and variations of the RG scheme. After Kadanoff's idea of a block spin RG [4] to describe magnetic phase transitions, it was Wilson's numerical renormalization group (NRG) [5,6] that led to the solution of the Kondo problem, i.e., the accurate, nonperturbative description of metallic conduction electrons coupled to a magnetic impurity below the Kondo temperature T_k and the explanation of the finite electrical resistivity that these systems exhibit at ultralow temperatures [7]. The density matrix renormalization group (DMRG) developed by White [8] to capture the formation of entanglement in the ground states of quantum many-body systems has basically solved the one-dimensional interacting quantum many-body problem [9]. Its application to two-dimensional systems [10] and its generalization to tensor network approaches [11] is one of the most active developments in contemporary computational physics.

When it comes to systems of interacting electrons in two and three spatial dimensions, a particularly appealing flavor of the RG is the functional renormalization group (FRG) [1,12]. This approach, which will be the foundation of this paper, is based on an infinite hierarchy of ordinary integr-differential equations; they govern the evolution of n-particle Green's functions or vertices controlled by a flow parameter Λ (usually chosen as an infrared cutoff). This allows us to systematically derive effective low-energy actions for

interacting electron problems and is routinely employed to elucidate the pairing mechanism in certain superconductors or other kinds of Fermi surface instabilities [13,14]. In practice, unless for the exactly solvable model originally studied by Polchinski [1], the FRG necessitates approximations imposed on the coupled integrodifferential flow equations to render their numerical solution feasible.

First, one needs to truncate their hierarchy to a level which covers the physics of interest but is still amenable to semianalytical or numerical approaches. Most often, one considers n-point functions with $n \leqslant 4$ and treats higher-order contributions only to a small extent. Truncations which completely neglect these Green's functions are especially justified when the bare interactions are weak and corrections to the flow are thus presumably small. As it turns out, FRG studies of itinerant fermion models have reached a remarkable degree of precision for determining ground-state phase diagrams of, e.g., the Hubbard model at, and even away, from half filling [13,15,16].

Second, there exists no unique way of implementing the RG parameter Λ into the generator of the vertices. Since the flow equations are only used in their truncated form, it naturally introduces a dependence of the results on the choice of regulator function. For FRG, this has often led to a certain inherent dependence of quantitative predictions on the actual choice of regularization.

Recently, the *multiloop* truncation [17,18] of the FRG flow equations (ml-FRG) has been developed to overcome some of these shortcomings. This is done by iteratively advancing the flow of the two-particle vertex to arbitrary orders in the bare interaction until convergence to the first-order parquet equation [19,20] is reached. Thereby, one recovers an independence of the choice of regulator while simultaneously keeping the additional numerical cost at a manageable level. For itinerant electron systems, this approximation has been found to improve the outcome of the FRG calculations, e.g., allowing for quantitative agreement with determinant quantum Monte Carlo simulations of the two-dimensional Hubbard model [21]. For intermediate interaction strengths, a high degree of convergence in the number of loops ℓ was found to already be reached at $\ell \approx 8$ [22], with the numerical effort scaling linearly in ℓ.

In this paper, we apply the multiloop scheme to the pseudofermion FRG (pf-FRG) approach to quantum spin systems [23–26]. Based on a decomposition of spin operators into fermionic partons [20], this adaptation of the FRG scheme allows us to study the physics of frustrated quantum magnets in two [23,24,27–45] and three spatial dimensions [38,46–57], which are commonly beyond the reach of other numerical quantum many-body schemes.

On a technical level, our multiloop pf-FRG approach introduced here is a transcription of the multiloop weak coupling implementations mentioned above. Besides certain subtleties that result from the bilocal parametrization of the two-particle vertex in real space, our technical formulation of the multiloop equations is in agreement with earlier studies [17]. Furthermore, we have implemented a characterization of the high-frequency structure of vertex functions which fully captures their asymptotic behavior [21,22,58,59] to attenuate numerical artifacts at higher loop orders and to stabilize the flow of all dressed couplings.

We benchmark our method by applying the ml-FRG to Heisenberg models on various three-dimensional lattices subject to different levels of frustration. For the antiferromagnets on the pyrochlore and cubic lattice, we distill the impact of higher loops on the signatures of the respective ground states, i.e., the symmetry-preserving Coloumb spin liquid phase for the former [51] and the symmetry-broken Néel state for the latter [47,60]. We then add a finite third-nearest neighbor coupling J_3 to the antiferromagnetic nearest-neighbor Heisenberg model on the simple cubic lattice and map out the phase diagram both in the unfrustrated regime $J_3/J_1 > 0$, as well as for mildly frustrated $J_3/J_1 < 0$. As a last step of exemplary numerical analysis, we study the rich phase diagram of the $J_1 - J_2$ Heisenberg model on the face centered cubic (fcc) lattice, featuring spin liquid candidates with subextensively degenerate ground state manifolds (GSMs) as well as magnetically ordered phases [53,61–64].

The paper is structured as follows. In Sec. II, we review the conventional formulation of pf-FRG as put forward in Refs. [23–26,47,65]. We further proceed by highlighting the parametrization of the high-frequency structure of the two-particle vertex [58] and the multiloop truncation. In Sec. III, we discuss our refinements of the numerical implementation of the pf-FRG procedure. Finally, for Sec. IV, we present our benchmark results for Heisenberg models on the pyrochlore, cubic and fcc lattice. In Sec. V, we conclude that the multiloop pf-FRG promises to rise up as one of the few numerical approaches available today that are capable of analyzing quantum magnetism in higher dimensions. We further speculate on the next potential methodological extensions and improvements of pf-FRG which can use our work as a reference point in terms of conceptual implementation and numerical performance.

II. METHOD

In this section, we briefly review the conventional formulation of pf-FRG as put forward in earlier studies [23,25,26,29,43,47,49,51–53,65,66], before we continue with a discussion of the methodological extensions which are subject to this paper.

A. Conventional pf-FRG

Our starting point is a spin-1/2 Heisenberg model of SU(2) spins,

$$\mathcal{H} = \sum_{ij} J_{ij} \mathbf{S}_i \mathbf{S}_j, \tag{1}$$

on a lattice with sites i, j subject to real exchange couplings J_{ij}. The spin operators are represented in terms of complex pseudofermions $f_{i\alpha}^{(\dagger)}$ with $\alpha \in \{\uparrow, \downarrow\}$ [20], i.e.,

$$S_i^\mu = \frac{1}{2} \sum_{\alpha,\beta} f_{i\alpha}^\dagger \sigma_{\alpha\beta}^\mu f_{i\beta}, \tag{2}$$

where $\sigma_{\alpha\beta}^\mu$ for $\mu \in \{x, y, z\}$ denote Pauli matrices. While this results in a purely quartic Hamiltonian which can directly be treated by established functional RG techniques [13], the pseudofermion representation of the spin algebra

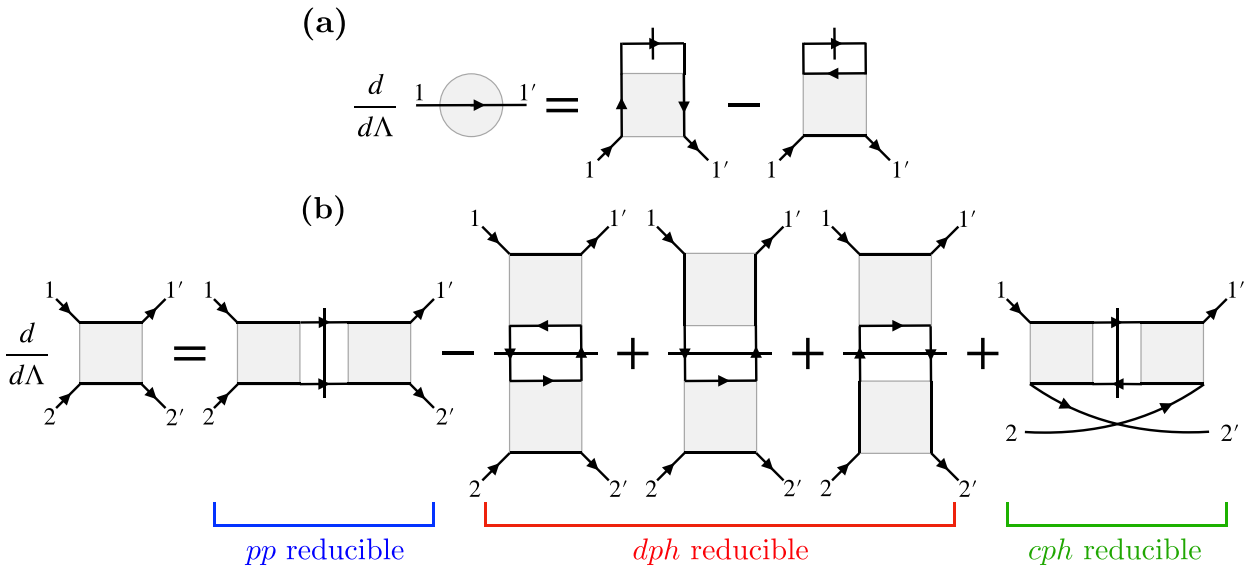

FIG. 1. Diagrammatic representation of the flow Eqs. (5) and (6) in terms of bilocal vertices where conserved lattice indices are indicated by thick black lines. The self-energy flow (a) is decomposed into a local Fock diagram and a nonlocal Hartree term which contains a summation over the full lattice. The two-particle vertex flow (b) can be written as a sum of five terms differing either in their two-particle reducibility or, in the case of the three diagrams reducible in the dph channel, in their spatial structure. Slashed lines denote pairs of differentiated propagators

is *a priori* not isomorphic to the original spin-1/2 representation, since the dimensions of the Hilbert spaces of pseudofermions ($d = 4$) and spin operators ($d = 2$) differ. However, unphysical Fock states with net zero spin can be projected out by an additional particle number constraint $\sum_\alpha f^\dagger_{i\alpha} f_{i\alpha} = 1$, which has to be fulfilled on all lattice sites individually.

In practice, this constraint is only enforced on average (corresponding to the $T \to 0$ limit of the Popov-Fedotov chemical potential [67]) by an explicit implementation of particle-hole symmetry on the level of irreducible vertex functions [25,43,65] (cf. Appendix A). Furthermore, the impact of occupation number fluctuations can be checked for by implementing local level repulsion terms $-AS^\mu_i S^\mu_i$, which gap out the unphysical states. Though these fluctuations are indeed further, though not entirely, suppressed for $A > 0$ [68], recent studies [25,43,49,68] suggest that physical observables extracted from the pf-FRG flows are remarkably unaffected, that is, they only differ by an overall energy rescaling between $A = 0$ and finite A [25,43,49]. As the $A \to \infty$ limit, unfortunately, spoils the numerical stability of the pf-FRG by introducing a new predominant energy scale [68], we, instead, consider the more stable Ansatz $A = 0$ in this paper. Note that the existence of unphysical states in the fermionic Hilbert space can be circumvented by decomposing the spin operators into Majorana instead of Abrikosov fermions [69], allowing us to transcribe the zero temperature pf-FRG approach considered here to finite temperatures within the pseudo-Majorana FRG [69]. At low temperatures $T \ll |J|$, on which we focus in the present paper, however, this approach suffers from unphysical divergencies due to an overcounting of physical Hilbert space sectors. How to cure these divergencies is a question of current research.

Due to the absence of kinetic contributions, the free propagator for the pseudofermion Hamiltonian takes the simple form

$$G_0(w) = (iw)^{-1}, \tag{3}$$

diagonal in real and spin space, where w is a fermionic Matsubara frequency. Similar to other flavors of FRG, a regulator function $\Theta^\Lambda(w)$ is introduced to cut off infrared divergencies in a controlled manner: For $\Lambda \to \infty$, the product of full propagator and regulator vanishes, while the original system is recovered for $\Lambda \to 0$. Here we choose

$$\Theta^\Lambda(w) = 1 - e^{-w^2/\Lambda^2}. \tag{4}$$

The FRG equations for the n-particle vertices then correspond to an interpolation between the simple limit where vertices collapse to the bare interaction J_{ij} and the physical limit of vanishing cutoff. Although these equations are in principle exact, the full hierarchy of integrodifferential equations is not closed, rendering approximations necessary in attempts to seek its solution.

Previous implementations of pf-FRG [23,25,26,43,47,66] have made extensive use of the Katanin scheme, which truncates the FRG equations after the two-particle vertex while simultaneously approximating contributions from the three-particle vertex by a self-energy feedback in the two-particle vertex flow. After truncation, the flows for the self-energy Σ^Λ and the two-particle vertex Γ^Λ (see Fig. 1) read

$$\begin{aligned}\frac{d}{d\Lambda}\Sigma^\Lambda(1) &= -\frac{1}{2\pi}\sum_2 \Gamma^\Lambda(1,2;1,2)S^\Lambda(2)\\ &\equiv -[\Gamma^\Lambda \circ S^\Lambda]_\Sigma\end{aligned} \tag{5}$$

$$\frac{d}{d\Lambda}\Gamma^\Lambda(1',2';1,2) = \frac{1}{2\pi}\sum_{3,4}[\Gamma^\Lambda(3,4;1,2)\Gamma^\Lambda(1',2';3,4) - \Gamma^\Lambda(1',4;1,3)\Gamma^\Lambda(3,2';4,2) - (3\leftrightarrow 4) + \Gamma^\Lambda(2',4;1,3)\Gamma^\Lambda(3,1';4,2) + (3\leftrightarrow 4)] \times G^\Lambda(3)S^\Lambda(4), \tag{6}$$

where the compound indices comprise a lattice and a spin index as well as a Matsubara frequency e.g., $1 = (i_1, \alpha_1, w_1)$. Conjugate Grassmann fields are discriminated by primes attached to the respective index, where $1'$ indicates an outgoing and 1 an incoming fermionic parton. Furthermore, $S^\Lambda \equiv -\frac{d}{d\Lambda}G^\Lambda|_{\Sigma^\Lambda=\text{const.}}$ is the single-scale propagator. Note that due to local U(1) and global SU(2) symmetry of the Hamiltonian in Eq. (1) the self-energy as well as the dressed propagators are diagonal in real and spin space. The Katanin truncation now amounts to the replacement

$$S^\Lambda \to -\frac{d}{d\Lambda}G^\Lambda \tag{7}$$

in the Γ^Λ flow. In this form, the pf-FRG equations become equivalent to mean-field gap equations in the limit of large spin length S, where they collapse to a mere resummation of RPA diagrams, as well as a large dimension of the spin algebra N [25,66], where only crossed particle-hole diagrams remain.

Transitions into phases with broken symmetries become visible in pf-FRG by an instability (indicated by a kink, cusp, or divergence) in the flowing spin-spin correlation

$$\chi^\Lambda_{ij}(iw=0) = \int_0^\beta d\tau \langle T_\tau S^\mu_i(\tau)S^\mu_j(0)\rangle^\Lambda, \tag{8}$$

where the renormalization has to be stopped to still extract sensible results. Here, T_τ is the imaginary time ordering operator and $\mu \in \{x, y, z\}$ can be chosen arbitrarily due to spin rotation invariance of Eq. (1). For long-range ordered states, the momentum $\mathbf{k}$ for which the susceptibility (i.e. the Fourier transform of χ_{ij}) is most dominant characterizes the respective type of order. The absence of a flow breakdown is, on the other hand, associated with putative spin liquid phases.

B. Asymptotic frequency parametrization

For the $T = 0$ implementation of pf-FRG, the spectrum of Matsubara frequencies becomes continuous and vertices need to be discretized on a finite number of frequency mesh points to compute a numerical RG flow. Moreover, a crucial ingredient for the solution of the truncated set of equations is the integration of products of Green's functions in frequency space during the evaluation of the inner sums in Eq. (6). Hence, numerical computations with limited resolution need to capture all relevant features of the vertices to obtain robust results. We employ an established parametrization scheme, which sorts all diagrams that may become finite during the flow into one of four classes and thereby tracks the high-frequency structure of the two-particle vertex in an efficient manner [58]. We start by grouping the contributions in Eq. (6) into three channels, which differ in their two-particle reducibility, i.e., the way in which external legs are assigned to vertices after cutting the two propagators in the respective diagrams. In this sense, the first term is particle-particle (pp) reducible, the second one direct particle-hole (dph) reducible, and the last one crossed particle-hole (cph) reducible. Equation (6) with the Katanin substitution Eq. (7) can therefore be compactly stated as

$$\frac{d}{d\Lambda}\Gamma^\Lambda = \dot{g}^\Lambda_{\text{pp}} + \dot{g}^\Lambda_{\text{dph}} + \dot{g}^\Lambda_{\text{cph}} \tag{9}$$

$$\dot{g}^\Lambda_c \equiv [\Gamma^\Lambda \circ \partial_\Lambda (G^\Lambda \times G^\Lambda) \circ \Gamma^\Lambda]_c, \tag{10}$$

where the precise definitions of the channels are given in Appendix B. As a consequence of imaginary time translation invariance and therefore Matsubara frequency conservation, each term can be associated with a specific bosonic frequency, corresponding to the energy transferred through the internal loop: pp with $s = w_{1'} + w_{2'}$, dph with $t = w_{1'} - w_1$, and cph with $u = w_{1'} - w_2$. If the frequency dependence of the channels is projected onto the respective transfer frequency, two independent fermionic frequency arguments remain to be determined, with our choice displayed in Fig. 2. This specific parametrization simplifies the internal symmetries of the channels under frequency inversions and exchange of fermionic frequencies (cf. Appendix D).

The diagrams contributing to each channel are classified according to the number of external arguments, which enter the internal summations [58], i.e.,

$$\dot{g}^\Lambda_c(w_c, v_c, v_c') = K^\Lambda_{1c}(w_c) + K^\Lambda_{2c}(w_c, v_c) + \bar{K}^\Lambda_{2c}(w_c, v_c') + K^\Lambda_{3c}(w_c, v_c, v_c') \tag{11}$$

for $c \in \{\text{pp}, \text{dph}, \text{cph}\}$. Note that we have only stated the frequency dependence explicitly while suppressing site and spin indices. Each kernel captures a certain asymptotic limit of the channels, since they decay to zero if one of their respective arguments is taken to infinity [58]. This can be seen by recalling that the full propagator effectively scales as $1/(iw)$ for large Matsubara frequencies. In this regard, one gains, in principle, explicit access to the asymptotic behavior of all contributions, allowing us to model different diagrams more effectively in numerical calculations, where only a finite number of frequencies can be used. For computational purposes, however, it is far more advantageous to define new kernels,

$$\begin{aligned} Q^\Lambda_{1c}(w_c) &\equiv \lim |v_c|, |v_c'| \to \infty \dot{g}^\Lambda_c(w_c, v_c, v_c'), \\ Q^\Lambda_{2c}(w_c, v_c) &\equiv \lim |v_c'| \to \infty \dot{g}^\Lambda_c(w_c, v_c, v_c'), \\ \bar{Q}^\Lambda_{2c}(w_c, v_c') &\equiv \lim |v_c| \to \infty \dot{g}^\Lambda_c(w_c, v_c, v_c'), \\ Q^\Lambda_{3c}(w_c, v_c, v_c') &\equiv \dot{g}^\Lambda_c(w_c, v_c, v_c'), \end{aligned} \tag{12}$$

where the limits are either performed numerically, by setting the respective frequency to a large value or by scanning the boundaries of Q_{3c} after evaluating the right-hand side of the flow equations. In the latter case, the asymptotic classes, though they can individually be extracted in each stage of the flow, only serve as efficient numerical buffers for constant extrapolations beyond the domain where Q_{3c} has been

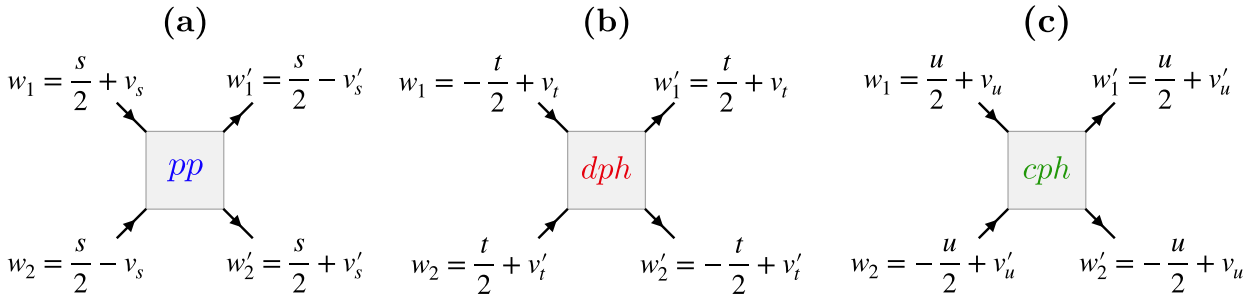

FIG. 2. Symmetrized frequency parametrization of the two-particle vertex channels. Shifting all arguments by half a transfer frequency allows for a more convenient implementation of symmetries on the level of vertex functions (see Appendix D for more details).

discretized. The new functions are related to the old kernels by

$$\begin{aligned} Q^{\Lambda}_{1c}(w_c) &= K^{\Lambda}_{1c}(w_c), \\ Q^{\Lambda}_{2c}(w_c, v_c) &= K^{\Lambda}_{1c}(w_c) + K^{\Lambda}_{2c}(w_c, v_c), \\ \bar{Q}^{\Lambda}_{2c}(w_c, v'_c) &= K^{\Lambda}_{1c}(w_c) + \bar{K}^{\Lambda}_{2c}(w_c, v'_c), \\ Q^{\Lambda}_{3c}(w_c, v_c, v'_c) &= K^{\Lambda}_{1c}(w_c) + K^{\Lambda}_{2c}(w_c, v_c) \\ &\quad + \bar{K}^{\Lambda}_{2c}(w_c, v'_c) + K^{\Lambda}_{3c}(w_c, v_c, v'_c). \end{aligned} \tag{13}$$

Keeping only these sums, one significantly reduces the number of memory accesses in a numerical implementation of the method, since for a given set of frequency arguments, only one function Q^{Λ} needs to be accessed instead of multiple kernels K^{Λ}. Another advantage of this definition is that the additional cost of extracting the asymptotic functions after computing limits of the flow [58] is avoided.

C. Multiloop extension

In the context of FRG for itinerant fermions [21,22,59], it has been shown that an extended truncation, dubbed the multiloop scheme, leads to a substantial improvement of functional RG calculations by (1) restoring independence of the choice of regulator function for $\Lambda \to 0$ [17,18] and (2) generation of all two-particle reducible (parquet) diagrams, which can be computed at a manageable numerical cost. This multiloop FRG (ml-FRG) scheme is based on the parquet equations. i.e., the Schwinger-Dyson equation (SDE) connecting the self-energy to the two-particle vertex and the Bethe-Salpeter equations (BSEs) for the two-particle reducible channels, which compactly written read

$$\Sigma = [(\Gamma_0 + [\Gamma_0 \circ (G \times G) \circ \Gamma]_{\mathrm{pp}}) \circ G]_{\Sigma}, \tag{14}$$

$$g_c = \left[\left(\Gamma - g_c\right) \circ (G \times G) \circ \Gamma\right]_c. \tag{15}$$

Note that we have already applied the well-known parquet approximation (PA), substituting the fully irreducible vertex with the bare vertex Γ_0. To construct from the parquet equations (in the PA) the ml-FRG flow, one regularizes the propagators as in Eq. (4). In consequence the SDE and BSEs become scale dependent and can be put into differential form by taking derivatives with respect to Λ on both sides of the equation. The multiloop flow in a channel g_c can then be computed via an iterative scheme which reads [17,18]

$$\dot{g}_c = \sum_{\ell \geqslant 1} \dot{g}_c^{(\ell)}, \tag{16}$$

$$\dot{g}_c^{(1)} = [\Gamma \circ \partial_{\Lambda}(G \times G) \circ \Gamma]_c, \tag{17}$$

$$\begin{aligned} \dot{g}_c^{(2)} &= \left[\dot{g}_{\bar{c}}^{(1)} \circ (G \times G) \circ \Gamma\right]_c + \left[\Gamma \circ (G \times G) \circ \dot{g}_{\bar{c}}^{(1)}\right]_c \\ &\equiv \dot{g}_c^{(2),L} + \dot{g}_c^{(2),R}, \end{aligned} \tag{18}$$

$$\begin{aligned} \dot{g}_c^{(\ell \geqslant 3)} &= \dot{g}_c^{(\ell),L} + \left[\dot{g}_c^{(\ell-1),R} \circ (G \times G) \circ \Gamma\right]_c + \dot{g}_c^{(\ell),R}, && (19) \\ &= \dot{g}_c^{(\ell),L} + \left[\Gamma \circ (G \times G) \circ \dot{g}_c^{(\ell-1),L}\right]_c + \dot{g}_c^{(\ell),R}, && (20) \\ &\equiv \dot{g}_c^{(\ell),L} + \dot{g}_c^{(\ell),C} + \dot{g}_c^{(\ell),R}, && (21) \end{aligned}$$

where we have defined the left, right, and central part of the ℓ loop contribution. The flow equation for the self-energy Eq. (5) is in principle exact, at least given an exact two-particle vertex Γ^{Λ}. One computes, however, an approximate RG flow for the latter, such that additional corrections become necessary [18,21,59]. The ml-FRG flow for the self-energy then reads

$$\dot{\Sigma} = \dot{\Sigma}_0 + \dot{\Sigma}_1 + \dot{\Sigma}_2, \tag{22}$$

$$\dot{\Sigma}_0 = -[\Gamma \circ S]_{\Sigma}, \tag{23}$$

$$\dot{\Sigma}_1 = \left[\sum_{\ell \geqslant 3} \left(\dot{g}_{pp}^{(\ell),C} + \dot{g}_{cph}^{(\ell),C}\right) \circ G\right]_{\Sigma}, \tag{24}$$

$$\dot{\Sigma}_2 = [\Gamma \circ (G \times \dot{\Sigma}_1 \times G)]_{\Sigma}. \tag{25}$$

Since the flow of the vertex requires the self-energy derivative, which itself builds on the central parts of the particle-particle and crossed particle-hole channels, one usually computes the vertex corrections using only the standard expression $\dot{\Sigma} = \dot{\Sigma}_0$ and accounts for self-energy corrections $\dot{\Sigma}_1$, $\dot{\Sigma}_2$ afterward. The revised value for $\dot{\Sigma}$ can in turn be used to recompute the vertex corrections until convergence is reached. In this paper, however, these numerically expensive self-energy loops are not considered, as the self-energy corrections already turn out to be small during the flow.

For systems of itinerant fermions, it is widely known [13] that truncation of the two-particle vertex flow equation bears

a resemblance to considering perturbative contributions up to some order in the bare interaction. Indeed, for a weakly coupled system, the inclusion of higher loops is therefore expected to improve upon the one-loop results in a systematic manner [17,18,21,59]. For inherently strongly coupled systems, such as the spin systems in the pseudofermion representation considered here, however, the question arises whether loop convergence can be achieved at all and, if so, how the loop expansion has to be interpreted.

To discuss the latter aspect further, we focus on the large-S (similar arguments can be made for large-N [26]) generalization of pf-FRG as put forward in Ref. [25]. It turns out that the leading $O(1)$ contribution to the two-particle vertex flow consists of a single diagram, namely, the nonlocal RPA loop in the direct particle-hole (dph) channel (see Fig. 1), whereas all other diagrams are $O(1/S)$. From Eqs. (16)–(21), it then becomes clear which diagrams are added to the pf-FRG flow at higher loop orders. Two-loop contributions augment the series of $O(1/S)$ diagrams by inserting contributions of $O(1)$ into subleading one-loop diagrams, while further contributions of $O(1/S^2)$ are generated by merging two $O(1/S)$ terms, such as the particle-particle (pp) and crossed particle-hole (cph) ladder. The $\ell = 3$ terms then complete the possible $O(1/S)$ contributions and simultaneously new $O(1/S^3)$ diagrams are generated. Every other odd loop order ℓ then finalizes the set of $O(1/S^{(\ell-1)/2})$ diagrams of the previous loops, while adding some new $O(1/S^\ell)$ diagrams.

This line of argument has three important consequences: (i) For $S \to \infty$, all higher loop contributions vanish, leaving, as expected, the already exact one-loop results unchanged [25]. (ii) For any finite $S < \infty$, multiloop corrections may, in the above sense, loosely be regarded as a $1/S$ series expansion, with, for example, $\ell = 1$ corresponding to a level-1 truncation of that series, that is, it generates the full set of leading-order diagrams and it consistently includes subleading corrections via the Katanin truncation (such that the exact results are recovered considering the $S(N) \to \infty$ limit [25,26]). (iii) The latter fact, however, renders the physical conclusiveness of a nonconverged $\ell > 1$ multiloop result in pf-FRG somewhat unclear. This is because, in contrast to itinerant FRG, where every loop by itself is controlled, higher loops in pf-FRG, where a small parameter is absent (usually $1/S = 2$ and $1/N = 1/2$), only partially include subleading $1/S$ and $1/N$ corrections, leading to an inconsistency in the respective orders of expansion.

Hence, only the two limits $\ell = 1$, contributing the essential leading order contributions for magnetic and spin liquid phases, and $\ell \to \ell_c < \infty$, where the multiloop expansion in pf-FRG has (up to this point hypothetically) converged to a self-consistent solution of the parquet equations should be regarded as physically relevant.

III. NUMERICAL IMPLEMENTATION

To treat the closed set of integrodifferential equations forming the truncated pf-FRG equations, we have to introduce a few more approximations to both the infinite real space lattice and the continuous Matsubara frequencies to make them numerically tractable.

A. Finite lattice graphs

The parton decomposed spin operators Eq. (2) are invariant under local U(1) transformations $f^{(\dagger)}_{i\alpha} \to e^{\pm i\phi} f^{(\dagger)}_{i\alpha}$, implying conservation of the number of spinons per lattice site. The site dependence of the two-particle vertex can therefore be efficiently reduced by the bilocal parametrization [65]

$$\Gamma^\Lambda(1',2';1,2) = \Gamma^{\Lambda=}_{i_1 i_2}(1',2';1,2)\delta_{i_{1'} i_1}\delta_{i_{2'} i_2} + \Gamma^{\Lambda\times}_{i_1 i_2}(1',2';1,2)\delta_{i_{1'} i_2}\delta_{i_{2'} i_1}, \tag{26}$$

where vertices with crossed fermion lines $\Gamma^{\Lambda\times}_{i_1 i_2}$ can be replaced by vertices with parallel fermion lines $\Gamma^{\Lambda=}_{i_1 i_2}$ (or vice versa) by making use of the crossing symmetry $\Gamma^\Lambda(1',2';1,2) = -\Gamma^\Lambda(2',1';1,2)$. We therefore focus only on vertices with parallel lines in the following and drop the additional superscript "=" for brevity [Fig. 1]. In addition, by treating all sites as symmetry equivalent, the site dependence of the self-energy can be entirely discarded, while lattice symmetries can be employed to obtain an effective dependence on a single site i_1^* for the two-particle vertex, i.e., $\Gamma^\Lambda_{i_1 i_2} \to \Gamma^\Lambda_{i_1^* i_0}$. Here i_0 is a fixed reference site, taken to be invariant under point-group symmetries, and i_1^* is the image of i_1 for i_2 mapped to i_0. Given a unit cell of the lattice, our code automatically performs this symmetry reduction by explicitly computing transformations, which leave the lattice invariant. Finally, vertices are truncated if the bond distance $d(i_1^*, i_0)$ exceeds a threshold L, which amounts to artificially introducing a maximal correlation length. In this paper, we choose $L = 6$ to keep the numerical effort for the multiloop truncation in conjunction with the three-dimensional lattices of interest at a manageable level.

B. Matsubara frequency discretization and integration

The pf-FRG flow equations have been derived in the $T = 0$ limit, where Matsubara frequencies become continuous and internal summations are promoted to integrals. To solve the flow equations numerically, one therefore has to make an appropriate choice both for the integration algorithm as well as the discretization of the vertices on a finite grid. To this end, one should carefully consider the interplay between the choice of regulator function, the propagators, and the vertices. In Fig. 3, we have schematically plotted the product $P_0^\Lambda(w,v) = -[G_0^\Lambda(w)G_0^\Lambda(v)]$ as it typically (up to self-energy corrections) appears for evaluations of the right-hand side of the multiloop flow. By integrating this function, one initially generates the frequency dependence of the vertices, and respecting its features is therefore crucial to obtain precise results.

The integration domain can roughly be split into three regions, two algebraically decaying tails that enclose a vivid structure residing symmetrically around $v = 0$. The position of the peaks is directly related to the transfer frequency of the respective channel w_c as well as the RG scale Λ necessitating a dynamical adjustment of integration breakpoints during the flow. Note that, although the outer domains formally require an integration up to infinity, one can in practice cut off the integral at a finite upper bound, where additional contributions to the integral become negligible.

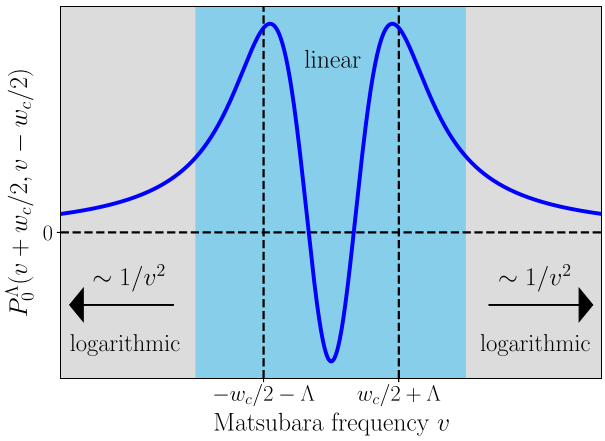

FIG. 3. Schematic plot of P_0^Λ. The numerical integration of this function can be separated into three domains, each featuring either a multiply peaked structure, where high resolution is required, or a simple $1/v^2$ decay. While successively lowering the value of the flow parameter, the peaks shift closer to $w_c/2$, making it necessary to dynamically adjust the breakpoints used for the integration to obtain precise results. See main text for further details on the quadrature rule utilized during the RG flow.

To cope with these characteristics, we utilize an adaptive quadrature rule, tailored toward the functions at hand. The integration domains are first split into linearly (for the inner domain) or logarithmically (for the outer domains) distributed intervals, where the interval's width is the smallest close to the peaks of P_0^Λ for the logarithmic part. In each of those subdomains, we then apply an adaptive trapezoidal rule ameliorated by a Richardson extrapolation for the final result, where the number of function evaluations is increased until we meet an absolute error tolerance of 10^{-10} or a relative error tolerance of 10^{-3}.

The vertices are discretized on non-negative frequency meshes composed of a linear part starting at $w = 0$ with spacing h and a logarithmic part from Nh to some large upper bound, where $N = 0.4N_{\text{tot}}$ is the number of linearly spaced frequencies. Negative frequencies are not used explicitly as they can always be mapped onto their positive counterpart by the symmetries outlined in Appendix D. In total, we monitor seven independent meshes throughout the flow: one for the self-energy ($N_\Sigma = 200$) and two for every channel, thereby one for the the transfer frequency axis ($N_\Omega = 40$) and one for the fermionic frequency axis ($N_\nu = 30$). Decoupling the frequency meshes for the different two-particle channels turned out to be crucial to stabilize our code for small values of the flow parameter because competing ground states, paramagnetic ones for the s/u channel, and magnetic ones for the t channel, could be resolved in an unbiased way.

Finally, the evaluation of the right-hand side of the flow equations requires knowledge of the vertices for frequencies, which do not necessarily align with the points in the chosen frequency mesh. To address this issue, we perform multilinear interpolations in between grid points for all (at most three) arguments of the different diagram classes, which in the worst case require eight kernel values to be taken into account.

C. Differential equation solver

To initialize the RG flow in the ml-FRG framework there are, in principle, two ways. As commonly done in FRG calculations, one can set the initial scale Λ_i to a value much larger than the spin coupling $|J| \equiv \sqrt{\sum_i J_i^2}$ (where J_i are the couplings with a finite value in the Hamiltonian) to approximate the $\Lambda \to \infty$ limit where only bare vertices remain. On the other hand, since the ml-FRG converges to the regularized PA by construction, one could also initialize the flow at a somewhat smaller value $\Lambda_i/|J|$ with a solution of the SDE and the BSEs [68]. Here, we chose the latter, as it allows us to remedy small numerical artifacts, primarily in the self-energy, that appear when the conventional option is selected.

Starting from an initial scale $\Lambda_i/|J| = 5$, we therefore first solve the parquet equations by simple fixed point iterations with a damping factor β (where $\beta = 1$ corresponds to a full update). The self-energy and two-particle channels are declared to have converged sufficiently once the maximumabsolute/relative deviation between two iterations is smaller than $10^{-10}/10^{-5}$. In practice, we found quick convergence as long as $\Lambda/|J| > 1$, where no damping was needed to reach the fixed point, while slowing down rapidly when $\Lambda/|J| \ll 1$. In the latter case, smaller and smaller values of β were required and directly solving the parquet equations soon became unfeasible, in agreement with Ref. [68].

The ml-FRG flow equations are integrated using the Bogacki-Shampine method [70] with adaptive step-size control. This causes the flow to first progress rapidly, while slowing down when instabilities, signaling spontaneous symmetry breaking, emerge at smaller energy scales. A third order solver, although it requires multiple (costly) evaluations of the right-hand side of the flow equations, in our opinion resembles a good compromise between reliability and numerical efficiency. We have set an absolute error tolerance of 10^{-10} and a relative error tolerance of 10^{-3} for one step of the solver, with a minimum step size of $h_{\text{min}} = 10^{-4}|J|$ and maximum size $h_{\text{max}} = 0.1\Lambda$, where Λ is the current cutoff value in units of $|J|$. To prevent the step size h increasing too rapidly whenever we meet the desired tolerances (and potential features in the flow are therefore overlooked), we limit its growth to at most 10% with respect to the old value. The RG flow is continued down to a minimal value $\Lambda_f/|J| = 0.05$ if the following sanity checks are fulfilled:

(1) The absolute maximum of the vertex is smaller than $50|J|$.

(2) The correlations do not show nonmonotonicities like peaks or cusps.

(3) The relative integration error of the ODE solver does not exceed the error tolerance by more than an order of magnitude.

The first and second criterium ensure that the solver is terminated whenever the flow breaks down at some large value of $\Lambda/|J|$ and the step size of the Bogacki-Shampine method therefore diminishes to h_{min}, resulting in a critical loss of performance. The last check secures that the adaptive step-size control of our ODE solver is still reliable and that h is properly reduced in critical regions of the flow to keep the errors inside the desired bounds. We found the latter test to be occasionally violated when either χ^Λ diverges or sufficient convergence

in loops cannot be achieved beyond a symmetry-breaking phase transition. That the flow in these cases becomes unstable is, however, an expected result and the ODE solver is only stopped to prevent excessive run times.

Furthermore, we found that to obtain stable results also at small $\Lambda/|J|$, resolving all relevant features of the vertices at different stages of the flow is of special importance. Therefore, we have developed a simple scanning routine (cf. Appendix E 3) which analyzes the vertices and subsequently proposes a new linear step width for the different frequency meshes after each Runge-Kutta step. The vertices are then transferred to the updated meshes via multilinear interpolations.

D. Algorithmic complexity

The asymptotic scaling of computation times with the different numerical parameters can be read off directly from the flow equations and is given by

$$O\big(N_L^2 \times N_I N_\Omega N_\nu^2 \times \ell\big),$$

where $N_L \sim L^d$ is the number of symmetry-reduced lattice sites for a lattice of dimension d, N_I the initial number of linearly/logarithmically spaced intervals for the adaptive frequency integration, N_Ω the number of mesh points for the transfer frequency axis of the channels, N_ν the respective number of points on the fermionic axes and ℓ the number of loops.

Let us examine in more detail how this scaling is obtained. To do so, we can focus on the computation of the two-particle vertex, as the effort of computing the self-energy derivative, the latter being a function of one frequency argument only, is negligible. After exploiting lattice symmetries and time translation invariance, each channel is parametrized by one site index, one transfer, and two fermionic frequencies. To compute the derivative for each of these components, one needs to evaluate the respective right-hand side of the flow equations, which comprise a single frequency integration over at least N_I frequency points and, in the case of the dph channel, another summation over the full lattice. Although, for large ℓ, the number of terms to compute within each loop stays constant, and as such the numerical effort asymptotically scales as $O(\ell)$, there is a computational overhead going from $\ell = 1$ to $\ell = 3$. The two-loop contribution consists of two terms, a left and right part, which both are as costly to evaluate as the one-loop terms. Furthermore, for $\ell \geqslant 3$, the central part additionally comes on top.

E. Code performance

Given the computational complexity outlined in the previous section, the question arises how the ml-FRG flow equations can be efficiently integrated down to small values of the infrared cutoff $\Lambda/|J|$, as their number N_{eq} rapidly grows for larger system sizes and increased frequency resolution (in this paper, for example $N_{\text{eq}} \approx 10^7$). Efficient code is therefore crucial to obtain results with modest computational resources and feasible run times.

Our code is written in the Julia programming language and so far utilizes two levels of parallelization [71]: vectorization utilizing on-core SIMD units and the invocation of multiple cores per CPU via Julia's native multithreading support.

To accelerate the evaluation of the integrands on the right-hand side of the flow equations, we buffer all spatial contributions for a given tuple of outer frequencies (w_c, v_c, v_c') in an array which is subsequently passed to the adaptive quadrature routine. This not only allows us to recycle interpolation parameters for different lattice sites but also makes it possible to vectorize the actual read-out process for the vertices.

Since different frequency components of the vertex can be computed independently, parallelizing the pf-FRG flow over several cores is in principle straightforward. The largest pitfall in distributing the calculations over multiple threads comes, however, from the adaptiveness of the quadrature routine. This is because every frequency component (w_c, v_c, v_c') may require a different number of integrand evaluations (and therefore computing time) before the trapezoidal rule converges in each domain. In consequence, the workload is highly asymmetric and load balancing becomes vital for boosting code performance to its full extent. The Julia language offers dynamic thread scheduling out of the box and is therefore well-suited for this problem.

Another possible level of parallelization that could in principle be exploited is the distribution of calculations across multiple computing nodes (for example via MPI). We found, however, that computing times are still tolerable when only a single node is used. For example, a $\ell = 4$ flow for the pyrochlore lattice with $\sim$460 sites was obtained in $\sim$10 hours with 48 threads on two Intel Xeon Platinum 8168 CPUs. Therefore, distributed memory parallelization is currently not implemented in our code.

IV. BENCHMARK CALCULATIONS

In this section, we present benchmark calculations of our multiloop pf-FRG machinery for a number of (frustrated) quantum spin models—the Heisenberg antiferromagnet on the pyrochlore lattice, a $J_1 - J_3$ Heisenberg model on the simple cubic (sc) lattice, and a $J_1 - J_2$ model on the fcc lattice, with respective Hamiltonians

$$\mathcal{H}_{\text{pyro}} = J_1 \sum_{\langle ij \rangle} \mathbf{S}_i \cdot \mathbf{S}_j, \tag{27}$$

$$\mathcal{H}_{\text{sc}} = J_1 \sum_{\langle ij \rangle} \mathbf{S}_i \cdot \mathbf{S}_j + J_3 \sum_{\langle\langle\langle ij \rangle\rangle\rangle} \mathbf{S}_i \cdot \mathbf{S}_j, \tag{28}$$

$$\mathcal{H}_{\text{fcc}} = J_1 \sum_{\langle ij \rangle} \mathbf{S}_i \cdot \mathbf{S}_j + J_2 \sum_{\langle\langle ij \rangle\rangle} \mathbf{S}_i \cdot \mathbf{S}_j, \tag{29}$$

where the nearest-neighbor coupling $J_1 > 0$ is always antiferromagnetic. Here J_n denotes the spin coupling to the nth nearest neighbor determined by spatial distance. We start by considering two limiting examples, the nearest-neighbor antiferromagnets on the pyrochlore and cubic lattices, respectively. While the former hosts an extensively degenerate (classical) GSM at $T = 0$ and in its quantum version is considered a candidate model for a quantum spin liquid ground state, the latter is free from geometric frustration and features a symmetry-broken ground state at low temperatures [60], even in the presence of a third-nearest neighbor coupling J_3. As a final benchmark, we consider the phase diagram of

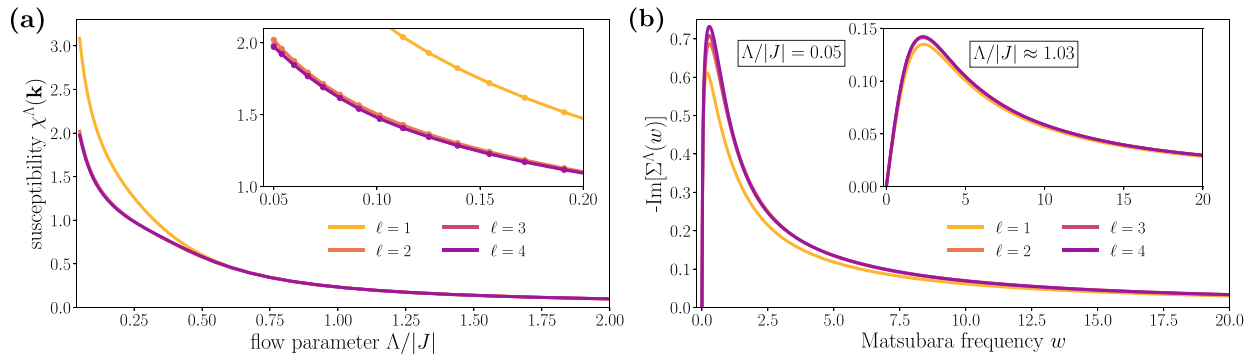

FIG. 4. Results for the $S = 1/2$ nearest-neighbor Heisenberg antiferromagnet on the pyrochlore lattice indicating a potential quantum spin liquid ground state. (a) Susceptibility flows depicted at the momentum with the largest amplitude. Increasing the loop order from $\ell = 1$ to $\ell = 4$ leads to rapid convergence (as demonstrated in the inset) and a substantial reduction of $\chi^\Lambda(\mathbf{k})$. (b) Multiloop self-energies obtained at two different stages of the flow. The inset shows that two-loop corrections already become relevant at relatively large scales $\Lambda \sim |J|$, with excellent convergence for $\ell > 2$. At small cutoffs, deviations between one and higher loops become more pronounced with respect to position and height of the quasiparticle peak. Though the self-energies seem well converged in loops for most frequencies, small differences around the peak are visible, indicating that loop convergence for small $\Lambda/|J|$ on the level of vertices is more difficult to reach than for the spin-spin correlations, in agreement with Ref. [68].

the $J_1 - J_2$ model on the fcc lattice, which in its classical limit is interesting for its appearance of degenerate GSMs of codimensions 2 (lines) and 1 (surfaces) at $T = 0$ [61,62], thus providing a promising playground to realize a competition between magnetically ordered and quantum spin liquid ground states.

From a technical point of view, these benchmark calculations show how the multiloop framework can capture the sometimes delicate balance between quantum fluctuations and ordering tendencies. Our case studies provide examples where either one of the two tendencies is strengthened when going to higher loop orders in our pf-FRG calculations.

A. Heisenberg model on the pyrochlore lattice

The $S = 1/2$ nearest-neighbor Heisenberg antiferromagnet on nonbipartite lattices, such as the kagome or pyrochlore lattices of corner-sharing triangles or tetrahedra, remains an unresolved problem in frustrated quantum magnetism. For the pyrochlore antiferromagnet, there are strong indications for a quantum paramagnetic ground state [51,73–77]; however, deciphering its nature has proven to be notoriously difficult [78–85]. Recently, there is mounting evidence in favor of a ground state which breaks only point-group symmetries while the nature of the symmetry-broken ground state remains under debate [78–80]. Indeed, while a DMRG calculation [78] has provided indications for inversion symmetry breaking, unconstrained many-variable variational Monte Carlo [79] and pf-FRG [80] calculations support a scenario where both inversion and C_3 symmetries are broken in the ground state [86]. Nonetheless, the competition of the recently proposed symmetric and chiral U(1) and $\mathbb{Z}_2$ quantum spin liquids [83,87,88] with the symmetry broken states of Refs. [78–80] remains to be investigated. In a recent $\ell = 1$ pf-FRG calculation, it was shown that the RG flow of the susceptibility does not develop a divergence at finite Λ for any wave vector in the extended Brillouin zone, indicating quantum paramagnetic behavior [51]. Here we show that this finding is remarkably robust up to $\ell = 4$, where our results have sufficiently converged (see Fig. 4), providing compelling evidence in favor of a quantum paramagnetic ground state. This low-temperature phase is characterized by the presence of a bowtie pattern in the susceptibility profile of the $[hhl]$, i.e., $k_x = k_y$ plane [72], with the points at the center of the bowties (called pinch points) being host to sharp features (singularities) in the case of the corresponding classical model at $T = 0$ [89]. These pinch points are reflective of dipolar spin correlations [90,91] which are hallmark of a cooperative paramagnetic state—a Coulomb phase [92], and have been argued to arise from the zero total spin moment rule (called ice-rule) on every tetrahedron [72,93,94]. In contrast, for a quantum model it is impossible to have a vanishing magnetization on every tetrahedron because the Hamiltonian does not commute with the total spin operator of any given tetrahedron. Hence, quantum fluctuations lead to violations of the ice rule, with the pinch points losing their sharpness and their singularity rounded off. Consequently, the pinch points [the $(0, 0, \pm 4\pi)$ (and symmetry related) points in Fig. 5(a)] smear out, acquiring a finite width [51,73,75,77,82,95–97], which serves as a measure of the degree of violation of the ice rule, i.e., the net magnetization acquired by the tetrahedra. To get a quantitative picture concerning the impact of diagrammatic contributions at higher loop orders, we plot the susceptibility along the $h = 0$ momentum cut [the vertical solid white line in Fig. 5(a)] for different loop orders in [Fig. 5(c)]. One observes that the width of the pinch point, as quantified by the full width at half maximum (σ) *increases* with ℓ and finally converges at $\ell = 4$ to $\sigma = 1.328\pi$ compared to $\sigma = 1.2\pi$ at $\ell = 1$ (see Refs. [51,77,82] for comparison of σ with other methods). This finding suggests that in the pyrochlore Heisenberg antiferromagnet *quantum fluctuations get amplified with increasing loop order*. In Fig. 5(d), we show the evolution of σ with Λ (effective temperature) [47] and find that it remarkably obeys (to a good accuracy) the same $\sqrt{\Lambda}$ scaling at small Λ expected of a classical model [72].

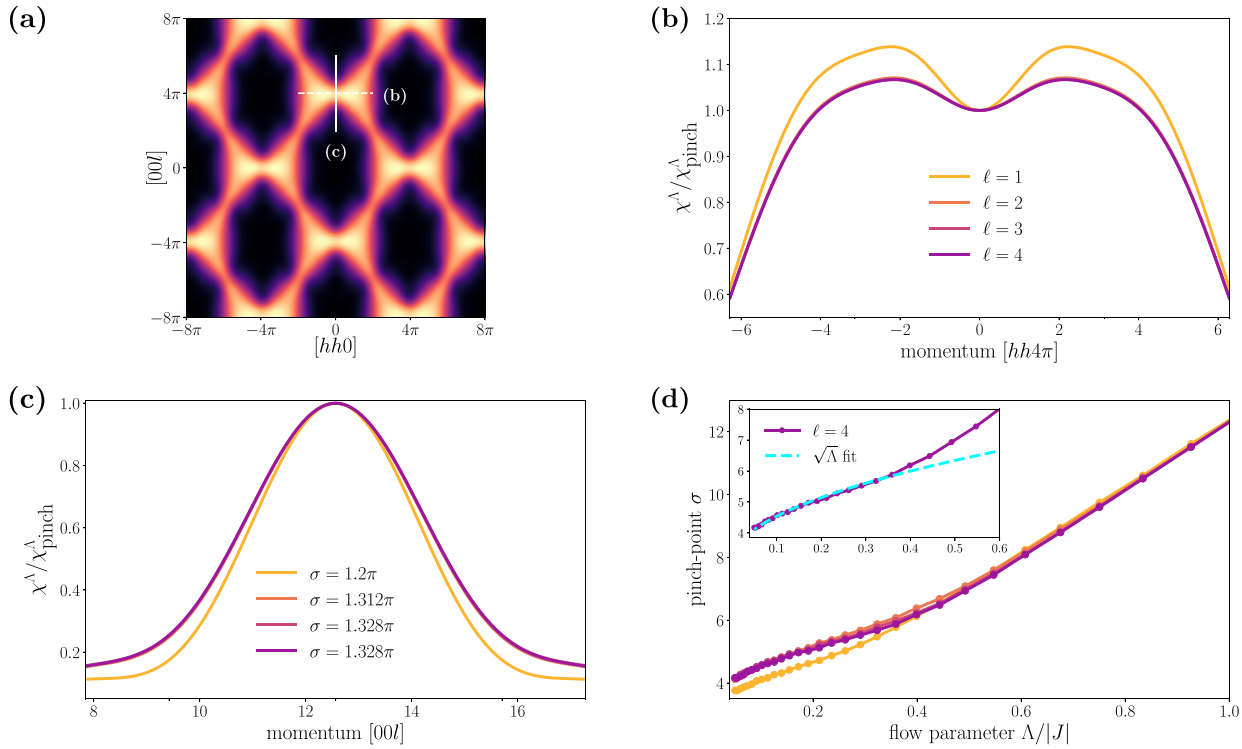

FIG. 5. Analysis of pinch points in the momentum-resolved susceptibility profile of the nearest-neighbor Heisenberg antiferromagnet on the pyrochlore lattice at $\Lambda = 0.05|J|$. (a) Susceptibility in the $[hhl]$ plane for $\ell = 4$. (b) Cut through momentum space along the $[hh4\pi]$ direction as indicated by the dashed horizontal line in (a). (c) Cut through momentum space along the $[00l]$ direction as indicated by the solid vertical line in (a) with the respective full width at half maximum σ. The latter increases upon the inclusion of higher loops, in contrast to the classical result, where one expects that the peaks become singular. (d) Flow of σ for different loop orders. The inset shows σ (for $\ell = 4$) at small values of $\Lambda/|J|$, which to good accuracy obeys a $\sqrt{\Lambda}$ behavior, a result hitherto expected only for the classical model [72]. However, for large cutoffs σ rather scales linear in Λ.

The variation of the intensity along a horizontal cut through the pinch point [dashed horizontal line in Fig. 5(a)] is shown in Fig. 5(b). It is interesting to note that the maxima of the static susceptibility in the $[hhl]$ plane is not located at the pinch points $[(0, 0, \pm 4\pi)]$ but rather in the two symmetrical lobes of the bowties in agreement with Ref. [73]. This should be compared with the findings from a recent finite-temperature matrix product state study [78,82] on clusters up to 128 sites (with fully periodic boundary conditions) which located the maxima of the equal-time structure factor $S(\mathbf{q})$ at the pinch points. Given the fact that all but two of the cluster geometries considered in this paper do not preserve the full cubic pyrochlore symmetry, it is difficult to reliably establish the behavior of $S(\mathbf{q})$ in the thermodynamic limit. A rotation-invariant Green's function method (RGM) [77] (computing $S(\mathbf{q})$) and bold-diagrammatic Monte Carlo simulations (computing static susceptibility) [75] find the intensity distribution to be essentially constant across the length of the bowtie. This variance in the findings between the three methods calls for further investigations since these different patterns of intensity distributions likely correspond to different quantum spin liquid mean-field ansätze [83]. Hence, for an accurate identification of the nature of the quantum spin liquid ground state [83,87,88] of the $S = 1/2$ Heisenberg antiferromagnet on the pyrochlore lattice, which still remains at large, it will be important to unambiguously resolve the behavior of $S(\mathbf{q})$ and the static susceptibility in the thermodynamic limit from other numerical approaches.

From a purely methodological perspective, we have demonstrated that loop convergence toward a symmetric ground state for the pyrochlore antiferromagnet can be obtained even at small values of the cutoff (percent level relative to the bare coupling) and already with a modest number of loops ($\ell \approx 4$). We would also like to mention that our ml-FRG framework and its implementation have the versatility to probe for different symmetry-breaking patterns by introducing a bias in the initialization of the two-particle vertex functions, and studying the evolution of the corresponding response functions under RG flow. In particular, it would be important to investigate the loop converge toward the different patterns of symmetry breaking recently studied at the $\ell = 1$ level in Ref. [80]. Such a ml-FRG analysis, which we defer to a future work, could possibly inform whether the inversion symmetry alone is broken or in combination with C_3 as these two gave similar responses at $\ell = 1$ level.

B. $J_1 - J_3$ Heisenberg model on the cubic lattice

We now turn our attention to a similar Heisenberg-type Hamiltonian, but for a lattice geometry devoid of any

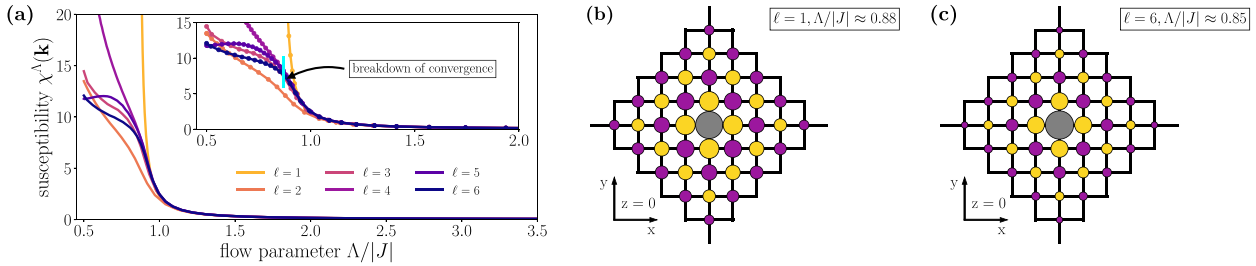

FIG. 6. Results for the $S = 1/2$ nearest-neighbor Heisenberg antiferromagnet on the simple cubic lattice. (a) Susceptibility flows at the dominant momentum $\mathbf{k} = (\pi, \pi, \pi)$. With increasing loop order, the $\ell = 1$ divergence is rounded off to a gentle shoulder in the $\ell > 1$ flows. However, beyond $\Lambda/|J| \approx 0.85$ (marked by the vertical turquoise line in the inset, where the deviation between the $\ell = 5$ and $\ell = 6$ flows exceeds 5%), the multiloop flows cannot be properly converged, indicating a breakdown of ml-FRG and therefore a phase transition. (b) Normalized real-space correlations in the $z = 0$ plane for a $L = 4$ patch of the full lattice obtained from $\ell = 1$ calculations right before the divergence. Here, purple (yellow) dots denote positive (negative) values of $\chi_{i_0 j}$ where the reference site i_0 is marked by a grey circle. (c) Same as (b) but for $\ell = 6$ at the point where loop convergence breaks down.

geometric frustration—the simple cubic lattice, which we, however, augment by a third-nearest-neighbor interaction J_3. This model system exhibits a magnetically ordered ground state for all couplings, with a transition from staggered Neél to collinear magnetic order for ferromagnetic $J_3 < -0.3\,J_1$. Indeed, quantum Monte Carlo simulations [47,60] have confirmed that the model orders at relatively large temperatures $T_c/|J| \sim 1$, a result which could already be reproduced by previous one-loop pf-FRG calculations [47]. For $J_3 < 0$, however, exchange frustration sets in and QMC approaches are not applicable due to the negative sign problem, though the classical ground states (at $T = 0$) are nondegenerate and the magnetic order simply changes from staggered to collinear at $J_3/J_1 = -0.25$. Here, we probe the effect of quantum fluctuations on the phase transition in the frustrated regime.

To start our analysis, we consider the limit $J_3 = 0$ and study the impact of higher loops on the formation of magnetic order for the cubic antiferromagnet [see Fig. 6(a)]. On the one-loop level, the susceptibility flow diverges at $\Lambda_c/|J| \approx 0.86$, where the real-space correlations are in line with an antiferromagnetic ground state [Fig. 6(b)], consistent with Refs. [47,60]. When higher loop orders are included, the one-loop divergence is diminished and only a soft shoulder appears in the $\ell > 1$ flows, though in close vicinity to the former. In addition, we were not able to properly converge the multiloop flows beyond $\Lambda_c/|J| \approx 0.85$ [see the inset in Fig. 6(a)] with the errors produced by our Runge-Kutta method growing relatively large such that the step size of the ODE solver was drastically reduced.

Considering the rapid convergence at higher loops for the pyrochlore model even at an order of magnitude smaller values of the cutoff, we can exclude that the nonsystematic behavior we observe beyond $\Lambda/|J| \approx 0.85$ in the present case is due to the numerical stability of our implementation. From this, and our analytical argument in Sec. II C, we therefore conclude that once magnetic order sets in, loop convergence apparently gets spoiled due to large couplings in the magnetic (dph) channel, causing the $1/S$ $(1/N)$ expansion presented by multiloop pf-FRG to break down at this point. In other words, a pf-FRG flow which lacks a bosonic field to describe order parameter fluctuations [67] seems insufficient to provide a solution to the PA in the symmetry-broken regime. Conversely, the correlations computed for $\Lambda_c/|J| \gtrsim 0.85$, where our flows still converged sufficiently well, support the formation of antiferromagnetic order [Fig. 6(c)] though their range and amplitude are reduced with respect to the $\ell = 1$ result [compare Figs. 6(b) and 6(c)].

For finite J_3, we found the behavior between one and higher loops to qualitatively agree with our findings for the nearest-neighbor antiferromagnet. Using the absence of loop convergence as an indicator for breakdown of the ml flow, we coarsely scanned the phase diagram of the $J_1 - J_3$ model in the frustrated ($J_3 < 0$) and nonfrustrated ($J_3 > 0$) parameter regime (see Fig. 7), determining the critical scales Λ_c where the flow cannot be faithfully continued for $\ell = 1$ and $\ell > 1$. We find that both at the one and higher loop levels, Λ_c is

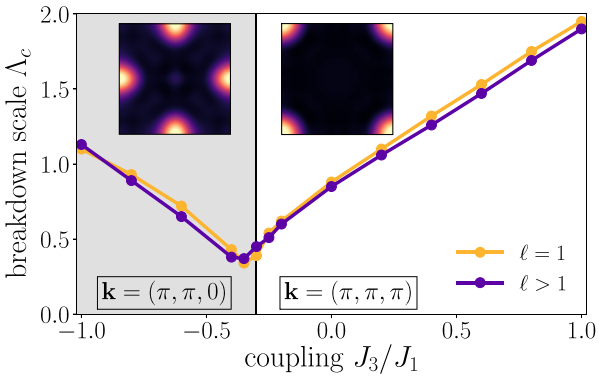

FIG. 7. Phase diagram for the $J_1 - J_3$ model on the simple cubic lattice. The pf-FRG data is obtained from one and higher loop calculations with at most $\ell = 6$. Antiferromagnetic third-nearest-neighbor couplings $J_3 > 0$ stabilize Neél order with wave vector $\mathbf{k} = (\pi, \pi, \pi)$. Ferromagnetic $J_3 < 0$ introduces exchange frustration, leading to a suppression of the breakdown scale Λ_c for intermediate values $-0.4 < J_3/J_1 < 0.0$. At $J_3/J_1 = -0.3$ (vertical black line), the magnetic order changes, promoting the momentum $\mathbf{k} = (\pi, \pi, 0)$ instead. Insets show the static susceptibilities (for $\ell = 6$) in the two phases, plotted in the first Brillouin zone for $k_z = \pi$. Though Λ_c slightly deviates between one and higher loops, the results are qualitatively consistent.

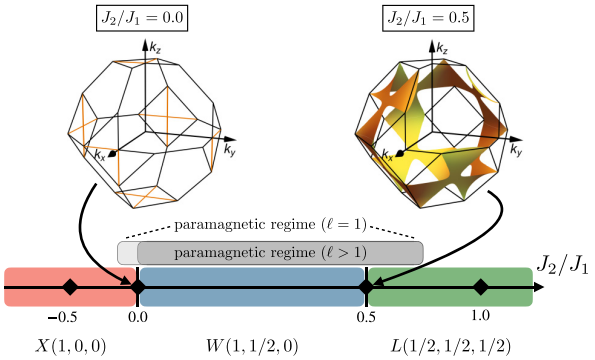

FIG. 8. Phase diagram of the $J_1 - J_2$ fcc model at $T = 0$. Classically, one finds three phases with energetically favorable momenta located at the X, W, and L high-symmetry points of the first Brillouin zone. These magnetic states are separated by two points, at $J_2/J_1 = 0.0$ and $J_2/J_1 = 0.5$, where sub-extensively degenerate ground-state manifolds (lines and surfaces) appear. In the quantum model, we find an extended regime ($J_2/J_1 \approx 0.0 - 0.65$) without a breakdown of the (ml-) FRG flows, marking a possible realm to realize quantum spin liquid behavior. Increasing the loop order leads to a small decrease in the extent of the paramagnetic regime with respect to the lower bound, which is shifted from $J_2/J_1 \approx -0.1$ for $\ell = 1$ to $J_2/J_1 \approx 0.0$ for $\ell > 1$. Black markers indicate the couplings for which we display the results more explicitly in Fig. 9.

suppressed close to the phase transition from (π, π, π) to $(\pi, \pi, 0)$ magnetic order at $J_3/J_1 = -0.3$. The value of the breakdown scale is similar between $\ell = 1$ and $\ell > 1$, with the higher loop result being slightly smaller in most cases. Given that the classical phase boundary at $J_3/J_1 = -0.25$ lies in close vicinity to our FRG result, we conclude, that quantum fluctuations, which were boosted for the strongly frustrated pyrochlore model, have only little influence on the ground state of the mildly frustrated model at hand.

C. Heisenberg model on the fcc lattice

The fcc crystal structure serves as another classic textbook example of a three-dimensional Bravais lattice which is not bipartite, thereby frustrating the two-sublattice Néel order. A measure of the degree of frustration is provided for by the dimensionality of the GSM, i.e., the set of wave vectors $\{\mathbf{Q}\}$ where $J(\mathbf{q})$ takes on its minimal value. At $T = 0$, the corresponding classical ($S \to \infty$) version of Eq. (29) with $J_2 = 0$ features a one-dimensional degenerate GSM [62,63] (see left plot in Fig. 8), while at $J_2 = 0.5$, the GSM takes the form of a two-dimensional spin spiral surface [61],

$$\cos\frac{Q_x a}{2} + \cos\frac{Q_y a}{2} + \cos\frac{Q_z a}{2} = 0, \tag{30}$$

(see right plot in Fig. 8) reflective of an increased frustration. This two-dimensional manifold can be topologically characterized as a triply periodic Schwarz-P surface with an Euler characteristic $\chi = -4$ [98], rationalized by an affine lattice construction [99], and can be associated with an electronic Fermi surface via a supersymmetry construction [100].

The origin of these degeneracies is manifest once the Hamiltonian is recast as a sum of complete squares of spins over edge-sharing tetrahedra (for $J_2 = 0$) and edge sharing octahedra (for $J_2 = 0.5$) which tessellate the fcc lattice [64],

$$\mathcal{H} = \frac{J_1}{4}\sum_{\text{tetra}}(\mathbf{S}_1 + \mathbf{S}_2 + \mathbf{S}_3 + \mathbf{S}_4)^2 - 2J_1 N, \tag{31}$$

$$\mathcal{H} = \frac{J_1}{4}\sum_{\text{octa}}(\mathbf{S}_1 + \mathbf{S}_2 + \mathbf{S}_3 + \mathbf{S}_4 + \mathbf{S}_5 + \mathbf{S}_6)^2 - \frac{3}{2}J_1 N, \tag{32}$$

where $\mathbf{S}_1, \ldots, \mathbf{S}_4$ [Eq. (31)] and $\mathbf{S}_1, \ldots, \mathbf{S}_6$ [Eq. (32)] refer to the four and six spins on the sites of a tetrahedron and octahedron, respectively. Since $J_1 > 0$, the Hamiltonian is minimized if and only if the spins sum up to zero on every tetrahedron (for $J_2/J_1 = 0$) and octahedron (for $J_2/J_1 = 0.5$), with the additional constants giving the ground-state energy. Every spin configuration satisfying this zero magnetization constraint is a valid classical ground state at $T = 0$. When the temperature $T \neq 0$ or/and the reciprocal spin $1/S \neq 0$, thermal and quantum fluctuations could potentially lift this degeneracy via the entropic order-by-disorder mechanism [101] and stabilize long-range magnetic order. However, if they fail to do so, one realizes a quantum paramagnet which could possibly be a quantum spin liquid. Thus, the J_1–J_2 fcc Heisenberg antiferromagnet serves as an ideal test bed to study the role of diagrammatic contributions at higher loop orders in distilling the nontrivial and subtle interplay of quantum and thermal selection effects for $S = 1/2$.

For the nearest-neighbor $S = 1/2$ Heisenberg antiferromagnet [see Fig. 9(a)], we find that the RG flows of the susceptibility at loop orders $\ell \leqslant 5$ do not display a divergence at finite $\Lambda/|J|$ for the wave vectors of either of the two classically degenerate orders present for $J_2 = 0$, namely, the $X(1,0,0)$ (type 1) or $W(1,1/2,0)$ (type III) orders (we henceforth adopt the notation where the points in the Brillouin zone are referred to by their names and coordinates in units of 2π, e.g., $Q_W = (2\pi, \pi, 0) = W(1,1/2,0)$, where the lattice constant $a = 1$). Furthermore, one observes that the susceptibility displays strongly broadened maxima at the $W(1,1/2,0)$ points [see $\ell = 5$ in Fig. 9(a)], consistent with earlier pf-FRG calculations [53], resembling the classical lines of degeneracy. Although loop convergence is excellent up to $\ell = 4$, small deviations become visible for $\ell = 5$ at the smallest cutoffs. We attribute the latter to numerical interpolation errors which become stronger the higher the loop order and the lower Λ, rather than a breakdown of the flow (as, e.g., in the cubic antiferromagnet), since lower loop orders were shown to be converged already. Further simulations with even higher frequency resolution will presumably remedy these artifacts and allow flows with large ℓ toward and beyond the minimum cutoff value of $\Lambda/|J| = 0.05$ chosen here. This is likely to shed light toward addressing a long-standing problem of whether the ground state of the $S = 1/2$ fcc Heisenberg antiferromagnet develops long-range magnetic order or is nonmagnetic in nature. The latter scenario (for which we see some signatures) provides a rare example of a frustrated model with a codimension-2 manifold where the combined effect of quantum and thermal fluctuations fails to lift the degeneracy thus realizing a paramagnetic ground state.

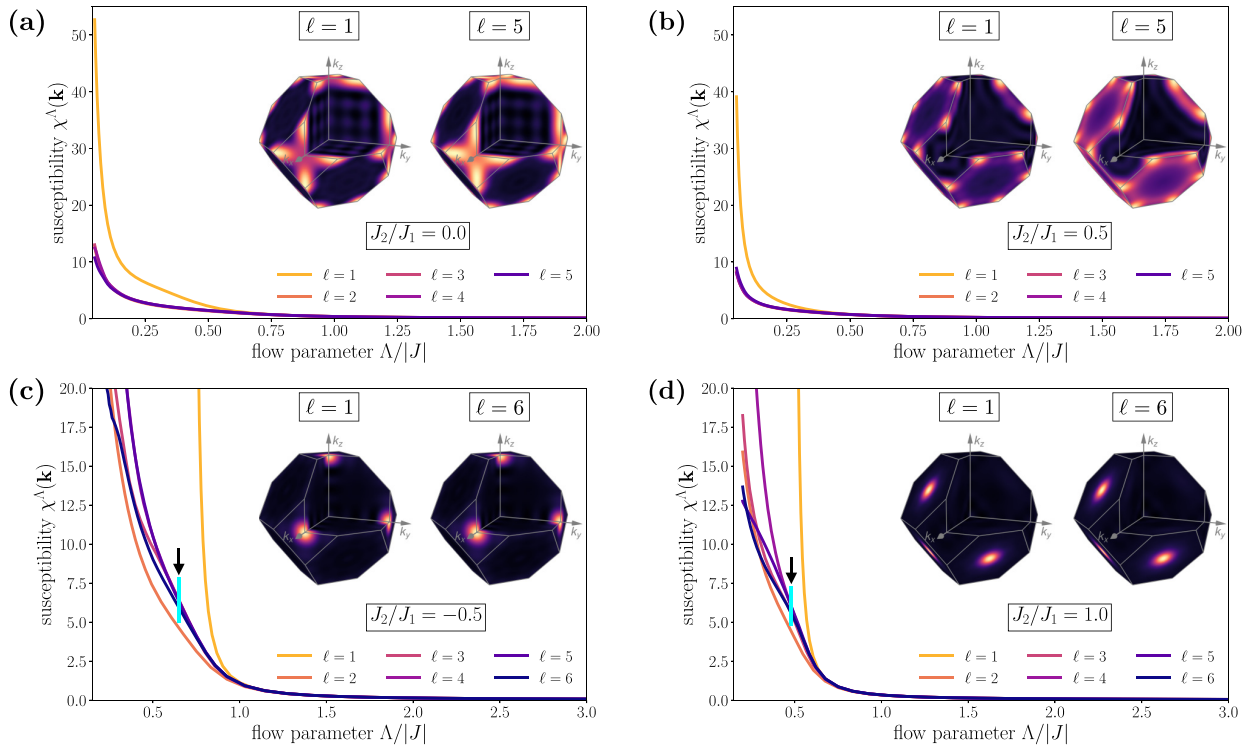

FIG. 9. Multiloop results for the $J_1 - J_2$ Heisenberg model on the fcc lattice. (a) Susceptibility flows for the fcc antiferromagnet, showing smooth and converging (for $\ell \leqslant 4$) flows down to the numerical lower bound set for Λ. Insets show the momentum-resolved susceptibilities in the first Brillouin zone, extracted at the lowest possible cutoff. (b) Same as (a) but for $J_2/J_1 = 0.5$. (c), (d) Results for $J_2/J_1 = -0.5$ and $J_2/J_1 = 1.0$ deep in the ordered phases (see Fig. 8). In contrast to the one-loop flow, which diverges at a finite Λ_c, the multiloop results remain regular, though they could not be converged far below the characteristic scale of the one-loop result, as indicated by a thick turquoise line. The susceptibilities plotted in the inset are computed from the results right before the divergence for $\ell = 1$ and before loop convergence breaks down for $\ell = 6$.

The classically degenerate point $J_2/J_1 = 0.5$ is a triple point of the $W(1, 1/2, 0)$ (type III), $L(1/2, 1/2, 1/2)$ (type II), and incommensurate spiral $(q, q, 0)$ orders [102], and the RG flows for the susceptibility tracked at the corresponding wave vectors display a smooth and monotonically increasing behavior down to the lowest simulated cutoff at all loop orders, with well-converged results to $\ell = 5$ [see Fig. 9(b)], similar to the nonmagnetic ground state probed for the pyrochlore antiferromagnet. The absence of a divergence at finite Λ (and the rapid convergence for $\ell > 1$) provides strong evidence in favor of a quantum paramagnetic ground state [103,104]. With increasing loop order, one observes a progressive smearing and softening of the spectral weight [compare $\ell = 1$ and $\ell = 5$ in Fig. 9(b)], and at $\ell = 5$ order we have a broadly homogeneous distribution of intensity over the surface of the Brillouin zone with soft maxima at the $W(1, 1/2, 0)$ points. A recent work [105] has identified two symmetric $\mathbb{Z}_2$ quantum spin liquids which could potentially serve as candidate ground states: (i) a gapped $\mathbb{Z}_2$ state and (ii) a $\mathbb{Z}_2$ spin liquid featuring a network of symmetry-protected linelike zero modes in reciprocal space. Within a self-consistent mean-field treatment, state (ii) was found to have a lower energy with the corresponding dynamical spin structure factor exhibiting enhanced intensity at the $L(1/2, 1/2, 1/2)$ point. This finding lends support to a scenario whereby a redistribution of spectral weight from the $W(1, 1/2, 0)$ to the $L(1/2, 1/2, 1/2)$ is likely to occur at a relatively lower energy scale. In contrast to $S = 1/2$, in the semiclassical limit ($1/S \ll 1$), quantum fluctuations (treated within the harmonic approximation) have been shown to select the $L(1/2, 1/2, 1/2)$ (type II) long-range magnetically ordered state [99].

For $J_2/J_1 = -0.5$ ($J_2/J_1 = 1.0$), i.e., deep in the magnetically ordered phases of the classical model, our results display the same behavior that we observed for the symmetry-broken ground state of the cubic lattice antiferromagnet [see Figs. 9(c) and 9(d)]. At the one-loop level, the susceptibility flows at the $X(1, 0, 0)$ [or $L(1/2, 1/2, 1/2)$, respectively] points diverge, with clearly resolved incipient Bragg peaks in the corresponding momentum-resolved susceptibilities. While the structure factors do not change qualitatively at higher loops, the divergence vanishes, though for cutoffs close to the respective $\Lambda_c/|J|$ of the $\ell = 1$ flows, loop convergence cannot be achieved up to $\ell = 6$.

Finally, we performed a rough scan of the full phase diagram of the antiferromagnetic $J_1 - J_2$ fcc model. In between the two degenerate points $J_2/J_1 = 0.0$ and $J_2/J_1 = 0.5$, we found an extended regime of paramagnetic ground states (see grey bar in Fig. 8), where one and higher loop results consistently show no flow breakdown. Furthermore, at $J_2/J_1 \approx 0.65$, both calculations with $\ell = 1$ and $\ell > 1$ predict a transition

into the $L(1/2, 1/2, 1/2)$ ordered state. For $J_2/J_1 \lesssim -0.1$ on the other hand, one-loop calculations predict type-I magnetic order, whereas higher loop calculations show no loop convergence down to the lowest cutoffs for $J_2/J_1 \lesssim 0.0$. The extent of the putative spin-liquid regime is therefore slightly reduced between $\ell = 1$ and $\ell > 1$.

V. CONCLUSIONS AND OUTLOOK

In this paper, we set out to add several methodological refinements to the pf-FRG approach for quantum spin models. Our primary goal was the employment of the multiloop truncation scheme [17,18] in pf-FRG, whose numerical implementation the manuscript at hand describes in meticulous detail. On a technical level, we found that the implementation of the multiloop pf-FRG approach necessitates a critical reevaluation of the (adaptive) integration schemes employed in solving the coupled integrodifferential equations, particularly with regard to the underlying frequency discretization. These methodological advancements we make accessible via the open-source package PFFRGSOLVER.JL written in the Julia programming language [106].

As a benchmark, we have employed this multiloop pf-FRG approach to a family of Heisenberg antiferromagnets, subject to varying levels of geometric frustration. For the model with the highest degree of frustration, i.e., the pyrochlore antiferromagnet (the GS is extensively degenerate in the classical limit), we find that the multiloop corrections strengthen quantum fluctuations, which we decipher via a careful analysis of the width of the pinch points characterizing the low-temperature quantum spin liquid phase. In addition, we found excellent convergence of χ^Λ already for $\ell = 4$ even at the smallest cutoff $\Lambda/|J| = 0.05$. These results are to be contrasted with the data obtained for the cubic antiferromagnet, which, due to the bipartite nature of the underlying lattice, is free from geometric frustration. Though we have shown that resolving a divergence of $\chi^\Lambda(\mathbf{k})$ for $\ell > 1$ is rather challenging due to long computation times and large errors of the ODE solver, we could demonstrate that converging the multiloop flows was not possible far beyond the characteristic scale of the one-loop result, indicating a breakdown of ml-FRG in this regime. Furthermore, the real space correlations, momentum-resolved susceptibilities, and phase boundary, when a finite third-nearest-neighbor coupling J_3 is included, are qualitatively consistent between $\ell = 1$ and $\ell > 1$. These two different scenarios, loop convergence at small cutoffs for putative spin liquids and the absence thereof when SU(2) symmetry is spontaneously broken, were shown to be consistent with our findings for the $J_1 - J_2$ Heisenberg model on the fcc lattice, settled between the cubic and pyrochlore antiferromagnets frustrationwise. Enclosed between the two degenerate points $J_2/J_1 = 0.0$ and $J_2/J_1 = 0.5$, we found an extended regime of paramagnetic states, whose full extent is, however, slightly reduced when higher loop calculations are employed.

Even though the inclusion of higher loop orders for FRG calculations on itinerant fermion systems has demonstrated that, already with a few iterations, convergence in several susceptibilities can be reached [21,59], for spin systems as considered here one could not anticipate that the RG flow is similarly well behaved. Formally, since the spinons do not carry kinetic energy, our parton decomposed Hamiltonian resembles the $U \to \infty$ limit of the Hubbard model and consequently there is no small parameter that one can build a perturbative argument on. Remarkably, our work shows that convergence in loop order can also be achieved for an FRG treatment of *strongly coupled* pseudofermions, complementing the initial development of multiloop FRG in the weakly coupled regime [17,18].

Employing the multiloop pf-FRG may pave an avenue for further systematic improvements. Besides the demonstration of loop convergence on the level of postprocessed susceptibilities, no difference between the latter and susceptibilities computed from response functions should remain at higher loops [22]. Similarly, self-energies and two-particle vertices should converge to solutions of the regularized PA at all cutoffs where the symmetries of the microscopic model are preserved. Note that, for moderate cutoffs, this has been shown in Ref. [68]. Although the PA provides a self-consistent many-body framework to derive flow equations for the self-energy and two-particle vertex, one could increase the diagrammatic complexity of the FRG equations even further by employing higher order approximations for the fully two-particle irreducible vertex to generate a more sophisticated starting point for strong-coupling FRG approaches. These methodological refinements are, however, beyond the scope of this paper. Furthermore, we want to emphasize that the generalization of our formulation to Hamiltonians with reduced spin symmetries [65,107,108] or additional degrees of freedom [43] is in principle straightforward, as it does not alter the principal structure of the multiloop equations.

Finally, a long-term objective of the further development of the pseudofermion FRG is to gain access not just to static correlators but also to dynamic correlations of frustrated quantum spin systems to facilitate an in-depth comparison between microscopic theoretical modeling and experimental evidence from, e.g., neutron scattering. It is likely that for all such enterprises, the refinements of pf-FRG reported in this paper are vital to achieve sufficient numerical performance.

ACKNOWLEDGMENTS

Recently, we learned of a parallel effort to implement multiloop pf-FRG by a group in Munich consisting of J. Thoenniss, M. K. Ritter, F. B. Kugler, J. von Delft, and M. Punk. We cordially thank them for insightful and detailed discussions on the subject, the open exchange of ideas and comments, and for coordinating the release of our papers [68]. We thank J. Reuther for insightful discussions on the technical aspects of pf-FRG and the implementation of higher loop orders therein. D. K. thanks M. M. Scherer, L. Gresista and D. Rohe for fruitful discussions on different aspects of pf-FRG and its numerical implementation. Y.I. thanks P. Balla, F. Becca, F. Ferrari, K. Penc, J. Richter, J. Sonnenschein, and M. Zhitomirsky for helpful discussions and collaboration on related topics. R.T. thanks L. Balents, A. V. Chubukov, M. Gingras, W. Metzner, F. Mila, R. Moessner, N. Perkins, M. Rice, M. Salmhofer, O. Starykh, O. Tchernyshyov, F. Verstraete, and J. Vidal for discussions. The Cologne group acknowledges partial support from the

Deutsche Forschungsgemeinschaft (DFG) – Projektnummer 277146847–SFB 1238 (Project No. C02). The Würzburg group is funded by the Deutsche Forschungsgemeinschaft (DFG, German Research Foundation) through Project-ID No. 258499086–SFB 1170 and through the Würzburg-Dresden Cluster of Excellence on Complexity and Topology in Quantum Matter-ct.qmat Project-ID No. 390858490–EXC 2147. R.T. thanks IIT Madras under the IoE program which facilitated the completion of this work. Y.I. acknowledges financial support by the Science and Engineering Research Board (SERB), Department of Science and Technology (DST), India through the Startup Research Grant No. SRG/2019/000056, MATRICS Grant No. MTR/2019/001042, and the Indo-French Centre for the Promotion of Advanced Research (CEFIPRA) Project No. 64T3-1. This research was supported in part by the National Science Foundation under Grant No. NSF PHY-1748958, the Abdus Salam International Centre for Theoretical Physics (ICTP) through the Simons Associateship scheme funded by the Simons Foundation, IIT Madras through the Institute of Eminence (IoE) program for establishing the QuCenDiEM group (Project No. SB20210813PHMHRD002720) and FORG group (Project No. SB20210822PHMHRD008268), the International Centre for Theoretical Sciences (ICTS), Bengaluru, India during a visit for participating in the program Novel Phases of Quantum Matter (Code ICTS/topmatter2019/12). Y.I. thanks IIT Madras for an IoE travel grant to visit Würzburg and Cologne, which facilitated progress on this paper. Y.I. acknowledges the use of the computing resources at HPCE, IIT Madras. The numerical simulations were performed on the CHEOPS cluster at RRZK Cologne, the JURECA Booster [109] and the JUWELS cluster [110] at the Forschungszentrum Juelich, the Julia cluster in Würzburg and the GCS Supercomputer SuperMUC-NG at the Leibniz Supercomputing Centre.

APPENDIX A: HALF-FILLING CONSTRAINT

The decomposition of the spin operators S_i into auxiliary fermionic partons introduces an artificial enlargement of the Hilbert space, which needs to be handled by a constraint on the occupation number on each lattice site i. However, enforcing the constraint exactly, in our case $\sum_\alpha f^\dagger_{i\alpha} f_{i\alpha} = 1$ with $\alpha \in \{\uparrow, \downarrow\}$, is technically difficult, since it would require the inclusion of an additional flowing gauge field in our FRG approach [67]. Therefore, we enforce the constraint only on average $\langle \sum_\alpha f^\dagger_{i\alpha} f_{i\alpha} \rangle = 1$, by imposing particle-hole symmetry on the level of vertices. The successful (numerical) implementation can be checked by computing the product $G_{i\alpha}(\tau) G_{i\alpha}(-\tau)$ for the single-particle Green's function

$$G_{i\alpha}(\tau) = -\langle \hat{T}_\tau f_{i\alpha}(\tau) f^\dagger_{i\alpha}(0) \rangle \tag{A1}$$

in imaginary time, which, written as the convolution of its Fourier transform $G_{i\alpha}(w)$, is given by

$$G_{i\alpha}(\tau) G_{i\alpha}(-\tau) = \frac{1}{(2\pi)^2} \int_{-\infty}^{\infty} dw \int_{-\infty}^{\infty} dv \; G_{i\alpha}(w) \times G_{i\alpha}(w - v) e^{iv\tau}. \tag{A2}$$

If the constraint is fulfilled, on average, one should then have

$$\lim_{\tau \to 0^+} G_{i\alpha}(\tau) G_{i\alpha}(-\tau) = G_{i\alpha}(0^+) G_{i\alpha}(0^-) = -\tfrac{1}{4}. \tag{A3}$$

For the $T = 0$ implementation of pf-FRG, one cannot directly compute $G_{i\alpha}(0^\pm)$, since the propagator is an odd function in frequency space, such that an integral over the full frequency domain vanishes. Note that Eq. (A3) should generally hold for any particle-hole symmetric self-energy, especially the one obtained in our FRG flow. Therefore, we have computed the double integral Eq. (A2) with our numerical $\Sigma^\Lambda(w)$ as input to check the consistency of our implementation. We find that, independent of the scale Λ, the coupling, the system size, and the loop order, the half-filling constraint is indeed fulfilled on average.

APPENDIX B: DEFINITION OF TWO-PARTICLE REDUCIBLE CHANNELS

In Eq. (10), we introduced the decomposition of the two-particle vertex flow in three two-particle reducible channels $\dot{g}^\Lambda_c$ with $c \in \{\text{pp}, \text{dph}, \text{cph}\}$, which were symbolically defined as

$$\dot{g}^\Lambda_c = [\Gamma^\Lambda \circ \partial_\Lambda (G^\Lambda \times G^\Lambda) \circ \Gamma^\Lambda]_c. \tag{B1}$$

Starting from Eq. (6), the concrete expressions read

$$\dot{g}^\Lambda_{\text{pp}}(1', 2'; 1, 2) = -\frac{1}{4\pi} \sum_{3,4} \Gamma^\Lambda(3, 4; 1, 2) \, \partial_\Lambda (G^\Lambda(3) G^\Lambda(4)) \, \Gamma^\Lambda(1', 2'; 3, 4), \tag{B2}$$

$$\dot{g}^\Lambda_{\text{dph}}(1', 2'; 1, 2) = \frac{1}{2\pi} \sum_{3,4} \Gamma^\Lambda(1', 4; 1, 3) \, \partial_\Lambda (G^\Lambda(3) G^\Lambda(4)) \, \Gamma^\Lambda(3, 2'; 4, 2), \tag{B3}$$

$$\dot{g}^\Lambda_{\text{cph}}(1', 2'; 1, 2) = -\frac{1}{2\pi} \sum_{3,4} \Gamma^\Lambda(2', 4; 1, 3) \, \partial_\Lambda (G^\Lambda(3) G^\Lambda(4)) \, \Gamma^\Lambda(3, 1'; 4, 2), \tag{B4}$$

where the pp channel needs to be defined with an additional prefactor $\frac{1}{2}$. Note that the crossing symmetry of the two-particle vertex $\Gamma^\Lambda(1', 2'; 1, 2) = -\Gamma^\Lambda(2', 1'; 1, 2)$ holds similarly for the pp channel, while the dph and cph channel are exchanged, that is,

$$\begin{aligned} \dot{g}^\Lambda_{\text{pp}}(1', 2'; 1, 2) &= -\dot{g}^\Lambda_{\text{pp}}(2', 1'; 1, 2), \\ \dot{g}^\Lambda_{\text{dph}}(1', 2'; 1, 2) &= -\dot{g}^\Lambda_{\text{cph}}(2', 1'; 1, 2), \\ \dot{g}^\Lambda_{\text{cph}}(1', 2'; 1, 2) &= -\dot{g}^\Lambda_{\text{dph}}(2', 1'; 1, 2). \end{aligned} \tag{B5}$$

APPENDIX C: TWO-PARTICLE REDUCIBLE CHANNELS IN BILOCAL PARAMETRIZATION

In Eq. (26), we introduced a bilocal parametrization for the real-space dependence of the two-particle vertex. This representation can be carried over to the two-particle reducible channels from Appendix B by plugging in the bilocal form and collecting terms with the same spatial structure. This procedure yields

$$\begin{aligned}
\dot{g}^{\Lambda}_{\mathrm{pp}\ i_1 i_2}(1',2';1,2) &= -\frac{1}{2\pi}\sum_{3,4}\Gamma^{\Lambda}_{i_1 i_2}(3,4;1,2)\,\partial_{\Lambda}(G^{\Lambda}(3)G^{\Lambda}(4))\,\Gamma^{\Lambda}_{i_1 i_2}(1',2';3,4),\\
\dot{g}^{\Lambda}_{\mathrm{dph}\ i_1 i_2}(1',2';1,2) &= \frac{1}{2\pi}\sum_{j,3,4}\Gamma^{\Lambda}_{i_1 j}(1',4;1,3)\,\partial_{\Lambda}(G^{\Lambda}(3)G^{\Lambda}(4))\,\Gamma^{\Lambda}_{j i_2}(3,2';4,2)\\
&\quad -\frac{1}{2\pi}\sum_{3,4}\Gamma^{\Lambda}_{i_1 i_2}(1',4;1,3)\,\partial_{\Lambda}(G^{\Lambda}(3)G^{\Lambda}(4))\,\Gamma^{\Lambda}_{i_2 i_2}(3,2';2,4)\\
&\quad -\frac{1}{2\pi}\sum_{3,4}\Gamma^{\Lambda}_{i_1 i_1}(1',4;3,1)\,\partial_{\Lambda}(G^{\Lambda}(3)G^{\Lambda}(4))\,\Gamma^{\Lambda}_{i_1 i_2}(3,2';4,2),\\
\dot{g}^{\Lambda}_{\mathrm{cph}\ i_1 i_2}(1',2';1,2) &= -\frac{1}{2\pi}\sum_{3,4}\Gamma^{\Lambda}_{i_1 i_2}(3,2';1,4)\,\partial_{\Lambda}(G^{\Lambda}(3)G^{\Lambda}(4))\,\Gamma^{\Lambda}_{i_1 i_2}(1',4;3,2).
\end{aligned} \tag{C1}$$

Here, the multi-indices on the right-hand side only contain a spin and frequency index, with spatial indices written out explicitly. Vertices Γ^{Λ} are to be understood as a shorthand notation for the bilocal vertex component with parallel legs, i.e., $\Gamma^{\Lambda=}$. For the local vertices $\Gamma^{\Lambda}_{i_1 i_1}$ and $\Gamma^{\Lambda}_{i_2 i_2}$ in the second and third terms of the dph channel, crossing symmetry was applied to map $\Gamma^{\Lambda\times}$ to $\Gamma^{\Lambda=}$. This is irrelevant as long as full vertices Γ^{Λ} are used in this expression. For the ml-FRG flow Eqs. (16)–(21), however, one also needs to insert only partial contributions to the full vertex. In this case, the channel mapping Eqs. (B5) needs to be accounted for explicitly.

APPENDIX D: SYMMETRIES OF TWO-PARTICLE REDUCIBLE CHANNELS

In previous work [65], a full symmetry analysis for the two-particle vertex in the presence of nondiagonal spin interactions has been performed. Although we focus our effort on Heisenberg spin systems here, we may nevertheless use the derived symmetries in the special case of diagonal interactions. To this end, we use the SU(2) symmetric parametrization of the bilocal vertex into a spin (s) and density (d) component,

$$\begin{aligned}
\Gamma^{\Lambda}_{i_1 i_2}(1',2';1,2) = \Bigg[&\Gamma^{\Lambda s}_{i_1 i_2}(s,t,u)\sum_{\mu}\sigma^{\mu}_{\alpha_{1'}\alpha_1}\sigma^{\mu}_{\alpha_{2'}\alpha_2}\\
&+\Gamma^{\Lambda d}_{i_1 i_2}(s,t,u)\delta_{\alpha_{1'}\alpha_1}\delta_{\alpha_{2'}\alpha_2}\Bigg]\\
&\times\delta(w_{1'}+w_{2'}-w_1-w_2),
\end{aligned} \tag{D1}$$

for which the symmetries read

$$\Gamma^{\Lambda s/d}_{i_1 i_2}(s,t,u) = \Gamma^{\Lambda s/d}_{i_2 i_1}(-s,t,u), \tag{D2}$$

$$\Gamma^{\Lambda s/d}_{i_1 i_2}(s,t,u) = \Gamma^{\Lambda s/d}_{i_1 i_2}(s,-t,u), \tag{D3}$$

$$\Gamma^{\Lambda s/d}_{i_1 i_2}(s,t,u) = \Gamma^{\Lambda s/d}_{i_2 i_1}(s,t,-u), \tag{D4}$$

$$\Gamma^{\Lambda s/d}_{i_1 i_2}(s,t,u) = \zeta\,\Gamma^{\Lambda s/d}_{i_1 i_2}(u,t,s), \tag{D5}$$

where $\zeta=+1$ for the spin part and $\zeta=-1$ for the density part. Combinations of one or more symmetries can directly be related to symmetries of the channels by recalling that the fermionic frequencies of each channel are directly related to linear combinations of the three bosonic transfer frequencies. This yields

$$g^{\Lambda s/d}_{\mathrm{pp}\ i_1 i_2}(s,v_s,v'_s) = g^{\Lambda s/d}_{\mathrm{pp}\ i_2 i_1}(-s,v_s,v'_s), \tag{D6}$$

$$g^{\Lambda s/d}_{\mathrm{pp}\ i_1 i_2}(s,v_s,v'_s) = \zeta\, g^{\Lambda s/d}_{\mathrm{cph}\ i_2 i_1}(s,-v_s,v'_s), \tag{D7}$$

$$g^{\Lambda s/d}_{\mathrm{pp}\ i_1 i_2}(s,v_s,v'_s) = \zeta\, g^{\Lambda s/d}_{\mathrm{cph}\ i_1 i_2}(s,v_s,-v'_s), \tag{D8}$$

$$g^{\Lambda s/d}_{\mathrm{pp}\ i_1 i_2}(s,v_s,v'_s) = g^{\Lambda s/d}_{\mathrm{pp}\ i_2 i_1}(s,v'_s,v_s) \tag{D9}$$

for the pp channel;

$$g^{\Lambda s/d}_{\mathrm{dph}\ i_1 i_2}(t,v_t,v'_t) = g^{\Lambda s/d}_{\mathrm{dph}\ i_1 i_2}(-t,v_t,v'_t), \tag{D10}$$

$$g^{\Lambda s/d}_{\mathrm{dph}\ i_1 i_2}(t,v_t,v'_t) = \zeta\, g^{\Lambda s/d}_{\mathrm{dph}\ i_1 i_2}(t,-v_t,v'_t), \tag{D11}$$

$$g^{\Lambda s/d}_{\mathrm{dph}\ i_1 i_2}(t,v_t,v'_t) = \zeta\, g^{\Lambda s/d}_{\mathrm{dph}\ i_1 i_2}(t,v_t,-v'_t), \tag{D12}$$

$$g^{\Lambda s/d}_{\mathrm{dph}\ i_1 i_2}(t,v_t,v'_t) = g^{\Lambda s/d}_{\mathrm{dph}\ i_2 i_1}(t,v'_t,v_t) \tag{D13}$$

for the dph channel, and, finally,

$$g^{\Lambda s/d}_{\mathrm{cph}\ i_1 i_2}(u,v_u,v'_u) = g^{\Lambda s/d}_{\mathrm{cph}\ i_2 i_1}(-u,v_u,v'_u), \tag{D14}$$

$$g^{\Lambda s/d}_{\mathrm{cph}\ i_1 i_2}(u,v_u,v'_u) = \zeta\, g^{\Lambda s/d}_{\mathrm{pp}\ i_2 i_1}(u,-v_u,v'_u), \tag{D15}$$

$$g^{\Lambda s/d}_{\mathrm{cph}\ i_1 i_2}(u,v_u,v'_u) = \zeta\, g^{\Lambda s/d}_{\mathrm{pp}\ i_1 i_2}(u,v_u,-v'_u), \tag{D16}$$

$$g^{\Lambda s/d}_{\mathrm{cph}\ i_1 i_2}(u,v_u,v'_u) = g^{\Lambda s/d}_{\mathrm{cph}\ i_1 i_2}(u,v'_u,v_u) \tag{D17}$$

for the cph channel. Given these symmetries, one can further conclude how they affect the respective kernel functions by successively eliminating certain kernels considering their asymptotic limit. Performing the full symmetry analysis, we were able to drastically reduce the numerical effort in computing the two-particle vertex flow. Most notably, all kernels need

to be saved only for positive Matsubara frequencies. Finally, the $v \leftrightarrow v'$ symmetry allows us to restrict $Q_{3\ c}^{s/d}$ to a mesh with $v \geqslant v'$.

APPENDIX E: NUMERICAL IMPLEMENTATION DETAILS

To clarify the implementation details of the code used for the numerical pf-FRG computations, we further elaborate on the general concepts outlined previously in Sec. III.

1. Finite lattice graphs

The finite lattice graphs are implemented by first enumerating all points within a bond distance L. Subsequently, using a small test lattice of two unit cells in all directions, the code determines the point group symmetry transformations with respect to a test site i_0 by trying to rotate pairs of connections onto other pairs of bonds. Afterward, the full lattice is checked for symmetry equivalent points and the set of symmetry-inequivalent points together with their respective multiplicity is determined. As a next step, a mapping table of any connection from point i_1 to i_2 in the full lattice to a symmetry equivalent connection i_0 to i_1^* within the reduced lattice is generated. This can then be used to construct the full overlap between two sites in the reduced lattice, i.e., a mapping table of pairs of connections i_0 to i_1 with an intermediate point i_2 located within the full lattice, as is needed for the site summation in the dph channel.

2. Discrete frequency meshes and interpolation

For a numerical treatment, we have to discretize the continuous, positive Matsubara frequency axis. We do this by constructing a mesh consisting of $0.4N_{\text{tot}}$ linearly spaced frequencies, amended by $0.6N_{\text{tot}}$ logarithmically spaced ones, where N_{tot} is the total number of nonzero frequencies. Additionally, $\omega = 0$ is always part of the mesh. This means the frequencies can be obtained as

$$\omega_i = i \cdot \frac{\omega_{\text{lin}}}{0.4N_{\text{tot}}} \qquad \text{for } i = 0, 1, \ldots, 0.4N_{\text{tot}}, \tag{E1}$$

$$\omega_i = \omega_{\text{lin}} \cdot \left(\frac{\omega_{\text{max}}}{\omega_{\text{lin}}}\right)^{\frac{i}{0.6N_{\text{tot}}}} \qquad \text{for } i = 0.4N_{\text{tot}} + 1, \ldots, N_{\text{tot}}, \tag{E2}$$

assuming that $0.4N_{\text{tot}}$ corresponds to an integer value (otherwise a `ceil / floor` operation has to be performed). The parameters ω_{lin} and ω_{max} are the extent of the linear part and full mesh, respectively, and are determined by the scanning routine outlined in Appendix E 3.

In the evaluation of the flow equations, values of the vertices are needed, which do not necessarily correspond to one of these discrete frequencies and, as such, we have to use a multilinear interpolation scheme to obtain them. In practice, this means that the value of a two-particle reducible channel at an arbitrary frequency combination (ω, ν, ν') is given by

$$\begin{aligned} g(\omega, \nu, \nu') = [&g(\omega_{i_<}, \nu_{i_<}, \nu'_{i_<})(\omega_{i_>} - \omega)(\nu_{i_>} - \nu)(\nu'_{i_>} - \nu') \\ &+ g(\omega_{i_>}, \nu_{i_<}, \nu'_{i_<})(\omega - \omega_{i_<})(\nu_{i_>} - \nu)(\nu'_{i_>} - \nu') \\ &+ g(\omega_{i_<}, \nu_{i_>}, \nu'_{i_<})(\omega_{i_>} - \omega)(\nu - \nu_{i_<})(\nu'_{i_>} - \nu') \\ &+ g(\omega_{i_<}, \nu_{i_<}, \nu'_{i_>})(\omega_{i_>} - \omega)(\nu_{i_>} - \nu)(\nu' - \nu'_{i_<}) \\ &+ g(\omega_{i_>}, \nu_{i_>}, \nu'_{i_<})(\omega - \omega_{i_<})(\nu - \nu_{i_<})(\nu'_{i_>} - \nu') \\ &+ g(\omega_{i_>}, \nu_{i_<}, \nu'_{i_>})(\omega - \omega_{i_<})(\nu_{i_>} - \nu)(\nu' - \nu'_{i_<}) \\ &+ g(\omega_{i_<}, \nu_{i_>}, \nu'_{i_>})(\omega_{i_>} - \omega)(\nu - \nu_{i_<})(\nu' - \nu'_{i_<}) \\ &+ g(\omega_{i_>}, \nu_{i_>}, \nu'_{i_>})(\omega - \omega_{i_<})(\nu - \nu_{i_<})(\nu' - \nu'_{i_<})] \\ &\times \frac{1}{(\omega_{i_>} - \omega_{i_<})(\nu_{i_>} - \nu_{i_<})(\nu'_{i_>} - \nu'_{i_<})}, \end{aligned} \tag{E3}$$

using subscripts $i_<(i_>)$ to indicate that the nearest smaller (larger) discrete frequency should be used. If one or both of the fermionic frequency arguments are larger than the respective maximum frequency of the mesh, the corresponding asymptotic kernels as defined in Eqs. (12) are used for the analogous interpolation in two or one dimensions. If the bosonic frequency exceeds the mesh boundary, the vertex is taken to be zero.

3. Scanning routine for frequency mesh adaptation

Continuing the ml-FRG flow to small values of the flow parameter requires that all relevant features of the vertices are well resolved in intermediate stages of the flow. Carefully analyzing the vertices, we found that most structures are usually located around the zero-frequency regime, where sharp peaks right at or close to $(w_c, v_c, v'_c) = (0, 0, 0)$ appear, and for lattice sites close to the reference site i_0. Our routine to scan the vertices after each step of the ODE solver and to determine from that a suitable linear spacing h for the frequency meshes uses the relative deviation $\Delta = \frac{|g_2 - g_1|}{\max(|g_2|, |g_1|)}$ as a control parameter. Here $\{g_i\}$ are the respective vertex values along a given frequency axis $\{w_i\}$ with $w_1 = 0$. More precisely, the mesh spacing h is increased or decreased such that $p_1 \leqslant \Delta \leqslant p_2$, where p_1 and p_2 are external parameters. We choose $p_1 = 0.05$ and $p_2 = 0.1$. As an additional sanity check, the spacing h must fulfill $p_3\Lambda \leqslant h \leqslant p_4\Lambda$ to avoid overambitious shrinking or expanding of the linear part of the mesh. We choose $p_3 = 0.05$ and $p_4 = 2.0$. The scanning is carried out for the bosonic and fermionic axis right at the reference site i_0 for all channels and with the respective other frequency arguments set to zero. Note that this scanning is only carried out when $\max(\{|g_i|\}) > 10^{-3}$ to prevent adapting the meshes according to noisy (i.e., not well captured with respect to the chosen error tolerances) data.

4. Frequency integration

For the quadrature of the frequency integrals on the right-hand side of the flow equations, we use an adaptive routine tailored to the structure of the propagator bubbles as outlined in Sec. III B. We first divide the integration into four intervals: $[-100 \times (\Lambda + \omega/2), -2 \times (\Lambda + \omega/2)]$, $[-2 \times (\Lambda + \omega/2), 0]$, $[0, 2 \times (\Lambda + \omega/2)]$, and $[2 \times (\Lambda + \omega/2), 100 \times (\Lambda + \omega/2)]$, where ω is the external bosonic frequency for the integration at hand. This is to accurately capture the features around $\pm(\Lambda + \omega/2)$ as well as the those at large frequencies. We have found empirically that $100 \times (\Lambda + \omega/2)$ is a good approximation for the infinite upper and lower boundaries in the integration.

The two outer intervals are then logarithmically [analogous to Eq. (E2)], the inner two linearly [cf. Eq. (E1)] divided into 30 subintervals. In each of those, we use an adaptive trapezoidal rule, which subdivides the intervals even further until an absolute error of less than 10^{-10} and a relative error of less than 10^{-3} is reached. Errors are computed by the difference between two subdivision steps. The final result is ameliorated by a Richardson extrapolation.

[1] J. Polchinski, Renormalization and effective Lagrangians, Nucl. Phys. B **231**, 269 (1984).

[2] R. Shankar, Renormalization-group approach to interacting fermions, Rev. Mod. Phys. **66**, 129 (1994).

[3] E. C. G. Stueckelberg and A. Petermann, Normalization of constants in the quanta theory, Helv. Phys. Acta **26**, 499 (1953).

[4] L. P. Kadanoff, Scaling laws for Ising models near T_c, Phys. Phys. Fiz. **2**, 263 (1966).

[5] K. G. Wilson, The renormalization group: Critical phenomena and the Kondo problem, Rev. Mod. Phys. **47**, 773 (1975).

[6] R. Bulla, T. A. Costi, and T. Pruschke, Numerical renormalization group method for quantum impurity systems, Rev. Mod. Phys. **80**, 395 (2008).

[7] J. Kondo, Resistance minimum in dilute magnetic alloys, Prog. Theor. Phys. **32**, 37 (1964).

[8] S. R. White, Density Matrix Formulation for Quantum Renormalization Groups, Phys. Rev. Lett. **69**, 2863 (1992).

[9] U. Schollwöck, The density-matrix renormalization group, Rev. Mod. Phys. **77**, 259 (2005).

[10] E. Stoudenmire and S. R. White, Studying two-dimensional systems with the density matrix renormalization group, Annu. Rev. Condens. Matter Phys. **3**, 111 (2012).

[11] R. Orús, Tensor networks for complex quantum systems, Nat. Rev. Phys. **1**, 538 (2019).

[12] C. Wetterich, Exact evolution equation for the effective potential, Phys. Lett. B **301**, 90 (1993).

[13] W. Metzner, M. Salmhofer, C. Honerkamp, V. Meden, and K. Schönhammer, Functional renormalization group approach to correlated fermion systems, Rev. Mod. Phys. **84**, 299 (2012).

[14] C. Platt, W. Hanke, and R. Thomale, Functional renormalization group for multi-orbital Fermi surface instabilities, Adv. Phys. **62**, 453 (2013).

[15] C. J. Halboth and W. Metzner, Renormalization-group analysis of the two-dimensional Hubbard model, Phys. Rev. B **61**, 7364 (2000).

[16] K.-M. Tam, S.-W. Tsai, and D. K. Campbell, Functional Renormalization Group Analysis of the Half-Filled One-Dimensional Extended Hubbard Model, Phys. Rev. Lett. **96**, 036408 (2006).

[17] F. B. Kugler and J. von Delft, Multiloop functional renormalization group for general models, Phys. Rev. B **97**, 035162 (2018).

[18] F. B. Kugler and J. von Delft, Multiloop Functional Renormalization Group that Sums up all Parquet Diagrams, Phys. Rev. Lett. **120**, 057403 (2018).

[19] I. T. Diatlov, V. V. Sudakov, and K. A. Ter-Martirosian, Asymptotic meson-meson scattering theory, Zh. Eksp. Teor. Fiz. **32**, 767 (1957); Y. A. Bychkov, L. P. Gor'kov, and I. E. Dzyaloshinskii, Possibility of superconductivity type phenomena in a one-dimensional system, *ibid.* **50**, 738 (1966); B. Roulet, J. Gavoret, and P. Nozières, Singularities in the x-ray absorption and emission of metals. I. First-order parquet calculation, Phys. Rev. **178**, 1072 (1969)..

[20] A. A. Abrikosov, Electron scattering on magnetic impurities in metals and anomalous resistivity effects, Phys. Phys. Fiz. **2**, 5 (1965).

[21] C. Hille, F. B. Kugler, C. J. Eckhardt, Y.-Y. He, A. Kauch, C. Honerkamp, A. Toschi, and S. Andergassen, Quantitative functional renormalization group description of the two-dimensional Hubbard model, Phys. Rev. Research **2**, 033372 (2020).

[22] A. Tagliavini, C. Hille, F. B. Kugler, S. Andergassen, A. Toschi, and C. Honerkamp, Multiloop functional renormalization group for the two-dimensional Hubbard model: Loop convergence of the response functions, SciPost Phys. **6**, 009 (2019).

[23] J. Reuther and P. Wölfle, J_1−J_2 frustrated two-dimensional Heisenberg model: Random phase approximation and functional renormalization group, Phys. Rev. B **81**, 144410 (2010).

[24] J. Reuther and R. Thomale, Functional renormalization group for the anisotropic triangular antiferromagnet, Phys. Rev. B **83**, 024402 (2011).

[25] M. L. Baez and J. Reuther, Numerical treatment of spin systems with unrestricted spin length S: A functional renormalization group study, Phys. Rev. B **96**, 045144 (2017).

[26] F. L. Buessen, D. Roscher, S. Diehl, and S. Trebst, Functional renormalization group approach to SU(N) Heisenberg models: Real-space renormalization group at arbitrary N, Phys. Rev. B **97**, 064415 (2018).

[27] J. Reuther, P. Wölfle, R. Darradi, W. Brenig, M. Arlego, and J. Richter, Quantum phases of the planar antiferromagnetic J_1 − J_2 − J_3 Heisenberg model, Phys. Rev. B **83**, 064416 (2011).

[28] J. Reuther, D. A. Abanin, and R. Thomale, Magnetic order and paramagnetic phases in the quantum J_1-J_2-J_3 honeycomb model, Phys. Rev. B **84**, 014417 (2011).

[29] J. Reuther, R. Thomale, and S. Trebst, Finite-temperature phase diagram of the Heisenberg-Kitaev model, Phys. Rev. B **84**, 100406(R) (2011).

[30] J. Reuther, R. Thomale, and S. Rachel, Magnetic ordering phenomena of interacting quantum spin Hall models, Phys. Rev. B **86**, 155127 (2012).

[31] J. Reuther and R. Thomale, Cluster functional renormalization group, Phys. Rev. B **89**, 024412 (2014).

[32] R. Suttner, C. Platt, J. Reuther, and R. Thomale, Renormalization group analysis of competing quantum phases in the J_1-J_2 Heisenberg model on the kagome lattice, Phys. Rev. B **89**, 020408(R) (2014).

[33] J. Reuther, R. Thomale, and S. Rachel, Spiral order in the honeycomb iridate Li_2IrO_3, Phys. Rev. B **90**, 100405(R) (2014).

[34] I. Rousochatzakis, J. Reuther, R. Thomale, S. Rachel, and N. B. Perkins, Phase Diagram and Quantum Order by Disorder in the Kitaev K_1 − K_2 Honeycomb Magnet, Phys. Rev. X **5**, 041035 (2015).

[35] Y. Iqbal, H. O. Jeschke, J. Reuther, R. Valentí, I. I. Mazin, M. Greiter, and R. Thomale, Paramagnetism in the kagome compounds $(Zn, Mg, Cd)Cu_3(OH)_6Cl_2$, Phys. Rev. B **92**, 220404(R) (2015).

[36] Y. Iqbal, W.-J. Hu, R. Thomale, D. Poilblanc, and F. Becca, Spin liquid nature in the Heisenberg $J_1 - J_2$ triangular antiferromagnet, Phys. Rev. B **93**, 144411 (2016).

[37] Y. Iqbal, P. Ghosh, R. Narayanan, B. Kumar, J. Reuther, and R. Thomale, Intertwined nematic orders in a frustrated ferromagnet, Phys. Rev. B **94**, 224403 (2016).

[38] F. L. Buessen and S. Trebst, Competing magnetic orders and spin liquids in two- and three-dimensional kagome systems: Pseudofermion functional renormalization group perspective, Phys. Rev. B **94**, 235138 (2016).

[39] M. Laubach, J. Reuther, R. Thomale, and S. Rachel, Three-band Hubbard model for Na_2IrO_3: Topological insulator, zigzag antiferromagnet, and Kitaev-Heisenberg material, Phys. Rev. B **96**, 121110(R) (2017).

[40] A. Keleş and E. Zhao, Absence of Long-Range Order in a Triangular Spin System with Dipolar Interactions, Phys. Rev. Lett. **120**, 187202 (2018).

[41] A. Keleş and E. Zhao, Renormalization group analysis of dipolar Heisenberg model on square lattice, Phys. Rev. B **97**, 245105 (2018).

[42] K. Iida, H. K. Yoshida, A. Nakao, H. O. Jeschke, Y. Iqbal, K. Nakajima, S. Ohira-Kawamura, K. Munakata, Y. Inamura, N. Murai, M. Ishikado, R. Kumai, T. Okada, M. Oda, K. Kakurai, and M. Matsuda, $q = 0$ long-range magnetic order in centennialite $CaCu_3(OD)_6Cl_2 \cdot 0.6D_2O$: A spin-$\frac{1}{2}$ perfect kagome antiferromagnet with $J_1 - J_2 - J_d$, Phys. Rev. B **101**, 220408(R) (2020).

[43] D. Kiese, F. L. Buessen, C. Hickey, S. Trebst, and M. M. Scherer, Emergence and stability of spin-valley entangled quantum liquids in moiré heterostructures, Phys. Rev. Research **2**, 013370 (2020).

[44] N. Astrakhantsev, F. Ferrari, N. Niggemann, T. Müller, A. Chauhan, A. Kshetrimayum, P. Ghosh, N. Regnault, R. Thomale, J. Reuther, T. Neupert, and Y. Iqbal, Pinwheel valence bond crystal ground state of the spin-$\frac{1}{2}$ Heisenberg antiferromagnet on the shuriken lattice, Phys. Rev. B **104**, L220408 (2021).

[45] M. Hering, F. Ferrari, A. Razpopov, I. I. Mazin, R. Valentí, H. O. Jeschke, and J. Reuther, Phase diagram of a distorted kagome antiferromagnet and application to y-kapellasite, npj Comput. Mater. **8**, 10 (2022).

[46] C. Balz, B. Lake, J. Reuther, H. Luetkens, R. Schönemann, T. Herrmannsdörfer, Y. Singh, A. T. M. Nazmul Islam, E. M. Wheeler, J. A. Rodriguez-Rivera, T. Guidi, G. G. Simeoni, C. Baines, and H. Ryll, Physical realization of a quantum spin liquid based on a complex frustration mechanism, Nat. Phys. **12**, 942 (2016).

[47] Y. Iqbal, R. Thomale, F. Parisen Toldin, S. Rachel, and J. Reuther, Functional renormalization group for three-dimensional quantum magnetism, Phys. Rev. B **94**, 140408(R) (2016).

[48] Y. Iqbal, T. Müller, K. Riedl, J. Reuther, S. Rachel, R. Valentí, M. J. P. Gingras, R. Thomale, and H. O. Jeschke, Signatures of a gearwheel quantum spin liquid in a spin-$\frac{1}{2}$ pyrochlore molybdate Heisenberg antiferromagnet, Phys. Rev. Materials **1**, 071201(R) (2017).

[49] F. L. Buessen, M. Hering, J. Reuther, and S. Trebst, Quantum Spin Liquids in Frustrated Spin-1 Diamond Antiferromagnets, Phys. Rev. Lett. **120**, 057201 (2018).

[50] Y. Iqbal, T. Müller, H. O. Jeschke, R. Thomale, and J. Reuther, Stability of the spiral spin liquid in $MnSc_2S_4$, Phys. Rev. B **98**, 064427 (2018).

[51] Y. Iqbal, T. Müller, P. Ghosh, M. J. P. Gingras, H. O. Jeschke, S. Rachel, J. Reuther, and R. Thomale, Quantum and Classical Phases of the Pyrochlore Heisenberg Model with Competing Interactions, Phys. Rev. X **9**, 011005 (2019).

[52] P. Ghosh, T. Müller, F. P. Toldin, J. Richter, R. Narayanan, R. Thomale, J. Reuther, and Y. Iqbal, Quantum paramagnetism and helimagnetic orders in the Heisenberg model on the body centered cubic lattice, Phys. Rev. B **100**, 014420 (2019).

[53] A. Revelli, C. C. Loo, D. Kiese, P. Becker, T. Fröhlich, T. Lorenz, M. Moretti Sala, G. Monaco, F. L. Buessen, J. Attig, M. Hermanns, S. V. Streltsov, D. I. Khomskii, J. van den Brink, M. Braden, P. H. M. van Loosdrecht, S. Trebst, A. Paramekanti, and M. Grüninger, Spin-orbit entangled $j = \frac{1}{2}$ moments in Ba_2CeIrO_6: A frustrated fcc quantum magnet, Phys. Rev. B **100**, 085139 (2019).

[54] N. Niggemann, M. Hering, and J. Reuther, Classical spiral spin liquids as a possible route to quantum spin liquids, J. Phys.: Condens. Matter **32**, 024001 (2020).

[55] P. Ghosh, Y. Iqbal, T. Müller, R. T. Ponnaganti, R. Thomale, R. Narayanan, J. Reuther, M. J. P. Gingras, and H. O. Jeschke, Breathing chromium spinels: A showcase for a variety of pyrochlore Heisenberg Hamiltonians, npj Quantum Mater. **4**, 63 (2019).

[56] S. Chillal, Y. Iqbal, H. O. Jeschke, J. A. Rodriguez-Rivera, R. Bewley, P. Manuel, D. Khalyavin, P. Steffens, R. Thomale, A. T. M. N. Islam, J. Reuther, and B. Lake, Evidence for a three-dimensional quantum spin liquid in $PbCuTe_2O_6$, Nat. Commun. **11**, 2348 (2020).

[57] I. Živković, V. Favre, C. Salazar Mejia, H. O. Jeschke, A. Magrez, B. Dabholkar, V. Noculak, R. S. Freitas, M. Jeong, N. G. Hegde, L. Testa, P. Babkevich, Y. Su, P. Manuel, H. Luetkens, C. Baines, P. J. Baker, J. Wosnitza, O. Zaharko, Y. Iqbal *et al.*, Magnetic Field Induced Quantum Spin Liquid in the Two Coupled Trillium Lattices of $K_2Ni_2(SO_4)_3$, Phys. Rev. Lett. **127**, 157204 (2021).

[58] N. Wentzell, G. Li, A. Tagliavini, C. Taranto, G. Rohringer, K. Held, A. Toschi, and S. Andergassen, High-frequency asymptotics of the vertex function: Diagrammatic parametrization and algorithmic implementation, Phys. Rev. B **102**, 085106 (2020).

[59] C. Hille, D. Rohe, C. Honerkamp, and S. Andergassen, Pseudogap opening in the two-dimensional Hubbard model: A functional renormalization group analysis, Phys. Rev. Research **2**, 033068 (2020).

[60] A. W. Sandvik, Critical Temperature and the Transition from Quantum to Classical Order Parameter Fluctuations in the Three-Dimensional Heisenberg Antiferromagnet, Phys. Rev. Lett. **80**, 5196 (1998).

[61] M. T. Heinilä and A. S. Oja, Long-range order produced by the interaction between spin waves in classical fcc Heisenberg models, Phys. Rev. B **48**, 16514 (1993).

[62] D. T. Haar and M. E. Lines, A molecular-field theory of anisotropic ferromagnetica, Philos. Trans. R. Soc. A **254**, 521 (1962).

[63] S. Alexander and P. Pincus, Phase transitions of some fully frustrated models, J. Phys. A: Math. Gen. **13**, 263 (1980).

[64] P. Balla, Y. Iqbal, and K. Penc, Degenerate manifolds, helimagnets, and multi-Q chiral phases in the classical Heisenberg antiferromagnet on the face-centered-cubic lattice, Phys. Rev. Research **2**, 043278 (2020).

[65] F. L. Buessen, V. Noculak, S. Trebst, and J. Reuther, Functional renormalization group for frustrated magnets with nondiagonal spin interactions, Phys. Rev. B **100**, 125164 (2019).

[66] F. L. Buessen, A functional renormalization group perspective on quantum spin liquids in three-dimensional frustrated magnets, Ph.D. thesis, University of Cologne, 2019.

[67] D. Roscher, N. Gneist, M. M. Scherer, S. Trebst, and S. Diehl, Cluster functional renormalization group and absence of a bilinear spin liquid in the J_1–J_2 Heisenberg model, Phys. Rev. B **100**, 125130 (2019).

[68] J. Thoenniss, M. K. Ritter, F. B. Kugler, J. von Delft, and M. Punk, Multiloop pseudofermion functional renormalization for quantum spin systems: Application to the spin-$\frac{1}{2}$ kagome Heisenberg model (unpublished).

[69] N. Niggemann, B. Sbierski, and J. Reuther, Frustrated quantum spins at finite temperature: Pseudo-Majorana functional renormalization group approach, Phys. Rev. B **103**, 104431 (2021).

[70] P. Bogacki and L. Shampine, A 3(2) pair of Runge - Kutta formulas, Appl. Math. Lett. **2**, 321 (1989).

[71] D. Rohe, Hierarchical parallelisation of functional renormalisation group calculations—hp-fRG, Comput. Phys. Commun. **207**, 160 (2016).

[72] S. V. Isakov, K. Gregor, R. Moessner, and S. L. Sondhi, Dipolar Spin Correlations in Classical Pyrochlore Magnets, Phys. Rev. Lett. **93**, 167204 (2004).

[73] B. Canals and C. Lacroix, Pyrochlore Antiferromagnet: A Three-Dimensional Quantum Spin Liquid, Phys. Rev. Lett. **80**, 2933 (1998).

[74] B. Canals and C. Lacroix, Quantum spin liquid: The Heisenberg antiferromagnet on the three-dimensional pyrochlore lattice, Phys. Rev. B **61**, 1149 (2000).

[75] Y. Huang, K. Chen, Y. Deng, N. Prokof'ev, and B. Svistunov, Spin-Ice State of the Quantum Heisenberg Antiferromagnet on the Pyrochlore Lattice, Phys. Rev. Lett. **116**, 177203 (2016).

[76] V. R. Chandra and J. Sahoo, Spin-$\frac{1}{2}$ Heisenberg antiferromagnet on the pyrochlore lattice: An exact diagonalization study, Phys. Rev. B **97**, 144407 (2018).

[77] P. Müller, A. Lohmann, J. Richter, and O. Derzhko, Thermodynamics of the pyrochlore-lattice quantum Heisenberg antiferromagnet, Phys. Rev. B **100**, 024424 (2019).

[78] I. Hagymási, R. Schäfer, R. Moessner, and D. J. Luitz, Possible Inversion Symmetry Breaking in the $S = 1/2$ Pyrochlore Heisenberg Magnet, Phys. Rev. Lett. **126**, 117204 (2021).

[79] N. Astrakhantsev, T. Westerhout, A. Tiwari, K. Choo, A. Chen, M. H. Fischer, G. Carleo, and T. Neupert, Broken-Symmetry Ground States of the Heisenberg Model on the Pyrochlore Lattice, Phys. Rev. X **11**, 041021 (2021).

[80] M. Hering, V. Noculak, F. Ferrari, Y. Iqbal, and J. Reuther, Dimerization tendencies of the pyrochlore Heisenberg antiferromagnet: A functional renormalization group perspective, Phys. Rev. B **105**, 054426 (2022).

[81] O. Derzhko, T. Hutak, T. Krokhmalskii, J. Schnack, and J. Richter, Adapting Planck's route to investigate the thermodynamics of the spin-half pyrochlore Heisenberg antiferromagnet, Phys. Rev. B **101**, 174426 (2020).

[82] R. Schäfer, I. Hagymási, R. Moessner, and D. J. Luitz, Pyrochlore $S = \frac{1}{2}$ Heisenberg antiferromagnet at finite temperature, Phys. Rev. B **102**, 054408 (2020).

[83] C. Liu, G. B. Halász, and L. Balents, Competing orders in pyrochlore magnets from a $\mathbb{Z}_2$ spin liquid perspective, Phys. Rev. B **100**, 075125 (2019).

[84] J. H. Kim and J. H. Han, Chiral spin states in the pyrochlore Heisenberg magnet: Fermionic mean-field theory and variational Monte Carlo calculations, Phys. Rev. B **78**, 180410(R) (2008).

[85] F. J. Burnell, S. Chakravarty, and S. L. Sondhi, Monopole flux state on the pyrochlore lattice, Phys. Rev. B **79**, 144432 (2009).

[86] In the pf-FRG analysis of Ref. [80] the breaking of C_3 rotations alone is also supported.

[87] C. Liu, G. B. Halász, and L. Balents, Symmetric U(1) and $\mathbb{Z}_2$ spin liquids on the pyrochlore lattice, Phys. Rev. B **104**, 054401 (2021).

[88] B. Schneider, J. C. Halimeh, and M. Punk, Projective symmetry group classification of chiral $\mathbb{Z}_2$ spin liquids on the pyrochlore lattice: Application to the spin-$\frac{1}{2}$ XXZ Heisenberg model, Phys. Rev. B **105**, 125122 (2022).

[89] M. P. Zinkin, M. J. Harris, and T. Zeiske, Short-range magnetic order in the frustrated pyrochlore antiferromagnet $CsNiCrF_6$, Phys. Rev. B **56**, 11786 (1997).

[90] D. A. Huse, W. Krauth, R. Moessner, and S. L. Sondhi, Coulomb and Liquid Dimer Models in Three Dimensions, Phys. Rev. Lett. **91**, 167004 (2003).

[91] R. Moessner and S. L. Sondhi, Three-dimensional resonating-valence-bond liquids and their excitations, Phys. Rev. B **68**, 184512 (2003).

[92] C. L. Henley, The "Coulomb phase" in frustrated systems, Annu. Rev. Condens. Matter Phys. **1**, 179 (2010).

[93] R. Moessner and J. T. Chalker, Low-temperature properties of classical geometrically frustrated antiferromagnets, Phys. Rev. B **58**, 12049 (1998).

[94] R. Moessner and J. T. Chalker, Properties of a Classical Spin Liquid: The Heisenberg Pyrochlore Antiferromagnet, Phys. Rev. Lett. **80**, 2929 (1998).

[95] S. Zhang, H. J. Changlani, K. W. Plumb, O. Tchernyshyov, and R. Moessner, Dynamical Structure Factor of the Three-Dimensional Quantum Spin Liquid Candidate $NaCaNi_2F_7$, Phys. Rev. Lett. **122**, 167203 (2019).

[96] K. W. Plumb, H. J. Changlani, A. Scheie, S. Zhang, J. W. Krizan, J. A. Rodriguez-Rivera, Y. Qiu, B. Winn, R. J. Cava, and C. L. Broholm, Continuum of quantum fluctuations in a three-dimensional S = 1 Heisenberg magnet, Nat. Phys. **15**, 54 (2019).

[97] A. B. Harris, A. J. Berlinsky, and C. Bruder, Ordering by quantum fluctuations in a strongly frustrated Heisenberg antiferromagnet, J. Appl. Phys. **69**, 5200 (1991).

[98] K. Grosse-Brauckmann, Triply periodic minimal and constant mean curvature surfaces, Interface Focus **2**, 582 (2012).

[99] P. Balla, Y. Iqbal, and K. Penc, Affine lattice construction of spiral surfaces in frustrated Heisenberg models, Phys. Rev. B **100**, 140402(R) (2019).

[100] J. Attig and S. Trebst, Classical spin spirals in frustrated magnets from free-fermion band topology, Phys. Rev. B **96**, 085145 (2017).

[101] J. Villain, R. Bidaux, J.-P. Carton, and R. Conte, Order as an effect of disorder, J. Phys. France **41**, 1263 (1980).

[102] Y. Yamamoto and T. Nagamiya, Spin arrangements in magnetic compounds of the rocksalt crystal structure, J. Phys. Soc. Jpn. **32**, 1248 (1972).

[103] We cannot rule out a scenario where long-range magnetic order sets in at $\Lambda/|J| < 0.05$, as has been hinted to in Ref. [111].

[104] A. N. Ignatenko, A. A. Katanin, and V. Y. Irkhin, Strong short-range magnetic order in a frustrated FCC lattice and its possible role in the iron structural transformation, JETP Lett. **87**, 555 (2008).

[105] J. Sonnenschein, A. Chauhan, Y. Iqbal, and J. Reuther, Projective symmetry group classifications of quantum spin liquids on the simple cubic, body centered cubic, and face centered cubic lattices, Phys. Rev. B **102**, 125140 (2020).

[106] PFFRGSolver.jl repository, https://github.com/dominikkiese/PFFRGSolver.jl.

[107] Y. Singh, S. Manni, J. Reuther, T. Berlijn, R. Thomale, W. Ku, S. Trebst, and P. Gegenwart, Relevance of the Heisenberg-Kitaev Model for the Goneycomb Lattice Iridates A_2IrO_3, Phys. Rev. Lett. **108**, 127203 (2012).

[108] M. Hering and J. Reuther, Functional renormalization group analysis of Dzyaloshinsky-Moriya and Heisenberg spin interactions on the kagome lattice, Phys. Rev. B **95**, 054418 (2017).

[109] Jülich Supercomputing Centre, JURECA: Modular supercomputer at Jülich Supercomputing Centre, J. Large-Scale Res. Facil. **4** (2018).

[110] Jülich Supercomputing Centre, JUWELS: Modular tier-0/1 supercomputer at the Jülich Supercomputing Centre, J. Large-Scale Res. Facil. **5** (2019).

[111] N.-N. Sun and H.-Y. Wang, The J_1-J_2 model on the face-centered-cubic lattices, J. Magn. Magn. Mater. **454**, 176 (2018).

Eur. Phys. J. B (2022)95:102
https://doi.org/10.1140/epjb/s10051-022-00349-2

THE EUROPEAN PHYSICAL JOURNAL B

Regular Article - Solid State and Materials

Benchmark calculations of multiloop pseudofermion fRG

Marc K. Ritter[1,a], Dominik Kiese[2], Tobias Müller[3], Fabian B. Kugler[4], Ronny Thomale[3], Simon Trebst[2], and Jan von Delft[1]

[1] Arnold Sommerfeld Center for Theoretical Physics, Center for NanoScience, and Munich Center for Quantum Science and Technology, Ludwig-Maximilians-Universität München, 80333 Munich, Germany
[2] Institute for Theoretical Physics, University of Cologne, 50937 Cologne, Germany
[3] Institute for Theoretical Physics, University of Würzburg, Am Hubland, 97074 Würzburg, Germany
[4] Department of Physics and Astronomy, Rutgers University, Piscataway, NJ 08854, USA

Received 30 March 2022 / Accepted 10 May 2022

Abstract. The pseudofermion functional renormalization group (pffRG) is a computational method for determining zero-temperature phase diagrams of frustrated quantum magnets. In a recent methodological advance, the commonly employed Katanin truncation of the flow equations was extended to include multiloop corrections, thereby capturing additional contributions from the three-particle vertex (Thoenniss et al. https://arxiv.org/abs/2011.01268; Kiese et al. https://arxiv.org/abs/2011.01269). This development has also stimulated significant progress in the numerical implementation of pffRG, allowing one to track the evolution of pseudofermion vertices under the renormalization group flow with unprecedented accuracy. However, cutting-edge solvers differ in their integration algorithms, heuristics to discretize Matsubara frequency grids, and more. To lend confidence in the numerical robustness of state-of-the-art multiloop pffRG codes, we present and compare results produced with two independently developed and algorithmically distinct solvers for Heisenberg models on three-dimensional lattice geometries. Using the cubic lattice Heisenberg (anti)ferromagnet with nearest and next-nearest neighbor interactions as a generic benchmark model, we find the two codes to quantitatively agree, often up to several orders of magnitude in digital precision, both on the level of spin-spin correlation functions and renormalized fermionic vertices for varying loop orders. These benchmark calculations further substantiate the usage of multiloop pffRG solvers to tackle unconventional forms of quantum magnetism.

1 Introduction

A fascinating phenomenon in the study of frustrated quantum magnets is the interplay of unconventional forms of magnetic order and the possible emergence of quantum spin liquid states near zero temperature [3]. The successful description of such low-energy states of quantum spin systems has, however, remained challenging, especially in the presence of competing interactions, geometric frustration, and in higher spatial dimensions.

Since its inception more than a decade ago [4], the pseudofermion functional renormalization group (pffRG) has become a powerful and flexible approach to map out the zero-temperature phase diagrams of various quantum spin models, both in two [4–20] and three spatial dimensions [16,21–29]. Although the problem obtained after representing the spin operators by complex fermions is treated approximately, one of the striking features of pffRG is its ability to track competing instabilities in different interaction channels, allowing one to discriminate putative spin-liquid phases from long-range ordered magnetic ground states. This ability can be traced back [30,31] to the inclusion of leading-order $1/S$ and $1/N$ diagrams (the former promoting classical magnetic order, the latter quantum fluctuations), which are treated on equal footing in pffRG by means of the routinely employed Katanin truncation [32].

Recently, the multiloop truncation scheme of the infinite hierarchy of fRG flow equations [33–35], previously used in the context of the Hubbard [36,37] and Anderson impurity model [38], was applied to the zero-temperature pffRG by some of us [1,2]. The convergence in the number of loops over a wide range of energy scales attested to the inner consistency of the pffRG method, despite being used in the strong-coupling limit. These developments were accompanied and facilitated by substantial improvements of the numerical implementation that remedy many shortcomings of previous studies. Yet, some of these advances, such as the employed integration routines and adaptive Matsubara frequency grids [1,2], rely on certain numerical heuristics, affecting, e.g., the minimal grid spacing and largest Matsubara frequencies considered. Therefore, quanti-

[a] e-mail: ritter.marc@physik.uni-muenchen.de (corresponding author)

Published online: 01 July 2022

tative agreement between different implementations is, although highly desired, not guaranteed *a priori*.

In the present work, we provide evidence for the numerical robustness of pffRG by benchmarking two independent state-of-the-art solvers, one provided by a research group at LMU Munich (dubbed code #1 in the following), and one by a Cologne–Würzburg collaboration (denoted by code #2) with an open-source release [39]. As a test case, we consider ferro- and antiferromagnetic Heisenberg models on the simple cubic lattice and compare our results both on the level of renormalized couplings (i.e. fermionic vertex functions) as well as for the (post-processed) spin-spin correlation functions.

The remainder of the paper is structured as follows. We begin by providing a brief overview of the multiloop pffRG in Sect. 2. This is followed by an in-depth comparison of the numerical results produced by the two codes at hand in Sect. 3. Finally, in Sect. 4, technical aspects of the implementation, such as the choice of frequency grids, integration routines and differential equation solvers are discussed, with special emphasis devoted to their influence on the numerical stability and accuracy of the two codes.

2 Multiloop pseudofermion fRG

Within the pffRG approach, one can study generic spin-1/2 Hamiltonians with bilinear spin couplings, i.e.,

$$\mathcal{H} = \tfrac{1}{2}\sum_{ij} J_{ij}^{\mu\nu} S_i^\mu S_j^\nu \,. \tag{1}$$

Here, the spin operators S_i^μ live on the sites i of an arbitrary lattice, and the exchange matrices $J_{ij}^{\mu\nu}$ are assumed to be real. The spin operators are represented in terms of complex pseudofermions $f_{i\alpha}^{(\dagger)}$ with $\alpha \in \{\uparrow,\downarrow\}$ as

$$S_i^\mu = \tfrac{1}{2}\sum_{\alpha,\beta} f_{i\alpha}^\dagger \sigma_{\alpha\beta}^\mu f_{i\beta} \,, \tag{2}$$

where $\sigma_{\alpha\beta}^\mu$ for $\mu \in \{x,y,z\}$ are the Pauli matrices. This yields a purely quartic Hamiltonian which can be treated by established functional RG techniques.

Note that the pseudofermion representation of the spin algebra comes with an artificial enlargement of the local Hilbert space dimension, which must be dealt with by an additional particle number constraint $\sum_\alpha f_{i\alpha}^\dagger f_{i\alpha} = 1$ on every lattice site. In practice, this constraint is not enforced, but holds on average due to particle-hole symmetry [1,2,4]. Nevertheless, the influence of fluctuations can be quantitatively gauged by explicitly computing the variance of the number operator, which can be expressed through the equal-time spin-spin correlation function $\langle S_i^\mu S_i^\mu \rangle$ [1]. Although fluctuations are not fully suppressed, even if a local level repulsion term $AS_i^\mu S_i^\mu$ (with $A<0$) is employed, recent studies [1,19,23,30] pointed out that observables extracted from pffRG flows are qualitatively unaffected by the unphysical Hilbert space sectors.

An alternate decomposition of the spin operators into Majorana instead of Abrikosov fermions allows one to circumvent the problem of unphysical states in the fermionic representation at the cost of redundant copies of physical Hilbert-space sectors [40]. For moderately high temperatures, the latter approach was recently shown to enable an accurate calculation of thermodynamic observables [41], such as the free energy and specific heat. However, the approach was also found to suffer from unphysical divergencies when approaching the $T \to 0$ limit, which we consider here (for the Abrikosov fermion decomposition).

Since kinetic contributions are absent in the pseudofermion representation of Eq. (1), the free propagator assumes the simple form

$$G_0(1'|1) = (i\omega_1)^{-1}\delta_{i_{1'}i_1}\delta_{\alpha_{1'}\alpha_1}\delta(\omega_{1'}-\omega_1)\,, \tag{3}$$

diagonal in all indices. To successively integrate out high-energy modes and thus provide an effective low-energy description of a given model, a cutoff parameter, here denoted as Λ, is introduced in the bare propagator. The fRG equations then govern the flow of the n-particle vertices from the UV limit $\Lambda \to \infty$, where the regularized bare propagator vanishes, to the infrared limit $\Lambda \to 0$, where one recovers the physical theory. As such, there is a certain degree of freedom in the cutoff implementation. A popular choice for the regulator in pffRG is a Heavyside step function, which sharply suppresses frequency contributions $|\omega| < \Lambda$. This choice is very useful for analytical treatments of pffRG in the large-S and large-N limit, where the flow equations can be solved exactly and reproduce mean-field gap equations [30,31]. However, if numerical calculations are employed away from these limits, a non-analytic regulator spoils the smoothness of the right-hand side of the flow equations, and therefore limits the applicability of higher-order integration routines. For this reason, we consider a smooth regulator

$$R^\Lambda(\omega) = 1 - e^{-\omega^2/\Lambda^2}\,, \tag{4}$$

throughout this manuscript, and implement the cutoff as $G_0^\Lambda(\omega) = R^\Lambda(\omega)G_0(\omega)$, with $G_0(\omega) \equiv (i\omega)^{-1}$.

To make the infinite hierarchy of fRG flow equations amenable to further calculations, a truncation is necessary. Usually, this is done by neglecting all n-particle vertices of $n=3$ and higher [32]. However, to capture the physics of interest in pffRG, one must already go beyond that using the Katanin truncation, which feeds the Λ derivative of the self-energy Σ^Λ back into the flow of the two-particle vertex Γ^Λ [4]. Within this truncation, the flow equations schematically read

$$\frac{d}{d\Lambda}\Sigma^\Lambda = -\left[\Gamma^\Lambda \circ S^\Lambda\right]_\Sigma \,, \tag{5}$$

$$\frac{d}{d\Lambda}\Gamma^\Lambda = \sum_c \dot{\gamma}_c^\Lambda = -\sum_c [\Gamma^\Lambda \circ \partial_\Lambda (G^\Lambda \times G^\Lambda) \circ \Gamma^\Lambda]_c \,. \tag{6}$$

Here, we introduced the loop function $[\Gamma \circ G]_\Sigma$ and the single-scale propagator $S^\Lambda \equiv -\frac{d}{d\Lambda} G^\Lambda|_{\Sigma^\Lambda=\text{const.}}$. We categorized the contributions to the flow of Γ into three distinct channels c: the particle-particle (s) channel, the direct particle-hole (t) channel, and the crossed particle-hole (u) channel. Each "bubble" term, with the general form $[\Gamma \circ (G \times G') \circ \Gamma']_c$, describes the flow of a two-particle reducible vertex γ_c. As all self-energies, vertices, and related correlators are Λ-dependent, we refrain from writing this dependence explicitly in the following.

The multiloop fRG (mfRG) flow [33–35], recently employed within pffRG [1,2], is an attempt to go beyond the Katanin truncation and capture even more contributions from n-particle vertices with $n \geq 3$. It can be derived from the parquet approximation [42], which self-consistently connects one- and two-particle correlation functions via the Schwinger–Dyson (SDE) and Bethe–Salpeter equations (BSE), and as such the inherent dependence of the $\Lambda \to 0$ fRG result on the specific choice of regulator is eliminated [34]. This approximation includes all those contributions to the flow of the two-particle vertex which can be efficiently calculated, i.e., with the same cost as the one-loop flow in Eqs. (5) and (6). Summarized briefly: To obtain the mfRG flow of γ_c, one iteratively computes multiloop corrections to the one-loop ($\ell = 1$) result, using bubble functions with undifferentiated propagators but differentiated vertices. In a similar fashion, one can recover equivalence to the SDE, by feeding back the so-determined vertex corrections into the self-energy flow.

One of the most important ingredients to achieve sufficient numerical accuracy throughout the multiloop flow is an appropriate treatment of the frequency dependence of the two-particle vertex. In Ref. [43], a parametrization in terms of one bosonic and two fermionic frequencies (the fourth frequency argument is fixed by energy conservation) for each two-particle reducible vertex was put forward. This parametrization captures the non-trivial high frequency asymptotics of the vertices while being numerically efficient. Code #1 uses precisely the proposal of Ref. [43], and the diagrams contributing to each channel are grouped into four asymptotic classes K_n as

$$\begin{aligned}\gamma_c(\omega_c, \nu_c, \nu_c') = {} & K_{1,c}(\omega_c) \\ & + K_{2,c}(\omega_c, \nu_c) + K_{2',c}(\omega_c, \nu_c') \\ & + K_{3,c}(\omega_c, \nu_c, \nu_c') \,,\end{aligned} \tag{7}$$

where we displayed only frequency arguments for brevity. Here, ω_c, ν_c and ν_c', denote the natural frequency arguments for diagrams reducible in channel c (see Ref. [1] for the conventions used). The K_n asymptotically decay to zero in each frequency, allowing one to reduce the necessary number of arguments when summing up the asymptotic classes to obtain γ_c. Code #2 chooses a slightly different approach, by defining asymptotic classes Q_n [44] as

$$\begin{aligned} Q_{1,c}(\omega_c) &= K_{1,c}(\omega_c) \\ Q_{2,c}(\omega_c, \nu_c) &= K_{1,c}(\omega_c) + K_{2,c}(\omega_c, \nu_c) \\ Q_{2',c}(\omega_c, \nu_c') &= K_{1,c}(\omega_c) + K_{2',c}(\omega_c, \nu_c') \\ Q_{3,c}(\omega_c, \nu_c, \nu_c') &= K_{1,c}(\omega_c) \\ &\quad + K_{2,c}(\omega_c, \nu_c) + K_{2',c}(\omega_c, \nu_c') \\ &\quad + K_{3,c}(\omega_c, \nu_c, \nu_c') \,, \end{aligned} \tag{8}$$

with the respective choice of natural frequency arguments outlined in Ref. [2]. Since the K_n classes decay to zero for large frequencies, the Q_n (at least for $n > 1$) are projected to a lower class. For instance, $Q_{3,c}(\omega_c, \nu_c, \nu_c') = Q_{2,c}(\omega_c, \nu_c)$ if $|\nu_c'| \to \infty$. Let us emphasize that both parametrizations contain the same information about the asymptotic structure of the two-particle vertices, as the K_n and Q_n parametrizations can be exactly transformed into each other. For an appropriate choice of numerical frequency grids, both parametrizations are therefore equally valid and differ only in numerical performance. The former approach allows for a more fine-grained adjustment of discrete frequencies to the asymptotic decay of individual classes, while the latter reduces the cost of evoking a two-particle vertex from a summation of up to four classes K_n to loading just a single Q_n.

The central observable computed from the pffRG equations is the flowing spin-spin correlation function,

$$\chi_{ij}^{\mu\nu}(i\omega = 0) = \int_0^\infty d\tau \langle T_\tau S_i^\mu(\tau) S_j^\nu(0) \rangle \,, \tag{9}$$

where we omit indication of the Λ-dependence for brevity. In all models considered here, the interactions in the Hamiltonian are diagonal and SU(2)-symmetric. This leads to spin-spin correlations that are symmetric as well, and we thus define $\chi_{ij} \equiv \chi_{ij}^{xx} = \chi_{ij}^{yy} = \chi_{ij}^{zz}$.

The spin-spin correlations can be used to identify transitions into phases with broken symmetries; there, the flow becomes unstable at some Λ_T and must be stopped. For long-range ordered states, the momentum $\boldsymbol{k}$ for which the structure factor

$$\chi(\boldsymbol{k}, i\omega) = \frac{1}{N_\text{sites}} \sum_{ij} e^{i\boldsymbol{k}\cdot(\boldsymbol{R}_i - \boldsymbol{R}_j)} \chi_{ij}(i\omega) \tag{10}$$

(i.e. the Fourier transform of χ_{ij}) is most dominant gives an indication of the emergent magnetic order, as exemplified in Fig. 1. A smooth flow down to the infrared $\Lambda \to 0$ is, on the other hand, associated with non-magnetic phases, such as spin liquids, dimerized, or plaquette-ordered states.

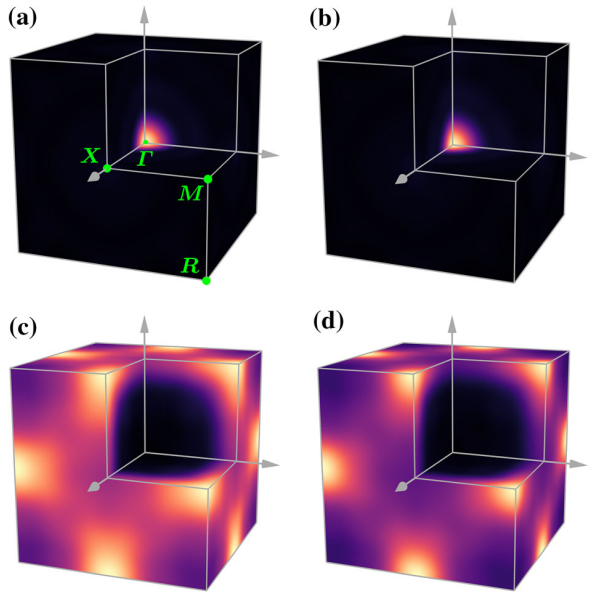

Fig. 1 Momentum-resolved structure factors within the first Brillouin zone of the cubic lattice for (**a**, **b**) the ferromagnetic case at $\Lambda/J = 0.8$ and (**c**, **d**) the paramagnetic case at $\Lambda/J = 0.3$, computed for (**a**, **c**) $\ell = 1$ and (**b**, **d**) $\ell = 3$ using code #2. The ferromagnet shows a sharp peak at the $\boldsymbol{\Gamma}$ point, without visible difference between the two loop orders. The putative paramagnet shows a broadened distribution of spectral weight centered around soft maxima at the $\boldsymbol{M}$ points in $\ell = 1$ calculations, while the structure factor peaks more distinctively for $\ell = 3$, signalling the onset of magnetic order instead

3 Results

To benchmark the two codes, we calculate the spin-spin correlations and pseudofermion vertices of an extended Heisenberg model on the cubic lattice with a maximum correlation length $\xi = 5$ in units of the lattice spacing [1]. The corresponding three-dimensional cluster contains $N = 515$ sites, small enough to efficiently compare the two codes but large enough to produce the (qualitatively) correct physics. The corresponding Hamiltonian with up to third-neighbor interactions (see inset in Fig. 2) reads

$$\mathcal{H} = J_1 \sum_{\langle ij \rangle} S_i^\mu S_j^\mu + J_2 \sum_{\langle\langle ij \rangle\rangle} S_i^\mu S_j^\mu + J_3 \sum_{\langle\langle\langle ij \rangle\rangle\rangle} S_i^\mu S_j^\mu \,, \tag{11}$$

where we fix $J \equiv \sqrt{J_1^2 + J_2^2 + J_3^2}$ as the unit of energy. We focus on two choices of these interaction parameters to highlight differences between fRG flows in different phases:

$$J_1 < 0, \qquad J_2 = 0, \qquad J_3 = 0, \tag{12}$$

$$J_1 > 0, \qquad J_2/J_1 = 0.6, \qquad J_3/J_1 = 0.25, \tag{13}$$

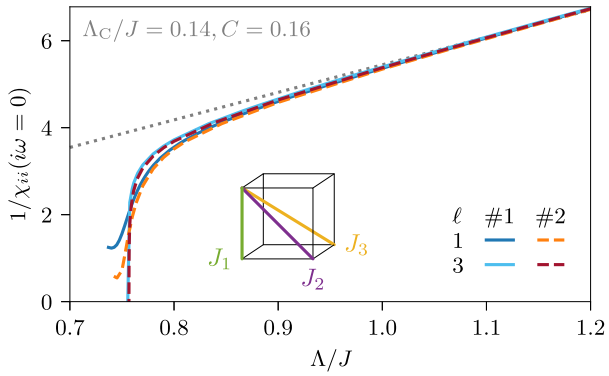

Fig. 2 Inverse spin-spin correlation function for the ferromagnet as a function of Λ. Shown here is a comparison of the $\ell = 1$ and $\ell = 3$ flows obtained from both codes. The dotted line is a Λ^{-1} fit $[\chi_C = CJ/(\Lambda - \Lambda_C)]$ to the data at $\Lambda/J \in [1.0, 4.0]$. The transition to a ferromagnetically ordered phase is visible as a sharp downturn away from Curie–Weiss behavior. Inset: Definition of the first, second, and third nearest-neighbor interaction, J_1 (green), J_2 (purple), and J_3 (yellow)

where Eq. (12) yields a nearest-neighbor ferromagnet and the setup of Eq. (13) was previously reported to result in a paramagnetic ground state [21].

Rewriting each spin operator S^μ in the Hamiltonian in terms of pseudofermions leads to an expression proportional to $f^\dagger_{\alpha'} f_\alpha f^\dagger_{\beta'} f_\beta$, with interactions proportional to $\sum_\mu \sigma^\mu_{\alpha'\alpha} \sigma^\mu_{\beta'\beta}$. Exploiting this SU(2) symmetry (the interactions are diagonal and of equal magnitude in every spin direction), the flowing pseudofermion vertex Γ (and each of its two-particle reducible parts γ_c) can be decomposed into a spin component Γ^s, proportional to the latter combination of Pauli matrices, and a density component Γ^d proportional to $\delta_{\alpha'\alpha}\delta_{\beta'\beta}$ [4,45]. Note that the density component, although initially vanishing for any typical spin model, becomes finite away from the UV limit and is essential for tracking the evolution of *all* symmetry-allowed couplings under the RG flow.

3.1 Ferromagnetic phase

With pure nearest-neighbor ferromagnetic interactions, the zero-temperature ground state is intuitively expected to be a ferromagnet. Therefore, in the context of pseudofermion fRG, there should be a transition at some finite $\Lambda_T > 0$ from a paramagnetic regime at large $\Lambda > \Lambda_T$ to the ferromagnetic phase at $\Lambda < \Lambda_T$. Approaching the transition, the spin-spin correlator χ_{ij} is expected to diverge, similar to a finite-temperature phase transition. In this case, a peak will form at the $\boldsymbol{\Gamma}$ point in reciprocal space, as is visible Fig. 1, since the correlations are uniform and positive in a ferromagnet.

Close to the transition, the flow is supposed to visibly deviate from its paramagnetic Curie–Weiss behavior $\chi_{ii} \approx CJ/(\Lambda - \Lambda_C)$ at large $\Lambda \gg \Lambda_T$. For this reason, it is convenient to plot the inverse correlator $1/\chi_{ii}$ as a function of Λ to locate the transition, as

shown in Fig. 2. Here, the $1/\Lambda$ behavior appears as a straight line with slope $1/C$ displaced horizontally by Λ_C/J and the transition to the ferromagnetic phase is visible as a sharp turn down to a smaller inverse correlation function at $\Lambda/J \approx 0.76$. The structure factor at Λ close to Λ_T, shown in Figs. 1 and 3, has a single peak at the $\boldsymbol{\Gamma}$ point, signifying an instability towards ferromagnetic order. This, as well as the Curie–Weiss fit parameters, are consistent across both considered loop orders $\ell = 1, 3$ and both codes, while Λ_T differs slightly.

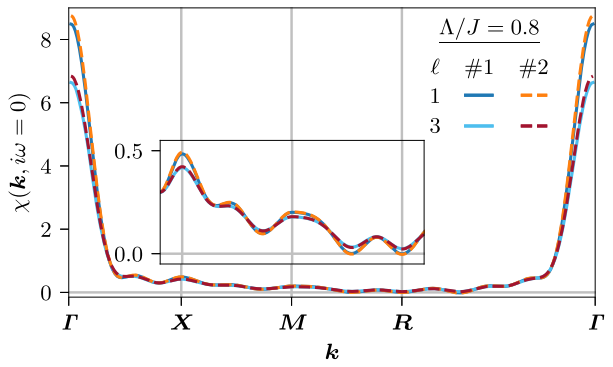

Fig. 3 Structure factor for the ferromagnet along a high-symmetry path of the cubic lattice Brillouin zone. The results are in excellent agreement between both codes, both for $\ell = 1$ and $\ell = 3$, showing dominant ferromagnetic correlations indicated by a sharp peak around the $\boldsymbol{\Gamma}$ point. Inset: Zoom into the path segment connecting the $\boldsymbol{X}, \boldsymbol{M}$, and $\boldsymbol{R}$ point

Since both implementations obtain the spin-spin correlations by post-processing the vertices, any discrepancy therein originates from differences in the vertices. Therefore, a more detailed examination of the $1/\chi_{ii}$-deviations between the codes for $\ell = 1$ will follow once the flow of the vertex components has been discussed. Moreover, even if the flows for the χ_{ij} agree perfectly (as, e.g., in the regime $\Lambda > \Lambda_T$), discrepancies in the vertices cannot be fully excluded, as post-processing spin-spin correlations from pseudofermion vertex data amounts to integrating a combination of several propagators and the vertex over two frequencies [1]. Hence, this additional step might hide potential differences in the vertex data.

To investigate this further, we focus on the t-reducible vertex γ_t plotted in Fig. 4 at various values of Λ: Its spin component γ_t^s (second and third column) is responsible for the transition and becomes sharply peaked at small bosonic frequencies $\omega \approx 0$. Its density component γ_t^d (last column) with its extended structures and peaks at non-zero fermionic frequencies ν is particularly difficult to resolve and thus most likely to contain numerical artifacts. Comparing γ_t, as well as the the self-energy Σ between the codes, we find quan-

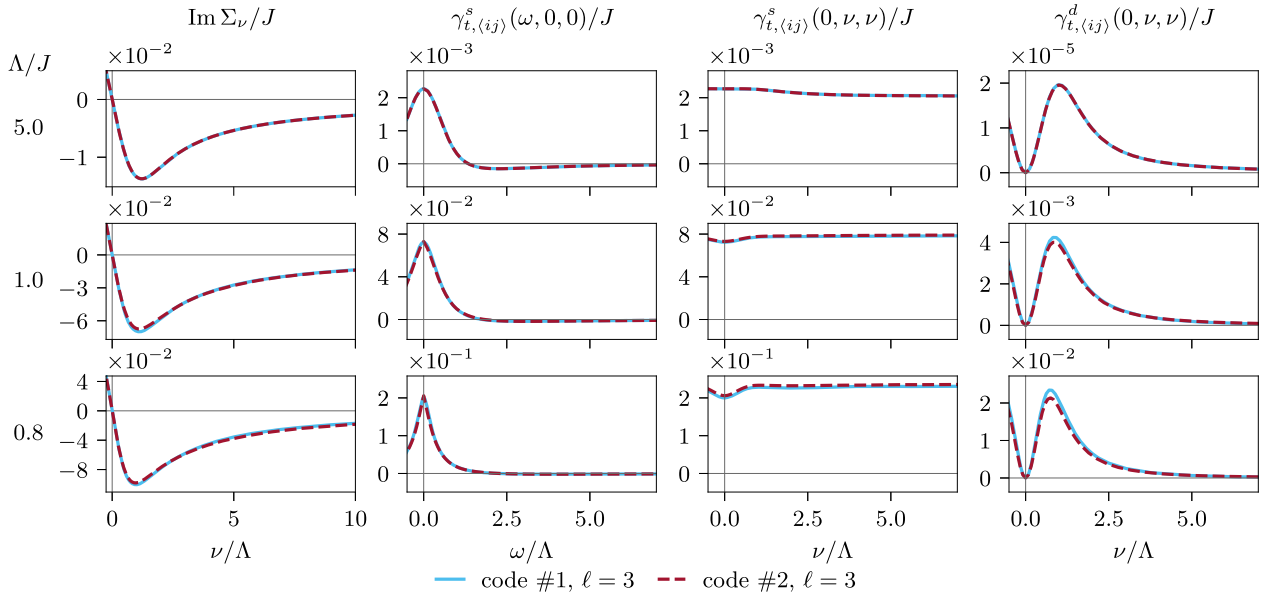

Fig. 4 Frequency structure of self-energy and t-reducible vertex for the ferromagnet at different values of Λ/J for $\ell = 3$ flows. The self-energy is purely imaginary and antisymmetric in frequency space, while all vertex components are real and symmetric along the directions plotted here. We show two cuts through the three-dimensional structure of $\gamma^{\Lambda,\mu}_{t,\langle ij\rangle}(\omega,\nu,\nu')$: A cut along the bosonic frequency axis ω, with both fermionic frequencies set to $\nu = \nu' = 0$, and a cut with equal fermionic frequencies $\nu = \nu'$, where the bosonic frequency was set to $\omega = 0$. The first cut is not shown for γ_t^d as $\gamma^d_{t,\langle ij\rangle}(\omega,0,0) = 0$ due to symmetry [1,2]. The most prominent structure in the t-reducible vertex is a peak around zero bosonic frequency $\omega = 0$ that grows in magnitude and becomes sharper as Λ is decreased. This indicates ferromagnetic correlations that grow stronger as the ordering phase transition is approached. In all components, there is quantitative agreement between the two codes

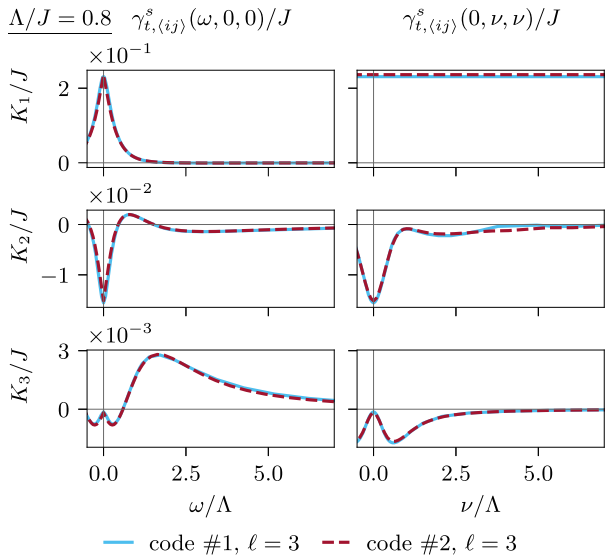

Fig. 5 Decomposition of the $\gamma^s_{t,\langle ij\rangle}(\omega,\nu,\nu')$ vertex for the ferromagnet into asymptotic classes $K_{1,t}, K_{2,t}, K_{3,t}$ (first, second, third row) for the $\ell = 3$ flows at $\Lambda/J = 0.8$. Frequency axes shown here are the same as in Fig. 4. As the flow is close to the ordering phase transition at this value of Λ, strong ferromagnetic correlations are present as a peak around $\omega = 0$ in $K_{1,t}$. The other classes are at least one order of magnitude smaller. In all classes, both codes show quantitative agreement

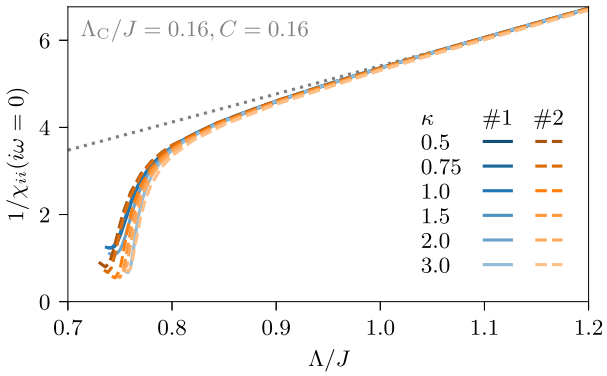

Fig. 6 Flows with rescaled frequency meshes. Comparison of the flow of inverse static on-site spin correlations $1/\chi_{ii}(i\omega = 0)$ obtained using frequency meshes with different scaling factors κ. The dotted line is a Λ^{-1} fit to the data at $\Lambda/J \in [1.0, 4.0]$. For all values of κ, a transition to a ferromagnet is visible as a sharp turn down. The predicted transition point as well as the slope of χ in the region $\Lambda/J < 0.8$ differs, while the behavior at large $\Lambda > J$ remains identical

titative agreement also on this very detailed level of inspection.

As outlined in Sect. 2, both codes use a decomposition of the reducible vertices $\gamma_s, \gamma_t, \gamma_u$ into four asymptotic classes each. The decomposition into asymptotic classes K_n is shown for γ^s_t at $\Lambda/J = 0.8$ in Fig. 5, where we omit $K^s_{2',t}$, as it is equal to $K^s_{2,t}$ by crossing symmetry [1,2]. Note that, while these vertices can directly be extracted from code #1, an additional transformation is applied to the Q_n decomposition of code #2 [see Eq. (8)]. The peak in γ^s_t at small bosonic frequencies in Fig. 4 is found to stem from the K_1 contribution, which is an order of magnitude larger than the other classes. In K_2 and K_3, extended structures with multiple maxima and minima exist. It is thus crucial to use a frequency mesh with enough mesh points in an extended region around the origin to control numerical interpolation errors (see Sect. 4).

Though the codes implement the vertex decomposition differently (see Sect. 2) and use different approaches to build appropriate frequency meshes (see [1,2] for a detailed description), all components of the vertex are consistent with each other. This demonstrates that it is possible to gain control over said interpolation errors by a careful adaptive implementation that places enough mesh points where they are needed.

Since the numerical error incurred by interpolation of the continuous frequency structure from a discrete mesh is particularly relevant whenever sharp structures are present in the vertex, different choices of frequency meshes have strong effects close to phase transitions, where some couplings are expected to diverge. For instance, in the ferromagnetic setup discussed above, the transition was induced by a peak in the spin component of the t-reducible vertex that grows quickly and starts to diverge, as can be seen in the second column of Fig. 4. As the transition is approached, this peak progressively becomes sharper and thus more difficult to resolve using discrete meshes. Thus, minor differences in mesh spacing can induce differences in the flow at the transition, though the qualitative, physical results remain unchanged.

To investigate the effects of changes in the mesh spacing explicitly, we compared results obtained from both codes with artificially modified meshes. Both implementations make use of adaptive frequency grids where, during the flow, the mesh spacing is adjusted according to the frequency structure of the vertex. The simplest way to manipulate the meshes is to rescale them by an artificial scaling factor κ. In Fig. 6, we show the effect of such a rescaling on the $\ell = 1$ flow from Fig. 2. Above $\Lambda/J \approx 0.8$, all frequency structures in the vertex are fairly broad and easy to resolve. Consequently, rescaling the frequency grid has little effect and values $\kappa = 0.5 \ldots 3.0$ result in the same flow and also the same Curie–Weiss fit parameters. Below that point, the flows differ more and more as structures become sharper and ultimately predict slightly different transition points Λ_T/J. Nevertheless, all flows predict a transition to the same ferromagnetic phase, which can be identified by a peak in the structure factor at the $\boldsymbol{\Gamma}$ point.

3.2 Paramagnetic phase

For the second set of parameters, Eq. (13), all interactions up to the third neighbor are antiferromagnetic.

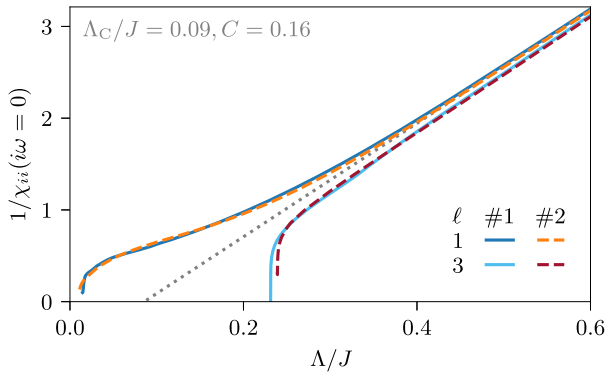

Fig. 7 Inverse spin-spin correlation function for the putative paramagnet as a function of Λ. Shown here is a comparison of the $\ell = 1$ and $\ell = 3$ flow obtained from both codes. The dotted line is a fit of a Λ^{-1} power law to the data at $\Lambda/J \in [1.0, 4.0]$. For $\Lambda/J \geq 0.5$, the Λ^{-1} behavior is followed almost perfectly. At smaller Λ/J, the $\ell = 1$ and $\ell = 3$ flows disagree: The $\ell = 1$ curve smoothly approaches $\Lambda = 0$ (staying above the power law), indicating antiferromagnetic correlations. By contrast, the $\ell = 3$ curve displays a downward cusp, similar to Fig. 2, and thus predicts an ordered state

Consistent with prior work using one-loop fRG [21], both codes find a paramagnetic ground state for $\ell = 1$, indicated by a smooth and regular flow down to $\Lambda = 0$ in Fig. 7.

Remarkably, the $\ell = 3$ data predicts a qualitatively different phase: There is a divergence in the spin correlations at $\Lambda_T/J \approx 0.24$, indicating an ordering transition at a scale roughly three times lower than for the ferromagnetic ordering instability discussed in the previous section. Such a reduced ordering scale is not unexpected for an exchange-frustrated spin system when compared to an unfrustrated one, but sometimes hard to establish.

Probing the structure factor in the vicinity of the divergence reveals a strong enhancement of magnetic correlations compared to the $\ell = 1$ flow, as indicated by sharpened Bragg peaks around the $\boldsymbol{M} = (0, \pi, \pi)$ points in Figs. 1 and 9. These correspond to antiferromagnetic correlations between planes orthogonal to the vector connecting the second nearest-neighbors along diagonals of the faces in the cubic unit cell (shown in purple in Fig. 2). Our result is consistent with earlier observations of long-range $(0, \pi, \pi)$ order neighboring the paramagnetic phase [21]. Yet, the mfRG flows obtained from both codes suggest a rather strong modification of the respective phase boundaries as the coupling parameters investigated here were previously predicted to be deep in the non-magnetic regime.

In the vertex (see Fig. 8) and self-energy, there is again very good quantitative agreement between both codes. At $\Lambda/J = 0.05$, small quantitative differences between code #1 and #2 appear in the density component γ_t^d of the t-reducible vertex, consistent with the earlier remark that it is the most difficult component to resolve well.

The $\ell = 1$ and $\ell = 3$ flows are very similar down to $\Lambda/J \geq 1$. Contributions of $\ell > 1$ terms become significant at $\Lambda/J \approx 1$ and eventually lead to an ordering instability induced by a peak in the γ_t^s component that diverges at $\Lambda/J \approx 0.24$. In contrast to the ferromagnetic case, this peak is negative, indicating anticorrelation. Along the fermionic ν frequency axis, the vertex shows an extended structure with multiple peaks of similar magnitude to the one on the bosonic axis. Since the K_1 class has no fermionic frequency, this means that, remarkably, other classes reach an order of magnitude comparable to K_1, as shown explicitly in Fig. 10. Consequently, vertex structures along fermionic frequency axes, in contrast to the ferromagnetic transition, become sizeable. It is therefore crucial to resolve the full three-dimensional frequency structure in K_3. Though numerically expensive, a large number of mesh points is necessary to ensure sufficient accuracy, as inadequate resolution of features along the fermionic frequency axes can strongly affect the fRG flow. This is even more important for multiloop flows, where interpolation errors might accumulate during the iteration over loop orders.

4 Technical aspects

To conclude our benchmark calculations, we discuss some of the particularly relevant technical aspects (see Table 1) which are needed to obtain confidence that we have sufficient degree of control over numerical errors. In doing so, we will also connect to the existing literature and scrutinize some of the algorithmic approaches which are routinely employed in the pffRG community.

4.1 Frequency grids

Both the self-energy and two-particle vertices are functions of Matsubara frequencies, which are continuous in the zero-temperature limit. A numerical implementation has to sample these functions on a finite grid and interpolate their values in between the sampling points. In many previous works (see e.g. Refs. [4,19,46]), the *same* frequency grid was chosen for the self-energy and all reducible vertices, usually featuring logarithmically increasing distances between adjacent grid points starting from some small but finite frequency. The intention behind such a choice of frequencies was to resolve the structure around zero frequency with high accuracy while coarse-graining high-frequency tails. Moreover, each vertex component was parametrized in terms of the three bosonic transfer frequencies, instead of the channel-specific mixed bosonic-fermionic frequency treatment utilized by codes #1 and #2.

Although most of the structure of the two-particle vertex is indeed centered around zero frequency, its precise extent strongly depends on the cutoff scale Λ (see, e.g., Figs. 4 and 8) and a *static* frequency grid will therefore fail to faithfully resolve the evolution of frequency structures under the fRG flow. Furthermore, multipeak

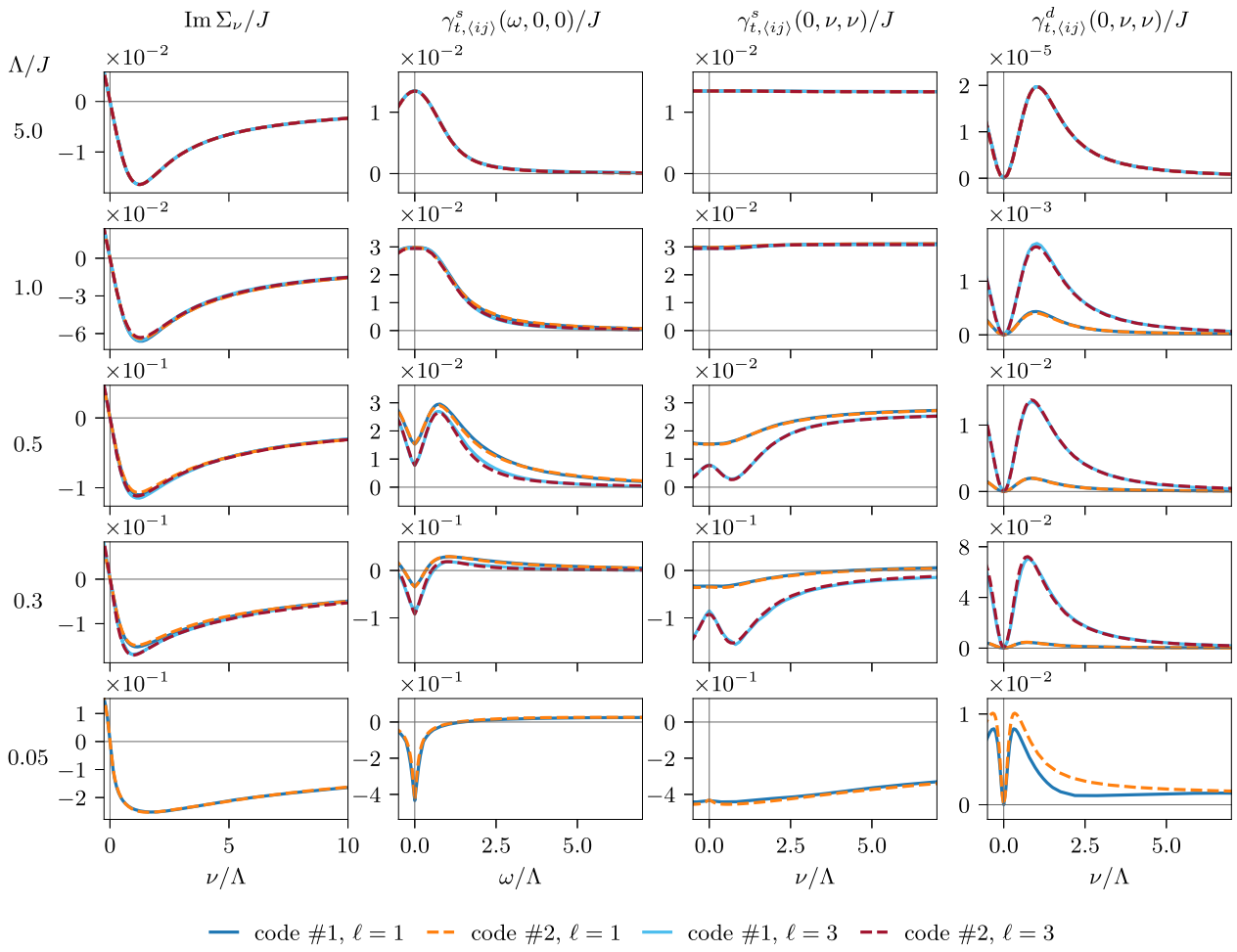

Fig. 8 Frequency structure of self-energy and t-reducible vertex for the putative paramagnet at different values of Λ/J for $\ell = 1$ and 3 flows. As the $\ell = 3$ flow diverges at $\Lambda/J \approx 0.24$, only $\ell = 1$ is shown at $\Lambda/J = 0.05$. The same cuts through the three-dimensional frequency structure of the vertices are shown as in Fig. 4. Again, a peak in the $\gamma^s_{t,\langle ij\rangle}$ component (second column) indicates strong correlations that become stronger as Λ is further decreased. In contrast to the ferromagnetic case, this peak is negative, indicative of antiferromagnetic correlations, and there is a sizeable contribution of γ^s_t for nonzero fermionic frequencies ν, ν' (third column), particularly for $\ell = 3$

structures that are present in several vertex components will in general not be captured by logarithmic sampling.

To address both shortcomings, codes #1 and #2 introduce hybrid frequency meshes using linear spacing around zero frequency augmented by an algebraic (code #1) or logarithmic (code #2) part to capture the high-frequency behavior in the asymptotic classes K_n or Q_n. The parameters of these meshes are then independently rescaled for different vertex components making use of sophisticated scanning routines (see [1,2] for further details).

4.2 Evaluation of bubble integrals

Having fixed the frequency discretization, the evaluation of frequency integrals in loop and bubble functions necessitates the use of a quadrature rule. In earlier implementations, a trapezoidal quadrature was used, with integration points coinciding with the frequency mesh of the vertex. As discussed above, this procedure yields good resolution around the origin of the integration variable. For 1ℓ calculations, the bubble function consists of a single-scale and a full propagator, the former being more strongly peaked than the latter. As the integration variable was usually shifted such that the origin coincided with the more important pole of the single-scale propagator, at least the dominant contribution was accounted for in previous implementations.

In higher loops, however, both propagators enter the bubble on equal footing, necessitating *adaptive* routines to deal with the enriched frequency structure. This is illustrated in Fig. 11, where we compare the results of integrating the bare susceptibility

$$\chi_0^\Lambda(\omega) = \frac{1}{4\pi}\int d\nu\, G_0^\Lambda(\nu+\tfrac{\omega}{2})\, G_0^\Lambda(\nu-\tfrac{\omega}{2})\,,$$

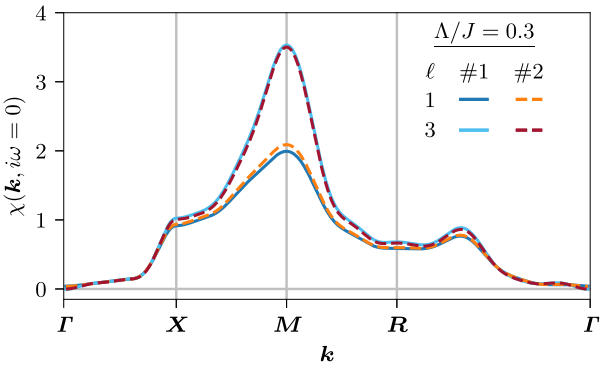

Fig. 9 Structure factor for the paramagnetic setup along a high-symmetry path of the cubic lattice Brillouin zone. The results are in good agreement between both codes, both for $\ell = 1$ and $\ell = 3$, showing that correlations are strongest around the $\boldsymbol{M}$ point. Here, the peak sharpens with increasing loop order, and the $\ell = 3$ flow predicts enhanced long-range correlations

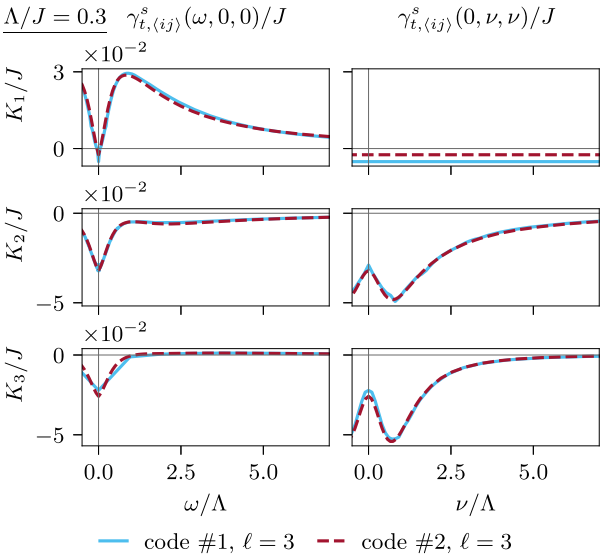

Fig. 10 Decomposition of the $\gamma^s_{t,\langle ij\rangle}(\omega, \nu, \nu')$ vertex in the paramagnetic setup as in Fig. 5, for the $\ell = 3$ flows at $\Lambda/J = 0.3$. Here, all asymptotic classes are of the same order of magnitude, and structures with multiple peaks are present along the fermionic frequency cut (second column)

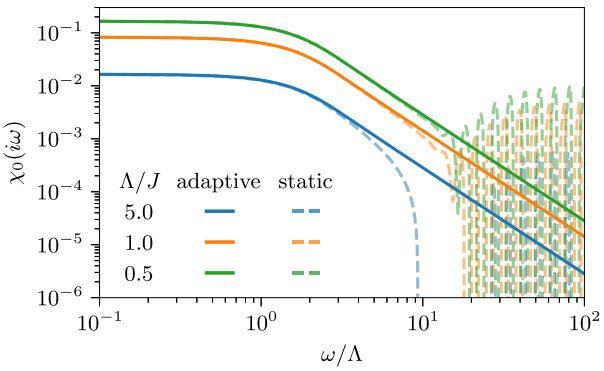

Fig. 11 Evaluation of bubble integrals. Comparison of the bare susceptibility $\chi_0^\Lambda(\omega) = \frac{1}{4\pi}\int d\nu\, G_0^\Lambda(\nu + \frac{\omega}{2})\, G_0^\Lambda(\nu - \frac{\omega}{2})$ obtained numerically via adaptive and static quadrature. The adaptive method utilizes the Simpson rule, while the static method applies a trapezoidal rule to a fixed logarithmic frequency discretization (see main text for more details). For frequencies larger than the scale set by the cutoff Λ, the non-adaptive integration becomes unstable and is plagued by rapid oscillations. By contrast, the adaptive routine yields stable results even beyond the small frequency regime and is therefore crucial to obtain accurate results for the vertex functions and their asymptotic behavior

i.e., the simplest bubble-like integral encountered during the fRG flow. Using trapezoidal quadrature over a fixed set of 60 logarithmically distributed integration points between $\nu_{\min} = 10^{-3}J$ and $\nu_{\max} = 250J$, we find strong deviations for frequencies $\omega/\Lambda \gtrsim 1 \sim 10$ compared to the results produced with the adaptive routine of code #2 (see Ref. [2] for further details). Moreover, at small cutoffs $\Lambda/J \lesssim 1$, the non-adaptive result is plagued by rapid oscillations, rendering it numerically unstable and thus inapplicable. Analytically, an asymptotic falloff with a power law ω^{-2} is expected, and this is reproduced perfectly by the adaptive integrator.

We emphasize that the test case considered here merely constitutes the simplest version of a bubble-like integral computed within the pffRG flow. In general, the propagators in bubble functions are dressed with self-energy insertions and additionally contracted with two-frequency dependent vertices. One should, therefore, expect even larger numerical errors for full fRG calculations that utilize non-adaptive quadrature.

Table 1 Technical summary of the algorithmic choices in code #1 and #2

	Code #1	Code #2
Vertex decomposition	K_1, K_2, K_3	Q_1, Q_2, Q_3
Frequency mesh	Adaptive linear and algebraic	Adaptive linear and logarithmic
Integration rule	Adaptive 21-point Gauss–Kronrod rule	Adaptive Simpson rule + Richardson extrapolation
ODE solver	5th order Cash–Carp	3rd order Bogacki–Shampine

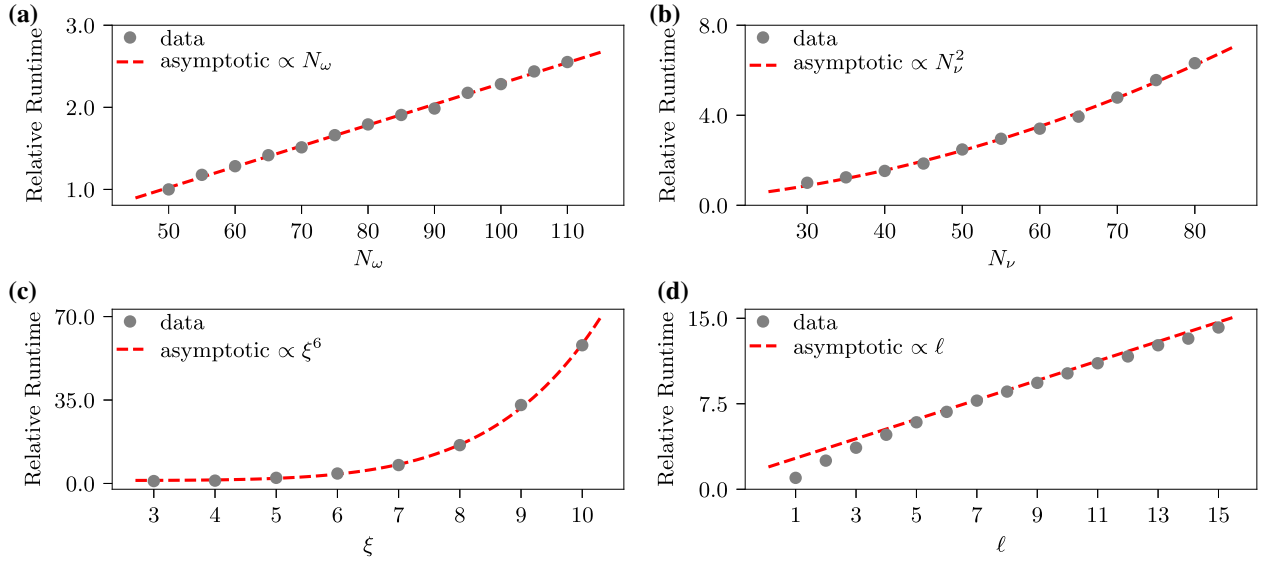

Fig. 12 Scaling of relative runtime with numerical parameters. Median computational runtime of 60 samples of a single calculation of the right-hand side of the flow equation for $\Lambda/J = 1$ relative to the runtime of the fastest computation in each series. Calculations start from a parquet solution to make the code integrate over non-trivial frequency structures. The numerical parameters for all plots are fixed to $N_\omega = 50$, $N_\nu = 30$, $\xi = 4$ and $\ell = 1$, if not varied. The asymptotic behavior expected analytically is achieved in all cases (dashed red lines)

4.3 Flow integration

The integration of the RG flow can, in principle, be performed using any standard solver for ordinary differential equations. While earlier works used an Euler scheme with decreasing step-sizes (see, e.g., Ref. [46]), we employ higher order solvers in the Runge–Kutta family with adaptive step-size control to achieve maximum accuracy while being numerically efficient to operate. It is of particular importance to implement an error-controlling method near ordering instabilities such as the ferromagnetic setup in Sect. 3, as otherwise numerical errors may become unacceptably large even at scales $\Lambda \approx J$.

4.4 Initial condition

The final ingredient to set up the pffRG flow is an appropriate initial condition. In the UV limit $\Lambda \to \infty$, the pseudofermion vertex is given by the bare spin coupling, which, in numerical calculations, is naturally implemented using J as the initial condition at a large but finite value of Λ. The mfRG flow will, by construction, reproduce a solution to the parquet equations [33–35], given an initial condition consistent with them. Therefore, we solve the regularized parquet equations iteratively for an initial scale $\Lambda/J = 5$ and use the resulting self-energy and reducible vertices as a dynamic, i.e., frequency-dependent starting point for the fRG flow [1].

4.5 Scaling analysis

Most of the runtime needed to evaluate the right-hand side of the flow equations is spent calculating the derivative of the high-dimensional two-particle vertex as given in Eq. (6). In comparison, the computation time spent for the self-energy derivative of Eq. (5) is negligible. Consequently, the (asymptotic) computational complexity is given by

$$\mathcal{O}\left(N_\xi^2 \times N_\omega N_\nu^2 \times \ell\right) ,$$

where N_ξ is the number of (symmetry reduced [1,2]) lattice sites, N_ω (N_ν) the number of bosonic (fermionic) frequencies, and ℓ denotes the number of loops. The total number of sites, in turn, is expected to follow a $\mathcal{O}(\xi^d)$ dependence, where ξ is the maximal correlation length considered and d is the spatial dimensionality of the underlying lattice, with $d = 3$ for the simple cubic lattice at hand.

To demonstrate that we indeed reach this asymptotic algorithmic scaling also in numerical implementations we show, in Fig. 12, the median runtime data for 60 evaluations of the right-hand side of the fRG equations obtained using code #2. For the number of bosonic and fermionic frequencies, the expected linear and quadratic behavior, respectively, is achieved over the whole parameter range. Note that, due to the adaptive integration and parallelization used, slight deviations from the theoretical scaling are to be expected. Similarly, the scaling in the maximal correlation length ξ is achieved for the whole parameter range. In the number of loops, the linear scaling sets in at $\ell = 5$, while for smaller ℓ a steeper slope is found. We attribute this behavior to the contributions of higher loops becoming successively smaller, leading to faster converging adaptive loop integrals for given absolute and relative tolerances. That way, the initial overhead of computing two

Table 2 Number of (symmetry reduced) vertex flow equations for Heisenberg models on the cubic lattice as a function of the maximum correlation length ξ. The number of positive frequencies is fixed to 60 (50) for the bosonic (fermionic) Matsubara axis

Max. correlation length ξ	No. flow equations
3	9 183 600
5	24 795 720
7	53 264 880
9	101 019 600
11	167 141 520
13	258 059 160

(three) loop corrections, which require twice (thrice) the number of integrals to be evaluated compared to $\ell = 1$, diminishes with increasing loop number and the analytically expected scaling, linear in ℓ, is recovered.

As a final remark, we mention that the number of vertex flow equations, another measure of algorithmic complexity, grows rapidly as one increases the maximal correlation length considered for a given lattice model. This is summarized in Table 2.

5 Conclusions

We benchmarked two state-of-the-art codes for solving pseudofermion functional renormalization group equations. Our analysis considered both physical observables, i.e. spin-spin correlation functions and structure factors, as well as fermionic vertex functions (self-energy and two-particle vertex) for ferro- and antiferromagnetic models on the simple cubic lattice.

For the nearest-neighbor ferromagnet, both codes were in quantitative agreement at least until $\Lambda/J \gtrsim 0.76$, where they consistently predicted a breakdown of the RG flow, indicated by a sharp peak (for $\ell = 1$) or a divergence (for $\ell = 3$) in the spin-spin correlations. The energy scale Λ_T associated with this numerical instability slightly differed, which necessitated an in-depth comparison of the influence of the numerical frequency grid on the obtained results. We found that both fRG solvers, due to the emergence of a singular peak in the t reducible vertex functions, become sensitive to the precise mesh spacing and thus predict marginally different critical scales, although the physical conclusion drawn from the RG flow, i.e. the onset of long-range ferromagnetic order, remains the same.

For the antiferromagnetic setup, the $\ell = 1$ results obtained by both codes were in agreement with one another and previous studies [21], predicting a paramagnetic state, signified by a regular RG flow down to the infrared. For $\ell = 3$, similar numerical agreement between the two codes was found. However, the physical results changed qualitatively: the flow of the spin-spin correlator diverged around $\Lambda/J \approx 0.24$, accompanied by sharp Bragg peaks at the $\boldsymbol{M}$ points indicating the formation of antiferromagnetic order at low temperatures. This reinstantiates the importance of including higher loop corrections in pffRG to avoid overestimating the extent of paramagnetic phases and to obtain more accurate predictions of ground states in frustrated quantum magnets.

We also elaborated on the importance of employing adaptive numerical algorithms to obtain robust results at all stages of the flow. More explicitly, there are extended structures with multiple peaks in the three-dimensional frequency dependence of several vertex components. As these structures are sizable, it is crucial to resolve them in an accurate manner. We found fixed logarithmic frequencies to be insufficient for structures not centered at zero frequency, and rely instead on adaptive frequency meshes that have been specifically optimized for pffRG vertices. Furthermore, we demonstrated that the commonly employed quadrature of a trapezoidal rule over a static, logarithmic mesh fails to produce the analytically expected behavior of bare bubble integrations at large frequencies. It is thus unsuitable for providing the essential Matsubara integrals for error-controlled fRG flows. By contrast, the implementations presented and benchmarked here solve these problems using highly accurate, yet efficient adaptive routines (see Table 1). We thus believe that, moving forward, they will be widely used for unbiased calculations of (multiloop) ground-state phase diagrams of frustrated magnets from pffRG.

Acknowledgements We thank L. Gresista, Y. Iqbal, M. Punk, and J. Reuther for useful and stimulating discussions and J. Thoenniss for his pioneering contribution to setting up the Munich multiloop pffRG code. The Cologne group gratefully acknowledges partial support from the Deutsche Forschungsgemeinschaft (DFG)—Projektnummer 277146847—SFB 1238 (project C02), the Munich group from DFG under Germany's Excellence Strategy EXC-2111 (Project No. 390814868), the Würzburg group from DFG through Project-ID 258499086-SFB 1170 and the Würzburg-Dresden Cluster of Excellence on Complexity and Topology in Quantum Matter—ct.qmat Project-ID 390858490-EXC 2147, and F.B.K. from the Alexander von Humboldt Foundation through a Feodor Lynen Fellowship. The numerical simulations were performed on the JURECA Booster and JUWELS cluster at the Forschungszentrum Juelich, the SuperMUC cluster and Linux clusters at the Leibniz Supercomputing Centre, as well as the CHEOPS cluster at RRZK Cologne. This research is also part of the Munich Quantum Valley, which is supported by the Bavarian State Government with funds from the Hightech Agenda Bayern Plus.

Funding Open Access funding enabled and organized by Projekt DEAL.

Data Availability Statement This manuscript has no associated data or the data will not be deposited. [Author's comment: The numerical data generated and analysed in this paper is available from the corresponding author on reasonable request. Furthermore, Code #2 is available as an open-source package [39].]

References

1. J. Thoenniss, M.K. Ritter, F.B. Kugler, J. von Delft, M. Punk. arXiv:2011.01268
2. D. Kiese, T. Müller, Y. Iqbal, R. Thomale, S. Trebst. arXiv:2011.01269
3. C. Lacroix, P. Mendels, F. Mila, *Introduction to Frustrated Magnetism*. Springer Series in Solid-State Sciences (Springer Berlin Heidelberg, 2011). https://doi.org/10.1007/978-3-642-10589-0
4. J. Reuther, P. Wölfle, Phys. Rev. B **81**, 144410 (2010). https://doi.org/10.1103/PhysRevB.81.144410
5. J. Reuther, R. Thomale, Phys. Rev. B **83**, 024402 (2011). https://doi.org/10.1103/PhysRevB.83.024402
6. J. Reuther, P. Wölfle, R. Darradi, W. Brenig, M. Arlego, J. Richter, Phys. Rev. B **83**, 064416 (2011). https://doi.org/10.1103/PhysRevB.83.064416
7. J. Reuther, D.A. Abanin, R. Thomale, Phys. Rev. B **84**, 014417 (2011). https://doi.org/10.1103/PhysRevB.84.014417
8. J. Reuther, R. Thomale, S. Trebst, Phys. Rev. B **84**, 100406 (2011). https://doi.org/10.1103/PhysRevB.84.100406
9. J. Reuther, R. Thomale, S. Rachel, Phys. Rev. B **86**, 155127 (2012). https://doi.org/10.1103/PhysRevB.86.155127
10. J. Reuther, R. Thomale, Phys. Rev. B **89**, 024412 (2014). https://doi.org/10.1103/PhysRevB.89.024412
11. R. Suttner, C. Platt, J. Reuther, R. Thomale, Phys. Rev. B **89**, 020408 (2014). https://doi.org/10.1103/PhysRevB.89.020408
12. J. Reuther, R. Thomale, S. Rachel, Phys. Rev. B **90**, 100405 (2014). https://doi.org/10.1103/PhysRevB.90.100405
13. Y. Iqbal, H.O. Jeschke, J. Reuther, R. Valentí, I.I. Mazin, M. Greiter, R. Thomale, Phys. Rev. B **92**, 220404 (2015). https://doi.org/10.1103/PhysRevB.92.220404
14. Y. Iqbal, W.J. Hu, R. Thomale, D. Poilblanc, F. Becca, Phys. Rev. B **93**, 144411 (2016). https://doi.org/10.1103/PhysRevB.93.144411
15. Y. Iqbal, P. Ghosh, R. Narayanan, B. Kumar, J. Reuther, R. Thomale, Phys. Rev. B **94**, 224403 (2016). https://doi.org/10.1103/PhysRevB.94.224403
16. F.L. Buessen, S. Trebst, Phys. Rev. B **94**, 235138 (2016). https://doi.org/10.1103/PhysRevB.94.235138
17. A. Keleş, E. Zhao, Phys. Rev. Lett. **120**, 187202 (2018). https://doi.org/10.1103/PhysRevLett.120.187202
18. A. Keleş, E. Zhao, Phys. Rev. B **97**, 245105 (2018). https://doi.org/10.1103/PhysRevB.97.245105
19. D. Kiese, F.L. Buessen, C. Hickey, S. Trebst, M.M. Scherer, Phys. Rev. Res. **2**, 013370 (2020). https://doi.org/10.1103/PhysRevResearch.2.013370
20. N. Astrakhantsev, F. Ferrari, N. Niggemann, T. Müller, A. Chauhan, A. Kshetrimayum, P. Ghosh, N. Regnault, R. Thomale, J. Reuther, T. Neupert, Y. Iqbal, Phys. Rev. B **104**, L220408 (2021). https://doi.org/10.1103/PhysRevB.104.L220408
21. Y. Iqbal, R. Thomale, F. Parisen Toldin, S. Rachel, J. Reuther, Phys. Rev. B **94**, 140408 (2016). https://doi.org/10.1103/PhysRevB.94.140408
22. Y. Iqbal, T. Müller, K. Riedl, J. Reuther, S. Rachel, R. Valentí, M.J.P. Gingras, R. Thomale, H.O. Jeschke, Phys. Rev. Mater. **1**, 071201 (2017). https://doi.org/10.1103/PhysRevMaterials.1.071201
23. F.L. Buessen, M. Hering, J. Reuther, S. Trebst, Phys. Rev. Lett. **120**, 057201 (2018). https://doi.org/10.1103/PhysRevLett.120.057201
24. Y. Iqbal, T. Müller, H.O. Jeschke, R. Thomale, J. Reuther, Phys. Rev. B **98**, 064427 (2018). https://doi.org/10.1103/PhysRevB.98.064427
25. Y. Iqbal, T. Müller, P. Ghosh, M.J.P. Gingras, H.O. Jeschke, S. Rachel, J. Reuther, R. Thomale, Phys. Rev. X **9**, 011005 (2019). https://doi.org/10.1103/PhysRevX.9.011005
26. P. Ghosh, T. Müller, F.P. Toldin, J. Richter, R. Narayanan, R. Thomale, J. Reuther, Y. Iqbal, Phys. Rev. B **100**, 014420 (2019). https://doi.org/10.1103/PhysRevB.100.014420
27. A. Revelli, C.C. Loo, D. Kiese, P. Becker, T. Fröhlich, T. Lorenz, M. Moretti Sala, G. Monaco, F.L. Buessen, J. Attig, M. Hermanns, S.V. Streltsov, D.I. Khomskii, J. van den Brink, M. Braden, P.H.M. van Loosdrecht, S. Trebst, A. Paramekanti, M. Grüninger, Phys. Rev. B **100**, 085139 (2019). https://doi.org/10.1103/PhysRevB.100.085139
28. P. Ghosh, Y. Iqbal, T. Müller, R.T. Ponnaganti, R. Thomale, R. Narayanan, J. Reuther, M.J.P. Gingras, H.O. Jeschke, NPJ Quant. Mater. **4**(1), 63 (2019). https://doi.org/10.1038/s41535-019-0202-z
29. S. Chillal, Y. Iqbal, H.O. Jeschke, J.A. Rodriguez-Rivera, R. Bewley, P. Manuel, D. Khalyavin, P. Steffens, R. Thomale, A.T.M.N. Islam, J. Reuther, B. Lake, Nat. Commun. **11**(1), 2348 (2020). https://doi.org/10.1038/s41467-020-15594-1
30. M.L. Baez, J. Reuther, Phys. Rev. B **96**, 045144 (2017). https://doi.org/10.1103/PhysRevB.96.045144
31. F.L. Buessen, D. Roscher, S. Diehl, S. Trebst, Phys. Rev. B **97**, 064415 (2018). https://doi.org/10.1103/PhysRevB.97.064415
32. A.A. Katanin, Phys. Rev. B **70**, 115109 (2004). https://doi.org/10.1103/PhysRevB.70.115109
33. F.B. Kugler, J. von Delft, Phys. Rev. B **97**, 035162 (2018). https://doi.org/10.1103/PhysRevB.97.035162
34. F.B. Kugler, J. von Delft, Phys. Rev. Lett. **120**, 057403 (2018). https://doi.org/10.1103/PhysRevLett.120.057403
35. F.B. Kugler, J. von Delft, New J. Phys. **20**(12), 123029 (2018). https://doi.org/10.1088/1367-2630/aaf65f

36. A. Tagliavini, C. Hille, F.B. Kugler, S. Andergassen, A. Toschi, C. Honerkamp, SciPost Phys. **6**, 9 (2019). https://doi.org/10.21468/SciPostPhys.6.1.009
37. C. Hille, F.B. Kugler, C.J. Eckhardt, Y.Y. He, A. Kauch, C. Honerkamp, A. Toschi, S. Andergassen, Phys. Rev. Res. **2**, 033372 (2020). https://doi.org/10.1103/PhysRevResearch.2.033372
38. P. Chalupa-Gantner, F.B. Kugler, C. Hille, J. von Delft, S. Andergassen, A. Toschi, Phys. Rev. Research **4**, 023050 (2022). https://doi.org/10.1103/PhysRevResearch.4.023050
39. `PFFRGSolver.jl` repository. https://github.com/dominikkiese/PFFRGSolver.jl
40. N. Niggemann, B. Sbierski, J. Reuther, Phys. Rev. B **103**(10) (2021). https://doi.org/10.1103/PhysRevB.103.104431
41. N. Niggemann, J. Reuther, B. Sbierski, SciPost Phys. **12**, 156 (2022). https://doi.org/10.21468/SciPostPhys.12.5.156
42. B. Roulet, J. Gavoret, P. Nozières, Phys. Rev. **178**, 1072 (1969). https://doi.org/10.1103/PhysRev.178.1072
43. N. Wentzell, G. Li, A. Tagliavini, C. Taranto, G. Rohringer, K. Held, A. Toschi, S. Andergassen, Phys. Rev. B **102**, 085106 (2020). https://doi.org/10.1103/PhysRevB.102.085106
44. G. Li, N. Wentzell, P. Pudleiner, P. Thunström, K. Held, Phys. Rev. B **93**, 165103 (2016). https://doi.org/10.1103/PhysRevB.93.165103
45. F.L. Buessen, V. Noculak, S. Trebst, J. Reuther, Phys. Rev. B **100**, 125164 (2019). https://doi.org/10.1103/PhysRevB.100.125164
46. F.L. Buessen, A functional renormalization group perspective on quantum spin liquids in three-dimensional frustrated magnets. Ph.D. thesis, University of Cologne (2019). https://kups.ub.uni-koeln.de/9986/

Eur. Phys. J. B (2022)95:119
https://doi.org/10.1140/epjb/s10051-022-00373-2

THE EUROPEAN PHYSICAL JOURNAL B

Regular Article - Computational Methods

Moments and multiplets in moiré materials

A pseudo-fermion functional renormalization group for spin–valley models

Lasse Gresista[a], Dominik Kiese, and Simon Trebst

Institute for Theoretical Physics, University of Cologne, 50937 Cologne, Germany

Received 1 March 2022 / Accepted 22 June 2022

Abstract. The observation of strongly correlated states in moiré systems has renewed the conceptual interest in magnetic systems with higher SU(4) spin symmetry, e.g., to describe Mott insulators where the local moments are coupled spin–valley degrees of freedom. Here, we discuss a numerical renormalization group scheme to explore the formation of spin–valley ordered and unconventional spin–valley liquid states at zero temperature based on a pseudo-fermion representation. Our generalization of the conventional pseudo-fermion functional renormalization group approach for $\mathfrak{su}(2)$ spins is capable of treating diagonal and off-diagonal couplings of generic spin–valley exchange Hamiltonians in the self-conjugate representation of the $\mathfrak{su}(4)$ algebra. To achieve proper numerical efficiency, we derive a number of symmetry constraints on the flow equations that significantly limit the number of ordinary differential equations to be solved. As an example system, we investigate a diagonal $\mathrm{SU}(2)_{\mathrm{spin}} \otimes \mathrm{U}(1)_{\mathrm{valley}}$ model on the triangular lattice which exhibits a rich phase diagram of spin and valley ordered phases.

1 Introduction

Moiré materials that exhibit flat bands such as twisted bilayer graphene (tBG) or certain van der Waals heterostructures such as trilayer graphene on hexagonal boron nitride (TLG/h-BN) have recently been established as novel, highly tunable platforms for the study of strongly correlated electrons. Relative to an almost vanishing bandwidth, residual interactions in these materials can induce a plethora of different many-body phenomena ranging from the formation of correlated insulators [1–4] and superconductors [5–7] to anomalous quantum Hall effects [8]. However, a microsopic description of these phenomena is a formidable challenge as the number of of low-energy degrees of freedom is often increased [9–11] in comparison to conventional Mott insulators.

More specifically, it has been argued [12,13] that multi-orbital Hubbard models can describe the flat band physics in, e.g., TLG/h-BN within the topologically trivial regime, where fully symmetric Wannier states may be constructed [14]. The proposed interaction terms for the corresponding Hamiltonians usually include a generalized Hubbard U [12,13,15] as well as Hund's type couplings. Performing a strong coupling expansion where one treats the interactions as the dominant energy scale, these extended Hubbard models can then be mapped to $\mathfrak{su}(4)$[1] spin–valley Hamiltonians that may be used as a starting point to investigate the nature of the correlated insulating states. The so-derived $\mathfrak{su}(4)$ models bear a close resemblance to Kugel–Khomskii models [16] that have a long history in the study of transition metal oxides, where they are used to capture the Jahn–Teller physics of intertwined spin and orbital degrees of freedom. Increasing the number of relevant microscopic degrees of freedom (in comparison to conventional quantum magnets) has been particularly appreciated to boost quantum fluctuations independent of, e.g., lattice geometries [17], which has made Kugel–Khomskii models a recurring target in the search for unusual many-body states such as quantum spin–orbital liquids [18–21]. As such, one might expect the $\mathfrak{su}(4)$ spin–valley physics relevant to the correlated insulating states of moiré materials to hold similar promise for the observation of spin–valley liquid states with macroscopic entanglement and potentially long-range, topological order.

In this manuscript, we present a powerful numerical scheme to analyze such $\mathfrak{su}(4)$ spin–valley (or spin–orbital) models based on a functional renormalization group (FRG) technique. Our approach is based on the pseudo-fermion FRG (pf-FRG) [22], approximating the elementary spin operators of the six-dimensional, self-conjugate representation of $\mathfrak{su}(4)$ by auxiliary complex fermions combined with an on-average constraint on the number of particles per site. Our approach allows to go beyond mean-field level by treating competing instabilities in different interaction channels on equal footing, and is able to capture both, long-ranged spin

[1] With $\mathfrak{su}(4)$, we refer to the Lie algebra of the Lie group SU(4).

[a] e-mail: gresista@thp.uni-koeln.de (corresponding author)

Published online: 30 July 2022

and/or valley ordered states as well as spin–valley liquid phases. In expanding previous work (by some of us) [21], we extend the range of applicability of this approach to models with off-diagonal interactions in either spin or valley space by formulating an efficient vertex parametrization derived from a meticulous symmetry analysis. We demonstrate the feasibility of this method by studying a spin–valley Hamiltonian with $\mathrm{SU}(2)_{\mathrm{spin}} \otimes \mathrm{U}(1)_{\mathrm{valley}}$ symmetry where we identify a plethora of spin and valley orderded phases from a state-of-the-art numerical implementation of pf-FRG [23,24].

The remainder of this manuscript is structured as follows. To begin with, we introduce the spin–valley Hamiltonian of interest on a general level and discuss its specific form for TLG/h-BN as a concrete example in Sect. 2. We will continue by reviewing the pf-FRG approach (Sect. 3), its generalization for $\mathfrak{su}(4)$ models as well as the implementation of model specific symmetries (Sect. 4). Finally, numerical results for the phase diagram of a $\mathrm{SU}(2)_{\mathrm{spin}} \otimes \mathrm{U}(1)_{\mathrm{valley}}$ model on the triangular lattice are presented and examined in Sect. 5.

2 Model

Microscopically, the SU(4) models of interest in this manuscript can be cast in terms of a general Hamiltonian

$$\mathcal{H} = \frac{1}{8} \sum_{\langle ij \rangle} J(1 + \boldsymbol{\sigma}_i \boldsymbol{\sigma}_j)(1 + \boldsymbol{\tau}_i \boldsymbol{\tau}_j)\,, \tag{1}$$

which couples two elementary $\mathfrak{su}(2)$ degrees of freedom, captured by the operators σ and τ, which might denote a spin and valley (or oribtal) degree of freedom. The overall SU(4) symmetry of the Hamiltonian arises from the balanced couplings of equal strength in both degrees of freedom, i.e., J is identical for the Heisenberg-like coupling of spins $\boldsymbol{\sigma}_i \boldsymbol{\sigma}_j$ on sites i and j (with $\boldsymbol{\sigma}_i = (\sigma_j^x, \sigma_j^y, \sigma_j^z)^T$) and a similar interaction of the valley degrees of freedom $\boldsymbol{\tau}_i \boldsymbol{\tau}_j$. Such valley degrees of freedom arise, in the context of tBG and related moiré materials, from the Dirac cones in the original graphene bands, which hybridize between the two layers upon twisting and thereby add an extra index [25] to the moiré bands, as illustrated in Fig. 1. Before drawing broad attention in the context of moiré materials, the spin–orbital variant of this model has been widely studied as Kugel–Khomskii model [16], often in connection with Jahn–Teller physics in transition metal oxides where spin and orbital ordering are intertwined [26]. We note that while we will frame our discussion of the SU(4) model (1) in the language of spin-valley physics relevant to moiré materials, the presented pf-FRG approach is equally applicable in the study of such spin–orbital models. We will return to this point in the discussion section at the end.

In what we will discuss in the following, we will put a focus on the self-conjugate representation of $\mathfrak{su}(4)$, where the spin–valley operators can be represented in terms of fermionic creation and annihilation operators as

$$\begin{aligned} \sigma_i^\mu \tau_i^\kappa &\equiv \sigma_i^\mu \otimes \tau_i^\kappa = f_{isl}^\dagger \theta_{ss'}^\mu \theta_{ll'}^\kappa f_{is'l'}^\dagger \\ \sigma_i^\mu &\equiv \sigma_i^\mu \otimes \tau_i^0 = f_{isl}^\dagger \theta_{ss'}^\mu f_{is'l}^\dagger \\ \tau_i^\kappa &\equiv \sigma_i^0 \otimes \tau_i^\kappa = f_{isl}^\dagger \theta_{ll'}^\kappa f_{isl'}^\dagger\,, \end{aligned} \tag{2}$$

with a local half-filling constraint

$$f_{isl}^\dagger f_{isl}^\dagger = 2 \tag{3}$$

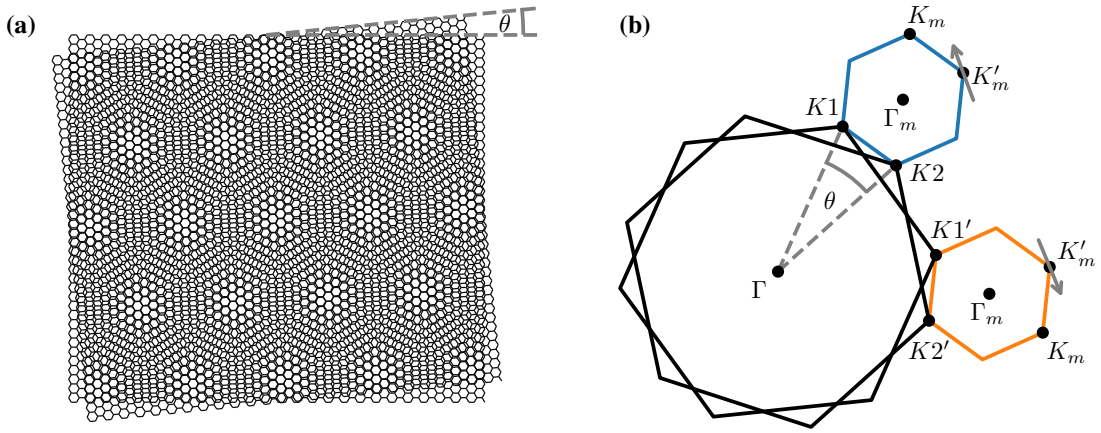

Fig. 1 **a** Moiré pattern emerging in two stacked layers of graphene with a relative twist angle θ. Clearly visible are the different regions with AA, AB, and BA stacking leading to a triangular super-lattice structure. **b** Construction of the two degenerate mini Brillouin zones from the difference of the K (or K') points of the two layers of graphene. In addition to the spin degree of freedom, indicated by the grey arrows, the electrons obtain a valley degree of freedom due to the possibility of being in either one of the mini Brillouin zones at the two valleys (at the K and K' points) of the graphene band structure

subject to every lattice site, where summation over repeated spin indices s and valley indices l is implied. Here, θ^μ denotes a Pauli matrix with $\mu \in \{0,1,2,3\}$ and $\theta^0 = \mathbb{1}$. Allowing also for more generic, i.e., SU(4) breaking, interactions, any bilinear spin–valley Hamiltonian can be written as

$$\begin{aligned}\mathcal{H} &= \frac{1}{8}\sum_{ij}\left[(\sigma_i^\mu J_{s,ij}^{\mu\nu}\sigma_j^\nu)(\tau_i^\kappa J_{v,ij}^{\kappa\lambda}\tau_j^\lambda) + I_{ij}\hat{n}_i\hat{n}_j\right] \\ &\equiv \frac{1}{8}\sum_{ij}\left[(\sigma_i^\mu \otimes \tau_i^\kappa)\left(J_{s,ij}^{\mu\nu}\otimes J_{v,ij}^{\kappa\lambda}\right)(\sigma_j^\nu\otimes\tau_j^\lambda)\right. \\ &\quad \left. + I_{ij}\hat{n}_i\hat{n}_j\right], \end{aligned} \tag{4}$$

where $J_{s,ij}^{\mu\nu}\otimes J_{v,ij}^{\kappa\lambda}$ is understood as the Kronecker product of the spin and valley exchange matrices and summation over repeating μ,ν,κ or λ is again implied. Here, $\hat{n}_i$ is the density operator $\hat{n}_i \equiv \sigma_i^0\tau_i^0 = f_{isl}^\dagger f_{isl}^\dagger$, and the term proportional to the coupling I_{ij} is needed to potentially cancel the density term $\sim \sigma_i^0\tau_i^0 J_{s,ij}^{00}J_{v,ij}^{00}\sigma_j^0\tau_j^0$, which does not appear in pure $\mathfrak{su}(4)$ spin models as, e.g., the SU(4) symmetric Hamiltonian in Eq. (1).

To keep the numerical effort for employing our pf-FRG approach at a manageable level, we assume a specific form of the exchange matrices, namely, that both, the spin and the valley exchange only couple bilinears of spin/valley or density operators and that the spin exchange is $\mathbb{Z}_2\times\mathbb{Z}_2\times\mathbb{Z}_2$ symmetric, and thus

$$\begin{aligned} J_{s,ij} &= \begin{pmatrix} J_{s,ij}^d & 0 & 0 & 0\\ 0 & J_{s,ij}^x & 0 & 0\\ 0 & 0 & J_{s,ij}^y & 0\\ 0 & 0 & 0 & J_{s,ij}^z \end{pmatrix} \\ J_{v,ij} &= \begin{pmatrix} J_{v,ij}^d & 0 & 0 & 0\\ 0 & J_{v,ij}^{xx} & J_{v,ij}^{xy} & J_{v,ij}^{xz}\\ 0 & J_{v,ij}^{yx} & J_{v,ij}^{yy} & J_{v,ij}^{yz}\\ 0 & J_{v,ij}^{zx} & J_{v,ij}^{zy} & J_{v,ij}^{zz} \end{pmatrix}. \end{aligned} \tag{5}$$

This form, although it spoils the generality of Eq. (4) it is nevertheless relevant to certain practical applications. For instance, the effective Hamiltonian for TLG/h-BN [11] can be recast to this form. Originally, the former is often given as

$$\begin{aligned}\mathcal{H} = &\frac{J_1}{8}\sum_{\langle ij\rangle}(1+\boldsymbol{\sigma}_i\boldsymbol{\sigma}_j)(1+\boldsymbol{\tau}_i\boldsymbol{\tau}_j) \\ &+\frac{J_2}{8}\sum_{\langle\langle ij\rangle\rangle}(1+\boldsymbol{\sigma}_i\boldsymbol{\sigma}_j)(1+\boldsymbol{\tau}_i\boldsymbol{\tau}_j) \\ &+\frac{1}{8}\sum_{\langle ij\rangle}J_{p;ij}^1(1+\boldsymbol{\sigma}_i\boldsymbol{\sigma}_j)(\tau_i^x\tau_j^x+\tau_i^y\tau_j^y) \\ &+\frac{1}{8}\sum_{\langle ij\rangle}J_{p;ij}^2(1+\boldsymbol{\sigma}_i\boldsymbol{\sigma}_j)(\tau_i^x\tau_j^y-\tau_i^y\tau_j^x)+O\left(\frac{t^3}{U^2}\right), \end{aligned} \tag{6}$$

which, in addition to SU(4) symmetric nearest-neighbour ($\sim J_1$) and next-nearest-neighbour ($\sim J_2$) interactions, contains both diagonal $\sim J_{p,ij}^1$ and off-diagonal $\sim J_{p,ij}^2$ valley exchange that breaks the SU(4) symmetry down to an $\mathrm{SU}(2)_{\mathrm{spin}}\otimes\mathrm{U}(1)_{\mathrm{valley}}$ symmetry. Comparing this model to the form of the general spin–valley Hamiltonian defined in Eq. (4), the nearest-neighbour exchange matrices can be written as

$$\begin{aligned} J_{s,ij} &= \mathbb{1} \\ J_{v,ij} &= \begin{pmatrix} J_1 & 0 & 0 & 0\\ 0 & J_1+J_{p;ij}^1 & J_{p;ij}^2 & 0\\ 0 & -J_{p;ij}^2 & J_1+J_{p;ij}^1 & 0\\ 0 & 0 & 0 & J_1 \end{pmatrix}, \end{aligned} \tag{7}$$

and the next-nearest-neighbour exchange is fully SU(4) symmetric, showing that they are indeed captured by the exchange matrices defined in Eq. (5).

3 pf-FRG for spin–valley models: an overview

We now proceed to the core methodological advancement of this manuscript, which will be laid out in this section—the extension of the conventional pf-FRG to spin–valley models described by Hamiltonians of the form given in Eq. (4), with general, diagonal, and off-diagonal couplings as defined by Eq. (5). To set the stage, we will first revisit the flow equations of the conventional pf-FRG approach for $\mathfrak{su}(2)$ spins and explain how the numerical solution of the flow equations can be used to determine whether and what type of magnetic order forms for a particular spin Hamiltonian at zero temperatures. We then proceed to the adapted pf-FRG approach for spin–valley models, for which we derive an efficient parametrization of the self-energy and two-particle vertex in what is a direct extension of the parametrization for $\mathfrak{su}(2)$ spin models with generic two-spin interactions [27]. Our particular focus is on constraints that symmetries of the spin–valley Hamiltonian pose on the parametrized vertex functions—very similar to the $\mathfrak{su}(2)$ case but with slight differences which we especially highlight. To put these equations into numerical practice, we discuss our implementation of the spin–valley pf-FRG approach and its algorithmic scaling. This section is intended as an overview stating the main results of our study important for the implementation of the pf-FRG for spin–valley models. Readers looking for a more detailed discussion of how the symmetries of the Hamiltonian lead to the parametrization and symmetry constraints are referred to Sect. 4.

3.1 Pseudo-fermion functional renormalization group

Let us set the stage by revisiting some of the conceptual steps of the pseudo-fermion FRG, which has orig-

inally been formulated for bilinear $\mathfrak{su}(2)$ spin models [22] with generic (diagonal and off-diagonal) interactions [27] and later generalized to SU(N) Heisenberg models [28], in the context of the spin–valley models at hand. By going to a pseudo-fermion representation of the original degrees of freedom, one arrives at a fermionic representation of the original model (with an additional half-filling constraint) as outlined in the previous section. One can then proceed to apply the well-established methods of the fermionic FRG [29,30].

An important distinction to electronic systems is that the pseudo-fermion Hamiltonian exhibits only a quartic interaction term and no quadratic kinetic terms. This readily implies that the free propagator is diagonal in all its arguments and takes the simple form

$$G_0(1',1) = G_0(\omega_1)\delta_{i_{1'}i_1}\delta_{s_{1'}s_1}\delta_{l_{1'}l_1}\delta_{\omega_{1'}\omega_1}, \tag{8}$$

with $G_0(\omega) = (i\omega)^{-1}$. The multi-index $1 = (i_1, s_1, l_1, \omega_1)$ consists of a lattice site index i_1, a spin index s_1, a fermionic Matsubara frequency ω_1 and, for spin–valley models, the additional valley index l_1. To implement the RG scale, or cut-off, Λ, we multiply a regulator to the free propagator

$$G_0^\Lambda(\omega) = G_0(\omega)(1 - e^{-\omega^2/\Lambda^2}), \tag{9}$$

where we choose a smooth regulator for improved numerical stability. The pf-FRG flow equations are then given as a special case of the general fermionic FRG equations by assuming that the flowing self-energy is, just as the free propagator, diagonal in all its arguments. This assumption is true for arbitrary spin-model bilinear in $\mathfrak{su}(2)$ spin operators [27]. For spin–valley Hamiltonians, however, we will show in Sect. 4 that this is only the case if the couplings are diagonal in either the spin or valley sector. That is why, in this work, we always consider couplings diagonal in the spin sector as stated in Eq. (5). In the context of moiré materials, most physically relevant spin–valley models are indeed of this form. This additional assumption, therefore, leaves our method still generally applicable to most models of interest.

In the original implementation of the pf-FRG [22] and most works since, then the flow equations are truncated using the Katanin truncation scheme [31], which we also adapt here[2]. In the Katanin truncation, only the self-energy Σ^Λ and the two-particle vertex Γ^Λ are considered, while higher order vertex functions are neglected.

[2] More recently, an alternative multi-loop truncation has been introduced in the context of electronic FRG calculations [32], which was subsequently also adapted in the context of pf-FRG [23,24]. Such a multi-loop approach can also be applied in the context of spin–valley pf-FRG calculations, but will be left to future exploration. Additionally, one may further improve the efficiency of the method by adapting the cluster FRG scheme [33].

The flow equations are then given by

$$\frac{d}{d\Lambda}\Sigma^\Lambda(1',1) = -\frac{1}{2\pi}\sum_2 \Gamma^\Lambda(1',2,1,2)S^\Lambda(\omega_2) \tag{10}$$

for the self-energy and

$$\begin{aligned}\frac{d}{d\Lambda}\Gamma^\Lambda(1',2',1,2) &= -\frac{1}{2\pi}\sum_{3,4}\Big[\Gamma^\Lambda(1',2',3,4)\Gamma^\Lambda(3,4,1,2)\\ &\quad -\Gamma^\Lambda(1',4,1,3)\Gamma^\Lambda(3,2',4,2) - (3\leftrightarrow 4)\\ &\quad +\Gamma^\Lambda(2',4,1,3)\Gamma^\Lambda(3,1',4,2) + (3\leftrightarrow 4)\Big]\\ &\quad \times G^\Lambda(\omega_3)\partial_\Lambda G^\Lambda(\omega_4),\end{aligned} \tag{11}$$

for the two-particle vertex. Here, the single-scale propagator is defined as $S^\Lambda \equiv -\partial_\Lambda G^\Lambda|_{\Sigma^\Lambda=\text{const.}}$. Note that the flow equations are formulated in the $T \to 0$ limit and the sums should therefore be understood as $\sum_1 \equiv \sum_{i_1 s_1 l_1}\int d\omega_1$.

The fermionic representation of the spin–valley operators, as presented in the previous section, necessitates the enforcement of a local half-filling constraint ($f^\dagger_{isl}f^\dagger_{isl} = 2$) to determine the dimensionality of the local Hilbert space. To this end, we employ the same technique used for $\mathfrak{su}(2)$ models, where the constraint is fulfilled only on average by explicitly implementing particle-hole symmetry on the level of the vertex functions [22–24], as will be discussed in detail in Sect. 4. Numerically, computing the expectation value $\langle f^\dagger_{isl}f^\dagger_{isl}\rangle$ from the self-energy and two-particle vertex, we confirm that the average constraint is indeed fulfilled during the entire pf-FRG flow. Although particle-number fluctuations violating the exact constraint have been shown to be sizeable, recent studies suggest that they leave the physical results obtained from the pf-FRG qualitatively unaffected [21,23,34]. We note that in contrast to $\mathfrak{su}(2)$ spin models, the physically relevant filling for spin–valley models depends on the considered material and may also be at quarter-filling ($f^\dagger_{isl}f^\dagger_{isl} = 1$) [11,35], corresponding to the fundamental representation of $\mathfrak{su}(4)$. At quarter-filling, however, the spin–valley Hamiltonian is no longer particle–hole symmetric and the constraint cannot be enforced in the same efficient manner. In this work, we therefore limit ourselves to half-filling.

To identify the ground state of a model of interest, we numerically solve the flow equations (as discussed in more detail below in Sect. 3.3) and thereby calculate the flow of various correlation functions from the flow of the vertex functions. In its most general we define a spin-valley-spin-valley correlation function

$$\begin{aligned}\chi_{ij}^{\mu\nu\kappa\lambda}(\omega) = \int_0^\infty d\tau e^{i\omega\tau}\,\big\langle T_\tau(\sigma_i^\mu\otimes\tau_i^\kappa)\,(\tau)\\ \times(\sigma_j^\nu\otimes\tau_j^\lambda)(0)\big\rangle\,,\end{aligned} \tag{12}$$

where T_τ is the time-ordering operator. From this general definition, we can then read off the form of spin–spin correlations

$$\chi_{ij}^{s,\mu\nu} \equiv \chi_{ij}^{\mu\nu 00} \sim \left\langle \sigma_i^\mu \sigma_j^\nu \right\rangle , \tag{13}$$

as well as valley–valley correlations

$$\chi_{ij}^{v,\kappa\lambda} \equiv \chi_{ij}^{00\kappa\lambda} \sim \left\langle \tau_i^\kappa \tau_j^\lambda \right\rangle . \tag{14}$$

A thermal phase transition to long-range, symmetry-breaking order in the spin or valley sector at some finite temperature can formally be detected by a divergence in the RG flow of the corresponding correlation at some breakdown scale Λ_c [28], as shown in Fig. 2a. Due to finite numerical resolution, however, they often manifest as a kink or a peak in the susceptibility. The momentum space profile of the dominant structure factor close to the breakdown scale, i.e., the Fourier transform of the static correlation $\chi_{ij}^{\Lambda s/v}(\omega = 0)$, then indicates the type of symmetry-breaking. Since the solution of the flow equation below the breakdown scale Λ_c is no longer physical, this only allows us to detect the phase transition that occurs at the largest breakdown scale if there are multiple subsequent transitions. This might be the case when spin and valley degrees of freedom exhibit different ordering transitions at two distinct energy scales. If, in this scenario, the spin sector orders at the larger of the two energy scales, we cannot directly determine the ground-state order of the valley sector from the flow of the valley–valley correlations. Instead, we need to fall back to, for instance, mean-field arguments as proposed in [21] to determine the most likely valley order. If, on the other hand, the correlations show *no* flow breakdown, both spin and valley degrees of freedom do not order, indicative of a ground state that remains paramagnetic or exhibits spin–valley liquid behavior.

These two scenarios are illustrated in Fig. 2a, b. Both panels show the flow of the structure factor at the dominant momentum for a magnetically ordered phase with dominant valley order (a) and the paramagnetic state at the SU(4) point [36] (b) where the spin–valley Hamiltonian corresponds to Eq. (1). In the magnetically ordered phase of panel (a), we see a clear flow breakdown in the valley structure factor $\chi^{\Lambda v}$, which manifests as a peak or divergence, depending on the vertex truncation length L (further discussed in Sect. 3.3). The spin structure factor $\chi^{\Lambda s}$ shown by the purple lines is strongly suppressed. At the SU(4) point, on the other hand, the flow of the structure factor is smooth and convex down to the lowest energy scale we can reliable calculate ($\Lambda = 0.02J$), indicating a paramagnetic ground state. Here, spin and valley correlations are identical due to the global SU(4) symmetry of the Hamiltonian (and indistinguishable in our plot).

3.2 Vertex parametrization and symmetry constraints

To make the solution of the flow equations numerically feasible, one needs to keep the overall number of differential equations needed to capture the flow equations as small as possible. Practically, this can be achieved by eliminating redundant calculations through implementing the symmetry constraints which the Hamiltonian poses on the self-energy and the two-particle vertex. A comprehensive symmetry analysis of this sort has been carried out for generic $\mathfrak{su}(2)$ spin models [27], which here will be generalized to the spin–valley Hamiltonians of interest. Details of this symmetry analysis will be discussed in Sect. 4, while we will report its main findings in the following.

The first important finding is that symmetries dictate that the self-energy is completely diagonal and can be

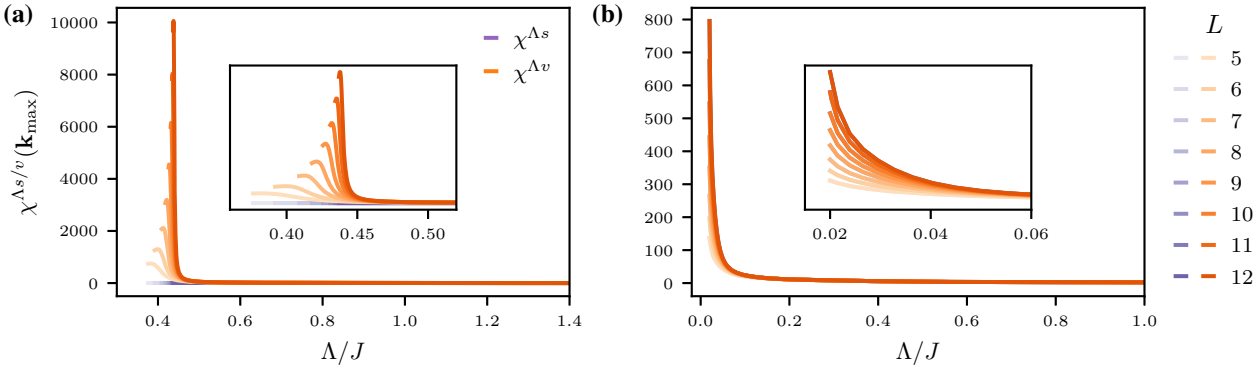

Fig. 2 Flow of the spin and valley structure factor in a magnetically ordered phase (**a**) and a paramaganetic phase (**b**) for different values of the vertex truncation length L. All structure factors are shown at the momentum at which they are maximal. The insets zoom into the flow at small cut-offs. In the magnetically ordered phase, we clearly see a breakdown of the flow in the valley sector, which manifests as a peak for small L and a more clear divergence when increasing L. In the paramagnetic phase, the flow is smooth and convex down to about $\Lambda/J = 0.02$, which is the smallest scale for which our calculations are numerically reliable

parametrized by a single function $\Sigma(\omega)$ as

$$\Sigma(1',1) = \Sigma(\omega)\delta_{s's}\delta_{l'l}\delta_{i'i}\delta_{\omega'\omega}. \tag{15}$$

We emphasize again that this is only the case if the interactions remain diagonal in either the spin or valley sector. For Hamiltonians with off-diagonal interactions in both sectors, the self-energy will not be diagonal in the spin and valley indices, greatly increasing the numerical cost for the solution of the flow equations. The two-particle vertex can be parametrized as

$$\begin{aligned}&\Gamma(1',2',1,2)\\ &= \Big[\Gamma^{\mu\kappa\lambda}_{i_1 i_2}(s,t,u)\ \theta^{\mu}_{s_{1'}s_1}\theta^{\mu}_{s_{2'}s_2}\theta^{\kappa}_{l_{1'}l_1}\theta^{\lambda}_{l_{2'}l_2}\ \delta_{i_{1'}i_1}\delta_{i_{2'}i_2}\\ &\quad -(1'\leftrightarrow 2')\Big]\ \delta_{\omega_{1'}+\omega_{2'}-\omega_1-\omega_2},\end{aligned} \tag{16}$$

with the three bosonic transfer frequencies

$$\begin{aligned} s &= \omega_{1'} + \omega_{2'}\\ t &= \omega_{1'} - \omega_1\\ u &= \omega_{1'} - \omega_2. \end{aligned} \tag{17}$$

This parametrization is of the same form as for $\mathfrak{su}(2)$ spin models—apart from an increased number of components due to the valley sector $\sim \theta^{\kappa}_{l_{1'}l_1}\theta^{\lambda}_{l_{2'}l_2}$ with the corresponding indices κ and λ. If we assume the Hamiltonian to be diagonal in the spin sector, we will only need to consider components diagonal in the spin $\sim \theta^{\mu}_{s_{1'}s_1}\theta^{\mu}_{s_{2'}s_2}$, with the corresponding index μ (and vice versa for a system with a diagonal valley Hamiltonian). The basis functions of the parametrization are constrained by the symmetries of the Hamiltonian as

$$\begin{aligned} \Sigma(\omega) &\in i\mathbb{R}\\ \Sigma(\omega) &= -\Sigma(-\omega)\\ \Gamma^{\mu\kappa\lambda}_{i_1 i_2}(s,t,u) &\in \begin{cases}\mathbb{R} & \text{if } \xi(\kappa)\xi(\lambda) = 1\\ i\mathbb{R} & \text{if } \xi(\kappa)\xi(\lambda) = -1\end{cases}\\ \Gamma^{\mu\kappa\lambda}_{i_1 i_2}(s,t,u) &= \Gamma^{\mu\lambda\kappa}_{i_2 i_1}(-s,t,u)\\ \Gamma^{\mu\kappa\lambda}_{i_1 i_2}(s,t,u) &= \xi(\kappa)\xi(\lambda)\Gamma^{\mu\kappa\lambda}_{i_1 i_2}(s,-t,u)\\ \Gamma^{\mu\kappa\lambda}_{i_1 i_2}(s,t,u) &= \xi(\kappa)\xi(\lambda)\Gamma^{\mu\lambda\kappa}_{i_2 i_1}(s,t,-u), \end{aligned} \tag{18, 19}$$

where we defined the sign function

$$\xi(\kappa) = \begin{cases} 1 & \text{if } \kappa = 0\\ -1 & \text{otherwise}\end{cases}. \tag{20}$$

These are the same relations as for the $\mathfrak{su}(2)$ case, apart from a missing constraint relating the s und u frequencies in the two-particle vertex (c.f. Eq. (14) in Ref. [27]). This is a consequence of the Hamiltonian only being invariant under a *global* particle–hole symmetry instead of the *local* particle–hole symmetry under which the $\mathfrak{su}(2)$ Hamiltonian is invariant. We discuss this in more detail in Sect. 4. The missing relation, however, does not change the key implications of the constraints, namely that the basis functions are either completely real or imaginary, and that values of the vertex functions at negative transfer frequencies can be inferred from the positive frequency axes.

The parametrization of the two-particle vertex using the three transfer frequencies in Eq. (17) is convenient for deriving the flow equations and symmetry constraints. However, to better capture the asymptotic frequency dependence of the two-particle vertex one can further refine the frequency parametrization [23,24,37]. The first step is to group the contributions in the flow equation of the two-particle vertex given in Eq. (11) into three channels according to their two-particle irreducibility. This results in a particle–particle (*pp*), direct particle–hole (*dph*), and crossed particle–hole (*cph*) channel, which correspond to the three contributions on the right-hand side (RHS) of Eq. (11), in the respective ordering. In these terms, the flow equation for the two-particle vertex can be written as

$$\frac{d}{d\Lambda}\Gamma^{\Lambda} = \dot{g}^{\Lambda}_{pp} + \dot{g}^{\Lambda}_{dph} + \dot{g}^{\Lambda}_{cph}, \tag{21}$$

and the vertex is parametrized (stating only the frequency dependence) as

$$\Gamma^{\Lambda}(s,t,u) = \Gamma^{\Lambda\to\infty} + \sum_c g^{\Lambda}_c(\omega_c, v_c, v'_c), \tag{22}$$

where $\Gamma^{\Lambda\to\infty}$ is the bare two-particle vertex at infinite cut-off. Each channel $g_c(\omega_c, v_c, v'_c)$ is parametrized by one bosonic transfer frequency ω_c and two additional fermionic frequencies v'_c, v'_c. The precise definition of the frequencies can be chosen in numerous ways. It is, however, advantageous to choose them, so that the symmetry constraints of the two-particle vertex given in Eq. (19) result in equally simple relations for each channel in the new parametrization. Here, we adapt the choice of Ref. [24]

$$\begin{aligned} \omega_{pp} &= s & v_{pp} &= \omega_1 - \frac{s}{2} & v'_{pp} &= \frac{s}{2} - \omega_{1'}\\ \omega_{dph} &= t & v_{dph} &= \omega_1 + \frac{t}{2} & v'_{dph} &= \omega_{1'} - \frac{t}{2}\\ \omega_{cph} &= u & v_{cph} &= \omega_1 - \frac{u}{2} & v'_{cph} &= \omega_{1'} - \frac{u}{2}, \end{aligned} \tag{23}$$

and give the resulting symmetry constraints for the channels in A. Compared to $\mathfrak{su}(2)$ spin models, no constraint relating the particle–particle and crossed particle–hole channel with each other is present, which can be traced back to the missing symmetry constraint relating the s and u frequency dependence[3].

[3] Fortunately, as we will explain in Sect. 3.3, this only results in an increase of numerical complexity by a factor of two, making numerical calculations only slightly more costly.

To complete the discussion, we still need to state the initial conditions of the flow equations corresponding to the self-energy and two-particle vertex in the limit $\Lambda \to \infty$, which are given by

$$\begin{aligned} \Sigma^{\Lambda\to\infty}(\omega) &= 0 \\ \Gamma^{\Lambda\to\infty\mu\kappa\lambda}_{i_1 i_2}(s,t,u) &= \frac{1}{8} J^{\mu}_{s,i_1 i_2} J^{\kappa\lambda}_{v,i_1 i_2}, \end{aligned} \tag{24}$$

with the couplings $J^{\mu}_{s,i_1 i_2}$ and $J^{\kappa\lambda}_{i_1 i_2}$ defined in Eq. (5).

3.3 Numerical implementation

The numerical solution of the pf-FRG flow equations poses several challenges and necessitates further approximations to be made. To overcome these challenges, we employ the state-of-the-art numerical implementation of Refs. [23,24], where additional details of the implementation are discussed. Here, we only give a short overview and discuss some slight technical differences in the implementation for spin–valley models.

First, one has to truncate the infinite lattice geometry by a finite lattice graph. Employing the symmetries of the lattice geometry for which the spin–valley model is formulated and the local U(1) symmetry present in all pseudo-fermion Hamiltonians, the spatial dependence of the two-particle vertex can be reduced to just one site index j and one arbitrary fixed reference site i_0, as will be derived in Sect. 4. To obtain a finite number of vertex components $\Gamma^{\Lambda}_{i_0 j}$ (considering only the lattice site dependence), we define a finite length scale L and truncate the vertex $\Gamma^{\Lambda}_{i_0,j}$ for bond distances $d(i_0, j) > L$, effectively enforcing a maximal correlation length. The finite-size effect of this truncation can be observed in Fig. 2, where several calculations with increasing values of L were performed for a magnetically ordered and a paramagnetic phase. In the ordered phase, the flow breakdown sharpens from a relatively broad peak for low values of L to a clear divergence for larger values of L, which is a typical observation. The paramagnetic phase is, in contrast, not affected by the increase of L (at least qualitatively). From an algorithmic point of view, the asymptotic scaling of the computation time is quadratic in the number of lattice points $N_L \sim L^d$, where d is the number of spatial dimensions. This is due to the fact that the number of vertex components as well as the sum over all lattice sites included in the flow equations scale linearly with N_L. In this work, we typically perform calculations at $L = 9$, above which the breakdown scale does not significantly change anymore and the numerical effort is still reasonable.

Since the pf-FRG approach is formulated at zero temperature, another point we need to address is how to discretize the continuous Matsubara frequencies. To accurately resolve all features of the two-particle vertex, it turns out that particular care needs to be taken in the choice of frequency meshes [23,24]. To this end, the frequencies are discretized on adaptive, hybrid linear-logarithmic meshes, which are updated using a scanning routine between each step of the ordinary differential equation (ODE) solver. In addition to continuous Matsubara frequencies, the flow equations at $T = 0$ include frequency integrals which have to be performed numerically. To calculate these integrals, we employ an adaptive quadrature which takes both the relevant features around the origin and the algebraic decay for large frequencies into account. Values of the vertex for frequencies not lying on the discrete frequency meshes are obtained by multi-linear interpolation. The computation time asymptotically scales with the number of (positive) bosonic frequencies N_Ω and (positive) fermionic frequencies N_ν as $\mathcal{O}(N_\Omega \cdot N_\nu^2)$. A typical setup for which the two-particle vertex is sufficiently well resolved is $N_\Omega = 40$ and $N_\nu = 30$, which we use for all calculations in this work. The computational effort to compute the self-energy is, compared to the vertex, negligible, as it only depends on one frequency. Here, we choose a frequency mesh with $N_\Sigma = 250$ frequencies. In the $\mathfrak{su}(2)$ case, only positive frequencies were required, as the symmetry constraints map all negative frequency components to some positive counterpart. For spin–valley models, however, due to the missing symmetry constraint relating the particle–particle and crossed particle–hole channel (discussed in Sect. 3.2), we have to also consider negative frequencies for either ν_c or ν'_c. This results in an additional factor of two in computation time compared to $\mathfrak{su}(2)$ spin models.

The adaptive frequency meshes and integration routine allow for an efficient evaluation of the RHS of the flow equations. For the solution of the ODEs themselves, we choose the Bogacki–Shampine method [38], which is a third-order Runge–Kutta method with adaptive step size control. We find that this method is a good compromise between computational cost and numerical precision.

Although the asymptotic scaling of the computation time with the number of lattice points and frequencies is the same as for the $\mathfrak{su}(2)$ case, more complex spin–valley models usually require a much larger numerical effort, as the extra valley index greatly increases the number of independent two-particle vertex components $\Gamma^{\Lambda,\mu\kappa\lambda}_{i_1 i_2}$, in which the computation time scales linearly. With the coupling matrices given in Eq. (5), there would be $N_\Gamma = 4 \cdot 4^2 = 64$ independent vertex components (only considering the spin–valley dependence). In comparison, the parametrization for generic $\mathfrak{su}(2)$ models only has $N_\Gamma = 4^2 = 16$ components. Fortunately, in almost all physical models, extra symmetries in the spin and valley space will greatly reduce the number of independent components. Considering, e.g., an SU(2) symmetry in the spin space and a U(1) symmetry in valley space, which is present in several models for moiré materials [11,35], the number is already reduced to $N_\Gamma = 2 \cdot 6 = 12$. For these models, the numerical effort is similar to $\mathfrak{su}(2)$ models with off-diagonal interactions and even allows for computations of relatively large-phase diagrams as will be presented in Sect. 5.

4 Symmetry classification

To proof the validity of the parametrization and the symmetry constraints presented in the previous section, we repeat the symmetry analysis of Ref. [27], where the pseudo-fermion Hamitonian for $\mathfrak{su}(2)$ spin models with generic diagonal and off-diagonal interactions is considered, but for the spin–valley Hamiltonian given in Eq. (4). We show that most of the symmetries of the $\mathfrak{su}(2)$ pseudo-fermion Hamiltonian are either also present in the spin–valley Hamiltonian, or can be generalized in a straightforward fashion. There are, however, some differences that we will highlight in the following. Most notably, we show that, even at the SU(4) point, the spin–valley model does not posses a *local* particle–hole symmetry that is present in the $\mathfrak{su}(2)$ case, but only the corresponding *global* symmetry. Consequently, it is also not present in generalizations of the SU(2) Heisenberg model to SU(N), which might not have been clearly stated before. This is the reason for the missing symmetry constraint for the two-particle vertex as presented in the previous section.

4.1 Local U(1) symmetry

The first symmetry transformation we consider, a local U(1) transformation, directly follows from the form of the spin–valley operator given by Eq. (2). It acts on the fermionic Hilbert space at site i by multiplying a local phase $\varphi_i \in [0, 2\pi)$ to the fermionic operators as

$$g_{\varphi_i} \begin{pmatrix} f^\dagger_{isl} \\ f^\dagger_{isl} \end{pmatrix} g^{-1}_{\varphi_i} = \begin{pmatrix} e^{i\varphi_i} f^\dagger_{isl} \\ e^{-i\varphi_i} f^\dagger_{isl} \end{pmatrix}, \tag{25}$$

which clearly leaves all spin–valley operators invariant. Interpreting the spin–valley Hamiltonian as a fermionic representation of an $\mathfrak{su}(4)$ spin model, it is simply a consequence of the choice for the fermionic representation of the spin operators. It is therefore also present in all conventional pf-FRG implementations using the standard pseudo-fermion representation. In that sense, it is sometimes also referred to as a gauge redundancy instead of a symmetry, as it is not a symmetry of the original spin Hamiltonian, but only of the pseudo-fermion representation. For our functional renormalization group approach, we are interested in the implication of the symmetry on the functional form[4] of the one-particle correlation function

$$\begin{aligned} G(1',1) &\equiv -\langle f^\dagger_{1'} f^\dagger_1 \rangle \\ &= -\int d\tau' d\tau e^{i\tau'\omega' - i\tau\omega} \left\langle f^\dagger_{i'\tau's'l'} f^\dagger_{i\tau sl} \right\rangle \end{aligned} \tag{26}$$

and the two-particle correlation function

$$\begin{aligned} G(1',2',1,2) &:= \langle f^\dagger_{1'} f^\dagger_{2'} f^\dagger_2 f^\dagger_1 \rangle \\ &= \int d\tau_{1'} d\tau_{2'} d\tau_1 d\tau_2 e^{i(\tau_{1'}\omega_{1'} + \tau_{2'}\omega_{2'} - \tau_1\omega_1 - \tau_2\omega_2)} \\ &\quad \times \left\langle f^\dagger_{i_{1'}\tau_{1'}s_{1'}l_{1'}} f^\dagger_{i_{2'}\tau_{2'}s_{2'}l_{2'}} f^\dagger_{i_2\tau_2 s_2 l_2} f^\dagger_{i_1\tau_1 s_1 l_1} \right\rangle, \end{aligned} \tag{27}$$

where we suppress the time-ordering operator as it becomes trivial in the path integral framework that the function renormalization group is formulated in. Acting with the local U(1) transformation given in Eq. (25) on the definition of the correlation functions and demanding their invariance leads to the corresponding symmetry constraint. It directly implies that we can restrict ourselves to a local one-particle correlation function

$$G(1',1) = G(1',1)\delta_{i_{1'} i_1}, \tag{28}$$

which only depends on one lattice site i_1, and a bi-local two-particle correlation function

$$\begin{aligned} G(1',2',1,2) = &\ G(1',2',1,2)\delta_{i_{1'} i_1}\delta_{i_{2'} i_2} \\ - &\ G(2',1',1,2)\delta_{i_{2'} i_1}\delta_{i_{1'} i_2}, \end{aligned} \tag{29}$$

which only depends on the two lattices sites i_1 and i_2.

4.2 Global particle–hole symmetry

In the pf-FRG for $\mathfrak{su}(2)$ spin models, spin operators S^a_i are represented using fermions with one spin index $\alpha = \pm 1$ as

$$S^a = \frac{1}{2} f^\dagger_{i\alpha} \theta^a_{\alpha\alpha'} f^\dagger_{i\alpha'}, \tag{30}$$

with $a \in \{1, 2, 3\}$. In addition to the U(1) gauge redundancy, there exists another redundancy in this representation that can be formulated as a *local* particle–hole symmetry [27]. It acts on the fermionic Hilbert space as

$$g_i \begin{pmatrix} f^\dagger_{i\alpha} \\ f^\dagger_{i\alpha} \end{pmatrix} g^{-1}_i = \begin{pmatrix} \alpha f^\dagger_{i\bar{\alpha}} \\ \alpha f^\dagger_{i\bar{\alpha}} \end{pmatrix}, \tag{31}$$

with $\bar{\alpha} \equiv -\alpha$. It leaves the fermionic representation of the $\mathfrak{su}(2)$ spin operators invariant and is therefore a symmetry of the pseudo-fermion Hamiltonian. We note that this symmetry is not anti-unitary and therefore does not correspond to the usual physical particle–hole symmetry [27]. Instead, it is again a consequence of the representation of the spin operators. The natural extension for spin–valley models with spin index $s = \pm 1$ and valley index $l = \pm 1$ is the transformation

$$g_i \begin{pmatrix} f^\dagger_{isl} \\ f^\dagger_{isl} \end{pmatrix} g^{-1}_i = \begin{pmatrix} sl f^\dagger_{i\bar{s}\bar{l}} \\ sl f^\dagger_{i\bar{s}\bar{l}} \end{pmatrix}, \tag{32}$$

[4] Note that our definition deviates from normal ordering to be in line with the conventional definition of retarded Greens functions.

under which the spin–valley operator transforms as

$$g_i\ \sigma_i^\mu \otimes \tau_i^\kappa\ g_i^{-1} = -\xi(\mu)\xi(\kappa)\sigma_i^\mu \otimes \tau_i^\kappa, \tag{33}$$

which can be shown straightforwardly using the anti-commutation relations of the fermionic operators and the identity

$$\bar{\alpha}\bar{\alpha}'\theta^\mu_{\alpha\alpha'} = \xi(\mu)\theta^\mu_{\bar{\alpha}'\bar{\alpha}}. \tag{34}$$

Spin–valley operators with either the spin index μ or the valley index κ set to zero—which correspond to the individual spin and valley operators as defined in Eq. (2)—are invariant under this transformation. General spin–valley operators, on the other hand, may change their sign. The Hamiltonian is, therefore, not invariant under the local particle–hole symmetry that acts on the Hilbert space of just one lattice site. Spin–valley operators, however, only appear in pairs in the spin–valley Hamiltonian. Performing the local particle–hole symmetry transformation on *all* lattice sites, such a pair of spin–valley operators transform as

$$g(\sigma_i^\mu \otimes \tau_i^\kappa)(\sigma_j^\nu \otimes \sigma_j^\lambda)g^{-1} = \xi(\mu)\xi(\kappa)\xi(\nu)\xi(\lambda) \times(\sigma_i^\mu \otimes \tau_i^\kappa)(\sigma_j^\nu \otimes \sigma_j^\lambda). \tag{35}$$

If an odd number of spin and valley indices is set to zero, this again implies a sign change. Recalling the definition of the spin–valley Hamiltonian in Eq. (4) and the following definition of the exchange matrices in Eq. (5), such terms are not included in our definition of the Hamiltonian. All terms that do appear in the Hamiltonian are indeed invariant. The main difference to the $\mathfrak{su}(2)$ pseudo-fermion Hamiltonian is, therefore, that the spin–valley Hamiltonian is invariant only under the *global* transformation, while the former was invariant under the *local* transformation. For the local single-particle correlation function, the global particle–hole symmetry implies

$$G(1',1)\delta_{i'i} = -ss'll'G(i-\omega\bar{s}\bar{l}, i-\omega'\bar{s}'\bar{l}')\delta_{i'i}, \tag{36}$$

and for the bi-local two-particle correlator, it implies

$$\begin{aligned} &G(1',2',1,2)\delta_{i_{1'}i_1}\delta_{i_{2'}i_2} \\ &\quad= s_{1'}s_1l_{1'}l_1s_{2'}s_2l_{2'}l_2\delta_{i_{1'}i_1}\delta_{i_{2'}i_2}G(i_1-\omega_1\bar{s}_1\bar{l}_1, i_2 \\ &\quad-\omega_2\bar{s}_2\bar{l}_2, i_1-\omega_{1'}\bar{s}_{1'}\bar{l}_{1'}, i_2-\omega_{2'}\bar{s}_{2'}\bar{l}_{2'}). \end{aligned} \tag{37}$$

These relations are, apart form the extra factors of valley indices, the same as for the $\mathfrak{su}(2)$ case when considering the global transformation. The invariance under the local transformation would yield additional constraints on the two-particle correlator acting only on multi-indices with the same lattice site (i_1 or i_2). For the parametrized two-particle vertex, these result in a constraint relating the s and u dependence or, in the asymptotic frequency parametrization defined in Eqs. (22, 23), the particle–particle and crossed particle–hole channel with each other. As already discussed in Sect. 3, this constraint is, consequently, missing for spin–valley models.

4.3 Generalized time-reversal symmetry

For $\mathfrak{su}(2)$ spin models, a genuinely physical symmetry is the invariance under time-reversal. In this setting, time-reversal reverses the sign of all spin operators $S^a \to -S^a$ and, as it is an anti-unitary symmetry, additionally applies complex conjugation to all complex numbers. Hamiltonians with real couplings in which spin operators only appear in pairs are therefore always invariant under time-reversal. On the Hilbert space of the $\mathfrak{su}(2)$ pseudo-fermions, it can be represented as

$$g\begin{pmatrix} f^\dagger_{i\alpha} \\ f^\dagger_{i\alpha} \end{pmatrix} g^{-1} = \begin{pmatrix} e^{i\pi\alpha/2}f^\dagger_{i\bar{\alpha}} \\ e^{-i\pi\alpha/2}f^\dagger_{i\bar{\alpha}} \end{pmatrix}. \tag{38}$$

We again consider a straightforward generalization of the transformation to spin–valley operators, which we define as the anti-unitary transformation

$$g\begin{pmatrix} f^\dagger_{isl} \\ f^\dagger_{isl} \end{pmatrix} g^{-1} = \begin{pmatrix} e^{i\pi s/2}e^{i\pi l/2}f^\dagger_{i\bar{s}\bar{l}} \\ e^{-i\pi s/2}e^{-i\pi l/2}f^\dagger_{i\bar{s}\bar{l}} \end{pmatrix}. \tag{39}$$

Using the relation $e^{i\pi(\alpha-\alpha')/2} = \alpha\alpha'$ and Eq. (34), it is straightforward to show that the spin–valley operator transforms as

$$g\ \sigma_i^\mu \otimes \tau_i^\kappa\ g^{-1} = \xi(\mu)\xi(\kappa)\sigma_i^\mu \otimes \tau_i^\kappa, \tag{40}$$

which, up to a minus sign, is the same transformation behavior as for the particle–hole symmetry in Eq. (33). As only pairs of spin–valley operators appear in the spin–valley Hamiltonian, for which the minus sign is irrelevant, the arguments for the invariance of Hamiltonian given there, consequently, also apply here. Applying this generalized version of time-reversal to the local one-particle correlator implies

$$G(1',1)\delta_{i',i} = ss'll'G(i-\omega'\bar{s}'\bar{l}', i-\omega\bar{s}\bar{l})^*\delta_{i',i}, \tag{41}$$

where the complex conjugation stems from the fact that the transformation is anti-unitary. For the bi-local two-particle correlation function, it implies

$$\begin{aligned} &G(1',2',1,2)\delta_{i_{1'}i_1}\delta_{i_{2'}i_2} \\ &\quad= s_{1'}s_1l_{1'}l_1s_{2'}s_2l_{2'}l_2\delta_{i_{1'}i_1}\delta_{i_{2'}i_2}G(i_1-\omega_{1'}\bar{s}_{1'}\bar{l}_{1'}, \\ &\quad\times i_2-\omega_{2'}\bar{s}_{2'}\bar{l}_{2'}, i_1-\omega_1\bar{s}_1\bar{l}_1, i_2-\omega_2\bar{s}_2\bar{l}_2)^*. \end{aligned} \tag{42}$$

Apart from extra valley indices, this is exactly the same as in the $\mathfrak{su}(2)$ case.

4.4 Hermitian symmetry

Just as the $\mathfrak{su}(2)$ spin operator, the spin–valley operator is Hermitian. The spin–valley Hamiltonian only consists of pairs of spin–valley operators and we have restricted ourselves to real couplings, making it Hermitian aswell. Complex transposition, therefore, leaves the Boltzman factor in the thermal expectation value invariant. Applying complex transposition on both sides of Eqs. (26, 27) and explicitly evaluating the RHS by "pulling" the complex transpose into the thermal expectation value, we obtain the constraint

$$G(1',1)\delta_{i',i} = G(i-\omega sl, i-\omega' s' l')^* \delta_{i',i} \tag{43}$$

for the local one-particle correlator and

$$\begin{aligned} G(1',2',1,2)\delta_{i_{1'}i_1}\delta_{i_{2'}i_2} &= \delta_{i_{1'}i_1}\delta_{i_{2'}i_2} \\ &\times G(i_1-\omega_1 s_1 l_2, i_2-\omega_2 s_2 l_2, \\ & i_1-\omega_{1'} s_{1'} l_{1'}, i_2-\omega_{2'} s_{2'} l_{2'})^* \end{aligned} \tag{44}$$

for the two-particle correlator. These constraints are again of the same form as for the $\mathfrak{su}(2)$ case.

4.5 Lattice symmetries

The spin models we consider are all formulated on lattices that can be specified in terms of an underlying Bravais lattice and a possibly multi-atomic basis. Therefore, lattice symmetries exist necessarily for any spin–valley model and are very important to efficiently implement the pf-FRG. Their implementation is the same whether one considers $\mathfrak{su}(2)$ spin models or spin–valley models. We can therefore use the same approach as for the conventional pf-FRG as, e.g., explained in Ref. [27]. There, all sites are assumed to be identical, in the sense that one can map any site to any other site via a lattice automorphism T that leaves the lattice itself invariant. On the fermionic operators, such a transformation acts as

$$g_T \begin{pmatrix} f^\dagger_{isl} \\ f^\dagger_{isl} \end{pmatrix} g_T^{-1} = \begin{pmatrix} f^\dagger_{T(i)sl} \\ f^\dagger_{T(i)sl} \end{pmatrix}. \tag{45}$$

In the case of bond-directional couplings, the transformation would additionally have to be combined with transformations in spin and valley space. For the one-particle correlation function, this implies

$$G(1',1)\,\delta_{i',i} = G(T(i)\,\omega' s' l', T(i)\omega s l)\,\delta_{i',i}. \tag{46}$$

The locality constraint in Eq. (28), resulting from the local U(1) symmetry, already reduces the spatial dependence of the self-energy to only one site index i_1. Using lattice automorphisms, we can map all sites to an arbitrary reference site i_0 and therefore completely remove the spatial dependence of the one-particle correlation function. Similarly, for the two-particle correlation function, it implies

$$\begin{aligned} G(1',2',1,2)\,\delta_{i_{1'}i_1}\delta_{i_{2'}i_2} &= \delta_{i_{1'}i_1}\delta_{i_{2'}i_2} \\ &\times G\big(T(i_1)\,\omega_{1'} s_{1'} l_{1'}, T(i_2)\,\omega_{2'} s_{2'} l_{2'}, \\ & T(i_1)\,\omega_1 s_1 l_1, T(i_2)\,\omega_2 s_2 l_2\big). \end{aligned} \tag{47}$$

Combining this with the bi-locality constraint in Eq. (29), and again mapping the first index i_1 to an arbitrary reference site i_0, the spatial dependence of the two-particle correlator can be reduced to just one lattice site.

4.6 Parametrization of correlation functions

To make use of the symmetry constraints on the correlation functions, it is advantageous to parametrize them, so that the symmetry constraints manifest in a more practical form. To this end, we can extent the parametrization for the correlation functions for generic $\mathfrak{su}(2)$ spin models introduced in [27] also to spin–valley models. This ultimately leads to the parametrization of the self-energy and two-particle vertex in Eqs. (15, 16) and the symmetry constraints in Eqs. (18, 19). Starting with the one-particle correlation function, we argued that due to the local U(1) symmetry and lattice symmetries, it is independent of the lattice site. Additionally, due to Matsubara frequency conservation, which is a consequence of translational invariance in imaginary time, it is diagonal in the frequency arguments. Expanding the spin and valley dependence in Pauli matrices $\theta^\mu\theta^\kappa$ $(\mu,\kappa = 0,1,2,3)$, the one-particle correlation function can be parametrized as

$$G(1',1) = G^{\mu\kappa}(w)\theta^\mu_{s's}\theta^\kappa_{l'l}\delta_{i'i}\delta_{\omega'\omega}. \tag{48}$$

Similarly, the two-particle correlation function depends only on two lattice sites and three frequencies, for which we choose the three transfer frequencies defined in Eq. (17). The parametrization then reads

$$\begin{aligned} &G(1',2',1,2) \\ &= \Big(G^{\mu\nu\kappa\lambda}_{i_1 i_2}(s,t,u)\theta^\mu_{s_{1'}s_1}\theta^\nu_{s_{2'}s_2}\theta^\kappa_{l_{1'}l_1}\theta^\lambda_{l_{2'}l_2}\delta_{i_{1'}i_1}\delta_{i_{2'}i_2} \\ &\quad -(1'\leftrightarrow 2')\Big)\delta_{\omega_{1'}+\omega_{2'}-\omega_1-\omega_2}. \end{aligned} \tag{49}$$

Plugging this parametrization into the symmetry constraints derived in Sects. 4.1–4.5, we obtain the symmetry constraints for the basis functions of the parametrization listed in Table 1. In the derivation of these constraints, we make heavy use of Eq. (34) and the particle-exchange symmetry

$$G(1',2',1,2) = G(2',1',2,1), \tag{50}$$

which is present in all purely fermionic models.

Table 1 Symmetry constraints for the basis functions of the parametrization of the correlation functions

$G^{\mu\kappa}(\omega) = \xi(\mu)\xi(\kappa)G^{\mu\kappa}(\omega)$	(H ∘ TR)
$G^{\mu\kappa}(\omega) = -G^{\mu\kappa}(-\omega)$	(H ∘ TR ∘ PH)
$G^{\mu\kappa}(\omega) = -G^{\mu\kappa}(\omega)^*$	(TR ∘ PH)
$G^{\mu\nu\kappa\lambda}_{i_1 i_2}(s,t,u) = \xi(\mu)\xi(\nu)\xi(\kappa)\xi(\lambda)$ $\times G^{\mu\nu\kappa\lambda}_{i_1 i_2}(s,t,u)^*$	(TR ∘ PH ∘ H ∘ TR)
$G^{\mu\nu\kappa\lambda}_{i_1 i_2}(s,t,u) = G^{\nu\mu\lambda\kappa}_{i_2 i_1}(-s,t,u)$	(H ∘ TR ∘ PH ∘ X)
$G^{\mu\nu\kappa\lambda}_{i_1 i_2}(s,t,u) = \xi(\mu)\xi(\nu)\xi(\kappa)\xi(\lambda)$ $\times G^{\mu\nu\kappa\lambda}_{i_1 i_2}(s,-t,u)$	(H ∘ TR)
$G^{\mu\nu\kappa\lambda}_{i_1 i_2}(s,t,u) = \xi(\mu)\xi(\nu)\xi(\kappa)\xi(\lambda)$ $\times G^{\nu\mu\lambda\kappa}_{i_2 i_1}(s,t,-u)$	(H ∘ TR ∘ X)

The labels specify which symmetries of the Hamiltonian were used in their derivation, where H stands for Hermitian, TR for generalized time-reversal, PH for global particle–hole and X for particle-exchange symmetry. The most notable implications are that all correlation functions will always be either only real or imaginary and all expression with negative frequencies can be related to those with positive frequencies

The list of symmetry constraints is very similar to the $\mathfrak{su}(2)$ case derived in Ref. [27], but has two significant differences. First, as already discussed in Sects. 3.2 and 4.2, the symmetry constraint relating s and u frequencies, or the particle-particle and crossed particle–hole channel, is missing because the spin–valley Hamiltonian is not invariant under a *local* particle–hole transformation but only under the *global* version. Second, the symmetry constraints do not imply that the one-particle correlation function is completely diagonal in all spin and valley indices. In the parametrization, this would manifest in G^{00} being the only non-vanishing basis function. Instead, for a general spin–valley Hamiltonian, also the terms G^{ab} with $a, b > 0$, which come with the factor $\sim \theta^a_{ss'}\theta^b_{ll'}$, are allowed. This would increase the number of flow equations and therefore also the numerical complexity significantly. Additionally, we could not use the conventional pf-FRG flow equations given in Eqs. (10, 11), where a diagonal one particle correlator (and self-energy) was assumed. Fortunately, in the context of moiré materials, many Hamiltonians of physical relevance posses additional symmetries in the spin and valley space [11,35] that further constrain the spin and valley dependence of the self-energy and two-particle vertex. It turns out that the minimal symmetry needed in order for the one-particle correlator to be diagonal is a $\mathbb{Z}_2 \times \mathbb{Z}_2 \times \mathbb{Z}_2$ symmetry in either the spin or valley sector. On the level of spin–valley operators, this means that the Hamiltonian is invariant under the transformation (for the case of the spin sector)

$$g_\mu \ \sigma_i^\mu \otimes \tau_i^\kappa \ g_\mu^{-1} = \xi(\mu)\sigma_i^\mu \otimes \tau_i^\kappa, \tag{51}$$

for each μ individually. This simply reverses the signs of all $\sigma_i^\mu \otimes \tau_i^\kappa$ with $\mu > 0$. Assuming a completely diagonal spin exchange matrix as in Eq. (5), the spin–valley Hamiltonian is indeed invariant under this transformation. This directly implies that all terms proportional to a single $\sim \theta^\mu$ (with $\mu > 0$) in the correlation functions have to vanish. More precisely, it imposes the constraint

$$G^{\mu\kappa}(\omega) = \delta_{\mu 0} G^{0\kappa}(\omega), \tag{52}$$

which in combination with the first equation in Table 1 implies

$$G^{\mu\kappa}(\omega) = \delta_{\mu 0}\delta_{\kappa 0} G^{00}(\omega) \equiv \delta_{\mu 0}\delta_{\kappa 0} G(\omega), \tag{53}$$

resulting in a completely diagonal one-particle correlation function parametrized by a single basis function $G(\omega)$. For the coupling matrices stated in Eq. (5), we can therefore use the standard pf-FRG approach also for spin–valley models. Assuming this additional symmetry, in the two-particle correlator, only diagonal components in the spin sector $\sim \theta^\mu\theta^\mu$ (no sum over μ) are allowed, resulting in the constraint

$$G^{\mu\nu\kappa\lambda}_{i_1 i_2}(s,t,u) = \delta_{\mu\nu} G^{\mu\mu\kappa\lambda}_{i_1 i_2}(s,t,u) \equiv \delta_{\mu\nu} G^{\mu\kappa\lambda}_{i_1 i_2}(s,t,u). \tag{54}$$

Imposing these additional constraints, all factors of $\xi(\mu)\xi(\nu)$ in Table 1 are equal to one and the relations reduce exactly to the constraints given in Eqs. (18, 19) with the self-energy and two-particle vertex replaced by the one- and two-particle correlation functions. We can therefore still consider a completely imaginary one-particle correlator that is odd in frequency space and completely diagonal. The two-particle correlator is either completely real or imaginary, depending on the sign of $\xi(\kappa, \lambda)$, and all negative frequency components can be mapped to a positive counterpart.

The argument why these constraints on the disconnected correlation functions carry over to the one-particle irreducible correlation functions, i.e., the self-energy and the vertex, is the same as given for the $\mathfrak{su}(2)$ case in [27]. For the self-energy, it simply follows from the Dyson equation [30]:

$$G(1',1) = \frac{1}{i\omega - \Sigma(1',1)}, \tag{55}$$

from which it is easy to see that all constraints carry over to the self-energy. For the two-particle vertex, the tree expansion (neglecting the three-particle vertex) relates it to the connected two-particle correlation function $G^{(c)}$ as [30]

$$G^{(c)}(1',2',1,2) = -\sum_{3,4,5,6} \Gamma(3,4,5,6) G(1',3)\, G(2',4)\, G(5,1) G(6,2). \tag{56}$$

As the one-particle correlation function is diagonal in all indices, it is clear that all constraints carry over from

the connected correlation function to the two-particle vertex. That the constraints from the disconnected two-particle correlation function carry over to the connected correlation function can be proven by their definition via generating functionals [30].

4.7 Symmetries of the flow equations

To verify that the parametrization and the symmetry constraints derived in the previous sections are indeed preserved also for the flowing self-energy and two-particle vertex for any value of Λ, they can additionally be proven using the pf-FRG flow equations given in Eqs. (10, 11) . That the parametrization for the self-energy in Eq. (15) and for the two-particle vertex in Eq. (16) is indeed complete can be seen by inserting them into the RHS of the flow equations and confirming that no additional terms are generated.

For the additional symmetry constraints, the proof can be performed via induction, as already explained in Refs. [27,39]. This essentially amounts to verifying the fulfillment of the constraints in the initial conditions and then showing that the derivatives $\frac{d}{d\Lambda}\Sigma$ and $\frac{d}{d\Lambda}\Gamma$ given by the RHS of the flow equations also fulfill them, assuming the self-energy and two-particle vertex themselves already do. The proof that the self-energy is odd, imaginary, and completely diagonal has to be repeated for spin–valley models due to slight differences in the flow equations. This is quite lengthy and, therefore, done in B. For the two-particle vertex, the proof of the symmetry constraints is much easier on the level of the unparametrized vertex, as there the flow equations still have a much simpler form. We therefore postulate the relations

$$\Gamma^{\Lambda}(1',2',1,2) = \Gamma^{\Lambda}(2',1',2,1) \tag{57}$$

$$\Gamma^{\Lambda}(1',2',1,2) = \Gamma^{\Lambda}(1,2,1',2')^{*} \tag{58}$$

$$\Gamma^{\Lambda}(1',2',1,2) = \Gamma^{\Lambda}(-2',-1',-2,-1) \tag{59}$$

$$\Gamma^{\Lambda}(1',2',1,2) = s_{1'}s_1l_{1'}l_1s_{2'}s_2l_{2'}l_2 \times\Gamma^{\Lambda}(\bar{1},\bar{2},\bar{1}',\bar{2}'), \tag{60}$$

where we defined $-1 = (i_1 - \omega_1 s_1 l_1)$ and $\bar{1} = (i_1\omega_1\bar{s}_1\bar{l}_1)$. When translated to the parametrized two-particle vertex and then combined, these relations yield exactly the symmetry constraints given in Eq. (19). Proving the relations for the unparametrized vertex, therefore, directly proves the symmetry constraints of the parametrized vertex. As Eq. (57) simply amounts to a simple particle exchange, no further proof is required. Eq. (58) is proven in [27] and Eq. (59) in [39] using the general pf-FRG flow equations. The only remaining relation still left to prove is Eq. (60), which we also show in B. This proves that the parametrization and the symmetry constraints are indeed valid also for the flowing self-energy and vertex, at any value of the cut-off Λ.

5 Results

To give an explicit example for the application of the pseudo-fermion functional renormalization group approach introduced in the manuscript and its efficient implementation in terms of the aforementioned symmetries, we apply it to elucidate the phase diagram of an $\mathrm{SU}(2)_{\mathrm{spin}} \otimes \mathrm{U}(1)_{\mathrm{valley}}$ symmetric spin–valley Hamiltonian on the triangular lattice. The explicit Hamiltonian we consider is

$$\begin{aligned}\mathcal{H} = \frac{J}{8}\sum_{\langle ij\rangle}(1+\boldsymbol{\sigma}_i\boldsymbol{\sigma}_j)(1+\boldsymbol{\tau}_i\boldsymbol{\tau}_j) \\ +\frac{J_x}{8}\sum_{\langle ij\rangle}(1+\boldsymbol{\sigma}_i\boldsymbol{\sigma}_j)(\tau_i^x\tau_j^x+\tau_i^y\tau_j^y) \\ +\frac{J_z}{8}\sum_{\langle ij\rangle}(1+\boldsymbol{\sigma}_i\boldsymbol{\sigma}_j)(\tau_i^z\tau_j^z),\end{aligned} \tag{61}$$

with a SU(4) symmetric term proportional to the coupling J and an in-plane J_x and out-of-plane J_z coupling that when non-zero break the SU(4) symmetry down to an SU(2) symmetry in the spin sector and a U(1) symmetry in the valley sector. We only include interactions between nearest neighbours $\langle ij\rangle$.

Such a model can be motivated, e.g., from including the effect of Hund's type couplings in a two-orbital extended Hubbard model and performing a strong coupling expansion [20]. It can therefore be regarded as a natural extension to previously studied models with either full SU(4) or reduced $\mathrm{SU}(2)_{\mathrm{spin}} \otimes \mathrm{SU}(2)_{\mathrm{valley}}$ symmetry [18–21] by adding an XXZ type perturbation to the orbital sector and likewise provides an intermediate, but important step towards the more complicated spin–valley Hamiltonians proposed for various moiré systems [10,11,20].

5.1 Phase diagram

To obtain the quantum phase diagram, we fix the coupling J in front of the SU(4) symmetric part of the Hamiltonian in Eq. (61) to a positive value and then vary the values of the in-plane coupling J_x and out-of-plane coupling J_z which break the SU(4) symmetry. As described in Sect. 3, to determine the magnetic order for a particular pair of couplings (J_x, J_z) we calculate the flow of the spin–spin and valley–valley correlations (and associated structure factors) as defined in Eqs. (13, 14), check whether or not a flow breakdown occurs and if so, which type of order is visible in the structure factor at the breakdown scale Λ_c. Due to the $\mathrm{SU}(2)_{\mathrm{spin}} \otimes \mathrm{U}(1)_{\mathrm{valley}}$ symmetry of the Hamiltonian all non-vanishing components of the spin–spin correlation are equivalent and we calculate only $\chi_{ij}^{\Lambda s} \equiv \chi_{ij}^{\Lambda s,xx} = \chi_{ij}^{\Lambda s,yy} = \chi_{ij}^{\Lambda s,zz}$. For the valley–valley correlation, we can distinguish between in-plane and out-of-plane order by calculating the in-plane valley–

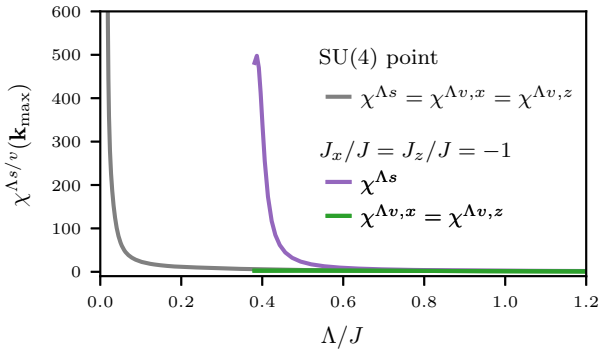

Fig. 3 Flow of the structure factor at points of higher symmetry. All structure factors are shown at the momentum where they are maximal. The grey line shows the structure factor at the SU(4) point, where the considered spin–valley model corresponds to the SU(4) symmetric Heisenberg model. Here, all structure factor components are identical. The flow is smooth and convex down to the lowest numerically reliable cut-off and no flow breakdown occurs, indicating a putative quantum spin–valley liquid (QSVL) ground state. The purple and green lines show the spin and valley structure factor for $J_x/J = J_z/J = -1$, where all terms containing valley operators cancel and the spin–valley model resembles an SU(2) symmetric Heisenberg model. In this case, the valley structure factors are strongly suppressed and the spin structure factor shows a sharp peak at the K and K' points, indicating 120° order in the spin sector

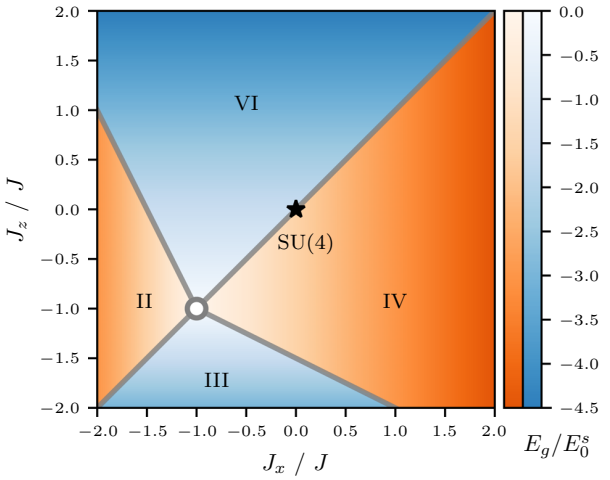

Fig. 4 Classical phase diagram in valley space for fixed spin ordering obtained from a Luttinger–Tisza analysis. The grey lines depict the phase boundaries and the color illustrates the (normalized) ground-state energy, where blue denotes out-of-plane and orange denotes in-plane ordering. At $J_x/J = J_z/J = -1$, where the phase boundaries meat, the classical mean-field Hamiltonian vanishes. Away from this point the Luttinger–Tisza analysis predicts the following types of valley order: (II) in-plane ferromagnetic (FM), (III) out-of-plane FM, (IV) in-plane 120°, and (VI) out-of-plane 120°. The so-obtained valley order is independent from the fixed nearest-neighbour spin order

valley correlation $\chi_{ij}^{\Lambda v,x} \equiv \chi_{ij}^{\Lambda v,xx} = \chi_{ij}^{\Lambda v,yy}$ and out-of-plane valley-valley correlation $\chi_{ij}^{\Lambda v,z} \equiv \chi_{ij}^{\Lambda v,zz}$.

Starting at the SU(4) point with $J_x/J = J_z/J = 0$, where all spin–spin and valley–valley correlations are equivalent, we observe no flow breakdown of the structure factors, as depicted by the grey line in Fig. 3. This indicates that no magnetic order is present in both the spin and the valley sector even for very-low-energy scales and indicates a putative quantum spin–valley liquid (QSVL) state [21]. Going away from the SU(4) point, however, we almost immediately observe a flow breakdown in either the spin or valley sector, indicating that the putative QSVL state is highly unstable in the presence of XXZ like perturbations. This is in line with results for the $\mathfrak{su}(2)$ XXZ model on the triangular lattice, where by varying the out-of-plane coupling a phase transition from in-plane 120° order to an "umbrella" order is observed at the SU(2) symmetric point [40]. Similarly, we observe a rich ensemble off different spin and valley ordered phases with both in- and out-of-plane ordering in the valley sector.

Before we present the full quantum phase diagram, however, let us first consider a classical mean-field approach to better understand the origin of the different phases. To this end, we note that the spin sector by itself will order either ferromagnetically (FM) or in a 120° order, depending on the sign of the exchange coupling. Assuming one of these states is realized, we decouple the spin and valley sector by approximating the pair of spin operators by its expectation value $\boldsymbol{\sigma}_i\boldsymbol{\sigma}_j \approx \langle\boldsymbol{\sigma}_i\boldsymbol{\sigma}_j\rangle$, with $\langle\boldsymbol{\sigma}_i\boldsymbol{\sigma}_j\rangle = 1$ for ferromagnetic (FM) and $\langle\boldsymbol{\sigma}_i\boldsymbol{\sigma}_j\rangle = \cos(2\pi/3) = -0.5$ for 120° order. The resulting mean-field Hamiltonian is then given, up to a constant, by

$$\mathcal{H}_{\mathrm{MF}} = E_0^s \sum_{\langle ij\rangle} \left[\left(1 + \frac{J_x}{J}\right)\left(\tau_i^x\tau_j^x + \tau_i^y\tau_j^y\right) + \left(1 + \frac{J_z}{J}\right)\tau_i^z\tau_j^z \right], \tag{62}$$

where the spin expectation value only appears in the positive factor $E_0^s \equiv J(1 + \langle\boldsymbol{\sigma}_i\boldsymbol{\sigma}_j\rangle)$ and, therefore, has no influence on the type of valley order. Approximating the valley operators by classical vectors with $|\boldsymbol{\tau}_i| = 1$, we perform a Luttinger–Tisza analysis [41,42] on the mean-field Hamiltonian. This analysis predicts in-plane (out-of-plane) valley order for large values of $|1 + J_x/J|$ ($|1 + J_z/J|$), which is either FM for positive, or 120° like for negative values. The precise phase boundaries along with the ground-state energies E_g are depicted in Fig. 4.

Special attention needs to be paid to the point at $J_x/J = J_z/J = -1$ where the phase boundaries meet. Exactly at this point, the couplings in front of the valley operators are equal to zero and the mean-field Hamiltonian vanishes. Going back to the full quantum Hamiltonian, it reduces to only the term $\sum_{ij} J(1 + \boldsymbol{\sigma}_i\boldsymbol{\sigma}_j)$, which resembles an SU(2) symmetric Heisenberg model

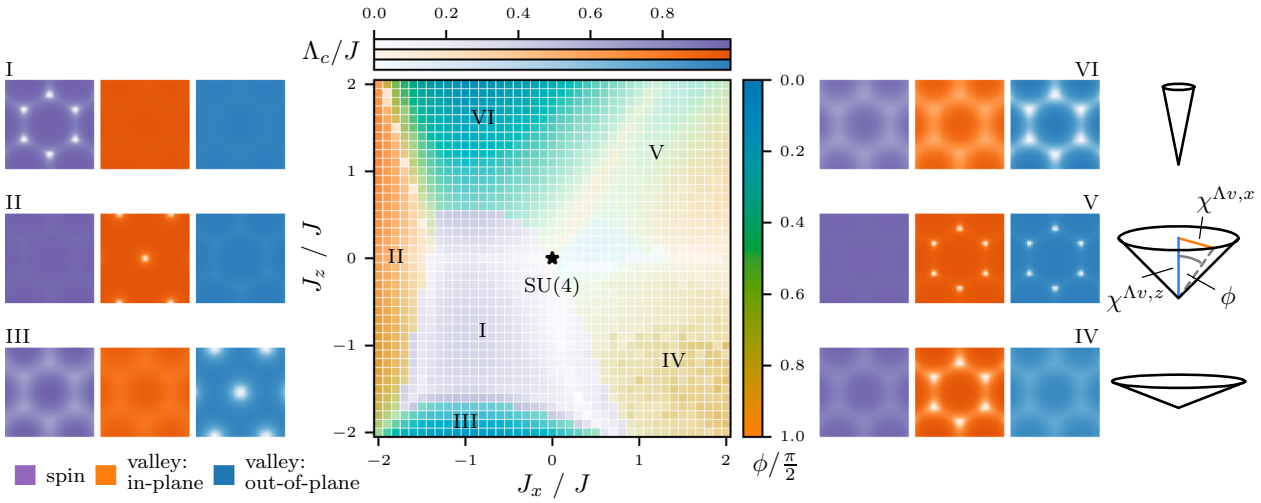

Fig. 5 Phase diagram of the $\mathrm{SU}(2)_{\mathrm{spin}} \otimes \mathrm{U}(1)_{\mathrm{valley}}$ **symmetric spin–valley model.** The color indicates which structure factor is dominant at the breakdown scale Λ_c, where purple implies dominant spin order, colors between orange and yellow indicate dominant order in the valley sector, and the opacity determines the magnitude of the breakdown scale Λ_c/J. In the case where we observe a flow breakdown in both the in-plane ($\chi^{\Lambda v,x}$) and out-of-plane ($\chi^{\Lambda v,x}$) valley structure factor the color determines the angle ϕ illustrated in the cones on the right of the figure. (I–VI) show the structure factors at Λ_c for the different types of order we observe: (I) 120° spin order, (II) out-of-plane FM valley order, (III) in-plane FM valley order, (IV-VI) 120° valley order shifting from an out-of-plane (IV) to an in-plane (VI) orientation, with competing order (V) in between. For $J_x/J = J_z/J = 0$, indicated by the star, the model is equivalent to the SU(4) symmetric Heisenberg model for which no flow breakdown is observed

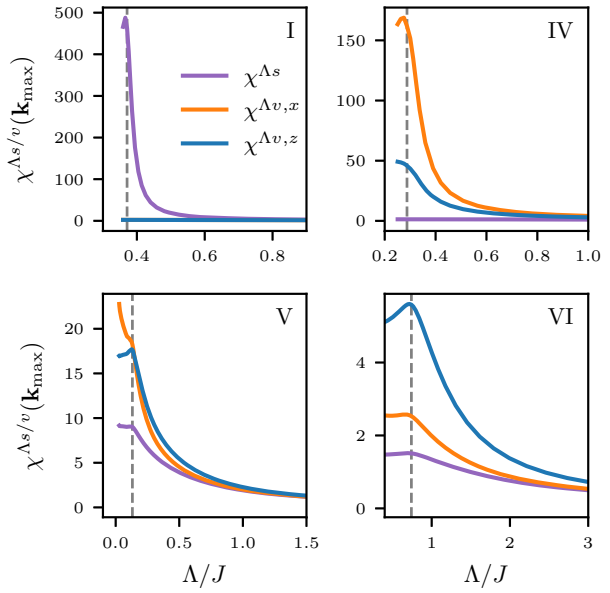

Fig. 6 Flow of the structure factors for different types of order as described under Fig. 5. The dashed lines show the breakdown scale Λ_c. (I) shows dominant spin order (purple) with the valley structure factors strongly suppressed. (IV–VI) shows dominant valley order which shifts from an in-plane (orange) to an out-of-plane (blue) orientation

with antiferromagnetic coupling J. Here, the flow of the spin structure factor shows a sharp peak, while the valley structure factors are strongly suppressed, as is depicted in Fig. 3. The same behavior occurs in a larger region around $J_x/J = J_z/J = -1$, which is shown in Fig. 5 along with the corresponding momentum resolved structure factor (annotated with the numeral I). The spin structure factor (in purple) shows strong peaks at the K and K' points, while the in-plane (orange) and out-of-plane (blue) valley structure factors show no distinct features when shown on the same color scale. This indicates 120° spin order, which again agrees with the results for the conventional $\mathfrak{su}(2)$ Heisenberg model [40,43].

In all other regions of the quantum phase diagram, the valley structure factors are clearly dominant and the spin structure factor shows only weak features. We enumerate the different types of valley order we find by the numerals II–VI, as shown in Fig. 5. The valley order at large negative couplings (II and III) agrees with the classically predicted results, as either the in- or out-of-plane structure factors show strong peaks at the Γ point, indicating FM order. At larger positive values for either the in-plane or out-of-plane coupling (VI–IV), the valley structure factors show peaks at the K and K' points indicating 120° like order. In contrast to the sharp phase boundary in the classical case, however, the valley order seems to gradually shift from mostly in-plane (IV), over competing in- and out-of-plane (V) to out-of-plane (VI) order. This is well visualized by the flow of the structure factors in Fig. 6. The valley structure factors both show flow breakdowns at approximately the same breakdown scale, but the magnitude at the breakdown scale shifts from a dominant $\chi^{\Lambda v,x}$ to

a dominant $\chi^{\Lambda v,z}$ when going from IV to VI. To quantify this transition, we define the angle

$$\phi = \arctan(\chi^{\Lambda_c v,x}/\chi^{\Lambda_c v,z}), \tag{63}$$

illustrated in Fig. 5 by the cones on the right and by the color scale ranging from from blue (in-plane) over green (competing in-plane and out-of-plane) to orange (out-of-plane)

To better illustrate the transitions between the different types of order, Figs. 7 and 8 show horizontal and vertical cuts through the phase diagram, respectively. The transitions between the phases are always accompanied by a dip or kink in the breakdown scale, indicating the positions of the phase boundaries. This is especially relevant for the transitions between mixed in- and out-of-plane valley order (V) to dominant in- or out-of-plane valley order (IV and VI), where the phase transition would not be as easily recognizable by just considering the evolution of the structure factors. The same is true for the transition from dominant valley to dominant spin order, as, e.g., depicted in the $J_x/J = 0$ cut in Fig. 8. Here, the at first very dominant out-of-plane valley order (III) gradually transitions to dominant spin order (I), with a region in between where the spin and valley structure factors are of similar magnitude. The kink in the breakdown scale appears at the largest J_z/J where the valley structure factor still shows a clear flow breakdown ($J_z/J \approx -1.6$), even though the spin structure factor is already dominant for smaller J_z/J. This is similar at all boundaries of phase I, which also becomes evident in the phase diagram of Fig. 5 by noting that the minima of the breakdown scale are positioned slightly inwards in the region of dominant spin order (colored in purple).

Of special interest are the cuts across the SU(4) point ($J_x/J = 0$ and $J_z/J = 0$), which show that even for very small values of the in- and out-of-plane couplings, the flow develops a breakdown at a finite Λ_c.

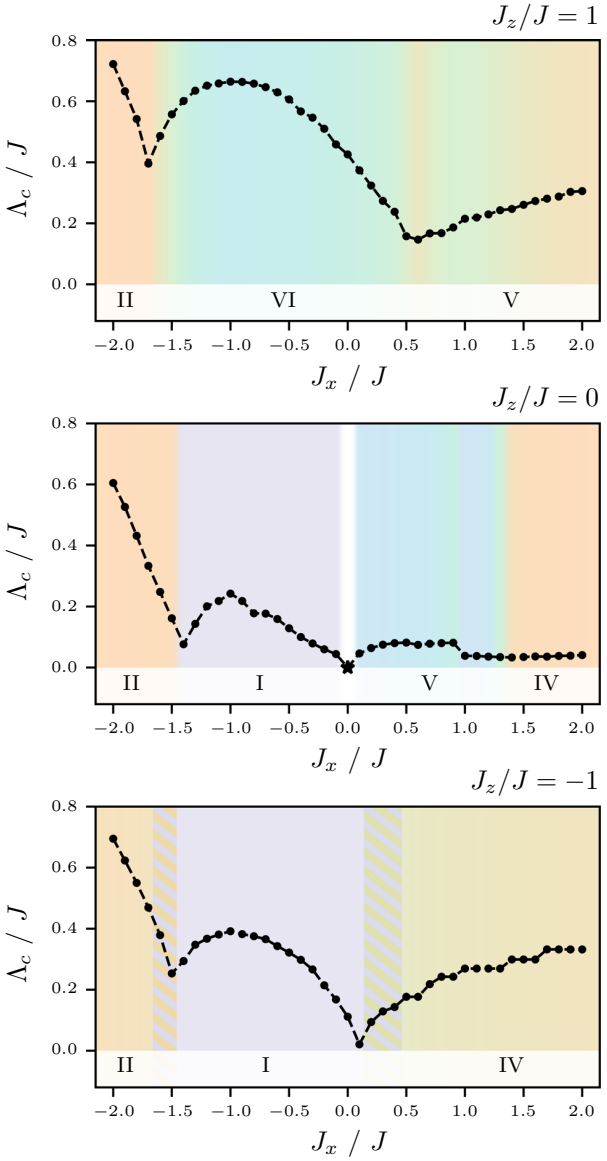

Fig. 7 Horizontal cuts through the phase diagram of Fig. 5 at $J_z/J = 1$ (top), $J_z/J = 0$ (middle) and $J_z/J = -1$ (bottom). The color-coding and the labels (I-VI) denote different types of order and are explained in Fig. 5. The transition between these phases is always accompanied by a dip or kink in the breakdown scale. In the transitions between dominant spin and valley order, there are regions where both the spin and valley structure factor show flow breakdowns at a similar Λ_c and with similar magnitudes. These regions are shaded and colored both orange and purple, as, e.g., visible in the transition between II and I along the $J_z/J = -1.0$ axis. At the SU(4) point (colored white), no flow breakdown occurs

6 Summary

In this manuscript, we have presented a generalization of the established pf-FRG approach to generic spin–valley Hamiltonians in the self-conjugate representation of $\mathfrak{su}(4)$, with either diagonal spin or valley interactions. We performed a careful symmetry analysis and derived a set of constraints on the vertex functions, which drastically lower the computational cost of tracking the flow of running couplings. Using a highly accurate solver for the functional flow equations, we subsequently applied this method to map out the quantum phase diagram of an $\mathrm{SU}(2)_{\mathrm{spin}} \otimes \mathrm{U}(1)_{\mathrm{valley}}$ model on the triangular lattice, which presents a simplified variant of the more general Hamiltonian proposed for TLG/h-BN, but already hosts a rich variety of spin and valley ordered ground states. In addition, we were able to demonstrate, that, by promoting the spin symme-

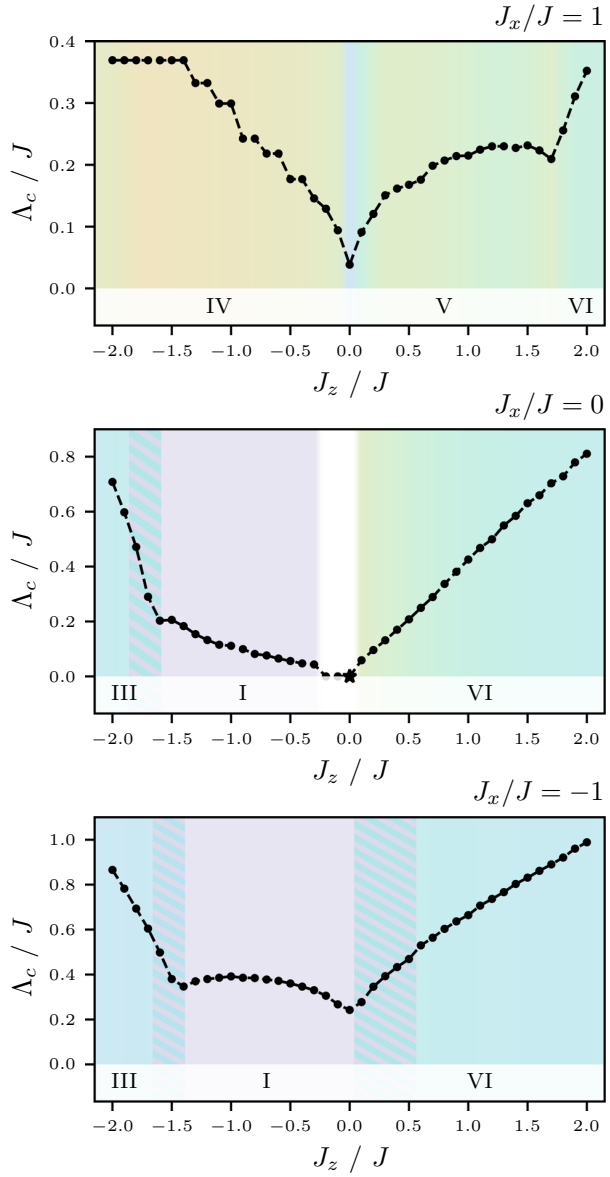

Fig. 8 Vertical cuts through the phase diagram of Fig. 5 at $J_x/J = 1$ (top), $J_x/J = 0$ (middle) and $J_x/J = -1$ (bottom). The color-coding and the labels (I–VI) denote different types of order and are explained in Fig. 5. The transition between these phases is always accompanied by a dip or kink in the breakdown scale. In the transitions between dominant spin and valley order, there are regions where both the spin and valley structure factor show flow breakdowns at a similar Λ_c and with similar magnitudes. These regions are shaded and colored both orange and blue, as e.g. visible in the transition between III and I along the $J_x/J = 0$ axis. The white regime close to the SU(4) point marks points for which no flow breakdown is observed

try group from SU(2) to SU(4), quantum fluctuations are boosted, ultimately resulting in a smooth RG flow down to the lowest energy scales, indicative of a spin–valley liquid state. However, this QSVL state appears to be very sensitive even to weak XXZ anisotropies in the valley sector, and we almost immediately detect the emergence of long-range order, when perturbing it.

While our focus in this manuscript has been on spin–valley Hamiltonians, we note that very similar models have been discussed for spin–orbit coupled systems that go beyond the celebrated Kugel–Khomskii model. The microscopic ingredients of such spin–orbital models are surprisingly similar to those of "Kitaev materials" [44]—a partially filled $4d$ or $5d$ orbital, the formation of a spin–orbital entangled local moment, and an edge-sharing octahedral crystalline environment. Specifically, a d^1 configuration can lead to local $j = 3/2$ moments subject to bond-directional exchanges that break the original SU(4) symmetry of the $j = 3/2$ moments. As a concrete material candidate exhibiting this microscopic mechanism, α-$ZrCl_3$ – a $4d$ sister compound of the isostructural Kitaev material $RuCl_3$—has been put forward [45]. To study the phase diagram of spin–orbital ground states in such a setting with varying diagonal and off-diagonal couplings, one can again rely on the pseudo-fermion FRG approach put forward in this manuscript.

Acknowledgements We thank F. L. Buessen, Y. Iqbal, and M. Scherer for discussions. Partial support from the Deutsche Forschungsgemeinschaft (DFG)—Projektnummer 277146847—SFB 1238 (project C02) is gratefully acknowledged. The numerical simulations were performed on the JURECA Booster and JUWELS cluster at the Forschungszentrum Juelich as well as the CHEOPS cluster at RRZK Cologne.

Author contributions

The main part of the PFFRG code was written by Dominik Kiese (with the Julia package PFFRGSolver.jl). Lasse Gresista (with help of Dominik Kiese) performed the symmetry analysis for the considered models, adapted the PFFRG code accordingly, and performed the calculations and data analysis. Simon Trebst supervised the study. All authors were involved in the preparation of the manuscript.

Funding Open Access funding enabled and organized by Projekt DEAL.

Data availability statement This manuscript has no associated data or the data will not be deposited. [Authors' comment: The numerical data generated and analyzed in this paper is available from the corresponding author on reasonable request.]

Appendix A: Symmetry constraints in the asymptotic frequency parametrization

In Eq. (19), we stated the symmetry constraints of the two-particle vertex in the frequency parametrization using the three transfer frequencies s, t, and u. As was discussed in Sect. 3.2, in our implementation of the pf-FRG, we use a refined frequency parametrization [23,24,37], where the vertex is split into three channels $g_c(\omega_c, v_c, v_c')$ as defined in Eq. (22), with our choice of frequencies given in Eq. (23). We can obtain symmetry constraints for the different channels by employing the same parametrization in the spin, valley, and site indices as for the full vertex

$$\begin{aligned} &g_c^\Lambda(1',2',1,2) \\ &= \Big[g_{c,i_1i_2}^{\Lambda\mu\kappa\lambda}(\omega_c,v_c,v_c')\ \theta^\mu_{s_1's_1}\theta^\mu_{s_2's_2}\theta^\kappa_{l_1'l_1}\theta^\lambda_{l_2'l_2}\ \delta_{i_1'i_1}\delta_{i_2'i_2} - \\ &\quad (1'\leftrightarrow 2')\Big]\,\delta_{\omega_{1'}+\omega_{2'},\omega_1+\omega_2}, \end{aligned} \tag{A.1}$$

and utilizing that the frequencies ω_c, v_c, v_c' can be written as linear combinations of the transfer frequencies. Combining one or more symmetry constraints of the two-particle vertex, this results in symmetry constraints for the particle–particle channel

$$\begin{aligned} g_{pp,i_1i_2}^{\Lambda\mu\kappa\lambda}(s,v_s,v_s') &= g_{pp,i_2i_1}^{\Lambda\mu\lambda\kappa}(-s,v_s,v_s') \\ g_{pp,i_1i_2}^{\Lambda\mu\kappa\lambda}(s,v_s,v_s') &= g_{pp,i_2i_1}^{\Lambda\mu\lambda\kappa}(s,-v_s,-v_s') \\ g_{pp,i_1i_2}^{\Lambda\mu\kappa\lambda}(s,v_s,v_s') &= \xi(\kappa)\xi(\lambda) g_{pp,i_2i_1}^{\Lambda,\mu\lambda\kappa},(s,v_s',v_s), \end{aligned} \tag{A.2}$$

the direct particle–hole channel

$$\begin{aligned} g_{dph,i_1i_2}^{\Lambda\mu\kappa\lambda}(t,v_t,v_t') &= \xi(\kappa)\xi(\lambda) g_{dph,i_1i_2}^{\Lambda\mu\kappa\lambda}(-t,v_t,v_t') \\ g_{dph,i_1i_2}^{\Lambda\mu\kappa\lambda}(t,v_t,v_t') &= \xi(\kappa)\xi(\lambda) g_{dph,i_1i_2}^{\Lambda\mu\kappa\lambda}(t,-v_t,-v_t') \\ g_{dph,i_1i_2}^{\Lambda\mu\kappa\lambda}(t,v_t,v_t') &= \xi(\kappa)\xi(\lambda) g_{dph,i_2i_1}^{\Lambda,\mu\lambda\kappa}(t,v_t',v_t), \end{aligned} \tag{A.3}$$

and the crossed particle–hole channel

$$\begin{aligned} g_{cph,i_1i_2}^{\Lambda\mu\kappa\lambda}(u,v_u,v_u') &= \xi(\kappa)\xi(\lambda) g_{cph,i_2i_1}^{\Lambda,\mu\lambda\kappa}(-u,v_u,v_u') \\ g_{cph,i_1i_2}^{\Lambda\mu\kappa\lambda}(u,v_u,v_u') &= \xi(\kappa)\xi(\lambda) g_{cph,i_2i_1}^{\Lambda,\mu\lambda\kappa}(u,-v_u,-v_u') \\ g_{cph,i_1i_2}^{\Lambda\mu\kappa\lambda}(u,v_u,v_u') &= \xi(\kappa)\xi(\lambda) g_{cph,i_1i_2}^{\Lambda\mu\kappa\lambda}(u,v_u',v_u), \end{aligned} \tag{A.4}$$

where for the fermionic frequencies v_c, v_c' we used the subscripts s,t,u instead of pp, dph, cph for brevity. Using these symmetry relations, we only have to explicitly calculate the two-particle vertex for positive values of ω_c and v_c, but have to also consider negative values for v_c'. Additionally, we only have to calculate components with $|v_c'| < |v_c|$. We note again that, compared to the $\mathfrak{su}2$ case, no constraints relating the particle–particle and crossed particle–hole channel are present.

Appendix B: Proof of symmetry constraints via flow equations

In Sect. 4.7, we claim that the completeness of the parametrization given in Eqs. (15, 16) and the symmetry constraints given in Eqs. (18, 19) can also be proven by induction using the flow equations, as was already done for the $\mathfrak{su}2$ case [27,39]. The proof amounts to checking that the constraints are fulfilled in the initial conditions and then showing that the RHS of the pf-FRG flow equations in Eqs. (10, 11) also fulfill the constraints, assuming the self-energy and two-particle vertex themselves already do. That the constraints are fulfilled in the initial conditions is easy to see, as for $\Lambda \to \infty$ the two-particle vertex is frequency independent and the self-energy vanishes. We will, therefore, only perform the induction step here.

Starting with the two-particle vertex, it is straightforward to see that the parametrization is complete by plugging it in the pf-FRG flow equations and showing that no additional terms are generated. To proof the symmetry constrains, we postulated equivalent constraints for the unparametrized two-particle vertex in Eqs. (57–60), which, when combined, lead to the symmetry constraints of the parametrized vertex. Fortunately, only the relation

$$\Gamma^\Lambda(1',2',1,2) = s_{1'}s_1l_{1'}l_1s_{2'}s_2l_{2'}l_2\Gamma^\Lambda(\bar{1},\bar{2},\bar{1}',\bar{2}') \tag{B.5}$$

differs from the $\mathfrak{su}(2)$ case and all other relations have already been proven [27,39]. The induction step for this relation is performed by writing down the flow equations for $s_{1'}s_1l_{1'}l_1s_{2'}s_2l_{2'}l_2\Gamma^\Lambda(\bar{1},\bar{2},\bar{1}',\bar{2}')$ and then manipulating the RHS

$$\begin{aligned} &s_{1'}s_1l_{1'}l_1s_{2'}s_2l_{2'}l_2\frac{d}{d\Lambda}\Gamma^\Lambda(\bar{1},\bar{2},\bar{1}',\bar{2}') \\ &\quad= -s_{1'}s_1l_{1'}l_1s_{2'}s_2l_{2'}l_2\frac{1}{2\pi}\sum_{3,4}\Big[\Gamma^\Lambda(\bar{1},\bar{2},3,4)\Gamma^\Lambda \\ &\quad(3,4,\bar{1}',\bar{2}') \\ &\quad -\Gamma^\Lambda(\bar{1},4,\bar{1}',3)\Gamma^\Lambda(3,\bar{2},4,\bar{2}') \\ &\quad -(3\leftrightarrow 4) + \Gamma^\Lambda(\bar{2},4,\bar{1}',3)\Gamma^\Lambda(3,\bar{1},4,\bar{2}') \\ &\quad +(3\leftrightarrow 4)\Big]G^\Lambda(\omega_3)\partial_\Lambda G^\Lambda(\omega_4) \\ &\quad\overset{(I)}{=} -\frac{1}{2\pi}\sum_{3,4}\Big[\Gamma^\Lambda(3,4,1,2)\Gamma^\Lambda(1',2',3,4) \\ &\quad -\Gamma^\Lambda(1',3,1,4)\Gamma^\Lambda(4,2',3,2) - (3\leftrightarrow 4) \\ &\quad +\Gamma^\Lambda(1',3,2,4)\Gamma^\Lambda(4,2',3,1) + (3\leftrightarrow 4)\Big] \\ &\quad\times G^\Lambda(\omega_3)\partial_\Lambda G^\Lambda(\omega_4) \\ &\quad\overset{(II)}{=} -\frac{1}{2\pi}\sum_{3,4}\Big[\Gamma^\Lambda(3,4,1,2)\Gamma^\Lambda(1',2',3,4) \end{aligned}$$

$$
\begin{aligned}
&-\Gamma^{\Lambda}(1',4,1,3)\Gamma^{\Lambda}(3,2',4,2)-(3\leftrightarrow 4)\\
&+\Gamma^{\Lambda}(3,1',4,2)\Gamma^{\Lambda}(2',4,1,3)+(3\leftrightarrow 4)\Big]\\
&\times G^{\Lambda}(\omega_3)\partial_{\Lambda}G^{\Lambda}(\omega_4)\\
=&\frac{d}{d\Lambda}\Gamma^{\Lambda}(1',2',1,2).
\end{aligned}
$$

In step I, we applied Eq. (B.5) and transformed the sum indices $\bar{3}$, $\bar{4}$ to 3 and 4 using that the propagator is odd in frequency space. In step II, we exchanged the indices $3 \leftrightarrow 4$ and applied the particle exchange symmetry [Eq. (57)] to the last term. This concludes the proof for the two-particle vertex. Due to the additional vertex components compared to the $\mathfrak{su}(2)$ case, we have to repeat the proof for the self-energy, although we will closely follow Ref. [27]. To this end, we first rewrite the relations in Eqs. (57, 60) for the parametrized vertex, but using natural frequencies

$$
\begin{aligned}
\Gamma^{\Lambda\mu\kappa\lambda}_{i_1i_2}(\omega_{1'},\omega_{2'},\omega_1,\omega_2)&=\Gamma^{\Lambda\mu\lambda\kappa}_{i_2i_1}(\omega_{2'},\omega_{1'},\omega_2,\omega_1)\\
\Gamma^{\Lambda\mu\kappa\lambda}_{i_1i_2}(\omega_{1'},\omega_{2'},\omega_1,\omega_2)&=\xi(\kappa)\xi(\lambda)\Gamma^{\Lambda\mu\kappa\lambda}_{i_1i_2}(\omega_1,\omega_2,\omega_{1'},\omega_{2'}),
\end{aligned}
$$

which directly implies

$$
\Gamma^{\Lambda\mu\kappa\lambda}_{i_1i_2}(\omega_1,\omega_2,\omega_1,\omega_2)=0 \quad \text{if} \quad \xi(\kappa)\xi(\lambda)=-1 \tag{B.6}
$$

$$
\Gamma^{\Lambda\mu\kappa\lambda}_{i_1i_1}(\omega_1,\omega_2,\omega_2,\omega_1)=\xi(\kappa)\xi(\kappa)\Gamma^{\Lambda\mu\lambda\kappa}_{i_1i_1}(\omega_1,\omega_2,\omega_2,\omega_1). \tag{B.7}
$$

Using these relations, we can simplify the self-energy flow equation

$$
\begin{aligned}
&2\pi\frac{d\Sigma(1',1)}{d\Lambda}\\
&\quad\overset{(I)}{=}\delta_{w_{1'}w_1}\delta_{i_{1'}i_1}\int d\omega_2\sum_{\mu,\kappa,\eta}\sum_{s_2,l_2}\Bigg[\sum_{i_2}\Gamma^{\Lambda\mu\kappa\lambda}_{i_1i_2}\\
&\quad\times(\omega_1,\omega_2,\omega_1,\omega_2)\theta^{\mu}_{s_{1'}s_1}\theta^{\mu}_{s_2s_2}\theta^{\kappa}_{l_{1'}l_1}\theta^{\lambda}_{l_2l_2}\\
&\quad-\Gamma^{\Lambda\mu\kappa\lambda}_{i_1i_1}(\omega_1,\omega_2,\omega_2,\omega_1)\theta^{\mu}_{s_{1'}s_2}\theta^{\mu}_{s_2s_1}\theta^{\kappa}_{l_{1'}l_2}\theta^{\lambda}_{l_2l_1}\Bigg]S^{\Lambda}(\omega_2)\\
&\quad\overset{(II)}{=}\delta_{w_{1'}w_1}\delta_{i_{1'}i_1}\delta_{s_{1'}s_1}\int d\omega_2\sum_{l_2}\Bigg[2\sum_{i_2}\Gamma^{\Lambda0\kappa\lambda}_{i_1i_2}\\
&\quad\times(\omega_1,\omega_2,\omega_1,\omega_2)\theta^{\kappa}_{l_1l_1}\theta^{\lambda}_{l_2l_2}\\
&-\sum_{\mu}\Bigg(\sum_{\kappa>\lambda>0}\Gamma^{\Lambda\mu\kappa\lambda}_{i_1i_1}(\omega_1,\omega_2,\omega_2,\omega_1)(\theta^{\kappa}_{l_{1'}l_2}\theta^{\lambda}_{l_2l_1}+\theta^{\lambda}_{l_{1'}l_2}\theta^{\kappa}_{l_2l_1})\\
&\quad+\sum_{\kappa>0}\Gamma^{\Lambda\mu\kappa0}_{i_1i_1}(\omega_1,\omega_2,\omega_2,\omega_1)(\theta^{\kappa}_{l_{1'}l_2}\theta^{0}_{l_2l_1}-\theta^{0}_{l_{1'}l_2}\theta^{\kappa}_{l_2l_1})\\
&\quad+\sum_{\kappa}\Gamma^{\Lambda\mu\kappa\kappa}_{i_1i_1}(\omega_1,\omega_2,\omega_2,\omega_1)\theta^{\kappa}_{l_{1'}l_2}\theta^{\kappa}_{l_2l_1}\Bigg)\Bigg]S^{\Lambda}(\omega_2)\\
&\quad\overset{(III)}{=}\delta_{w_{1'}w_1}\delta_{i_{1'}i_1}\delta_{s_{1'}s_1}\delta_{l_{1'}l_1}\int d\omega_2\\
&\quad\times\Bigg[4\sum_{i_2}\Gamma^{\Lambda000}_{i_1i_2}(\omega_1,\omega_2,\omega_1,\omega_2)\\
&\quad-\sum_{\mu,\kappa}\Gamma^{\Lambda\mu\kappa\kappa}_{i_1i_1}(\omega_1,\omega_2,\omega_2,\omega_1)\Bigg]S^{\Lambda}(\omega_2).
\end{aligned}
$$

In step I, we simply wrote out the self-energy flow equation using the vertex parametrization. In step II, we performed the sum over s_2 using $(\theta^{\mu})^2=\mathbb{1}$ and $\mathrm{Tr}\,\theta^{\mu}=2\delta_{\mu,0}$ and applied Eq. (B.7) to rearrange the sum over κ and λ. In step III, we perform the sum over l_2 again using $\mathrm{Tr}\,\theta^{\lambda}=2\delta_{\lambda,0}$ and $(\theta^{\kappa})^2=\mathbb{1}$ and the (anti)commutation relations $[\theta^{\kappa},\theta^{0}]=0$ and $\{\theta^{\kappa},\theta^{\lambda}\}=2\delta_{\kappa\lambda}$ (for $\kappa,\lambda>0$). In this form of the flow equation, it is clear that the self-energy indeed stays diagonal during the flow and, as all two-particle vertex components appearing in the last line are real and the single-scale propagator is imaginary, the self-energy is completely imaginary. That the self-energy is also odd in frequency space can easily be seen using Eq. (58) and the particle-exchange symmetry [Eq. (57)]. This concludes the proof for the self-energy.

References

1. Y. Cao, V. Fatemi, A. Demir, S. Fang, S.L. Tomarken, J.Y. Luo, J.D. Sanchez-Yamagishi, K. Watanabe, T. Taniguchi, E. Kaxiras, R.C. Ashoori, P. Jarillo-Herrero, Nature **556**(7699), 80 (2018). https://doi.org/10.1038/nature26154
2. C. Shen, Y. Chu, Q. Wu, N. Li, S. Wang, Y. Zhao, J. Tang, J. Liu, J. Tian, K. Watanabe et al., Nat. Phys. **16**(5), 520–525 (2020). https://doi.org/10.1038/s41567-020-0825-9
3. X. Liu, Z. Hao, E. Khalaf, J.Y. Lee, Y. Ronen, H. Yoo, D. Haei Najafabadi, K. Watanabe, T. Taniguchi, A. Vishwanath, et al., Nature **583**(7815), 221–225 (2020). https://doi.org/10.1038/s41586-020-2458-7
4. Y. Cao, D. Rodan-Legrain, O. Rubies-Bigorda, J.M. Park, K. Watanabe, T. Taniguchi, P. Jarillo-Herrero, Nature **583**(7815), 215–220 (2020). https://doi.org/10.1038/s41586-020-2260-6
5. Y. Cao, V. Fatemi, S. Fang, K. Watanabe, T. Taniguchi, E. Kaxiras, P. Jarillo-Herrero, Nature **556**(7699), 43 (2018). https://doi.org/10.1038/nature26160
6. X. Lu, P. Stepanov, W. Yang, M. Xie, M.A. Aamir, I. Das, C. Urgell, K. Watanabe, T. Taniguchi, G. Zhang, A. Bachtold, A.H. MacDonald, D.K. Efetov, Nature **574**(7780), 653 (2019). https://doi.org/10.1038/s41586-019-1695-0
7. G. Chen, A.L. Sharpe, P. Gallagher, I.T. Rosen, E.J. Fox, L. Jiang, B. Lyu, H. Li, K. Watanabe, T. Taniguchi, J. Jung, Z. Shi, D. Goldhaber-Gordon, Y. Zhang, F. Wang, Nature **572**(7768), 215 (2019). https://doi.org/10.1038/s41586-019-1393-y
8. A.L. Sharpe, E.J. Fox, A.W. Barnard, J. Finney, K. Watanabe, T. Taniguchi, M.A. Kastner, D. Goldhaber-Gordon, Science **365**(6453), 605 (2019). https://doi.org/10.1126/science.aaw3780
9. M. Koshino, N.F.Q. Yuan, T. Koretsune, M. Ochi, K. Kuroki, L. Fu, Phys. Rev. X **8**, 031087 (2018). https://doi.org/10.1103/PhysRevX.8.031087
10. L. Xian, D.M. Kennes, N. Tancogne-Dejean, M. Altarelli, A. Rubio, Nano Lett. **19**(8), 4934–4940 (2019). https://doi.org/10.1021/acs.nanolett.9b00986
11. Y.H. Zhang, T. Senthil, Phys. Rev. B **99**, 205150 (2019). https://doi.org/10.1103/PhysRevB.99.205150
12. C. Xu, L. Balents, Phys. Rev. Lett. **121**(8), 087001 (2018). https://doi.org/10.1103/PhysRevLett.121.087001

13. N.F.Q. Yuan, L. Fu, Phys. Rev. B **98**, 045103 (2018). https://doi.org/10.1103/PhysRevB.98.045103
14. H.C. Po, L. Zou, A. Vishwanath, T. Senthil, Phys. Rev. X **8**, 031089 (2018). https://doi.org/10.1103/PhysRevX.8.031089
15. L. Classen, C. Honerkamp, M.M. Scherer, Phys. Rev. B **99**(19), 195120 (2019). https://doi.org/10.1103/PhysRevB.99.195120
16. K.I. Kugel, D.I. Khomskiĭ, Sov. Phys. Usp. **25**(4), 231 (1982). https://doi.org/10.1070/pu1982v025n04abeh004537
17. L.F. Feiner, A.M. Oleś, J. Zaanen, Phys. Rev. Lett. **78**, 2799 (1997). https://doi.org/10.1103/PhysRevLett.78.2799
18. P. Corboz, M. Lajkó, A.M. Läuchli, K. Penc, F. Mila, Phys. Rev. X **2**, 041013 (2012). https://doi.org/10.1103/PhysRevX.2.041013
19. W.M.H. Natori, E.C. Andrade, R.G. Pereira, Phys. Rev. B **98**(19), 195113 (2018). https://doi.org/10.1103/PhysRevB.98.195113
20. W.M.H. Natori, R. Nutakki, R.G. Pereira, E.C. Andrade, Phys. Rev. B **100**(20) (2019). https://doi.org/10.1103/PhysRevB.100.205131
21. D. Kiese, F.L. Buessen, C. Hickey, S. Trebst, M.M. Scherer, Phys. Rev. Res. **2**(1), 013370 (2020). https://doi.org/10.1103/PhysRevResearch.2.013370
22. J. Reuther, P. Wölfle, Phys. Rev. B **81**(14), 144410. https://doi.org/10.1103/PhysRevB.81.144410
23. J. Thoenniss, M.K. Ritter, F.B. Kugler, J. von Delft, M. Punk, arXiv:2011.01268
24. D. Kiese, T. Mueller, Y. Iqbal, R. Thomale, S. Trebst, arXiv:2011.01269
25. R. Bistritzer, A.H. MacDonald, PNAS **108**(30), 12233 (2011). https://doi.org/10.1073/pnas.1108174108
26. D.I. Khomskii, *Transition Metal Compounds* (Cambridge University Press, 2014)
27. F.L. Buessen, V. Noculak, S. Trebst, J. Reuther, Phys. Rev. B **100**(12), 125164 (2019). https://doi.org/10.1103/PhysRevB.100.125164
28. F.L. Buessen, D. Roscher, S. Diehl, S. Trebst, Phys. Rev. B **97**(6), 064415 (2018). https://doi.org/10.1103/PhysRevB.97.064415
29. C. Wetterich, Phys. Lett. B **301**, 90 (1993). https://doi.org/10.1016/0370-2693(93)90726-X
30. P. Kopietz, L. Bartosch, F. Schütz, *Introduction to the Functional Renormalization Group* (Springer, Berlin, 2010)
31. A.A. Katanin, Phys. Rev. B **70**(11), 115109 (2004). https://doi.org/10.1103/PhysRevB.70.115109
32. F.B. Kugler, J. von Delft, Phys. Rev. B **97**(3), 035162 (2018). https://doi.org/10.1103/PhysRevB.97.035162
33. J. Reuther, R. Thomale, Phys. Rev. B **89**, 024412 (2014). https://doi.org/10.1103/PhysRevB.89.024412
34. F.L. Buessen, M. Hering, J. Reuther, S. Trebst, Phys. Rev. Lett. **120**, 057201 (2018). https://doi.org/10.1103/PhysRevLett.120.057201
35. J.W.F. Venderbos, R.M. Fernandes, Phys. Rev. B **98**(24), 245103 (2018). https://doi.org/10.1103/PhysRevB.98.245103
36. A. Keselman, L. Savary, L. Balents, SciPost Phys. **8**, 76 (2020). https://doi.org/10.21468/SciPostPhys.8.5.076
37. N. Wentzell, G. Li, A. Tagliavini, C. Taranto, G. Rohringer, K. Held, A. Toschi, S. Andergassen, Phys. Rev. B**102**(8), 085106 (2020). https://doi.org/10.1103/PhysRevB.102.085106
38. P. Bogacki, L.F. Shampine, Appl. Math. Lett. **2**(4), 321 (1989). https://doi.org/10.1016/0893-9659(89)90079-7
39. J. Reuther, PhD thesis, Karlsruhe (2011). https://doi.org/10.5445/IR/1000023236
40. D. Sellmann, X.F. Zhang, S. Eggert, Phys. Rev. B **91**(8), 081104 (2015). https://doi.org/10.1103/PhysRevB.91.081104
41. J.M. Luttinger, L. Tisza, Phys. Rev. **70**(11–12), 954 (1946). https://doi.org/10.1103/PhysRev.70.954
42. J.M. Luttinger, Phys. Rev. **81**(6), 1015 (1951). https://doi.org/10.1103/PhysRev.81.1015
43. J. Reuther, R. Thomale, Phys. Rev. B **83**, 024402 (2011). https://doi.org/10.1103/PhysRevB.83.024402
44. S. Trebst, C. Hickey, Phys. Rep. **950**, 1 (2022). https://doi.org/10.1016/j.physrep.2021.11.003
45. M. Yamada, M. Oshikawa, G. Jackeli, Phys. Rev. Lett. **121**, 097201 (2018). https://doi.org/10.1103/PhysRevLett.121.097201

6 fRG studies on strongly correlated electrons

6.1 Overview

In this section, we present model studies of different strongly correlated electron systems. Starting in the weak-coupling limit, we employ N-patch and truncated-unity fRG to compute the renormalized interaction for spin-polarized fermions on the triangular lattice (see Ref. [P4]). For once, this allows us to study Fermi liquid instabilities of electrons in isolated bands of transition metal dichalcogenide heterostructures. The simplicity of the model, on the other hand, enables a detailed comparison of the two momentum space approximations. Considering both, attractive and repulsive nearest-neighbor interactions, we demonstrate agreement of the methods with regard to the produced phase diagrams, especially close to van-Hove filling. The predicted critical scales, however, are slightly off, which could be attributed to the neglect of fluctuations away from the Fermi level in the N-patch scheme.

In Ref. [P5], we consider antiferromagnetic Heisenberg models on the kagome lattice. The latter have a long history in the quest for finding spin liquid materials, with herbertsmithite ($ZnCu_3(OH)_6Cl_2$) being one of the most prominent candidates. One intriguing feature of the kagome antiferromagnet (KAFM) is the possibility to rewrite its Hamiltonian in terms of local constraints on every triangular plaquette, which, if simultaneously fulfilled, make for a *classical* ground state. Since many such configurations exist, this gives rise to an extensive degeneracy of minimal energy states - a Coloumb spin liquid with algebraically decaying real space correlations and pinch points in the static structure factor. This Coloumb phase has recently been demonstrated to survive even upon perturbing the KAFM with second and third neighbor interactions of equal strength J [145]. If J is further increased, however, the pinch points give rise to arc-like features dubbed half-moons. For $J/J_1 = 1$, where J_1 characterizes the nearest-neighbor Heisenberg interaction, the half-moons from different Brillouin zones merge into stars, bringing about yet another configuration of the classical spins. In our publication, we access the quantum phase diagram of this model from different many-body methods such as pffRG, DMRG and variational Monte Carlo simulations. Our main findings can be summarized as follows: (a) We find the quantum spin liquid phase of the KAFM to be stable beyond its classical extent. (b) For $J \approx 0.27 - 0.3$, one observes the opening of half-moons in the structure factor. In real space, the half-moon phase corresponds to a pinwheel VBC in which reflection symmetries of the lattice are broken. Such a state was recently suggested as one possible instability of the QSL phase [146]. (c) For large J, we find a long-range ordered ground state characterized by incipient Bragg peaks forming a star pattern. Our results provide solid evidence for a regime of enhanced stability of the KAFM spin liquid, which has so far been regarded as quite susceptible to additional perturbations [117, 147, 148]. Hereby, the QSL candidate $YCu_3(OH)_6Br_2[Br_x(OH)_{1-x}]$ [149] might serve as motivation for further explorations of the phase diagram and the investigation of exotic many-body states possibly emerging therein.

Refs. [P6, P7] are devoted to two exemplary pffRG studies of frustrated magnets in moiré heterostructures. In particular, we map out the phase diagram of twisted tungsten diselenide in Ref. [P6], finding an overly rich variety of commensurate and incommensurate magnetic orders with small regimes of spin liquid behavior. The effective model considered for $tWSe_2$ resembles a pure spin-1/2 Hamiltonian, albeit with Dzyaloshinski-Moriya interactions which break inversion symmetry [82, 83]. In Ref. [P7], on the contrary, we study the effect of Hund's type couplings on the stability of quantum spin-valley liquids (QSVLs), finding that the QSVL states are remarkably robust with respect to SU(4)-breaking interactions. Both our papers establish moiré materials as an exciting platform not only for the emergence of superconducting phases, but also for exhibiting fascinating physics in the insulating regime.

Relevant publications:

[P4] *Functional renormalization of spinless triangular-lattice fermions: N-patch vs. truncated-unity scheme*
N. Gneist, **D. Kiese**, R. Henkel, L. Classen, and M. M. Scherer
arXiv:2205.12547

[P5] *Pinch-points to half-moons and up in the stars: the kagome skymap*
D. Kiese, F. Ferrari, N. Astrakhantsev, N. Niggemann, P. Ghosh, T. Müller, R. Thomale, T. Neupert, J. Reuther, M. J. P. Gingras, S. Trebst, and Y. Iqbal
arXiv:2206.00264

[P6] *TMDs as a platform for spin liquid physics: A strong coupling study of twisted bilayer WSe_2*
D. Kiese, Y. He, C. Hickey, A. Rubio, and D. M. Kennes
APL Materials 10, 031113 (2022)

[P7] *Emergence and stability of spin-valley entangled quantum liquids in moiré heterostructures*
D. Kiese, F. L. Buessen, C. Hickey, S. Trebst, and M. M. Scherer
Physical Review Research 2, 013370 (2020)

Author contributions: *D. Kiese implemented and operated the N-patch fRG code used to produce the results in Ref. [P4]. The author of this thesis was responsible for setting up the pffRG simulations in Refs. [P5–P7], where he also prepared the respective plots. D. Kiese actively participated in the writing of all manuscripts.*

EPJ manuscript No.
(will be inserted by the editor)

Functional renormalization of spinless triangular-lattice fermions: N-patch vs. truncated-unity scheme

Nico Gneist[1], Dominik Kiese[1], Ravn Henkel[1], Ronny Thomale[2], Laura Classen[3], and Michael M. Scherer[4]

[1] Institute for Theoretical Physics, University of Cologne, 50937 Cologne, Germany
[2] Institute for Theoretical Physics, University of Würzburg, Am Hubland, D-97074 Würzburg, Germany
[3] Max Planck Institute for Solid State Research, D-70569 Stuttgart, Germany
[4] Institute for Theoretical Physics III, Ruhr-University Bochum, D-44801 Bochum, Germany

May 26, 2022

Abstract. We study competing orders of spinless fermions in the triangular-lattice Hubbard model with nearest-neighbor interaction. We calculate the effective, momentum-resolved two-particle vertex in an unbiased way in terms of the functional renormalization group method and compare two different schemes for the momentum discretization, one based on dividing the Fermi surface into patches and one based on a channel decomposition. We study attractive and repulsive nearest-neighbor interaction and find a competition of pairing and charge instabilities. In the attractive case, a Pomeranchuk instability occurs at Van Hove filling and f-wave and p-wave pairing emerge when the filling is reduced. In the repulsive case, we obtain a charge density wave at Van Hove filling and extended p-wave pairing with reduced filling. The p-wave pairing solution is doubly degenerate and can realize chiral $p + ip$ superconductivity with different Chern numbers in the ground state. We discuss implications for strongly correlated spin-orbit coupled hexagonal electron systems such as moiré heterostructures.

1 Introduction

For decades the single-band Hubbard model has been the Standard Model of Correlated Electron Physics. Not only has it been thought of as capturing essential features of the phase diagram of high-temperature superconductors and related materials, it has also served as a reference model for the development of quantum many-body methods [1].

In terms of Fermi surface instabilities, the square lattice has been the dominating focus of theoretical research as it has been hosting the majority of quasi-two dimensional candidate materials for strongly correlated electron systems. More recently, however, the discovery of strongly-correlated states in moiré materials, i.e. systems based on few-layer stacks of two-dimensional materials such as graphene or transition metal dichalcogenides (TMD) [2–6], has made a strong case for revisiting hexagonal lattice systems of correlated electrons from the viewpoint of state-of-the-art quantum many-body approaches [7–14].

Kagome, honeycomb, and triangular lattices all share the same hexagonal point group symmetry but differ in terms of Wyckoff positions taken by their respective lattice sites. The triangular lattice stands out as the local site symmetry matches that of the hexagonal point group symmetry. It has a high potential to offer exotic many-body states due an intricate interplay between frustration and correlations, see, e.g., [15–23] for a recent series of studies on that matter.

In systems such as TMDs, a sizable spin-orbit coupling breaks the spin-rotation invariance. As a consequence, effective models for moiré TMDs often involve several spin-split bands [24–26] which need to be taken into account by adequate quantum many-body approaches. In an attempt to boil down moiré TMDs to its fermiological essence, this can thus lead to an effective model of spin-polarized interacting electrons (or spinless fermions). Note that in the absence of local Hubbard repulsion due to the removed spin degree of freedom, nearest-neighbor density-density interactions are the most elementary terms to consider, which we adopt for our paradigmatic toy model in the following.

A method that has been shown to be quite flexible when it comes to the description of competing instabilities of correlated-electron systems on various lattice geometries and for a broad range of fillings and interactions, is the functional renormalization group (FRG) [27–29]. The FRG has been used in numerous studies to identify the leading Fermi-surface instabilities with all competing interaction channels being treated on equal footing [30,31] Within the correlated-electron FRG different schemes have been employed for numerical implementations, most prominently the N-patch scheme, which divides the Brillouin zone into a number of N patches with the representative momenta lying on the Fermi surface [32]. The N-patch scheme allows for a relatively simple and straightforward numerical implementation, but becomes numerically expensive for high

momentum resolution and also does not faithfully incorporate momentum conservation. More recently, an alternative scheme – the truncated-unity scheme [33] (TUFRG) – based on a decomposition of the different interaction channels [34] has been devised, which separates stronger and weaker momentum dependencies and therefore allows for a more efficient numerical evaluation at high momentum resolution.

In this work, we establish the correlated phase diagram of of spinless electrons on the triangular lattice in the presence of competing interaction channels around Van Hove filling. To that end, we set up both, an N-Patch- and a TUFRG approach for correlated fermions without spin-SU(2) invariance. We carefully study the convergence within both schemes and compare them to each other. The motivation of our work is twofold:

1. The FRG represents a very promising scheme for setting up sophisticated numerical implementations that can capture accurate multi-orbital/-band models for moiré TMDs. Our results can then be used for future reference of such implementations.

2. The systematic quantitative comparison between the two FRG schemes provides guidance to the choice of transfer-momentum resolution and form-factor expansions in future TUFRG studies, which are likely to be more appropriate for a faithful description of more involved models due to numerical efficiency.

2 Model

We consider a tight-binding model for spinless fermions on the triangular lattice where we add a nearest-neighbor density-density interaction, reading

$$H = -t\sum_{\langle ij\rangle}\left(c_i^\dagger c_j + \text{h.c.}\right) - \mu\sum_i n_i + V_1\sum_{\langle ij\rangle} n_i n_j\,. \quad (1)$$

Here the operator $c_i^{(\dagger)}$ annihilates (creates) a fermion on lattice site i, such that we allow for nearest-neighbor fermion hopping with rate t. The fermion density operator $n_i = c_i^\dagger c_i$ couples to the chemical potential μ to change the filling of the system and $V_1 > 0$ (< 0) is the strength of the repulsive (attractive) density interaction of neighboring fermions (see Fig. 1). We will study the effects of attractive and repulsive interactions for an extended range of fillings corresponding to μ. The energy band of this model is given via a Fourier transform, yielding

$$\xi(\boldsymbol{k}) = -2t[\cos(k_x) + 2\cos(k_x/2)\cos(\sqrt{3}k_y/2)] - \mu\,, \quad (2)$$

with wavevector $\boldsymbol{k} = (k_x, k_y)$. We note that at $\mu/t = 2$ the band dispersion features saddle points at the three inequivalent $\boldsymbol{M}$ points of the Brillouin zone (BZ) (Fig. 1), giving rise to a Van Hove singularity (VHS). Our investigations of the emergent many-body instabilities of the system will be carried out in the vicinity of the VHS, but also beyond.

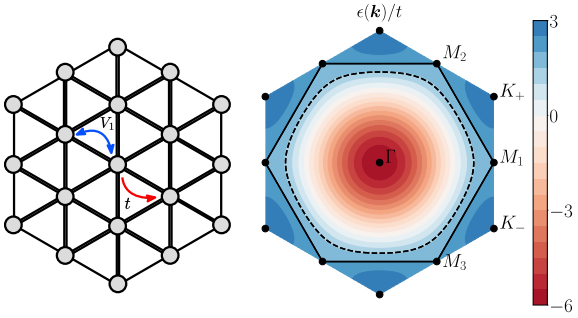

Fig. 1. Real-space lattice and dispersion in the BZ. The solid line in the right panel shows the perfectly nested Fermi surface for $\mu/t = 2$ which corresponds to Van Hove filling. The dashed line shows the Fermi surface for $\mu/t = 1.4$.

3 Fermionic functional renormalization group

The fermionic functional renormalization group (FRG) [27, 28] has been established as a versatile approach to treat strongly-correlated electrons without bias towards a specific mean-field channel [30, 31]. It is rooted in the functional integral description of quantum many-body systems and it allows for the investigation of a broad range of models without specific limitations for their kinetic or interaction parameters. Generally, the FRG acts as functional implementation of the Wilsonian renormalization-group (RG) idea, namely, one starts at an ultraviolet (UV) cutoff scale Λ_{UV} and successively takes effects of fermionic fluctuations into account by approaching the infrared (IR) limit $\Lambda_{\text{IR}} = 0$.

While the FRG description of a selected model is at a formal level exact, one needs to decide for truncations of the description to derive a feasible numerical application from the general principles. In the situation of competing interactions, this truncation will mostly concentrate on the evolution of the two-particle vertex as an indicator for emerging Fermi-surface instabilities. In the past, this has led to many successful applications of the method to strongly-correlated electron systems, for example, for models of spin-rotational invariant electrons on triangular and honeycomb lattices, see, e.g., [8–13, 35–39]. In addition more specific models of these geometries have been investigated aiming at the description moiré materials [23, 40–44].

The FRG flow is realized by solving a system of coupled differential equations interpolating between the UV and the IR limit. In this work, we want to compare two specific computational schemes to track this FRG evolution of running couplings: (1) the N-*patch* scheme, which was one of the first well-established methods within the fermionic FRG framework, and (2) the *truncated-unit FRG*, a more recent approach which goes beyond the patching scheme and allows for a finer grained momentum resolution.

3.1 Flow equations

Our starting point is the action for a many-electron system

$$S[\bar{\psi},\psi] = -(\bar{\psi}, G_0^{-1}\psi) + S_{\text{int}}[\bar{\psi},\psi]\,, \tag{3}$$

where $\bar{\psi},\psi$ are Grassmann-valued fields. Here, the quadratic term includes the free propagator $G_0(\omega,\boldsymbol{k}) = 1/(i\omega - \xi(\boldsymbol{k}))$ with Matsubara frequency ω and single-particle dispersion $\xi(\boldsymbol{k})$, and the bracket $(.,.)$ denotes integrations over continuous and summations over discrete indices. The second term $S_{\text{int}}[\bar{\psi},\psi]$ in Eq. (3) is an interaction term, which can be read off directly from the interaction part of the microscopic Hamiltonian in Eq. (1). With the help of the action S, we can define the Schwinger functional $\mathcal{G}[\bar{\eta},\eta] = -\ln\int D\psi D\bar{\psi}\exp(-S[\bar{\psi},\psi])\exp[(\bar{\eta},\psi)+(\bar{\psi},\eta)]$ and its Legendre transform - the effective action - $\Gamma[\bar{\psi},\psi] = (\bar{\eta},\psi)+(\bar{\psi},\eta)+G[\bar{\eta},\eta]$ with $\psi = -\partial G/\partial\bar{\eta}$ and $\bar{\psi} = \partial G/\partial\eta$, which generates the one-particle irreducible (1PI) correlation functions [45].

The central step for setting up the renormalization group scheme amounts to regularizing the free propagator by an infrared cutoff Λ, such that $G_0(\omega,\boldsymbol{k}) \to G_0^{\Lambda}(\omega,\boldsymbol{k})$. The cutoff implementation is, in some sense, arbitrary, as long as the ultraviolet ($\Lambda\to\infty$) and infrared limit ($\Lambda\to 0$) are smoothly connected. Here, we opt for implementing the temperature flow scheme introduced by Honerkamp and Salmhofer [46] which is employed for both FRG implementations. For now, however, we will keep the discussion general and refer the reader to App. A for details on the T-flow.

Having regularized the bare propagator, the effective action $\Gamma[\bar{\psi},\psi]$ becomes scale dependent and its flow is governed by an exact differential equation [47], which reads

$$\frac{\partial}{\partial\Lambda}\Gamma^{\Lambda} = -(\bar{\psi},(\dot{G}_0^{\Lambda})^{-1}\psi) - \frac{1}{2}\mathrm{Tr}\left((\dot{\mathbf{G}}_0^{\Lambda})^{-1}(\mathbf{\Gamma}^{(2)\Lambda})^{-1}\right)\,, \tag{4}$$

where $\mathbf{\Gamma^{(2)\Lambda}} = (\partial_{\bar{\psi}},\partial_{\psi})^T(\partial_{\psi},\partial_{\bar{\psi}})\Gamma^{\Lambda}$ is the matrix of second derivatives of Γ^{Λ}. Here, the appearance of the matrix of second functional derivatives of the effective action $\mathbf{\Gamma}^{(2)}$ necessitates some truncation to derive a closed set of equations for the 1PI vertex functions. We employ a standard approximation scheme, which (1) neglects self-energy insertions, such that undifferentiated fermion lines correspond to bare, unrenormalized propagators, (2) sets external Matsubara frequency arguments to zero and, simultaneously, does not account for the frequency dependence of the two-particle vertex and (3) truncates the three-particle vertex from the flow equations (an in-depth discussion of these approximations is reviewed in [30]). As a result, we obtain flow equations for the static two-particle vertex $V(\boldsymbol{k}_1,\boldsymbol{k}_2,\boldsymbol{k}_3)$ (the fourth momentum is fixed by momentum conservation), which allow us to determine Fermi liquid instabilities in an unbiased way.

For spinless fermions, the flow equations read [48, 49]

$$\frac{d}{d\Lambda}V^{\Lambda} = \tau_{\text{pp}} + \tau_{\text{ph,c}} + \tau_{\text{ph,d}}\,. \tag{5}$$

where

$$\begin{aligned}\tau_{\text{pp}} = -\frac{1}{2}\int_q \frac{d}{d\Lambda}&[G_0^{\Lambda}(i\omega,\boldsymbol{q}+\boldsymbol{k}_1+\boldsymbol{k}_2)G_0^{\Lambda}(-i\omega,-\boldsymbol{q})]\\ &\times V^{\Lambda}(\boldsymbol{k_1},\boldsymbol{k_2},\boldsymbol{q}+\boldsymbol{k_1}+\boldsymbol{k_2})\\ &\times V^{\Lambda}(\boldsymbol{q}+\boldsymbol{k}_1+\boldsymbol{k}_2,-\boldsymbol{q},\boldsymbol{k}_3)\,,\end{aligned} \tag{6}$$

denotes the pairing or particle-particle channel

$$\begin{aligned}\tau_{\text{ph,c}} = -\int_q \frac{d}{d\Lambda}&[G_0^{\Lambda}(i\omega,\boldsymbol{q}+\boldsymbol{k}_1-\boldsymbol{k}_4)G_0^{\Lambda}(i\omega,\boldsymbol{q})]\\ &\times V^{\Lambda}(\boldsymbol{k}_1,\boldsymbol{q},\boldsymbol{q}+\boldsymbol{k}_1-\boldsymbol{k}_4)\\ &\times V^{\Lambda}(\boldsymbol{q}+\boldsymbol{k}_1-\boldsymbol{k}_4,\boldsymbol{k}_2,\boldsymbol{k}_3)\,,\end{aligned} \tag{7}$$

the crossed particle-hole channel and

$$\begin{aligned}\tau_{\text{ph,d}} = +\int_q \frac{d}{d\Lambda}&[G_0^{\Lambda}(i\omega,\boldsymbol{q}+\boldsymbol{k}_1-\boldsymbol{k}_3)G_0^{\Lambda}(i\omega,\boldsymbol{q})]\\ &\times V^{\Lambda}(\boldsymbol{k}_1,\boldsymbol{q},\boldsymbol{k}_3)\\ &\times V^{\Lambda}(\boldsymbol{q}+\boldsymbol{k}_1-\boldsymbol{k}_3,\boldsymbol{k}_2,\boldsymbol{q})\,,\end{aligned} \tag{8}$$

the direct particle-hole channel, respectively. Here the integral is defined as $\int_k = A_{\text{BZ}}^{-1}T\int_{\text{BZ}}d\boldsymbol{k}\sum_{i\omega}$ and $k=(\boldsymbol{k},\omega)$ where A_{BZ} is the area of the Brillouin zone.

Integrating these equations starting with the bare coupling in the $\Lambda\to\infty$ limit, Fermi liquid instabilities are signified by singular contributions to V. We note that V is a function of three momenta and it is therefore costly to compute. For this reason, we rely on further approximations for its momentum dependence, two of which are presented in the following.

3.2 N-patch FRG

The first, well-established approximation of the momentum dependence assumes that the two-particle vertex is constant along elongated *patches* in momentum space [30].

To implement the patching scheme, we define a mapping $\pi : 1.\text{BZ} \to \mathbb{Z}_{\text{FS}}^N$, identifying momenta $\boldsymbol{k}$ in the first Brillouin zone with their nearest-neighbor $\pi(\boldsymbol{k})$ in an angular discretization $\mathbb{Z}_{\text{FS}}^N$ of the Fermi surface, which consists of N points, see Fig. 2. This way, irrelevant couplings perpendicular to the Fermi surface are projected out and the vertex is fully determined by its value on the central patch points, which we place equidistantly. Note, that this treatment of the momentum dependence of the vertex spoils momentum conservation, since the fourth momentum $\boldsymbol{k}_4 = \pi(\boldsymbol{k}_1)+\pi(\boldsymbol{k}_2)-\pi(\boldsymbol{k}_3)$ of the projected vertex $V(\pi(\boldsymbol{k}_1),\pi(\boldsymbol{k}_2),\pi(\boldsymbol{k}_3))$ will in general not align with a patch point and therefore require an additional transformation with π.

N-patch FRG calculations were successfully employed to track the flow of marginal couplings for prototypical model systems of high-T_c superconductivity such as iron

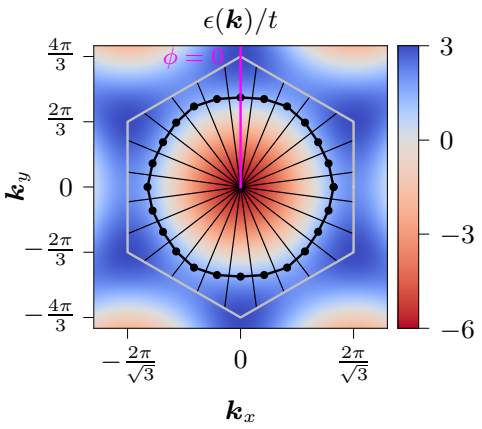

Fig. 2. Illustration of the N-patch FRG scheme for $N = 24$ points on the Fermi surface (thick black line). The patches, indicated by thin black lines, range from the $\boldsymbol{\Gamma}$ point to the boundary of the first Brillouin zone (thick grey line). Our results are produced with $N = 192$. The reference patch for the angular discretization is indicated by a thin magenta line.

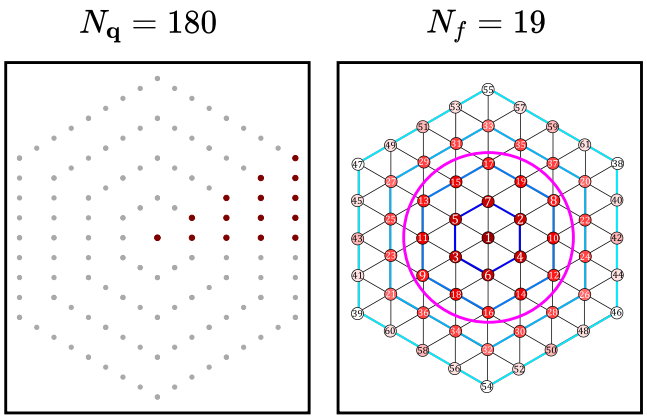

Fig. 3. Illustration of the TUFRG resolutions. Left: for the comparison with the patching scheme, $N_{\boldsymbol{q}} = 180$ momentum points were chosen which are evenly spaced in the Brillouin zone. Only the contributions of the red points have to be calculated since the rest can be obtained by symmetry operations. Right: The plane-wave form factors are $f_l(\boldsymbol{k}) = \exp(i\boldsymbol{k}\boldsymbol{R}_l)$, where $\boldsymbol{R}_l$ are the real space vectors. Our results are produced with $N_f = 19$ (inside the magenta circle) unless stated otherwise. For more details see App. B.2.

pnictides and cuprates, see, e.g., Refs. [29–31] and references therein. This legitimates the method as a valid starting point to determine the leading instabilities around the Fermi surface fixed point.

In summary, the patching scheme describes the vertex with three projected momenta, i.e. $V(\pi(\boldsymbol{k}_1), \pi(\boldsymbol{k}_2), \pi(\boldsymbol{k}_3))$, such that for a selection of N patches, the numerical cost will scale with N^3. In this work, we implemented a resolution of the Fermi surface using $N = 192$ patches.

3.3 Truncated-unity FRG

The truncated-unity FRG (TUFRG) [33] allows for a high resolution of the full Brillouin zone, i.e. in contrast to the N-patch scheme, it is not restricted to the Fermi surface. Instead, one can chose arbitrary points of momenta to evaluate the flow equations. The derivation of the TUFRG approach is based on the fact that the singular behaviour of instabilities are mainly depending on the transfer momenta inside the loops in Eqs. (6)–(8) connecting the two vertices [34]. Specifically, they are $\boldsymbol{k}_1 + \boldsymbol{k}_2$ in τ_{pp}, $\boldsymbol{k}_1 - \boldsymbol{k}_4$ in $\tau_{ph,c}$ and $\boldsymbol{k}_1 - \boldsymbol{k}_3$ in $\tau_{ph,d}$. Consequently, the interaction is reparametrized into different channels such that each object is accounting for one of the transfer momenta. In practice, V^Λ is decomposed as

$$\begin{aligned} V^\Lambda(\boldsymbol{k}_1, \boldsymbol{k}_2, \boldsymbol{k}_3, \boldsymbol{k}_4) = V^{\Lambda,0}(\boldsymbol{k}_1, \boldsymbol{k}_2, \boldsymbol{k}_3, \boldsymbol{k}_4) \\ + \Phi^{\Lambda,P}(\boldsymbol{k}_1 + \boldsymbol{k}_2; -\boldsymbol{k}_2, -\boldsymbol{k}_4) \\ + \Phi^{\Lambda,C}(\boldsymbol{k}_1 - \boldsymbol{k}_4; \boldsymbol{k}_4, \boldsymbol{k}_2) \\ + \Phi^{\Lambda,D}(\boldsymbol{k}_1 - \boldsymbol{k}_3; \boldsymbol{k}_3, \boldsymbol{k}_2)\,, \end{aligned} \tag{9}$$

where $V^{\Lambda,0}(\boldsymbol{k}_1, \boldsymbol{k}_2, \boldsymbol{k}_3, \boldsymbol{k}_4)$ accounts for the initial conditions of the model. The channels carry the important transfer momentum as first argument and each channel can be interpreted as representing a specific kind of interaction. The choice of these three channels was initially motivated by models of spinful fermions, where P will represent a pairing interaction, and depending on spin combinations, C and D represent magnetic and density-density interactions. Since our model Eq. (1) is spinless, both channel C and D will eventually represent density-density interactions and this choice is therefore redundant We keep this representation anyway such that a transfer of this method to a spinful model can be done in a transparent way.

To relate the channels to the diagrams with the same important momentum, we define the flow equations

$$\frac{d}{d\Lambda}\Phi^P(\boldsymbol{k}_1 + \boldsymbol{k}_2; -\boldsymbol{k}_2, -\boldsymbol{k}_4) = \tau_{\mathrm{pp}}(\boldsymbol{k}_1, \boldsymbol{k}_2, \boldsymbol{k}_3, \boldsymbol{k}_4)\,, \tag{10}$$

$$\frac{d}{d\Lambda}\Phi^C(\boldsymbol{k}_1 - \boldsymbol{k}_4; \boldsymbol{k}_4, \boldsymbol{k}_2) = \tau_{\mathrm{ph,c}}(\boldsymbol{k}_1, \boldsymbol{k}_2, \boldsymbol{k}_3, \boldsymbol{k}_4)\,, \tag{11}$$

$$\frac{d}{d\Lambda}\Phi^D(\boldsymbol{k}_1 - \boldsymbol{k}_3; \boldsymbol{k}_3, \boldsymbol{k}_2) = \tau_{\mathrm{ph,d}}(\boldsymbol{k}_1, \boldsymbol{k}_2, \boldsymbol{k}_3, \boldsymbol{k}_4)\,, \tag{12}$$

where Λ was dropped for brevity. Since the the last two momenta of the channels are deemed as less important, we will expand them in form-factors:

$$\Phi^X(\boldsymbol{q}, \boldsymbol{k}, \boldsymbol{k}') = \sum_{l,l'} X^{l,l'}(\boldsymbol{q}) f_l(\boldsymbol{k}) f^*_{l'}(\boldsymbol{k}') \tag{13}$$

with $X \in \{P, C, D\}$. This expansion can be imposed as long as the form-factors are forming a unity:

$$A_{\mathrm{BZ}}^{-1} \sum_l f^*_l(\boldsymbol{p}) f_l(\boldsymbol{k}) = \delta(\boldsymbol{p} - \boldsymbol{k})\,, \tag{14}$$

$$A_{\mathrm{BZ}}^{-1} \int d\boldsymbol{k} f^*_l(\boldsymbol{k}) f_{l'}(\boldsymbol{k}) = \delta_{l,l'}\,. \tag{15}$$

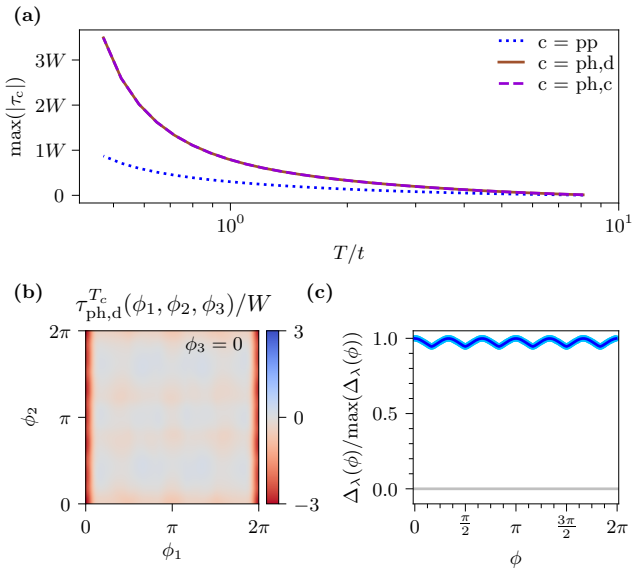

Fig. 4. Patching results for $V_1/t = -1$ and $\mu/t = 2$. The flow of the largest couplings in each channel is plotted in (a) and indicates an instability in the particle-hole channels. Solving the respective gap equation using the renormalized vertex in (b), yields the largest eigenvalue for transfer momentum $\boldsymbol{q} = 0$. The so-determined order parameter, indicated by light blue dots in (c), has an extended s-wave symmetry and transforms in the A_1 irrep. with both first and second neighbor harmonics (a fit to the numerical data is plotted as a dark blue line).

The channel decomposition and the unity of the form-factors can now be used to reformulate the initial flow equations into a form which offers a computational advantage.

In the TUFRG approach we derive flow equations for $P^{l,l'}(\boldsymbol{q}), C^{l,l'}(\boldsymbol{q}), D^{l,l'}(\boldsymbol{q})$ by taking the derivative $\frac{d}{d\Lambda}$ and inserting form-factor resolved unities on the right hand side of Eqs. (6)–(8) between the vertices and the loops, eventually leading to separating the three objects momentum-wise while connecting them in terms of form-factors. The sum of the form factors introduced with the unity Eq. (15) can then be truncated safely to gain a numerical advantage. The final form of the TUFRG flow equations reads

$$\frac{d}{d\Lambda}P^{l,l'}(\boldsymbol{q}) = +\frac{1}{2}\sum_{l_1,l_2} V^P(\boldsymbol{q})_{l,l_1}\dot{B}(\boldsymbol{q})^{(-)}_{l_1,l_2}V^P(\boldsymbol{q})_{l_2,l'}\,, \quad (16)$$

$$\frac{d}{d\Lambda}C^{l,l'}(\boldsymbol{q}) = +\sum_{l_1,l_2} V^C(\boldsymbol{q})_{l,l_1}\dot{B}(\boldsymbol{q})^{(+)}_{l_1,l_2}V^C(\boldsymbol{q})_{l_2,l'}\,, \quad (17)$$

$$\frac{d}{d\Lambda}D^{l,l'}(\boldsymbol{q}) = -\sum_{l_1,l_2} V^D(\boldsymbol{q})_{l,l_1}\dot{B}(\boldsymbol{q})^{(+)}_{l_1,l_2}V^D(\boldsymbol{q})_{l_2,l'}\,, \quad (18)$$

for details of the objects see App. B.1.

The flow equations now scale with $N_{\boldsymbol{q}} \times N_f^2$, where $N_{\boldsymbol{q}}$ is the number of momenta $\boldsymbol{q}$ which discretize the Brillouin zone and N_f is the number of chosen form-factors, see Fig. 3. In practice one has to choose much less form-factors than patches in the patching scheme. Therefore, we gain a numerical advantage over the scaling of the N-patch scheme ($\sim N^3$) and the freedom to choose a larger number of momenta $N_{\boldsymbol{q}}$ in the Brillouin zone. In this work, we use $N_{\boldsymbol{q}} = 180$ and $N_f = 19$ for comparison with 192 patches in the other approach. To discuss single points in the phase diagram we use $N_{\boldsymbol{q}} = 540$ and $N_f = 19$. In the convergence checks we go up to $N_{\boldsymbol{q}} = 792$ and $N_f = 61$. For details about the choice of momenta and form factors, see App. B.2.

3.4 Linearized gap equation

To obtain the gap function $\Delta(\boldsymbol{k})$ for the superconducting instabilities encountered during the FRG flow, we utilize standard BCS theory [50], that is, we perform a mean-field decoupling in the superconducting channel and derive a self consistent gap equation for $\Delta(\boldsymbol{k})$. Close to the critical temperature, where the gap is presumably small, the gap equation can be linearized and resembles an eigenvalue equation, which reads

$$\Delta(\boldsymbol{k}) = -\frac{1}{N}\sum_{\boldsymbol{k}'} V_{\mathrm{BCS}}(\boldsymbol{k},\boldsymbol{k}')\frac{\Delta(\boldsymbol{k}')}{2\xi_{\boldsymbol{k}'}}\tanh\left(\frac{\xi_{\boldsymbol{k}'}}{2T_c}\right). \quad (19)$$

The only input required to solve Eq. (19) and determine the leading contributions to the gap function as the eigenvectors with the largest negative eigenvalues, is then given by the pairing potential $V_{\mathrm{BCS}}(\boldsymbol{k},\boldsymbol{k}') = V(\boldsymbol{k},-\boldsymbol{k},\boldsymbol{k}',-\boldsymbol{k}')$.

For the patching approach, we rewrite the right hand side of Eq. (19) as an integral over a small energy shell $-\epsilon_c \leq \xi_{\boldsymbol{k}} \leq \epsilon_c \ll \epsilon_{\mathrm{FS}}$ around the Fermi surface, where the most dominant contribution to the momentum sum stems from. The gap equation thus becomes

$$\Delta(\boldsymbol{k}) \approx -\left[\int_{-\epsilon_c}^{\epsilon_c} d\xi\ \frac{1}{2\xi}\tanh\left(\frac{\xi}{2T_c}\right)\right] \times \langle V_{\mathrm{BCS}}(\boldsymbol{k},\boldsymbol{k}')\Delta(\boldsymbol{k}')\rangle_{\boldsymbol{k}'\in\mathrm{FS}}\,, \quad (20)$$

where the integral evaluates to

$$\int_{-\epsilon_c}^{\epsilon_c} d\xi\ \frac{1}{2\xi}\tanh\left(\frac{\xi}{2T_c}\right) \approx \ln\left(1.13\frac{\epsilon_c}{T_c}\right). \quad (21)$$

Finally, substituting $V_{\mathrm{BCS}}(\boldsymbol{k},\boldsymbol{k}') = \tau^{T_c}_{\mathrm{pp}}(\boldsymbol{k},-\boldsymbol{k},\boldsymbol{k}',-\boldsymbol{k}')$ in Eq. (21) allows to straightforwardly obtain $\Delta(\boldsymbol{k})$ on the Fermi surface within the patching approach.

If we work with the TUFRG approach instead, we can restore the pairing interaction straightforwardly by calculating the pairing interaction from the P channel, which is just given by the form-factor expansion in Eq. (13):

$$\Phi^P(\boldsymbol{q},\boldsymbol{k},\boldsymbol{k}') = \sum_{l,l'} P^{l,l'}(\boldsymbol{q}) f_l(\boldsymbol{k}) f^*_{l'}(\boldsymbol{k}'). \quad (22)$$

Since the divergence has a sharp peak at $q = 0$, we set the superconducting pairing interaction as:

$$\Phi^P(\boldsymbol{q}=0,\boldsymbol{k},\boldsymbol{k}') := \Phi^P(\boldsymbol{k},\boldsymbol{k}')\,, \quad (23)$$

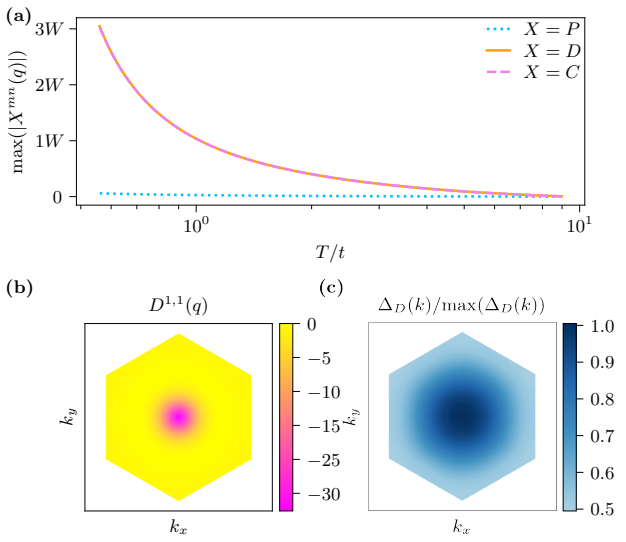

Fig. 5. TUFRG results for $V_1/t = -1$ and $\mu/t = 2$. Tracking the evolution of the P, C, D channels, we can compare the maximal value of the respective vertices and detect a divergence in the C/D channel, see (a). Moreover we notice the expected alignment of the D and C channel due to symmetry. The momentum resolved on-site vertex $D^{1,1}(q)$ in (b) peaks at the $\boldsymbol{\Gamma}$ point, indicating the possibility of a Pomeranchuck instability. The reconstructed order parameter $\Delta_D(k)$ of the D channel is in the A_1 irrep., see (c). We use $N_{\boldsymbol{q}} = 540$, $N_f = 19$.

and identify $V_{\mathrm{BCS}}(\boldsymbol{k}, \boldsymbol{k}') = \Phi^P(\boldsymbol{k}, \boldsymbol{k}')$. Thereafter, the gap function is obtained by diagonalization of the $N_{\boldsymbol{q}} \times N_{\boldsymbol{q}}$ matrix $\Phi^P(\boldsymbol{k}, \boldsymbol{k}')$.

Note, that while we have focused on pairing instabilities for the sake of brevity, one can generalize the discussion above directly to instabilities in the particle-hole channels by performing the respective mean-field decoupling and deriving a gap equation with an appropriate density instead of a pairing potential.

4 Attractive case $V_1 < 0$

We first investigate the case of attractive interactions $V_1 < 0$ at and away from Van Hove filling $\mu/t = 2$. To that end, we apply both, the N-patch and the TUFRG scheme, and work out the qualitative and quantitative differences between these approaches. In order to generate a common starting point we initialize both methods as follows: the RG flow starts at

$$T_{\mathrm{UV}} = W\,, \tag{24}$$

where $W = 9t$ is the bandwidth of the model. The respective flow equations are integrated down to the infrared, which we numerically define by $T_{\mathrm{IR}}/t = 10^{-5}$. If one of the channels diverges, signified by its maximum exceeding $3W$, the integration is terminated preemptively. As initial value for the vertex, we set $V^W(\pi(\boldsymbol{k}_1), \pi(\boldsymbol{k}_2), \pi(\boldsymbol{k}_3)) = V_1$ in the patching scheme, and $V^W(\boldsymbol{k}_1, \boldsymbol{k}_2, \boldsymbol{k}_3, \boldsymbol{k}_4) = V_1$, $\Phi^{W,X} = 0$ in the TUFRG.

4.1 Pomeranchuk instability at Van Hove filling

Tracking the evolution of the attractive case under the RG flow both employed approaches eventually detect a divergence of the particle-hole channels between $T/t = 1$ and $T/t = 0.1$, see Figs. 4 and 5. Due to crossing symmetry, which relates the direct and crossed particle-hole contributions, the flows of the respective maxima align and we, thus, reduce our discussion to $\tau_{\mathrm{ph,d}}$ for brevity.

In the patching scheme, we find the most singular eigenvalue to emerge from the linearized gap equation (see App. **??** for further details) with transfer momentum $\boldsymbol{q} = \boldsymbol{k_1} - \boldsymbol{k_3} = 0$, corresponding to a Pomeranchuk instability [51]. The respective order parameter $\langle \bar{\psi}_{\boldsymbol{k}} \psi_{\boldsymbol{k}} \rangle$ (see (c) in Fig. 4) is found to live in the A_1 irreducible representation (irrep.) of C_{6v} with an extended s-wave form factor including nearest and second-nearest neighbors. The momentum modulation, induced by the second neighbor harmonic, is, however, quite weak to the constant offset presented by the nearest-neighbor A_1 basis function.

In the TUFRG scheme, the instability almost exclusively affects the onsite-component $D^{1,1}(q)$ of the direct particle-hole channel, with a pronounced peak at the $\boldsymbol{\Gamma}$ point (see Fig. 5 (b)) and in agreement with the patching results. The reconstructed order parameter Δ_D (see (c) in Fig. 5) likewise transforms in the A_1 irrep., including a momentum modulation on the Fermi line. Note that, due to this modulation being weak compared to the nearest-neighbor A_1 contribution, this is rather difficult to see from the colormap in Fig. 5.

4.2 Superconductivity below Van Hove filling

For fillings $\mu/t < 2$, the Fermi surface is deformed and at some point the Pomeranchuck instability is overruled by a superconducting instability. We observe that, depending on the combination of chemical potential and interaction strength, both employed FRG schemes consistently predict two different kinds of superconductivity with $\boldsymbol{q} = 0$ for an extended range of fillings.

More specifically, moving away from $\mu/t = 2$ towards smaller values, the Pomeranchuck instability will at first be replaced by a region of f-wave superconductivity. Using the FRG data, we can reconstruct a gap function as detailed in Sec. 3.4. Indeed, we find that the gap function belongs to the one-dimensional B_1 irrep. of C_{6v} (see Figs. 6 and 7). The size of the filling range where the f-wave superconductivity instability occurs grows for decreasing interaction strength $|V_1|$. In the case of $V_1 = -0.4$ this type of superconductivity is even the only one which persists. Notably, in the case of $V_1 = -1.0$, where the region is the smallest, the N-patch FRG scheme does not detect f-wave at all while TUFRG still resolves a small domain of this instability.

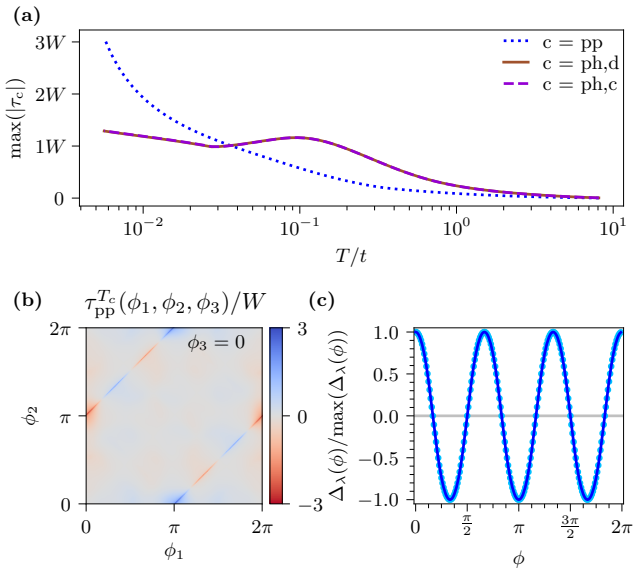

Fig. 6. Patching results for $V_1/t = -0.6$ and $\mu/t = 1.8$. Here, the flows of the channel maxima (see (a)) signifies a pairing instability. The superconducting gap, extracted from the renormalized vertex in (b), has f-wave symmetry (light blue dots) and can be fitted by the nearest-neighbor harmonic of the B_1 irrep. (dark blue line).

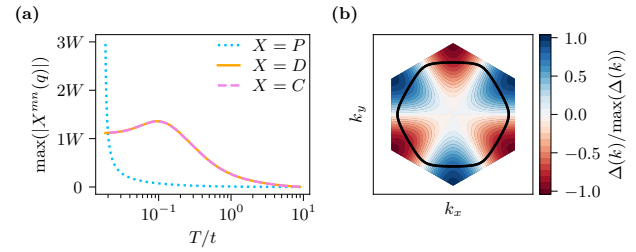

Fig. 7. TUFRG results for $V_1/t = -0.6$ and $\mu/t = 1.8$. Tracking similar to Fig.5 we can now find a divergence of the P channel away from Van Hove filling, indicating the emergence of superconductive instability (see (a)). The reconstructed leading gap $\Delta(k)$ of this instability (see (b)) depicts a function in the B_1 irrep. of C_{6v}. The black line represents the Fermi surface, featuring 6 zero crossings. We use $N_{\boldsymbol{q}} = 540$, $N_f = 19$.

Lowering μ further, p-wave superconductivity becomes the leading instability, which is described by the two-dimensional E_1 irrep. of the same point group (see Figs. 8 and 9). On a mean-field level, it is energetically beneficial for the superconducting order to open a full gap in the quasi-particle spectrum, which can be accomplished, for example, by constructing the superconducting gap $\Delta(\boldsymbol{k})$ as a complex superposition of the E_1 lattice harmonics. This leads to a $p + ip$ superconducting state featuring a finite Chern number $\mathcal{C} = -1$ which is thus topologically non-trivial (see App. D).

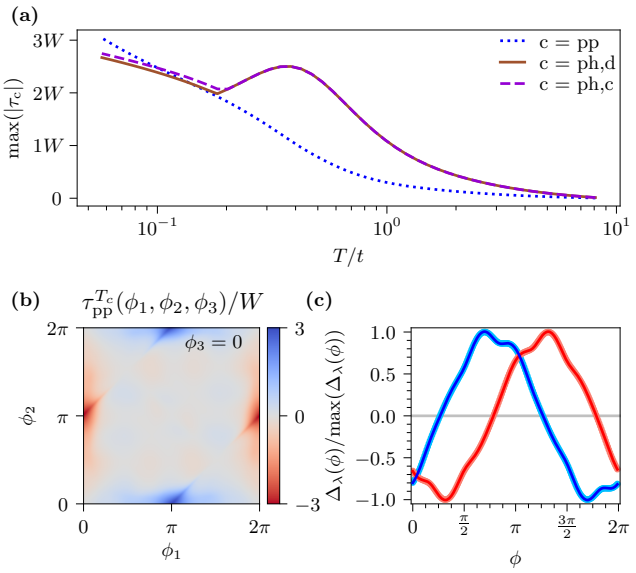

Fig. 8. Patching results for $V_1/t = -1$ and $\mu/t = 1.2$. Similar to Fig. 6, the vertex flows, plotted in (a), hint towards a superconducting instability. The respective gap equation, which requires the renormalized vertex from (b) as input, has a two-fold degenerate leading eigenvalue. The respective eigenvectors (superconducting gaps), displayed as light blue (light red) dots in (c), have p-wave symmetry and are well described by the nearest-neighbor lattice harmonics of the E_1 representation of C_{6v}, which we indicate by a dark blue (dark red) line.

Qualitatively, the two superconducting instabilities we find here are also consistent with the mean-field study presented in Ref. [52]. We note, however, that our FRG study includes additional fluctuations, which induce the Pomeranchuk instability when approaching Van Hove filling.

4.3 Phase diagram of the attractive case

In Fig. 10, we have mapped out the phase diagram for various $V_1/t < 0$ using both, the N-patch FRG and the TUFRG. Generally, the phase boundaries, the respective ground state instabilities, and the critical scales are in reasonable agreement. Some deviations in the critical temperatures are visible, in particular, in the regions where the superconducting instabilities occur at very low scales. Notably, the transition from Pomeranchuk to the f-wave superconductivity is in good alignment in both methods while the second transition point towards p-wave superconductivity has a larger difference although deep into this particular phase the methods apparently converge.

To establish the reliability of our results, we have further studied the convergence of the TUFRG approach with respect to the momentum- and form-factor resolution $(N_{\boldsymbol{q}}, N_f)$ in more detail, see App. B.2.

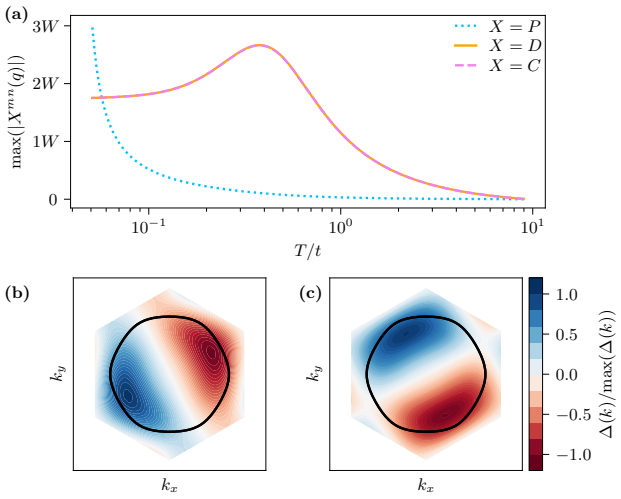

Fig. 9. TUFRG results for $V_1/t = -1$ and $\mu/t = 1.2$ with $N_{\boldsymbol{q}} = 540$, $N_f = 19$ For even lower fillings we still find a divergence of the P channel (a). But the reconstructed (degenerate) leading gaps $\Delta(k)$ of the emerging superconductivity instability (see (b)) depict now functions in the E_1 irrep. of C_{6v}. The black line represents the Fermi surface, featuring 2 zero crossings.

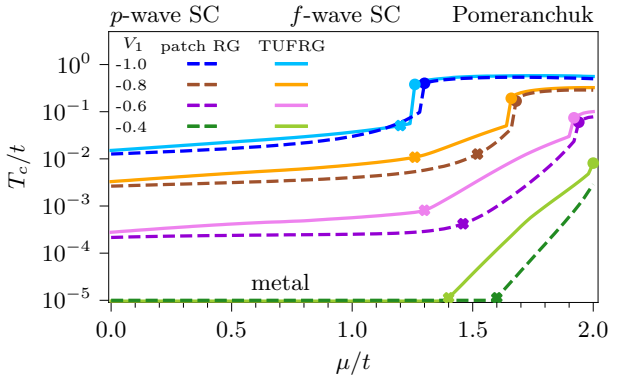

Fig. 10. Phase diagram for attractive interactions from patching and TUFRG. At Van Hove filling and for sufficiently strong interactions, both methods consistently predict a Pomeranchuk instability (see Figs. 4 & 5 for more details). Below $\mu/t = 2.0$, two kinds of pairing instabilities can be found: an f-wave superconductor in vicinity of Van Hove filling (see Figs. 6 & 7) and a p-wave instability (see Figs. 8 & 9) at even smaller values of μ/t. The boundaries are indicated by colored crosses (for the f-wave superconductor) or dots (for the Pomeranchuk instability), respectively.

5 Repulsive case $V_1 > 0$

We now consider the repulsive case $V_1/t > 0$. Here, we can expect that the occurring instabilities result from an interplay of the perfect nesting at the Van Hove point, whose effect can be mitigated by changing the filling, and

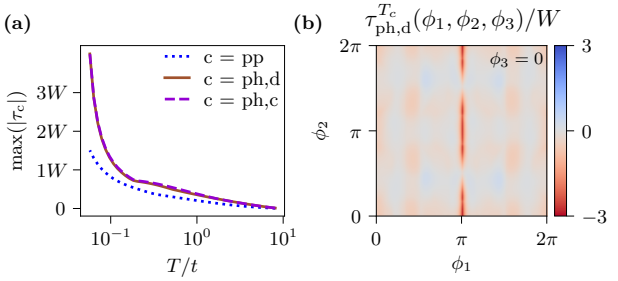

Fig. 11. Patching results for $V_1/t = 1$ at Van Hove filling. (a) Flow of the channel maxima, indicating a simultaneous divergence in both particle-hole channels, consistent with the TUFRG result in Fig. 12. (b) Plot of the direct particle-hole channel right at the critical scale T_c. The corresponding plot for $\tau_{\mathrm{ph,c}}$ can be obtained via crossing symmetry, i.e. a permutation ϕ_1 and ϕ_2 and a flip of the overall sign.

a divergent susceptibility in the pairing channel, which eventually induces a superconducting instability.

5.1 CDW at Van Hove filling

Similar to the attractive case, both methods detect a divergence of the particle-hole channels for $\mu/t = 2$. An analysis of the possible order parameters $\langle \bar{\psi}_{\boldsymbol{k}+\boldsymbol{q}} \psi_{\boldsymbol{k}} \rangle$ (see Figs. 11 and 12), however, reveals that the leading instability occurs for transfer momenta $\boldsymbol{q}$, which coincide with the nesting vector $\boldsymbol{M}$. The FRG results thus indicates the instability towards a charge density wave.

5.2 $\tilde{p}$-wave superconductivity below Van Hove filling

As we have discussed for the attractive case, the Fermi surface loses its nesting property below Van Hove filling, and, thus, fluctuations in the particle-hole channels are weaker (but still finite). In contrast to our previous considerations, however, putative superconducting instabilities would now arise from a different mechanism. Since $V_1/t > 0$, pairing is not directly encapsulated by the bare vertex and an attractive interaction in τ_{pp} henceforth needs to be generated by inter-channel feedback during the RG flow.

Indeed, both methods find an instability of the particle-particle channel for various fillings $\mu/t < 0$ and, remarkably, the flows of the maxima in the different channels plotted in Figs. 13(a) and 14(a) underline the importance of particle-hole fluctuations for the emergence of superconductivity. While the pairing channel is negligible (in TUFRG) or at least smaller than the other contributions (in the patching scheme), the particle-hole channels first sharply increase and then converge to a constant value, which dominates the vertex. In the low temperature regime, however, an abrupt upturn in the τ_{pp} flow can be observed, which ultimately results in a divergence of the RG flow. The respective gap function again transforms in the E_1 representation of C_{6v}, but requires both nearest- and

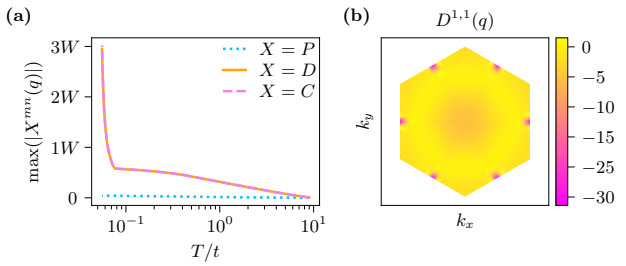

Fig. 12. TUFRG results for $V_1/t = 1$ and $\mu/t = 2$ with $N_{\boldsymbol{q}} = 540$, $N_f = 19$. Tracking the evolution of the channels P, C, D, we will find a CDW instability as the maximal absolute value of the C and D diverge while the P channel remains small, see (a). The alignment of the C and D channel is still expected because of the symmetric connection of the diagrams. The on-site, momentum resolved D channel $D^{1,1}(q)$ inhabits peaks at the $\boldsymbol{M}$ points, indicating the emergence of the CDW with modulation $\exp(i\boldsymbol{MR})$.

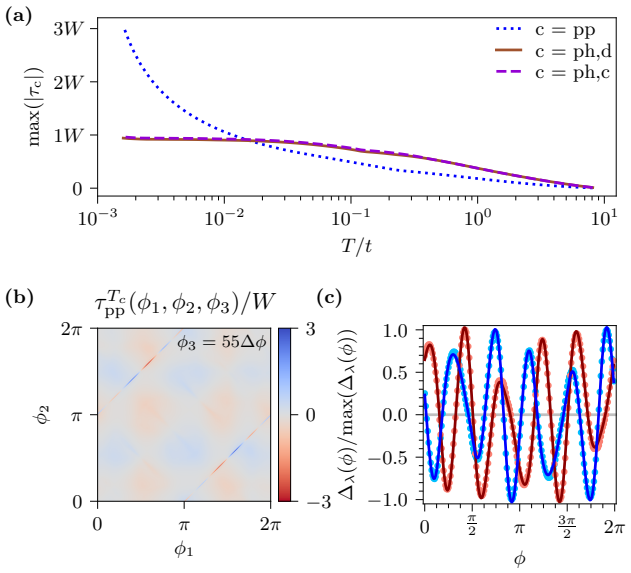

Fig. 13. Patching results for $V_1/t = 1$ and $\mu/t = 1.7$. A superconducting instability, driven by strong particle-hole fluctuations, becomes visible as a divergence of the particle-particle channel (see (a) and (b)). The pairing potential, constructed from τ_{pp} at the critical scale T_c, has two degenerate gaps (light red and light blue dots in (c)), which can be fit by a linear combination of first and second neighbor lattice harmonics of the two-dimensional E_1 representation of C_{6v} (dark red/blue line).

second-nearest neighbor lattice harmonics, as indicated by an increased number of nodes on the Fermi surface (see Fig. 13(c) or Fig. 14(b)). We dub this instability $\tilde{p}$-wave to set it apart from its counterpart in the attractive case.

Notably, a complex order parameter constructed solely from the second neighbor E_1 basis functions likewise yields $\mathcal{C} = -1$, whereas superpositions of both the first and second neighbor harmonics can generate an enhanced quantum Hall response due to Chern numbers $|\mathcal{C}| > 1$ (see Fig. 19 for more details).

5.3 Phase diagram of the repulsive case

In Fig. 15 we finally show results for the phase diagram obtained from the patching scheme and TUFRG for various fillings and repulsive interactions. Interestingly, the temperature scales for the $\tilde{p}$-wave superconductor measured in the patching scheme are almost one order of magnitude higher than in TUFRG, though the nature of the instability remains the same. Moreover, the sharp drop in T_c between the CDW and superconducting regime is absent in the patching results, where only a soft shoulder is indicative of the transition. Close to Van Hove filling on the other hand, the agreement is more reasonable. Since the central patch points coincide with the saddle points in the latter case, this generates the suspicion that the projection to the Fermi surface might be responsible for the observed discrepancy away from perfect nesting.

6 Discussion

We analyzed competing orders in a model of spinless electrons on the triangular lattice with nearest-neighbor interaction. Our study was motivated by the observation of correlated states in moiré bilayers of transition metal dichalcogenides. These systems are effectively described by interacting electrons on a triangular lattice, although equipped with (pseudo)spin and/or orbital degrees of freedom. To distill out the minimal degrees of freedom, we considered the paradigmatic toy model of spinless electrons and showed that it still possesses a rich interplay of ordering tendencies in the vicinity of a Van Hove singularity. To resolve this interplay, we calculated the effective two-particle interaction vertex in an unbiased way with the functional renormalization group. It is crucial to accurately resolve the momentum dependence of the vertex and we used two different parameterizations - a patching scheme for the Fermi surface and a channel decomposition for the momentum transfers. Both of them give qualitatively consistent results.

With an attractive bare interaction, we find a Pomeranchuk instability in the s-wave channel directly around Van Hove filling and f- and p-wave pairing instabilities in its vicinity for smaller fillings. Within RPA, both the charge and pairing channel can develop an instability, although at weak coupling the pairing channel has a stronger divergence (logarithmic vs double logarithmic). Interestingly, in our calculations, the Pomeranchuk instability in the charge channel develops first due to non-universal effects (beyond the logarithmic scaling). The s-wave Pomeranchuk instability corresponds to a singular compressibility but is not associated with any symmetry-breaking order. This can signal the tendency to phase separation with domains of different density. Another possibility is that

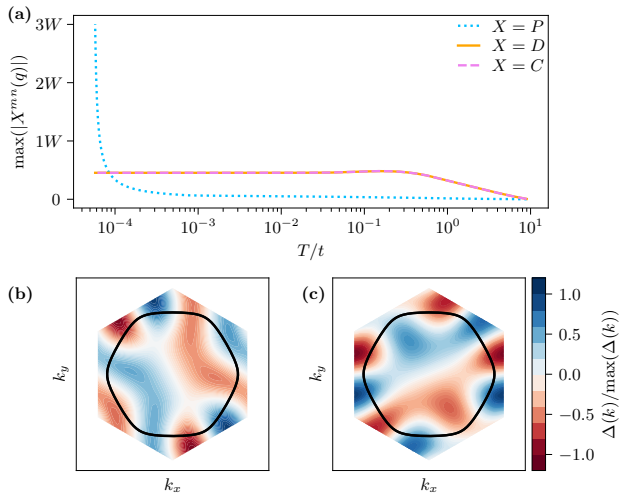

Fig. 14. TUFRG results for $V_1/t = 1$ and $\mu/t = 1.7$ with $N_{\boldsymbol{q}} = 540$, $N_f = 19$ The RG flow for repulsive interactions away from Van Hove filling features the divergence of the P channel and hence a superconductive instability (a). The reconstructed degenerate leading gaps $\Delta(k)$ of this instability (see (b)) depict a higher harmonic function of the E_1 irrep. of C_{6v}. The black line represents the Fermi surface, featuring 10 zero crossings each.

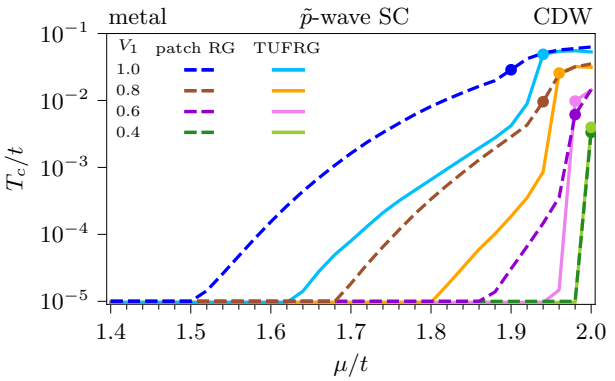

Fig. 15. Phase diagram for repulsive interactions from patching and TUFRG. Both approaches predict one transition from a metallic state, where no instability of the RG flow is observed down to $T/t = 10^{-5}$, to an extended $\tilde{p}$-wave superconductor (see Figs. 13 & 14), followed by another transition (indicated by a colored dot) to a charge density wave with transfer momentum $\boldsymbol{q} = \boldsymbol{M}$ close to Van Hove filling (see Figs. 11 & 12).

the divergence is cured by terms outside of our truncation, e.g., by self-energy terms, and makes room for a subleading instability. The p-wave pairing solution is two-fold degenerate and can form chiral $p+ip$ superconductivity in the ground state. This topological triplet superconducting state breaks time-reversal symmetry and can host Majorana modes on its boundaries.

In the case of a repulsive bare interaction, we obtain a CDW instability closest to Van Hove filling, whose fluctuations mediate unconventional p-wave pairing at smaller fillings. The wave vectors of the CDW are the three nonequivalent M points of the Brillouin zone and the exact charge pattern of the associated order depends on their combination in the ground state. Due to the bare nearest-neighbor repulsion, we find the unconventional p-wave pairing to be of extended size described by nearest- and next-nearest-neighbor harmonics. This can yield topological $p + ip$ states with higher Chern numbers, which increases, e.g., the number of chiral edge modes and the quantum Hall response.

Acknowledgements.— We thank P. Bonetti for helpful discussions. R.T. is funded by Deutsche Forschungsgemeinschaft (DFG, German Research Foundation) through Project-ID 258499086 - SFB 1170 and through the Würzburg-Dresden Cluster of Excellence on Complexity and Topology in Quantum Matter - ct.qmat Project-ID 390858490 - EXC 2147. N.G., D.K., and M.M.S. acknowledge support through the SFB 1238 (project C02, project id 277146847). M.M.S. is funded by the DFG Heisenberg programme (project id 452976698).

Author contributions

NG implemented the TUFRG code and ran the respective calculations. DK implemented the patch code and ran these calculations. RH ran additional TUFRG calculations and helped in the benchmarking process. RT, LC and MMS supervised the study. All authors were involved in the preparation of the manuscript.

Data availability statement

This manuscript has no associated data or the data will not be deposited. [Authors' comment: The data generated in this study for both methods is available from the respective authors on reasonable request.]

References

1. T. Schäfer, N. Wentzell, F. Šimkovic, Y.Y. He, C. Hille, M. Klett, C.J. Eckhardt, B. Arzhang, V. Harkov, F.m.c.M. Le Régent, A. Kirsch, Y. Wang, A.J. Kim, E. Kozik, E.A. Stepanov, A. Kauch, S. Andergassen, P. Hansmann, D. Rohe, Y.M. Vilk, J.P.F. LeBlanc, S. Zhang, A.M.S. Tremblay, M. Ferrero, O. Parcollet, A. Georges, Phys. Rev. X **11**, 011058 (2021). DOI 10.1103/PhysRevX.11.011058. URL https://link.aps.org/doi/10.1103/PhysRevX.11.011058
2. Y. Cao, V. Fatemi, S. Fang, K. Watanabe, T. Taniguchi, E. Kaxiras, P. Jarillo-Herrero, Nature **556**(7699), 43 (2018)
3. Y. Cao, V. Fatemi, A. Demir, S. Fang, S.L. Tomarken, J.Y. Luo, J.D. Sanchez-Yamagishi, K. Watanabe, T. Taniguchi, E. Kaxiras, R.C. Ashoori, P. Jarillo-Herrero, Nature **556**(7699), 80 (2018)

4. S. Manzeli, D. Ovchinnikov, D. Pasquier, O.V. Yazyev, A. Kis, Nature Reviews Materials **2**(8), 17033 (2017)
5. L. Wang, E.M. Shih, A. Ghiotto, L. Xian, D.A. Rhodes, C. Tan, M. Claassen, D.M. Kennes, Y. Bai, B. Kim, et al., Nature materials **19**, 861 (2020)
6. Y. Tang, L. Li, T. Li, Y. Xu, S. Liu, K. Barmak, K. Watanabe, T. Taniguchi, A.H. MacDonald, J. Shan, K.F. Mak, Nature **579**, 353 (2020)
7. R. Nandkishore, L.S. Levitov, A.V. Chubukov, Nature Physics **8**(2), 158 (2012)
8. M.L. Kiesel, C. Platt, W. Hanke, D.A. Abanin, R. Thomale, Phys. Rev. B **86**, 020507 (2012). DOI 10.1103/PhysRevB.86.020507. URL https://link.aps.org/doi/10.1103/PhysRevB.86.020507
9. W.S. Wang, Y.Y. Xiang, Q.H. Wang, F. Wang, F. Yang, D.H. Lee, Phys. Rev. B **85**, 035414 (2012). DOI 10.1103/PhysRevB.85.035414. URL https://link.aps.org/doi/10.1103/PhysRevB.85.035414
10. M.L. Kiesel, C. Platt, R. Thomale, Phys. Rev. Lett. **110**, 126405 (2013). DOI 10.1103/PhysRevLett.110.126405. URL https://link.aps.org/doi/10.1103/PhysRevLett.110.126405
11. M.L. Kiesel, C. Platt, W. Hanke, R. Thomale, Phys. Rev. Lett. **111**, 097001 (2013). DOI 10.1103/PhysRevLett.111.097001. URL https://link.aps.org/doi/10.1103/PhysRevLett.111.097001
12. A.V. Maharaj, R. Thomale, S. Raghu, Phys. Rev. B **88**, 205121 (2013). DOI 10.1103/PhysRevB.88.205121. URL https://link.aps.org/doi/10.1103/PhysRevB.88.205121
13. M.H. Fischer, T. Neupert, C. Platt, A.P. Schnyder, W. Hanke, J. Goryo, R. Thomale, M. Sigrist, Phys. Rev. B **89**, 020509 (2014). DOI 10.1103/PhysRevB.89.020509. URL https://link.aps.org/doi/10.1103/PhysRevB.89.020509
14. R. Nandkishore, R. Thomale, A.V. Chubukov, Phys. Rev. B **89**, 144501 (2014). DOI 10.1103/PhysRevB.89.144501. URL https://link.aps.org/doi/10.1103/PhysRevB.89.144501
15. S. Goto, S. Kurihara, D. Yamamoto, Phys. Rev. B **94**, 245145 (2016). DOI 10.1103/PhysRevB.94.245145. URL https://link.aps.org/doi/10.1103/PhysRevB.94.245145
16. A. Szasz, J. Motruk, M.P. Zaletel, J.E. Moore, Phys. Rev. X **10**, 021042 (2020). DOI 10.1103/PhysRevX.10.021042. URL https://link.aps.org/doi/10.1103/PhysRevX.10.021042
17. Y. Gannot, Y.F. Jiang, S.A. Kivelson, Phys. Rev. B **102**, 115136 (2020). DOI 10.1103/PhysRevB.102.115136. URL https://link.aps.org/doi/10.1103/PhysRevB.102.115136
18. A. Szasz, J. Motruk, Phys. Rev. B **103**, 235132 (2021). DOI 10.1103/PhysRevB.103.235132. URL https://link.aps.org/doi/10.1103/PhysRevB.103.235132
19. B.B. Chen, Z. Chen, S.S. Gong, D. Sheng, W. Li, A. Weichselbaum, arXiv preprint arXiv:2102.05560 (2021). URL https://arxiv.org/abs/2102.05560
20. A. Wietek, R. Rossi, F. Šimkovic, M. Klett, P. Hansmann, M. Ferrero, E.M. Stoudenmire, T. Schäfer, A. Georges, Phys. Rev. X **11**, 041013 (2021). DOI 10.1103/PhysRevX.11.041013. URL https://link.aps.org/doi/10.1103/PhysRevX.11.041013
21. Z. Zhu, D. Sheng, A. Vishwanath, arXiv:2007.11963 (2020). URL https://arxiv.org/abs/2007.11963
22. X.Y. Song, A. Vishwanath, Y.H. Zhang, Phys. Rev. B **103**, 165138 (2021). DOI 10.1103/PhysRevB.103.165138. URL https://link.aps.org/doi/10.1103/PhysRevB.103.165138
23. M.M. Scherer, D.M. Kennes, L. Classen, arXiv:2108.11406 (2021). URL https://arxiv.org/abs/2108.11406
24. F. Wu, T. Lovorn, E. Tutuc, I. Martin, A.H. MacDonald, Phys. Rev. Lett. **122**, 086402 (2019). DOI 10.1103/PhysRevLett.122.086402. URL https://link.aps.org/doi/10.1103/PhysRevLett.122.086402
25. J. Zang, J. Wang, J. Cano, A.J. Millis, Physical Review B **104**(7) (2021). DOI 10.1103/physrevb.104.075150. URL http://dx.doi.org/10.1103/PhysRevB.104.075150
26. H. Pan, F. Wu, S. Das Sarma, Phys. Rev. Research **2**, 033087 (2020). DOI 10.1103/PhysRevResearch.2.033087. URL https://link.aps.org/doi/10.1103/PhysRevResearch.2.033087
27. C. Wetterich, Physics Letters B **301**(1), 90 (1993). DOI https://doi.org/10.1016/0370-2693(93)90726-X. URL https://www.sciencedirect.com/science/article/pii/037026939390726X
28. M. Salmhofer, C. Honerkamp, Progress of Theoretical Physics **105**(1), 1 (2001). DOI https://doi.org/10.1143/PTP.105.1
29. N. Dupuis, L. Canet, A. Eichhorn, W. Metzner, J.M. Pawlowski, M. Tissier, N. Wschebor, Physics Reports **910**, 1 (2021)
30. W. Metzner, M. Salmhofer, C. Honerkamp, V. Meden, K. Schönhammer, Reviews of Modern Physics **84**(1), 299 (2012). DOI 10.1103/revmodphys.84.299. URL https://doi.org/10.1103%2Frevmodphys.84.299
31. C. Platt, W. Hanke, R. Thomale, Advances in Physics **62**(4-6), 453 (2013)
32. C. Honerkamp, M. Salmhofer, N. Furukawa, T.M. Rice, Phys. Rev. B **63**, 035109 (2001). DOI 10.1103/PhysRevB.63.035109. URL https://link.aps.org/doi/10.1103/PhysRevB.63.035109
33. J. Lichtenstein, D. Sánchez de la Peña, D. Rohe, E. Di Napoli, C. Honerkamp, S. Maier, Computer Physics Communications **213**, 100 (2017). DOI https://doi.org/10.1016/j.cpc.2016.12.013. URL https://www.sciencedirect.com/science/article/pii/S0010465516303927
34. C. Husemann, M. Salmhofer, Phys. Rev. B **79**, 195125 (2009). DOI 10.1103/PhysRevB.79.195125. URL https://link.aps.org/doi/10.1103/PhysRevB.79.195125
35. C. Honerkamp, Phys. Rev. B **68**, 104510 (2003). DOI 10.1103/PhysRevB.68.104510. URL https://link.aps.org/doi/10.1103/PhysRevB.68.104510
36. C. Honerkamp, Phys. Rev. Lett. **100**, 146404 (2008). DOI 10.1103/PhysRevLett.100.146404. URL https://link.aps.org/doi/10.1103/PhysRevLett.100.146404
37. M.M. Scherer, S. Uebelacker, C. Honerkamp, Phys. Rev. B **85**, 235408 (2012). DOI 10.1103/PhysRevB.85.235408. URL https://link.aps.org/doi/10.1103/PhysRevB.85.235408
38. M.M. Scherer, S. Uebelacker, D.D. Scherer, C. Honerkamp, Phys. Rev. B **86**, 155415 (2012). DOI 10.1103/PhysRevB.86.155415. URL https://link.aps.org/doi/10.1103/PhysRevB.86.155415

39. W. Wu, M.M. Scherer, C. Honerkamp, K. Le Hur, Phys. Rev. B **87**, 094521 (2013). DOI 10.1103/PhysRevB.87.094521. URL https://link.aps.org/doi/10.1103/PhysRevB.87.094521
40. D.M. Kennes, J. Lischner, C. Karrasch, Phys. Rev. B **98**, 241407 (2018). DOI 10.1103/PhysRevB.98.241407. URL https://link.aps.org/doi/10.1103/PhysRevB.98.241407
41. Q.K. Tang, L. Yang, D. Wang, F.C. Zhang, Q.H. Wang, Phys. Rev. B **99**, 094521 (2019). DOI 10.1103/PhysRevB.99.094521. URL https://link.aps.org/doi/10.1103/PhysRevB.99.094521
42. L. Classen, C. Honerkamp, M.M. Scherer, Phys. Rev. B **99**, 195120 (2019). DOI 10.1103/PhysRevB.99.195120. URL https://link.aps.org/doi/10.1103/PhysRevB.99.195120
43. N. Gneist, L. Classen, M.M. Scherer, arXiv preprint arXiv:2203.01226 (2022)
44. L. Klebl, A. Fischer, L. Classen, M.M. Scherer, D.M. Kennes, arXiv e-prints arXiv:2204.00648 (2022)
45. J.W. Negele, H. Orland, Quantum Many-particle Systems (1st ed.) (CRC Press, 1998). DOI https://doi.org/10.1201/9780429497926
46. C. Honerkamp, M. Salmhofer, Phys. Rev. B **64**, 184516 (2001). DOI 10.1103/PhysRevB.64.184516. URL https://link.aps.org/doi/10.1103/PhysRevB.64.184516
47. W. Metzner, M. Salmhofer, C. Honerkamp, V. Meden, K. Schönhammer, Rev. Mod. Phys. **84**, 299 (2012). DOI 10.1103/RevModPhys.84.299. URL https://link.aps.org/doi/10.1103/RevModPhys.84.299
48. D.D. Scherer, M.M. Scherer, C. Honerkamp, Phys. Rev. B **92**, 155137 (2015). DOI 10.1103/PhysRevB.92.155137. URL https://link.aps.org/doi/10.1103/PhysRevB.92.155137
49. S. Hesselmann, D.D. Scherer, M.M. Scherer, S. Wessel, Phys. Rev. B **98**, 045142 (2018). DOI 10.1103/PhysRevB.98.045142. URL https://link.aps.org/doi/10.1103/PhysRevB.98.045142
50. M. Sigrist, K. Ueda, Rev. Mod. Phys. **63**, 239 (1991). DOI 10.1103/RevModPhys.63.239. URL https://link.aps.org/doi/10.1103/RevModPhys.63.239
51. A.V. Chubukov, M. Khodas, R.M. Fernandes, Phys. Rev. X **6**, 041045 (2016). DOI 10.1103/PhysRevX.6.041045. URL https://link.aps.org/doi/10.1103/PhysRevX.6.041045
52. M. Cheng, K. Sun, V. Galitski, S. Das Sarma, Phys. Rev. B **81**, 024504 (2010). DOI 10.1103/PhysRevB.81.024504. URL https://link.aps.org/doi/10.1103/PhysRevB.81.024504
53. C. Honerkamp, Phys. Rev. B **98**, 155132 (2018). DOI 10.1103/PhysRevB.98.155132. URL https://link.aps.org/doi/10.1103/PhysRevB.98.155132
54. S.J. O, Y.H. Kim, O.G. Pak, K.H. Jong, C.W. Ri, H.C. Pak, Phys. Rev. B **103**, 235150 (2021). DOI 10.1103/PhysRevB.103.235150. URL https://link.aps.org/doi/10.1103/PhysRevB.103.235150
55. N. Read, D. Green, Phys. Rev. B **61**, 10267 (2000). DOI 10.1103/PhysRevB.61.10267. URL https://link.aps.org/doi/10.1103/PhysRevB.61.10267
56. A.M. Black-Schaffer, C. Honerkamp, Journal of Physics: Condensed Matter **26**(42), 423201 (2014). DOI 10.1088/0953-8984/26/42/423201. URL https://doi.org/10.1088/0953-8984/26/42/423201

A Temperature regulator

Both codes applied in this manuscript make use of the temperature flow scheme developed by Honerkamp and Salmhofer [46]. As such, the bare propagator is regularized as

$$G_0(i\omega, \boldsymbol{k}) \to G_0^T(i\omega, \boldsymbol{k}) = \frac{T^{1/2}}{i\omega - \xi(\boldsymbol{k})}\,, \tag{25}$$

while the fermionic fields $\bar{\psi}, \psi$ are simultaneously rescaled by a factor $T^{-3/4}$. This way, the temperature only appears in the Gaussian part of the action and the flow equations (5) apply up to a substitution $\Lambda \to T$. Another prominent advantage of this regularization, apart from being able to directly identify Λ with a physical quantity (temperature), is that contributions from particle-hole loops are fully taken into account even for small total momenta. In contrast to, for example, momentum shell schemes (see Ref. [47]), instabilities with transfer momenta at the $\boldsymbol{\Gamma}$ point are therefore not artificially suppressed, allowing to treat all channels in an unbiased way [46].

B Flow equations and numerical implementation of TUFRG

B.1 Elements of flow equations

Each flow equation Eqs. (16)-(18) consists of a product of a particle-particle $(-)$ or particle-hole $(+)$ bubble integral $\dot{B}(\boldsymbol{q})^{\pm}_{l,l'}$ connecting two cross-channel projections V^X, with $X = P, C, D$. For completeness, both objects will be described here explicitly. The bubble integrals emerge by insertion of the form-factor resolved unities in Eqs. (6)-(8) to separate the loops of the diagrams from the vertices. Their explicit form is given by

$$\dot{B}(\boldsymbol{q})^{(\pm)}_{l,l'} = -\int_p \frac{d}{d\Lambda}[G_0^\Lambda(i\omega, \boldsymbol{q}+\boldsymbol{p}) \times G_0^\Lambda(\pm i\omega, \pm\boldsymbol{q})] f_l(\boldsymbol{p}) f^*_{l'}(\boldsymbol{p})\,. \tag{26}$$

By implementing the temperature flow as shown in App. A and performing the Matsubara summations explicitly the bubbles are cast into:

$$\dot{B}(\boldsymbol{q})^{(+)}_{l,l'} = +\int_{\boldsymbol{p}} \frac{n'_F(\xi(\boldsymbol{q}+\boldsymbol{p})) - n'_F(\xi(\boldsymbol{q}))}{\xi(\boldsymbol{q}+\boldsymbol{p}) - \xi(\boldsymbol{q})} f_l(\boldsymbol{p}) f^*_{l'}(\boldsymbol{p}), \tag{27}$$

$$\dot{B}(\boldsymbol{q})^{(-)}_{l,l'} = -\int_{\boldsymbol{p}} \frac{n'_F(\xi(\boldsymbol{q}+\boldsymbol{p})) + n'_F(\xi(-\boldsymbol{q}))}{\xi(\boldsymbol{q}+\boldsymbol{p}) + \xi(-\boldsymbol{q})} f_l(\boldsymbol{p}) f^*_{l'}(\boldsymbol{p}), \tag{28}$$

where $n'_F(x)$ is the Fermi function after performing the temperature-derivative i.e. $n'_F(x) = \frac{d}{dT} n_F(x)$. After inserting the form-factor resolved unities into the initial flow equations, the vertices will also gain a dependency on the form-factors. The emergent objects will be the cross-channel projections:

$$V^P_{l,l'}(\boldsymbol{q}) = \int_{\boldsymbol{k},\boldsymbol{k}'} f_l(\boldsymbol{k}) f^*_{l'}(\boldsymbol{k}') V^\Lambda(\boldsymbol{k}+\boldsymbol{q}, -\boldsymbol{k}, \boldsymbol{k}'+\boldsymbol{q}, -\boldsymbol{k}'), \tag{29}$$

$$V^C_{l,l'}(\boldsymbol{q}) = \int_{\boldsymbol{k},\boldsymbol{k}'} f_l(\boldsymbol{k}) f^*_{l'}(\boldsymbol{k}') V^\Lambda(\boldsymbol{k}+\boldsymbol{q}, \boldsymbol{k}', \boldsymbol{k}'+\boldsymbol{q}, \boldsymbol{k})\,, \tag{30}$$

$$V^D_{l,l'}(\boldsymbol{q}) = \int_{\boldsymbol{k},\boldsymbol{k}'} f_l(\boldsymbol{k}) f^*_{l'}(\boldsymbol{k}') V^\Lambda(\boldsymbol{k}+\boldsymbol{q}, \boldsymbol{k}', \boldsymbol{k}, \boldsymbol{k}'+\boldsymbol{q})\,, \tag{31}$$

where the integral includes the Brillouin zone area: $\int_{\boldsymbol{k}} = A_{\mathrm{BZ}}^{-1} \int d\boldsymbol{k}$. These expressions can also be simplified by plugging in the plane wave form-factors $\exp(i\boldsymbol{k}\boldsymbol{R}_l)$ (see App. B.2) and expressing V^Λ by the decomposition Eq. (9). Therefore the double integral over the Brillouin zone is exchanged by a simple sum over the selected form-factors $\sum_L$:

$$V^P_{l,l'}(\boldsymbol{q}) = V^{P,0}_{l,l'}(\boldsymbol{q}) + V^{P\measuredangle C}_{l,l'}(\boldsymbol{q}) + V^{P\measuredangle D}_{l,l'}(\boldsymbol{q}) + P_{l,l'}(\boldsymbol{q})\,, \tag{32}$$

$$V^{P\measuredangle C}_{l,l'}(\boldsymbol{q}) = \sum_L \tilde{C}_{\boldsymbol{R}_L, -\boldsymbol{R}_L+\boldsymbol{R}_l+\boldsymbol{R}_{l'}}(-\boldsymbol{R}_L+\boldsymbol{R}_{l'}) e^{-i(\boldsymbol{R}_L-\boldsymbol{R}_{l'})\boldsymbol{q}}\,,$$

$$V^{P\measuredangle D}_{l,l'}(\boldsymbol{q}) = \sum_L \tilde{D}_{\boldsymbol{R}_L, -\boldsymbol{R}_L+\boldsymbol{R}_l-\boldsymbol{R}_{l'}}(-\boldsymbol{R}_L-\boldsymbol{R}_{l'}) e^{-i\boldsymbol{R}_L\boldsymbol{q}}\,.$$

$$V^{C}_{l,l'}(\boldsymbol{q}) = V^{C,0}_{l,l'}(\boldsymbol{q}) + V^{C\nleftarrow P}_{l,l'}(\boldsymbol{q}) + V^{C\nleftarrow D}_{l,l'}(\boldsymbol{q}) + C_{l,l'}(\boldsymbol{q}) \,, \tag{33}$$

$$\begin{aligned} V^{C\nleftarrow P}_{l,l'}(\boldsymbol{q}) &= \sum_{L} \tilde{P}_{\boldsymbol{R}_L, -\boldsymbol{R}_L + \boldsymbol{R}_l + \boldsymbol{R}_{l'}}(-\boldsymbol{R}_L + \boldsymbol{R}_{l'}) e^{-i(\boldsymbol{R}_L - \boldsymbol{R}_{l'})\boldsymbol{q}} \,, \\ V^{C\nleftarrow D}_{l,l'}(\boldsymbol{q}) &= \sum_{L} \tilde{D}_{\boldsymbol{R}_L, \boldsymbol{R}_L - \boldsymbol{R}_l + \boldsymbol{R}_{l'}}(-\boldsymbol{R}_l) e^{-i\boldsymbol{R}_L \boldsymbol{q}} \,, \end{aligned}$$

$$V^{D}_{l,l'}(\boldsymbol{q}) = V^{D,0}_{l,l'}(\boldsymbol{q}) + V^{D\nleftarrow P}_{l,l'}(\boldsymbol{q}) + V^{D\nleftarrow C}_{l,l'}(\boldsymbol{q}) + D_{l,l'}(\boldsymbol{q}) \,, \tag{34}$$

$$\begin{aligned} V^{D\nleftarrow P}_{l,l'}(\boldsymbol{q}) &= \sum_{L} \tilde{P}_{\boldsymbol{R}_L, \boldsymbol{R}_L - \boldsymbol{R}_l - \boldsymbol{R}_{l'}}(-\boldsymbol{R}_l) e^{-i(\boldsymbol{R}_L - \boldsymbol{R}_{l'})\boldsymbol{q}} \,, \\ V^{D\nleftarrow C}_{l,l'}(\boldsymbol{q}) &= \sum_{L} \tilde{C}_{\boldsymbol{R}_L, \boldsymbol{R}_L - \boldsymbol{R}_l + \boldsymbol{R}_{l'}}(-\boldsymbol{R}_l) e^{-i\boldsymbol{R}_L \boldsymbol{q}} . \end{aligned}$$

The objects $V^{X,0}_{l,l'}(\boldsymbol{q})$ encode the initial interaction of the model Eq. (1) by projecting it into the respective channels, see App. C. $\tilde{X}_{l,l'}$ represents the Fourier-transformed channels, for example for the pairing channel P:

$$\tilde{P}_{l,l'}(R_i) = A^{-1}_{\mathrm{BZ}} \int d\boldsymbol{p}\, P_{l,l'}(\boldsymbol{p}) e^{-i\boldsymbol{p}\boldsymbol{R}_i} . \tag{35}$$

B.2 Choice of momenta and form-factors and convergence

One has the freedom to select different sets of form-factors as long as the unity condition Eqs. (14)-(15) are fulfilled. The simplest choice of form-factors have the form of plane waves: $f_l(\boldsymbol{k}) = \exp(i\boldsymbol{k}\boldsymbol{R}_l)$ where $\boldsymbol{R}_l$ is a real space vector of the lattice of the investigated model, i.e. in our case the triangular lattice. This choice has the advantage, that the truncation of form-factors can be done within an interpretable reasoning: the inclusion of a form-factor $f_l(\boldsymbol{k})$ will correspond to taking effects of fermionic bilinears with distance $\boldsymbol{R}_l$ into account [53]. Since we assume that the emerging physics in the RG flow will be predominately influenced by short-range effects, we will truncate all form-factors which exceed a chosen distance. In our calculations we mostly select $N_f = 19$ form-factors, corresponding to on-site (i.e. $\boldsymbol{R}_1 = 0$), first-, second- and third-nearest neighbors effects. For the convergence checks in Figs. 17,18 we will also use $N_f = 37$ (i.e. up to 5th nearest-neighbors effects) and $N_f = 61$ (i.e. up to 8th nearest-neighbors effects), see Fig.16. This specific choice of amount of form-factors is based on keeping a *hexagonal-shell* N_s into account. This means, that we will include all plane waves with $\boldsymbol{R}_l$ which are on or inside the $N_s - th$ hexagon of the real space lattice, cf. Fig.16. Therefore the numbers $N_f = 19, 37, 61$ correspond to the hexagon-shells $N_s = 2, 3, 4$.

For the momentum resolution, we choose evenly placed points in the Brillouin zone. Most of our calculations are done with $N_{\boldsymbol{q}} = 180$ momenta to compare it with the 192 patching points of the other approach, while for the convergence checks in Figs. 17,18 we also choose $N_{\boldsymbol{q}} = 336$, $N_{\boldsymbol{q}} = 540$ and $N_{\boldsymbol{q}} = 792$.

Actually, one does not have to calculate the RG flow for all momenta $N_{\boldsymbol{q}}$, but only for a fraction $1/12 \times N_{\boldsymbol{q}}$. The rest of the contributions can then be restored by symmetry relations since the symmetries of the initial model Eq. (1) are inherited by the flow equations, see [54] for details.

C Initial conditions

The initial condition for the FRG flow is given by the bare two-particle vertex V_0, which can be directly read off the microscopic model in Eq. (1). For this purpose, one needs to identify the action S_{int} with the vertex at the UV scale, i.e $S_{\mathrm{int}} = V^{\Lambda_{\mathrm{UV}}} = V_0$, and additionally account for crossing symmetries, such as $V(\boldsymbol{k}_1, \boldsymbol{k}_2, \boldsymbol{k}_3, \boldsymbol{k}_4) = -V(\boldsymbol{k}_2, \boldsymbol{k}_1, \boldsymbol{k}_3, \boldsymbol{k}_4)$. The initial condition needs to be properly (anti-) symmetrized henceforth. On the level of the Hamiltonian, crossing symmetry can already be made explicit by reordering the Fock space operators as

$$V_1 \sum_{\langle ij \rangle} n_i n_j = V_1 \sum_{\langle ij \rangle} c^\dagger_i c^\dagger_j c_j c_i = \frac{1}{4} V_1 \sum_{\langle ij \rangle} \Big(c^\dagger_i c^\dagger_j c_j c_i - c^\dagger_i c^\dagger_j c_i c_j - c^\dagger_j c^\dagger_i c_j c_i + c^\dagger_j c^\dagger_i c_i c_j \Big). \tag{36}$$

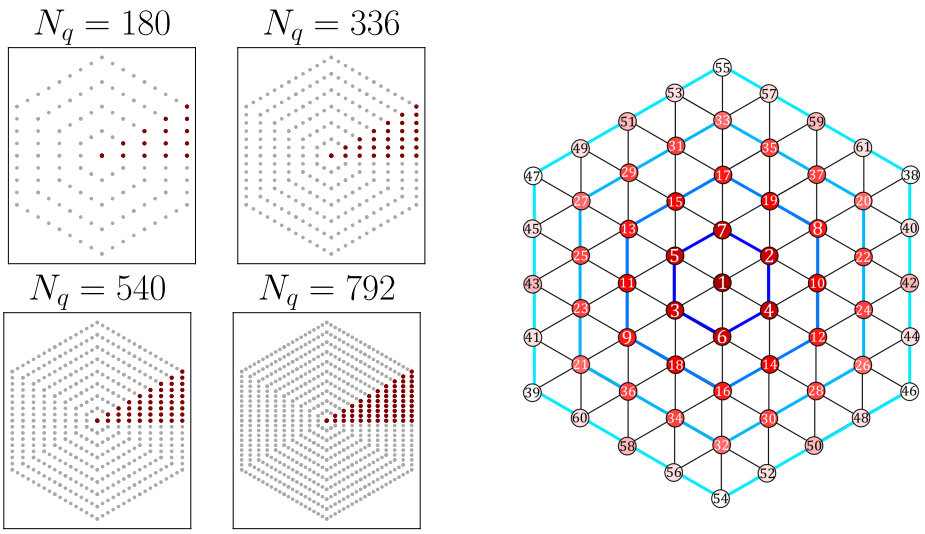

Fig. 16. Momentum resolutions and form-factors choice. Left: different resolutions of the Brillouin zone. Only 1/12 of the momenta (red) actually have to be calculated in the RG flow while the rest can be derived by symmetry relations. Right: real space vectors $\boldsymbol{R}_l$ for the plane wave form-factors.

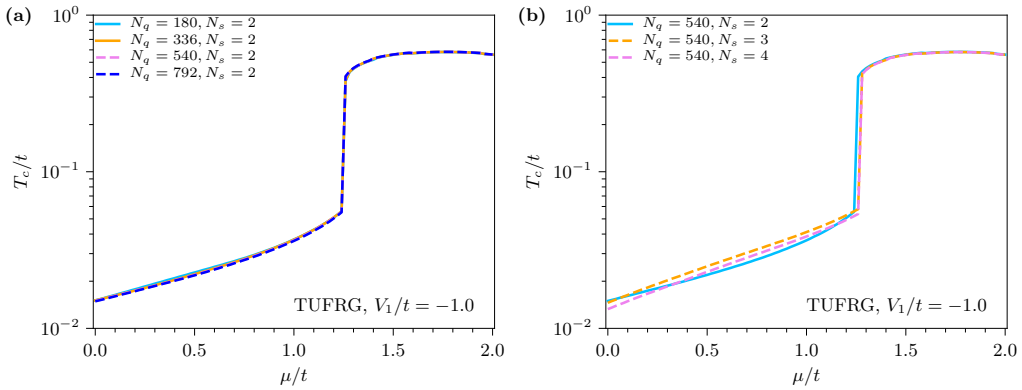

Fig. 17. Convergence of critical RG scales from TUFRG for the attractive case $V_1/t < 0$**.** (a) Study for convergence for increasing momentum resolution. All calculations align qualitatively and quantitatively for the checked region. (b) Study for convergence in form factors. While the results match qualitatively, minor deviations in the critical temperature regarding the superconductive instabilities occur.

Transforming to momentum space, the initial condition for the FRG flow is thus

$$V_0(\boldsymbol{k}_1, \boldsymbol{k}_2, \boldsymbol{k}_3, \boldsymbol{k}_4) = \frac{V_1}{2} \sum_{\boldsymbol{\delta}} \left(e^{-i(\boldsymbol{k}_2 - \boldsymbol{k}_4)\boldsymbol{\delta}} - e^{-i(\boldsymbol{k}_2 - \boldsymbol{k}_3)\boldsymbol{\delta}} - e^{-i(\boldsymbol{k}_1 - \boldsymbol{k}_4)\boldsymbol{\delta}} + e^{-i(\boldsymbol{k}_1 - \boldsymbol{k}_3)\boldsymbol{\delta}} \right), \tag{37}$$

where we sum over the nearest-neighbor displacement vectors $\boldsymbol{\delta}$. Projecting all momenta to the Fermi surface via $\pi : 1.\mathrm{BZ} \to \mathbb{Z}_{\mathrm{FS}}^N$, Eq. (37) directly serves as the initial condition for the patching scheme.

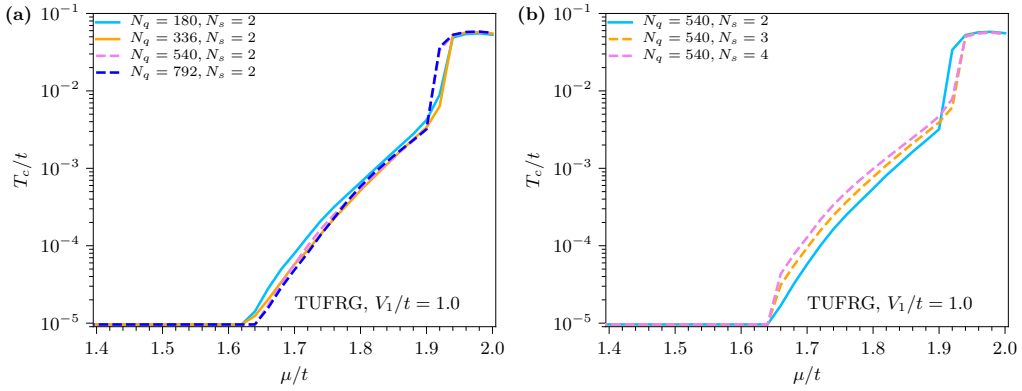

Fig. 18. Convergence of critical RG scales from TUFRG for the repulsive case $V_1/t > 0$.(a) For the investigation of convergence in increasing momentum resolution $N_{\boldsymbol{q}}$ we find qualitatively the same phase diagram which quantitative deviations diminish for higher resolution. (b) The the investigation of including more form factors N_f we still find qualitative alignment, while the critical temperature slightly grows for including more shells. Since we are primarily interested in the qualitative behaviour and the deviations are not too strong, we use $N_s = 2$ for the calculations in the sections 4 and 5.

For the TUFRG approach, we additionally insert Eq. (37) into Eqs. (29)-(31) to derive explicit expressions for $V^{X,0}_{l,l'}$, with $X \in \{P, C, D\}$. This procedure finally yields

$$V^{C,0}_{\mathbf{R}_1,\mathbf{R}_1}(\mathbf{q}) = -V^{D,0}_{\mathbf{R}_1,\mathbf{R}_1}(\mathbf{q}) = -V_1 \sum_{\boldsymbol{\delta}} e^{i\mathbf{q}\boldsymbol{\delta}} \tag{38}$$

$$V^{P,0}_{\mathbf{R}_l,\mathbf{R}_l}(\mathbf{q}) = V^{C,0}_{\mathbf{R}_l,\mathbf{R}_l}(\mathbf{q}) = -V^{D,0}_{\mathbf{R}_l,\mathbf{R}_l}(\mathbf{q}) = V_1 \tag{39}$$

$$V^{P,0}_{\mathbf{R}_{-l},\mathbf{R}_l}(\mathbf{q}) = -V_1 e^{-i\mathbf{q}\mathbf{R}_l}\,, \tag{40}$$

with $l \in \{2, 3, 4, 5, 6, 7\}$ as the initial condition for the TUFRG flow.

D Chern numbers

To access possible topological properties of pairing instabilities, we consult a Skyrmion winding number formula [55,56]

$$\mathcal{C} = \frac{1}{4\pi} \int_{1.\mathrm{BZ}} d^2k \left\langle \boldsymbol{m}(\boldsymbol{k}) \middle| \frac{\partial \boldsymbol{m}(\boldsymbol{k})}{\partial k_x} \times \frac{\partial \boldsymbol{m}(\boldsymbol{k})}{\partial k_y} \right\rangle , \tag{41}$$

where $\langle . \mid . \rangle$ is the Euclidean scalar product. Here, $\boldsymbol{m}(\boldsymbol{k})$ denotes the pseudospin vector or Skyrmion magnetization, which follows the winding of the superconducting gap around the Fermi surface. In algebraic form, $\boldsymbol{m}(\boldsymbol{k})$ is given by

$$\boldsymbol{m}(\boldsymbol{k}) = \frac{1}{E(\boldsymbol{k})} \begin{pmatrix} \mathrm{Re}(\Delta(\boldsymbol{k})) \\ \mathrm{Im}(\Delta(\boldsymbol{k})) \\ \xi(\boldsymbol{k}) \end{pmatrix} , \tag{42}$$

where $E(\boldsymbol{k}) = \sqrt{|\Delta(\boldsymbol{k})|^2 + \xi(\boldsymbol{k})^2}$ is the Bogoliubov quasi-particle spectrum.

It is immediately clear, that any real or purely imaginary gap function will result in a topologically trivial state with $\mathcal{C} = 0$. In contrast, for a gap function corresponding to a two-dimensional irreducible representation, such as the p-wave instabilities we found in the main text, the possibility of non-trivial topology arises. In principle, one would need to minimize the mean-field free energy for a linear superposition of the respective lattice harmonics and determine whether or not a complex gap function prevails. Here, we resign from employing this variational approach and instead use a heuristic argument. Consider the ground state energy $E_0 = -\langle |\Delta(\boldsymbol{k})| \rangle_{\mathrm{FS}}$ for a gap function $\Delta(\boldsymbol{k})$ which we suppose to live in the complex two-dimensional space corresponding to a doubly degenerate eigenvalue of the linearized gap equation. If this linear combination is either real or purely imaginary, there will be momenta on the Fermi surface where $|\Delta(\boldsymbol{k})|$ is gapless and no contribution to the ground state energy is obtained henceforth. If one assumes a complex linear combination instead, $|\Delta(\boldsymbol{k})|$ will be fully gapped at the Fermi level and thus, a lower ground state energy is obtained. It is therefore natural to assume, that the energetically more beneficial superposition

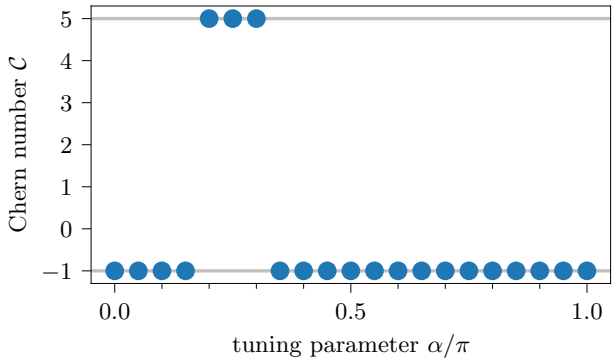

Fig. 19. Example calculations for Chern numbers in the E_1 representation for $\mu/t = 1.7$. Motivated by our finding of a higher-harmonic $\tilde{p}$-wave instability for repulsive interactions $V_1/t > 0$ (see Figs. 13 & 14), we perform exemplary computations of $\mathcal{C}$ for superconducting gaps of the form $\Delta(\boldsymbol{k}) = [\cos(\alpha)\delta_1^{E_1}(\boldsymbol{k}) + \sin(\alpha)\tilde{\delta}_1^{E_1}(\boldsymbol{k})] + i \times [\cos(\alpha)\delta_2^{E_1}(\boldsymbol{k}) + \sin(\alpha)\tilde{\delta}_2^{E_1}(\boldsymbol{k})]$, where $\delta_{1(2)}^{E_1}$ denotes the nearest-neighbor lattice harmonics of the E_1 irrep. and $\tilde{\delta}_{1(2)}^{E_1}$ the respective second neighbor functions. The model is chosen such that we recover the pure first (second) neighbor limit for $\alpha = 0$ (π).

of lattice harmonics is a complex one. Computing $\mathcal{C}$ from the ansatz $\Delta(\boldsymbol{k}) = \delta_1^{E_1}(\boldsymbol{k}) + i\delta_2^{E_1}(\boldsymbol{k})$ for the nearest-neighbor or second neighbor lattice harmonics δ^{E_1} of the E_1 irrep., for example, we find $\mathcal{C} = -1$ over the entire range of fillings where the p-wave instability occurs. An admixture of both, the first and second neighbor functions may, however, yield a strongly enhanced Chern number, as exemplified in Fig. 19.

Pinch-points to half-moons and up in the stars: the kagome skymap

Dominik Kiese,[1,*] Francesco Ferrari,[2,*] Nikita Astrakhantsev,[3,*] Nils Niggemann,[4,5,6,*] Pratyay Ghosh,[7,6,*] Tobias Müller,[7] Ronny Thomale,[6,7] Titus Neupert,[3] Johannes Reuther,[4,5,6] Michel J. P. Gingras,[8] Simon Trebst,[1] and Yasir Iqbal[6,†]

[1]*Institute for Theoretical Physics, University of Cologne, 50937 Cologne, Germany*
[2]*Institut für Theoretische Physik, Goethe-Universität Frankfurt, Max-von-Laue-Straße 1, D-60438 Frankfurt am Main, Germany*
[3]*Department of Physics, University of Zürich, Winterthurerstrasse 190, 8057 Zürich, Switzerland*
[4]*Dahlem Center for Complex Quantum Systems and Fachbereich Physik, Freie Universität Berlin, D-14195 Berlin, Germany*
[5]*Helmholtz-Zentrum Berlin für Materialien und Energie, D-14109 Berlin, Germany*
[6]*Department of Physics and Quantum Centers in Diamond and Emerging Materials (QuCenDiEM) group, Indian Institute of Technology Madras, Chennai 600036, India*
[7]*Institute for Theoretical Physics and Astrophysics, Julius-Maximilian's University of Würzburg, Am Hubland, D-97074 Würzburg, Germany*
[8]*Department of Physics and Astronomy, University of Waterloo, Waterloo, Ontario, Canada N2L 3G1*

(Dated: June 2, 2022)

Pinch point singularities, associated with flat band magnetic excitations, are tell-tale signatures of Coulomb spin liquids. While their properties in the presence of quantum fluctuations have been widely studied, the fate of the complementary non-analytic features – shaped as half-moons and stars – arising from adjacent shallow dispersive bands has remained unexplored. Here, we address this question for the spin $S = 1/2$ Heisenberg antiferromagnet on the kagome lattice with second and third neighbor couplings, which allows one to tune the classical ground state from flat bands to being governed by shallow dispersive bands for intermediate coupling strengths. Employing the complementary strengths of variational Monte Carlo, pseudo-fermion functional renormalization group, and density-matrix renormalization group, we establish the quantum phase diagram. The U(1) Dirac spin liquid ground state of the nearest-neighbor antiferromagnet remains remarkably robust till intermediate coupling strengths when it transitions into a pinwheel valence bond crystal displaying signatures of half-moons in its structure factor. Our work thus identifies a microscopic setting that realizes one of the proximate orders of the Dirac spin liquid identified in a recent work [Song, Wang, Vishwanath, He, Nat. Commun. **10**, 4254 (2019)]. For larger couplings, we obtain a collinear magnetically ordered ground state characterized by star-like patterns.

Classical spin models which admit a completion of squares belong to the distinct *genre* of "maximally frustrated" Hamiltonians which feature an exponentially large degenerate ground-state manifold [1, 2]. In two spatial dimensions, a celebrated example is the classical nearest-neighbor Heisenberg antiferromagnet (NNHAF) on the kagome lattice

$$\mathcal{H} = J_1 \sum_{\langle ij \rangle} \mathbf{S}_i \cdot \mathbf{S}_j = \frac{J_1}{2} \sum_{\triangle,\triangledown} (\mathbf{S}_1 + \mathbf{S}_2 + \mathbf{S}_3)^2 - J_1 N \quad (1)$$

with $|\mathbf{S}_i| = 1$ and N the total number of spins. By virtue of the right-hand-side of Eq. (1), any spin configuration which satisfies $(\mathbf{S}_1+\mathbf{S}_2+\mathbf{S}_3) = 0$ on each triangle qualifies as a classical ground state. The emergence of such a local constraint leads to the formation of a Coulomb spin liquid [3], with algebraically decaying spin-spin correlations in real space, which gives structure to the exponentially large manifold of degenerate ground states. In Fourier space, these correlations most strikingly manifest themselves in the presence of non-analytic features in the structure factor called *pinch points* [4, 5]. Remarkably, this classical Coulomb phase remains stable [6, 7] even in the presence of additional couplings along a fine-tuned line when second neighbor (J_2) and third neighbor along edges (J_{3a}) [see Fig. 1(a)] are concurrently introduced and of equal strength, i.e. $J_2 = J_{3a}$ ($\equiv J$ henceforth). This can be readily understood when diagonalizing the spin exchange Hamiltonian $\mathcal{H}(\mathbf{k})$ in momentum space [8–10], which reveals that the characteristic flat band of the NNHAF persists [6] up to $J/J_1 = 1/5$. For $J/J_1 > 1/5$, a shallow dispersive band starts to cut below the flat band in parts of the Brillouin zone [6], which in turn gives rise to pairs of *half-moons*, i.e., crescent shaped arcs in the static structure factor [11], with the flat band remaining close-by with a multitude of low-energy excitations [12]. On a deeper level, the formation of half-moons in the static structure factor results from a non-analyticity in the dispersive-band eigenvectors as a function of momentum and, given the completeness of the eigenvector basis, can be viewed as necessarily arising in order to complement the singularity in the momentum dependence of the flat-band eigenvectors [6, 13]. With increasing J/J_1, the radius of the half-moon continuously grows and at $J/J_1 = 1$, the half-moons from different Brillouin zones coalesce, giving rise to a *star* pattern in the static structure factor. While in the case of Ising spins, which show a similar sequence of momentum space signatures as a function of J/J_1, the nature of the half-moons and star phases has a well-understood real-space picture in terms of magnetic clustering of topological charges [14–16], for continuous (Heisenberg) spins, the nature of the real-space clustering and its freedom to continuously evolve with J is far more involved and not yet completely understood [6].

Much of the interest in the kagome *quantum* antiferromagnet as a potential host to highly entangled quantum states owes its origin to the realization that its classical ground state is governed by flat bands – an opportunity for otherwise resid-

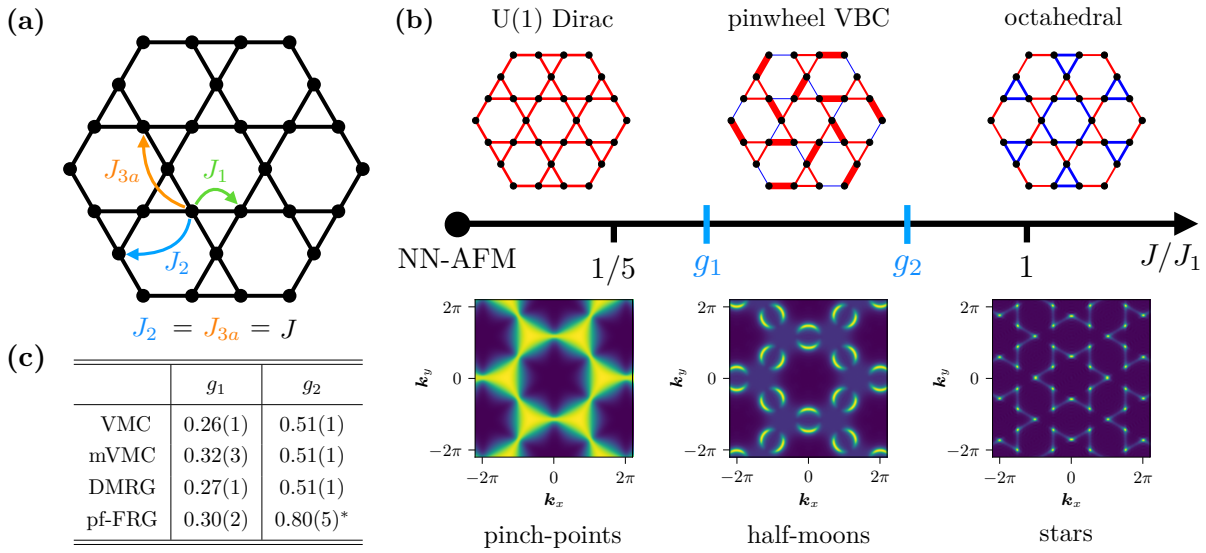

(c)

	g_1	g_2
VMC	0.26(1)	0.51(1)
mVMC	0.32(3)	0.51(1)
DMRG	0.27(1)	0.51(1)
pf-FRG	0.30(2)	0.80(5)*

FIG. 1. **The kagome skymap.** (a) Illustration of first- (J_1), second- (J_2), and third-neighbor interactions along edges (J_{3a}) of the kagome lattice for the considered model. (b) The $S = 1/2$ quantum phase diagram with (top panel) representative real-space spin-spin correlation profiles, with red (blue) bonds denoting antiferromagnetic (ferromagnetic) correlations, and (lower panel) spin structure factors of the different phases evaluated at $J/J_1 = 0.1$ (DSL), $J/J_1 = 0.4$ (pinwheel VBC), and $J/J_1 = 0.9$ (collinear order) from pf-FRG. (c) estimates of the phase boundaries (g_1 and g_2) obtained from the various approaches employed in this work. While we see agreement, within error bars, for g_1 for all approaches, the pf-FRG result for g_2 (marked by an asterisk), shows a notable deviation whose origin we discuss in Appendix I B.

ual quantum effects to dictate the macroscopic ground state. Thence, tuning the pairwise exchange along the maximally frustrated axis ($J_2 = J_{3a} \equiv J$) which, classically, is tuned to have a flat band over an extended region in parameter space, should provide a fertile playground to potentially realize novel states of matter also in the quantum model. For one, the U(1) Dirac spin liquid (DSL) [17–19] ground state of the NNHAF [20–23] is indeed known to be fragile to magnetic order when perturbed by longer-range Heisenberg couplings [24, 25] or Dzyaloshinskii-Moriya interactions [26], as expected for algebraic spin liquids, but its fate along the maximally frustrated direction of interest here is unknown. In particular, this parameter axis may afford a higher degree of stability to the U(1) DSL against long-range order, and one may wonder whether the DSL naturally gives way to other exotic quantum phases as one marches along this direction. On a conceptual level, instabilities of the DSL have recently been rigorously classified [19] in field theoretical work. But it remains an open challenge to identify microscopic settings in which these instabilities manifest themselves and what telltale signatures they come along with that might be accessible in experimental studies.

In this manuscript, we take an important step in this direction by establishing the quantum counterpart to the classical half-moon phase as a pinwheel valence bond crystal state which the DSL transitions into only for finite coupling strength. We do so by employing complementary numerical quantum many-body approaches to build a detailed picture of the $S = 1/2$ quantum phase diagram along the maximally frustrated axis for $J/J_1 > 0$, resolving the characteristic real-space and Fourier-space signatures of all quantum phases. The numerical approaches include fermionic variational Monte Carlo (VMC) with versatile Gutzwiller projected Jastrow wave functions [27], many-variable variational Monte Carlo (mVMC) with unconstrained optimization of the Bardeen-Cooper-Schrieffer (BCS) pairing function (supplemented with symmetry projectors) [28, 29], one-loop pseudofermion functional renormalization group (pf-FRG) [30], and density-matrix renormalization group (DMRG) [31]. The resulting quantum phase diagram is shown in Fig. 1, where cumulative and complementary evidence from all employed approaches shows that the ground state remains nonmagnetic over an appreciably wide span of parameter space [see Fig. 1(b)], notably extending far beyond the classical domain ($0 \leqslant J/J_1 \leqslant 0.2$) where flat bands are lowest in energy. This nonmagnetic region is composed of two phases: (i) the U(1) Dirac spin liquid (DSL) for $0 \leqslant J/J_1 \lesssim 0.26$ characterized by soft maxima at the pinch points in its spin structure factor $\chi(\mathbf{k})$, and (ii) a 12-site unit cell, C_6 symmetric pinwheel valence bond crystal (VBC) for $0.26 \lesssim J/J_1 \lesssim 0.51$, displaying signatures of half-moons in $\chi(\mathbf{k})$, see Fig. 1(b). Our analysis indicates the DSL-VBC transition to be first-order as ascertained on finite systems from a sudden change in the spin-spin correlation profile and a crossing of the energies. For $J/J_1 \gtrsim 0.51$, the VBC gives way, via a first-order transition, to collinear long-range magnetic order [32, 33] with signatures of a star-like pattern in $\chi(\mathbf{k})$.

Results. We set the stage, by observing that across our nu-

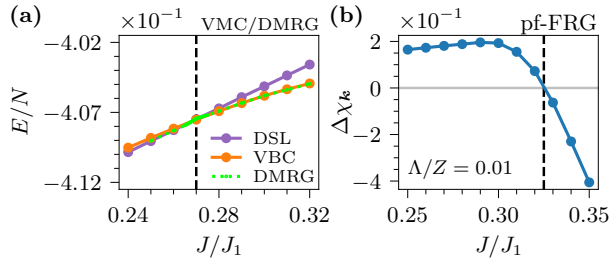

FIG. 2. **Transition into half-moon phase.** (a) From VMC, the evolution with J/J_1 of the energy per site of the DSL and VBC states ($3 \times 12 \times 12$ lattice). DMRG energies are also shown for comparison. (b) From pf-FRG, the variation of the spectral measure $\Delta\chi_{\boldsymbol{k}}$ (see text below) with J/J_1 evaluated at the lowest simulated RG cutoff $\Lambda/Z = 0.01$ where $Z = \sqrt{J_1^2 + 2J^2}$.

merical approaches we find that the ground state energy is seen to *increase* with J/J_1, reflecting an enhanced degree of frustration at variance with conventional expectation that the NNHAF represents the point of maximal frustration, which is relieved upon inclusion of long-range couplings. The presence of a pronounced kink in the evolution of the ground state energy is indicative of a phase transition [see Fig. 2(a)] which we estimate to be at $g_1 = 0.27(1)$ via an analysis of its derivative (from our DMRG calculations). This value is also corroborated by the behavior of the von Neumann entanglement entropy which starts decreasing sharply at g_1 [see Fig. S12] indicating the formation of a less entangled state.

To probe the nature of the ensuing states, let us start by discussing results from our fermionic VMC approach with versatile Gutzwiller-projected wave functions constructed in a manner enabling us to accurately study the competition between nonmagnetic quantum spin liquid (QSL) and VBC phases, together with magnetically ordered states. Such a unified framework has been met with success in its application to a wide range of frustrated spin models [24, 25, 34–36]. Our calculations are performed on $3 \times L \times L$ clusters respecting the full symmetry of the kagome lattice. For the $S = 1/2$ NNHAF, there is emerging consensus towards a U(1) DSL ground state [20, 23, 37, 38], which is known to yield the lowest variational energy [20, 37]. Upon including a J coupling, we investigate for the potential instability of the U(1) DSL to symmetric $\mathbb{Z}_2$ [39], chiral U(1) [40], chiral $\mathbb{Z}_2$ [41], and lattice nematic $\mathbb{Z}_2$ [42] QSLs. We also probe for possible dimerization tendencies into VBCs with various unit cell sizes up to 36 sites and different symmetries [17, 18, 43–45]. Our analysis finds a remarkable robustness of the U(1) DSL to the above-mentioned potential instabilities over a wide range along the maximally frustrated axis extending up till $J/J_1 = 0.26(1)$, which we note is beyond the range of J/J_1 for the classical model where the flat band is the lowest in energy [6].

At $J/J_1 = 0.26(1)$, we detect a *dimer instability* of the DSL towards a VBC ground state in our VMC calculations. This VBC state is found to be characterized by a 2×2 enlarged unit cell with a C_6 invariant *pinwheel* structure of spin-spin correlations in real space which breaks reflection symmetries [see Fig. 1(b)]. The formation of such a VBC state is further corroborated by an enhanced dimer response (see Fig. S4). Interestingly, such a pattern of strong/weak bonds has previously been identified as descending from confinement transitions of $\mathbb{Z}_2$ spin liquids [46] (left panel of Fig. 1 therein), and recently proposed in Ref. [19] [Fig. 3(c) therein] as a potential instability of the U(1) DSL resulting from a condensation of a C_6 invariant mass and the associated monopole terms. Our finding of a C_6 symmetric VBC, as opposed to other less symmetric patterns [Fig. 2(c) in Ref. [47]], is likely connected to the fact that the imaginary expectation value of the monopole condensation responsible for this reflection symmetry breaking pattern also optimizes the Landau potential [19]. It is worth pointing out that our VBC pattern is distinct from the 2×2 enlarged VBC patterns previously proposed in Fig. 4 of Ref. [17] and Fig. 5 of Ref. [18] which do not break reflections (though these pattern also minimize the Landau potential as noted in Ref. [19]). While, the DSL to VBC transition is allowed to be continuous, our microscopic calculations find it to be first-order as inferred from a level-crossing of the energies of the two states [see Fig. 2(a)] together with the observation of an abrupt change in the nearest-neighbor spin-spin correlation profile. We show that the energy gain of the VBC w. r. t. the U(1) DSL is non-zero for $J/J_1 > 0.26(1)$ and remains so on all finite size systems we simulated, indicating size-consistency of the VBC state and its stability in the thermodynamic limit.

Further support for the pinwheel VBC state comes from mVMC calculations at $J/J_1 = 0.4$, for which we measure the real-space dimer-dimer correlation pattern (see Fig. S6) where the emergence of the C_6 symmetric pinwheel VBC is also manifest. We also construct a symmetry-breaking dimer operator with non-vanishing susceptibility extrapolated to the thermodynamic limit (see Fig. S7). An analysis of the latter suggests a triply-degenerate C_3-related order parameter, with the three M-points momenta setting the spatial dependence, which signals a VBC behavior with the spontaneous C_3-symmetry breaking. However, the equal-weight sum of these three basis functions of the dominant irreducible representations results into an effective C_6 symmetric pinwheel pattern as obtained within VMC [see Fig. 1 (b)], which we illustrate in the inset of Fig. S7. The corresponding susceptibility decreases rapidly as $J/J_1 \to 0$, substantiating a transition to a quantum spin liquid phase from the VBC.

To probe the aforementioned VBC order within DMRG, we start by imposing the pinwheel VBC pattern (via small pinning fields) in a trial wavefunction that is then used as initial state for subsequent DMRG calculations performed with the original unperturbed Hamiltonian deep within the three phases of interest, namely, at $J/J_1 = 0.2$, $J/J_1 = 0.4$, and $J/J_1 = 0.65$. This procedure allows us to probe the stability of the initial pinwheel VBC state for these three phases or, alternatively, see its melting into different quantum states. We see that for $J/J_1 = 0.4$ [see Fig. 3(c)], the removal of the bias

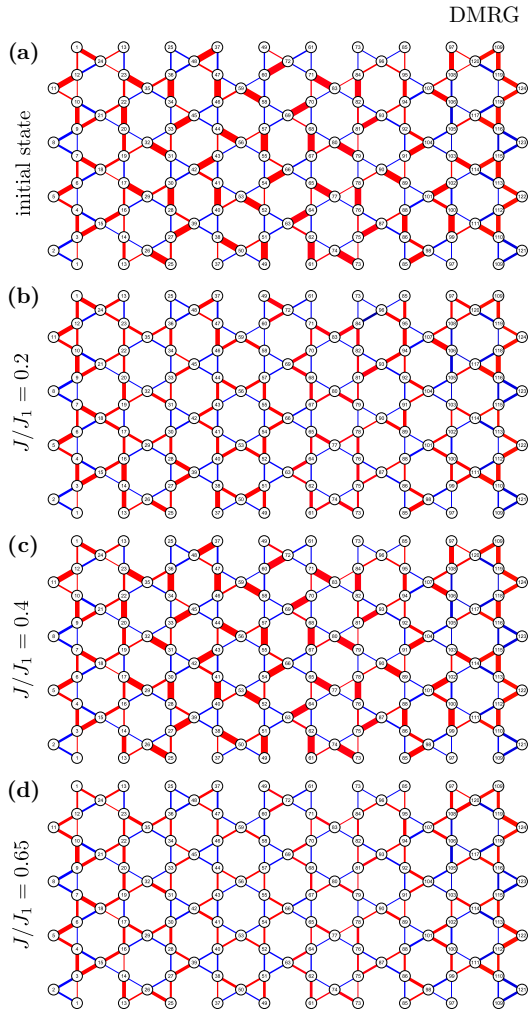

FIG. 3. **Nearest-neighbor spin-spin correlations** obtained from DMRG. (a) the initial state obtained at $J/J_1 = 0.4$ with a bias in the Hamiltonian (5% of J_1) that favours the onset of the pinwheel VBC. The final converged states obtained after 24 sweeps at (b) $J/J_1 = 0.2$, (c) $J/J_1 = 0.4$ and (d) $J/J_1 = 0.65$.

hardly affects the initial state thus providing strong support for the pinwheel VBC as true ground state in this regime. This is further corroborated by the fact that at $J/J_1 = 0.2$ and 0.65, the VBC pattern is progressively washed out [see Fig. 3(b) and see Fig. 3(d)]. Together, these results provide a smoking gun signature for the formation of the pinwheel VBC state in the range $J \in (g_1, g_2)$ [see Fig. 1(c)].

In Fourier space, the hallmark of the onset of the VBC order, as obtained within pf-FRG, is the splitting of the pinch points (M-points of the extended Brillouin zone), where the maxima of $\chi(\mathbf{k})$ are located for the DSL, into two symmetric half-moons resulting in the maxima of the intensity now being located at generic $(0, q_y)$ (and symmetry related) incommensurate points, as captured in an earlier pf-FRG study of the same model [49]. Given that the DSL and VBC phases can

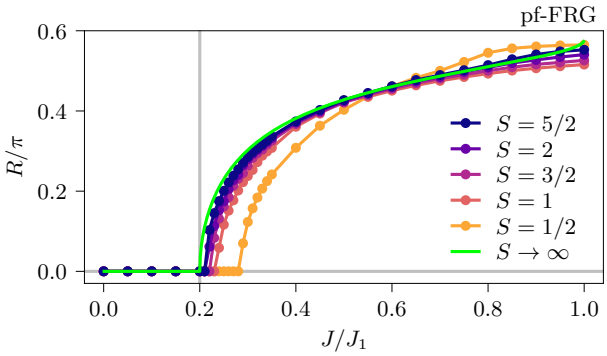

FIG. 4. **Half-moon radii.** From pf-FRG, we show for different values of spin-S [48], the evolution with J/J_1 of the radius of the half-moons characterizing the pinwheel VBC. The large-S (classical) result is from Ref. [6].

also be distinguished by comparing $\chi(\mathbf{k})$ along two cuts in momentum space, i.e., $\Gamma - K$ and $\Gamma - M$ segments, more precisely, we define a "spectral measure" $\Delta\chi_{\boldsymbol{k}}$ as the difference between the maxima along these two cuts, i.e., $\Delta\chi_{\boldsymbol{k}} = \chi^{\max}(\mathbf{k} \in \Gamma - K) - \chi^{\max}(\mathbf{k} \in \Gamma - M)$. The splitting of the pinch point into half-moons correspond to a downturn in the value of $\Delta\chi$ while the zero crossing of $\Delta\chi$ indicates that the half-moons become the dominant feature in $\chi(\mathbf{k})$. Based on these two signatures, we estimate the onset of VBC from pf-FRG at $J/J_1 = 0.30(2)$ [see Fig. 2(b) and Fig. S1], in good agreement with the other employed approaches. The evolution of the radius of the half-moon as a function of J/J_1 obtained from pf-FRG is shown in Fig. 4, where for $S = 1/2$ one observes an appreciable deviation from the reported large-S result [6]. For progressively increasing values of S, the known large-S behavior [6] is approached. Within the VMC calculation, the splitting of the pinch point maxima into half-moons is observed deep inside the VBC phase as shown in Fig. S8. Similarly, deep inside the VBC phase, the $\chi(\mathbf{k})$ obtained from mVMC shows maxima at incommensurate $(0, k_y)$ points as shown in Fig. S5.

Finally, let us turn to the transition into the star phase. To this end, we show, in Fig. 5, the evolution of the square of the sublattice magnetization m^2 with J/J_1, as obtained from mVMC, VMC, and DMRG. One observes a sudden change to a finite value of m^2 for $J/J_1 > 0.51(1)$, indicating the onset of long-range collinear spin order with a 12-site magnetic unit cell (see inset of Fig. 5) [32]. While the estimate of the phase boundary from these three approaches shows remarkable agreement, the comparatively smaller values of m^2 inside the ordered phase obtained in DMRG can be ascribed to the quasi one-dimensional character of the cylindrical geometries. The abrupt nature of the jump in the value of m^2 observed in mVMC and VMC, together with the crossing of the energies of the disordered VBC and magnetically ordered states across the transition point (see inset of Fig. 5), lends evidence in favor of a first-order character of the transition.

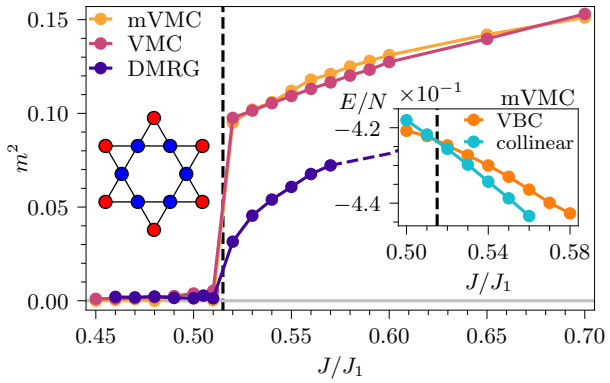

FIG. 5. **Transition into the star phase.** The behavior of the square of the sublattice magnetization m^2 with J/J_1 near the transition from the pinwheel VBC into collinear magnetic order [illustrated in the inset, with blue and red spins pointing in opposite directions]. The results from VMC and mVMC are for a $3 \times 8 \times 8$ site cluster [see Fig. S10 for finite-size scaling results of m^2 from VMC to the thermodynamic limit], while those from DMRG are obtained on a YC8-8 cylinder.

Similar conclusions are drawn from VMC via finite-size scaling of m^2 for different values of J/J_1 (see Fig. S10), wherein one observes a jump in the value of m^2 in the thermodynamic limit. The collinear magnetically ordered state displays a star-like pattern of intensity distribution in $\chi(\mathbf{k})$ [see Fig. 1(b)] with maxima at the location expected for the octahedral regular magnetic order [33]. It is worth noting that for $S = 1/2$ the phase boundary between the half-moon and star phases considerably shifts to a smaller value of $J/J_1 = 0.51(1)$, compared to the classical boundary at $J/J_1 = 1$, highlighting significant effects of quantum fluctuations.

Discussion. Moving the ground state of the kagome antiferromagnet along the maximally frustrated line is a complicated endeavor – as such it is quite fulfilling to see the remarkable agreement between our complementary numerical approaches yielding a consistent understanding of momentum and real space signatures of the ground state phases and their respective boundaries; a feat that would not have been imaginable only a few years ago. One might hope that the U(1) DSL, half-moon, and star phases will have a window of stability away from the maximally frustrated axis. It would thus be of interest to search and identify materials promising to realize the Dirac spin liquid phase and which lie within this region of stability. The recently studied material $YCu_3(OH)_6Br_2[Br_x(OH)_{1-x}]$ [50] wherein signatures of DSL behavior has been presented, could serve as a potential material candidate warranting further investigation. Another interesting candidate material might be the distorted kagome compound $Rb_2Cu_3SnF_{12}$ [51] where indications for a pinwheel VBC have been reported. One may be able to approach the maximally frustrated line by effectively varying the super-exchange couplings by application of hydrostatic or uniaxial pressure to vary the super-exchange bond angles [52]. On the theoretical front, given the persistent and enhanced frustration upon inclusion of J, it would be interesting to ascertain the extent of the nonmagnetic phase of the spin $S = 1$ NNHAF, and decipher the corresponding real-space nature of the half-moon phase. Finally, it would be worth exploring the corresponding quantum phase diagram on the pyrochlore lattice, which similarly at the classical level is host to persistent flat bands, as well as half-moon and star phases [6, 15].

During completion of this manuscript, we were made aware of a paper by Lugan *et al.* studying the same model with a complementary bosonic method.

Acknowledgments. We thank Federico Becca, Subhro Bhattacharjee, Ludovic Jaubert, Harald Jeschke, Arnaud Ralko, and Arnab Sen for insightful discussions. D. K., N. N., J. R., and S. T acknowledge support from the Deutsche Forschungsgemeinschaft (DFG, German Research Foundation), within Project-ID 277101999 CRC 183 (Project A04). F. F. acknowledges support from the Alexander von Humboldt Foundation through a postdoctoral Humboldt fellowship. N. A. is funded by the Swiss National Science Foundation, grant number: PP00P2_176877. The mVMC simulations were supported by the RSF grant (project No. 21-12-00237). The work in Wurzburg was supported by the Deutsche Forschungsgemeinschaft (DFG, German Research Foundation) through Project-ID 258499086-SFB 1170 and the Wurzburg-Dresden Cluster of Excellence on Complexity and Topology in Quantum Matter – ct.qmat Project-ID 390858490-EXC 2147. M.J.P.G is supported by the NSERC of Canada and the Canada Research Chair program (M. J. P. G., Tier 1). Y. I. acknowledges financial support by the Science and Engineering Research Board (SERB), Department of Science and Technology (DST), India through the Startup Research Grant No. SRG/2019/000056, MATRICS Grant No. MTR/2019/001042, and the Indo-French Centre for the Promotion of Advanced Research (CEFIPRA) Project No. 64T3-1. This research was supported in part by the National Science Foundation under Grant No. NSF PHY-1748958, the Abdus Salam International Centre for Theoretical Physics (ICTP) through the Simons Associateship scheme funded by the Simons Foundation, IIT Madras through the Institute of Eminence (IoE) program for establishing the QuCenDiEM group (Project No. SB20210813PHMHRD002720) and FORG group (Project No. SB20210822PHMHRD008268), the International Centre for Theoretical Sciences (ICTS), Bengaluru, India during a visit for participating in the program "Novel phases of quantum matter" (Code: ICTS/topmatter2019/12). N. N. thanks IIT Madras for funding a three-month stay through an International Graduate Student Travel award which facilitated completion of this research work. J. R. thanks IIT Madras for a Visiting Faculty Fellow position under the IoE program during which part of the research work and manuscript writing were carried out. D. K. and S. T. acknowledge usage of the JURECA Booster and JUWELS cluster at the Forschungszentrum Juelich and the Noctua2 cluster at the Paderborn Center for Parallel Computing (PC^2). N. N. and J. R. acknowledges the use of the CURTA cluster at FU Berlin [53]. N. A. acknowledges the usage of computing resources of the federal

collective usage center "Complex for simulation and data processing for mega-science facilities" at NRC "Kurchatov Institute". T. M., P. G., and R. T. gratefully acknowledge the Gauss Centre for Supercomputing e. V. for funding this project by providing computing time on the GCS Supercomputer SuperMUC at Leibniz Supercomputing Centre. Y. I. acknowledges the use of the computing resources at HPCE, IIT Madras.

* These authors contributed equally to this work.
† yiqbal@physics.iitm.ac.in

[1] J. T. Chalker, P. C. W. Holdsworth, and E. F. Shender, Hidden order in a frustrated system: Properties of the Heisenberg Kagomé antiferromagnet, Phys. Rev. Lett. **68**, 855 (1992).
[2] I. Ritchey, P. Chandra, and P. Coleman, Spin folding in the two-dimensional Heisenberg kagomé antiferromagnet, Phys. Rev. B **47**, 15342 (1993).
[3] C. L. Henley, The "Coulomb Phase" in Frustrated Systems, Annu. Rev. Condens. Matter Phys. **1**, 179 (2010).
[4] D. A. Garanin and B. Canals, Classical spin liquid: Exact solution for the infinite-component antiferromagnetic model on the kagomé lattice, Phys. Rev. B **59**, 443 (1999).
[5] M. E. Zhitomirsky, Octupolar ordering of classical kagome antiferromagnets in two and three dimensions, Phys. Rev. B **78**, 094423 (2008).
[6] T. Mizoguchi, L. D. C. Jaubert, R. Moessner, and M. Udagawa, Magnetic clustering, half-moons, and shadow pinch points as signals of a proximate Coulomb phase in frustrated Heisenberg magnets, Phys. Rev. B **98**, 144446 (2018).
[7] T. Li, A continuous family of fully frustrated Heisenberg models on the Kagome lattice, EPL (Europhysics Letters) **133**, 47001 (2021).
[8] J. M. Luttinger, A Note on the Ground State in Antiferromagnetics, Phys. Rev. **81**, 1015 (1951).
[9] J. M. Luttinger and L. Tisza, Theory of Dipole Interaction in Crystals, Phys. Rev. **70**, 954 (1946).
[10] D. H. Lyons and T. A. Kaplan, Method for Determining Ground-State Spin Configurations, Phys. Rev. **120**, 1580 (1960).
[11] J. Robert, B. Canals, V. Simonet, and R. Ballou, Propagation and Ghosts in the Classical Kagome Antiferromagnet, Phys. Rev. Lett. **101**, 117207 (2008).
[12] Half-moons also appear for Ising models on the kagome and pyrochlore lattices for $0 < J/J_1 < 1/3$ [14] and $0 < J/J_1 < 1/4$ [15, 16], respectively.
[13] H. Yan, R. Pohle, and N. Shannon, Half moons are pinch points with dispersion, Phys. Rev. B **98**, 140402 (2018).
[14] T. Mizoguchi, L. D. C. Jaubert, and M. Udagawa, Clustering of Topological Charges in a Kagome Classical Spin Liquid, Phys. Rev. Lett. **119**, 077207 (2017).
[15] J. G. Rau and M. J. P. Gingras, Spin slush in an extended spin ice model, Nat. Commun. **7**, 12234 (2016).
[16] M. Udagawa, L. D. C. Jaubert, C. Castelnovo, and R. Moessner, Out-of-equilibrium dynamics and extended textures of topological defects in spin ice, Phys. Rev. B **94**, 104416 (2016).
[17] M. B. Hastings, Dirac structure, RVB, and Goldstone modes in the kagomé antiferromagnet, Phys. Rev. B **63**, 014413 (2000).
[18] M. Hermele, Y. Ran, P. A. Lee, and X.-G. Wen, Properties of an algebraic spin liquid on the kagome lattice, Phys. Rev. B **77**, 224413 (2008).
[19] X.-Y. Song, C. Wang, A. Vishwanath, and Y.-C. He, Unifying description of competing orders in two-dimensional quantum magnets, Nat. Commun. **10**, 4254 (2019).
[20] Y. Iqbal, F. Becca, S. Sorella, and D. Poilblanc, Gapless spin-liquid phase in the kagome spin-$\frac{1}{2}$ Heisenberg antiferromagnet, Phys. Rev. B **87**, 060405 (2013).
[21] Y. Iqbal, D. Poilblanc, and F. Becca, Vanishing spin gap in a competing spin-liquid phase in the kagome Heisenberg antiferromagnet, Phys. Rev. B **89**, 020407 (2014).
[22] Y. Iqbal, F. Becca, and D. Poilblanc, Projected wave function study of $\mathbb{Z}_2$ spin liquids on the kagome lattice for the spin-$\frac{1}{2}$ quantum Heisenberg antiferromagnet, Phys. Rev. B **84**, 020407 (2011).
[23] Y.-C. He, M. P. Zaletel, M. Oshikawa, and F. Pollmann, Signatures of Dirac Cones in a DMRG Study of the Kagome Heisenberg Model, Phys. Rev. X **7**, 031020 (2017).
[24] Y. Iqbal, F. Ferrari, A. Chauhan, A. Parola, D. Poilblanc, and F. Becca, Gutzwiller projected states for the $J_1 - J_2$ Heisenberg model on the Kagome lattice: Achievements and pitfalls, Phys. Rev. B **104**, 144406 (2021).
[25] Y. Iqbal, D. Poilblanc, and F. Becca, Spin-$\frac{1}{2}$ Heisenberg $J_1 - J_2$ antiferromagnet on the kagome lattice, Phys. Rev. B **91**, 020402 (2015).
[26] C.-Y. Lee, B. Normand, and Y.-J. Kao, Gapless spin liquid in the kagome heisenberg antiferromagnet with dzyaloshinskii-moriya interactions, Phys. Rev. B **98**, 224414 (2018).
[27] F. Becca and S. Sorella, *Quantum Monte Carlo Approaches for Correlated Systems* (Cambridge University Press, Cambridge, United Kingdom ; New York, NY, 2017).
[28] T. Misawa, S. Morita, K. Yoshimi, M. Kawamura, Y. Motoyama, K. Ido, T. Ohgoe, M. Imada, and T. Kato, mVMC—Open-source software for many-variable variational Monte Carlo method, Comput. Phys. Commun **235**, 447 (2019).
[29] D. Tahara and M. Imada, Variational Monte Carlo Method Combined with Quantum-Number Projection and Multi-Variable Optimization, J. Phys. Soc. Jpn. **77**, 114701 (2008).
[30] J. Reuther and P. Wölfle, $J_1 - J_2$ frustrated two-dimensional Heisenberg model: Random phase approximation and functional renormalization group, Phys. Rev. B **81**, 144410 (2010).
[31] S. R. White, Density matrix formulation for quantum renormalization groups, Phys. Rev. Lett. **69**, 2863 (1992).
[32] V. Grison, P. Viot, B. Bernu, and L. Messio, Emergent Potts order in the kagome $J_1 - J_3$ Heisenberg model, Phys. Rev. B **102**, 214424 (2020).
[33] L. Messio, C. Lhuillier, and G. Misguich, Lattice symmetries and regular magnetic orders in classical frustrated antiferromagnets, Phys. Rev. B **83**, 184401 (2011).
[34] Y. Iqbal, W.-J. Hu, R. Thomale, D. Poilblanc, and F. Becca, Spin liquid nature in the Heisenberg $J_1 - J_2$ triangular antiferromagnet, Phys. Rev. B **93**, 144411 (2016).
[35] N. Astrakhantsev, F. Ferrari, N. Niggemann, T. Müller, A. Chauhan, A. Kshetrimayum, P. Ghosh, N. Regnault, R. Thomale, J. Reuther, T. Neupert, and Y. Iqbal, Pinwheel valence bond crystal ground state of the spin-$\frac{1}{2}$ Heisenberg antiferromagnet on the shuriken lattice, Phys. Rev. B **104**, L220408 (2021).
[36] Y. Iqbal, D. Poilblanc, R. Thomale, and F. Becca, Persistence of the gapless spin liquid in the breathing kagome Heisenberg antiferromagnet, Phys. Rev. B **97**, 115127 (2018).
[37] Y. Ran, M. Hermele, P. A. Lee, and X.-G. Wen, Projected-Wave-Function Study of the Spin-$1/2$ Heisenberg Model on the Kagomé Lattice, Phys. Rev. Lett. **98**, 117205 (2007).
[38] W. Zhu, X. Chen, Y.-C. He, and W. Witczak-Krempa, Entanglement signatures of emergent Dirac fermions: Kagome spin

liquid and quantum criticality, Sci. Adv. **4**, eaat5535 (2018).
[39] Y.-M. Lu, Y. Ran, and P. A. Lee, $\mathbb{Z}_2$ spin liquids in the $S = \frac{1}{2}$ Heisenberg model on the kagome lattice: A projective symmetry-group study of Schwinger fermion mean-field states, Phys. Rev. B **83**, 224413 (2011).
[40] S. Bieri, L. Messio, B. Bernu, and C. Lhuillier, Gapless chiral spin liquid in a kagome Heisenberg model, Phys. Rev. B **92**, 060407 (2015).
[41] S. Bieri, C. Lhuillier, and L. Messio, Projective symmetry group classification of chiral spin liquids, Phys. Rev. B **93**, 094437 (2016).
[42] R. Schaffer, Y. Huh, K. Hwang, and Y. B. Kim, Quantum spin liquid in a breathing kagome lattice, Phys. Rev. B **95**, 054410 (2017).
[43] Y. Iqbal, F. Becca, and D. Poilblanc, Valence-bond crystals in the kagomé spin-1/2 Heisenberg antiferromagnet: a symmetry classification and projected wave function study, New J. Phys. **14**, 115031 (2012).
[44] Y. Iqbal, F. Becca, and D. Poilblanc, Valence-bond crystal in the extended kagome spin-$\frac{1}{2}$ quantum Heisenberg antiferromagnet: A variational Monte Carlo approach, Phys. Rev. B **83**, 100404 (2011).
[45] R. R. P. Singh and D. A. Huse, Ground state of the spin-1/2 kagome-lattice Heisenberg antiferromagnet, Phys. Rev. B **76**, 180407 (2007).
[46] Y. Huh, M. Punk, and S. Sachdev, Vison states and confinement transitions of $\mathbb{Z}_2$ spin liquids on the kagome lattice, Phys. Rev. B **84**, 094419 (2011).
[47] S. Yan, D. A. Huse, and S. R. White, Spin-Liquid Ground State of the $S = 1/2$ Kagome Heisenberg Antiferromagnet, Science **332**, 1173 (2011).
[48] M. L. Baez and J. Reuther, Numerical treatment of spin systems with unrestricted spin length S: A functional renormalization group study, Phys. Rev. B **96**, 045144 (2017).
[49] F. L. Buessen and S. Trebst, Competing magnetic orders and spin liquids in two- and three-dimensional kagome systems: Pseudofermion functional renormalization group perspective, Phys. Rev. B **94**, 235138 (2016).
[50] Z. Zeng, X. Ma, S. Wu, H.-F. Li, Z. Tao, X. Lu, X.-h. Chen, J.-X. Mi, S.-J. Song, G.-H. Cao, G. Che, K. Li, G. Li, H. Luo, Z. Y. Meng, and S. Li, Possible Dirac quantum spin liquid in the kagome quantum antiferromagnet $YCu_3(OH)_6Br_2[Br_x(OH)_{1-x}]$, Phys. Rev. B **105**, L121109 (2022).
[51] K. Matan, T. Ono, Y. Fukumoto, T. J. Sato, J. Yamaura, M. Yano, K. Morita, and H. Tanaka, Pinwheel valence-bond solid and triplet excitations in the two-dimensional deformed kagome lattice, Nat. Phys. **6**, 865 (2010).
[52] Y. Iqbal, H. O. Jeschke, J. Reuther, R. Valentí, I. I. Mazin, M. Greiter, and R. Thomale, Paramagnetism in the kagome compounds $(Zn, Mg, Cd)Cu_3(OH)_6Cl_2$, Phys. Rev. B **92**, 220404 (2015).
[53] L. Bennett, B. Melchers, and B. Proppe, Curta: A General-purpose High-Performance Computer at ZEDAT, Freie Universität Berlin (2020).
[54] J. Thoenniss, M. K. Ritter, F. B. Kugler, J. von Delft, and M. Punk, Multiloop Pseudofermion Functional Renormalization for Quantum Spin Systems: Application to the Spin-$\frac{1}{2}$ Kagome Heisenberg Model, arxiv (2020), arXiv:2011.01268v1.
[55] D. Kiese, F. L. Buessen, C. Hickey, S. Trebst, and M. M. Scherer, Emergence and stability of spin-valley entangled quantum liquids in moiré heterostructures, Phys. Rev. Research **2**, 013370 (2020).
[56] F. L. Buessen, M. Hering, J. Reuther, and S. Trebst, Quantum Spin Liquids in Frustrated Spin-1 Diamond Antiferromagnets, Phys. Rev. Lett. **120**, 057201 (2018).
[57] D. Kiese, T. Müller, Y. Iqbal, R. Thomale, and S. Trebst, Multi-loop Functional Renormalization Group Approach to Quantum Spin Systems, arxiv (2020), arXiv:2011.01269.
[58] `PFFRGSolver.jl` repository, `https://github.com/dominikkiese/PFFRGSolver.jl`.
[59] M. Hering, V. Noculak, F. Ferrari, Y. Iqbal, and J. Reuther, Dimerization tendencies of the pyrochlore Heisenberg antiferromagnet: A functional renormalization group perspective, Phys. Rev. B **105**, 054426 (2022).
[60] Y. Iqbal, P. Ghosh, R. Narayanan, B. Kumar, J. Reuther, and R. Thomale, Intertwined nematic orders in a frustrated ferromagnet, Phys. Rev. B **94**, 224403 (2016).
[61] A. Keleş and E. Zhao, Rise and fall of plaquette order in the Shastry-Sutherland magnet revealed by pseudofermion functional renormalization group, Phys. Rev. B **105**, L041115 (2022).
[62] T. Misawa and M. Imada, Origin of high-T_c superconductivity in doped Hubbard models and their extensions: Roles of uniform charge fluctuations, Phys. Rev. B **90**, 115137 (2014).
[63] M. Casula, C. Attaccalite, and S. Sorella, Correlated geminal wave function for molecules: An efficient resonating valence bond approach, J. Chem. Phys. **121**, 7110 (2004).
[64] S. Morita, R. Kaneko, and M. Imada, Quantum Spin Liquid in Spin 1/2 J_1–J_2 Heisenberg Model on Square Lattice: Many-Variable Variational Monte Carlo Study Combined with Quantum-Number Projections, J. Phys. Soc. Jpn **84**, 024720 (2015).
[65] Y. Nomura and M. Imada, Dirac-Type Nodal Spin Liquid Revealed by Refined Quantum Many-Body Solver Using Neural-Network Wave Function, Correlation Ratio, and Level Spectroscopy, Phys. Rev. X **11**, 031034 (2021).
[66] S. Sorella, Green Function Monte Carlo with Stochastic Reconfiguration, Phys. Rev. Lett. **80**, 4558 (1998).
[67] G. Carleo and M. Troyer, Solving the quantum many-body problem with artificial neural networks, Science **355**, 602 (2017).
[68] N. Astrakhantsev, T. Westerhout, A. Tiwari, K. Choo, A. Chen, M. H. Fischer, G. Carleo, and T. Neupert, Broken-Symmetry Ground States of the Heisenberg Model on the Pyrochlore Lattice, Phys. Rev. X **11**, 041021 (2021).
[69] Additional superconducting pairing terms can be included in the auxiliary Hamiltonian of Eq. (S9), but for the model under consideration they do not provide any energy gain in the thermodynamic limit.
[70] M. Fishman, S. R. White, and E. M. Stoudenmire, The ITensor Software Library for Tensor Network Calculations (2020), arXiv:2007.14822 [cs.MS].

I. PSEUDO-FERMION FUNCTIONAL RENORMALIZATION GROUP

The pseudo-fermion functional renormalization group approach (pf-FRG) [S30] approximates the original spin model by a fermionic Hamiltonian using an Abrikosov fermion representation

$$S_i^\mu = \frac{1}{2}\sum_{\alpha,\beta} f_{i,\alpha}^\dagger \sigma_{\alpha,\beta}^\mu f_{i,\beta}\,, \tag{S1}$$

of the spin operators together with the soft-constraint $\langle\sum_\alpha f_{i,\alpha}^\dagger f_{i,\alpha}\rangle = 1$ on every lattice site. Fluctuations around this average decrease during the RG flow and can be further suppressed adding level repulsion terms to the Hamiltonian [S54], yet the qualitative results, especially with respect to the nature of the ground state, appear robust with respect to small variations of the number of particles per site [S48, S54–S56].

The flow equations are generated by implementing an infrared cutoff Λ into the bare propagator $G_0(\omega) = (i\omega)^{-1}$ of the pseudo-fermion Hamiltonian and taking derivatives of one-particle irreducible vertices with respect to it. The resulting hierarchy of ordinary differential equations is not closed and thus needs to be truncated, usually by discarding all n-particle vertices with $n > 2$. In pf-FRG one needs to incorporate some contributions from the three-particle vertex by means of the so called Katanin truncation [S30], which feeds back the self-energy flow into the flow of the two-particle vertex. The corresponding flow equations for the self-energy Σ and two-particle vertex Γ then read

$$\begin{aligned}\frac{d}{d\Lambda}\Sigma^\Lambda(1) &= -\frac{1}{2\pi}\sum_2 \Gamma^\Lambda(1,2|1,2)S^\Lambda(2)\\ \frac{d}{d\Lambda}\Gamma^\Lambda(1',2'|1,2) &= -\frac{1}{2\pi}\sum_{3,4}\big[\Gamma^\Lambda(3,4|1,2)\Gamma^\Lambda(1',2'|3,4)\\ &\quad - \Gamma^\Lambda(1',4|1,3)\Gamma^\Lambda(3,2'|4,2) - (3\leftrightarrow 4)\\ &\quad + \Gamma^\Lambda(2',4|1,3)\Gamma^\Lambda(3,1'|4,2) + (3\leftrightarrow 4)\big]\\ &\quad \times \partial_\Lambda(G^\Lambda(3)G^\Lambda(4))\,,\end{aligned} \tag{S2}$$

where G^Λ denotes the full fermionic propagator and $S^\Lambda \equiv -\frac{d}{d\Lambda}G^\Lambda|_{\Sigma^\Lambda=\text{const.}}$ the single-scale propagator. Here, multi-indices $1 = (i_1, \alpha_1, \omega_1)$ comprise a lattice, spin and Matsubara frequency index.

To characterize the physical field theory that the pf-FRG is flowing towards, one usually computes spin-spin correlators

$$\chi_{ij} = \chi_{ij}^{zz}(i\omega = 0) = \int_0^\beta d\tau \langle T_\tau S_i^z(\tau) S_j^z(0)\rangle\,, \tag{S3}$$

from renormalized pseudo-fermion vertices (we suppress the Λ dependence here for brevity) and checks whether long-range order manifests as an instability in their flow. The associated spin configuration can then be determined by Fourier transforming χ_{ij} to momentum space and locating the position of the incipient Bragg peaks. A paramagnetic phase, on the other hand, is signified by a smooth flow down to the infrared $\Lambda \to 0$ with broadened features in the structure factor $\chi(\boldsymbol{k})$.

We use the `PFFRGSolver.jl` [S57, S58] software package to perform the integration of the flow equations in this manuscript. All calculations are performed on a 48×36^2 frequency grid with absolute error tolerances $a_{\text{tol}} = 10^{-8}$ and a relative error tolerance $r_{\text{tol}} = 10^{-2}$ (10^{-4}) for the differential equation solver (Matsubara frequency integrals). The real-space truncation is set to $L = 24$ bonds away from the origin.

A. Pinch-point to half-moon transition in pf-FRG

To support the data regarding the pinch-point to half-moon transition presented in the main text, we explicitly present the pf-FRG data, from which the phase boundary was distilled. In Fig. S1, we plot structure factors close to the transition

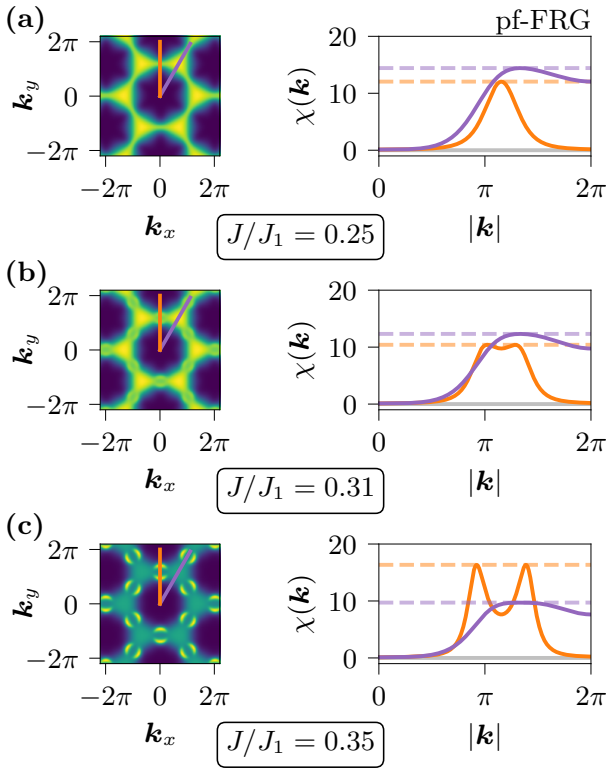

FIG. S1. **Pinch-point to half-moon transition** from pf-FRG data at $\Lambda/Z = 0.01$. We plot the structure factor in the $\boldsymbol{k}_x - \boldsymbol{k}_y$ plane (left column) and along two distinct cuts through momentum space (right column). In the spin liquid phase (a), the maximum intensity is centered around the corners of the kagome Brillouin zone (magenta line), with subdominant peaks at the pinch-points (orange line). Approaching the half-moon phase (b) and (c), the pinch-points first flatten and split into two peaks and finally also carry the maximum intensity in the structure factor.

at $J/J_1 \approx 0.33$ for $\Lambda/Z = 0.01$, both in the two dimensional $\boldsymbol{k}_x - \boldsymbol{k}_y$ plane as well as along two distinct momentum space cuts. In the spin-liquid phase (see panel (a) in Fig. S1), the structure factor peaks at the corners of the kagome Brillouin zone, as well as at the pinch-points, with more spectral weight distributed around the corners. Thus, the spectral measure $\Delta\chi_{\boldsymbol{k}}$, i.e the difference between the magenta and orange dashed line in the right column of Fig. S1, is positive. Around $J/J_1 \approx 0.31$, the peaks at the pinch-points flatten and give rise to two peaks (the half-moons), yet $\Delta\chi_{\boldsymbol{k}} > 0$ holds. Only at larger J/J_1, shown, e.g. in panel (c) of Fig. S1, the spectral measure changes sign, and the half-moons indeed pose the most distinct feature in the structure factor.

B. Half-moon to star transition in pf-FRG

In contrast to the transition from the spin liquid (pinch-point) to the VBC (half-moon) phase, which could easily be identified in pf-FRG calculations by measuring the half-moon radius and the spectral parameter $\Delta\chi_{\boldsymbol{k}}$, determining the transition from the non-magnetic VBC to the magnetic collinear phase turns out to be more difficult. All other numerical approaches employed here consistently predict a finite magnetization around $J/J_1 \approx 0.5$, yet, the pf-FRG flows show no sign of a flow breakdown at this point (see Fig. S2). Here, magnetic order sets in at larger couplings $J/J_1 \geq 0.8$ and only for extremely small cutoffs $\Lambda/Z \gtrsim 0.011$, close to the lower limit $\Lambda/Z = 0.01$ which is still numerically feasible. Probing the real-space correlations $\chi_{0\,\Delta x\boldsymbol{a}_1} = \chi(\Delta x)$ along the $\boldsymbol{a}_1 = (1, 0)$ direction (i.e. along one axis of the kagome lattice), we indeed find fairly long-range correlations extending over the whole $L = 24$ real space cluster considered in the numerical simulations. In the spin liquid and half-moon phase, in contrast, correlations decay more rapidly and already for few bonds away from the origin, their magnitude is strongly diminished (see Fig. S3). The discrepancy in the precise location of the phase boundary could be related to the fulfillment of the half-filling constraint in pf-FRG. After all, it is only enforced on average and there may still exist fluctuations which populate unphysical, i.e. non-magnetic pseudofermion states [S54]. These might be responsible for impeding the formation of a clear divergence of the RG flow already at smaller values of J/J_1. Furthermore, we cannot rule out a scenario in which the critical scale lies below the numerical threshold $\Lambda/Z = 0.01$.

C. Dimer response from pf-FRG

While the order parameter corresponding to a VBC state is of order S^4 and would require higher vertex functions that are out of reach for the pf-FRG, a qualitative picture of a system's tendency to select a particular dimer pattern may still be obtained. To achieve this, the unit cell needs to be enlarged so that translational symmetry is broken by slightly increasing

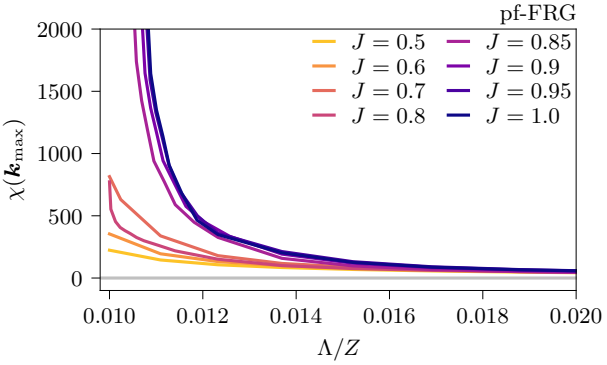

FIG. S2. **pf-FRG flows of the structure factor** at the momenta with maximum intensity. For $J/J_1 < 0.8$ the flows are featureless and can be continued down to the smallest considered energy scale $\Lambda/Z = 0.01$. For $J/J_1 = 0.8$ the flow shows a sharp upturn at the lowest values of Λ/Z, which evolves into a divergence for $J/J_1 > 0.8$, signalling the onset of long-range magnetic order.

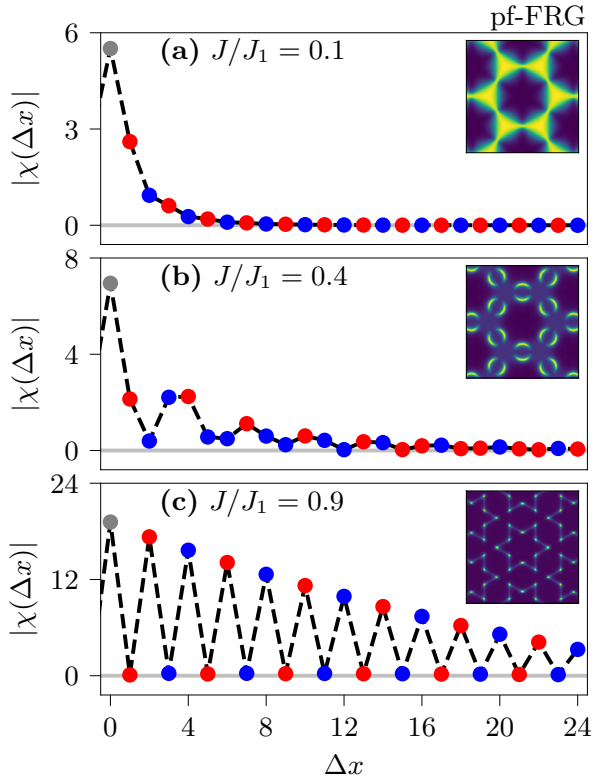

FIG. S3. **Spin-spin correlations along the $\boldsymbol{a}_1$ direction of the kagome lattice** extracted from pf-FRG vertices at $\Lambda/Z \approx 0.011$ deep in the three different phases. Here blue (red) markers denote (anti-) ferromagnetic correlations to the reference site marked in grey. In (a) the spin liquid and (b) the half-moon phase, correlations decay particularly fast, and beyond $6 \sim 10$ bonds away from the origin their magnitude become negligible. In the star phase (c), however, magnetic correlations spread over the whole range of the lattice considered in the numerical calculations, explaining the observed flow breakdowns.

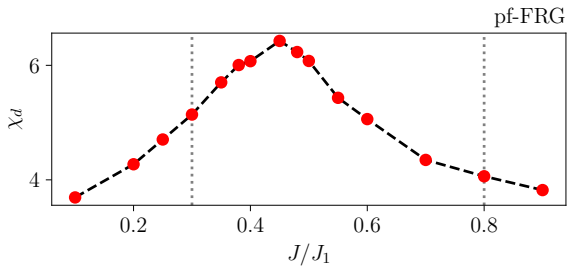

FIG. S4. **pf-FRG dimer response for the pinwheel VBC pattern** in Fig. 1 of the main text as a function of J/J_1. The dimer response is calculated via Eq. (S4). The phase boundaries shown as grey dotted lines are obtained as described in the sections above.

the strength of dimerized bonds while weakening the others, i.e. $J_1 \to J_1 \pm \delta$ with $\delta = 0.01 J_1$ [S59–S61]. Defining the equal time, real-space spin-spin correlation along such a strengthened dimer bond as $\langle S_i^z S_j^z \rangle_+$ and a completely unperturbed (i.e. $\delta = 0$) reference value $\langle S_i^z S_j^z \rangle_0$, we may define the dimer response as

$$\chi_d = \frac{J_1}{\delta} \times \frac{\langle S_i^z S_j^z \rangle_+ - \langle S_i^z S_j^z \rangle_0}{\langle S_i^z S_j^z \rangle_0}. \tag{S4}$$

Note that this definition requires the evaluation of two separate FRG runs to compute $\langle S_i^z S_j^z \rangle_0$ and $\langle S_i^z S_j^z \rangle_+$. From pf-FRG, equal-time correlators can be computed as $\langle S_i^z S_j^z \rangle \equiv \langle S_i^z S_j^z \rangle (t = 0) = \int d\nu \chi_{ij}(\nu)$.

Fig. S4 shows the response obtained for the pinwheel VBC pattern displayed in Fig. 1, where thick red bonds are strengthened and thin bonds are weakened by δ: In the QSL phase, we observe a relatively small value of the dimer response which rises steadily towards the VBC phase up until a distinct maximum at $J_2 \approx 0.45$ after which it decreases once more. This is in good agreement with the phase diagram presented in Fig. 1 of the main text.

II. MANY-VARIABLE WAVE FUNCTION (MVMC)

The many-variable variational Monte Carlo (mVMC) method can be successfully used in studies of strongly correlated spin and electronic systems [S62, S63]. In particular, the method can be applied to distinguish between quantum spin liquid and valence bond solid phases, such as in the case of the J_1-J_2 Heisenberg model on the square lattice [S64, S65]. In this work, we employ the mVMC implementation from Ref. [S28, S29]. The construction of the variational states relies on the Abrikosov fermion representation of spin degrees of freedom, as given in Eq. (S1).

Inspired by the Anderson resonating valence-bond wave function, the mVMC ansatz has the form

$$|\phi_{\text{pair}}\rangle = \hat{\mathcal{P}}_{\text{G}}^{\infty} \exp\left(\sum_{i,j} F_{i,j} \hat{f}_{i,\uparrow}^{\dagger} \hat{f}_{j,\downarrow}^{\dagger}\right) |0\rangle, \tag{S5}$$

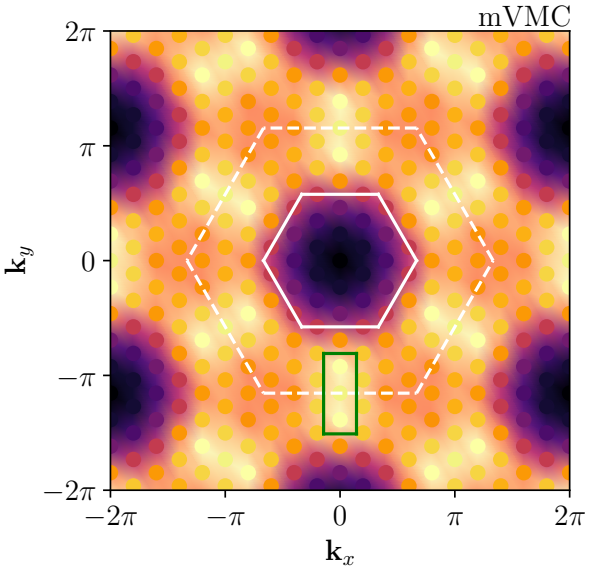

FIG. S5. **Static (equal-time) spin structure factor** at $J/J_1 = 0.4$ as computed by mVMC. The color plot shows the isotropic structure factor $\chi(\mathbf{k})$ [Eq. (S8)] in the $\boldsymbol{k}_x - \boldsymbol{k}_y$ plane. The results have been obtained on a $3 \times 8 \times 8$ finite cluster. The white hexagon with solid (dashed) lines delimits the first (extended) Brillouin zone. The green box highlights the "half-moon" feature of the correlation pattern.

where single occupation is ensured by the Gutzwiller projector

$$\hat{\mathcal{P}}_{\text{G}}^{\infty} = \prod_i (f_{i,\uparrow}^{\dagger} f_{i,\uparrow} - f_{i,\downarrow}^{\dagger} f_{i,\downarrow})^2, \tag{S6}$$

which maps the fermionic Hilbert space to the original Hilbert space of spin operators. The wave-function value $\langle \boldsymbol{\sigma} | \phi_{\text{pair}} \rangle$ of a specific spin configuration $|\boldsymbol{\sigma}\rangle$ is evaluated using the Slater determinant of the matrix with elements $F_{i,j}$. Here, $\boldsymbol{\sigma}$ represents a string of ± 1, which, for each lattice site, stands for the respective spin eigenstate in the S^z basis. The parameters $F_{i,j}$ are optimised using the stochastic reconfiguration technique [S66], which can be seen as a way of performing imaginary-time evolution in the variational parameters manifold [S27, S67].

To improve the accuracy of the variational wave functions, we employ quantum-number projections. The point-group symmetry $\hat{G}$ is enforced by applying its generators until the symmetry orbit is exhausted

$$|\Psi_\xi\rangle = \hat{P}|\Psi\rangle = \sum_n \xi^n \hat{G}^n |\Psi\rangle, \tag{S7}$$

where ξ is the desired projection quantum number and $|\Psi_\xi\rangle$ the resulting symmetrized state. The projection onto the total spin S is performed by superposing the $SU(2)$–rotated wave functions [S29]. In this work, for systems with more than 36 sites, we partially impose translational symmetry directly on the variational parameters $F_{i,j}$. Namely, we introduce translational symmetry modulo 2×2 unit cells sublattice structure

and enforce the 2×2 translations and the point-group symmetries using Eq. (S7). The resulting procedure amounts into $2\times2\times3^2\times L^2$ variational parameters with L being the number of unit cells in each lattice direction. Such partial translational symmetry imposition is a reasonable compromise between the ability to express complicated wave function and the required time to optimize the wave function.

Magnetic properties of variational wave functions can be assessed by computing the structure factor $\chi(\mathbf{k})$ as the equal-time momentum-resolved spin-spin correlation function

$$\chi(\mathbf{k}) = \frac{1}{3L^2}\sum_{i,\,j} e^{i\mathbf{k}\cdot(\mathbf{r}_i-\mathbf{r}_j)}\langle\hat{\mathbf{S}}_i\cdot\hat{\mathbf{S}}_j\rangle, \qquad \text{(S8)}$$

where $\mathbf{r}_i$ indicates the position of the lattice site i including sublattice displacement. In Fig. S5, we present the spin structure factor at $J/J_1 = 0.4$ as computed by mVMC.

In a non-magnetic phase, the properties of the wave function are assessed by measuring the dimer-dimer correlation function $\chi^D_{b,\,b'} = \langle\hat{D}_b\hat{D}_{b'}\rangle - \langle\hat{D}_b\rangle\langle\hat{D}_{b'}\rangle$ for all pairs of bonds in the system, $0 \leqslant b, b' < N_{\text{bonds}}$, where $\hat{D}_b = \hat{\mathbf{S}}_i\cdot\hat{\mathbf{S}}_j$, with i, j being sites at ends of the bond b. In Fig. S6, we show the dimer-dimer correlations between the base bond (located in a distant unit cell) and other bonds. To carry out a quantitative assessment of the VBC character of the ground state, we need to define suitable scalar order parameters to perform an infinite-volume extrapolation of the dimer order. Thus, we regard $\chi^D_{b,\,b'}$ as a matrix in the bond indices and we diagonalize it; the resulting set of eigenvalues/eigenvectors pairs $(\lambda,\ A^\lambda_b)$ is used to define the operators $\hat{\mathcal{O}}_\lambda = \sum_b A^\lambda_b\hat{D}_b$, each of them corresponding to a certain momentum and irreducible representation of the lattice point group. The tendency to establish a finite expectation value of one of these operators, and thus spontaneously break the corresponding lattice symmetry, is measured by the susceptibility $\chi_{\hat{\mathcal{O}}_\lambda} = \langle\hat{\mathcal{O}}^\dagger_\lambda\hat{\mathcal{O}}_\lambda\rangle - \langle\hat{\mathcal{O}}^\dagger_\lambda\rangle\langle\hat{\mathcal{O}}_\lambda\rangle = \lambda$ extrapolated to the thermodynamic limit [S68].

Following this procedure, we obtain leading eigenvalues and eigenstates of the $\chi^D_{b,\,b'}$ matrix at $J/J_1 = 0.2,\ 0.3,\ 0.4$ on finite-size lattices with $L = 4,\ 6,\ 8$ and 10. In Fig. S7, we show an equal-weight superposition of the three degenerate leading eigenstates at the M–points. Other eigenvalues are an order of magnitude smaller, and are thus not shown. We extrapolate the corresponding susceptibility to the thermodynamic limit and obtain, for $J/J_1 = 0.4$, non-vanishing susceptibility extrapolation of $7.6(3)\times10^{-3}$. This signals presence of symmetry breaking through establishment of a dimer order at $J/J_1 = 0.4$. Similar extrapolations at $J/J_1 = 0.2,\ 0.25,\ 0.3$ and 0.35 yield $3.8(2)\times10^{-3}$, $4.1(2)\times10^{-3}$, $5.1(3)\times10^{-3}$ and $6.9(2)\times10^{-3}$, respectively. By fitting the susceptibility dependence on J/J_1 with a hyperbolic tangent ansatz, we estimate the inflection point to be at $J/J_1 = 0.32(3)$. This provides an estimate of the transition point from the QSL to the VBC phase. We emphasize that the dimer-dimer susceptibility within mVMC remains finite in the QSL phase. This is related to the fact that the mVMC wave function cannot efficiently express the ground state of the $U(1)$ DSL phase, unlike the dimerized VBC case. This is confirmed by the comparison of the mVMC variational energy to the one of the DMRG approach in the two phases.

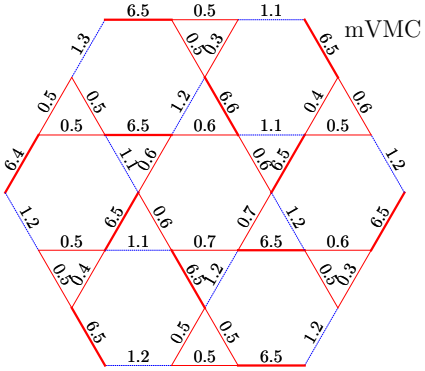

FIG. S6. **Real-space correlations pattern** $\langle\hat{D}_a\hat{D}_b\rangle - \langle\hat{D}_a\rangle\langle\hat{D}_b\rangle$ measured within mVMC on the $3\times8\times8$ kagome lattice for $J/J_1 = 0.4$. Here $\hat{D}_a$ is the dimer operator placed on the "base" bond (in a distant unit cell) and $\hat{D}_b$ is the dimer operator on other bonds. Red (blue) color in the figure represents positive (negative) values of the correlator, while its absolute magnitude (multiplied by 100) is marked near each bond. The correlations were measured on a non-symmetrized mVMC wave function for which the pinwheel dimer pattern is more pronounced.

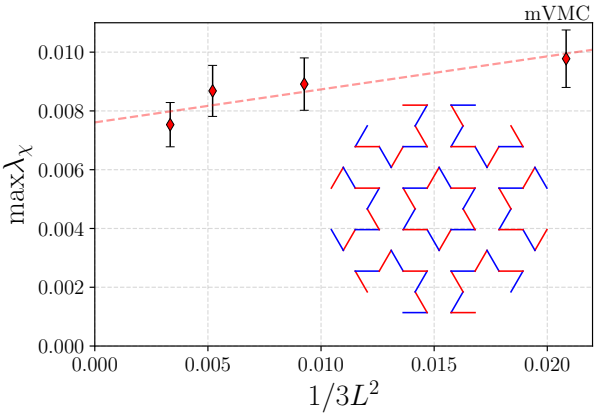

FIG. S7. **Extrapolation of the maximum eigenvalue of the χ^D_{ij} dimer-dimer correlation matrix** at $J/J_1 = 0.4$ as the function of inverse lattice volume. The leading eigenvalue is triply-degenerate, while the other eigenvalues are an order of magnitude smaller. The inset shows an equal-weight superposition of the three basis functions of the dominant irreducible representation, all three connected by $2\pi/3$–rotations.

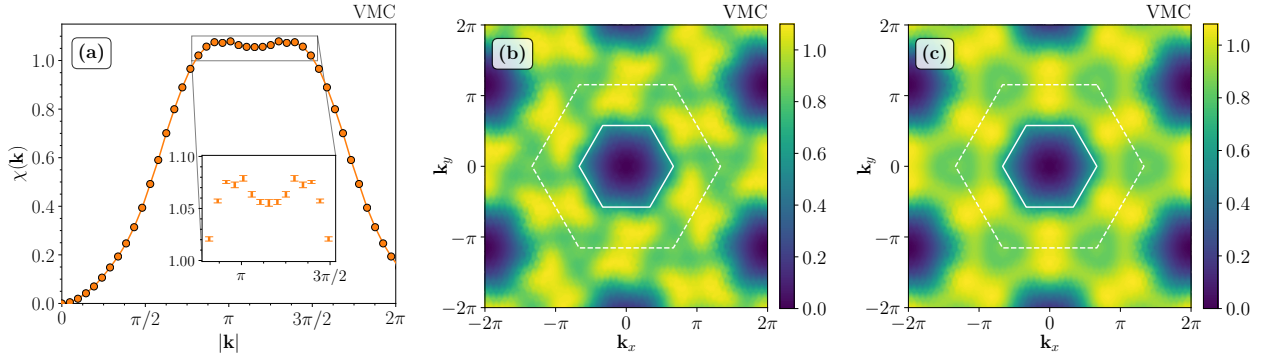

FIG. S8. **Static (equal-time) spin structure factor of the VBC phase** as computed by VMC [Eq. (S8)]. Results for $J/J_1 = 0.5$ are shown (on a $3 \times 24 \times 24$ lattice). In (a) we plot $\chi(\mathbf{k})$ as a function of $|\mathbf{k}|$, along the $\mathbf{k}_x = 0$ cut in momentum space shown in Fig. S1 (orange vertical line). The inset highlights the dip in the profile of $\chi(\mathbf{k})$ (with error bars) at the pinch-point positions, which signals the appearance of half-moons. The color plots in (b) and (c) show the value of $\chi(\mathbf{k})$ in the $\boldsymbol{k}_x - \boldsymbol{k}_y$ plane. The results of (b) are obtained with the bare VBC wave function, which breaks the reflection symmetry of the kagome lattice. In (c) we show symmetrized results for the structure factor, where the reflection symmetry is imposed *a posteriori*. The white hexagon with solid (dashed) lines delimits the first (extended) Brillouin zone.

III. VARIATIONAL MONTE CARLO (VMC)

The variational Monte Carlo (VMC) [S27] approach employed in this work shares several common aspects with the mVMC method introduced in the previous section. Both techniques rely on the Abrikosov fermion representation of spin operators, introduced in Eq. (S1). Within this fermionic formulation, suitable variational states for the Heisenberg model are obtained by projecting a fermionic wave function to the spin Hilbert space. The projection, which enforces the single fermionic occupation of each lattice site, is achieved by means of a Gutzwiller-projector $\mathcal{P}_G^\infty$ [see Eq. (S6)], and can be performed exactly by an appropriate Monte Carlo sampling [S27]. The variational *Ansätze* of VMC, discussed in this section, differ from those of the mVMC approach in the choice of the fermionic states to be projected.

Within the VMC approach, the variational state is obtained by projecting a Slater determinant, $|\Phi_0\rangle$, which is the ground state of an auxiliary quadratic Hamiltonian

$$\mathcal{H}_0 = \sum_{i,j} t_{ij}(f^\dagger_{i,\uparrow} f_{j,\uparrow} + f^\dagger_{i,\downarrow} f_{j,\downarrow}) + \sum_i \sum_{\mu=x,y,z} h_i^\mu S_i^\mu \,. \quad \text{(S9)}$$

The parameters t_{ij} (hoppings) and h_i^μ (fictitious magnetic field) of $\mathcal{H}_0$ are optimized in order to minimize the variational energy of the projected state [S69]. The complete expression for the variational wave function is

$$|\Psi_{\text{var}}\rangle = \mathcal{J}\mathcal{P}_G^\infty |\Phi_0\rangle \,, \quad \text{(S10)}$$

where, in addition to the projected Slater determinant, we have included the long-range spin-spin Jastrow factor [S27]

$$\mathcal{J} = \exp\Big(\sum_{i,j} v_{i,j} S_i^z S_j^z\Big) \,. \quad \text{(S11)}$$

The pseudopotential parameters $v_{i,j}$ are assumed to be translationally invariant, and numerically optimized along with the fermionic parameters t_{ij} and h_i^μ. The optimization of the variational wave function is achieved through the stochastic reconfiguration method [S27, S66, S67]

A. Spin liquid to pinwheel VBC transition in VMC

For small values of the ratio J/J_1, the optimal variational wave function for the model is the U(1) DSL [S20, S37]. Upon increasing J/J_1, the system undergoes a phase transition to the pinwheel VBC at $J/J_1 = 0.26(1)$ (see Fig. 2 of the main text). The variational Ansatz for the VBC is obtained by considering a 2×2 enlarged unit cell of 12 sites, which can accommodate the pinwheel pattern depicted in Fig. 1 (b) of the main text. The variational parameters of the VBC Ansatz are the inequivalent hoppings within the enlarged unit cell, from first- to third-neighbors (the latter ones being limited to the J_{3a}-bonds). The number of independent hopping parameters is reduced from 72 to 12 by applying the C_6 rotational symmetry of the kagome lattice. Finally, an underlying sign structure for the hoppings is imposed, to reproduce the flux pattern of the U(1) DSL (similarly to the approach used in Ref. [S43]). For this reason, the VBC wave function can be regarded as an instability of the DSL state. We find that the energy of the VBC state is lower than the one of the DSL for $J/J_1 > 0.26$, signalling the transition to the pinwheel VBC phase. Deep inside the VBC phase, the static structure factor $\chi(\mathbf{k})$ displays signatures of half-moons, as shown in Fig. S8.

B. Pinwheel VBC to collinear magnetic order transition in VMC

At $J/J_1 = 0.51(1)$, a phase transition from the pinwheel VBC to the magnetic phase with collinear order is observed. The auxiliary Hamiltonian $\mathcal{H}_0$ for the magnetic state features

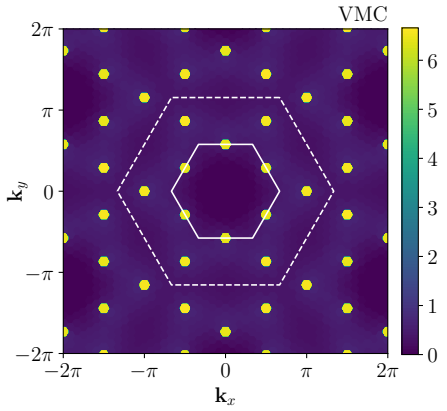

FIG. S9. **Static (equal-time) spin structure factor of the collinear ordered phase** at $J/J_1 = 0.6$ as computed by VMC. The color plot shows the isotropic structure factor $\chi(\mathbf{k})$ in the $\boldsymbol{k}_x - \boldsymbol{k}_y$ plane. The results have been obtained on a $3 \times 12 \times 12$ finite cluster. The white hexagon with solid (dashed) lines delimits the first (extended) Brillouin zone.

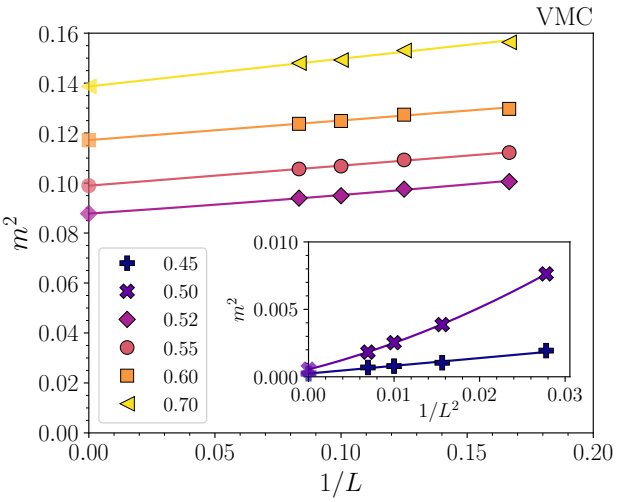

FIG. S10. **Finite-size scalings of the square of the sublattice magnetization** m^2 for the collinear spin order showing its behavior at the VBC-magnetic order transition. We employed $3 \times L \times L$ clusters with $L = 6, 8, 10, 12$. The values of J/J_1 are reported in the box in the lower-left corner. The inset shows the finite-size scaling of m^2 within the VBC regime, as a function of $1/L^2$. For $J/J_1 > 0.51$ (i.e., within the collinear magnetic phase), m^2 extrapolates to a non-zero value for $L \to \infty$.

the same hopping parametrization of the VBC Ansatz, with the addition of a fictitious magnetic field h_i^μ which reproduces the collinear order sketched in the inset of Fig. 5. The fictitious collinear field h_i^μ is taken along the S_x direction. Thus, the presence of the Jastrow factor, which is a function of S_z operators, introduces transverse spin fluctuations on top of the ordered fermionic state. Although the variational parametrization allows for a continuous transition between the VBC and the collinear ordered states, the transition turns out to be of the first order. Indeed, we detect the presence of two energy minima when optimizing the variational energy, i.e. an absolute minimum and a metastable state with higher energy. One of the minima corresponds to the VBC state, i.e., it is characterized by a vanishingly small magnetic field h_i^μ in the thermodynamic limit and a dimer pattern like the one of Fig. 1 (b); the other minumum, instead, corresponds to the magnetically ordered phase. The relative positions of the two minima swap at $J/J_1 = 0.51(1)$, and magnetic order sets in for larger values of J/J_1. In the collinear ordered phase, the static structure factor shows the presence of Bragg peaks at the ordering vectors, as shown in Fig. S9 for $J/J_1 = 0.6$. The first-order nature of the VBC-collinear order transition is confirmed by the sudden jump of the sublattice magnetization, shown in Fig. S5 of the main text for a $3 \times 8 \times 8$ lattice. A finite-size scaling analysis of m^2 confirms the presence of an abrupt change at the phase boundary also in the thermodynamic limit (see Fig. S10).

IV. DENSITY MATRIX RENORMALIZATION GROUP

Our density matrix renormalization group (DMRG) calculations are performed with the matrix product state (MPS) algorithm using the ITensor library [S70] on YC4-4 (38 sites) and YC8-8 (124 sites) spin tubes as illustrated in Fig. S11, with 4 and 8 sites lying on the y-axis with a periodic boundary condition implemented along the y-axis. Along x-axis the system is open.The maximum bond dimension used for these calculations is 2048. In general, for each DMRG run we are performing 12 full sweeps.

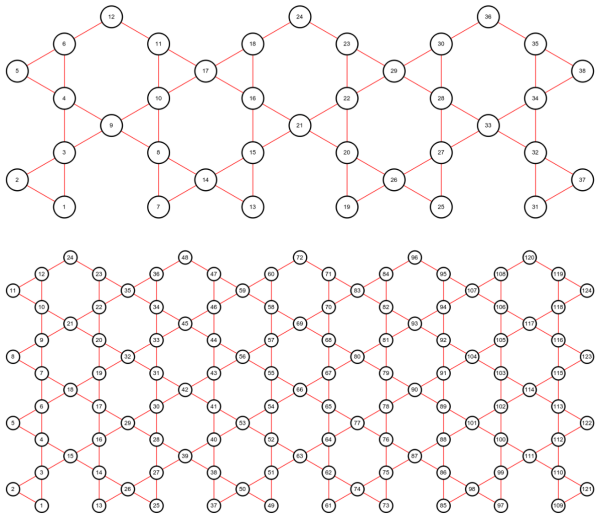

FIG. S11. **DMRG clusters.** The YC4-4 (38 sites) and YC8-8 (124 sites) spin tubes used for the DMRG calculations.

A. Spin liquid to pinwheel VBC transition in DMRG

In our DMRG calculations, we find g_1 is occurring at $J/J_1 = 0.27(1)$ which is signalled in (i) a discontinuity in the derivative of ground state energy with respect to J as plotted in Fig. 2(a) of the main text, and (ii) a sharp kink in the von Neumann entanglement entropy right at this transition as shown in Fig. S12. Both signatures are consistent with a first-order transition.

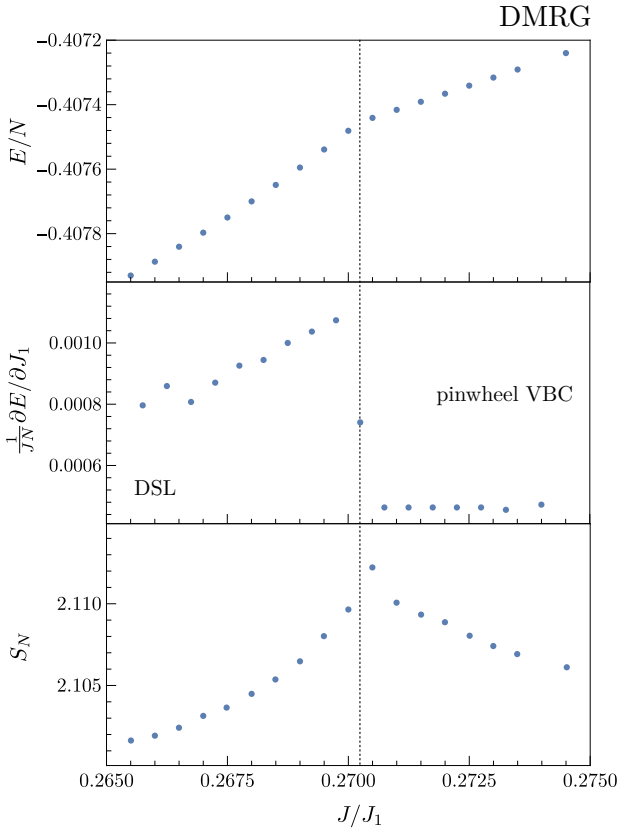

FIG. S12. **DMRG results for the spin liquid to pinwheel VBC transition.** Top: The ground state energy as a function of J/J_1 and its derivative (middle panel). Bottom: The von Neumann entanglement entropy S_N calculated across the central bond using the matrix product ground state obtained via DMRG. The kink in the ground state energy, leading to a step-function behavior in its derivative, and the sharply kinked, non-monotonous behavior of S_N are all indicative of a first-order phase transition. Its location is estimated at $J/J_1 \approx 0.27(1)$ indicated by the dashed line, consistent with results from VMC calculations, see Fig. 2(a).

APL Materials ARTICLE scitation.org/journal/apm

TMDs as a platform for spin liquid physics: A strong coupling study of twisted bilayer WSe_2

Cite as: APL Mater. 10, 031113 (2022); doi: 10.1063/5.0077901
Submitted: 8 November 2021 • Accepted: 2 March 2022 •
Published Online: 18 March 2022

Dominik Kiese,[1] Yuchi He,[2] Ciarán Hickey,[1] Angel Rubio,[3,4,5,a)] and Dante M. Kennes[2,3,b)]

AFFILIATIONS

[1] Institute for Theoretical Physics, University of Cologne, 50937 Cologne, Germany
[2] Institut für Theorie der Statistischen Physik, RWTH Aachen University and JARA-Fundamentals of Information Technology, 52056 Aachen, Germany
[3] Max Planck Institute for the Structure and Dynamics of Matter and Center for Free Electron Laser Science, Luruper Chaussee 149, 22761 Hamburg, Germany
[4] Center for Computational Quantum Physics, Simons Foundation Flatiron Institute, New York, New York 10010, USA
[5] Nano-Bio Spectroscopy Group, Departamento de Fisica de Materiales, Universidad del País Vasco, UPV/EHU, 20018 San Sebastián, Spain

Note: This paper is part of the Special Topic on Moire Materials.

[a)] Electronic mail: angel.rubio@mpsd.mpg.de
[b)] Author to whom correspondence should be addressed: dante.kennes@rwth-aachen.de

ABSTRACT

The advent of twisted moiré heterostructures as a playground for strongly correlated electron physics has led to a plethora of experimental and theoretical efforts seeking to unravel the nature of the emergent superconducting and insulating states. Among these layered compositions of two-dimensional materials, transition metal dichalcogenides are now appreciated as highly tunable platforms to simulate reinforced electronic interactions in the presence of low-energy bands with almost negligible bandwidth. Here, we focus on the twisted homobilayer WSe_2 and the insulating phase at half-filling of the flat bands reported therein. More specifically, we explore the possibility of realizing quantum spin liquid (QSL) physics on the basis of a strong coupling description, including up to second-nearest neighbor Heisenberg couplings J_1 and J_2 as well as Dzyaloshinskii–Moriya (DM) interactions. Mapping out the global phase diagram as a function of an out-of-plane displacement field, we indeed find evidence for putative QSL states, albeit only close to SU(2) symmetric points. In the presence of finite DM couplings and XXZ anisotropy, long-range order is predominantly present with a mix of both commensurate and incommensurate magnetic phases.

I. INTRODUCTION

Twisted moiré materials, such as the prominent magic-angle twisted bilayer graphene (tBG), have recently been established as a new platform to study many-body electron physics.[1–27] The key mechanism promoting strongly enhanced electronic correlations is the formation of large moiré unit cells hosting low-energy bands with an extremely narrow bandwidth.[28–30] These flat bands have been shown to give rise to exotic low temperature phase diagrams featuring superconducting and insulating states while offering a high degree of experimental control,[5] e.g., over twist angle and doping.

Recently, twisted bilayer transition metal dichalcogenides (tTMDs) have moved to the center of experimental attention as a tunable platform to simulate electronic many-body states.[31–41] The decisive difference between tBG and tTMDs is the reduction in effective degrees of freedom in going from the former to the latter, allowing for the construction of simplified microscopic Hamiltonians, such as generalized Hubbard models, more amenable to (numerical) quantum many-body methods.[35,36,42,43]

Here, we consider a specific TMD bilayer, twisted WSe_2 ($tWSe_2$), for which a correlated insulating phase at half-filling of the flat bands has recently been reported.[31,32] These results have

triggered corollary theoretical activity in deciphering the ground state phase diagram of the effective strong coupling Hamiltonian,[44,45] where the full rotation symmetry of the underlying triangular superlattice is broken down to C_3 by an anisotropic modulation of the spin couplings. The latter is parameterized by a phase ϕ inherited from the respective Hubbard model and can be tuned by an out-of-plane displacement field V_z. Notably, there is evidence from microscopic considerations[44] that large values of $|V_z| > 50$ meV support the emergence of second-nearest neighbor, SU(2) symmetric Heisenberg exchange interactions. For the pure triangular lattice Heisenberg model, these are believed to undermine magnetic order in favor of a spin liquid ground state,[46–50] and as such, the intriguing possibility of realizing exotic phases in the exceptionally tunable experimental setup provided by twisted TMDs remains an interesting research direction. If experimentally realized, this would add elusive spin liquid states to the list of phases of matter accessible by controlled moiré engineering.[5]

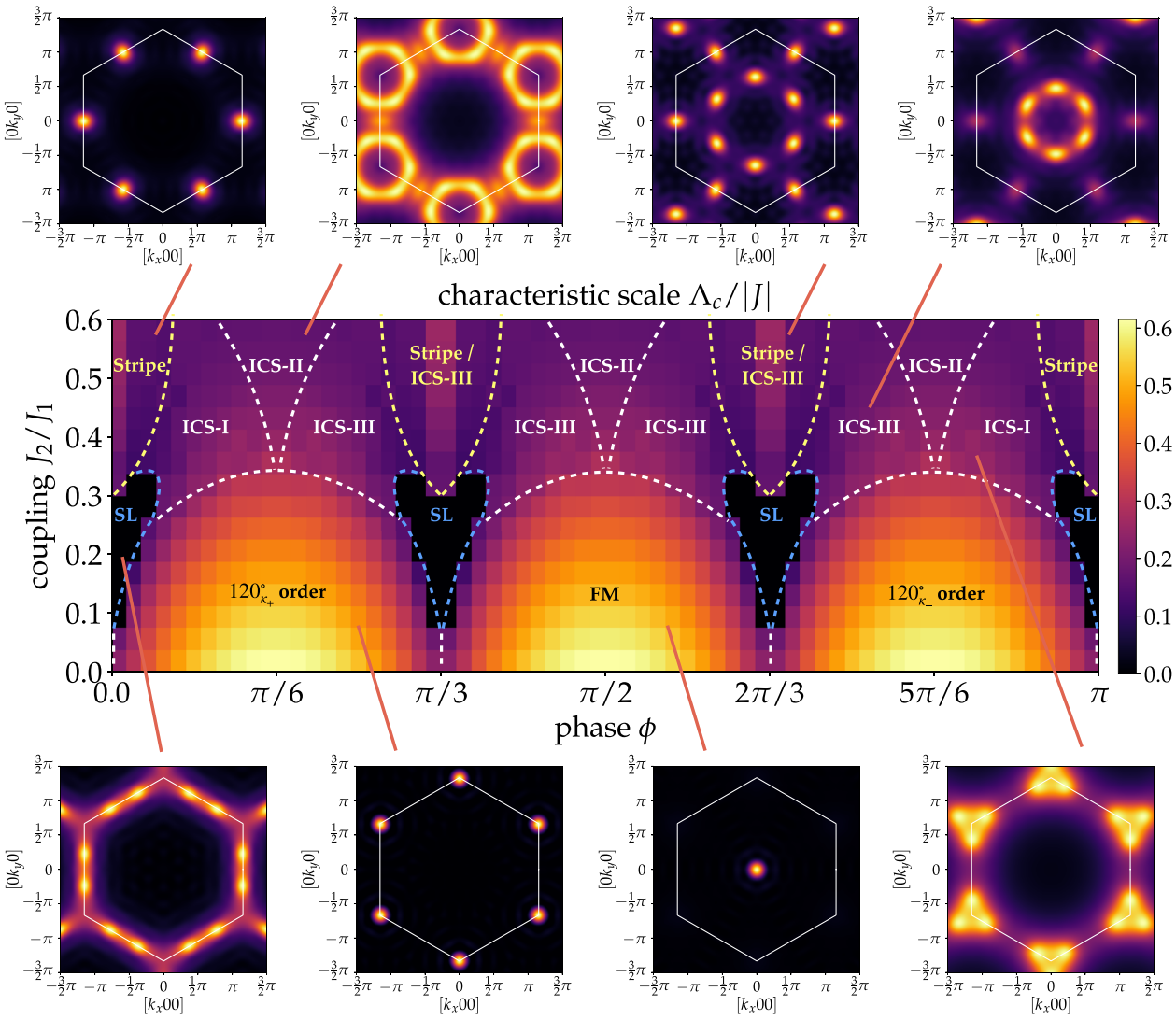

FIG. 1. Magnetic phase diagram for $tWeS_2$ obtained from pf-FRG. We plot the characteristic RG scale Λ_c indicating the emergence of magnetic long-range order or the absence thereof. In total, we identify a plethora of nine potential phases (SL: spin liquid, ICS: incommensurate spin spiral, and FM: ferromagnet), including a putative quantum spin liquid for ϕ close to integer multiples of $\pi/3$ and finite second-nearest neighbor Heisenberg coupling J_2/J_1. The surrounding heat maps display the full elastic component of the structure factor [i.e., $\sum_\mu \chi^{\Lambda_c}_{\mu\bar{\mu}}(\boldsymbol{k}, iw = 0)$], measurable, for example, by neutron scattering experiments. Further details about the different phases and how they are identified in our numerical calculations can be found in Secs. III A, III B 1, and III C of the main text.

In this article, we set out to study the effective spin model proposed for $tWSe_2$,[44,45] augmented by an antiferromagnetic second-nearest neighbor Heisenberg coupling J_2 previously not considered, using both classical *and* quantum many-body methods. In the classical limit, we first use the Luttinger–Tisza (LT) method to determine the likely magnetic orders at zero temperature. We then investigate their stability with respect to thermal fluctuations and a strictly enforced constraint on the length of the classical $O(3)$ spins by performing classical Monte Carlo (MC) simulations. The quantum phase diagram is mapped out utilizing state-of-the-art pseudo-fermion functional renormalization group (pf-FRG) calculations and (infinite) density matrix renormalization group[51–53] techniques (iDMRG).

Our key results are summarized in Fig. 1. In order to discuss them in a concise manner, we first focus on the regime $\phi \in [0, \frac{\pi}{6}]$ as the remainder of the phase diagram can be related via a simple three-sublattice mapping (see Sec. II). The three main features of this regime can then be phrased in the following way: (1) Both classically and quantum mechanically, we find that the 120° order, featuring, for $\phi > 0$, a finite vector chirality κ (discussed in the following), becomes more stable with increasing ϕ. (2) At large J_2, finite ϕ tends to favor one of the two incommensurate spin spiral states over the stripe order expected for the pure J_1–J_2 model. Classically, any finite ϕ suffices to generate incommensurate correlations, whereas quantum mechanically, the stripe order seems to remain stable for small ϕ. (3) Close to the Heisenberg limit, a paramagnetic region is identified for finite values of J_2, indicating a putative realm for quantum spin liquid (QSL) physics. This regime, however, quickly diminishes with increasing ϕ. These observations can straightforwardly be generalized to the parameter space beyond $\phi = \pi/6$, albeit with new labels for the different phases. For example, close to $\phi = \pi/3$, one finds a ferromagnetic (FM) ground state instead of the chiral 120° orders found at $\phi = 0$ and $\phi = 2\pi/3$.

The remainder of this article is structured as follows: First, following the arguments of previous microscopic considerations,[44] the derivation of the effective $tWSe_2$ spin model, starting from the corresponding tight-binding Hamiltonian, is recapped. We then summarize known results for the $J_2 = 0$ limit and elaborate on symmetry properties of the strong coupling Hamiltonian. Second, the results obtained within the Luttinger–Tisza method and classical Monte Carlo simulations are discussed. Next, we introduce the pf-FRG and iDMRG methods and present their implications for the quantum phase diagram. We conclude by evaluating the relevance of our results for future experimental studies of $tWSe_2$ and pointing out further possible research directions.

II. MODEL

We focus on homobilayers of $tWSe_2$, which have recently been studied both experimentally,[31,54] using transport and scanning tunneling microscopy (STM) measurements, as well as theoretically,[31,44,45] using mean-field approaches. The STM measurements have demonstrated that the moiré valence bands originate from the $\pm K$ valleys of the two TMD layers, while the Γ valley is energetically disfavored. Spin degrees of freedom are thereby locked to one of the two valleys, giving rise to an effective spin–orbit coupling in the corresponding tight-binding Hamiltonian on the triangular superlattice,[44,45]

$$H_t = \sum_{\alpha\in\{\uparrow,\downarrow\}} \sum_{\langle ij\rangle} t_{ij}^{\alpha} c_{i\alpha}^{\dagger} c_{j\alpha}^{\dagger} + \text{h.c.}, \tag{1}$$

which is a valid description of $tWSe_2$ for small commensurate twist angles $\theta \gtrsim 3°$, where lattice relaxation effects and further neighbor hoppings can be neglected.[44] Note that because of the aforementioned spin-valley locking, the sum over spin degrees of freedom α should be a understood as a simultaneous sum over valleys.

Due to time-reversal and point group symmetries, the hoppings t_{ij}^{α} have to obey $t_{ij}^{\alpha} = \bar{t}_{ji}^{\alpha}$ and $t_{ij}^{\alpha} = \bar{t}_{ij}^{\bar{\alpha}}$, while also being invariant under only threefold lattice rotations.[44] More specifically, the dispersion for the tight-binding Hamiltonian in Eq. (1) reads

$$\varepsilon_{\alpha}(\boldsymbol{k}) = -2|t| \sum_{\boldsymbol{\delta}_{nn}} \cos(\boldsymbol{k}\boldsymbol{\delta}_{nn} + \alpha\phi) \tag{2}$$

with $|t| = |t_{\langle ij\rangle}^{\alpha}| \sim 1$ meV defining the energy scale of the model.[44] Here, $\boldsymbol{\delta}_{nn}$ sums over three out of six nearest neighbor displacement vectors of the triangular lattice with an equal phase ϕ (see Fig. 2). Density functional theory (DFT) calculations imply that the latter can be varied between $\pm\pi/3$ by an out-of-plane displacement field $|V_z| \lesssim 100$ meV, which shifts the energies at the K and K' points of the mini-Brillouin zone in opposite directions and thus breaks the approximate inversion symmetry of the bilayer system.[31,44,45] A spin–orbit coupled generalized Hubbard model results by combining the tight-binding Hamiltonian (1) with an on–site interaction U. This on–site interaction has been found to be about one order of magnitude larger than the kinetic contribution,[44] motivating a strong coupling description.

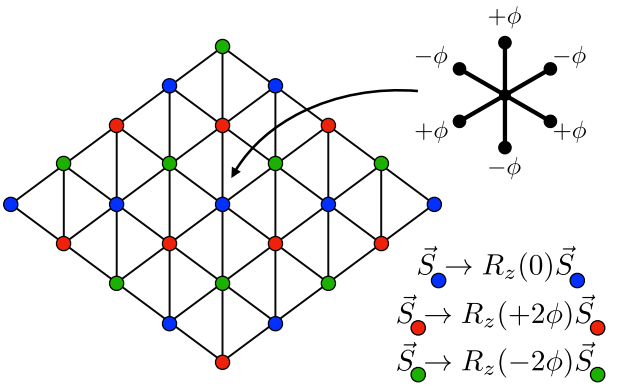

FIG. 2. Three-sublattice rotation for the triangular lattice model. The anisotropic phase ϕ_{ij} changes sign between nearest neighbor bonds (as shown in the upper right corner). The Hamiltonian (3) can be recast in terms of out-of-plane rotation matrices $R_z(-2\phi_{ij})$ [see Eq. (4)]. By rotating the spins on the three sublattices (see the lower right corner), each nearest neighbor term in Eq. (4) can be transformed into an SU(2) symmetric Heisenberg interaction, except for terms coupling the red and green sublattices. The remaining rotation, by -6ϕ, vanishes for $\phi = n\frac{\pi}{3}$ with $n \in \mathbb{Z}$.

In this work, we consider the $U \gg |t|$ limit at half-filling, where one can derive an effective spin model[44,45] with residual U(1) symmetry about the z axis,

$$H = J_1 \sum_{\langle ij \rangle} \left[\cos(2\phi_{ij}) (S_i^x S_j^x + S_i^y S_j^y) + S_i^z S_j^z \right] + J_1 \sum_{\langle ij \rangle} \sin(2\phi_{ij})\, \hat{z} \cdot (\mathbf{S}_i \times \mathbf{S}_j) + J_2 \sum_{\langle\langle ij \rangle\rangle} \mathbf{S}_i \cdot \mathbf{S}_j, \tag{3}$$

featuring XXZ, off-diagonal Dzyaloshinskii–Moriya (DM) and SU(2) symmetric next-nearest neighbor Heisenberg interactions. The phase ϕ_{ij} varies sign between nearest neighbor bonds (see Fig. 2), thus inheriting the reduction from sixfold to threefold lattice rotational symmetry from the tight-binding model (1). As pointed out in Ref. 44, the form of the underlying second-nearest neighbor hopping motivates the inclusion of a fully SU(2) symmetric Heisenberg interaction J_2, which has previously not been considered. For large displacement fields $|V_z| > 50$ meV, this J_2 is the next largest interaction beyond the nearest neighbor J_1 terms (with $J_1 \sim 1$ meV).[44]

For $J_2 = 0$, the ground state phase diagram of Eq. (3) has previously been studied using classical Luttinger–Tisza and self-consistent Hartree–Fock mean-field calculations.[44,45] For $\phi \in [0, \pi]$, both works find a ferromagnetic phase $(\pi/3 < \phi < 2\pi/3)$ sandwiched between two antiferromagnetic 120° orders with opposite vector chiralities $\kappa_\pm$ with $\kappa = \mathrm{sgn}(\hat{z} \cdot (\mathbf{S}_1 \times \mathbf{S}_2 + \mathbf{S}_2 \times \mathbf{S}_3 + \mathbf{S}_3 \times \mathbf{S}_2))$, where $\mathbf{S}_1, \mathbf{S}_2$, and $\mathbf{S}_3$ are spins on a triangular plaquette. For finite J_2, however, the situation has not yet been studied and quantum fluctuations could stabilize more exotic phases especially since the several numerical works[46–48,50] suggest that the pure J_1–J_2 Heisenberg model on the triangular lattice hosts a quantum spin liquid ground state.

For finite $\phi = n\frac{\pi}{3}$ with $n \in \mathbb{Z}$, the nearest neighbor terms can be transformed into a fully SU(2) symmetric form by performing a three-sublattice rotation (see Fig. 2), thus opening up the possibility to experimentally tune the system close to the (effective) Heisenberg limit by variation of the displacement field.[44,45] This can be clearly seen by rewriting the Hamiltonian as

$$H = J_1 \sum_{\langle ij \rangle} \mathbf{S}_i^{\mathrm{T}} R_z(-2\phi_{ij}) \mathbf{S}_j + J_2 \sum_{\langle\langle ij \rangle\rangle} \mathbf{S}_i \cdot \mathbf{S}_j, \tag{4}$$

where $R_z(-2\phi_{ij})$ is an out-of-plane rotation matrix with rotation angle $-2\phi_{ij}$ and then performing the transformation shown in Fig. 2. Indeed, more generally, the energetics at ϕ, $\phi + n\pi/3$, and $n\pi/3 - \phi$ are identical although crucially the wavefunctions do change.

With these observations in mind, we therefore focus our efforts on the regime $\phi \in [0, \frac{\pi}{6}]$ and study the respective ground states by classical Luttinger–Tisza and Monte Carlo simulations as well as quantum pf-FRG and iDMRG calculations that go beyond mean-field theory. The global phase diagram can then be straightforwardly obtained using the sublattice rotation outlined above and adjusting the labels of the phases accordingly.

III. RESULTS

A. Classical limit

First, we explore the classical $S \to \infty$ limit of the model. In order to determine the likely classical magnetic orders, we turn to the Luttinger–Tisza (LT) method.[55] This method treats the spin as an unconstrained vector, allowing for a straightforward Fourier transform and subsequent diagonalization of any quadratic spin Hamiltonian. For the model in Eq. (3), the corresponding energy eigenvalues are

$$E_H(\mathbf{k}) = J_1 \sum_{\boldsymbol{\delta}_1} \cos(\mathbf{k} \cdot \boldsymbol{\delta}_1) + J_2 \sum_{\boldsymbol{\delta}_2} \cos(\mathbf{k} \cdot \boldsymbol{\delta}_2),$$
$$E_\pm(\mathbf{k}) = J_1 \sum_{\boldsymbol{\delta}_1} \cos(\mathbf{k} \cdot \boldsymbol{\delta}_1 \pm 2\phi_{ij}) + J_2 \sum_{\boldsymbol{\delta}_2} \cos(\mathbf{k} \cdot \boldsymbol{\delta}_2), \tag{5}$$

where $\boldsymbol{\delta}_1$ and $\boldsymbol{\delta}_2$ are the set of nearest and next-nearest neighbor lattice vectors. $E_H(\mathbf{k})$ is independent of ϕ and is identical to the Heisenberg result (i.e., $\phi = 0$) with the eigenvalue lying purely along the z axis. On the other hand, $E_\pm(\mathbf{k})$ are explicitly ϕ dependent with eigenvalues lying purely within the xy-plane. For a given set of parameters, the absolute minimum eigenvalue provides a strict lower bound to the classical energy, and the corresponding momenta, which we denote by $\mathbf{k}^\star$, provide candidate classical ordering wavevectors. They also provide crucial clues as to what correlations one might expect in the quantum case, where the spins are not subject to a hard classical constraint.

For $\phi = 0$, i.e., the J_1–J_2 Heisenberg model, there is a transition from 120° order with ordering wavevector $\mathbf{k}^\star = K$ to stripe order with $\mathbf{k}^\star = M$ at a critical value of $J_2/J_1 = 1/8$. Turning on a small finite $\phi \neq 0$ has three important consequences: (i) it forces the spins to order within the xy-plane [$E_\pm(\mathbf{k})$ are always favored], (ii) it selects a definite chirality and helps stabilize the 120° order, increasing its extent to a maximum of $J_2/J_1 = 1/3$ at $\phi = \pi/6$, and (iii) it immediately turns the stripe order incommensurate, which we label ICS-I, with ordering wavevectors $\mathbf{k}^\star$ that lie along the high-symmetry $M - K$ line (and $M - K'$ line although from here on we will simply use K when no further distinction is necessary). It also generates a new ordered phase, clustered close to $\phi = \pi/6$, with incommensurate magnetic order and associated ordering wavevectors that do not lie on any high-symmetry line, which we label ICS-II. Note that due to the low-symmetry when $\phi \neq 0$, the Luttinger–Tisza method does not support classical coplanar spirals with just a single $\mathbf{k}^\star$,[56] meaning that the ICS phases must be multi-$\mathbf{k}$ spirals (see the supplementary material for further information).

As noted in Sec. II, the physics of the model for $\phi > \pi/6$ can be related to the region $\phi \in [0, \frac{\pi}{6}]$ discussed above via a simple three-sublattice transformation. Indeed, this can also be seen from the form of the LT eigenvalues with $E_\pm(\mathbf{k}) \to E_\pm(\mathbf{k} \pm n\mathbf{K})$ for $\phi \to \phi + n\pi/3$. Thus, the 120° order gets mapped to FM order, and the ICS-I phase with $\mathbf{k}^\star$ along the $M - K$ line gets mapped to a new ICS-III phase with $\mathbf{k}^\star$ along the $K - \Gamma$ line. All phases remain ordered within the xy-plane. The classical Luttinger–Tisza phase diagram is summarized in Fig. 3(a).

Classical Monte Carlo (MC) simulations allow us to explore the relative stability of the different phases as well as to confirm that the

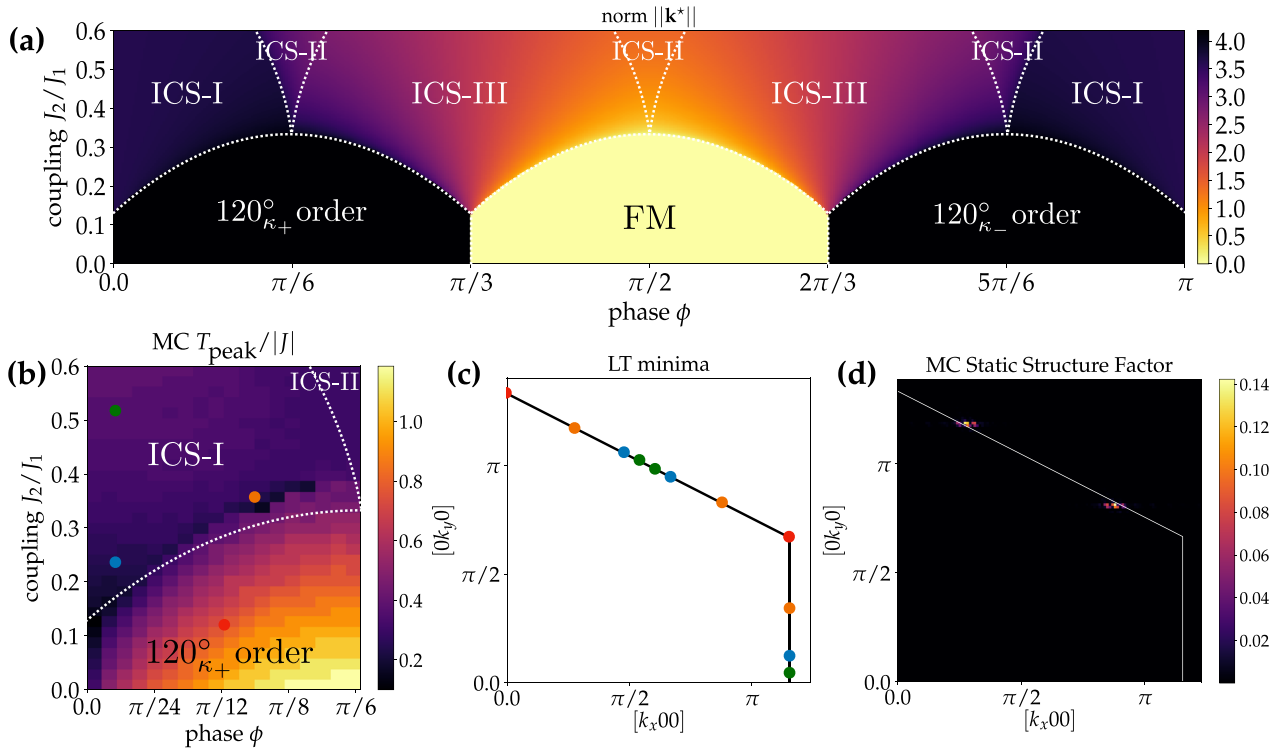

FIG. 3. Classical phase diagram with (a) the Luttinger–Tisza (LT) result. Six distinct phases are visible, a simple ferromagnetic order (FM), two 120° orders with vector chirality κ_+ and κ_-, and three incommensurate phases, ICS-I, ICS-II, and ICS-III. The background color indicates the norm of the ordering wavevector $\|\mathbf{k}^\star\|$. (b) Classical Monte Carlo results on a 96 × 96 lattice for the peak temperature T_{peak} from the specific heat across the phase diagram with the LT phase boundaries overlaid on top. (c) Locations of the LT ordering wavevectors $\mathbf{k}^\star$ for the four points marked in (b) with, for example, the green dots in (c) marking the LT ordering wavevectors for the green parameter point in (b) (see Fig. 4 for the spin-1/2 pf-FRG structure factors at the same points). (d) Classical static spin structure factor at low temperature obtained by Monte Carlo simulations at the point $J_2/J_1 = 0.36$ and $\phi = \pi/10$ [orange point in (b) and (c)] within the ICS-I phase. The two sharp peaks lie at the same incommensurate momenta as the LT minima shown in (c).

Luttinger–Tisza $\mathbf{k}^\star$ are correct. As the model contains a continuous U(1) rotational symmetry about the z axis, the Mermin–Wagner theorem precludes a finite in-plane magnetization at finite temperature. However, a peak in specific heat at T_{peak} related to a Berezinskii–Kosterlitz–Thouless (BKT) transition due to ordering in the xy-plane is still possible,[57,78] as seen, for example, in the triangular lattice XXZ model [the first term in Eq. (3)].[58] A map of T_{peak} is shown in Fig. 3(b) with, as expected, the highest $T_{\text{peak}} \sim 1.5J_1$ occurring for $J_2/J_1 = 0$ and $\phi = \pi/6$, a consequence of the enhanced stability for the 120° order that finite ϕ provides. On the other hand, within the incommensurate phases, T_{peak} shows little variation, lying between 0.4 and $0.5J_1$ for the whole range shown. Finally, Fig. 3(d) shows an example of the static spin structure factor taken from the MC within the ICS-I phase. There are two peaks at incommensurate wavevectors located along the $M - K$ and $M - K'$ high-symmetry lines whose location precisely matches two of the ordering wavevectors $\mathbf{k}^\star$ predicted by the Luttinger–Tisza method [the orange dots in Fig. 3(c)]. This is accompanied by a complex real space structure (see the supplementary material for examples).

B. Pseudo-fermion functional renormalization group

1. Method

In the past decade, the pseudo-fermion functional renormalization group (pf-FRG) developed by Reuther and Wölfle[59] has been widely employed to investigate ground state phase diagrams of quantum spin models on two[59,60] and three[61] dimensional lattices. The method utilizes the parton decomposition,

$$S_i^\mu = \frac{1}{2}\sum_{\alpha,\beta} f_{i\alpha}^\dagger \sigma_{\alpha\beta}^\mu f_{i\beta}, \tag{6}$$

to recast the original Hamiltonian in terms of fermionic creation and annihilation operators. Here, $\sigma_{\alpha\beta}^\mu$ for $\mu \in \{x, y, z\}$ denote Pauli matrices. Changing the representation space of the spin algebra, however, comes with a caveat: The dimensions of the (local) Hilbert space of pseudo-fermions ($d = 4$) and spin-1/2 operators ($d = 2$) are different, and as such, the respective representations are not isomorphic. Although unphysical states can be eliminated by an additional local constraint $\sum_\alpha f_{i\alpha}^\dagger f_{i\alpha} = 1$ on every lattice site, an exact treatment of

this constraint is rather difficult, and in practice, the softened condition $\langle \sum_\alpha f^\dagger_{i\alpha} f^\dagger_{i\alpha} \rangle = 1$ is employed. Fluctuations around the mean have been found to leave observables computed within pf-FRG qualitatively unchanged,[62,63] advocating an on-average treatment of the fermionic number constraint at zero temperature.

Having rewritten the spin Hamiltonian in terms of fermions, a regulator function, here chosen as

$$\Theta^\Lambda(w) = 1 - e^{-w^2/\Lambda^2} \tag{7}$$

with flow parameter Λ, is implemented in the bare propagator as

$$G_0(w) \to G_0^\Lambda(w) = \Theta^\Lambda(w) G_0(w). \tag{8}$$

This procedure gives rise to Λ-dependent n-point correlation functions whose flow from the ultraviolet $G_0^{\Lambda\to\infty}(w) = 0$ to the infrared $G_0^{\Lambda\to 0}(w) = G_0(w)$ limit is governed by a hierarchy of ordinary integro-differential flow equations. To be amenable to numerical algorithms, the latter has to be truncated. Here, we utilize the Katanin truncation,[59,62,64] which cuts off the flow equations beyond the two-particle vertex and has been demonstrated to efficiently capture competing magnetic and non-magnetic phases.[65]

The main observable extracted from the pf-FRG is the flowing spin–spin correlation function,

$$\chi^{\mu\nu\Lambda}_{ij}(iw = 0) = \int_0^\beta d\tau \langle T_\tau S^\mu_i(\tau) S^\nu_j(0) \rangle^\Lambda, \tag{9}$$

which shows an instability (such as a cusp, kink, or divergence) once the RG flow selects a ground state with broken symmetries. The absence of such a breakdown is consequently associated with paramagnetic phases such as spin liquids. Furthermore, for long-range ordered states, the respective type of magnetic order can be characterized by Fourier transforming $\chi^{\mu\nu\Lambda}_{ij}$ to momentum space ($F[\chi^{\mu\nu\Lambda}_{ij}](\mathbf{k}) = \chi^\Lambda_{\mu\nu}(\mathbf{k})$) and determining the wavevectors $\mathbf{k}_{\max}$ with the largest spectral weight. Further information on the method and its numerical implementation is provided in Sec. I of the supplementary material.

Due to the symmetry properties of Eq. (3), we consider two distinct susceptibilities $\chi^\Lambda_{XX}(\mathbf{k})$ ($= \chi^\Lambda_{YY}(\mathbf{k})$) and $\chi^\Lambda_{ZZ}(\mathbf{k})$ in momentum space to distinguish possible in-plane and out-of-plane magnetic orders. While finite, in general, for $\phi_{ij} > 0$, off-diagonal correlation functions $\chi^\Lambda_{XY}(\mathbf{k})$ ($= -\chi^\Lambda_{YX}(\mathbf{k})$) turn out to be rather small compared to their diagonal counterparts in our pf-FRG calculations and are therefore only considered as a benchmark to check for a switch in vector chirality between the two 120° orders.

2. Phase diagram

We now turn to the discussion of the $\phi \in [0, \frac{\pi}{6}]$ region of the phase diagram of our model Hamiltonian Eq. (3), as obtained within pf-FRG and summarized in Fig. 4.

For small $\phi \lesssim \pi/48$ and intermediate next-nearest neighbor coupling, we find a small region of spin liquid behavior, where the RG flow [see the blue curve in Fig. 4(c)] stays smooth and featureless down to the lowest simulated cutoff value $\Lambda/|J| = 0.05$, where $|J| = \sqrt{J_1^2 + J_2^2}$. For $\phi = 0$, corresponding to the pure J_1–J_2 Heisenberg model, the estimated range of the spin liquid regime $0.12 \lesssim J_2/J_1 \lesssim 0.32$ is larger than the respective literature values 0.06–0.08 $\lesssim J_2/J_1 \lesssim$ 0.15–0.17, which we attribute to our softened treatment of the fermionic number constraint and the exclusion of higher loop corrections in the current framework. Since the FRG calculation is nevertheless capable of reproducing the existence of a paramagnetic regime between the adjacent 120° and stripe ordered phases (consistent with previous studies[60]), we are confident that its qualitative predictions of the phase diagram are reliable. The structure factor $\sum_\mu \chi^\Lambda_{\mu\mu}(\mathbf{k})$ within the SL phase is displayed in Fig. 4(d). It resembles an interpolation between the 120° and stripe orders [Figs. 4(e) and 4(f)] in the sense that its peaks move on the high-symmetry line between the K and M points of the first Brillouin zone as J_2 and ϕ are increased. In this regard, the spin liquid region appears similar to a molten version of the neighboring incommensurate spin spiral phase [ICS-I in Figs. 4(a) and 4(b)], albeit with a washed out distribution of the subleading weight along the Brillouin zone edges. The spectral weight for the ICS-I phase is, in contrast, much more localized although, of course, the maxima still reside at incommensurate positions between the K and M points [Fig. 4(g)].

For larger ϕ, we find the pf-FRG phase diagram to be roughly consistent with the classical result (Fig. 3), predicting, for $J_2/J_1 \gtrsim 0.32$, a transition from in-plane 120° order to one of the two incommensurate phases that can be distinctly identified by the position of their ordering wavevector $\mathbf{k}_{\max}$ within the first Brillouin zone [Fig. 4(b)]. The phase boundary is, however, shifted upward in favor of the 120° order within the FRG. We generally find the dominant contributions to the structure factor to stem from the in-plane correlations, i.e., $\chi^\Lambda_{XX} + \chi^\Lambda_{YY}$, where flow breakdowns are most visible although out-of-plane correlations become sizable with increasing J_2. This finding is in line with the Luttinger–Tisza result Eq. (5) as the eigenvalues corresponding to in-plane and out-of-plane order move closer together.

Notably, our pf-FRG approach also finds a stripe ordered ground state for $J_2/J_1 \gtrsim 0.32$–0.36 and close to $\phi = 0$. In contrast, our classical calculations predict the stripe order to be unstable to incommensurate ordering for any finite ϕ. This could be, on the one hand, due to finite size effects in the pf-FRG calculations (although for increased lattice truncation ranges, no changes are observed), which would make it difficult to decipher the extremely weak classical incommensuration at small ϕ. On the other hand, quantum fluctuations may also favor the commensurate stripe order over the ICS-I phase especially since their classical energies for small ϕ and large J_2 are almost degenerate. We also note that the signatures for magnetic ordering as characterized by a breakdown of the RG flow [see Fig. 4(c)] are rather weak in the incommensurate phases (pronounced shoulder vs sharp peak or divergence in the stripe and 120° phase), hinting toward strongly competing magnetic and non-magnetic channels within the FRG approach for this part of the phase diagram.

For $\phi > \pi/6$, as before, the structure of the model outlined in Sec. II allows us to straightforwardly generalize our results (see Fig. 1), while adjusting the labels for the different phases. For $\pi/3 < \phi < 2\pi/3$, antiferromagnetic 120° order is replaced by a ferromagnetic ground state, which yet again becomes 120° ordered although with opposite vector chirality for $2\pi/3 < \phi < \pi$. At large J_2 and $\pi/6 < \phi < 5\pi/6$, the ICS-I order gets mapped to another incommensurate spin spiral phase (ICS-III) with susceptibility maxima located on the high-symmetry line between the Γ and K points. Finally, the stripe order found close to the Heisenberg limit $\phi = 0$ re-appears

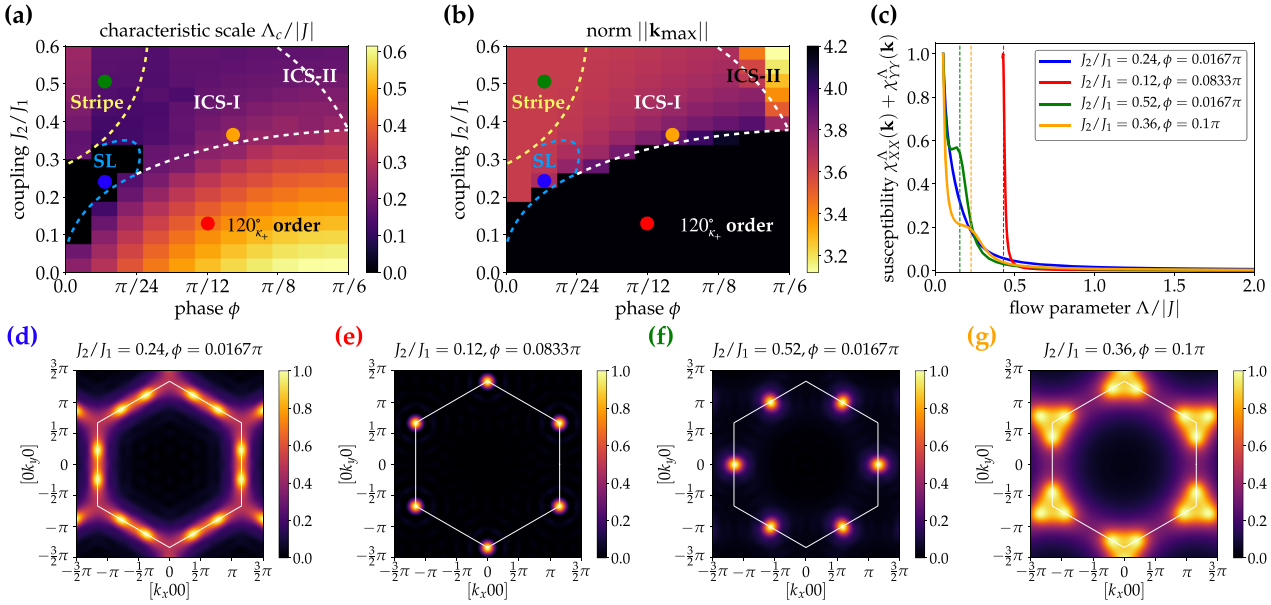

FIG. 4. Phase diagram for $\phi \in [0, \frac{\pi}{6}]$ obtained from pf-FRG. In (a), the characteristic RG scale Λ_c is shown as a function of antiferromagnetic next-nearest neighbor coupling J_2/J_1 and phase $0 \leq \phi \leq \pi/6$ with approximate phase boundaries drawn as a guide to the eye. We find a small region of quantum spin liquid (SL) behavior for small $\phi < \pi/24$ and intermediate values of $0.12 < J_2/J_1 < 0.32$, where the RG flow [see the blue curve in panel (c)] stays smooth and featureless down to the lowest accessible cutoff values. The rest of the phase diagram is occupied by four different magnetically ordered phases, which can be distinguished by their ordering wavevector $\mathbf{k}_{\max}$ and its respective norm, as displayed in (b). For the stripe and 120° ordered phases (with definite vector chirality κ_+), $\mathbf{k}_{\max}$ resides at the *M* and *K* points, respectively, whereas it continuously changes the position in the spin liquid and incommensurate spin spiral (ICS) phases, as apparent from the color gradient in (b). In (c), we show representative flows of the magnetic susceptibility as a function of the RG scale $\Lambda/|J|$ with dashed lines highlighting the position of the characteristic scale $\Lambda_c/|J|$ (which is most visible for the in-plane correlators). The latter can be distinctly identified for the stripe and 120° phase, whereas the incommensurate phases only show a pronounced shoulder, indicating strongly competing tendencies between magnetic and non-magnetic channels in the pf-FRG equations. The flows have been normalized by their respective maximum for better comparability. Finally, (d)–(g) display the full, diagonal structure factors $\sum_\mu \chi^\Lambda_{\mu\mu}(\mathbf{k})$ computed at the characteristic scale Λ_c for the four points marked with colored dots in (a) and (b).

close to $\phi = \pi/3$ and $\phi = 2\pi/3$ in coexistence with the ICS-III order (see Fig. 1 in the supplementary material for further details).

C. Density matrix renormalization group

To complement our numerical results, we now present our iDMRG calculations of the model for two representative J_2 cuts at $\phi = \pi/48$ and $\pi/12$ on an infinite cylinder geometry. We use the two-site iDMRG algorithm[51,52] to optimize infinite matrix product states (iMPSs) as approximations to the ground state wavefunctions. We chose the bond dimension such that the error is smaller than the marker size in every plot.[66] The two-site iDMRG truncation errors are at most of the order of 10^{-7}.

The cylinder geometry is illustrated in Fig. 5(a). We choose a circumference $L_y = 6$, compatible with the possible 120° and stripe orders, with an example of the latter shown in the same inset. The infinite cylinder geometry then allows us to probe possible incommensurate correlations along the infinite direction.

Recall that finite ϕ explicitly breaks SU(2) symmetry down to a residual in-plane U(1) symmetry. According to the Mermin–Wagner theorem for quasi-one-dimensional systems (such as our cylindrical iDMRG geometry), an in-plane 120° order that spontaneously breaks U(1) symmetry is forbidden. However, the existence of a possible two-dimensional 120° phase can be inferred by studying spin–spin correlations. On the other hand, long-range out-of-plane stripe order does not break any continuous symmetry and can therefore be directly observed within our iDMRG calculations.

We study the out-of-plane, $\langle S^z_0 S^z_{n\mathbf{a}_2}\rangle$, and in-plane, $\langle S^+_0 S^-_{n\mathbf{a}_2}\rangle$, spin–spin correlation functions, where $\mathbf{a}_2$ is the lattice vector along the infinite direction [see Fig. 5(a)] and $S^\pm_i = S^x_i \pm iS^y_i$. Using the iMPS data, it is known that static correlation functions of this form can be written as $\sum_j C_j e^{ik_j n} e^{-n/\xi_j}$,[53] where j sums over eigenvectors of the iMPS transfer matrix. The largest ξ_j corresponds to the dominant correlation length, while the respective k_j then characterizes the momentum of the lowest-lying excitation along the infinite direction. The correlation length spectrum has, for example, been used to study the $\phi = 0$ case in Ref. 47.

Within the correlation length spectrum, the 120° order for the SU(2) symmetric case corresponds to a dominant correlation length at $k = \pm 2\pi/3$, equal in magnitude for both in- and out-of-plane components. For finite ϕ, however, our classical and pf-FRG calculations indicate that 120° order is not only locked to the *xy*-plane but

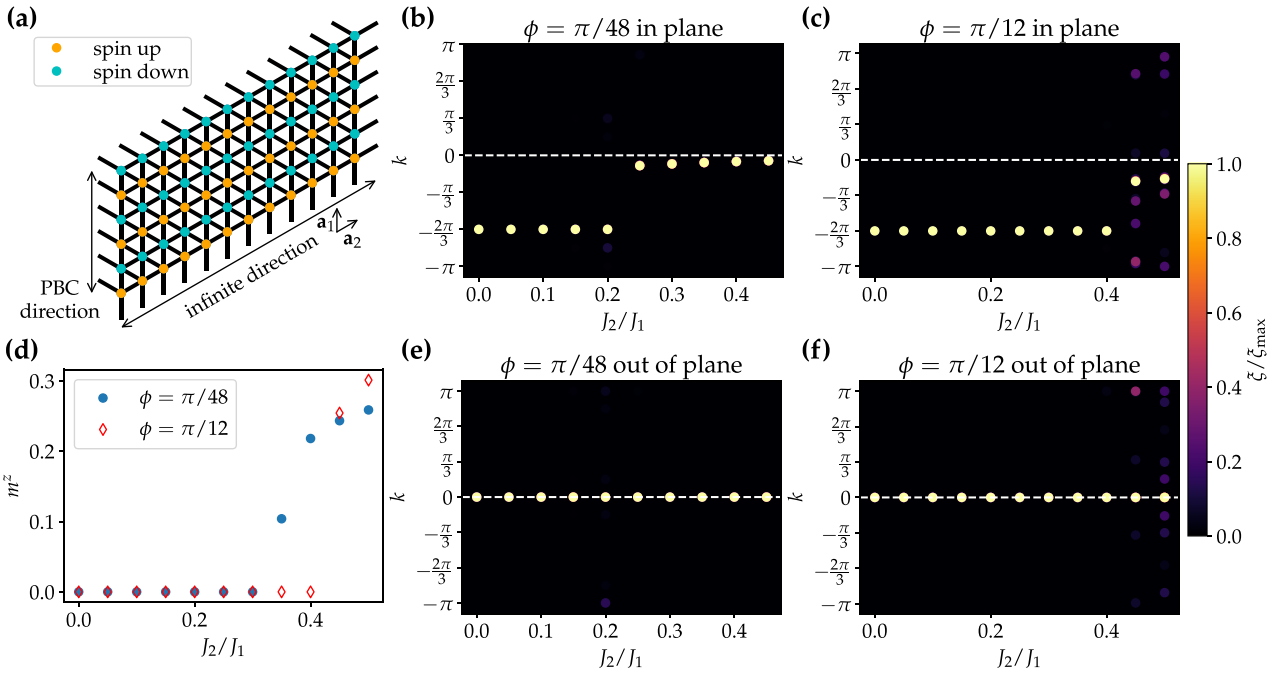

FIG. 5. Correlation length spectrum on an infinite cylinder geometry. (a) shows the triangular lattice on an infinite cylinder geometry with an $L_y = 6$ site circumference. A configuration of the possible out-of-plane stripe order is illustrated by the coloring of sites in orange (cyan), indicating an out-of-plane spin up (down). (b)–(f) show the correlation length spectra (see the main text for definition) along the infinite direction for $\phi = \pi/48$ and $\pi/12$. For each value of J_2/J_1, we plot the 20 largest correlation lengths at their respective k values. For most cases, few points are visible as they share the same k. Finally, in (d), the out-of-plane staggered magnetization along the cylinder direction, m^z, is plotted. The evidence for the in-plane 120° phase is the dominant in-plane correlation length at $-2\pi/3$. In-plane incommensurate correlations are visible for relatively large J_2 in both (b) and (c), where the momenta are not locked to high-symmetry points, but are instead distributed around $-\pi/10$ and $-\pi/6$, respectively. The indication for out-of-plane stripe order is given by a non-vanishing m^z in (d).

also locked to a certain chirality. Our DMRG data (see Fig. 5) are consistent with these results as we observe that only in-plane correlations display a peak at $k = -2\pi/3$.

For large J_2 and $\phi \neq 0$, we find incommensurate correlations characterized by a continuously varying momentum in Figs. 5(b) and 5(c). Curiously, the incommensurate correlations can exist either with or without an accompanying finite out-of-plane staggered magnetization along the cylinder direction, $m^z = \sum_y |\langle S^z_y e^{iny}\rangle|/L_y$.[79] For the chosen cylinder geometry, an out-of-plane stripe order with stripes parallel to the infinite $\mathbf{a}_2$ direction [shown in Fig. 5(a)] has a finite m^z. For $\phi = \pi/48$, we observe a relatively large region, $0.2 \lesssim J_2/J_1 \lesssim 0.3$, with in-plane incommensurate correlations and with negligible out-of-plane components, $S^z_i \approx 0$. This is consistent with the pf-FRG structure factor computed in the putative spin liquid phase, Fig. 4(d), where residual but broadened incommensurate peaks are visible. On the other hand, for larger J_2, we obtain a finite out-of-plane m^z [see Fig. 5(d)], consistent with the onset of out-of-plane stripe order. For $\phi = \pi/12$, we observe, however, at least within our resolution, just a single direct transition from in-plane 120° order to out-of-plane stripe order, not inconsistent with the absence of a spin liquid in the pf-FRG calculations.

Note, however, that at $\phi = \pi/12$, the pf-FRG predicts that out-of-plane stripe order is much weaker compared to the in-plane incommensurate correlations [see Fig. 4(e), where peaks at the M point, coming from the out-of-plane component of the structure factor, are overshadowed by the in-plane incommensurate peaks]. The stripe order that we identify in iDMRG may be a finite size artifact of the quasi-one-dimensional cylinder geometry with the possibility that stripe order is molten in favor of the incommensurate in-plane order when going to two dimensions. As the incommensurate correlations are frustrated along the finite direction of the cylinder, the finite size effects should, in fact, be rather large. Our iDMRG calculations may, in turn, be biased toward commensurate stripe order, as opposed to an incommensurate phase. Further simulations with larger L_y, beyond the scope of this work, are necessary to settle on a final conclusion regarding this issue.

IV. DISCUSSION

Twisted TMDs have been predicted to provide an exciting opportunity to realize the physics of the triangular lattice Hubbard model and potentially access the magnetism of its strong coupling limit. By focusing on the particular case of $tWSe_2$ and including both first- and second-nearest neighbor couplings as well as a finite displacement field, we have mapped out the strong coupling phase diagram. Perhaps the most intriguing phase, the QSL that appears

in the pure J_1–J_2 limit, unfortunately only inhabits a small portion of the larger phase diagram, which includes XXZ anisotropy and an effective DM interaction. Accessing QSL physics thus requires tuning the displacement field such that $\phi \sim n\pi/3$ and the twist angle such that J_2/J_1 is within the required range. It is an open question whether further interactions, generated by taking into account further hoppings t_{ij}^{α} and interactions U_{ij} of the underlying Hubbard model, can lead to a wider, more stable QSL window.

A large part of the phase diagram, above a sufficiently large $J_2/J_1 \sim 0.3$, hosts incommensurate magnetic phases. Such phases can be expected to host gapless phason modes due to the low-energy cost of translating the incommensurate magnetic structure. This is on top of the underlying moiré structure, which, at the atomic level, is generically incommensurate. If it is possible to tune to such a large J_2/J_1 ratio, it would allow to explore the interplay between the moiré scale incommensurate magnetic structure and its gapless phason modes with the atomic scale incommensurate lattice structure and its gapless phonon modes.[67,68]

For smaller ratios of $J_2/J_1 \lesssim 0.3$, the 120° order is stabilized. For $\phi = \pi/6$, it is particularly stable and has a fixed chirality, which leaves only a single BKT transition at finite temperature, with an expected $T_{\mathrm{BKT}} \gtrsim J_1$. It thus provides a particularly clean example of BKT physics within potential experimental reach and the possibility of exploring moiré scale magnetic vortices.

An important additional tuning parameter to consider in the future is an external magnetic field. Its effects on the 120° order and J_1–J_2 QSL are already known,[69,70] but how it will distort the incommensurate phases found at finite ϕ is not immediately clear. An interesting possibility would be the formation of multi-Q states. Indeed, such a possibility is actually realized for incommensurate phases found within the pure J_1–J_2 Heisenberg model.[71] In that case, it is even possible to stabilize a skyrmion lattice phase at finite temperature. Realizing a similar scenario for the model at hand with incommensurate phases ICS-I, II, and III would open up a path to studying moiré scale skyrmion lattices within $tWSe_2$.[72]

The phase diagram uncovered in this work expands our view on the landscape of opportunities arising within tTMDs. In particular, the strong coupling physics of $tWSe_2$ has the potential to realize and tune between QSLs, incommensurate magnetic orders, and extremely stable, chiral 120° and ferromagnetic orders. Adding QSL states and incommensurate magnetic orders to the catalog of moiré-controllable phases of matter is an exciting open experimental question, which might be in reach using highly tunable TMDs. We note that the case of $tWSe_2$ was taken here as a prominent experimentally characterized homobilayer example, but the available range of TMDs might help to fabricate other twisted van der Waals materials. In those, e.g., the QSL state could take a more prominent stage in the respective phase diagram.

Note added in proof. During the completion of this article, we became aware of the publication of related (but previously inaccessible) work by Zare and Mosadeq.[73] In contrast to our study, they focus on a honeycomb lattice model, rather than a triangular lattice model, which is then analyzed using the Luttinger–Tisza method (combined with a variational approach to optimize the classical ground states) and DMRG simulations. They find similar conclusions regarding the fate of the quantum spin liquid phases and the stability of magnetic orders.

SUPPLEMENTARY MATERIAL

In addition to the results presented in the main text, further analysis can be found in the supplementary material. This includes a discussion of the real space spin configurations obtained from the classical Monte Carlo simulations, the full trajectory of Luttinger–Tisza wavevectors within the first Brillouin zone upon variation of ϕ, and details on the pf-FRG implementation.

ACKNOWLEDGMENTS

We thank M. Claassen, M. M. Scherer, and Zhenyue Zhu for useful discussions. D.K. thanks L. Gresista and T. Müller for related work on the `PFFRGSolver.jl` package[74] used for the FRG calculations. The DMRG calculations are based on the Tenpy package.[75] D.K. and C.H. acknowledge support from the Deutsche Forschungsgemeinschaft (DFG, German Research Foundation), Project No. 277146847, SFB 1238 (Project No. C03). Y.H. and D.M.K. acknowledge funding by the Deutsche Forschungsgemeinschaft (DFG, German Research Foundation) under Grant No. RTG 1995 within the Priority Program SPP 2244 "2DMP" and within Germany's Excellence Strategy—Cluster of Excellence Matter and Light for Quantum Computing (ML4Q) Grant No. EXC 2004/1-390534769. This work was supported by the Max Planck-New York City Center for Nonequilibrium Quantum Phenomena. The numerical simulations were performed on the CHEOPS cluster at RRZK Cologne, the JURECA Booster[76] and JUWELS cluster[77] at the Forschungszentrum Juelich, and the Raven cluster at MPCDF of the Max Planck society.

AUTHOR DECLARATIONS

Conflict of Interest

We have no conflicts of interest.

DATA AVAILABILITY

The data that support the findings of this study are available from the corresponding author upon reasonable request.

REFERENCES

[1] Y. Cao, V. Fatemi, A. Demir, S. Fang, S. L. Tomarken, J. Y. Luo, J. D. Sanchez-Yamagishi, K. Watanabe, T. Taniguchi, E. Kaxiras *et al.*, "Correlated insulator behaviour at half-filling in magic-angle graphene superlattices," Nature **556**, 80–84 (2018).

[2] Y. Cao, V. Fatemi, S. Fang, K. Watanabe, T. Taniguchi, E. Kaxiras, and P. Jarillo-Herrero, "Unconventional superconductivity in magic-angle graphene superlattices," Nature **556**, 43–50 (2018).

[3] G. Chen, A. L. Sharpe, E. J. Fox, Y.-H. Zhang, S. Wang, L. Jiang, B. Lyu, H. Li, K. Watanabe, T. Taniguchi *et al.*, "Tunable correlated Chern insulator and ferromagnetism in a moiré superlattice," Nature **579**, 56–61 (2020).

[4] X. Liu, Z. Hao, E. Khalaf, J. Y. Lee, Y. Ronen, H. Yoo, D. Haei Najafabadi, K. Watanabe, T. Taniguchi, A. Vishwanath *et al.*, "Tunable spin-polarized correlated states in twisted double bilayer graphene," Nature **583**, 221–225 (2020).

[5] D. M. Kennes, M. Claassen, L. Xian, A. Georges, A. J. Millis, J. Hone, C. R. Dean, D. N. Basov, A. N. Pasupathy, and A. Rubio, "Moiré heterostructures as a condensed-matter quantum simulator," Nat. Phys. **17**, 155–163 (2021).

[6] H. Yoo, R. Engelke, S. Carr, S. Fang, K. Zhang, P. Cazeaux, S. H. Sung, R. Hovden, A. W. Tsen, T. Taniguchi, K. Watanabe, G.-C. Yi, M. Kim, M. Luskin, E. B. Tadmor, E. Kaxiras, and P. Kim, "Atomic and electronic reconstruction at the van der Waals interface in twisted bilayer graphene," Nat. Mater. **18**, 448–453 (2019).

[7]L. Balents, C. R. Dean, D. K. Efetov, and A. F. Young, "Superconductivity and strong correlations in moiré flat bands," Nat. Phys. **16**, 725–733 (2020).
[8]G. Chen, A. L. Sharpe, P. Gallagher, I. T. Rosen, E. J. Fox, L. Jiang, B. Lyu, H. Li, K. Watanabe, T. Taniguchi *et al.*, "Signatures of tunable superconductivity in a trilayer graphene moiré superlattice," Nature **572**, 215–219 (2019).
[9]G. Chen, L. Jiang, S. Wu, B. Lyu, H. Li, B. L. Chittari, K. Watanabe, T. Taniguchi, Z. Shi, J. Jung *et al.*, "Evidence of a gate-tunable Mott insulator in a trilayer graphene moiré superlattice," Nat. Phys. **15**, 237–241 (2019).
[10]C. Shen, Y. Chu, Q. Wu, N. Li, S. Wang, Y. Zhao, J. Tang, J. Liu, J. Tian, K. Watanabe *et al.*, "Correlated states in twisted double bilayer graphene," Nat. Phys. **16**, 520–525 (2020).
[11]Y. Cao, D. Rodan-Legrain, O. Rubies-Bigorda, J. M. Park, K. Watanabe, T. Taniguchi, and P. Jarillo-Herrero, "Tunable correlated states and spin-polarized phases in twisted bilayer–bilayer graphene," Nature **583**, 215–220 (2020).
[12]G. W. Burg, J. Zhu, T. Taniguchi, K. Watanabe, A. H. MacDonald, and E. Tutuc, "Correlated insulating states in twisted double bilayer graphene," Phys. Rev. Lett. **123**, 197702 (2019).
[13]M. He, Y. Li, J. Cai, Y. Liu, K. Watanabe, T. Taniguchi, X. Xu, and M. Yankowitz, "Symmetry breaking in twisted double bilayer graphene," Nat. Phys. **17**, 26–30 (2021).
[14]M. Yankowitz, S. Chen, H. Polshyn, Y. Zhang, K. Watanabe, T. Taniguchi, D. Graf, A. F. Young, and C. R. Dean, "Tuning superconductivity in twisted bilayer graphene," Science **363**, 1059–1064 (2019).
[15]X. Lu, P. Stepanov, W. Yang, M. Xie, M. A. Aamir, I. Das, C. Urgell, K. Watanabe, T. Taniguchi, G. Zhang *et al.*, "Superconductors, orbital magnets and correlated states in magic-angle bilayer graphene," Nature **574**, 653–657 (2019).
[16]P. Stepanov, I. Das, X. Lu, A. Fahimniya, K. Watanabe, T. Taniguchi, F. H. L. Koppens, J. Lischner, L. Levitov, and D. K. Efetov, "Untying the insulating and superconducting orders in magic-angle graphene," Nature **583**, 375–378 (2020).
[17]A. L. Sharpe, E. J. Fox, A. W. Barnard, J. Finney, K. Watanabe, T. Taniguchi, M. A. Kastner, and D. Goldhaber-Gordon, "Emergent ferromagnetism near three-quarters filling in twisted bilayer graphene," Science **365**, 605–608 (2019).
[18]M. Serlin, C. L. Tschirhart, H. Polshyn, Y. Zhang, J. Zhu, K. Watanabe, T. Taniguchi, L. Balents, and A. F. Young, "Intrinsic quantized anomalous Hall effect in a moiré heterostructure," Science **367**, 900–903 (2020).
[19]C. Xu and L. Balents, "Topological superconductivity in twisted multilayer graphene," Phys. Rev. Lett. **121**, 087001 (2018).
[20]C.-C. Liu, L.-D. Zhang, W.-Q. Chen, and F. Yang, "Chiral spin density wave and $d + i\,d$ superconductivity in the magic-angle-twisted bilayer graphene," Phys. Rev. Lett. **121**, 217001 (2018).
[21]M. Claassen, D. M. Kennes, M. Zingl, M. A. Sentef, and A. Rubio, "Universal optical control of chiral superconductors and Majorana modes," Nat. Phys. **15**, 766–770 (2019).
[22]L. Xian, D. M. Kennes, N. Tancogne-Dejean, M. Altarelli, and A. Rubio, "Multiflat bands and strong correlations in twisted bilayer boron nitride: Doping-induced correlated insulator and superconductor," Nano Lett. **19**, 4934–4940 (2019).
[23]K. Kim, A. DaSilva, S. Huang, B. Fallahazad, S. Larentis, T. Taniguchi, K. Watanabe, B. J. LeRoy, A. H. MacDonald, and E. Tutuc, "Tunable moiré bands and strong correlations in small-twist-angle bilayer graphene," Proc. Natl. Acad. Sci. U. S. A. **114**, 3364–3369 (2017).
[24]A. Kerelsky, L. J. McGilly, D. M. Kennes, L. Xian, M. Yankowitz, S. Chen, K. Watanabe, T. Taniguchi, J. Hone, C. Dean, A. Rubio, and A. N. Pasupathy, "Maximized electron interactions at the magic angle in twisted bilayer graphene," Nature **572**, 95–100 (2019).
[25]A. Kerelsky, C. Rubio-Verdú, L. Xian, D. M. Kennes, D. Halbertal, N. Finney, L. Song, S. Turkel, L. Wang, K. Watanabe, T. Taniguchi, J. Hone, C. Dean, D. N. Basov, A. Rubio, and A. N. Pasupathy, "Moiréless correlations in ABCA graphene," Proc. Natl. Acad. Sci. U. S. A. **118**, e2017366118 (2021).
[26]D. Halbertal, N. R. Finney, S. S. Sunku, A. Kerelsky, C. Rubio-Verdú, S. Shabani, L. Xian, S. Carr, S. Chen, C. Zhang, L. Wang, D. Gonzalez-Acevedo, A. S. McLeod, D. Rhodes, K. Watanabe, T. Taniguchi, E. Kaxiras, C. R. Dean, J. C. Hone, A. N. Pasupathy, D. M. Kennes, A. Rubio, and D. N. Basov, "Moiré metrology of energy landscapes in van der Waals heterostructures," Nat. Commun. **12**, 242 (2021).
[27]C. Rubio-Verdú, S. Turkel, Y. Song, L. Klebl, R. Samajdar, M. S. Scheurer, J. W. F. Venderbos, K. Watanabe, T. Taniguchi, H. Ochoa, L. Xian, D. Kennes, R. M. Fernandes, A. Rubio, and A. N. Pasupathy, "Moiré nematic phase in twisted double bilayer graphene," Nature Phys. **18**, 196–202 (2021).
[28]R. Bistritzer and A. H. MacDonald, "Moiré bands in twisted double-layer graphene," Proc. Natl. Acad. Sci. U. S. A. **108**, 12233–12237 (2011).
[29]G. Trambly de Laissardière, D. Mayou, and L. Magaud, "Localization of Dirac electrons in rotated graphene bilayers," Nano Lett. **10**, 804–808 (2010).
[30]J. M. B. Lopes dos Santos, N. M. R. Peres, and A. H. Castro Neto, "Continuum model of the twisted graphene bilayer," Phys. Rev. B **86**, 155449 (2012).
[31]L. Wang, E.-M. Shih, A. Ghiotto, L. Xian, D. A. Rhodes, C. Tan, M. Claassen, D. M. Kennes, Y. Bai, B. Kim *et al.*, "Correlated electronic phases in twisted bilayer transition metal dichalcogenides," Nat. Mater. **19**, 861–866 (2020).
[32]L. An, X. Cai, D. Pei, M. Huang, Z. Wu, Z. Zhou, J. Lin, Z. Ying, Z. Ye, X. Feng, R. Gao, C. Cacho, M. Watson, Y. Chen, and N. Wang, "Interaction effects and superconductivity signatures in twisted double-bilayer WSe_2," Nanoscale Horiz. **5**, 1309–1316 (2020).
[33]H. S. Arora, R. Polski, Y. Zhang, A. Thomson, Y. Choi, H. Kim, Z. Lin, I. Z. Wilson, X. Xu, J.-H. Chu *et al.*, "Superconductivity in metallic twisted bilayer graphene stabilized by WSe_2," Nature **583**, 379–384 (2020).
[34]L. Xian, M. Claassen, D. Kiese, M. M. Scherer, S. Trebst, D. M. Kennes, and A. Rubio, "Realization of nearly dispersionless bands with strong orbital anisotropy from destructive interference in twisted bilayer MoS_2," Nat. Commun. **12**, 5644 (2021).
[35]F. Wu, T. Lovorn, E. Tutuc, and A. H. MacDonald, "Hubbard model physics in transition metal dichalcogenide moiré bands," Phys. Rev. Lett. **121**, 026402 (2018).
[36]F. Wu, T. Lovorn, E. Tutuc, I. Martin, and A. H. MacDonald, "Topological insulators in twisted transition metal dichalcogenide homobilayers," Phys. Rev. Lett. **122**, 086402 (2019).
[37]M. Angeli and A. H. MacDonald, "Γ valley transition metal dichalcogenide moiré bands," Proc. Natl. Acad. Sci. U. S. A. **118**, e2021826118 (2021).
[38]M. H. Naik and M. Jain, "Ultraflatbands and shear solitons in moiré patterns of twisted bilayer transition metal dichalcogenides," Phys. Rev. Lett. **121**, 266401 (2018).
[39]E. C. Regan, D. Wang, C. Jin, M. I. Bakti Utama, B. Gao, X. Wei, S. Zhao, W. Zhao, Z. Zhang, K. Yumigeta, M. Blei, J. D. Carlström, K. Watanabe, T. Taniguchi, S. Tongay, M. Crommie, A. Zettl, and F. Wang, "Mott and generalized Wigner crystal states in WSe_2/WS_2 moiré superlattices," Nature **579**, 359–363 (2020).
[40]X. Qian, J. Liu, L. Fu, and J. Li, "Quantum spin Hall effect in two-dimensional transition metal dichalcogenides," Science **346**, 1344–1347 (2014).
[41]M. M. Scherer, D. M. Kennes, and L. Classen, "$\mathcal{N} = 4$ chiral superconductivity in moiré transition metal dichalcogenides," arXiv:2108.11406 [cond-mat.str-el] (2021).
[42]Y. Tang, L. Li, T. Li, Y. Xu, S. Liu, K. Barmak, K. Watanabe, T. Taniguchi, A. H. MacDonald, J. Shan *et al.*, "Simulation of Hubbard model physics in WSe_2/WS_2 moiré superlattices," Nature **579**, 353–358 (2020).
[43]M. Koshino, N. F. Yuan, T. Koretsune, M. Ochi, K. Kuroki, and L. Fu, "Maximally localized Wannier orbitals and the extended Hubbard model for twisted bilayer graphene," Phys. Rev. X **8**, 031087 (2018).
[44]H. Pan, F. Wu, and S. Das Sarma, "Band topology, Hubbard model, Heisenberg model, and Dzyaloshinskii-Moriya interaction in twisted bilayer WSe_2," Phys. Rev. Res. **2**, 033087 (2020).
[45]J. Zang, J. Wang, J. Cano, and A. J. Millis, "Hartree-Fock study of the moiré Hubbard model for twisted bilayer transition metal dichalcogenides," Phys. Rev. B **104**, 075150 (2021).
[46]Y. Iqbal, W.-J. Hu, R. Thomale, D. Poilblanc, and F. Becca, "Spin liquid nature in the Heisenberg $J_1 - J_2$ triangular antiferromagnet," Phys. Rev. B **93**, 144411 (2016).
[47]S. Hu, W. Zhu, S. Eggert, and Y.-C. He, "Dirac spin liquid on the spin-1/2 triangular Heisenberg antiferromagnet," Phys. Rev. Lett. **123**, 207203 (2019).
[48]Z. Zhu and S. R. White, "Spin liquid phase of the $S = \frac{1}{2}$ $J_1 - J_2$ Heisenberg model on the triangular lattice," Phys. Rev. B **92**, 041105 (2015).
[49]Y. Shimizu, K. Miyagawa, K. Kanoda, M. Maesato, and G. Saito, "Spin liquid state in an organic Mott insulator with a triangular lattice," Phys. Rev. Lett. **91**, 107001 (2003).

[50]A. Szasz, J. Motruk, M. P. Zaletel, and J. E. Moore, "Chiral spin liquid phase of the triangular lattice Hubbard model: A density matrix renormalization group study," Phys. Rev. X **10**, 021042 (2020).
[51] S. R. White, "Density matrix formulation for quantum renormalization groups," Phys. Rev. Lett. **69**, 2863–2866 (1992).
[52]I. P. McCulloch, "Infinite size density matrix renormalization group, revisited," arXiv:0804.2509 [cond-mat.str-el] (2008).
[53]V. Zauner, D. Draxler, L. Vanderstraeten, M. Degroote, J. Haegeman, M. M. Rams, V. Stojevic, N. Schuch, and F. Verstraete, "Transfer matrices and excitations with matrix product states," New J. Phys. **17**, 053002 (2015).
[54]Z. Zhang, Y. Wang, K. Watanabe, T. Taniguchi, K. Ueno, E. Tutuc, and B. J. LeRoy, "Flat bands in twisted bilayer transition metal dichalcogenides," Nat. Phys. **16**, 1093–1096 (2020).
[55]J. M. Luttinger and L. Tisza, "Theory of dipole interaction in crystals," Phys. Rev. **70**, 954–964 (1946).
[56]C. Liu, R. Yu, and X. Wang, "Semiclassical ground-state phase diagram and multi-Q phase of a spin-orbit-coupled model on triangular lattice," Phys. Rev. B **94**, 174424 (2016).
[57]Note that for a BKT transition, the specific heat T_{peak} does not mark the location of the phase transition but instead slightly overestimates it, e.g., $T_{\text{peak}} \sim 1.1 - 1.2T_{\text{BKT}}$ for the triangular lattice XXZ model.[58,78]
[58]L. Capriotti, R. Vaia, A. Cuccoli, and V. Tognetti, "Phase transitions induced by easy-plane anisotropy in the classical Heisenberg antiferromagnet on a triangular lattice: A Monte Carlo simulation," Phys. Rev. B **58**, 273–281 (1998).
[59]J. Reuther and P. Wölfle, "$J_1 - J_2$ frustrated two-dimensional Heisenberg model: Random phase approximation and functional renormalization group," Phys. Rev. B **81**, 144410 (2010).
[60]J. Reuther and R. Thomale, "Functional renormalization group for the anisotropic triangular antiferromagnet," Phys. Rev. B **83**, 024402 (2011).
[61] Y. Iqbal, R. Thomale, F. Parisen Toldin, S. Rachel, and J. Reuther, "Functional renormalization group for three-dimensional quantum magnetism," Phys. Rev. B **94**, 140408 (2016).
[62]M. L. Baez and J. Reuther, "Numerical treatment of spin systems with unrestricted spin length S: A functional renormalization group study," Phys. Rev. B **96**, 045144 (2017).
[63]J. Thoenniss, M. K. Ritter, F. B. Kugler, J. von Delft, and M. Punk, "Multiloop pseudofermion functional renormalization for quantum spin systems: Application to the spin-$\frac{1}{2}$ kagome Heisenberg model," arXiv:2011.01268 [cond-mat.str-el] (2020).
[64]F. L. Buessen, D. Roscher, S. Diehl, and S. Trebst, "Functional renormalization group approach to SU(N) Heisenberg models: Real-space renormalization group at arbitrary N," Phys. Rev. B **97**, 064415 (2018).
[65]Recently, an advanced "multi-loop" truncation scheme has been successfully employed within the pf-FRG,[63,74] improving on certain aspects of the Katanin truncation. Since the respective one and higher loop ground state phase diagrams were, however, qualitatively the same, we refrain from performing higher loop calculations in this work to reduce the numerical effort involved in treating the off-diagonal DM interaction in combination with breaking of C_6 symmetry.
[66]We use bond dimension 3600 for Figs. 5(b), 5(c), 5(e), and 5(f) while using bond dimensions 3600 and 5000 for extrapolating[79] the non-vanishing m^z in Fig. 5(d).
[67]M. Koshino and Y.-W. Son, "Moiré phonons in twisted bilayer graphene," Phys. Rev. B **100**, 075416 (2019).
[68]I. Maity, M. H. Naik, P. K. Maiti, H. R. Krishnamurthy, and M. Jain, "Phonons in twisted transition-metal dichalcogenide bilayers: Ultrasoft phasons and a transition from a superlubric to a pinned phase," Phys. Rev. Res. **2**, 013335 (2020).
[69]M. Ye and A. V. Chubukov, "Quantum phase transitions in the Heisenberg $J_1 - J_2$ triangular antiferromagnet in a magnetic field," Phys. Rev. B **95**, 014425 (2017).
[70]H. Nakano and T. Sakai, "Magnetization process of the spin-1/2 triangular-lattice Heisenberg antiferromagnet with next-nearest-neighbor interactions—Plateau or nonplateau," J. Phys. Soc. Jpn. **86**, 114705 (2017).
[71] T. Okubo, S. Chung, and H. Kawamura, "Multiple-q states and the skyrmion lattice of the triangular-lattice Heisenberg antiferromagnet under magnetic fields," Phys. Rev. Lett. **108**, 017206 (2012).
[72]M. Akram, H. LaBollita, D. Dey, J. Kapeghian, O. Erten, and A. S. Botana, "Moiré skyrmions and chiral magnetic phases in twisted CrX_3 (X = I, Br, and Cl) bilayers," Nano Lett. **21**, 6633–6639 (2021).
[73]M.-H. Zare and H. Mosadeq, "Spin liquid in twisted homobilayers of group-VI dichalcogenides," Phys. Rev. B **104**, 115154 (2021).
[74]D. Kiese, T. Mueller, Y. Iqbal, R. Thomale, and S. Trebst, "Multiloop functional renormalization group approach to quantum spin systems," arXiv:2011.01269 [cond-mat.str-el] (2021).
[75]J. Hauschild and F. Pollmann, "Efficient numerical simulations with tensor networks: Tensor network Python (TeNPy)," SciPost Physics Lecture Notes 5, 2018.
[76]Jülich Supercomputing Centre, "JURECA: Modular supercomputer at Jülich Supercomputing Centre," J. Large-Scale Res. Facil. **4**, A132 (2018).
[77]Jülich Supercomputing Centre, "JUWELS: Modular tier-0/1 supercomputer at the Jülich Supercomputing Centre," J. Large-Scale Res. Facil. **5**, A171 (2019).
[78]R. Gupta and C. F. Baillie, "Critical behavior of the two-dimensional XY model," Phys. Rev. B **45**, 2883–2898 (1992).
[79]S. R. White and A. L. Chernyshev, "Neél order in square and triangular lattice Heisenberg models," Phys. Rev. Lett. **99**, 127004 (2007).

Emergence and stability of spin-valley entangled quantum liquids in moiré heterostructures

Dominik Kiese, Finn Lasse Buessen, Ciarán Hickey, Simon Trebst, and Michael M. Scherer
Institute for Theoretical Physics, University of Cologne, 50937 Cologne, Germany

(Received 26 July 2019; revised manuscript received 7 February 2020; accepted 12 February 2020; published 30 March 2020)

Twisting moiré heterostructures to the flatband regime allows for the formation of strongly correlated quantum states, since the dramatic reduction of the bandwidth can cause the residual electronic interactions to set the principal energy scale. An effective description for such correlated moiré heterostructures, derived in the strong-coupling limit at integer filling, generically leads to spin-valley Heisenberg models. Here we explore the emergence and stability of spin-liquid behavior in an $SU(2)^{spin} \otimes SU(2)^{valley}$ Heisenberg model upon inclusion of Hund's-induced and longer-ranged exchange couplings, employing a pseudofermion functional renormalization group approach. We consider two lattice geometries, triangular and honeycomb (relevant to different moiré heterostructures), and find, for both cases, an extended parameter regime surrounding the SU(4) symmetric point where no long-range order occurs, indicating a stable realm of quantum spin-liquid behavior. For large Hund's coupling, we identify the adjacent magnetic orders, with both antiferromagnetic and ferromagnetic ground states emerging in the separate spin and valley degrees of freedom. For both lattice geometries the inclusion of longer-ranged exchange couplings is found to have both stabilizing and destabilizing effects on the spin-liquid regime depending on the sign of the additional couplings.

DOI: 10.1103/PhysRevResearch.2.013370

I. INTRODUCTION

Spurred by the discovery of a plethora of insulating and superconducting states in twisted bilayer graphene (TBG) [1,2], a growing stream of experimental evidence points to the generic emergence of correlated electronic behavior in various moiré heterostructures [3–12]. The basic mechanism that gives rise to strongly enhanced correlation effects in these materials is the formation of long-wavelength moiré patterns with (almost) flat low-energy bands whose narrow bandwidth becomes comparable to the otherwise negligible energy scale of the electronic interactions [13–15]. Due to a high degree of control, e.g., in the regulation of the twist angle, tunable bandwidths, or fillings, and a low level of disorder, such systems are discussed as ideal platforms for detailed studies of quantum many-body states. Despite a vast amount of concomitant theoretical activity [16–41], the precise nature of the observed insulators and superconductors, however, remains to be explored and settled through the construction of faithful models and application of appropriate quantum *many-body* approaches.

Several model constructions for correlated moiré materials have been put forward in terms of effective tight-binding descriptions on the moiré superlattice, augmented by various interaction terms [38,39,41]. Whereas details of the models may differ, they feature a series of universal traits: (1) an emergent hexagonal superlattice, (2) a multiorbital structure, and (3) extended Hubbard and Hund's interactions. More specifically, while TBG is preferably described using a honeycomb superlattice [38,39,41], related structures such as, e.g., twisted double-bilayer graphene (TDBG) or trilayer graphene/hexagonal boron nitride heterostructures (TLG/h-BN) are better captured by a triangular superlattice [6,41–44]. The orbital degrees of freedom are inherited from the valleys in the original bands, e.g., the two Dirac valleys in the Brillouin zone of graphene.

Beyond these universal traits it has been argued that band topology can play an important role in moiré heterostructures [35,41,45–48]. Faithfully incorporating a nontrivial band topology in an effective tight-binding model and simultaneously maintaining all symmetries, for example, for TBG, is a formidable task, which can lead to complex multiband models that refuse a reduction to the flat bands only [49–51]. However, at least in some flat-band moiré heterostructures, including TLG/h-BN, the quantum valley topological number can be tuned from being nontrivial to being trivial by applying a perpendicular electric field [35,41,43]. In that latter case, the universal traits (1)–(3) may be combined into a minimal two-orbital extended Hubbard model [16,17] serving as a paradigmatic starting point. Its kinetic term

$$H_t = -t \sum_{\langle ij \rangle} \sum_{\alpha=1}^{4} (c_{i\alpha}^{\dagger} c_{j\alpha} + \text{H.c.}), \tag{1}$$

for the electrons combines the spin projection $s \in \{\uparrow, \downarrow\}$ and valley quantum number $l \in \{+, -\}$ in a flavor index $\alpha \in \{(\uparrow,+), (\uparrow,-), (\downarrow,+), (\downarrow,-)\}$, reflecting an effective SU(4) symmetry. On the triangular lattice this results in a set of four degenerate bands, which can potentially describe, e.g., the set

of minibands above charge neutrality in TDBG or TLG/h-BN at appropriately tuned out-of-plane electric field.

The simplest conceivable interaction term retaining the SU(4) symmetry is a Hubbard interaction $H_{\text{int}} = U \sum_i (\sum_{\alpha=1}^{4} n_{i\alpha})^2$, which can arise in the limit of large lattice periods where the interaction depends primarily on the total charge on a site and becomes the dominant interaction scale. In this strong-coupling limit, the kinetic term can then be treated perturbatively [16,17,41,43]. With an integer number of electrons per site this leads to an effective spin-valley Heisenberg Hamiltonian with SU(4) symmetric superexchange coupling $J_H \propto t^2/U$. Additional symmetry-breaking interactions are also expected, in particular in the form of further Hund's-type couplings in either the spin or valley degrees of freedom [16,17]. Moreover, Wannier state constructions suggest that further-neighbor interactions can become sizable [38] and should augment any minimal model. We note that for TLG/h-BN an intersite Hund's interaction has been argued to provide a leading ferromagnetic contribution to the nearest-neighbor exchange coupling in the strong-coupling limit [43]. Away from the strict limit, however, antiferromagnetic superexchange may dominate [43]. In this regime, the triangular geometry together with the additional valley degrees of freedom augments the role of quantum fluctuations suggesting that the system may host exotic quantum liquid behavior. In view of the large and ever-growing number of different correlated moiré heterostructures and the persistent interest in exotic quantum liquid behavior, we take this observation as a motivation to study generic antiferromagnetic spin-valley Heisenberg models. Further possible applications of such models are, e.g., Mott insulators with strong spin-orbit coupling [52–54].

More specifically, in this work, we explore antiferromagnetic nearest-neighbor spin-valley Heisenberg models with $\text{SU}(2)^{\text{spin}} \otimes \text{SU}(2)^{\text{valley}}$ symmetry for both triangular and honeycomb lattice geometries, which we later supplement with further-neighbor interaction terms. Our focus is on the case of half-filling of the underlying Hubbard model, i.e., two electrons per site. For the effective Heisenberg model at strong coupling, this implies that we are working with the six-dimensional self-conjugate representation of SU(4) spins. This is in contrast to the four-dimensional fundamental representation of SU(4) relevant to, e.g., the case of quarter-filling.

For both lattice geometries, we find extended parameter regimes surrounding the SU(4) symmetric point where no long-range symmetry-breaking order occurs, indicating a stable realm for a spin-valley entangled quantum liquid. Moving further away from the SU(4) symmetric point, we find magnetic order in the spin and valley degrees of freedom that can be either antiferromagnetic or ferromagnetic. To explore the effect of longer-range interactions, we augment our model by a next-nearest neighbor coupling and determine its role in stabilizing quantum spin-valley liquid (QSVL) behavior versus long-range order for different signs of the coupling and the two lattice geometries. Our work complements earlier work for the case of quarter-filling, where it was argued that a QSVL state with neutral gapless fermionic excitations forms on the honeycomb lattice [53], while on the triangular lattice extended parameter regimes without any net magnetization have been identified in DMRG simulations [55].

II. SPIN-VALLEY MODEL

The starting point of our study is an SU(4) spin-valley Heisenberg model [16,41], $\mathcal{H}_{\text{SU(4)}} = J_H \sum_{\langle ij \rangle} \hat{T}_i^{\mu} \hat{T}_j^{\mu}$, where J_H is the antiferromagnetic exchange coupling between nearest neighbors on either the triangular or honeycomb lattice, and $\hat{T}_i$ denote SU(4) spins. The $\mu = 1, \ldots, 15$ components of the spin operators can be represented on a fermionic Hilbert space via the parton construction $\hat{T}_i^{\mu} = f_{i\alpha}^{\dagger} T_{\alpha\beta}^{\mu} f_{i\beta}$, where the index α enumerates four different fermion flavors and the matrices T^{μ} are the SU(4) generators [56]. At half-filling of the underlying Hubbard model, the local spin-valley Hilbert space is six-dimensional (4 choose 2), which leads to a local filling constraint of two partons per lattice site $\sum_{\alpha} f_{i\alpha}^{\dagger} f_{i\alpha} = 2$.

Upon inclusion of Hund's couplings, the SU(4) symmetry of the model is explicitly broken [16]. Omitting other sources of SU(4) breaking, a residual separate spin-valley $\text{SU}(2)^{\text{s}} \otimes \text{SU}(2)^{\text{v}}$ symmetry remains which is reflected by the extended Hamiltonian

$$\mathcal{H} = \sum_{\langle ij \rangle} J \left(\hat{\sigma}_i^a \otimes \hat{\tau}_i^b \right) \left(\hat{\sigma}_j^a \otimes \hat{\tau}_j^b \right) + J_s \hat{\sigma}_i^a \hat{\sigma}_j^a + J_v \hat{\tau}_i^b \hat{\tau}_j^b \,, \quad (2)$$

where the spin-valley operators read $\hat{\sigma}_i^a = f_{is'l'}^{\dagger} \theta_{s's}^a \delta_{l'l} f_{isl}$, $\hat{\tau}_i^b = f_{is'l'}^{\dagger} \delta_{s's} \theta_{l'l}^b f_{isl}$, and $\hat{\sigma}_i^a \otimes \hat{\tau}_i^b = f_{is'l'}^{\dagger} \theta_{s's}^a \theta_{l'l}^b f_{isl}$. Instead of enumerating the four fermion types by a single index, we have exposed the spin quantum number $s \in \{\uparrow, \downarrow\}$ and the valley quantum number $l \in \{+, -\}$ explicitly; Pauli matrices are denoted by θ^a, $a \in \{1, 2, 3\}$. At the high-symmetry point $J = J_s = J_v$ the full SU(4) symmetry is restored. We assume that the Hund's interactions are weak enough such that all exchange couplings are antiferromagnetic [55], i.e., $J, J_v, J_s > 0$.

III. PSEUDOFERMION FUNCTIONAL RG

Parton-decomposed quartic Hamiltonians of the general type defined in Eq. (2) can readily be analyzed by the pseudofermion functional renormalization group (pf-FRG) [57–60]. For SU(N) spins, the approach is already naturally formulated with a local constraint of $N/2$ fermions per site. It combines aspects of an expansion in spin length S [61] (which naturally favors magnetic order) and in the SU(N) spin symmetry [62,63] (which typically favors quantum spin-liquid states), and it becomes exact on a mean-field level in the separate limits of large S and large N. It is thus suited to resolve the competition between ordered ground states and QSVL phases in the spin-valley model at hand. We extend the standard implementation of pf-FRG to incorporate the $\text{SU}(2)^{\text{s}} \otimes \text{SU}(2)^{\text{v}}$ symmetry, thereby obtaining flow equations for the one-particle irreducible vertices as a function of an RG frequency cutoff scale Λ. Numerically solving the set of $\mathcal{O}(10^6)$ flow equations at up to 84 Matsubara frequencies and using a real-space vertex truncation of $L = 7$ lattice bonds in each spatial direction, spontaneous symmetry breaking, e.g., the onset of long-range magnetic or valence bond order, is indicated by an instability of the RG flow [57,64] which occurs at some critical scale Λ_c.

In the case of long-range order, to identify the precise nature of the ordered state we can separately gain access to the elastic component ($\omega = 0$) of the correlation functions in

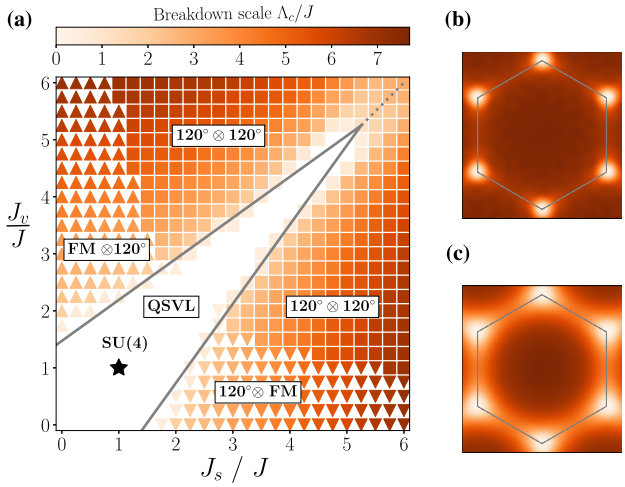

FIG. 1. Phase diagram on the triangular lattice. (a) Colors indicate the magnitude of the breakdown scale Λ_c in units of J, triangles (squares) denote regions with negative (positive) effective coupling Eq. (4); see text for details. (b) Structure factor in the spin (valley) subspace at dominant J_s (J_v), plotted at Λ_c, indicating the onset of 120° order. (c) Structure factor at the SU(4) point where no instability of the RG flow occurs. Local correlations are reminiscent of 120° order albeit broadened. The same color scale is applied to both (b) and (c). The solid gray lines mark the phase boundaries between the QSVL and the ordered phases, the dotted line marks the diagonal $J_s/J = J_v/J$.

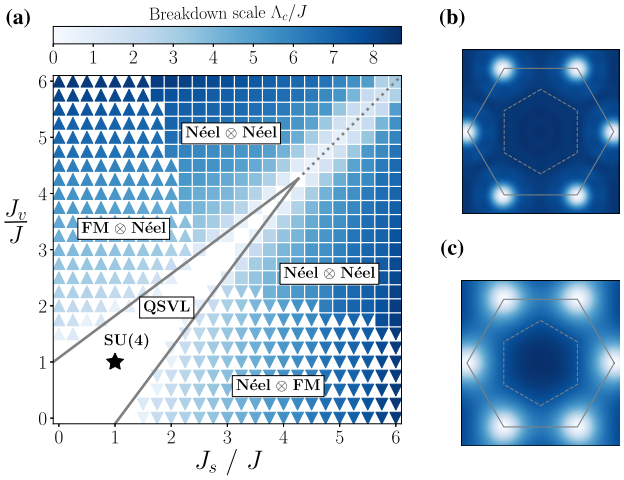

FIG. 2. Phase diagram on the honeycomb lattice. (a) Colors indicate the magnitude of the breakdown scale Λ_c in units of J, triangles (squares) denote regions with negative (positive) effective coupling Eq. (4); see text for details. (b), (c) Structure factors for a state deep in the Néel ordered phase versus the SU(4) symmetric state, with the same color scale applied.

the spin sector and in the valley sector,

$$\chi_{ij}^{s\Lambda} = \left\langle \hat{\sigma}_i^a \hat{\sigma}_j^a \right\rangle^{\Lambda}, \quad \text{and/or} \quad \chi_{ij}^{v\Lambda} = \left\langle \hat{\tau}_i^b \hat{\tau}_j^b \right\rangle^{\Lambda}. \tag{3}$$

Sharp features emerging in the respective structure factors $\chi^{s/v}(\vec{q}) \propto \sum_{ij} e^{i\vec{q}\cdot(\vec{r}_i - \vec{r}_j)} \chi_{ij}^{s/v}$ allow us to deduce the type of long-range order in either the spin or the valley degrees of freedom, cf. Figs. 1 and 2.

IV. EMERGENT SPIN-VALLEY LIQUID BEHAVIOR

We begin our analysis with the SU(4) symmetric point, $J_s/J = J_v/J = 1$. For both the triangular and honeycomb lattice, no instabilities are detected in the pf-FRG flow, indicating a fully symmetric ground state. In addition, upon varying the vertex range L we observe no finite-size dependence of the flows, consistent with a ground state without symmetry-breaking long-range order. This rules out not just magnetically ordered states, but also valence bond or dimer crystals [65], an ordering which spins in the self-conjugate representation are often prone to [66,67]. For SU(4) spins in the self-conjugate representation we can further use the Lieb-Schultz-Mattis-Hastings [68–70] theorem to rule out a featureless Mott insulator as the ground state in the case of the triangular lattice, whereas such a state is in principle still a possibility on the honeycomb lattice. We note that the spin/valley structure factors have features resembling 120°/Néel order, albeit significantly broadened; see Figs. 1(c) and 2(c).

V. STABILITY OF SPIN-VALLEY LIQUID AND ADJACENT MAGNETISM

Moving towards parameter regimes with broken SU(4) symmetry, $J_s/J, J_v/J \neq 1$, we find that an extended paramagnetic region emanates from the SU(4) symmetric point, see the white wedges in Figs. 1 and 2. Importantly, this finding supports the stability of the emergent spin-valley liquid behavior even in the presence of SU(4) breaking perturbations such as the Hund's coupling. Comparing the two lattice geometries, the triangular lattice gives rise to a parametrically larger QSVL phase than the bipartite honeycomb lattice, which can likely be traced back to the geometric frustration of the former. Along the diagonal line of equal coupling $J_v = J_s$, the QSVL region eventually collapses and disappears, being replaced by long-range antiferromagnetic order. Moving along the dotted diagonal line in the respective phase diagrams we observe a strongly suppressed breakdown scale Λ_c, relative to the surrounding parameter space, indicating that quantum fluctuations are strongest when $J_v = J_s$.

For sufficiently strong dominance of either spin or valley coupling, different ordered phases occur for both lattice geometries. The transition towards an ordered state is indicated by a leading instability in the RG flow, either in the spin or valley sector. To explore the subleading instabilities in the remaining sector, we employ a heuristic mean-field-like approach to estimate the effective spin or valley couplings between nearest-neighbor sites i and j,

$$J_v^{\text{eff}} = J_v + J\chi_{ij}^{s\Lambda_c} \quad \text{and} \quad J_s^{\text{eff}} = J_s + J\chi_{ij}^{v\Lambda_c}. \tag{4}$$

Note that for 120° or Néel order in one of the SU(2) sectors the corresponding nearest-neighbor correlation becomes negative. Therefore, the effective couplings J_v^{eff} and J_s^{eff} may, too, turn negative and drive a *ferromagnetic* instability in the other sector, despite the antiferromagnetic nature of all couplings in

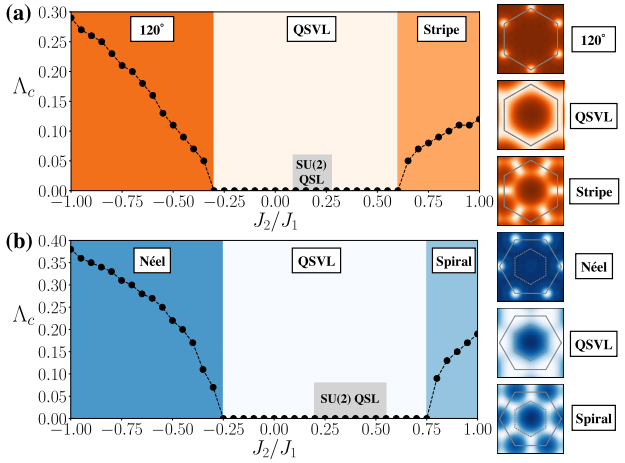

FIG. 3. Phase diagrams for SU(4) J_1-J_2 models on the triangular lattice (a) and the honeycomb lattice (b). Gray boxes indicate the extent of the quantum spin-liquid (QSL) regime for the respective spin-1/2 SU(2) model. Structure factors for the respective phases are shown to the right, where the same color scale is applied to all plots of the underlying lattice.

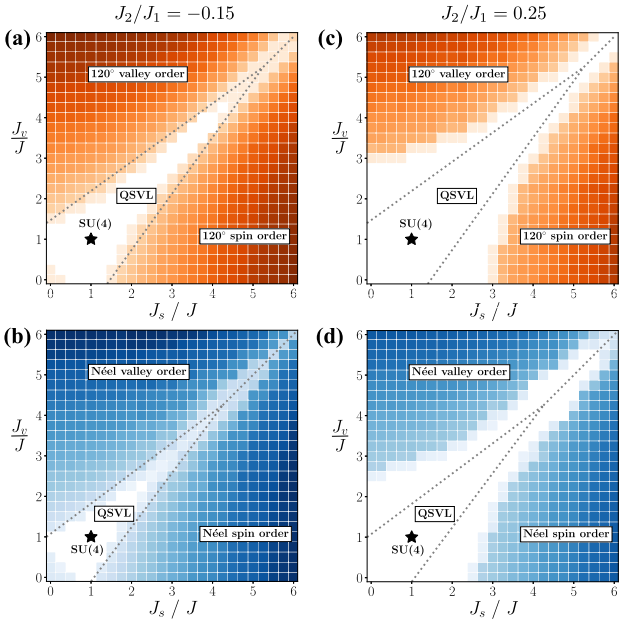

FIG. 4. Phase diagrams for longer-ranged spin-valley model showing the effect of ferromagnetic $J_2/J_1 = -0.15$ for (a) the triangular and (b) the honeycomb model. The same for antiferromagnetic $J_2/J_1 = 0.25$ for (c) the triangular and (d) the honeycomb model. Colors correspond to critical scales as indicated in Figs. 1 and 2. For reference, the phase boundaries at $J_2/J_1 = 0$ and the diagonal are marked by dotted lines.

the microscopic spin-valley model [55]. This kind of mechanism may be at the origin of the spin polarization observed at half-filling in TDBG [9,10], as first pointed out in Ref. [55] for quarter-filling. Extracting the sign of the effective coupling according to Eq. (4) at the transition scale of the leading sector allows us to distinguish two regimes with either ferro- or antiferromagnetic correlations in the subleading sector [71]. In Figs. 1 and 2 the so-determined order in the subleading regimes is indicated by triangle (ferromagnetic) or square (antiferromagnetic) symbols.

VI. LONGER-RANGE INTERACTIONS

In the ongoing search for an effective microscopic description for moiré heterostructures it has been pointed out that longer-ranged Coulomb interactions should not be neglected [38], which in the effective spin model will give rise to exchange couplings beyond nearest-neighbor. To probe the stability of the QSVL regime in our model we here consider the effect of a next-nearest neighbor coupling J_2.

Let us first recapitulate the effect a next-nearest-neighbor coupling J_2 for the spin-1/2 SU(2) case on the triangular and the honeycomb lattices. Here the bare nearest-neighbor coupling leads to magnetic ordering and only an antiferromagnetic J_2 of intermediate coupling strength facilitates the formation of a narrow quantum spin-liquid (QSL) regime [59,72–74], as indicated by the gray boxes in Fig. 3. Notably, the induced QSL regime is somewhat larger for the honeycomb lattice where the next-nearest neighbor interaction introduces geometric frustration.

For the model at hand, we first concentrate on the SU(4) symmetric point and explore the effect of $J_2/J_1 \in [-1, 1]$. As shown in Fig. 3, the QSVL region for the SU(4) model is significantly expanded for both lattice geometries in comparison to the SU(2) QSL case. The impact of J_2 on the the full spin-valley (J_s, J_v) phase diagrams of Figs. 1 and 2 is illustrated in Fig. 4 for both ferromagnetic and antiferromagnetic J_2. While an antiferromagnetic J_2 is found to further widen the wedge-shaped QSVL region, the converse occurs for ferromagnetic J_2, which drives the system closer to the ordered states. This means that, depending on the sign of J_2, longer-range interactions can actually stabilize and even expand the region of QSVL behavior.

VII. CONCLUSIONS

In this work, we studied $\mathrm{SU}(2)^{\mathrm{s}} \otimes \mathrm{SU}(2)^{\mathrm{v}}$-symmetric spin-valley Heisenberg models in the self-conjugate representation for both the triangular and honeycomb lattice. Seen as the effective Hamiltonians generated in the strong-coupling limit of an underlying Hubbard model, such models are relevant as minimal models in the exploration of the correlated insulating states of recently synthesized moiré heterostructures. Depending on which set of minibands the Hubbard model is designed to describe, the half-filling case studied here can potentially describe different candidate correlated insulators, e.g., the insulator at half-filling $n = +n_s/2$ in the triangular system TDBG.

In particular, we focused on the study of Hund's-induced as well as longer-ranged exchange couplings and their impact on the spin-valley liquid which has been found to emerge in the limit of SU(4) symmetry in both lattice geometries. We find extended parameter regimes where this phase is stabilized, with no signatures of long-range order, providing evidence for a stable realm of spin-valley liquid behavior. Experimentally,

such a phase would be consistent with a correlated insulator lacking spin and valley polarization. However, the precise nature of the phase and potential experimental fingerprints are left for future study, though we note that a recent projective-symmetry-group classification of fermionic partons on the half-filled triangular lattice suggests the possibility of a U(1) spin liquid with four Fermi surfaces [75], which would be consistent with our analysis. Our findings hint at the possibility of spin-valley entangled quantum liquids lurking within the correlated insulating regimes of moiré heterostructures.

ACKNOWLEDGMENTS

We thank L. Classen, P. Corboz, A. Laeuchli, and A. Paramekanti for discussions. C.H. thanks the Aspen Center for Theoretical Physics, where parts of this paper were written, for hospitality and support under Grant No. NSF 1066293. We acknowledge partial support from the Deutsche Forschungsgemeinschaft (DFG, German Research Foundation), Project No. 277146847, SFB 1238 (Project No. C03) and Project No. 277101999, TRR 183 (Projects No. B01 and No. A02). The numerical simulations were performed on the CHEOPS cluster at RRZK Cologne and the JURECA Booster at the Forschungszentrum Juelich.

APPENDIX A: HEXAGONAL MOIRÉ STRUCTURES

As noted in the main text, the minimal model that covers the necessary universal aspects of the various moiré heterostructures is a two-orbital extended Hubbard model. With four flavors of fermions per site, two spin and two valley degrees of freedom, this leads to a four band model on the triangular lattice and an eight band model on the honeycomb lattice (where the doubling is simply due to the doubling of the unit cell). Which of these lattices is appropriate to use depends on the particular moiré heterostructure one is interested in.

For TBG, TLG/h-BN, and TDBG there are a total of eight minibands near charge neutrality, four above and four below, that are separated from the rest of the spectrum by trivial band gaps. Filling of these minibands is thus typically denoted as ranging from $n = -n_s$ to $n = +n_s$, as indicated in Fig. 5 [where, for convenience, we plot $n/(n_s/4)$]. In the case of TBG, the bands above/below charge neutrality are connected via Dirac points, meaning that any effective Hubbard model must describe all eight bands. This naturally motivates the use of the honeycomb lattice Hubbard model. Half-filling, i.e., the scenario focused on in the main text, thus corresponds to charge neutrality $n = 0$. However, in the case of TDBG and TLG/h-BN the bands above/below charge neutrality are disconnected from one another, meaning that an effective Hubbard model description need only focus on one or the other set of four bands. This naturally leads to a triangular lattice description, with half-filling now corresponding to $n = \pm n_s/2$.

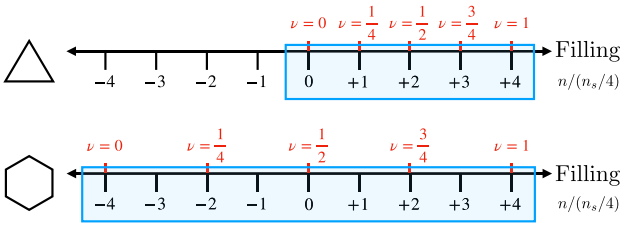

FIG. 5. Comparison of filling for the effective Hubbard model, ν, and for the minibands in the experimental cases of interest, $n/(n_s/4)$ (where $n = \pm n_s$ corresponds to fully empty or filled bands) in the case of a triangular (upper) and honeycomb (lower) lattice description. Depending on the lattice description the effective Hubbard model can either apply to all of, or just half of, the minibands, with its region of applicability denoted by the blue boxes.

APPENDIX B: PSEUDOFERMION FUNCTIONAL RG APPROACH

The pseudofermion functional renormalization group (pf-FRG) has recently been established as a versatile tool for the investigation of ground state phase diagrams for a wide class of spin models [57,76,77]. In doing so, the free fermion propagator $G_0 = (i\omega)^{-1}$ of a pseudofermion decomposed quartic Hamiltonian, e.g., Eq. (1) (main text), is modified by a step-like regularization function $\Theta(|\omega| - \Lambda)$ with frequency cutoff scale Λ, i.e., $G_0 \to G_0^\Lambda = G_0\Theta^\Lambda$. The artificial scale dependence of this theory results in a hierarchy of coupled one-loop RG flow equations for the one-particle-irreducible (1PI) interaction vertices. We employ a standard approximation scheme, where the hierarchy is truncated to exclusively account for the frequency-dependent self-energy Σ^Λ and two-particle interaction vertex Γ^Λ; see, e.g., Ref. [62] for more details and technicalities.

Here, we describe the aspects of the pf-FRG which are particular to the present spin-valley model, i.e., the vertex parametrization for the $\mathrm{SU}(2) \otimes \mathrm{SU}(2)$ symmetry and the implementation of the filling constraint.

1. Vertex parametrization for SU(2)⊗SU(2) symmetry

The flow equations for the special case of $\mathrm{SU}(2)^{\mathrm{s}} \otimes \mathrm{SU}(2)^{\mathrm{v}}$ symmetry can be extracted from the general fermionic FRG equations. Here we consider the flows of the self-energy and the two-particle vertex given by

$$\frac{d}{d\Lambda}\Sigma^\Lambda(1';1) = -\frac{1}{2\pi}\sum_2 \Gamma^\Lambda(1',2;1,2)S^\Lambda(2), \tag{B1}$$

$$\begin{aligned}\frac{d}{d\Lambda}&\Gamma^\Lambda(1',2';1,2)\\ &= -\frac{1}{2\pi}\sum_{3,4}[\Gamma^\Lambda(1',2';3,4)\Gamma^\Lambda(3,4;1,2)\\ &\quad - \Gamma^\Lambda(1',4;1,3)\Gamma^\Lambda(3,2';4,2) - (3 \leftrightarrow 4)\\ &\quad + \Gamma^\Lambda(2',4;1,3)\Gamma^\Lambda(3,1';4,2) + (3 \leftrightarrow 4)]\\ &\quad \times G^\Lambda(3)\frac{d}{d\Lambda}G^\Lambda(4)\,,\end{aligned} \tag{B2}$$

where the numbers $n = \{i_n, s_n, l_n, w_n\}$ represent tuples, comprising a lattice site index i_n, a spin index s_n, a valley index l_n and a Matsubara frequency w_n. We already employed that both the full G^Λ and single-scale S^Λ propagator are diagonal

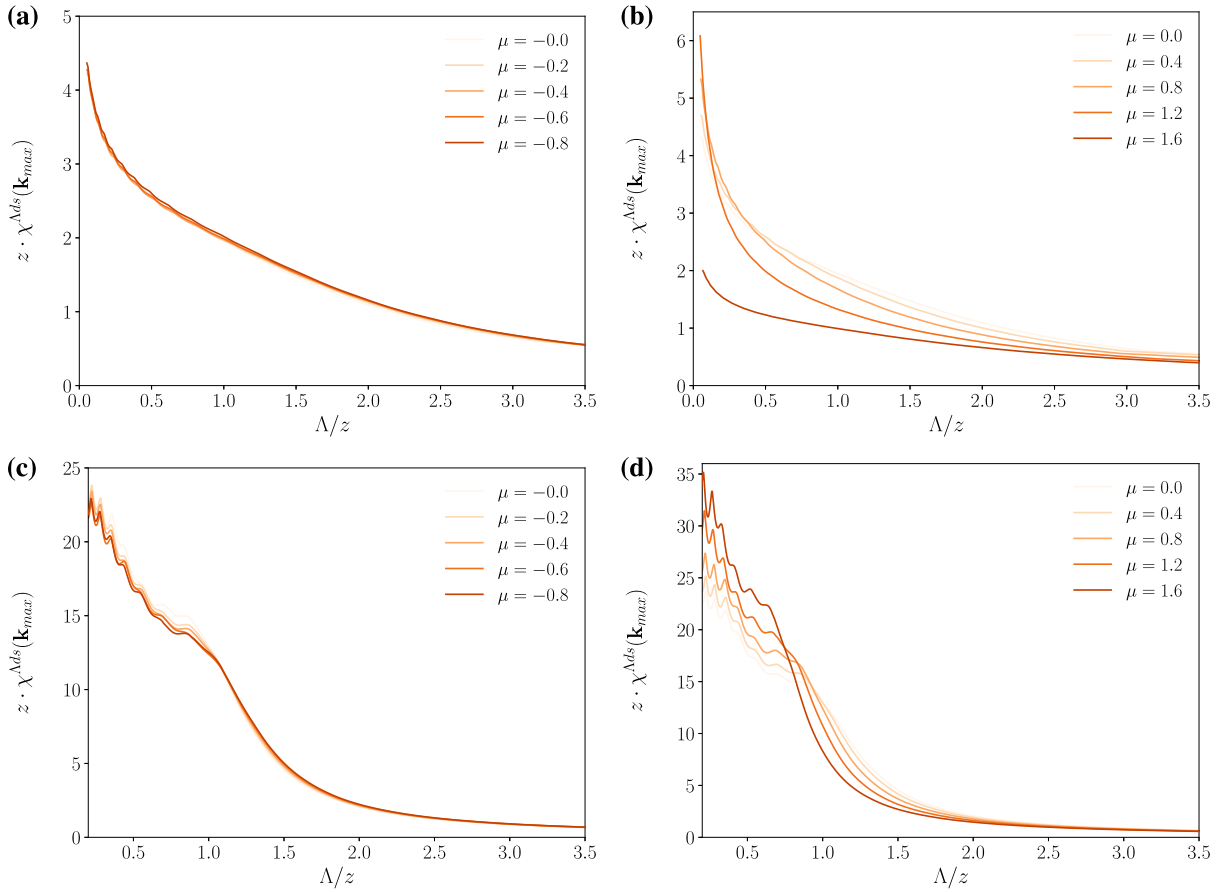

FIG. 6. Effect of level terms on the static structure factor $\chi^{\Lambda ds}(\mathbf{k})$ for the triangular lattice. (a), (b) $J_s/J = J_v/J = 1.0$. (c), (d) $J_s/J = 0.5$, $J_v/J = 4.0$. Negative μ yield no qualitative changes at $\mathbf{k} = \mathbf{k}_{\max}$ where the structure factor exhibits its peak value. For $\mu > 0$, especially in the QSVL phase, the flows differ visibly. Note that all axis have been normalized to a common energy scale by $z = \sqrt{J^2 + J_s^2 + J_v^2 + \mu^2}$ to account for the change of initial conditions.

in all arguments. Their remaining frequency dependence is given by

$$G_i^\Lambda(w) = \frac{\theta(|\omega| - \Lambda)}{iw - \Sigma_i^\Lambda(w)}, \tag{B3}$$

$$S_i^\Lambda(w) = \frac{\delta(|\omega| - \Lambda)}{iw - \Sigma_i^\Lambda(w)}. \tag{B4}$$

The spin/valley dependence of the 1PI irreducible vertices can then be expanded in terms of an $\mathfrak{su}(2)$ basis. Augmenting this scheme by symmetry-allowed SU(2)-invariant density terms and making use of translation invariance in imaginary time, as well as local $U(1)$ symmetry, the parametrization of the vertices reads

$$\Sigma^\Lambda(1';1) = \sum_{\alpha,\beta} \Sigma_{i_1}^{\Lambda\alpha\beta}(w_1)\theta^\alpha_{s_{1'}s_1}\theta^\beta_{l_{1'}l_1}\delta_{i_{1'}i_1}\delta(w_{1'} - w_1)\,, \tag{B5}$$

$$\begin{aligned}\Gamma^\Lambda(1',2';1,2) &= \sum_{\alpha,\alpha',\beta,\beta'} \Gamma^{\Lambda\alpha\alpha'\beta\beta'}_{i_1 i_2}(w_{1'}w_{2'};w_1w_2)\theta^\alpha_{s_{1'}s_1}\theta^{\alpha'}_{s_{2'}s_2}\theta^\beta_{l_{1'}l_1}\theta^{\beta'}_{l_{2'}l_2}\delta_{i_{1'}i_1}\delta_{i_{2'}i_2} \\ &\quad\times \delta(w_{1'} + w_{2'} - w_1 - w_2) - (1 \leftrightarrow 2),\end{aligned} \tag{B6}$$

where $\alpha, \beta \in \{0, 1, 2, 3\}$ with $\theta^0 = \mathbf{1}$. Exploiting SU(2) symmetry in both spin and valley indices we are left with pure density contributions for the self-energy, while the two-particle vertex may also contain off-diagonal terms albeit with equal spin directions, i.e.,

$$\Sigma^\Lambda(1';1) = \Sigma^\Lambda_{i_1}(w_1)\delta_{s_{1'}s_1}\delta_{l_{1'}l_1}\delta_{i_{1'}i_1}\delta(w_{1'} - w_1)\,, \tag{B7}$$

$$\begin{aligned}&\Gamma^\Lambda(1',2';1,2) \\ &= [\Gamma^{\Lambda ss}_{i_1 i_2}(w_{1'}w_{2'};w_1w_2)\theta^a_{s_{1'}s_1}\theta^a_{s_{2'}s_2}\theta^b_{l_{1'}l_1}\theta^b_{l_{2'}l_2} \\ &\quad+ \Gamma^{\Lambda sd}_{i_1 i_2}(w_{1'}w_{2'};w_1w_2)\theta^a_{s_{1'}s_1}\theta^a_{s_{2'}s_2}\delta_{l_{1'}l_1}\delta_{l_{2'}l_2} \\ &\quad+ \Gamma^{\Lambda ds}_{i_1 i_2}(w_{1'}w_{2'};w_1w_2)\delta_{s_{1'}s_1}\delta_{s_{2'}s_2}\theta^b_{l_{1'}l_1}\theta^b_{l_{2'}l_2} \\ &\quad+ \Gamma^{\Lambda dd}_{i_1 i_2}(w_{1'}w_{2'};w_1w_2)\delta_{s_{1'}s_1}\delta_{s_{2'}s_2}\delta_{l_{1'}l_1}\delta_{l_{2'}l_2}] \\ &\quad\times \delta_{i_{1'}i_1}\delta_{i_{2'}i_2}\delta(w_{1'} + w_{2'} - w_1 - w_2) - (1 \leftrightarrow 2)\,,\end{aligned} \tag{B8}$$

where $a, b \in \{1, 2, 3\}$. The superscripts ss, sd, ds, dd hereby denote if the coupling in the spin (valley) sector is spin like (s) or density like (d).

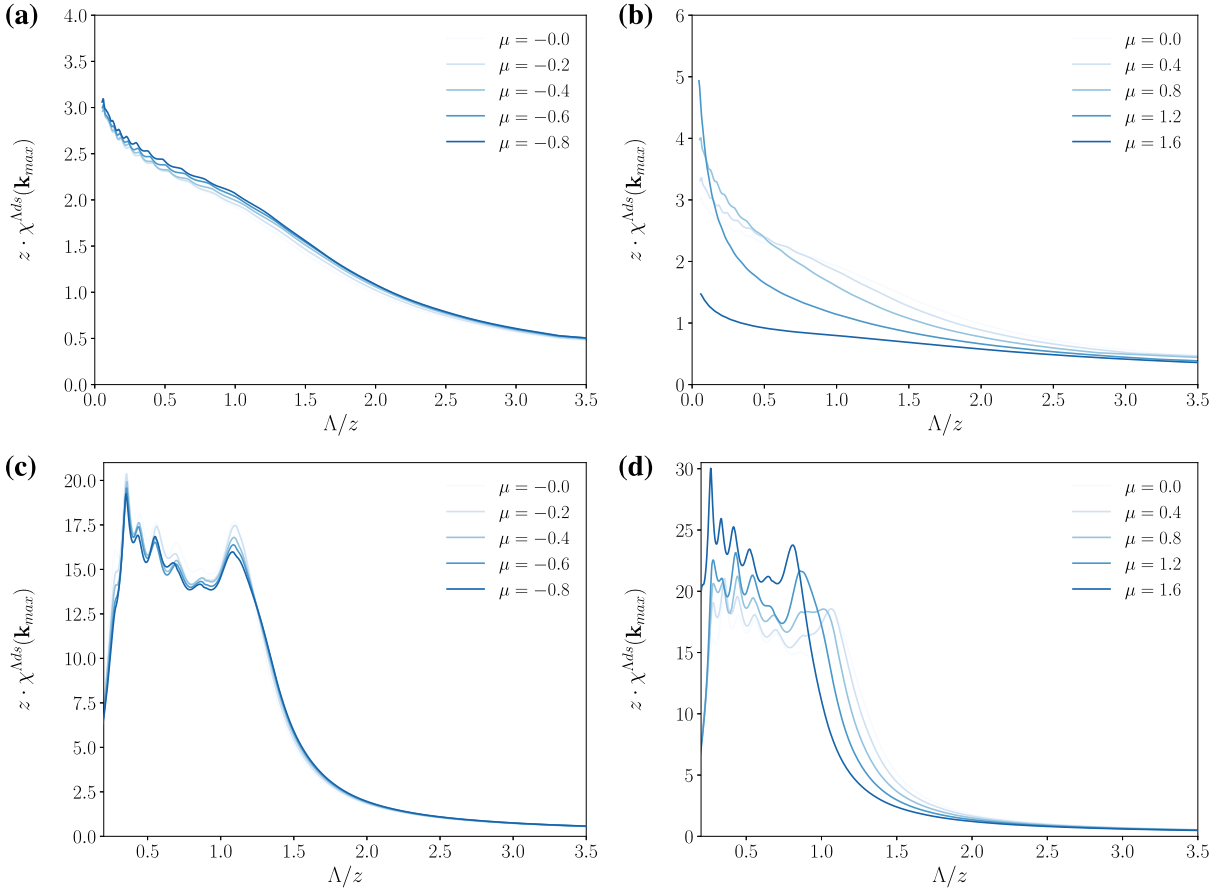

FIG. 7. Effect of level terms on the static structure factor $\chi^{\Lambda ds}(\mathbf{k})$ for the honeycomb lattice. (a), (b) $J_s/J = J_v/J = 1.0$. (c), (d) $J_s/J = 0.5$, $J_v/J = 4.0$. Similar to what is seen in Fig. 6, unphysical contributions become relevant only at $\mu > 0$, while for negative μ no qualitative change is observed.

The initial conditions at the UV scale then read $\Sigma^{\infty}_{i_1}(w) = 0$ for the self-energy and

$$\Gamma^{\infty ss}_{i_1 i_2}(w_{1'} w_{2'}; w_1 w_2) = J\,, \quad \Gamma^{\infty sd}_{i_1 i_2}(w_{1'} w_{2'}; w_1 w_2) = J_s\,,$$
$$\Gamma^{\infty ds}_{i_1 i_2}(w_{1'} w_{2'}; w_1 w_2) = J_v\,, \quad \Gamma^{\infty dd}_{i_1 i_2}(w_{1'} w_{2'}; w_1 w_2) = 0\,, \tag{B9}$$

for the two-particle interaction vertices. Further details on the inner workings of the pf-FRG approach can be found in Ref. [78].

2. Particle-hole symmetry and the half-filling constraint

In the model studied here, the local Hilbert space for fermionic flavors $\alpha \in \{(\uparrow +), (\uparrow -), (\downarrow +), (\downarrow -)\}$ is equipped with the particle-number basis $B = \{|n_1, ..., n_4\rangle\}$. We define the linear unitary operator $\mathcal{P}$ acting on the basis by exchanging each occupied state with an empty state $\mathcal{P}|n_1, ..., n_4\rangle = |1 - n_1, ..., 1 - n_4\rangle$. By computing the corresponding matrix elements, one finds that $\mathcal{P}$ transforms creation and annihilation operators into each other, i.e., $\mathcal{P}^\dagger f^\dagger_\alpha \mathcal{P} = f_\alpha$, $\mathcal{P}^\dagger f_\alpha \mathcal{P} = f^\dagger_\alpha$. This transformation leaves the spin-valley Hamiltonian and its groundstate at $\Lambda \to \infty$ invariant. On the level of vertex functions, we obtain the identities $\Sigma^\Lambda(1'; 1) = -\Sigma^\Lambda(-1; -1')$ and $\Gamma^\Lambda(1', 2'; 1, 2) = \Gamma^\Lambda(-1, -2; -1', -2')$, where the minus sign applies only to Matsubara frequencies. The vertex components therefore obey $\Sigma^\Lambda_{i_1}(w) = -\Sigma^\Lambda_{i_1}(-w)$ and $\Gamma^{\Lambda\zeta}_{i_1 i_2}(s, t, u) = \Gamma^{\Lambda\zeta}_{i_1 i_2}(-s, t, -u)$ where $\zeta \in \{ss, sd, ds, dd\}$.

These symmetries are explicitly implemented in our pf-FRG approach. However, only one local subspace, namely the one with two occupied states, is mapped to itself by $\mathcal{P}$, i.e., by enforcing the symmetries of that respective subspace half-filling at each lattice site is expected to be well-enforced on average. Furthermore, since the particle number per site must be conserved as a consequence of local U(1) symmetry, hopping processes that alter the filling would trigger a measurable nonmagnetic instability of the flow, which we do not observe here.

To test the validity of the above considerations we have employed a numerical scheme first exploited in [61]. The spin-valley Hamiltonian is extended by local level terms $\mu \hat{T}^v_i \hat{T}^v_i$ diagonal in the parton representation of $SU(4)$ spins. Each of them contributes an energy $E(n) = \frac{5}{2}\mu(n - \frac{1}{4}n^2)$ where n is the fermion occupation number. For $\mu < 0$ half-filling (i.e.,

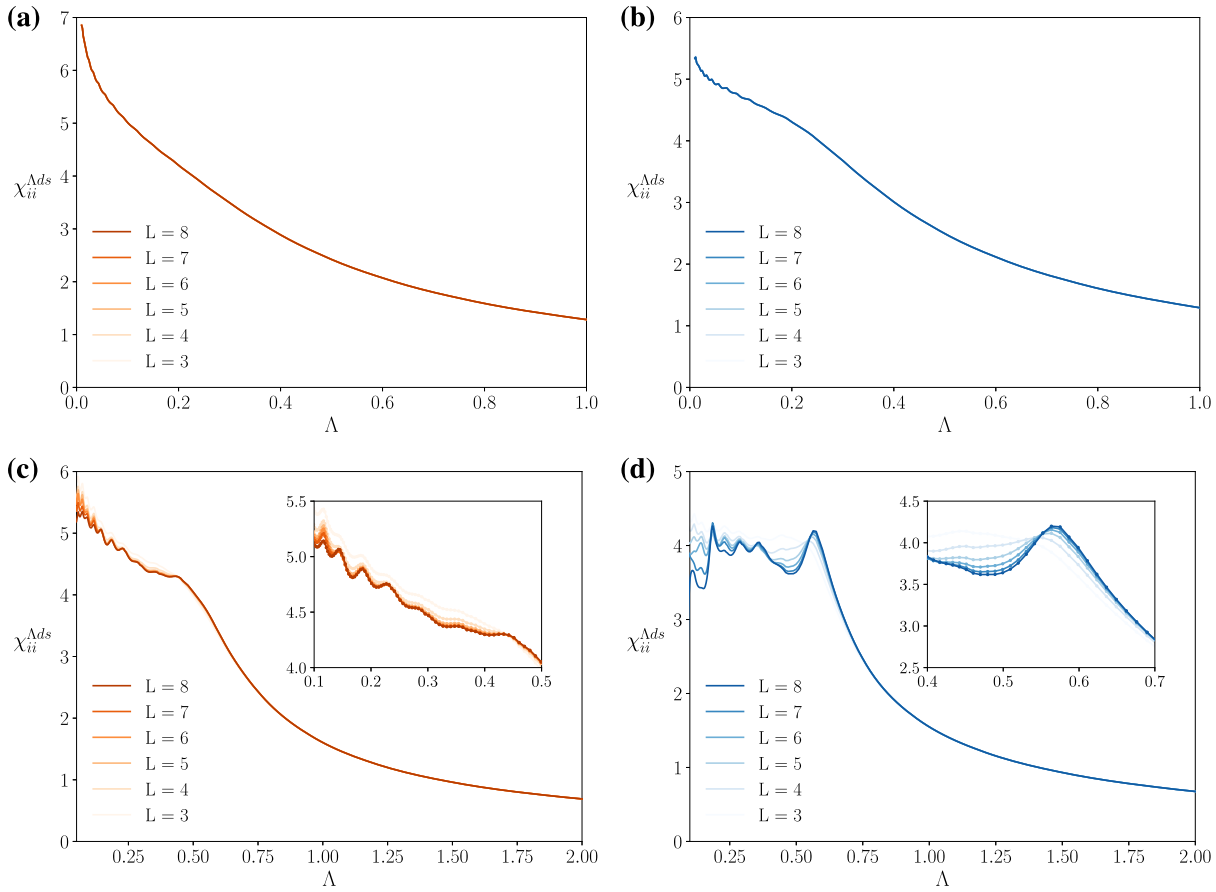

FIG. 8. Finite-size analysis of the onsite correlation function $\chi_{ii}^{\Lambda ds} = \chi_{ii}^{v\Lambda}$ for the triangular lattice (orange) and the honeycomb lattice (blue). (a), (b) $J_s/J = J_v/J = 1.0$. (c), (d) $J_s/J = 0.5$, $J_v/J = 4.0$. For a paramagnetic ground state the flow shows neither dependence on L nor an instability and correlations quickly decay to zero beyond nearest neighbors.

$n = 2$) is favored, whereas for $\mu > 0$ $E(n)$ is minimized for either $n = 0$ or $n = 4$. Hence, if the assumption of half-filling is correct, then our results at $\mu = 0$ should be consistent with those obtained for negative μ (up to an overall shift of the energy scale). However level attractions ($\mu > 0$) should lead to qualitative changes, since a subspace with different filling is populated.

By repeating our pf-FRG calculations with finite level (repulsion or attraction) terms, such behavior can indeed be observed. While negative values of μ seem to have no qualitative impact, level attraction terms lead to visible changes of the susceptibility flows. In the absence of a breakdown (top row in Figs. 6 and 7) susceptibilities start to vanish, consistent with effective lattice vacancies at $n = 0(4)$. For coupling parameters supporting long-range order (bottom row in Figs. 6 and 7) the effect of positive μ is however less pronounced, numerical instabilities a merely shifted towards lower values of Λ. Since the exchange couplings relevant to these phases are usually higher than the simulated ratios μ/J this behavior is expected. In light of these results we are confident that half-filling is well enforced even without an explicit projection scheme.

3. Finite-size analysis of the RG flow

An instability in the vertex function during the RG flow indicates spontaneous breaking of symmetries that have been implemented in the initial conditions [62]. Most prominently, magnetic instabilities appear as pronounced kinks or cusps in the flow of the momentum resolved two-spin correlations. Alternatively, one may check the behavior of an on-site correlation function, i.e., χ_{ii}^{Λ}, for different values of the vertex range L. Formally, L does not determine the system size (which is in fact infinite in pf-FRG) but rather sets the scale on which spins can be correlated. It is then natural to expect sensitivity to this parameter near the critical scale since the physics is governed by the collective behavior of all spins. However, if the system does not develop an instability down to the smallest energy scales, i.e., the pf-FRG flow stays regular, then real-space correlations should be robust with respect to variations of L.

Indeed as shown in Fig. 8, flows of the spin correlation in the dominant interaction channel for different L are aligned within the paramagnetic regions of the spin-valley phase diagrams, but deviate from each other around the critical scale in the ordered phases. We find, however, that this effect is

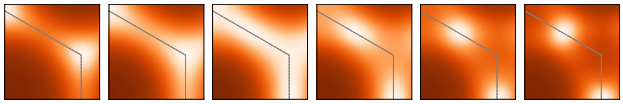

FIG. 9. Structure factors for the SU(4) model on the triangular lattice within the paramagnetic phase. Lines denote the first Brillouin zone boundary. From left to right $J_2/J_1 = 0.0/0.1/0.2/0.3/0.4/0.5$. At a ratio of $J_2/J_1 \approx 0.2$ a deformation from local 120° correlations to local stripe correlations is observed.

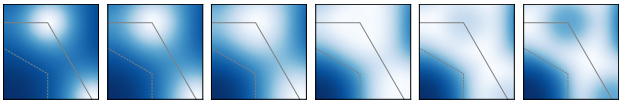

FIG. 10. Structure factors for the SU(4) model on the honeycomb lattice within the paramagnetic phase. Dashed lines denote the first, full lines the extended Brillouin zone. From left to right $J_2/J_1 = 0.0/0.1/0.2/0.3/0.4/0.5$. At a ratio of $J_2/J_1 \approx 0.3$ a deformation from local Néel to local spiral correlations is observed.

more subtle for the triangular than the honeycomb lattice, which we attribute to the inherent geometric frustration of the former.

4. Structure factor evolution in the spin-valley liquid of the J_1-J_2 model

The spin-valley entangled liquid ground states of the nearest-neighbor SU(4) Heisenberg models (on both the triangular and honeycomb lattice) remain stable upon inclusion of moderate longer-ranged exchange interactions as illustrated in Fig. 3 of the main text.

Here, we provide further information about the evolution of the structure factors upon varying J_2/J_1. First, we recall that for $J_2/J_1 = 0$, local correlations are reminiscent of 120° (Néel) order for the triangular (honeycomb) model. Going to large antiferromagnetic $J_2 > 0$, stripe (spiral) order emerges with the evolution of the structure factor being plotted in Figs. 9 and 10 at the onset of these orders. Around $J_2/J_1 \approx 0.2$ for the triangular and at about $J_2/J_1 \approx 0.3$ for the honeycomb lattice, the topology of the momentum resolved correlation functions changes visibly, indicating a Lifshitz transition.

[1] Y. Cao, V. Fatemi, A. Demir, S. Fang, S. L. Tomarken, J. Y. Luo, J. D. Sanchez-Yamagishi, K. Watanabe, T. Taniguchi, E. Kaxiras, *et al.*, Correlated insulator behavior at half-filling in magic-angle graphene superlattices, Nature **556**, 80 (2018).

[2] Y. Cao, V. Fatemi, S. Fang, K. Watanabe, T. Taniguchi, E. Kaxiras, and P. Jarillo-Herrero, Unconventional superconductivity in magic-angle graphene superlattices, Nature **556**, 43 (2018).

[3] M. Yankowitz, S. Chen, H. Polshyn, Y. Zhang, K. Watanabe, T. Taniguchi, D. Graf, A. F. Young, and C. R. Dean, Tuning superconductivity in twisted bilayer graphene, Science **363**, 1059 (2019).

[4] A. L. Sharpe, E. J. Fox, A. W. Barnard, J. Finney, K. Watanabe, T. Taniguchi, M. A. Kastner, and D. Goldhaber-Gordon, Emergent ferromagnetism near three-quarters filling in twisted bilayer graphene, Science **365**, 605 (2019).

[5] X. Lu, P. Stepanov, W. Yang, M. Xie, M. A. Aamir, I. Das, C. Urgell, K. Watanabe, T. Taniguchi, G. Zhang *et al.*, Superconductors, orbital magnets, and correlated states in magic angle bilayer graphene, Nature **574**, 653 (2019).

[6] G. Chen, L. Jiang, S. Wu, B. Lyu, H. Li, B. L. Chittari, K. Watanabe, T. Taniguchi, Z. Shi, J. Jung *et al.*, Evidence of a gate-tunable Mott insulator in a trilayer graphene moiré superlattice, Nat. Phys. **15**, 237 (2019).

[7] G. Chen, A. L. Sharpe, P. Gallagher, I. T. Rosen, E. J. Fox, L. Jiang, B. Lyu, H. Li, K. Watanabe, T. Taniguchi, and *et al.*, Signatures of gate-tunable superconductivity in trilayer graphene/boron nitride moiré superlattice, Nature **572**, 215 (2019).

[8] E. Codecido, Q. Wang, R. Koester, S. Che, H. Tian, R. Lv, S. Tran, K. Watanabe, T. Taniguchi, F. Zhang, *et al.*, Correlated insulating and superconducting states in twisted bilayer graphene below the magic angle, Sci. Adv. **5**, eaaw9770 (2019).

[9] X. Liu, Z. Hao, E. Khalaf, J. Y. Lee, K. Watanabe, T. Taniguchi, A. Vishwanath, and P. Kim, Spin-polarized correlated insulator and superconductor in twisted double bilayer graphene, arXiv:1903.08130.

[10] Y. Cao, D. Rodan-Legrain, O. Rubies-Bigordà, J. M. Park, K. Watanabe, T. Taniguchi, and P. Jarillo-Herrero, Electric field tunable correlated states and magnetic phase transitions in twisted bilayer-bilayer graphene, arXiv:1903.08596.

[11] C. Shen, N. Li, S. Wang, Y. Zhao, J. Tang, J. Liu, J. Tian, Y. Chu, K. Watanabe, T. Taniguchi *et al.*, Observation of superconductivity with Tc onset at 12K in electrically tunable twisted double bilayer graphene, arXiv:1903.06952.

[12] M. Serlin, C. L. Tschirhart, H. Polshyn, Y. Zhang, J. Zhu, K. Watanabe, T. Taniguchi, L. Balents, and A. F. Young, Intrinsic quantized anomalous Hall effect in a moiré heterostructure, Science **367**, 900 (2020).

[13] G. Trambly de Laissardière, D. Mayou, and L. Magaud, Localization of dirac electrons in rotated graphene bilayers, Nano Lett. **10**, 804 (2010).

[14] R. Bistritzer and A. H. MacDonald, Moiré bands in twisted double-layer graphene, Proc. Natl. Acad. Sci. U.S.A. **108**, 12233 (2011).

[15] J. M. B. Lopes dos Santos, N. M. R. Peres, and A. H. Castro Neto, Continuum model of the twisted graphene bilayer, Phys. Rev. B **86**, 155449 (2012).

[16] C. Xu and L. Balents, Topological Superconductivity in Twisted Multilayer Graphene, Phys. Rev. Lett. **121**, 087001 (2018).

[17] N. F. Q. Yuan and L. Fu, Model for the metal-insulator transition in graphene superlattices and beyond, Phys. Rev. B **98**, 045103 (2018).

[18] J. F. Dodaro, S. A. Kivelson, Y. Schattner, X. Q. Sun, and C. Wang, Phases of a phenomenological model of twisted bilayer graphene, Phys. Rev. B **98**, 075154 (2018).

[19] D. M. Kennes, J. Lischner, and C. Karrasch, Strong correlations and $d + id$ superconductivity in twisted bilayer graphene, Phys. Rev. B **98**, 241407(R) (2018).

[20] Q.-K. Tang, L. Yang, D. Wang, F.-C. Zhang, and Q.-H. Wang, Spin-triplet f-wave pairing in twisted bilayer graphene near $\frac{1}{4}$-filling, Phys. Rev. B **99**, 094521 (2019).

[21] H. Isobe, N. F. Q. Yuan, and L. Fu, Unconventional Superconductivity and Density Waves in Twisted Bilayer Graphene, Phys. Rev. X **8**, 041041 (2018).

[22] Y.-P. Lin and R. M. Nandkishore, Kohn-Luttinger superconductivity on two orbital honeycomb lattice, Phys. Rev. B **98**, 214521 (2018).

[23] Y.-P. Lin and R. M. Nandkishore, A chiral twist on the high-T_c phase diagram in Moiré heterostructures, Phys. Rev. B **100**, 085136 (2019).

[24] L. Rademaker and P. Mellado, Charge-transfer insulation in twisted bilayer graphene, Phys. Rev. B **98**, 235158 (2018).

[25] T. Huang, L. Zhang, and T. Ma, Antiferromagnetically ordered Mott insulator and $d + id$ superconductivity in twisted bilayer graphene: A quantum Monte Carlo study, Sci. Bull. **64**, 310 (2019).

[26] M. Fidrysiak, M. Zegrodnik, and J. Spałek, Unconventional topological superconductivity and phase diagram for an effective two-orbital model as applied to twisted bilayer graphene, Phys. Rev. B **98**, 085436 (2018).

[27] H. Guo, X. Zhu, S. Feng, and R. T. Scalettar, Pairing symmetry of interacting fermions on a twisted bilayer graphene superlattice, Phys. Rev. B **97**, 235453 (2018).

[28] B. Roy and V. Juričć, Unconventional superconductivity in nearly flat bands in twisted bilayer graphene, Phys. Rev. B **99**, 121407(R) (2019).

[29] C.-C. Liu, L.-D. Zhang, W.-Q. Chen, and F. Yang, Chiral Spin Density Wave and $d + id$ Superconductivity in the Magic-Angle-Twisted Bilayer Graphene, Phys. Rev. Lett. **121**, 217001 (2018).

[30] Y. Da Liao, Z. Y. Meng, and X. Y. Xu, Valence Bond Orders at Charge Neutrality in a Possible Two-Orbital Extended Hubbard Model for Twisted Bilayer Graphene, Phys. Rev. Lett. **123**, 157601 (2019).

[31] Y.-Z. You and A. Vishwanath, Superconductivity from valley fluctuations and approximate SO(4) symmetry in a weak coupling theory of twisted bilayer graphene, npj Quantum Mater. **4**, 16 (2019).

[32] A. Thomson, S. Chatterjee, S. Sachdev, and M. S. Scheurer, Triangular antiferromagnetism on the honeycomb lattice of twisted bilayer graphene, Phys. Rev. B **98**, 075109 (2018).

[33] Y. Sherkunov and J. J. Betouras, Electronic phases in twisted bilayer graphene at magic angles as a result of Van Hove singularities and interactions, Phys. Rev. B **98**, 205151 (2018).

[34] J. Kang and O. Vafek, Strong Coupling Phases of Partially Filled Twisted Bilayer Graphene Narrow Bands, Phys. Rev. Lett. **122**, 246401 (2019).

[35] Y.-H. Zhang, D. Mao, Y. Cao, P. Jarillo-Herrero, and T. Senthil, Nearly flat chern bands in moiré superlattices, Phys. Rev. B **99**, 075127 (2019).

[36] C. Schrade and L. Fu, Spin-valley density wave in moiré materials, Phys. Rev. B **100**, 035413 (2019).

[37] K. Seo, V. N. Kotov, and B. Uchoa, Ferromagnetic Mott State in Twisted Graphene Bilayers at the Magic Angle, Phys. Rev. Lett. **122**, 246402 (2019).

[38] M. Koshino, N. F. Q. Yuan, T. Koretsune, M. Ochi, K. Kuroki, and L. Fu, Maximally Localized Wannier Orbitals and the Extended Hubbard Model for Twisted Bilayer Graphene, Phys. Rev. X **8**, 031087 (2018).

[39] J. Kang and O. Vafek, Symmetry, Maximally Localized Wannier States, and a Low-Energy Model for Twisted Bilayer Graphene Narrow Bands, Phys. Rev. X **8**, 031088 (2018).

[40] L. Classen, C. Honerkamp, and M. M. Scherer, Competing phases of interacting electrons on triangular lattices in moiré heterostructures, Phys. Rev. B **99**, 195120 (2019).

[41] H. C. Po, L. Zou, A. Vishwanath, and T. Senthil, Origin of Mott Insulating Behavior and Superconductivity in Twisted Bilayer Graphene, Phys. Rev. X **8**, 031089 (2018).

[42] L. Xian, D. M. Kennes, N. Tancogne-Dejean, M. Altarelli, and A. Rubio, Multiflat bands and strong correlations in twisted bilayer boron nitride: Doping-induced correlated insulator and superconductor, Nano Lett. **19**, 4934 (2019).

[43] Y.-H. Zhang and T. Senthil, Bridging hubbard model physics and quantum Hall physics in trilayer graphene/$h-$BN moiré superlattice, Phys. Rev. B **99**, 205150 (2019).

[44] T. M. R. Wolf, J. L. Lado, G. Blatter, and O. Zilberberg, Electrically Tunable Flat Bands and Magnetism in Twisted Bilayer Graphene, Phys. Rev. Lett. **123**, 096802 (2019).

[45] J. C. W. Song, P. Samutpraphoot, and L. S. Levitov, Topological Bloch bands in graphene superlattices, Proc. Natl. Acad. Sci. USA **112**, 10879 (2015).

[46] Q. Tong, H. Yu, Q. Zhu, Y. Wang, X. Xu, and W. Yao, Topological mosaics in moiré superlattices of van der Waals heterobilayers, Nat. Phys. **13**, 356 (2017).

[47] T. M. R. Wolf, O. Zilberberg, I. Levkivskyi, and G. Blatter, Substrate-induced topological minibands in graphene, Phys. Rev. B **98**, 125408 (2018).

[48] B. L. Chittari, G. Chen, Y. Zhang, F. Wang, and J. Jung, Gate-Tunable Topological Flat Bands in Trilayer Graphene Boron-Nitride Moiré Superlattices, Phys. Rev. Lett. **122**, 016401 (2019).

[49] L. Zou, H. C. Po, A. Vishwanath, and T. Senthil, Band structure of twisted bilayer graphene: Emergent symmetries, commensurate approximants, and Wannier obstructions, Phys. Rev. B **98**, 085435 (2018).

[50] H. C. Po, L. Zou, T. Senthil, and A. Vishwanath, Faithful tight-binding models and fragile topology of magic-angle bilayer graphene, Phys. Rev. B **99**, 195455 (2019).

[51] S. Carr, S. Fang, H. C. Po, A. Vishwanath, and E. Kaxiras, Derivation of Wannier orbitals and minimal-basis tight-binding Hamiltonians for twisted bilayer graphene: First-principles approach, Phys. Rev. Res. **1**, 033072 (2019).

[52] G. Khaliullin, Orbital order and fluctuations in Mott insulators, Prog. Theor. Phys. Suppl. **160**, 155 (2005).

[53] P. Corboz, M. Lajkó, A. M. Läuchli, K. Penc, and F. Mila, Spin-Orbital Quantum Liquid on the Honeycomb Lattice, Phys. Rev. X **2**, 041013 (2012).

[54] W. M. H. Natori, R. Nutakki, R. G. Pereira, and E. C. Andrade, SU(4) Heisenberg model on the honeycomb lattice with exchange-frustrated perturbations: Implications for twistronics and Mott insulators, Phys. Rev. B **100**, 205131 (2019).

[55] X.-C. Wu, A. Keselman, C.-M. Jian, K. A. Pawlak, and C. Xu, Ferromagnetism and spin-valley liquid states in moiré correlated insulators, Phys. Rev. B **100**, 024421 (2019).

[56] D. P. Arovas and A. Auerbach, Functional integral theories of low-dimensional quantum Heisenberg models, Phys. Rev. B **38**, 316 (1988).

[57] J. Reuther and P. Wölfle, J_1-J_2 frustrated two-dimensional Heisenberg model: Random phase approximation and functional renormalization group, Phys. Rev. B **81**, 144410 (2010).

[58] J. Reuther and R. Thomale, Functional renormalization group for the anisotropic triangular antiferromagnet, Phys. Rev. B **83**, 024402 (2011).

[59] J. Reuther, D. A. Abanin, and R. Thomale, Magnetic order and paramagnetic phases in the quantum J_1-J_2-J_3 honeycomb model, Phys. Rev. B **84**, 014417 (2011).

[60] C. Wetterich, Exact evolution equation for the effective potential, Phys. Lett. B **301**, 90 (1993).

[61] M. L. Baez and J. Reuther, Numerical treatment of spin systems with unrestricted spin length S: A functional renormalization group study, Phys. Rev. B **96**, 045144 (2017).

[62] F. L. Buessen, D. Roscher, S. Diehl, and S. Trebst, Functional renormalization group approach to SU(N) Heisenberg models: Real-space renormalization group at arbitrary N, Phys. Rev. B **97**, 064415 (2018).

[63] D. Roscher, F. L. Buessen, M. M. Scherer, S. Trebst, and S. Diehl, Functional renormalization group approach to SU(N) Heisenberg models: Momentum-space renormalization group for the large-N limit, Phys. Rev. B **97**, 064416 (2018).

[64] D. Roscher, N. Gneist, M. M. Scherer, S. Trebst, and S. Diehl, Cluster functional renormalization group and absence of a bilinear spin liquid in the J_1-J_2-Heisenberg model, Phys. Rev. B **100**, 125130 (2019).

[65] Generally, an instability can be observed for any (quantum) order which is captured by a fermionic bilinear operator; see Ref. [62]. More complicated order whose order parameter involves higher order operators does not necessarily manifest in a flow breakdown .

[66] J. B. Marston and I. Affleck, Large-n limit of the Hubbard-Heisenberg model, Phys. Rev. B **39**, 11538 (1989).

[67] D. S. Rokhsar, Quadratic quantum antiferromagnets in the fermionic large-N limit, Phys. Rev. B **42**, 2526 (1990).

[68] E. Lieb, T. Schultz, and D. Mattis, Two soluble models of an antiferromagnetic chain, Ann. Phys. **16**, 407 (1961).

[69] M. B. Hastings, Lieb-Schultz-Mattis in higher dimensions, Phys. Rev. B **69**, 104431 (2004).

[70] Y. Yao, C.-T. Hsieh, and M. Oshikawa, Anomaly Matching and Symmetry-Protected Critical Phases in $SU(N)$ Spin Systems in 1+1 Dimensions, Phys. Rev. Lett. **123**, 180201 (2019).

[71] We finally note that, in principle, the FRG setup can also be extended to allow for a continuation of the flow into the ordered regime [63,64,79]; however, such modifications are beyond the scope of this work.

[72] Z. Zhu and S. R. White, Spin liquid phase of the $S = \frac{1}{2}J_1 - J_2$ Heisenberg model on the triangular lattice, Phys. Rev. B **92**, 041105(R) (2015).

[73] W.-J. Hu, S.-S. Gong, W. Zhu, and D. N. Sheng, Competing spin-liquid states in the spin-$\frac{1}{2}$ Heisenberg model on the triangular lattice, Phys. Rev. B **92**, 140403(R) (2015).

[74] Y. Iqbal, W.-J. Hu, R. Thomale, D. Poilblanc, and F. Becca, Spin liquid nature in the heisenberg $J_1 - J_2$ triangular antiferromagnet, Phys. Rev. B **93**, 144411 (2016).

[75] Y.-H. Zhang and D. Mao, Spin liquids and pseudogap metals in $SU(4)$ Hubbard model in moiré superlattice, Phys. Rev. B **101**, 035122 (2020).

[76] Y. Iqbal, R. Thomale, F. Parisen Toldin, S. Rachel, and J. Reuther, Functional renormalization group for three-dimensional quantum magnetism, Phys. Rev. B **94**, 140408(R) (2016).

[77] J. Reuther and R. Thomale, Cluster functional renormalization group, Phys. Rev. B **89**, 024412 (2014).

[78] F. L. Buessen, A functional renormalization group perspective on quantum spin liquids in three-dimensional frustrated magnets, Ph.D. thesis, University of Cologne, 2019.

[79] M. Salmhofer, C. Honerkamp, W. Metzner, and O. Lauscher, Renormalization group flows into phases with broken symmetry, Prog. Theor. Phys. **112**, 943 (2004).

7 Novel platforms for frustrated magnetism

7.1 Overview

Quantum spin liquids (QSLs) are enigmatic states of matter, in which conventional magnetic order is impeded by strong quantum fluctuations. In the past, several QSL materials have been proposed, albeit many of them ultimately order at low temperatures. Their respective coupling parameters, however, place them in vicinity of theoretically predicted spin liquid phases and certain QSL signatures, such as the temperature dependence of spin-spin correlation functions, can, thus, still be observed [150]. This has raised the intriguing question, whether its possible to artificially prohibit long-range order in these materials by tuning the interactions in such a way that frustration increases and magnetic states are consequently penalized. In the following, two routes for achieving this ambitious goal are proposed.

The twist angle between multi-layer composition of van der Waals materials, such as twisted bilayer graphene (tBG) [53, 73], has recently been established as a promising tuning knob for modifying electronic correlations. In Ref. [P8], we study the properties of bilayer molybdenum disulfite ($tMoS_2$) using large-scale density functional theory (DFT) and many-body calculations. Remarkably, $tMoS_2$ realizes a honeycomb superlattice with two flat bands, which result from the destructive interference of certain elements in the hopping matrix. In contrast to tBG, however, we find that the band structure of $tMoS_2$ at small twist angles is well described by a strongly-asymmetric p_x-p_y Hamiltonian. If augmented by Hubbard-Kanamori type interactions, the latter gives rise to an intricate Kugel-Khomski model with competing interactions in the orbital sector[1], which has been proposed to give rise to exotic spin dimer and spin-orbital liquid phases [151, 152]. Twisted moiré heterostructures, in which models with competing spin and orbital fluctuations can be crafted by stacking different materials and varying their relative twist angle, thus open up a promising avenue for the realization of elusive spin liquid states.

In the second publication, Ref. [P9], we engineer algebraically decaying Heisenberg couplings (γ) on top of an ordinary square antiferromagnet by utilizing the light of an optical cavity. The former, for $\gamma \to \infty$ and sufficiently long-range interactions, resemble a global singlet constraint and thus assure to suppress Néel order. Employing a Schwinger-Boson mean-field approach, we could indeed demonstrate the emergence of two spin liquid phases, one opening a spinon gap, the other one becoming gapless in the thermodynamic limit. This is remarkable insofar that the square lattice Heisenberg antiferromagnet is non-frustrated and yet our protocol is able to successfully destroy magnetic order. Cavity mediated interactions could thus become a powerful tool for generating QSLs both in condensed matter systems as well as in quantum simulators made from ultracold atoms.

Relevant publications:

[P8] *Realization of Nearly Dispersionless Bands with Strong Orbital Anisotropy from Destructive Interference in Twisted Bilayer MoS_2*
L. Xian, M. Claassen, **D. Kiese**, M. M. Scherer, S. Trebst, D. M. Kennes and A. Rubio
Nature Communications 12, 5644 (2021)

[P9] *Cavity-induced quantum spin liquids*
A. Chiocchetta, **D. Kiese**, C. P. Zelle, F. Piazza and S. Diehl
Nature Communications 12, 5901 (2021)

Author contributions: *The author performed the mean-field calculations in Ref. [P8] and prepared the corresponding section in the manuscript. D. Kiese was also responsible for writing the Schwinger-Boson code on which Ref. [P9] is based. Furthermore, he performed the numerical simulations, generated the respective figures and participated in the writing of that paper.*

[1] The spin sector has SU(2) symmetry and is non-frustrated.

nature COMMUNICATIONS

ARTICLE

https://doi.org/10.1038/s41467-021-25922-8 OPEN

Realization of nearly dispersionless bands with strong orbital anisotropy from destructive interference in twisted bilayer MoS_2

Lede Xian [1,2], Martin Claassen[3,4], Dominik Kiese[5], Michael M. Scherer[5], Simon Trebst [5], Dante M. Kennes [1,6]✉ & Angel Rubio [1,3,7]✉

Recently, the twist angle between adjacent sheets of stacked van der Waals materials emerged as a new knob to engineer correlated states of matter in two-dimensional heterostructures in a controlled manner, giving rise to emergent phenomena such as superconductivity or correlated insulating states. Here, we use an ab initio based approach to characterize the electronic properties of twisted bilayer MoS_2. We report that, in marked contrast to twisted bilayer graphene, slightly hole-doped MoS_2 realizes a strongly asymmetric p_x-p_y Hubbard model on the honeycomb lattice, with two almost entirely dispersionless bands emerging due to destructive interference. The origin of these dispersionless bands, is similar to that of the flat bands in the prototypical Lieb or Kagome lattices and co-exists with the general band flattening at small twist angle due to the moiré interference. We study the collective behavior of twisted bilayer MoS_2 in the presence of interactions, and characterize an array of different magnetic and orbitally-ordered correlated phases, which may be susceptible to quantum fluctuations giving rise to exotic, purely quantum, states of matter.

[1] Max Planck Institute for the Structure and Dynamics of Matter and Center for Free Electron Laser Science, Hamburg, Germany. [2] Frontier Research Center, Songshan Lake Materials Laboratory, Dongguan, China. [3] Center for Computational Quantum Physics, Simons Foundation Flatiron Institute, New York, NY, USA. [4] Department of Physics and Astronomy, University of Pennsylvania, Philadelphia, PA, USA. [5] Institute for Theoretical Physics, University of Cologne, Cologne, Germany. [6] Institut für Theorie der Statistischen Physik, RWTH Aachen University and JARA-Fundamentals of Information Technology, Aachen, Germany. [7] Nano-Bio Spectroscopy Group, Departamento de Fisica de Materiales, Universidad del País Vasco, San Sebastián, Spain. ✉email: dante.kennes@rwth-aachen.de; angel.rubio@mpsd.mpg.de

Two-dimensional van der Waals materials constitute a versatile platform to realize quantum states by design, as they can be synthesized in many different stacking conditions[1], offer a wide variety of chemical compositions, and are easily manipulated by back gates, strain and the like. Stacking two sheets of van der Waals materials atop each other at a relative twist has recently emerged as a vibrant research direction to enhance the role of electronic interactions, with first reports on twisted bilayer graphene[2–6] and another van der Waals materials stacked atop each other at a twist[7–17] displaying features of correlated physics that afford a high level of control. In particular, bi-, tri-, and quadruple-layer graphene[18] as well as twisted few-layer transition metal dichalcogenides (TMDs)[19,20] are currently under intense experimental scrutiny[13,21–29]. By forming a moiré supercell at small twist angles, a large unit cell in real space emerges for twisted systems, which due to quantum interference effects leads to a quasi-two-dimensional system with strongly quenched kinetic energy scales. This reduction in kinetic energy scale, signaled by the emergence of flat electron bands, in turn enhances the role of electronic interactions in these systems. Therefore, twisted systems enable the realization of new correlated condensed matter models, establishing a solid-state quantum simulator platform[30].

Whereas the flatting of band dispersions in two-dimensional moiré superlattices results mainly from the localization of charge density distributions by the moiré potential, a well-known alternate pathway to flat bands can occur in certain lattices such as the Lieb and the Kagome lattices. Here, purely geometric considerations lead to the formation of perfectly localized electronic states that have weight only on single plaquettes or hexagons, respectively, and that are eigenstates of the kinetic Hamiltonian due to destructive interference between lattice hopping matrix elements[31]. To put it differently, linear combinations of the macroscopically degenerate extended Bloch states in these systems allows to form localized Wannier-like eigenstates (living on single plaquettes or hexagons in the examples above) with no dispersion (for a review on the subject see, e.g,[32]). Such flat band systems can give rise to many interesting phenomena, such as the formation of nontrivial topology when time-reversal symmetry is broken, or other exotic quantum phases of matter due to their susceptibility to quantum fluctuations and electronic correlations[32].

Here, we demonstrate that both flat band mechanisms can be engineered to coexist in twisted bilayers of MoS_2 ($tbMoS_2$): a TMD of direct experimental relevance that has been extensively studied from synthesis to applications[33,34]. We confirm that families of flat bands emerge when two sheets of MoS_2 in the 2H structure are stacked at a twist[12,35] due to moiré potentials. Our large-scale ab initio based simulations show that while the first set of engineered flat bands closest to the edge of the bandgap with twist angles close to $\Theta \approx 0°$ can be used to effectively engineer a non-degenerate electronic flat band in analogy to a single layer of graphene at meV energy scales, more intriguingly, the next set of flat bands instead realizes a strongly asymmetric flat band p_x–p_y honeycomb lattice[36,37]. Both of these families of bands should be accessible experimentally via gating. The strongly asymmetric nature of this p_x–p_y honeycomb lattice is in marked contrast to the much-discussed case of twisted bilayer graphene, where an approximately symmetric version of such a Hamiltonian is now believed to describe the low-energy flat band structures found at small twist angle[38–42]. The strongly asymmetric p_x–p_y honeycomb model itself features two almost entirely dispersionless flat bands that touch the top and the bottom of graphene-like Dirac bands at the Gamma point, respectively. These flat bands in this model originate from destructive interference, in analogy to flat bands in the Lieb and the Kagome lattices[31] discussed above, and will be referred to as ultra-flat bands in the following discussion. On top of that, the total bandwidth of the strongly asymmetric p_x–p_y honeycomb effective model realized here (all four bands) can be further flattened by decreasing the twist angle. In addition, these ultra-flat bands can be topologically nontrivial in the presence of spin-orbital coupling (SOC)[43]. Although all the flat bands discussed here originate from the Γ-point states of MoS_2 and are not affected by intrinsic SOC (see Supplementary Fig. 3), we expect that substrate engineering[44] can be used to introduce SOC coupling into these bands and invoke topologically nontrivial behavior of the ultra-flat band states. Previously, the p_x-p_y model was studied in the context of cold gases where exotic correlated phases were predicted[36,45,46], as well as in semiconductor microcavities[47] and certain 2D systems such as organometallic frameworks[48,49] and Bismuth deposited on SiC[50] with a focus on their nontrivial topology properties. Our findings elevate $tbMoS_2$ to an interesting platform where effects of ultra-flat bands can be studied systematically in a strongly correlated solid-state setting.

Notably, in the strong-coupling regime, the p_x–p_y model amended by Hubbard and Hund's interactions gives rise to a spin-orbital honeycomb model which – depending on the specific parameters and symmetries of the model – hosts magnetic, orbital as well as valence-bond orderings, or even more exotic quantum spin-orbital liquid phases[51–53]. With this, our work adds an interesting type of lattice model – the highly asymmetric p_x–p_y Hubbard model – to the growing list of systems that can effectively be engineered using the twist angle between multiple layers. This is particularly intriguing as we maintain the full advantages that come with two-dimensional van der Waals materials, such as relative simplicity of the chemical composition and controllability of the material properties; e.g. of the filling (by a back gate), electric tunability (by displacement fields) or the bandwidth of the model (by the twist angle).

Results

Ab initio characterization of twisted MoS_2. We first characterize the low-energy electronic properties of twisted bilayer MoS_2 using density functional theory (DFT) calculations (see Methods). DFT in particular has established itself as a reliable tool to provide theoretical guidance and to predict the band structure of many twisted bi- and multilayer materials[8,13,15]. However, such a first-principles characterization becomes numerically very demanding as the twist angle Θ approaches small values and the unit cell becomes very large entailing many atoms (of the order of a few thousands and more). Nevertheless, it is that limit in which strong band-narrowing effects and as a consequence prominent effects of correlations are expected. The results of such a characterization are summarized in Fig. 1. Note that atomic relaxation has been shown to affect the electronic properties of twisted 2D materials[12,35,54]. While for twisted bilayer graphene this effect is only significant at twist angles smaller than 1 degree[54], it noticeably alters the low-energy band dispersions and charges density localization for twisted transition metal dichalcogenides bilayer (such as MoS_2) even with relatively large twist angles above 1 degree[12,35]. Therefore, we relax all the systems in our DFT calculations. Panel (a) shows the relaxed atomic structure of two sheets of MoS_2 in real space, twisted with respect to each other. A moiré interference pattern forms at a small twist angle yielding a large unit cell, within which we identify different local patterns of stacking of the two sheets of MoS_2, indicated via areas framed by cyan, magenta or purple dashed lines. The local stacking arrangements of the respective areas are given in the right sub-panels of the panel (a). Note that the $B^{Mo/S}$ and the $B^{S/Mo}$ regions are equivalent as they are related by C2 symmetry. These equivalent $B^{Mo/S}/B^{Mo/S}$ regions form a hexagonal network.

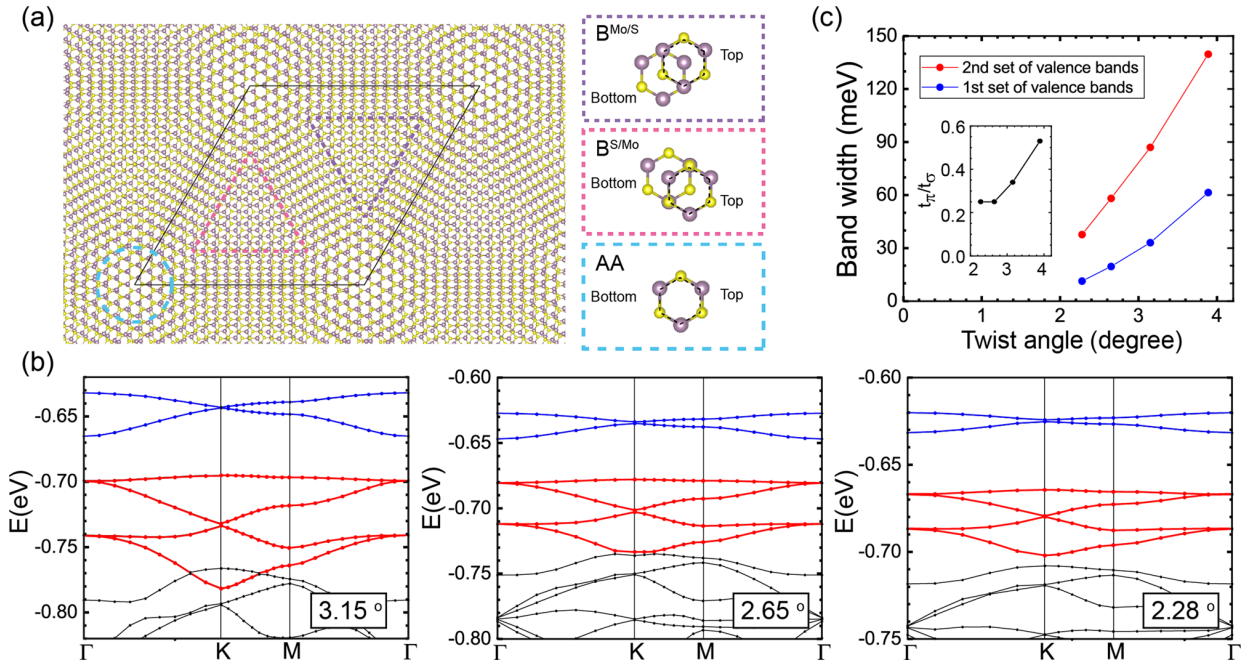

Fig. 1 Atomic and electronic structures of twisted bilayer MoS_2. a Atomic structure of $tbMoS_2$ at $\Theta = 3.15°$. Local atomic arrangements of the three different regions in the moiré unit cell are indicated in the right panels. The Mo (S) atoms are indicated with purple (yellow) balls. **b** Evolution of low-energy band structures at the top of the valence bands of $tbMoS_2$ with decreasing small twist angles. The first set and the second set of valence bands are highlighted with blue and red lines, respectively. **c** Evolution of the bandwidth of the first set and the second set of valence bands with decreasing twist angles. Inset: twist angle dependence of the ratio of the hopping amplitudes t_π and t_σ in the p_x–p_y honeycomb lattice.

In panel (b) we show the ab initio band structure of the twisted material after relaxation, where we find two families of bands that will become increasingly flat and start to detach from all other bands, as the twist angle is lowered. We mark these bands by blue and red color in panel (b), which shows results for decreasing angles from $\Theta = 3.16°$–$2.28°$. The bandwidth of these two energetically separated groups of bands is summarized in panel (c) of Fig. 1. We find that the bandwidth of these two bands shrinks drastically as the angle is decreased, yielding bandwidths of the order of 10 meV as the angle approaches $\Theta \approx 2°$. Similar features are also shown in the work of Naik et al.[35]. The bandwidth and the shape of the flat bands (in particular for the second set) in our calculations are slightly quantitatively different from the previous work probably because we relax the structure directly with DFT while the authors of ref. [35] use a force-field approach. Note that these flat bands near the top of the valence bands originate from the states around the Γ point in the Brillouin zone of the primitive unit cell of untwisted MoS_2, with both S p_z and Mo d_{z^2} characters (see Supplementary Fig. 2 for a DFT characterization of the orbital contribution to the different bands). This is different to the case of twisted WSe_2, where the top valence flat bands originate from the states around the K point in the Brillouin zone of the primitive unit cell (dominated by W $d_{x^2-y^2}$ and d_{xy} orbitals), which experience different interlayer moiré potentials compared with those of the Γ-point flat bands discussed here leading to an effective triangular lattice Hubbard model[13]. Since also in other TMDs, such as $MoSe_2$ and WS_2, the top of the valence band in the untwisted bilayer is also located at the Γ point in the Brillouin zone[55,56], the physics we discussed here transfers also to those materials being twisted.

The upper bands in Fig. 1 (marked in blue) show a Dirac cone at the K point and behave very similar to the bands found for monolayer graphene (with the exception of a reduced bandwidth). They are spin degenerate in nature, but feature no additional degeneracy except at certain high symmetry points. Instead, the next set of bands (marked in red) is essential to our work. They too feature a Dirac cone at the K point, but also feature two additional ultra-flat bands at the top and bottom in addition to a band structure similar to graphene. The ratio between the width of the ultra-flat and the flat bands decreases as the angle is decreased, but saturates in our calculations as a twist angle of $\Theta \approx 2.28°$ is approached. We attribute this saturation to lattice relaxation effects; note however that the overall bandwidth keeps decreasing. To access this second set of bands we need to empty the bands marked in blue first. The effects of this doping are of minor quantitative nature (see Supplementary Fig. 5).

Remarkably, this second family of flat bands is well-described by an effective p_x–p_y tight-binding model on a honeycomb lattice, depicted schematically in Fig. 2a, and conveniently described by the following Hamiltonian:

$$H_0 = \sum_{\langle i,j\rangle,s} (t_\sigma \mathbf{c}^\dagger_{i,s} \cdot \mathbf{n}^{\parallel}_{ij}\mathbf{n}^{\parallel}_{ij} \cdot \mathbf{c}_{j,s} - t_\pi \mathbf{c}^\dagger_{i,s} \cdot \mathbf{n}^{\perp}_{ij}\mathbf{n}^{\perp}_{ij} \cdot \mathbf{c}_{j,s}) + \sum_{\langle\langle i,j\rangle\rangle,s} (t^N_\sigma \mathbf{c}^\dagger_{i,s} \cdot \mathbf{n}^{\parallel}_{ij}\mathbf{n}^{\parallel}_{ij} \cdot \mathbf{c}_{j,s} - t^N_\pi \mathbf{c}^\dagger_{i,s} \cdot \mathbf{n}^{\perp}_{ij}\mathbf{n}^{\perp}_{ij} \cdot \mathbf{c}_{j,s}), \quad (1)$$

where $\mathbf{c}_{i,s} = (c_{i,\mathrm{x},s}, c_{i,\mathrm{y},s})^T$ with $c_{i,\mathrm{x(y)},s}$ annihilating an electron with $p_{\mathrm{x(y)}}$-orbital at site i and with spin $s = \uparrow, \downarrow$. $\langle i,j\rangle$ ($\langle\langle i,j\rangle\rangle$) denotes (next) nearest neighbors. For each sum in Eq. (1), the first term describes the σ hopping (head to tail) between the p-orbitals and the second term denotes the π hopping (shoulder to shoulder). Furthermore, $\mathbf{n}^{\parallel}_{ij} = (\mathbf{r}_i - \mathbf{r}_j)/|\mathbf{r}_i - \mathbf{r}_j|$, with $\mathbf{r}_i$ being the position of site i and $\mathbf{n}^{\perp}_{ij} = U\mathbf{n}^{\parallel}_{ij}$ with U being the two-dimensional 90 degree rotation matrix $U = \begin{pmatrix} 0 & -1 \\ 1 & 0 \end{pmatrix}$. Finally, t_σ and t_π (t^N_σ and t^N_π) are the nearest neighbor (next-nearest neighbor) hopping amplitudes

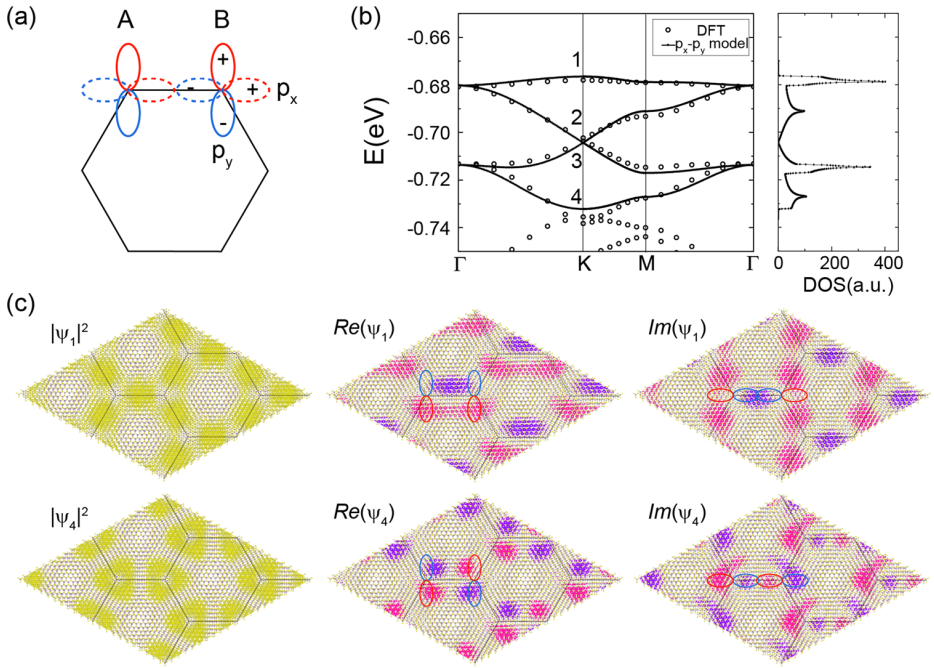

Fig. 2 p_x-p_y honeycomb model for twisted bilayer MoS_2. a Illustration of the model: in a honeycomb lattice composed of sublattices A and B, there are two orthogonal orbitals (p_x and p_y) at each of the two sublattice sites. The solid and the dashed lines denote the p_y and the p_x orbitals, respectively, and the red and the blue color denotes the positive and the negative side of the orbital, respectively. **b** Fitting the dispersion of the p_x-p_y model to the second set of valence bands of $tbMoS_2$ calculated with DFT for $tbMoS_2$ at 2.65°. The left panel shows the corresponding density of states displaying the signature four-peak structure. **c** Charge density, real and imaginary parts of the wave function calculated with DFT for the states in the two quasi-flat bands 1 and 4 shown in (**b**). The isosurface of the charge density is colored yellow. The positive and the negative parts of the isosurfaces of the wave function are colored in pink and purple, respectively. The solutions of the corresponding states from the p_x-p_y model are indicated with the blue and red ovals and agree with the DFT results.

for the σ-bonding term and π-bonding term, respectively. Figure 2b, c depict the corresponding dispersions, density of states, and wave functions in comparison to model predictions, illustrating that the four moiré bands at low energies are well captured by Eq. (1) upon the choice of hopping parameters $t_\pi = 0.25t_\sigma$, $t_\sigma^N = 0.07t_\sigma$ and $t_\pi^N = -0.04t_\sigma$. The density of states exhibits a characteristic four van Hove singularities structure, with two originating from the Dirac bands and two stemming from the additional two ultra-flat bands. The small ratio between the nearest neighbor hopping amplitudes t_π/t_σ determines the residual small dispersion in the ultra-flat bands we report. This ratio is controllable by the twist angle, which is summarized in the inset of Fig. 1c. All these parameters are related to the interlayer moiré potential and are thus expected to be also affected and controllable by the uniaxial pressure perpendicular to the layers as demonstrated for twisted bilayer graphene[4].

The flat band wavefunctions consist of atomic wavefunctions from the p_z orbital on S atoms and the d_{z^2} orbital on Mo atoms. Modulated by the moiré potential, the weighting of the atomic wavefunctions and their modulus square (i.e., charge density) vary at different atomic sites across the whole supercell, showing distinct patterns for different flat band states at the K point in the supercell Brillouin zone as shown in Panel (c) of Fig. 2. These patterns of the charge density as well as the real and the imaginary part of the total wavefunctions obtained from DFT show features consistent with those of the p_x–p_y Hamiltonian of Eq. (1). Note, that we call this the p_x-p_y Hamiltonian to connect to established literature on the subject; whereas the actual moiré wave functions are composed of p_z and d_z orbitals, they transform like p_x, p_y orbitals according to the irreps of the reduced symmetry group of the moiré supercell. Interestingly, the charge density distribution of the top ultra-flat band state displays a Kagome lattice structure. We have thus unambiguously established twisted MoS_2 to be a candidate system to realize a p_x–p_y model on the honeycomb lattice with strongly asymmetric hoppings t_σ and t_π, giving rise to a new set of ultra-flat bands.

Correlations and magnetic properties. We now study the role of electronic interactions. As the highly-anisotropic p_x-p_y orbital structure constitutes the essential novelty of twisted bilayer MoS_2, we focus on quarter filling (one electron per sublattice in the Moié unit cell) where orbital fluctuations can be expected to be crucial. This filling fraction is straightforwardly accessible in the experiment via back gating, and we defer a discussion of the half-filled case to Supplementary Note 1. To proceed, we assume purely local electronic interactions, which can be generically parameterized in terms of the Hubbard-Kanamori Hamiltonian:

$$H_U = U\sum_{i,\alpha} n_{i\alpha\uparrow}n_{i\alpha\downarrow} + (U-2J)\sum_i n_{ix}n_{iy} + J\sum_{i,s,s'} c^\dagger_{ixs}c^\dagger_{iys'}c_{ixs'}c_{iys} + J\sum_{i,\alpha\neq\beta} c^\dagger_{i\alpha\uparrow}c^\dagger_{i\alpha\downarrow}c_{i\beta\downarrow}c_{i\beta\uparrow} \quad (2)$$

for two orbitals with rotational symmetry. More realistic modelling should include long-range interactions. However, for our choice of commensurate quarter filling, any longer-ranged component of the Coulomb interaction at strong-coupling will serve merely to renormalize the effective spin-orbital interactions of the resulting Kugel-Khomskii model and we therefore concentrate on purely local interactions for simplicity. Furthermore, our DFT

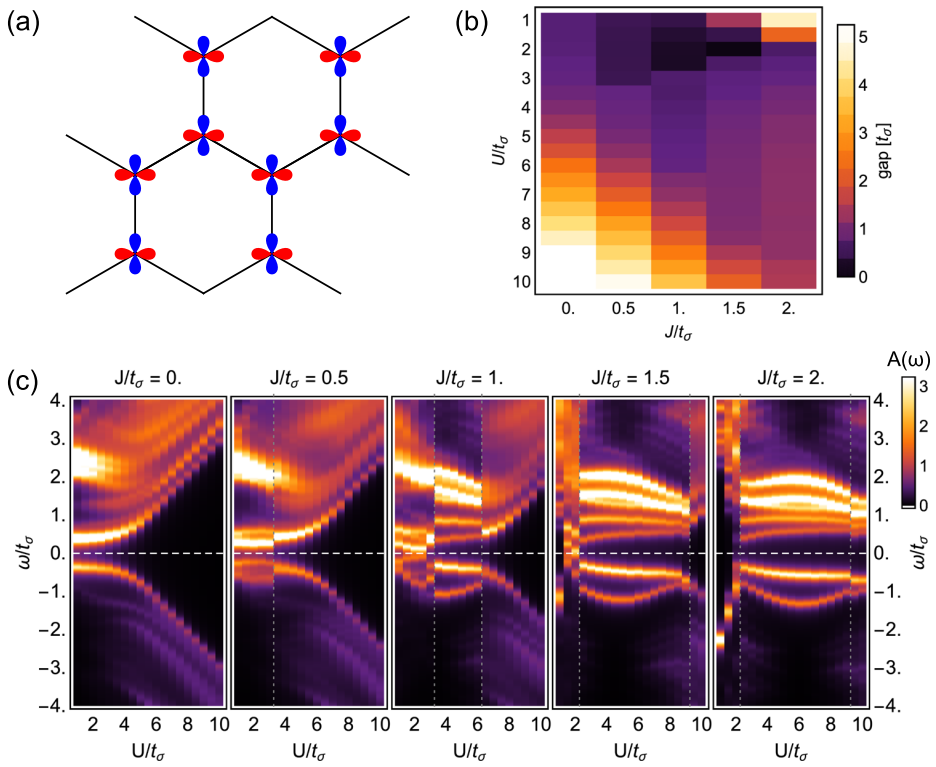

Fig. 3 Charge gap and correlations for twisted bilayer MoS_2 at vanishing temperature. a depicts the 16-orbital cluster geometry employed for exact diagonalization of the Hubbard-Kanamori Hamiltonian. **b** depicts the charge gap as a function of Hubbard U and Hund's exchange J interactions, calculated for the 16-orbital cluster and extracted from (**c**) the local density of states, which is readily accessible via scanning tunnelling microscopy. A well-defined charge gap develops beyond $U/t_\sigma \sim 4$ at small J that scales linearly with the Hubbard interaction U. Vertical gray dotted lines indicate phase transitions to charge-ordered states at large J/U, coinciding with a closing of the charge gap.

calculations suggest $t_\pi \approx 0.25 t_\sigma$ and only weak next-nearest neighbor hopping at small twist angles; we therefore neglect next-nearest neighbor hopping in the analysis below (see Supplementary Fig. 4 for a comparison of the band structures with and without next-nearest neighbor hopping). An ab initio based characterization of the values of U and J requires numerically expansive Wannierzation of the wave functions and is unfortunately beyond the scope of this work. However, by substrate engineering[22] it is likely that a whole range of values can be accessed and therefore it is useful to vary these parameters to explore all possible phases accessible in experiments to make concrete predictions. Vice versa given a future experimental observation our results can be used to estimate the strength of correlations.

Figure 3c depicts the local density of states as a function of Hubbard U and Hund's exchange J interactions, calculated via an exact diagonalization study of Eqs. (1) and (2) for a cluster depicted schematically in (a). Clear evidence of a charge gap beyond $U/t_\sigma \sim 4$ at small J signifies the onset of a correlated insulator which could be directly observed via transport and scanning tunnelling microscopy. The behavior of the gap is depicted in Fig. 3b as a function of U, J and signifies that charge fluctuations are strongly suppressed for large U. Establishing the existence of a charge gap motivates to set up a strong-coupling Hamiltonian routinely employed for the types of systems under scrutiny here.

In this regime, a natural follow-up questions concerns possible orderings of the orbital and magnetic degrees of freedom. The corresponding strong-coupling Kugel-Khomskii Hamiltonian[57–59] for the p_x-p_y model at quarter filling is given in refs. [51–53] and reads:

$$H = \sum_{\langle ij \rangle} \frac{1}{U-3J} \xi^1_{ij} \left[t_\sigma t_\pi \bar{Q}_{ij} - (t_\sigma^2 + t_\pi^2)(P^{xy}_{ij} + P^{yx}_{ij}) \right] - \frac{1}{U+J} \xi^0_{ij} \left[t_\sigma t_\pi Q_{ij} + 2t_\sigma^2 P^{xx}_{ij} + 2t_\pi^2 P^{yy}_{ij} \right] + \frac{1}{U-J} \xi^0_{ij} \left[t_\sigma t_\pi (Q_{ij} - \bar{Q}_{ij}) - 2t_\sigma^2 P^{xx}_{ij} - 2t_\pi^2 P^{yy}_{ij} - (t_\sigma^2 + t_\pi^2)(P^{xy}_{ij} + P^{yx}_{ij}) \right]. \quad (3)$$

Here, $\xi^1_{ij} = 3/4 + \mathbf{S}_i \mathbf{S}_j$ denotes the projector onto triplet states, whereas $\xi^0_{ij} = 1/4 - \mathbf{S}_i \mathbf{S}_j$ selects the singlet spin states instead. Note that the orbital operators, for example Q_{ij}, are bond dependent, giving rise to a strong spatial anisotropy of the resulting spin-orbit model. To be more precise following ref. [52], the operators Q_{ij} and $\bar{Q}_{ij}$ describe processes where orbital occupations of sites i and j are reversed, that is they are defined as $Q_{ij} = (\tau_i^+ \tau_j^+ + \tau_i^- \tau_j^-)/2$ and $\bar{Q}_{ij} = (\tau_i^+ \tau_j^- + \tau_i^- \tau_j^+)/2$, with $\tau_i^\pm = \mathbf{n}_{ij}^\perp \boldsymbol{\tau}_i \pm i\tau_i^y$ where $\boldsymbol{\tau}_i = (\tau_i^z, \tau_i^x, \tau_i^y)^T$. The orbital projection operators can then be expressed as $P^{xx}_{ij} = (1 + \mathbf{n}^\parallel_{ij} \boldsymbol{\tau}_i)(1 + \mathbf{n}^\parallel_{ij} \boldsymbol{\tau}_j)/4$, $P^{yy}_{ij} = (1 - \mathbf{n}^\parallel_{ij} \boldsymbol{\tau}_i)(1 - \mathbf{n}^\parallel_{ij} \boldsymbol{\tau}_j)/4$, $P^{xy}_{ij} = (1 + \mathbf{n}^\parallel_{ij} \boldsymbol{\tau}_i)(1 - \mathbf{n}^\parallel_{ij} \boldsymbol{\tau}_j)/4$ and $P^{yx}_{ij} = (1 - \mathbf{n}^\parallel_{ij} \boldsymbol{\tau}_i)(1 + \mathbf{n}^\parallel_{ij} \boldsymbol{\tau}_j)/4$, where e.g. P^{xx}_{ij} selects states where the superposition $(p_x \mathbf{e}_x + p_y \mathbf{e}_y)\mathbf{n}^\parallel_{ij}$ is occupied on nearest neighbor sites i and j connected by the bond $\mathbf{n}^\parallel_{ij}$.

To study its ground state phase diagram using the ab initio parameters found in the previous section, we employ a mean-field analysis of competing for orbital orderings with ferromagnetic and antiferromagnetic spin order. Note, that the simplifying

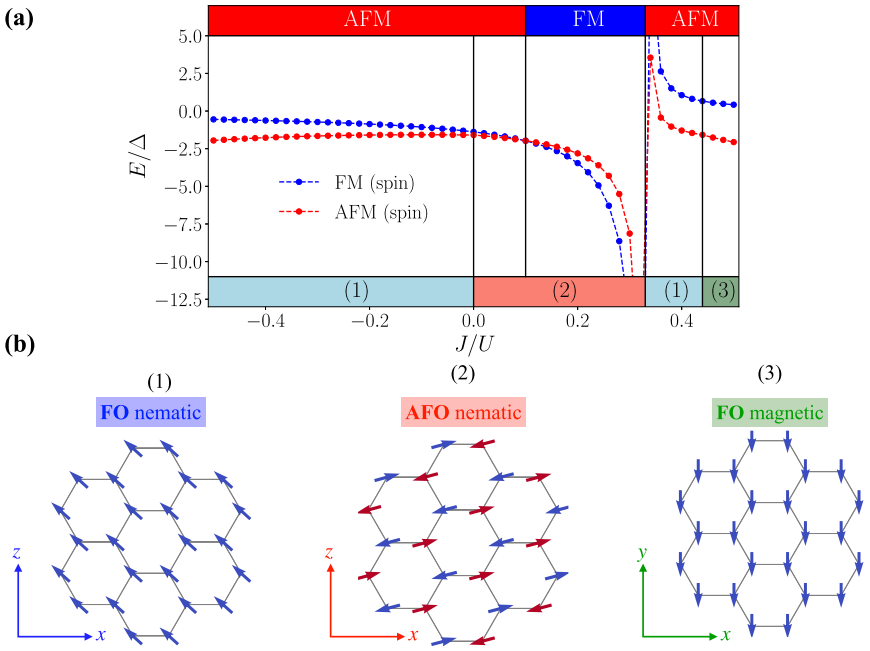

Fig. 4 Magnetic phase diagram for twisted bilayer MoS_2. a Classical ground state energy per orbital in units of $\Delta = t_\sigma^2/U$, assuming ferro- (blue) or antiferromagnetic (red) order for the spin degrees of freedom. We take the ab initio parameters, $t_\pi = 0.25t_\sigma$ and use an iterative energy minimization. The lower panel determines the phase boundaries for the orbital degrees of freedom given the energetically more favorable spin order shown in the top panel. At $J/U = 0.1$ we find the spin order to change from AFM to FM, with AFO nematic order for the orbital degrees of freedom remaining stable in agreement with ref. [53]. **b** Configurations of orbital vectors are found at the end of iterative minimization. Note that we display the projection of $\boldsymbol{\tau}$ to the plane in $\mathbb{R}^3$ (indicated by the axis shown in the bottom left), such that nematic states with finite contributions only in xz direction ((1) & (2)) can be distinguished from magnetic states (3) which point perpendicular, i.e along the y-axis.

assumption of vanishing temperature – a standard one in condensed matter research – still allows to draw conclusions for the low-temperature physics accessible in experiments as fingerprints of the phases we discuss extend into this regime as well. To this end, we note that on the bipartite honeycomb lattice the SU(2) invariant spin sector would, on its own, order either ferro- or antiferromagnetically, depending on the sign of the exchange couplings. As an Ansatz, we therefore assume that one of the respective states is stabilized and decouple the spin from the orbital degrees of freedom by replacing $\mathbf{S}_i\mathbf{S}_j$ with its expectation value $\langle \mathbf{S}_i\mathbf{S}_j\rangle = \pm 1/4$ such that $\xi_{ij}^1 = 1, \xi_{ij}^0 = 0$ for ferromagnetic spin order and $\xi_{ij}^1 = \xi_{ij}^0 = 1/2$ for Neél order.

After such a mean-field decoupling corresponding to the ground state in the spin sector, we analyze the ground states of the resulting Hamiltonian for the orbital degrees of freedom, which we approximate as classical vectors. We use an iterative energy minimization combined with simulated annealing techniques (see Methods) to converge the mean-field equations and find the phase diagram summarized in Fig. 4. Panel (a) shows the energy of ferromagnetic and antiferromagnetic spin configurations from which the magnetic phase diagram can be read off. This is given in the upper part of the plot and we find antiferromagnetic ordering with an intermittent ferromagnetic phase at intermediate ratios of $0.1 < J/U < 1/3$. In the lower part of the plot, we show the corresponding subsidiary orbital order. From our simulations, we identify three different configurations of orbital vectors $\boldsymbol{\tau}$, which can be classified according to their projection on a single definite plane in space, shown in the lower left of the plots: (1) ferro-orbital (FO) nematic order[5,6,60–62], where the vectors on all lattice sites align in parallel to the xz-plane. Quantum mechanically, finite values of $\langle \tau_i^{x/z}\rangle$ indicate an imbalance of the occupation of p_x and p_y orbitals, breaking rotation symmetry and thereby motivating the notion of a nematic state. (2) AFO nematic order; each vector is aligned anti-parallel with its nearest neighbors corresponding to $\langle \tau_i^{x/z}\rangle \neq 0$ on each sublattice, but without finite projections τ_i^y on individual sites. (3) FO magnetic order; all vectors order along the y-axis, such that $\langle \tau_i^y\rangle \neq 0$, which, in the quantum mechanical system, would indicate time-reversal symmetry breaking. The inclusion of quantum fluctuations can change this picture and more exotic ground states may emerge. For example, for our ab initio band structure parameters, a noncollinear spin dimer phase is predicted in a certain range of interaction couplings and even a quantum spin-orbital liquid is found in its proximity[53]. Since these exotic phases primarily occur for weak Hund's coupling and strong orbital anisotropies, the assumptions made for our calculations can therefore be justified for sizable J_H and modest distances to the isotropic $t_\sigma = t_\pi$ point.

Discussion

We have established that twisted bilayer MoS_2 is a promising platform to realize the orbital anisotropic p_x–p_y Hubbard model by employing large-scale ab initio calculations. We find that families of flat bands emerge where the first family of flat bands shows s-orbital character and the second family is an intriguing realization of a strongly asymmetric p_x–p_y Hubbard model both on a honeycomb lattice, adding a lattice with nontrivial almost perfectly-flat bands due to destructive interference to the growing list of systems that can be engineered in twisted heterostructures. The symmetry of these flat bands is inherited from the hexagonal lattice formed by the equivalent $B^{Mo/S}$ and $B^{S/Mo}$ regions. At an even smaller angle, the sequence in the family of flat bands found with respect to their orbital character continues. Our analysis shows that the low-energy DFT band structures in this system can

be well captured by a free electron gas model modulated by a simple harmonic potential that has hexagonal (D_6) symmetry, which is consistent with a recent study[63]. This simple model further shows that the next family would exhibit a d-orbital character on the honeycomb lattice. Such a lattice would effectively realize a multi-orbital generalization of a Kagome lattice – a prototypical model for quantum spin liquids. However, at such small angles strong relaxation is likely to become dominant, prohibiting access to this regime and potentially spoiling its experimental realization. Currently, the ab initio characterization of such small angles is numerically too exhaustive and this work sparks a direct need for novel computational methods to tackle this question.

Furthermore, our combined exact diagonalization and strong-coupling expansion approaches classify the magnetic and orbital phase diagrams, however, the inclusion of quantum fluctuations stipulates an intriguing avenue of future theoretical research.

Indeed, previous theoretical works provide some evidence for a quantum spin liquid in the SU(4)-symmetric Kugel-Khomskii model on the honeycomb lattice[64], the square lattice as a related system without frustration[65] and studied the role of perturbations that break SU(4) symmetry and isotropy[53] In twisted MoS_2, this regime would in fact map to larger twist angles, where the anisotropy of the p_x-p_y model is less pronounced, as well as to a regime of vanishing Hund's coupling, placing such a putative quantum spin liquid at the transition between FO nematic and AFO nematic phases.

In addition, by proximity or variations in the chemical composition of the twisted bilayer, it might be possible to induce spin-orbit coupling splitting of the ultra-flat bands at the top and bottom of the asymmetric p_x–p_y dispersion. Such a bandgap opening would induce interesting topological properties[66] in a highly tunable materials setting.

Methods

Details on ab initio calculations. We calculate the electronic properties of twisted bilayer MoS_2 with ab initio methods based on density functional theory (DFT) as implemented in the Vienna ab initio Simulation Package (VASP)[67]. We employ plane-wave basis sets with an energy cutoff of 550 eV and pseudopotentials as constructed with the projector augmented wave (PAW) method[68]. The exchange-correlation functionals are treated at the generalized gradient approximations (GGA) level[69]. The supercell lattice constants are chosen such that they correspond to 3.161 Å for the 1×1 primitive cell of MoS_2. Vacuum spacing larger than 15 Å is introduced to avoid artificial interaction between the periodic images along the z-direction. Because of the large supercells, a $1 \times 1 \times 1$ k-grid is employed for the ground state and the relaxation calculations. For all the calculations, all the atoms are relaxed until the force on each atom is less than 0.01 eV/Å. Van der Waals corrections are considered with the method of Tkatchenko and Scheffler[70]. We extract the real and the imaginary parts of the DFT wavefunctions with the VASPKIT code[71].

Details on exact diagonalization. Exact diagonalization calculations were performed for the electronic tight-binding model in Eq. (1) with Hubbard-Kanamori interactions defined in Eq. (2). All calculations were performed for a two-orbital eight-site cluster with periodic boundary conditions at quarter filling, corresponding to eight spin-1/2 particles in sixteen orbitals. Rotationally symmetric Kanamori interactions are adopted, with $U' = U - 2J$. As the magnitudes of the Hubbard U and Hund's exchange J interactions cannot be reliably predicted for a Moié supercell from first principles, all presented results are shown as a function of U, J. Calculations of the single-particle Green's functions and local density of states are performed starting from the ground state in the total momentum $K_{\mathrm{tot}} = 0$ and total spin $S_z = 0$ sectors, using the Lanczos method and continued-fraction representation, and a spectral broadening (imaginary part of the self-energy) of $\eta = 0.1$ is imposed.

Details on minimization procedure for classical Hamiltonian. Metropolis Monte Carlo simulations are a prime tool for the investigation of classical spin models, since they allow for off-diagonal, spatially anisotropic spin couplings to be included, even when one-spin terms, such as magnetic fields, are involved. Here we employ a special variant of the algorithm to the mean-field version of (3), keeping in mind that the 'spins' used in the simulation are approximations to orbital operators $\boldsymbol{\tau}$. First, a lattice site i is randomly chosen, and its respective gradient field

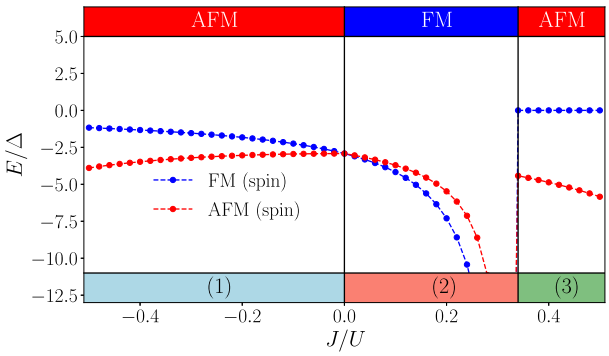

Fig. 5 Magnetic phase diagram of the strong-coupling Hamiltonian (3) in the isotropic limit $t_\sigma = t_\pi$. Our results from iterative minimization are in agreement with ref. [52], stabilizing FO nematic order (1) for $J/U < 0$ (see main text) and FO magnetic order (3) (see main text) for $J/U > 1/3$. In the intermediate range of parameters $0 < J/U < 1/3$ the ferromagnetic spin sector is selected, such that, due to vanishing ξ^0_{ij}, rotation invariance is restored for the orbital vectors, giving rise to AFM order (2) but without any preferred axis in euclidean space.

$\mathrm{h}_i = \nabla_i H$ is computed for the current spin configuration $\{\boldsymbol{\tau}_i\}$. Second, a random orientation $\boldsymbol{\tau}'_i$ for the vector at site i is proposed and the weight

$$g = \min\left(e^{-\beta(\boldsymbol{\tau}'_i - \boldsymbol{\tau}_i)\mathbf{h}_i}, 1\right), \tag{4}$$

is computed for an effective inverse temperature β. Performing several Metropolis updates with increasing values of β we are able to efficiently lower the energy of a random initial configuration, minimizing the odds to converge to a local minimum by only allowing optimal updates (i.e. $\tau_i = -\mathrm{h}_i$) right from the start. After N_a sweeps over the full lattice, the so-obtained configuration is ameliorated by N_o optimization sweeps, where the randomly selected spin is rotated anti-parallel to the local gradient field such that the energy is deterministically lowered in every step and we converge as close to the global energy minimum as possible. Hence, this algorithm is reminiscent of Monte Carlo simulations with simulated annealing, but at zero temperature where thermal fluctuations are frozen out.

To benchmark our implementation we have carried out the minimization procedure in the isotropic limit $t_\sigma = t_\pi$ for $N_a = N_o = 10^5$, where the optimization sweeps are terminated when the energy change after one sweep, ϵ, becomes small (usually $\epsilon \leq 10^{-10}$). Mapping out the phase diagram for both the FM, $\langle \mathrm{S}_i \mathrm{S}_j \rangle = 1/4$, as well as the AFM, $\langle \mathrm{S}_i \mathrm{S}_j \rangle = -1/4$, spin sector on a lattice with $N = 1250$ spins subject to periodic boundary conditions we find the result in Fig. 5, which is consistent with the one presented in ref. [52]. For $J < 0$ the AFM spin sector has lower energy, with the orbitals forming a ferro-orbital (FO) nematic state where $\langle \tau_i^{x/z} \rangle \neq 0$ and $\langle \tau_i^{y} \rangle = 0$. For $J > 0$ one finds the FM spin sector (for which the orbital degrees of freedom restore their rotation invariance) to dominate as long as $J < 1/3$, where the AFM sector takes over again and establishes a FO magnetic state, i.e. $\langle \tau_i^{x/z} \rangle = 0$ and $\langle \tau_i^{y} \rangle \neq 0$.

Data availability

The raw data sets used for the presented analysis within the current study are available from the corresponding authors on reasonable request.

Code availability

The tailored developed codes used in this work can be provided from the corresponding author on reasonable request. Ab initio calculations are done with the code VASP (version 5.4.4).

Received: 10 December 2020; Accepted: 1 September 2021;
Published online: 24 September 2021

References

1. Liu, F. et al. Disassembling 2d van der waals crystals into macroscopic monolayers and reassembling into artificial lattices. *Science* **367**, 903–906 (2020).
2. Cao, Y. et al. Unconventional superconductivity in magic-angle graphene superlattices. *Nature* **556**, 43–50 (2018).

3. Cao, Y. et al. Correlated insulator behaviour at half-filling in magic-angle graphene superlattices. *Nature* **556**, 80–84 (2018).
4. Yankowitz, M. et al. Tuning superconductivity in twisted bilayer graphene. *Science* **363**, 1059–1064 (2019).
5. Kerelsky, A. et al. Maximized electron interactions at the magic angle in twisted bilayer graphene. *Nature* **572**, 95–100 (2019).
6. Choi, Y. et al. Electronic correlations in twisted bilayer graphene near the magic angle. *Nat. Phys.* **15**, 1174–1180 (2019).
7. Jin, C. et al. Observation of moiré excitons in wse_2/ws_2 heterostructure superlattices. *Nature* **567**, 76–80 (2019).
8. Tran, K. et al. Evidence for moiré excitons in van der waals heterostructures. *Nature* **567**, 71–75 (2019).
9. Alexeev, E. M. et al. Resonantly hybridized excitons in moiré superlattices in van der waals heterostructures. *Nature* **567**, 81–86 (2019).
10. Seyler, K. L. et al. Signatures of moiré-trapped valley excitons in $mose_2/wse_2$ heterobilayers. *Nature* **567**, 66–70 (2019).
11. Xian, L., Kennes, D. M., Tancogne-Dejean, N., Altarelli, M. & Rubio, A. Multiflat bands and strong correlations in twisted bilayer boron nitride: Doping-induced correlated insulator and superconductor. *Nano Lett.* **19**, 4934–4940 (2019).
12. Naik, M. H. & Jain, M. Ultraflatbands and shear solitons in moiré patterns of twisted bilayer transition metal dichalcogenides. *Phys. Rev. Lett.* **121**, 266401 (2018).
13. Wang, L. et al. Correlated electronic phases in twisted bilayer transition metal dichalcogenides. *Nat. Mater.* **19**, 861–866 (2020).
14. Scuri, G. et al. Electrically tunable valley dynamics in twisted wse_2/wse_2 bilayers. *Phys. Rev. Lett.* **124**, 217403 (2020).
15. Kerelsky, A. et al. Moiréless correlations in abca graphene. *Proc. Natl. Acad. Sci. U.S.A.* **118**, e2017366118 (2021).
16. Andersen, T. I. et al. Excitons in a reconstructed moiré potential in twisted wse_2/wse_2 homobilayers. *Nat. Mater.* **20**, 480–487 (2021).
17. Kennes, D. M., Xian, L., Claassen, M. & Rubio, A. One-dimensional flat bands in twisted bilayer germanium selenide. *Nat. Commun.* **11**, 1124 (2020).
18. Rozhkov, A., Sboychakov, A., Rakhmanov, A. & Nori, F. Electronic properties of graphene-based bilayer systems. *Phys. Rep.* **648**, 1–104 (2016).
19. Wu, F., Lovorn, T., Tutuc, E. & MacDonald, A. H. Hubbard model physics in transition metal dichalcogenide Moiré Bands. *Phys. Rev. Lett.* **121**, 026402 (2018).
20. Wu, F., Lovorn, T., Tutuc, E., Martin, I. & MacDonald, A. H. Topological insulators in twisted transition metal dichalcogenide homobilayers. *Phys. Rev. Lett.* **122**, 086402 (2019).
21. Lu, X. et al. Superconductors, orbital magnets and correlated states in magic-angle bilayer graphene. *Nature* **574**, 653–657 (2019).
22. Stepanov, P. et al. Untying the insulating and superconducting orders in magic-angle graphene. *Nature* **583**, 375–378 (2020).
23. Arora, H. S. et al. Superconductivity in metallic twisted bilayer graphene stabilized by wse_2. *Nature* **583**, 379–384 (2020).
24. Chen, G. et al. Tunable correlated chern insulator and ferromagnetism in a moiré superlattice. *Nature* **579**, 56–61 (2020).
25. Liu, X. et al. Tunable spin-polarized correlated states in twisted double bilayer graphene. *Nature* **583**, 221–225 (2020).
26. Shen, C. et al. Correlated states in twisted double bilayer graphene. *Nat. Phys.* **16**, 520–525 (2020).
27. Cao, Y. et al. Tunable correlated states and spin-polarized phases in twisted bilayer–bilayer graphene. *Nature* **583**, 215–220 (2020).
28. He, M. et al. Symmetry breaking in twisted double bilayer graphene. *Nat. Phys.* **17**, 26–30 (2020).
29. Burg, G. W. et al. Correlated insulating states in twisted double bilayer graphene. *Phys. Rev. Lett.* **123**, 197702 (2019).
30. Kennes, D. M. et al. Moiré heterostructures as a condensed-matter quantum simulator. *Nat. Phys.* **17**, 155–163 (2021).
31. Liu, Z., Liu, F. & Wu, Y.-S. Exotic electronic states in the world of flat bands: from theory to material. *Chin. Phys. B* **23**, 077308 (2014).
32. Leykam, D., Andreanov, A. & Flach, S. Artificial flat band systems: from lattice models to experiments. *Adv. Phys.: X* **3**, 1473052 (2018).
33. Mak, K. F., Lee, C., Hone, J., Shan, J. & Heinz, T. F. Atomically thin mos_2: a new direct-gap semiconductor. *Phys. Rev. Lett.* **105**, 136805 (2010).
34. Wang, H., Li, C., Fang, P., Zhang, Z. & Zhang, J. Z. Synthesis, properties, and optoelectronic applications of two-dimensional mos_2 and mos_2-based heterostructures. *Chem. Soc. Rev.* **47**, 6101–6127 (2018).
35. Naik, M. H., Kundu, S., Maity, I. & Jain, M. Origin and evolution of ultraflat bands in twisted bilayer transition metal dichalcogenides: Realization of triangular quantum dots. *Phys. Rev. B* **102**, 075413 (2020).
36. Wu, C., Bergman, D., Balents, L. & Das Sarma, S. Flat bands and wigner crystallization in the honeycomb optical lattice. *Phys. Rev. Lett.* **99**, 070401 (2007).
37. Wu, C. & Das Sarma, S. $p_{x,y}$-orbital counterpart of graphene: cold atoms in the honeycomb optical lattice. *Phys. Rev. B* **77**, 235107 (2008).
38. Bistritzer, R. & MacDonald, A. H. Moiré bands in twisted double-layer graphene. *Proc. Natl. Acad. Sci. U.S.A.* **108**, 12233–12237 (2011).
39. Yuan, N. F. Q. & Fu, L. Model for the metal-insulator transition in graphene superlattices and beyond. *Phys. Rev. B* **98**, 045103 (2018).
40. Po, H. C., Zou, L., Senthil, T. & Vishwanath, A. Faithful tight-binding models and fragile topology of magic-angle bilayer graphene. *Phys. Rev. B* **99**, 195455 (2019).
41. Carr, S., Fang, S., Po, H. C., Vishwanath, A. & Kaxiras, E. Derivation of wannier orbitals and minimal-basis tight-binding hamiltonians for twisted bilayer graphene: First-principles approach. *Phys. Rev. Research* **1**, 033072 (2019).
42. Kennes, D. M., Lischner, J. & Karrasch, C. Strong correlations and $d+id$ superconductivity in twisted bilayer graphene. *Phys. Rev. B* **98**, 241407 (2018).
43. Zhang, G.-F., Li, Y. & Wu, C. Honeycomb lattice with multiorbital structure: topological and quantum anomalous hall insulators with large gaps. *Phys. Rev. B* **90**, 075114 (2014).
44. Qi, J., Li, X., Niu, Q. & Feng, J. et al. Giant and tunable valley degeneracy splitting in $mote_2$. *Phys. Rev. B* **92**, 121403 (2015).
45. Lee, W.-C., Wu, C. & Das Sarma, S. *f*-wave pairing of cold atoms in optical lattices. *Phys. Rev. A* **82**, 053611 (2010).
46. Wu, C. Orbital ordering and frustration of *p*-band mott insulators. *Phys. Rev. Lett.* **100**, 200406 (2008).
47. Jacqmin, T. et al. Direct observation of dirac cones and a flatband in a honeycomb lattice for polaritons. *Phys. Rev. Lett.* **112**, 116402 (2014).
48. Liu, Z., Wang, Z.-F., Mei, J.-W., Wu, Y.-S. & Liu, F. Flat chern band in a two-dimensional organometallic framework. *Phys. Rev. Lett.* **110**, 106804 (2013).
49. Su, N., Jiang, W., Wang, Z. & Liu, F. Prediction of large gap flat chern band in a two-dimensional metal-organic framework. *Appl. Phys. Lett.* **112**, 033301 (2018).
50. Reis, F. et al. Bismuthene on a sic substrate: a candidate for a high-temperature quantum spin hall material. *Science* **357**, 287–290 (2017).
51. Smerald, A. & Mila, F. Exploring the spin-orbital ground state of $ba_3cusb_2o_9$. *Phys. Rev. B* **90**, 094422 (2014).
52. Venderbos, J. W. F. & Fernandes, R. M. Correlations and electronic order in a two-orbital honeycomb lattice model for twisted bilayer graphene. *Phys. Rev. B* **98**, 245103 (2018).
53. Natori, W. M. H., Nutakki, R., Pereira, R. G. & Andrade, E. C. Su(4) heisenberg model on the honeycomb lattice with exchange-frustrated perturbations: Implications for twistronics and mott insulators. *Phys. Rev. B* **100**, 205131 (2019).
54. Yoo, H. et al. Atomic and electronic reconstruction at the van der waals interface in twisted bilayer graphene. *Nat. Mater.* **18**, 448 (2019).
55. Kuc, A., Zibouche, N. & Heine, T. Influence of quantum confinement on the electronic structure of the transition metal sulfide ts_2. *Phys. Rev. B* **83**, 245213 (2011).
56. Zhang, Y. et al. Direct observation of the transition from indirect to direct bandgap in atomically thin epitaxial $mose_2$. *Nat. Nanotechnol.* **9**, 111 (2014).
57. Tokura, Y. & Nagaosa, N. Orbital physics in transition-metal oxides. *Science* **288**, 462–468 (2000).
58. Corboz, P., Lajkó, M., Läuchli, A. M., Penc, K. & Mila, F. Spin-orbital quantum liquid on the honeycomb lattice. *Phys. Rev. X* **2**, 041013 (2012).
59. Khomskii, D. & Mostovoy, M. Orbital ordering and frustrations. *J. Phys. A: Math. Gen.* **36**, 9197 (2003).
60. Sboychakov, A. O., Rozhkov, A. V., Rakhmanov, A. L. & Nori, F. Many-body effects in twisted bilayer graphene at low twist angles. *Phys. Rev. B* **100**, 045111 (2019).
61. Sboychakov, A., Rozhkov, A., Rakhmanov, A. & Nori, F. Spin density wave and electron nematicity in magic-angle twisted bilayer graphene. *Phys. Rev. B* **102**, 155142 (2020).
62. Rubio-Verdú, C. et al. Universal moiré nematic phase in twisted graphitic systems. Preprint at https://arxiv.org/abs/2009.11645 (2020).
63. Angeli, M. & MacDonald, A. H. γ valley transition metal dichalcogenide moiré bands. *Proc. Natl. Acad. Sci. USA* **118**, e2021826118 (2021).
64. Corboz, P., Lajkó, M., Läuchli, A. M., Penc, K. & Mila, F. Spin-orbital quantum liquid on the honeycomb lattice. *Phys. Rev. X* **2**, 041013 (2012).
65. Wang, F. & Vishwanath, A. z_2 spin-orbital liquid state in the square lattice kugel-khomskii model. *Phys. Rev. B* **80**, 064413 (2009).
66. Zhang, G.-F., Li, Y. & Wu, C. Honeycomb lattice with multiorbital structure: topological and quantum anomalous hall insulators with large gaps. *Phys. Rev. B* **90**, 075114 (2014).
67. Kresse, G. & Hafner, J. Ab initio molecular dynamics for liquid metals. *Phys. Rev. B* **47**, 558 (1993).
68. Blöchl, P. E. Projector augmented-wave method. *Phys. Rev. B* **50**, 17953 (1994).
69. Perdew, J. P., Burke, K. & Ernzerhof, M. Generalized gradient approximation made simple. *Phys. Rev. Lett.* **77**, 3865 (1996).
70. Tkatchenko, A. & Scheffler, M. Accurate molecular van der waals interactions from ground-state electron density and free-atom reference data. *Phys. Rev. Lett.* **102**, 073005 (2009).

71. Wang, V., Xu, N., Liu, J.-C., Tang, G. & Geng, W.-T. Vaspkit: a user-friendly interface facilitating high-throughput computing and analysis using vasp code. *Comput. Phys. Commun.* **267**, 108033 (2021).

Acknowledgements

We are grateful to Abhay Pasupathy, Cory Dean and Dmitri Basov for fruitful discussions. This work is supported by the European Research Council (ERC-2015-AdG-694097), Grupos Consolidados (IT1249-19), and SFB925. MC and AR are supported by the Flatiron Institute, a division of the Simons Foundation. We acknowledge funding by the Deutsche Forschungsgemeinschaft (DFG, German Research Foundation) under Germany's Excellence Strategy - Cluster of Excellence Matter and Light for Quantum Computing (ML4Q) EXC 2004/1 - 390534769 and Advanced Imaging of Matter (AIM) EXC 2056 - 390715994 and funding by the Deutsche Forschungsgemeinschaft (DFG, German Research Foundation) under RTG 1995 and RTG 2247. Support by the Max Planck Institute - New York City Center for Non-Equilibrium Quantum Phenomena is acknowledged. DK, MMS, and ST acknowledge support from the Deutsche Forschungsgemeinschaft (DFG, German Research Foundation), Projektnummer 277146847 – CRC 1238 (projects C02, C03).

Author contributions

L.X., D.M.K. and A.R. conceived the project. D.M.K., S.T. and A.R. designed and coordinated the research. L.X., M.C., D.K. and M.S. performed all the simulations. All authors discussed and analyzed the results and contributed to writing the manuscript.

Funding

Open Access funding enabled and organized by Projekt DEAL.

Competing interests

The authors declare no competing interests.

Additional information

Supplementary information The online version contains supplementary material available at https://doi.org/10.1038/s41467-021-25922-8.

Correspondence and requests for materials should be addressed to Dante M. Kennes or Angel Rubio.

Peer review information *Nature Communications* thanks Fengcheng Wu and the other, anonymous, reviewer(s) for their contribution to the peer review of this work. Peer reviewer reports are available.

nature COMMUNICATIONS

ARTICLE

https://doi.org/10.1038/s41467-021-26076-3 OPEN

Cavity-induced quantum spin liquids

Alessio Chiocchetta[1✉], Dominik Kiese[1], Carl Philipp Zelle[1], Francesco Piazza[2] & Sebastian Diehl[1]

Quantum spin liquids provide paradigmatic examples of highly entangled quantum states of matter. Frustration is the key mechanism to favor spin liquids over more conventional magnetically ordered states. Here we propose to engineer frustration by exploiting the coupling of quantum magnets to the quantized light of an optical cavity. The interplay between the quantum fluctuations of the electro-magnetic field and the strongly correlated electrons results in a tunable long-range interaction between localized spins. This cavity-induced frustration robustly stabilizes spin liquid states, which occupy an extensive region in the phase diagram spanned by the range and strength of the tailored interaction. This occurs even in originally unfrustrated systems, as we showcase for the Heisenberg model on the square lattice.

[1] Institute for Theoretical Physics, University of Cologne, 50937 Cologne, Germany. [2] Max Planck Institute for the Physics of Complex Systems, 01187 Dresden, Germany. ✉email: achiocch@uni-koeln.de

Quantum spin liquids (QSLs) represent strongly correlated phases of matter, which are characterized by quantum fluctuations so dominant as to suppress magnetic ordering down to the lowest temperatures. Yet, the spins may be quantum mechanically entangled over long distances[1–3]. In Nature, QSLs are expected to occur in proximity to magnetic phases, but their existence often remains elusive. The key ingredient behind quantum spin liquid formation is, however, clearly identified: it is the presence of strong frustration, which disallows magnetic symmetry breaking, but need not be averse to, e.g., quantum mechanical singlet ordering. The routes towards frustration are manifold: one promising avenue is the focus on materials where magnetic ordering is penalized by the geometry of the lattice, such as for triangular, Kagomé or pyrochlore lattices[4–7]. Another one proceeds via the energetic competition of couplings of different ranges, like in the antiferromagnetic (AFM) J_1–J_2 Heisenberg model or dipolar-interacting systems[8–10], where the simultaneous appearance of nearest- and beyond-nearest-neighbour couplings counteracts global antiferromagnetism.

The challenge is then out to engineer robust QSL states of quantum condensed matter. Here, we will achieve this task by coupling an ordinary Heisenberg antiferromagnet on a square lattice to the electromagnetic field of an optical cavity.

The physical mechanism stabilizing the QSL takes the second route towards strong frustration to the extreme, by considering long-range AFM interactions described by an algebraically decaying spin–spin interaction $\sim r^{-\alpha}$ including the case of all-to-all couplings $\alpha = 0$, mediated by the cavity, cf. Fig. 1a. For the limiting case $\alpha = 0$ and a cavity-induced interaction γ dominating over the nearest-neighbour Heisenberg coupling J, $J/\gamma = 0$, this realizes a state with long-range correlations mediated by singlets of arbitrarily large size (LRS). Away from this limit, and for decay exponents $\alpha \lesssim 1$, within a Schwinger–Boson approach, we find that the frustration imprinted by the cavity creates an extensive regime of QSL states. It is characterized by the absence of spontaneous symmetry breaking, and fractional excitations of both of a gapped (SL-I) and of gapless (SL-II) nature, cf. Fig. 1b. As a consequence of the underlying long-ranged interactions, correlations decay algebraically in both these phases.

In terms of physical implementation, we draw motivation from recent developments exploring the interplay of quantum materials with quantized light. This idea has been researched in the context of weakly correlated systems, mainly as a tool to reinforce superconductivity and other coherent many-body phases[11–20]. First works have also addressed the strong coupling regime, showing how existing phases can be manipulated in this way[12,21,22]. Here, we demonstrate that the coupling to a cavity can even induce phases that are not present in its absence: an unfrustrated AFM system is turned into a quantum spin liquid, provided the AFM interaction mediated by the cavity is sufficiently long-ranged and strong. To achieve these requirements, we develop a solid-state implementation harnessing localized electronic orbitals as effective spin degrees of freedom, coupled to the cavity modes via additional coherent laser drive, cf. Fig. 1a. This gives rise to quantum mechanically fluctuating, effective magnetic fields in all linearly independent spatial directions, which vanish on average. They thus counteract dynamically magnetization in any direction, but do not suppress the spin-singlet ordering, crucial for QSL states.

Results

Model. We consider a long-range SU(2)-symmetric Heisenberg model on a square lattice

$$H = J \sum_{\langle i,j \rangle} \mathbf{S}_i \cdot \mathbf{S}_j + \gamma \sum_{i \neq j} \frac{\mathbf{S}_i \cdot \mathbf{S}_j}{|\mathbf{r}_{ij}|^{\alpha}}, \tag{1}$$

with $\mathbf{S}_i = (S_i^x, S_i^y, S_i^z)$ spin-1/2 operators on the lattice site i, $J > 0$ the nearest-neighbour AFM exchange, $\gamma > 0$ the strength of the long-range interaction modulated by the exponent α and $\mathbf{r}_{ij} \equiv \mathbf{r}_i - \mathbf{r}_j$. Periodic boundary conditions are assumed. Before analysing the ground-state phase diagram of the Hamiltonian (1), let us qualitatively discuss the expected phases, starting with some known limiting cases. For $\gamma = 0$, the ground state of the Hamiltonian (1) displays Néel-like order[23]. For $\alpha = 0$ and $\gamma \gg J$, the long-range Hamiltonian is proportional to the total spin $(\sum_i \mathbf{S}_i)^2$: this imposes a constraint on this singlet manifold, energetically penalizing states with a finite value of the total spin S, including states with finite magnetization. As a result, the ground state of the total Hamiltonian is given by the ground state of the short-range Hamiltonian projected on the singlet manifold. This is similar to the analysis in ref. [24], where resonating valence bond (RVB) states with singlets of arbitrarily large size were used as variational wavefunctions. We will denote this state as a long-range singlet state (LRS). Finally, for $J = 0$, different scenarios are possible: for α large enough, only nearest-neighbouring sites experience an appreciable interaction, and therefore Néel-like order is expected. For smaller values of α, the frustrating nature of the interaction is expected to penalize AFM order, thus favoring disordered phases. This was shown to be the case for $\alpha = 3$ on the triangular lattice[8], and on the square lattice[9] (although only for

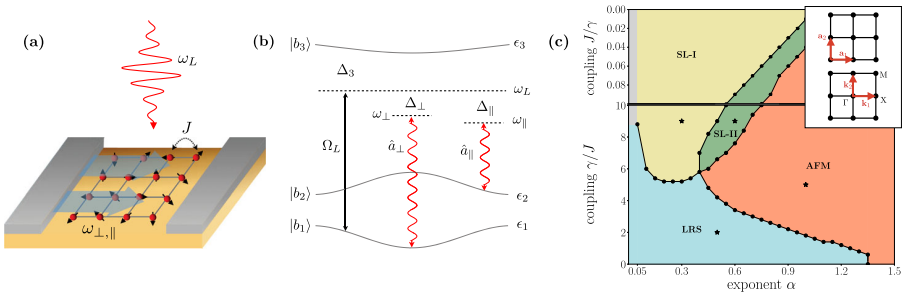

Fig. 1 Implementation of a cavity-induced quantum spin liquid and phase diagram. a Setup: a two-dimensional material, with nearest-neighbour exchange interaction J, is coupled to a cavity with fundamental frequencies $\omega_{\perp,\parallel}$, whose field is represented by the light-blue arrows. The system is driven by an external laser with frequency ω_L. **b** Level scheme: the electronic orbitals $|b_{1,2}\rangle$, with energies $\sim\epsilon_{1,2}$ are coupled to the auxiliary band $|b_3\rangle$, with energy $\sim\epsilon_3$ via the laser with Rabi frequency Ω_L and the cavity modes $a_{\perp,\parallel}$. The third band is detuned from the laser by Δ_3, and from the cavity modes by $\Delta_{\perp,\parallel}$. **c** Phase diagram for the ground state of Hamiltonian (1), obtained from the bosonic spinon decomposition, as a function of the exponent α and of the coupling ratio γ/J, featuring spin-liquid (SL), long-range-single (LRS) and antiferromagnetic (AFM) phases. Error bars on the phase boundaries are within the symbols' size. The inset shows the square lattice and the reciprocal one, with the respective primitive vectors.

spatially anisotropic interactions in the latter case), where a QSL phase was found.

Summarizing, by varying γ/J and α, we expect three kinds of phases: (i) Néel-like AFM, (ii) a disordered QSL phase, and (iii) an LRS phase. This is substantiated below using a Schwinger–Boson approach, which is capable of capturing all the phases mentioned above. In particular, it provides a natural interpolation scheme between the well-understood RVB and Néel physics discussed above.

In order to unveil the nature of the ground state of the Hamiltonian (1), we apply the bosonic spinon decomposition pioneered in refs. [25–27], where the spin operators are represented in terms of new bosonic degrees of freedom, ultimately interpreted as emergent fractional excitations. While this method represents an approximation[25,26], it still provides useful information to identify candidate spin liquids. Moreover, the main advantage of this method is its flexibility to interpolate between the different states previously identified. On the one hand, SU(2)-symmetric bosonic ground states are identified with candidate spin liquids. On the other hand, the onset of magnetic order is signalled by the Bose–Einstein condensation of these bosons.

The spin operators on the lattice site j are decomposed as (using sum convention for the Greek indices)

$$\mathbf{S}_j = \frac{1}{2} b^\dagger_{j,\mu} \boldsymbol{\sigma}_{\mu\nu} b_{j,\nu}, \tag{2}$$

where $b_{j,\mu}$ is a boson (spinon) with spin $\mu \in \{\uparrow, \downarrow\}$, and $\boldsymbol{\sigma}$ the vector of Pauli matrices. The mapping is then completed by the constraint $b^\dagger_{j\mu} b_{j\mu} = 1$. Insights on the nature of the state are then obtained from the expectation values of the SU(2)-invariant bilinears $\mathcal{A}_{ij} = i\sigma^y_{\mu\nu}\langle b_{i\mu} b_{j\nu}\rangle/2$, and $\mathcal{B}_{ij} = \langle b^\dagger_{i\mu} b_{j\mu}\rangle/2$, which indicate the tendency of the spins at the sites i and j of forming a singlet or to align, respectively. For SU(2)-symmetric states, finite values of $\mathcal{A}_{ij}$ and $\mathcal{B}_{ij}$ determine a finite spinon hopping between the lattice sites i and j, thus signalling the emergence of propagating fractional excitations.

After performing a mean-field decoupling of the spinonic Hamiltonian (see 'Methods' for further details), the values of $\mathcal{A}_{ij}$ and $\mathcal{B}_{ij}$ are self-consistently determined by minimizing the ground-state energy. This task is enabled in practice by using an Ansatz for the values of $\mathcal{A}_{ij}$ and $\mathcal{B}_{ij}$. The most natural choice is the manifestly translational-invariant Ansatz $\mathcal{A}_{ij} = \mathcal{A}_{i-j}$, $\mathcal{B}_{ij} = \mathcal{B}_{i-j}$, which follows from a projective-symmetry-group analysis[28]. The resulting saddle-point equations, reported in Eq. (9a, b, c), are reduced to a system of $2N+1$ coupled non-linear equations, for finite-size systems with $N = L \times L$ lattice sites. The numerical complexity of the problem still limits the size N of the systems for which a solution can be found.

For finite-size systems, a spontaneous symmetry breaking cannot occur, and therefore the AFM order parameter always vanishes. Accordingly, other criteria are needed to assess the onset of an ordered phase. Here, we identify the onset of an AF-ordered phase when the two following conditions are met: (i) the gap $E_g \equiv \min_{\mathbf{q}} E_{\mathbf{q}}$ in the spinon dispersion closes upon increasing the system size N and (ii) the squared magnetization $M^2 \equiv \sum_j |\mathbf{S}_j \cdot \mathbf{S}_0|/N$ approaches a constant value upon increasing N. Notice that these two indicators also naturally lend themselves to characterize the other phases outlined before: a phase with $M^2 = 0$ corresponds to either a gapped ($E_g \neq 0$) or a gapless $E_g = 0$ QSL, while a phase with $M^2 \neq 0$ and $E_g \neq 0$ can be naturally identified with an LRS state. These criteria are summarized in Table 1.

Let us finally discuss the phase diagram in Fig. 1c. The first, main result, is the emergence of a gapped QSL phase (denoted as SL-I) for $\alpha \lesssim 1.25$, and $\gamma \gtrsim 5J$, characterized by the presence of a gap and by the absence of long-range correlations. This phase appears for any $\alpha > 0.05$, corresponding to the minimum value here considered, suggesting that the LRS phase is unstable in this region and only exists for $\alpha = 0$. In addition, our data also show the existence of a gapless QSL phase (denoted SL-II) for intermediate values of α, clearly manifested in the largest available system sizes, as shown in Fig. 2a, b.

Table 1 Ground-state phases.

	SL-I	SL-II	LRS	AFM
Gap	Yes	No	Yes	No
LRO	No	No	Yes	Yes

The summary of the four phases identified in this work was according to the criteria discussed in the main text.

For $\gamma \lesssim 5J$, the LRS phase is remarkably stable for $\alpha \lesssim 1.25$. Here, the system is simultaneously gapped and characterized by long-range correlations (cf. Table 1), which, however, do not correspond to a spontaneous symmetry breaking. Finally, we observe that, as expected, for large values of α, as well as for $\gamma = 0$, the system is always in the ordinary Néel–AFM phase.

An example of extrapolated values of M^2 and E_g used to build the phase diagram in Fig. 1c is shown in Fig. 2d, as a function of α for $\gamma = 7J$. The fitting function used to extrapolate the $L \to \infty$ limit of these observables has the form $\mathcal{O}_L = \mathcal{O}_\infty + b_\mathcal{O} L^{-\omega_\mathcal{O}}$, with $\mathcal{O}_\infty$, $b_\mathcal{O}$ and $\omega_\mathcal{O}$ fitting parameters. The slightly negative extrapolated values of M^2 and E_g are due to the simplified form of the extrapolation function above, which neglects subleading terms in $1/L$ (cf. ref. [29]). This fitting function was identified by a preliminary evaluation of the quantity $\xi_\mathcal{O}(L) = 1/\ln\left(\frac{\mathcal{O}_{L-4}-\mathcal{O}_{L-2}}{\mathcal{O}_{L-2}-\mathcal{O}_L}\right)$, which displays a linear behaviour in L for algebraic finite-size scaling, while it saturates for an exponential one[30]. The algebraic finite-size scaling occurring also for gapped phases is imprinted by the algebraic character of the interactions[31]. For the same reason, the spin–spin correlation functions in the QSL phases also display an algebraically decaying behaviour, rather than the usual short-range one, with an exponent depending continuously on the interaction's exponent α (cf. Fig. 2e). Algebraic correlations were similarly found for gapped, disordered phases in spin chains with long-range interactions[32–34], further substantiating the generality of this mechanism.

Besides gap and long-range order, we provide a further observable to characterize the phases here identified, i.e., the dynamical structure factor $S_{\mathbf{q}}(\omega) = \int_t e^{i\omega t}\langle \mathbf{S}_{-\mathbf{q}}(t) \cdot \mathbf{S}_{\mathbf{q}}(0)\rangle$, with $\mathbf{S}_{\mathbf{q}}$ the Fourier transform of the spin operators with momentum $\mathbf{q}$. $S_{\mathbf{q}}(\omega)$, which can be straightforwardly computed from the spinon decomposition[35], leads to markedly different features depending on the phase. For the SL-I and SL-II phases (Fig. 3a, b, respectively), the DSF features a broadening originated in the continuum of fractional excitations. On the contrary, the AFM phase (Fig. 3c) shows a sharper signal close to the gapless quasi-particle dispersion, corresponding to the magnonic dispersion expected in the AFM phase. We emphasize that the presence of a gap in the DSF for the SL-II phase is a finite-size effect, and it is expected to close in the thermodynamic limit. Finally, the LRS phase (Fig. 3d) features a broadening similar to the SL-I phase, suggesting the presence of fractionalized excitations.

A final word of caution concerns the accuracy of the bosonic spinon decomposition used here. As a mean-field theory, it provides a qualitatively correct topology of the phase diagram, while the phase borders cannot be expected to be quantitatively accurate.

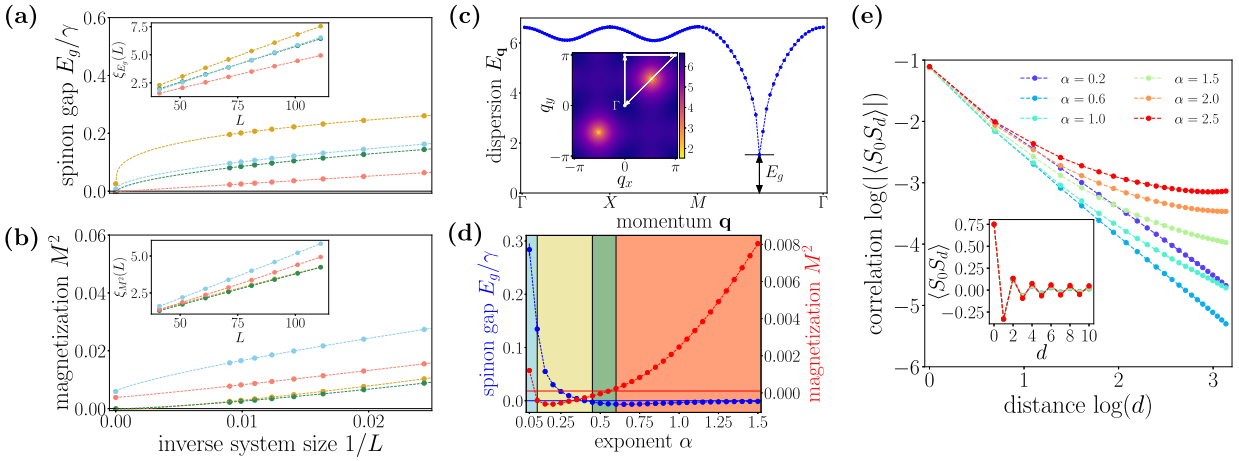

Fig. 2 Numerical characterization of the ground state. a, **b** Dependence of the spinon gap (upper panel) and square magnetization (lower panel) on the inverse linear system size. The curves refer to values of α and γ/J denoted in Fig. 1c by star symbols, according to the corresponding background colours. The maximum linear size considered is $L = 110$. Insets: values of the functions $\xi_{E_g,M^2}(L)$ as functions of the linear system size L. **c** Spinon dispersion for $\gamma = 7J$ and $\alpha = 0.3$ (SL-I phase), for given cuts in the first Brillouin zone. Inset: spinon dispersion in the first Brillouin zone. The white lines denote the cuts of the main plot. **d** Extrapolated gap (blue curve) and square magnetization (red curve) as functions of the exponent α. The background colours reflect the phases illustrated in Fig. 1c. **e** Spin–spin correlation functions along the lattice axis for different values of the exponent α and for $\gamma = 7J$. Inset: spin–spin correlations at short distances.

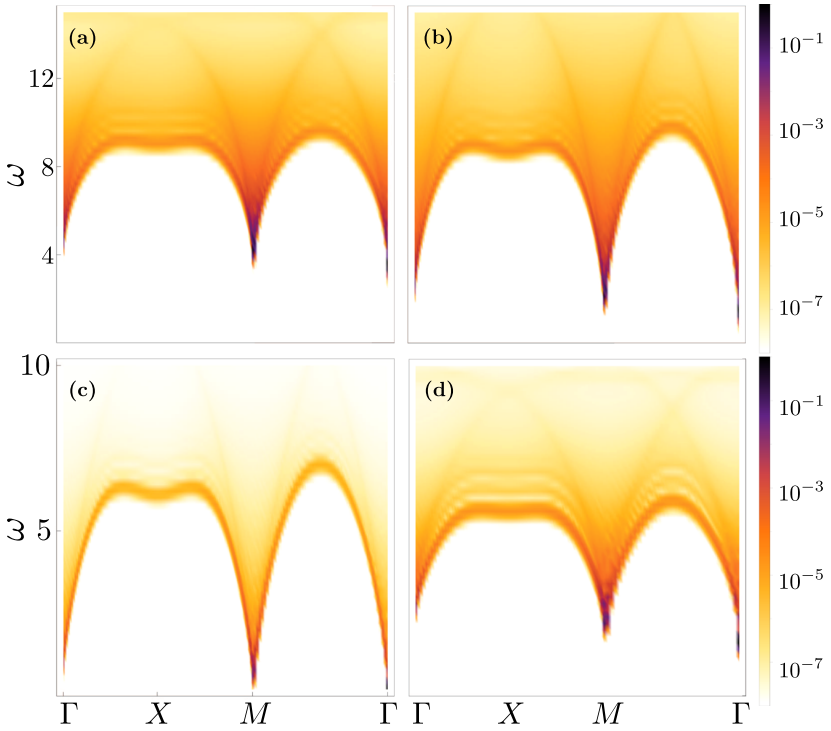

Fig. 3 Dynamical structure factor. $\mathbf{S_q}(\omega)$ as a function of the frequency ω and of the momentum $\mathbf{q}$. Results are shown for: SL-I [panel **a**, $\gamma = 9J$, $\alpha = 0.3$], SL-II [panel **b**, $\gamma = 9J$, $\alpha = 0.6$], AFM [panel **c**, $\gamma = 5J$, $\alpha = 1.0$] and LRS [panel **d**, $\gamma = 4.4J$, $\alpha = 0.35$].

Implementation. The Hamiltonian Eq. (1) (or variations of it) can be realized in quantum simulators using trapped ions or ultracold atoms[8,36,37]. While these platforms provide unprecedented controllability, the realization of low-temperature strongly correlated phases remains challenging. On the converse, solid-state platforms naturally feature strongly correlated physics at cryogenically accessible temperatures. Moreover, the controllability in 2D materials is progressing fast, making them, among others, candidates for quantum simulators[38]. In the following, we will focus on a scheme for implementing the Hamiltonian (1) in a solid-state system.

Our proposal uses two electronic orbital degrees of freedom, constituting a pseudospin of length $S = 1/2$. In the absence of a cavity, the pseudospins are assumed to be described by a short-range AFM Heisenberg model, emerging as a strong Mott limit of a Hubbard model for the electronic degrees of freedom: this is the case, e.g., of iridate and ruthenate materials[39–41]. We assume SU(2) symmetry for the sake of simplicity.

As substantiated further below, the coupling of the localized electronic states to the cavity will result in a coupling between the pseudospins and quantized effective magnetic fields. The setup we consider is sketched in Fig. 1a. Two aspects of the long-range Hamiltonian (1) are essential to unveil QSL phases: (i) an AFM character of the induced interaction and (ii) a high degree of symmetry, ideally SU(2). In order to control the symmetry of the emerging cavity-mediated interaction, we propose to use two cavity modes. While a single mode is sufficient to mediate a U(1)-symmetric interaction, a second mode allows for an enhancement to SU(2) symmetry. The required selectivity in the cavity–spin coupling can be achieved via an auxiliary third band which is driven far off-resonance by a laser [see Fig. 1b]. The resulting two-photon transitions involve virtual excitations to the third band and back to one of the two bands implementing the pseudospin degree of freedom. The sign of the cavity-mediated interaction is then finally determined by the detuning between the laser and each cavity mode.

The paramagnetic and diamagnetic coupling terms between electrons and electromagnetic field are given by:

$$H_{\rm int} = \frac{1}{2m}\int_{\mathbf{r}} \psi^\dagger(\mathbf{r})[2e\ \mathbf{p}\cdot\mathbf{A}(\mathbf{r},t) + e^2\mathbf{A}^2(\mathbf{r},t)]\psi(\mathbf{r})\ , \qquad (3)$$

with ψ the electronic operators, e the electronic charge and $\mathbf{A}(\mathbf{r},t)$ the vector potential. $\mathbf{A}(\mathbf{r},t)$ includes the external laser with frequency ω_L and the cavity modes $a_{\perp,\parallel}$ with frequencies $\omega_{\perp,\parallel}$. By choosing the proper polarization for the cavity modes and the laser, the scheme depicted in Fig. 1b can be realized: the laser and the cavity mode $a_\perp$ induces transitions between orbitals 1 and 3, while the cavity mode $a_\parallel$ couples only orbitals 2 and 3. As we assume the electrons to be localized by the strong interaction between particles, due to the strong localization, the field operators can be conveniently expanded onto localized orbitals[23]: $\psi(\mathbf{r}) = \sum_{i,b=1,2,3} w_{ib}(\mathbf{r})c_{ib}$, where $w_{ib}(\mathbf{r}) = w_b(\mathbf{r}-\mathbf{r}_i)$, with $\mathbf{r}_i$ the position of the centre of the unit cell. Here, the index i runs over the lattice sites and b is the band index. The interaction Hamiltonian (3) thus reads (see 'Methods' for further details)

$$H_{\rm int} = \sum_i \left[c^\dagger_{i3}c_{i1}(\rho^L_{31} + a_\perp\rho^\perp_{31}) + c^\dagger_{i3}c_{i2}a_\parallel\rho^\parallel_{32} + \text{h.c.}\right], \qquad (4)$$

where we neglected counter-rotating terms and changed to the frame rotating with the laser frequency, where $c_{i3} \to c_{i3}e^{-i\omega_L t}$, $a_\ell \to a_\ell e^{-i\omega_L t}$. Correspondingly, the third electron band and the fundamental frequencies of the cavity modes ω_ℓ are shifted as $\Delta_3 = \epsilon_3 - \omega_L$ and $\Delta_\ell = \omega_\ell - \omega_L$. The matrix elements $\rho^\ell_{bb'}$, $\ell \in \{L, \perp, \parallel\}$ correspond to the transition rates between the bands b and b'.

The effective cavity–spin coupling is then obtained by eliminating the third band adiabatically, assuming the band detuning $|\Delta_3|$ to be much larger than the matrix elements $\rho^\ell_{bb'}$, $\ell \in \{L, \perp, \parallel\}$ and the cavity detunings $\Delta_{\perp,\parallel}$. The resulting interaction Hamiltonian describes spins coupled to global, quantum mechanically fluctuating effective magnetic fields:

$$H_{\rm int} = \sum_i \left(B^x S^x_i + B^y S^y_i + B^z S^z_i\right), \qquad (5)$$

with $B^z = -(\rho^L_{13}\rho^\perp_{31}a_\perp + \text{h.c.})/\Delta_3$, $B^x = -(\rho^L_{13}\rho^\parallel_{32}a_\parallel + \text{h.c.})/\Delta_3$ and $B^y = -(i\rho^L_{13}\rho^\parallel_{32}a_\parallel + \text{h.c.})/\Delta_3$, and $\mathbf{S}_i = c^\dagger_{ib}\boldsymbol{\sigma}_{bb'}c_{ib'}/2$ is the pseudo-spin operator. The values of the effective fluctuating effective magnetic fields B^a, $a = x, y, z$, reflect the laser-assisted processes illustrated in Fig. 1. For instance, B^x and B^y, which couple the first and second orbital, result from the laser-assisted excitation of an electron from the first to the third auxiliary band, followed by a decay to the second band with the emission of a cavity photon. The U(1) symmetry of the Hamiltonian results from neglecting the counter-rotating terms, and it is evident from the fact that an excitation from the first to the second band is accompanied only by the creation of a cavity photon, and vice versa. Equation (5) is one of the main results of this paper: the effective quantum magnetic fields B^a couple to all the spins, generating an effective long-range coupling. To further consolidate this insight, we integrate out the cavity field at the level of the Heisenberg equations and obtain an effective Hamiltonian for the spins only[42]:

$$H_{\rm int} = \sum_{ij}\left[\gamma_z S^z_i S^z_j + \gamma_\perp(S^x_i S^x_j + S^y_i S^y_j)\right], \qquad (6)$$

with the long-range exchange $\gamma_z = |\rho^L_{13}\rho^\perp_{13}|^2/(\Delta_3^2\Delta_\perp)$ and $\gamma_\perp = |\rho^L_{13}\rho^\parallel_{23}|^2/(\Delta_3^2\Delta_\parallel)$. The interaction is thus naturally U(1)-symmetric, and full SU(2) symmetry can be achieved by adjusting the cavity-mode detunings. Importantly, by choosing the latter to be positive (i.e. a blue-detuned laser), the cavity-mediated interaction is AFM.

We now briefly show how multi-mode cavities can generate spatially dependent effective spin–spin interactions. To this end, we consider a cavity with a large number of modes. For simplicity, we assume them to correspond to photons propagating as plane waves along the transverse direction with a dispersion $\Delta_{\ell,\mathbf{q}} = \sqrt{\omega_\ell^2 + (c\mathbf{q})^2} - \omega_L$, with c the speed of light in the medium. The form of the Hamiltonian (5) is then preserved, with the fluctuating magnetic fields now possessing a spatial structure according to

$$B^a = \sum_{\mathbf{q}} g^a_{\mathbf{q}}\ a_{\mathbf{q}}\ e^{i\mathbf{q}\cdot\mathbf{r}_j} + \text{h.c.}\,, \qquad (7)$$

with $g^a_{\mathbf{q}}$ the momentum-dependent version of the coupling reported below Eq. (5). By integrating out the cavity photons, one obtains an effective Hamiltonian as in Eq. (6), where the effective exchange interaction between the spins S^a and S^b is given by $\Gamma^{ab}_{ij} = \sum_{\mathbf{q}} g^a_{\mathbf{q}} g^b_{\mathbf{q}}\ e^{-i\mathbf{q}\cdot\mathbf{r}_{ij}}/\Delta_{\ell,\mathbf{q}}$. While the precise form of Γ^{ab}_{ij} depends on the details of $g^a_{\mathbf{q}}$, its spatial structure is expected to be long-ranged. In fact, the length scale governing the spatial behaviour is proportional to $\Delta_\ell^{-1/2}$: in THz cavities, the ratio between the lattice size and this length scale is of order 10^{-4}, see, e.g., ref. [14], and, therefore Γ^{ab}_{ij}, can be effectively modelled as a slowly decaying function. For photonic crystal cavities, the form of Γ^{ab}_{ij} can be even further engineered by exploiting the band dispersion of the cavity photons[43]. The precise form of this function is not expected to qualitatively affect the phase diagram. Accordingly, we choose to parametrize the interaction as $\Gamma^{ab}_{ij} \simeq |\mathbf{r}_i - \mathbf{r}_j|^{-\alpha}$, with the value of α compactly encoding the interaction range. The values of α achievable with realistic cavity parameters are of order 10^{-1}, and therefore favourable to observe the SL phases (see 'Methods' for further details).

We finally provide an estimate for the values of γ in Eq. (1) achievable with this setup (see 'Methods' for further details). The dipole matrix elements can be estimated assuming a lattice spacing of few angstroms. For THz cavities with a compression factor of $\sim 10^{-5}$ or smaller, a drive with an intensity of $\sim$10 MW cm^{-2} leads to values of γ of order $\sim$100 K. This number is comparable or larger than typical couplings in antiferromagnets, which range from $\sim$5 K for vanadates[44] to $\sim$600 K for iridates[45]. For α-$RuCl_3$, the (ferromagnetic) Heisenberg interaction is $\sim$40 K, while the Kitaev one is $\sim$80 K, see ref. [46]. Accordingly, the spin–liquid phases predicted in the phase diagram in Fig. 1c are achievable with current setups.

Discussion

In this work, we showed that long-range spin–exchange interactions can be robustly induced by coupling a strongly correlated electron system to the quantum fluctuations of a driven cavity. The electron–cavity coupling gives rise to a variety of tunable spin interactions, including frustrated ones. The thus created cavity-mediated frustration can destroy the magnetic order, favoring disordered spin–liquid states, absent in the cavity-less configuration. We have demonstrated this for an ordinary Heisenberg antiferromagnet, whose ground state manifests an extensive and robust quantum spin–liquid phase when coupled to a cavity. Our results open avenues for engineering quantum spin liquids, sparking the challenge to devise new schemes to control electronic degrees of freedom with quantum light, and to uncover phases of matter that are usually inaccessible. This also represents an exciting perspective for the experimental detection of strongly correlated phases: photons emitted from the cavities carry signatures of the quantum many-body state, which become accessible to standard optical measurements. Our findings are immediately relevant also for quantum simulations. Artificial spin systems with tunable long-range interactions can be currently created using either trapped ions[36,47] or ultracold atoms coupled to an optical cavity[48–51]. These platforms represent, therefore, ideal candidates to simulate quantum spin liquid phases.

Methods

Saddle-point equations for bosonic spinons. In this section, we outline the derivation of the saddle point equations for the spinon bilinear expectation values $\mathcal{A}_{ij}$ and $\mathcal{B}_{ij}$.

The spin-exchange terms appearing in Eq. (1) can be recast as $\mathbf{S}_i\mathbf{S}_j =: B_{ij}^\dagger B_{ij} : -A_{ij}^\dagger A_{ij}$ for $i \neq j$, where $A_{ij} = i\sigma^y_{\mu\nu} b_{i\mu} b_{j\nu}/2$ and $B_{ij} = b^\dagger_{i\mu} b_{j\mu}/2$ are SU(2)-invariant spinonic bilinears. A finite expectation value of these operators indicates the tendency of the spins at the sites i and j of forming a singlet (A_{ij}) or to align (B_{ij}); moreover, it induces a finite bosonic hopping rate between the lattice sites i and j, signalling the existence of propagating fractional excitations. In order to solve for the value of these quantities, we build on the approach of ref. [25]. First, the bosonized version of the Hamiltonian (1) is represented as a path integral, with the constraint implemented by a space- and time-dependent Lagrange multiplier $\lambda_i(t)$. After decoupling the bilinear products by using a Hubbard–Stratonovich transformation, the expectation values $\mathcal{A}_{ij} = \langle A_{ij}\rangle$ and $\mathcal{B}_{ij} = \langle B_{ij}\rangle$ are obtained as saddle point values of the corresponding action. This approximation imposes the constraint only on average, and the now position- and time-independent Lagrange multiplier λ has to be determined self-consistently. This approximation is equivalent to decoupling the Hamiltonian (1) in bosonic bilinears as:

$$H = \frac{1}{2}\sum_{i,j}\left(\epsilon_{ij} b^\dagger_{i\mu} b_{j\mu} + i\Delta^*_{ij}\sigma^y_{\mu\nu} b_{i\mu} b_{j\nu}\right) + \text{h.c.} + \varepsilon_0, \tag{8}$$

where $\epsilon_{ij} = J_{ij}\mathcal{B}^*_{ij} + \delta_{ij}\lambda/2$, $\Delta^*_{ij} = -J_{ij}\mathcal{A}^*_{ij}$ and $\varepsilon_0 = \sum_{i,j}(-|\mathcal{B}_{ij}|^2 + |\mathcal{A}_{ij}|^2) - 2SN\lambda$. As discussed in the main text, we assume a translational-invariant ansatz, i.e. $\mathcal{A}_{ij} = \mathcal{A}_{i-j}$ and $\mathcal{B}_{ij} = \mathcal{B}_{i-j}$, able to interpolate between all the expected phases. The two degenerate eigenvalues of H are given by $E^2_{\mathbf{q}} = \epsilon^2_{\mathbf{q}} - |\Delta_{\mathbf{q}}|^2$, with $\epsilon_{\mathbf{q}}$ and $\Delta_{\mathbf{q}}$ the Fourier transform of the functions appearing in Eq. (8). By minimizing the ground-state energy $E_0 = \sum_{\mathbf{q}}\left(E_{\mathbf{q}} - \epsilon_{\mathbf{q}}\right) + \varepsilon_0$ with respect to the variational parameters $\epsilon_{\mathbf{q}}$, $\Delta_{\mathbf{q}}$ and λ, one obtains the saddle-point equations:

$$1 = \frac{1}{2N}\sum_{\mathbf{q}}\frac{\epsilon_{\mathbf{q}}}{E_{\mathbf{q}}}, \tag{9a}$$

$$\epsilon_{\mathbf{p}} = \lambda + \frac{1}{2N}\sum_{\mathbf{q}} J_{\mathbf{p}-\mathbf{q}}\left(\frac{\epsilon_{\mathbf{q}}}{E_{\mathbf{q}}} - 1\right), \tag{9b}$$

$$\Delta_{\mathbf{p}} = \frac{1}{2N}\sum_{\mathbf{q}} J_{\mathbf{p}-\mathbf{q}}\frac{\Delta_{\mathbf{q}}}{E_{\mathbf{q}}}, \tag{9c}$$

with $J_{\mathbf{q}}$ the Fourier transform of J_{ij}. These equations provide the full momentum dependence of the functions $\epsilon_{\mathbf{q}}$ and $\Delta_{\mathbf{q}}$. The actual number of unknowns increases with the range of the interaction. In fact, for short-range interactions, the momentum dependence can be found analytically, and only a few parameters are left to be computed self-consistently. For long-range interactions, instead, the full momentum dependence needs to be found numerically. Equation (9a, b, c) amounts to a system of $2N + 1$ coupled non-linear equations, with N the total number of sites. To find the roots of these equations, we used a trust region solver as provided by the Julia NLSolve library, with the accepted residual norm set to 10^{-8}. The error of the numerical solution for a finite system of N sites is, therefore, negligible compared to the extrapolation to the thermodynamic limit. Determining $\xi_{\mathcal{O}}(L)$ by a least-squares fit resulted in relative errors between 0.5 and 2%, which we consider to be sufficient for the analysis performed here. The root-finding algorithm is accelerated by exploiting vectorization for the evaluation of the saddle-point equations where possible, and by parallelization via OpenBLAS.

Implementation details. Here, we provide additional details to the set-up described in the main text. The vector potential can be written as

$$\mathbf{A}(\mathbf{r}, t) = \Omega_L \mathbf{u}_L \varphi_L(\mathbf{r}) e^{i\omega_L t} + \sum_{\ell=\parallel,\perp} \mathcal{N}_\ell \mathbf{u}_\ell a_\ell \varphi_\ell(\mathbf{r}) + \text{h.c.}, \tag{10}$$

where Ω_L^2 and ω_L denote the laser intensity and frequency, respectively. Here $\mathbf{u}$ and $\varphi(\mathbf{r})$ are the polarization vector and the mode wavefunction. For the cavity modes, labelled by $\ell = \parallel, \perp$, the wave function is normalized over the finite volume V_c and $\mathcal{N}_\ell = \sqrt{1/2\omega_\ell \epsilon_0 \epsilon_r}$, where ω_ℓ is the mode fundamental frequency and ϵ_0, ϵ_r are the vacuum and relative permittivity of the material, respectively.

We assume that that the mode wavefunctions $\varphi(\mathbf{r})$ does not vary significantly over the extent of the Wannier functions. By tuning the polarization vectors $\mathbf{u}$ to selectively couple the orbitals as in Fig. 1, and by performing the rotating-wave approximation, the resulting paramagnetic Hamiltonian term is given by Eq. (4), with

$$\rho^\ell_{bb'} = \frac{e\mathcal{N}_\ell}{m}\varphi_\ell \mathbf{u}_\ell \cdot \langle w_{ib}|\mathbf{p}|w_{ib'}\rangle. \tag{11}$$

The expression for $\rho^L_{bb'}$ can be obtained from the previous equation by replacing $\mathcal{N}_\ell$ with Ω_L.

The diamagnetic part of the Hamiltonian (3) reads, after neglecting higher-order electron-photon processes of the type $c_3^\dagger c_3(a + a^\dagger)$ and $c_3^\dagger c_3 a^\dagger a$:

$$H_{\text{int,dia}} = \sum_{\ell=\perp,\parallel} \delta_\ell\, a^\dagger_\ell a_\ell + \sum_i \delta_3\, c^\dagger_{i3} c_{i3}, \tag{12}$$

plus a term linear in the cavity fields, which vanishes as the laser and cavity wavefunctions are orthogonal. The shifts

$$\delta_\ell = \frac{e^2}{m} V_e\, \mathcal{N}_\ell^2 |\varphi_\ell|^2, \tag{13a}$$

$$\delta_3 = \frac{e^2\Omega_L^2}{m}|\varphi_L|^2 + \sum_{\ell=\perp,\parallel}\frac{e^2\mathcal{N}_\ell^2}{2m}|\varphi_\ell|^2, \tag{13b}$$

renormalize the energies of the cavity modes and of the third band, respectively. By assuming that the band detuning $|\widetilde{\Delta}_3|$ is much larger than the coupling strengths and the cavity detunings $\widetilde{\Delta}_\ell$, the third band can be adiabatically eliminated, leading to Eq. (5) in the main text, including an additional term $B_0 \sum_i S^z_i$, with $B_0 = |\rho^L_{13}|^2/\widetilde{\Delta}_3$. This effective classical magnetic field breaks explicitly the SU(2) symmetry, but it is much smaller than the spin exchange and therefore it can be safely neglected.

Estimate of interaction strength and range. We consider a THz laser ($\omega_L = 100$ THz) with intensity $\Omega_L^2 = 10$ MW cm^{-2}, with a small detuning from the cavity frequency $\Delta_\perp = \Delta_\parallel = 10^{-2}$ THz. The compression factor of the cavity is assumed to be $\Lambda = 10^{-5}$. The detuning from the third band is $\Delta_3 = 1$ THz, thus satisfying the condition $\Delta_3 \gg \Delta_\perp$. We estimate the matrix as follows: $\langle w_{i1}|\mathbf{p}|w_{i3'}\rangle \sim m\omega_{13}\langle w_{i1}|\mathbf{r}|w_{i3'}\rangle$, with $\omega_{13} = \omega_L + \Delta_L$ and $\langle w_{i1}|\mathbf{r}|w_{i3'}\rangle = 10$ A, the same order of magnitude of a typical lattice spacing. Using the formulas derived in the text, one then estimates a long-range interaction with strength $\gamma \sim 100$ K.

We also provide an estimate of the values of α. To this end, we evaluate the explicit form of $\Gamma(\mathbf{r}_{ij})$ as reported in the text below Eq. (7). For simplicity, we assume $\Delta_\perp = \Delta_\parallel \equiv \Delta$ and $\omega_\perp = \omega_\parallel \equiv \omega$. The Rabi-like couplings $g_{\mathbf{q}}$ inherits the momentum dependence from the normalization of every mode, i.e. $g_{\mathbf{q}} \propto (\omega^2 + (c\mathbf{q})^2)^{-1/4}$. Accordingly, the cavity-mediated exchange is given by:

$$\Gamma(\mathbf{r}_{ij}) \propto \sum_{\mathbf{q}} \frac{e^{-i\mathbf{q}\cdot\mathbf{r}_{ij}}}{\sqrt{\omega^2 + (c\mathbf{q})^2}\left(\sqrt{\omega_c^2 + (c\mathbf{q})^2} - \omega_L\right)}. \tag{14}$$

The corresponding integral is computed numerically, and the results shown in Fig. 4 over a range of 50 lattice sites, for different values of the cavity detuning. The values of α obtained are reported in the figure.

Heating effects. A possible advantage of our scheme is that it does not rely on the laser being resonant with any electronic or phononic excitation, with the only tradeoff of a decreasing coupling strength as the detuning increases. Exploiting the variability of the detuning, as well as the knowledge of the relevant excitation modes of the quantum material and the cavity, resonances can be avoided and heating is pushed to later times. This said, we can on the other hand consider the worst-case scenario, where heating does efficiently take place, and estimate the amount of it, following ref. [52]. As a paradigmatic material, we consider $RuCl_3$,

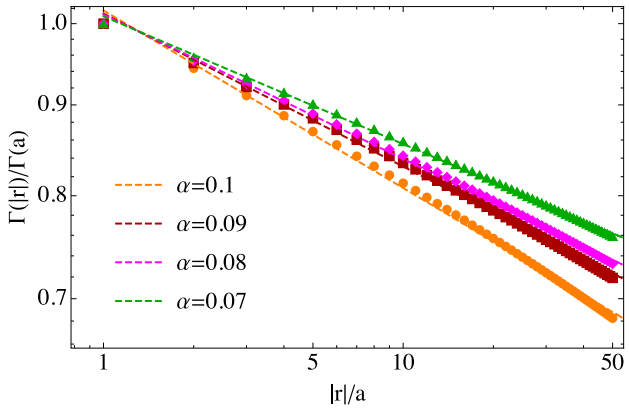

Fig. 4 Normalized long-range spin-exchange Γ(|r|) as a function of the distance between sites |r|. The cavity fundamental wavelength is $\lambda = 2\pi c/\omega = 10^5 a$, with a the lattice spacing. The symbols correspond to different values of the cavity detuning: $\Delta = 0.5\omega$ (orange), $\Delta = 0.1\omega$ (red), $\Delta = 0.05\omega$ (purple) and $\Delta = 0.01\omega$ (green). The dashed curves correspond to the fitted power laws, with exponents reported in the legend.

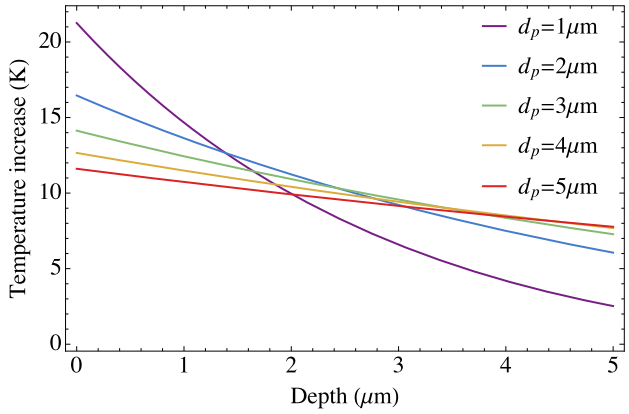

Fig. 5 Heating effects. Laser-induced temperature increase as a function of the depth in the sample, for different values of the laser penetration depths.

which features orbital pseudospin, and whose low-temperature properties have been intensely studied[46]. In order to estimate the heating of the material surface due to the external laser, we evaluate the energy density deposited by the laser using the formula:

$$\epsilon(z) = (1-R)\frac{\mathcal{F}}{d_{\rm p}} e^{-\frac{z}{d_{\rm p}}}, \tag{15}$$

with z the depth in the sample, $R \sim 0.05$ the material reflectivity at the laser frequency considered, i.e. 100 THz (cf. ref. [53]), $d_{\rm p}$ the penetration depth, chosen of an order of micrometres and $\mathcal{F}$ is the excitation energy density. In order to achieve lasing in the desired frequency range, a short-pulse protocol can be used. By considering pulses of ~10 ps, and maximal laser intensity of 10 MW cm^{-2}, we require $\mathcal{F} = 10^{-5}$ J cm^{-2}. In order to estimate the increase in temperature due to the deposited energy density $\epsilon(z)$, we assume that thermalization time is fast, and use the following relation:

$$\epsilon(z) = \frac{1}{V_{\rm m}} \int_{T_0}^{T_{\rm f}(z)} C_{\rm p}(T) {\rm d}T, \tag{16}$$

where $V_{\rm m} = 53.32$ cm^3 mol^{-1} is the molar volume of α-$RuCl_3$, and $C_{\rm p}$ is the molar heat capacity, for which we use the value fitted from the measurements of ref. [54], and T_0 is the initial temperature in the sample. For an initial temperature of $T_0 = 2$ K, the rise in temperature as a function of z and for different values of the penetration length $d_{\rm p}$ are reported in Fig. 5 here. The estimated temperature increase in the first layers is in between 5 and 20 K, depending on the penetration depth. In order to understand the impact of heating on the candidate QSL phases, a simple criterion compares the temperature increase with the gap (at least for the gapped spin liquid phase, which we dubbed SL-I in the main text). Robustness of the QSL phase then requires the temperature increase to be smaller than the gap, whose scale is given by the material couplings and by the cavity-induced interaction. For α-$RuCl_3$, as discussed in the main text, interactions lie between 40 and 80 K. Accordingly, the heating induced by the laser is not expected to destabilize the gapped QSL phase. For what concerns the gapless QSL phase (SL-II in the main text), the previous argument is clearly inapplicable, and its robustness against thermal fluctuations must be assessed using a more sophisticated approach, e.g. by solving the saddle-point equations at finite temperature.

Code availability

The code that supports the plots within this paper is available from the corresponding author upon reasonable request.

Received: 22 October 2020; Accepted: 16 September 2021;
Published online: 08 October 2021

References

1. Savary, L. & Balents, L. Quantum spin liquids: a review. *Rep. Prog. Phys.* **80**, 016502 (2016).
2. Zhou, Y. I., Kanoda, K. & Ng, Tai-Kai Quantum spin liquid states. *Rev. Mod. Phys.* **89**, 025003 (2017).
3. Knolle, J. & Moessner, R. A field guide to spin liquids. *Annu. Rev. Condens. Matter Phys.* **10**, 451–472 (2019).
4. Balents, L. Spin liquids in frustrated magnets. *Nature* **464**, 199–208 (2010).
5. Castelnovo, C., Moessner, R. & Sondhi, S. L. Spin ice, fractionalization, and topological order. *Annu. Rev. Condens. Matter Phys.* **3**, 35–55 (2012).
6. Gingras, M. J. P. & McClarty, P. A. Quantum spin ice: a search for gapless quantum spin liquids in pyrochlore magnets. *Rep. Prog. Phys.* **77**, 056501 (2014).
7. Norman, M. R. Colloquium: Herbertsmithite and the search for the quantum spin liquid. *Rev. Mod. Phys.* **88**, 041002 (2016).
8. Yao, N. Y., Zaletel, M. P., Stamper-Kurn, D. M. & Vishwanath, A. A quantum dipolar spin liquid. *Nat. Phys.* **14**, 405–410 (2018).
9. Zou, H., Zhao, E. & Liu, W. V. Frustrated magnetism of dipolar molecules on a square optical lattice: prediction of a quantum paramagnetic ground state. *Phys. Rev. Lett.* **119**, 050401 (2017).
10. Keleş, A. & Zhao, E. Absence of long-range order in a triangular spin system with dipolar interactions. *Phys. Rev. Lett.* **120**, 187202 (2018).
11. Sentef, M. A., Ruggenthaler, M. & Rubio, A. Cavity quantum-electrodynamical polaritonically enhanced electron-phonon coupling and its influence on superconductivity. *Sci. Adv.* **4**, eaau6969 (2018).
12. Mazza, G. & Georges, A. Superradiant quantum materials. *Phys. Rev. Lett.* **122**, 017401 (2019).
13. Andolina, G. M., Pellegrino, F. M. D., Giovannetti, V., MacDonald, A. H. & Polini, M. Cavity quantum electrodynamics of strongly correlated electron systems: a no-go theorem for photon condensation. *Phys. Rev. B* **100**, 121109 (2019).
14. Schlawin, F., Cavalleri, A. & Jaksch, D. Cavity-mediated electron-photon superconductivity. *Phys. Rev. Lett.* **122**, 133602 (2019).
15. Curtis, J. B., Raines, Z. M., Allocca, A. A., Hafezi, M. & Galitski, V. M. Cavity quantum eliashberg enhancement of superconductivity. *Phys. Rev. Lett.* **122**, 167002 (2019).
16. Thomas, A. et al. Exploring superconductivity under strong coupling with the vacuum electromagnetic field. Preprint at *arXiv* https://arxiv.org/abs/1911.01459 (2019).
17. Gao, H., Schlawin, F., Buzzi, M., Cavalleri, A. & Jaksch, D. Photoinduced electron pairing in a driven cavity. *Phys. Rev. Lett.* **125**, 053602 (2020).
18. Ashida, Y. et al. Quantum electrodynamic control of matter: cavity-enhanced ferroelectric phase transition. *Phys. Rev. X* **10**, 041027 (2020).
19. Schuler, M., Bernardis, DanieleDe, Läuchli, A. M. & Rabl, P. The vacua of dipolar cavity quantum electrodynamics. *SciPost Phys.* **9**, 66 (2020).
20. Chakraborty, A. & Piazza, F. Non-bcs-type enhancement of superconductivity from long-range photon fluctuations. Preprint at *arXiv* https://arxiv.org/abs/2008.06513 (2020).
21. Sentef, M. A., Li, J., Künzel, F. & Eckstein, M. Quantum to classical crossover of floquet engineering in correlated quantum systems. *Phys. Rev. Res.* **2**, 033033 (2020).
22. Kiffner, M., Coulthard, J. R., Schlawin, F., Ardavan, A. & Jaksch, D. Manipulating quantum materials with quantum light. *Phys. Rev. B* **99**, 085116 (2019).
23. Auerbach, A. *Interacting Electrons and Quantum Magnetism* (Springer Science & Business Media, 2012)
24. Liang, S., Doucot, B. & Anderson, P. W. Some new variational resonating-valence-bond-type wave functions for the spin- antiferromagnetic heisenberg model on a square lattice. *Phys. Rev. Lett.* **61**, 365–368 (1988).

25. Arovas, D. P. & Auerbach, A. Functional integral theories of low-dimensional quantum heisenberg models. *Phys. Rev. B* **38**, 316–332 (1988).
26. Read, N. & Sachdev, S. Large-n expansion for frustrated quantum antiferromagnets. *Phys. Rev. Lett.* **66**, 1773–1776 (1991).
27. Ceccatto, H. A., Gazza, C. J. & Trumper, A. E. Nonclassical disordered phase in the strong quantum limit of frustrated antiferromagnets. *Phys. Rev. B* **47**, 12329–12332 (1993).
28. Wen, Xiao-Gang Quantum orders and symmetric spin liquids. *Phys. Rev. B* **65**, 165113 (2002).
29. Sorella, S., Otsuka, Y. & Yunoki, S. Absence of a spin liquid phase in the hubbard model on the honeycomb lattice. *Sci. Rep.* **2**, 992 (2012).
30. Golinelli, O., Jolicoeur, T. H. & Lacaze, R. Finite-lattice extrapolations for a haldane-gap antiferromagnet. *Phys. Rev. B* **50**, 3037–3044 (1994).
31. Campa, A., Dauxois, T., Fanelli, D., & Ruffo, S. *Physics of Long-Range Interacting Systems* (Oxford Univ. Press, 2014).
32. Hauke, P. et al. Complete devil's staircase and crystal-superfluid transitions in a dipolarXXZspin chain: a trapped ion quantum simulation. *N. J. Phys.* **12**, 113037 (2010).
33. Koffel, T., Lewenstein, M. & Tagliacozzo, L. Entanglement entropy for the long-range ising chain in a transverse field. *Phys. Rev. Lett.* **109**, 267203 (2012).
34. Peter, D., Müller, S., Wessel, S. & Büchler, H. P. Anomalous behavior of spin systems with dipolar interactions. *Phys. Rev. Lett.* **109**, 025303 (2012).
35. Messio, L., Cépas, O. & Lhuillier, C. Schwinger-boson approach to the kagome antiferromagnet with dzyaloshinskii-moriya interactions: phase diagram and dynamical structure factors. *Phys. Rev. B* **81**, 064428 (2010).
36. Richerme, P. et al. Non-local propagation of correlations in quantum systems with long-range interactions. *Nature* **511**, 198–201 (2014).
37. Mivehvar, F., Piazza, F., Donner, T., & Ritsch, H. Cavity qed with quantum gases: new paradigms in many-body physics. Preprint at *arXiv* https://doi.org/10.22331/q-2021-07-13-501 (2021).
38. Kennes, D. M. et al. Moiréheterostructures as a condensed-matter quantum simulator. *Nat. Phys.* **17**, 155–163 (2021).
39. Jackeli, G. & Khaliullin, G. Mott insulators in the strong spin-orbit coupling limit: From heisenberg to a quantum compass and kitaev models. *Phys. Rev. Lett.* **102**, 017205 (2009).
40. Georges, A., de' Medici, L. & Mravlje, J. Strong correlations from hund's coupling. *Annu. Rev. Condens. Matter Phys.* **4**, 137–178 (2013).
41. Rau, J. G., Lee, EricKin-Ho & Kee, Hae-Young Spin-orbit physics giving rise to novel phases in correlated systems: Iridates and related materials. *Annu. Rev. Condens. Matter Phys.* **7**, 195–221 (2016).
42. Mivehvar, F., Ritsch, H. & Piazza, F. Cavity-quantum-electrodynamical toolbox for quantum magnetism. *Phys. Rev. Lett.* **122**, 113603 (2019).
43. Joannopoulos, J. D., Johnson, S. G., Winn, J. N., & Meade, R. D. *Photonic Crystals: Molding the Flow of Light* 2nd edn (Princeton Univ. Press, 2008).
44. Melzi, R. et al. $li_2VO(si, ge)O_4$, a prototype of a two-dimensional frustrated quantum heisenberg antiferromagnet. *Phys. Rev. Lett.* **85**, 1318–1321 (2000).
45. Kim, J. et al. Magnetic excitation spectra of sr_2iro_4 probed by resonant inelastic x-ray scattering: establishing links to cuprate superconductors. *Phys. Rev. Lett.* **108**, 177003 (2012).
46. Banerjee, A. et al. Proximate kitaev quantum spin liquid behaviour in a honeycomb magnet. *Nat. Mater.* **15**, 733–740 (2016).
47. Jurcevic, P. et al. Quasiparticle engineering and entanglement propagation in a quantum many-body system. *Nature* **511**, 202–205 (2014).
48. Landini, M., Dogra, N., Kroeger, K., Hruby, L., Donner, T. & Esslinger, T. Formation of a spin texture in a quantum gas coupled to a cavity. *Phys. Rev. Lett.* **120**, 223602 (2018).
49. Kroeze, R. M., Guo, Y., Vaidya, V. D., Keeling, J. & Lev, B. L. Spinor self-ordering of a quantum gas in a cavity. *Phys. Rev. Lett.* **121**, 163601 (2018).
50. Krešić, I. et al. Spontaneous light-mediated magnetism in cold atoms. *Commun. Phys.* **1**, 1–9 (2018).
51. Davis, E. J., Bentsen, G., Homeier, L., Li, T. & Schleier-Smith, M. H. Photon-mediated spin-exchange dynamics of spin-1 atoms. *Phys. Rev. Lett.* **122**, 010405 (2019).
52. Gao, H., Schlawin, F., Buzzi, M., Cavalleri, A. & Jaksch, D. Photoinduced electron pairing in a driven cavity. *Phys. Rev. Lett.* **125**, 053602 (2020).
53. Reschke, S., Mayr, F., Wang, Z., Do, Seung-Hwan, Choi, K.-Y. & Loidl, A. Electronic and phonon excitations in $\alpha - RuCl_3$. *Phys. Rev. B* **96**, 165120 (2017).
54. Cao, H. B. et al. Low-temperature crystal and magnetic structure of $\alpha - rucl_3$. *Phys. Rev. B* **93**, 134423 (2016).

Acknowledgements

We warmly acknowledge discussions with C. Hickey, G. Mazza, A. Rosch, M. Scherer and especially S. Trebst. We acknowledge support by the funding from the European Research Council (ERC) under the Horizon 2020 research and innovation programme, Grant Agreement No. 647434 (DOQS), and by the DFG Collaborative Research Centre (CRC) 1238 Project No. 277146847—projects C02, C03 and C04.

Author contributions

S.D. and A.C. designed the research, D.K. performed the numerical simulations, A.C. and F.P. developed the implementation scheme. C.P.Z. computed and analysed the dynamical structure factor data. All authors analysed the results and contributed to the manuscript.

Funding

Open Access funding enabled and organized by Projekt DEAL.

Competing interests

The authors declare no competing interests.

Additional information

Correspondence and requests for materials should be addressed to Alessio Chiocchetta.

Peer review information *Nature Communications* thanks the anonymous reviewers for their contribution to the peer review of this work.

Reprints and permission information is available at http://www.nature.com/reprints

Publisher's note Springer Nature remains neutral with regard to jurisdictional claims in published maps and institutional affiliations.

8 Conclusion and Outlook

In this thesis, two efficient numerical implementations of the functional renormalization group were developed. More specifically, N-patch fRG was employed to study competing orders of weakly-coupled spinless fermions on the triangular lattice. Even for purely repulsive interactions, we were able to demonstrate the opening of superconducting gaps with different symmetries. Here, Cooper pairing was prominently driven by charge fluctuations, which become sizable enough to mediate inter-electron attraction in vicinity of van-Hove filling. To tackle quantum spin systems, corresponding to localized electrons in the strong-coupling limit, we picked up the pseudofermion functional renormalization group method. In the last decade, pffRG has become an auspicious tool to map out phase diagrams of frustrated magnets, yet, elementary questions about the validity of its inherent approximations have been left unanswered. Going beyond the widely used 1ℓ truncation of the flow equations using multiloop fRG, we could prove convergence to solutions of the parquet approximation for several energy scales, which attests to the method's consistency. Moreover, we scrutinized fulfillment of the pseudofermion constraint by explicitly computing occupation number fluctuations. Although sites are half-filled on average, sizable fluctuations persisted even if the RG scale Λ was reduced below the energy scale set by the spin coupling. Qualitative features of the flow, on the other hand, appeared remarkably robust against the occupation of unphysical states with net-spin zero. Finally, a generalization of pffRG to spin-valley coupled Hamiltonians in the self-conjugate representation of $\mathfrak{su}(4)$ was presented and fRG results for additional model systems were discussed.

A central message we wanted to convey with this work is that highly accurate fRG flows and feasible computing times do not exclude themselves. Many implementations, be it for weakly [153, 154] or strongly-coupled electron systems [17, 18], have opted for inferior integration techniques regarding both precision and robustness of the obtained results. From our point of view, this is for one of two reasons: One could, in principle, argue that systematic deficiencies, such as the regulator dependence of 1ℓ flows induced by truncating the three-particle vertex, overshadow numerical errors. In other words, no matter how accurate the numerical results, principal approximations cannot be made up for. Second, fRG calculations appear to be quite expensive from the outset. Recall that the two-particle vertex for itinerant electron models requires three momentum and frequency arguments even after exploiting translation invariance. For two-dimensional systems, this implies that the number of effective couplings grows as $N_{\boldsymbol{k}}^6 N_\omega^3$, where $N_{\boldsymbol{k}}$ is the number of momenta along one axis of the Brillouin zone and N_ω the number of Matsubara frequencies. It might therefore seem appealing to reduce computing times by falling back to low-confidence methods. Both lines of reasoning, however, come with their own flaws. Indeed, fRG is based on systematic and sometimes even uncontrolled approximations, but how are we supposed to gauge their impact on the results if we allow ourselves to be sloppy with the numerical implementation? As an example, consider the multiloop truncation. In theory, mfRG should overcome many shortcomings of traditional 1ℓ flows. Yet, this approach is based on successive insertions of bubble integrals into each other. Hence, numerical errors invoked by 1ℓ diagrams will proliferate into higher orders, which makes conclusions regarding loop convergence appear like mere speculation. The second argument, on the other hand, is likely based on the perception that adaptive quadrature based on higher-order methods is too expensive to pursue. As we have demonstrated for the calculation of loop functions in N-patch fRG and Matsubara integrals in pffRG, this does not adhere to the truth. For sure, performing integrations with higher-order quadrature rules initially requires more function evaluations, which, especially in fRG, are quite costly. Tuning these in such a way that they cope with the structure of the integrand, however, renders them extremely efficient, since subsequent refinements of the integration domain are only necessary in regions where sharp features emerge. In all other cases, convergence is rapid and thus numerically cheap. Moreover, already the calculation of bare susceptibilities revealed that this procedure is essential for producing stable results especially in the low-energy regime.

Through publishment of the `PFFRGSolver` Julia package [P1, P2], we aimed at providing a coherent numerical standard for the simulation of quantum spin systems with pseudofermion fRG, while reducing the entry barrier for newcomers to the field. Our code combines the technical achievements of this thesis embedded into a performance oriented backend with a plug-and-play style user interface. In the spirit of similar efforts from the weak-coupling community [153], we strongly believe that this step helps to advance the method by bringing it forth to a wider audience. This way, long-standing quests, such as the calculation of dynamic structure factors from a full-fledged Keldysh pffRG implementation or the generalization to finite temperatures in conjuction with the Popov-Fedotov trick, come within

reach.

With the advent of (twisted) moiré heterostructures, many new and exciting platforms for the study of strongly correlated electron physics have emerged. One of their most fascinating trademarks is the broad landscape of quantum models they can harbor, ranging from extensions of the Hubbard model [82, 83, 155–157] to spin-valley entangled Hamiltonians in the strong-coupling limit [16, P3, P7, 152], which hold promise for the realization of elusive spin-valley liquids [158, 159]. Their unbiased theoretical simulation using fRG, however, poses numerous challenges. First of all, the dimension of the local Hilbert space is usually enhanced by additional orbital degrees of freedom, such that their electronic band structure involves multiple bands with intricate Fermi surface topologies [54, 77–79, 82, 83]. Second, mapping out phase diagrams for hexagonal superlattices with frustrated interactions will certainly require fine grained momentum space grids to resolve the interplay of competing orders at low temperatures. For field-theoretical approaches such as fRG, compact representations of two-particles vertices are therefore of paramount importance. Fortunately, several techniques for reducing the numerical cost of computing and storing Γ have recently been proposed. These include, for example, truncated unity approximations [39, 45, 46, 153, 154] or the single boson exchange decomposition [160, 161], the former based on an expansion of the vertex's momentum dependence into analytic form factors, the latter representing Γ in terms of three-leg Hedin vertices coupled by bosonic fluctuations. Their implementation within (multiloop) fRG, combined with the methodological advances and numerical achievements of this thesis, paves a promising avenue for future explorations of exotic ground states in the ever growing manifold of moiré materials.

Bibliography

[P1] D. Kiese et al., *Multiloop Functional Renormalization Group Approach to Quantum Spin Systems*, Physical Review Research **4**, 023185 (2022).

[P2] M. K. Ritter et al., *Benchmark calculations of multiloop pseudofermion fRG*, The European Physical Journal B **95**, 102 (2022).

[P3] L. Gresista, D. Kiese, and S. Trebst, *Moments and multiplets in moiré materials*, The European Physical Journal B **95**, 119 (2022).

[P4] N. Gneist et al., *Functional renormalization of spinless triangular-lattice fermions: N-patch vs. truncated-unity scheme*, arXiv:2205.12547 (2022).

[P5] D. Kiese et al., *Pinch-points to half-moons and up in the stars: the kagome skymap*, arXiv:2206.00264 (2022).

[P6] D. Kiese et al., *TMDs as a platform for spin liquid physics: A strong coupling study of twisted bilayer WSe_2*, APL Materials **10**, 031113 (2022).

[P7] D. Kiese et al., *Emergence and stability of spin-valley entangled quantum liquids in moiré heterostructures*, Physical Review Research **2**, 013370 (2020).

[P8] L. Xian et al., *Realization of nearly dispersionless bands with strong orbital anisotropy from destructive interference in twisted bilayer MoS2*, Nature Communications **12**, 5644 (2021).

[P9] A. Chiocchetta et al., *Cavity-induced quantum spin liquids*, Nature Communications **12**, 5901 (2021).

[1] D. P. Arovas, E. Berg, S. A. Kivelson, and S. Raghu, *The Hubbard Model*, Annual Review of Condensed Matter Physics **13**, 239274 (2022).

[2] Editorial, *The Hubbard model at half a century*, Nature Physics **9**, 523 (2013).

[3] G. Benfatto, A. Giuliani, and V. Mastropietro, *Fermi Liquid Behavior in the 2D Hubbard Model at Low Temperatures*, Annales Henri Poincaré **7**, 809898 (2006).

[4] L. N. Cooper, *Bound Electron Pairs in a Degenerate Fermi Gas*, Physical Review **104**, 11891190 (1956).

[5] S. Maiti and A. V. Chubukov, *Superconductivity from repulsive interaction*, AIP Conference Proceedings, 373 (2013).

[6] J. Bardeen, L. N. Cooper, and J. R. Schrieffer, *Theory of Superconductivity*, Physical Review **108**, 11751204 (1957).

[7] A. Kitaev, *Anyons in an exactly solved model and beyond*, Annals of Physics **321**, 2111 (2006).

[8] Y. Kasahara et al., *Majorana quantization and half-integer thermal quantum Hall effect in a Kitaev spin liquid*, Nature **559**, 227231 (2018).

[9] X.-G. Wen, *Quantum orders and symmetric spin liquids*, Physical Review B **65**, 165113 (2002).

[10] L. Balents, *Spin liquids in frustrated magnets*, Nature **464**, 199208 (2010).

[11] W. Metzner et al., *Functional renormalization group approach to correlated fermion systems*, Reviews of Modern Physics **84**, 299352 (2012).

[12] A. Georges, G. Kotliar, W. Krauth, and M. J. Rozenberg, *Dynamical mean-field theory of strongly correlated fermion systems and the limit of infinite dimensions*, Reviews of Modern Physics **68**, 13125 (1996).

[13] U. Schollwöck, *The density-matrix renormalization group in the age of matrix product states*, Annals of Physics **326**, 96192 (2011).

[14] R. Orús, *Tensor networks for complex quantum systems*, Nature Reviews Physics **1**, 538550 (2019).

[15] P. Kopietz, *Introduction to the Functional Renormalization Group*, Lecture Notes in Physics **798** (2009).

[16] Y.-H. Zhang and T. Senthil, *Bridging Hubbard model physics and quantum Hall physics in trilayer graphene/h − BN moiré superlattice*, Physical Review B **99**, 205150 (2019).

[17] F. L. Buessen, *A Functional Renormalization Group Perspective on Quantum Spin Liquids in Three-Dimensional Frustrated Magnets*, PhD thesis, University of Cologne (2019).

[18] J. Reuther, *Frustrated Quantum Heisenberg Antiferromagnets: Functional Renormalization-Group Approach in Auxiliary-Fermion Representation*, PhD thesis, Institute of Technology Karlsruhe (2011).

[19] J. Polchinski, *Renormalization and effective lagrangians*, Nuclear Physics B **231**, 269295 (1984).

[20] C. Wetterich, *Exact evolution equation for the effective potential*, Physics Letters B **301**, 9094 (1993).

[21] Honerkamp, C., Salmhofer, M., and Rice, T. M., *Flow to strong coupling in the two-dimensional Hubbard model*, The European Physical Journal B **27**, 127134 (2002).

[22] J. Reuther and P. Wölfle, J_1-J_2 *frustrated two-dimensional Heisenberg model: Random phase approximation and functional renormalization group*, Physical Review B **81**, 144410 (2010).

[23] N. Niggemann, B. Sbierski, and J. Reuther, *Frustrated quantum spins at finite temperature: Pseudo-Majorana functional renormalization group approach*, Physical Review B **103**, 104431 (2021).

[24] S. Andergassen et al., *Functional renormalization group for Luttinger liquids with impurities*, Physical Review B **70**, 075102 (2004).

[25] C. Karrasch et al., *A finite-frequency functional renormalization group approach to the single impurity Anderson model*, Journal of Physics: Condensed Matter **20**, 345205 (2008).

[26] A. A. Katanin, *Fulfillment of Ward identities in the functional renormalization group approach*, Physical Review B **70**, 115109 (2004).

[27] A. Eberlein, *Fermionic two-loop functional renormalization group for correlated fermions: Method and application to the attractive Hubbard model*, Physical Review B **90**, 115125 (2014).

[28] F. B. Kugler and J. von Delft, *Multiloop functional renormalization group for general models*, Physical Review B **97**, 035162 (2018).

[29] B. Roulet, J. Gavoret, and P. Nozières, *Singularities in the X-Ray Absorption and Emission of Metals. I. First-Order Parquet Calculation*, Physical Review **178**, 10721083 (1969).

[30] F. B. Kugler, *Renormalization group approaches to strongly correlated electron systems*, PhD thesis, Ludwig-Maximilians-Universität München (2019).

[31] N. E. Bickers and D. J. Scalapino, *Critical behavior of electronic parquet solutions*, Physical Review B **46**, 80508056 (1992).

[32] F. B. Kugler and J. von Delft, *Derivation of exact flow equations from the self-consistent parquet relations*, New Journal of Physics **20** (2018).

[33] P. Chalupa-Gantner et al., *Fulfillment of sum rules and Ward identities in the multiloop functional renormalization group solution of the Anderson impurity model*, arXiv:2110.07455 (2021).

[34] R. Shankar, *Renormalization-group approach to interacting fermions*, Reviews of Modern Physics **66**, 129192 (1994).

[35] H. Zhai, F. Wang, and D.-H. Lee, *Antiferromagnetically driven electronic correlations in iron pnictides and cuprates*, Physical Review B **80**, 064517 (2009).

[36] D. Zanchi and H. J. Schulz, *Weakly correlated electrons on a square lattice: Renormalization-group theory*, Physical Review B **61**, 1360913632 (2000).

[37] L. Klebl et al., *Competition of Density Waves and Superconductivity in Twisted Tungsten Diselenide*, arXiv:2204.00648 (2022).

[38] L. Klebl et al., *Moiré engineering of spin–orbit coupling in twisted platinum diselenide*, Electronic Structure **4**, 014004 (2022).

[39] N. Gneist, L. Classen, and M. M. Scherer, *Competing instabilities of the extended Hubbard model on the triangular lattice: Truncated-unity functional renormalization group and application to moiré materials*, arXiv:2203.01226 (2022).

[40] M. M. Scherer, D. M. Kennes, and L. Classen, $\mathcal{N} = 4$ *chiral superconductivity in moiré transition metal dichalcogenides*, arXiv:2108.11406 (2021).

[41] C. Hille et al., *Quantitative functional renormalization group description of the two-dimensional Hubbard model*, Physical Review Research **2**, 033372 (2020).

[42] C. Husemann and M. Salmhofer, *Efficient parametrization of the vertex function, Ω scheme, and the t, t' Hubbard model at van Hove filling*, Physical Review B **79**, 195125 (2009).

[43] F. B. Kugler and J. von Delft, *Multiloop Functional Renormalization Group That Sums Up All Parquet Diagrams*, Physical Review Letters **120**, 057403 (2018).

[44] J. Beyer, F. Goth, and T. Müller, *Better Integrators for Functional Renormalization Group Calculations*, arXiv:2203.15306 (2022).

[45] J. Lichtenstein et al., *High-performance functional Renormalization Group calculations for interacting fermions*, Computer Physics Communications **213**, 100110 (2017).

[46] J. B. Hauck and D. M. Kennes, *TU^{2}FRG: a scalable approach for truncated unity functional renormalization group in generic fermionic models*, The European Physical Journal B **95**, 60 (2022).

[47] A. Tagliavini et al., *Multiloop functional renormalization group for the two-dimensional Hubbard model: Loop convergence of the response functions*, SciPost Physics **6**, 9 (2019).

[48] C. Hille, D. Rohe, C. Honerkamp, and S. Andergassen, *Pseudogap opening in the two-dimensional Hubbard model: A functional renormalization group analysis*, Physical Review Research **2**, 033068 (2020).

[49] H. Kamerlingh Onnes, *Further experiments with liquid helium. C. On the change of electric resistance of pure metals at very low temperatures etc. IV. The resistance of pure mercury at helium temperatures*, Koninklijke Nederlandse Akademie van Wetenschappen Proceedings Series B Physical Sciences **13**, 12741276 (1910).

[50] W. Meissner and R. Ochsenfeld, *Ein neuer Effekt bei Eintritt der Supraleitfähigkeit*, Die Naturwissenschaften **21**, 787788 (1933).

[51] S. Kittaka et al., *Multiband Superconductivity with Unexpected Deficiency of Nodal Quasiparticles in* $CeCu_2Si_2$, Physical Review Letters **112**, 067002 (2014).

[52] Y. Maeno et al., *Superconductivity in a layered perovskite without copper*, Nature **372**, 532534 (1994).

[53] Y. Cao et al., *Unconventional superconductivity in magic-angle graphene superlattices*, Nature **556**, 4350 (2018).

[54] R. Bistritzer and A. H. MacDonald, *Moiré bands in twisted double-layer graphene*, Proceedings of the National Academy of Sciences **108**, 1223312237 (2011).

[55] X. Lu et al., *Superconductors, orbital magnets and correlated states in magic-angle bilayer graphene*, Nature **574**, 653657 (2019).

[56] D. M. Kennes et al., *Moiré heterostructures as a condensed-matter quantum simulator*, Nature Physics **17**, 155163 (2021).

[57] B. R. Ortiz et al., CsV_3Sb_5*: A* $\mathbb{Z}_2$ *Topological Kagome Metal with a Superconducting Ground State*, Physical Review Letters **125**, 247002 (2020).

[58] M. L. Kiesel and R. Thomale, *Sublattice interference in the kagome Hubbard model*, Physical Review B **86**, 121105 (2012).

[59] M. Sigrist and K. Ueda, *Phenomenological theory of unconventional superconductivity*, Reviews of Modern Physics **63**, 239311 (1991).

[60] C. Platt, *A Common Thread in Unconventional Superconductivity: The Functional Renormalization Group in Multi-Band Systems*, PhD thesis, Universität Würzburg (2012).

[61] A. M. Black-Schaffer and C. Honerkamp, *Chiral d-wave superconductivity in doped graphene*, Journal of Physics: Condensed Matter **26**, 423201 (2014).

[62] A. Altland and M. R. Zirnbauer, *Nonstandard symmetry classes in mesoscopic normal-superconducting hybrid structures*, Physical Review B **55**, 11421161 (1997).

[63] G. E. Volovik, *On edge states in superconductors with time inversion symmetry breaking*, Journal of Experimental and Theoretical Physics Letters **66**, 522527 (1997).

[64] D. J. Thouless, M. Kohmoto, M. P. Nightingale, and M. den Nijs, *Quantized Hall Conductance in a Two-Dimensional Periodic Potential*, Physical Review Letters **49**, 405408 (1982).

[65] M. Z. Hasan and C. L. Kane, *Colloquium: Topological insulators*, Reviews of Modern Physics **82**, 30453067 (2010).

[66] C. Honerkamp, D. Rohe, S. Andergassen, and T. Enss, *Interaction flow method for many-fermion systems*, Physical Review B **70**, 235115 (2004).

[67] C. Honerkamp and M. Salmhofer, *Temperature-flow renormalization group and the competition between superconductivity and ferromagnetism*, Physical Review B **64**, 184516 (2001).

[68] P. Bogacki and L. Shampine, *A 3(2) pair of Runge - Kutta formulas*, Applied Mathematics Letters **2**, 321325 (1989).

[69] W. H. Press, S. A. Teukolsky, W. T. Vetterling, and B. P. Flannery, *Numerical Recipes 3rd Edition: The Art of Scientific Computing*, Cambridge University Press (2007).

[70] F. L. Buessen, D. Roscher, S. Diehl, and S. Trebst, *Functional renormalization group approach to SU(N) Heisenberg models: Real-space renormalization group at arbitrary N*, Physical Review B **97**, 064415 (2018).

[71] H. Zhai, F. Wang, and D.-H. Lee, *Antiferromagnetically driven electronic correlations in iron pnictides and cuprates*, Physical Review B **80**, 064517 (2009).

[72] T. Schäfer et al., *Tracking the Footprints of Spin Fluctuations: A MultiMethod, MultiMessenger Study of the Two-Dimensional Hubbard Model*, Physical Review X **11**, 011058 (2021).

[73] Y. Cao et al., *Correlated insulator behaviour at half-filling in magic-angle graphene superlattices*, Nature **556**, 8084 (2018).

[74] L. Wang et al., *Correlated electronic phases in twisted bilayer transition metal dichalcogenides*, Nature Materials **19**, 861866 (2020).

[75] L. An et al., *Interaction effects and superconductivity signatures in twisted double-bilayer WSe_2*, Nanoscale Horizons **5**, 13091316 (2020).

[76] H. S. Arora et al., *Superconductivity in metallic twisted bilayer graphene stabilized by WSe_2*, Nature **583**, 379384 (2020).

[77] F. Wu, T. Lovorn, E. Tutuc, and A. H. MacDonald, *Hubbard Model Physics in Transition Metal Dichalcogenide Moiré Bands*, Physical Review Letters **121**, 026402 (2018).

[78] F. Wu et al., *Topological Insulators in Twisted Transition Metal Dichalcogenide Homobilayers*, Physical Review Letters **122**, 086402 (2019).

[79] M. Angeli and A. H. MacDonald, Γ *valley transition metal dichalcogenide Moiré bands*, Proceedings of the National Academy of Sciences **118**, 2021826118 (2021).

[80] M. H. Naik and M. Jain, *Ultraflatbands and shear solitons in moiré patterns of twisted bilayer transition metal dichalcogenides*, Physical Review Letters **121**, 266401 (2018).

[81] E. C. Regan et al., *Mott and generalized Wigner crystal states in WSe_2/WS_2 moiré superlattices*, Nature **579**, 359363 (2020).

[82] J. Zang, J. Wang, J. Cano, and A. J. Millis, *Hartree-Fock study of the moiré Hubbard model for twisted bilayer transition metal dichalcogenides*, Physical Review B **104** (2021).

[83] H. Pan, F. Wu, and S. Das Sarma, *Band topology, Hubbard model, Heisenberg model, and Dzyaloshinskii-Moriya interaction in twisted bilayer WSe_2*, Physical Review Research **2**, 033087 (2020).

[84] M. Cheng, K. Sun, V. Galitski, and S. Das Sarma, *Stable topological superconductivity in a family of two-dimensional fermion models*, Physical Review B **81**, 024504 (2010).

[85] M. L. Baez and J. Reuther, *Numerical treatment of spin systems with unrestricted spin length S: A functional renormalization group study*, Physical Review B **96**, 045144 (2017).

[86] J. Reuther and R. Thomale, *Functional renormalization group for the anisotropic triangular antiferromagnet*, Physical Review B **83**, 024402 (2011).

[87] J. Reuther et al., *Quantum phases of the planar antiferromagnetic $J_1 - J_2 - J_3$ Heisenberg model*, Physical Review B **83**, 064416 (2011).

[88] J. Reuther, D. A. Abanin, and R. Thomale, *Magnetic order and paramagnetic phases in the quantum J_1-J_2-J_3 honeycomb model*, Physical Review B **84**, 014417 (2011).

[89] J. Reuther, R. Thomale, and S. Trebst, *Finite-temperature phase diagram of the Heisenberg-Kitaev model*, Physical Review B **84**, 100406 (2011).

[90] J. Reuther, R. Thomale, and S. Rachel, *Magnetic ordering phenomena of interacting quantum spin Hall models*, Physical Review B **86**, 155127 (2012).

[91] J. Reuther and R. Thomale, *Cluster functional renormalization group*, Physical Review B **89**, 024412 (2014).

[92] R. Suttner, C. Platt, J. Reuther, and R. Thomale, *Renormalization group analysis of competing quantum phases in the J_1-J_2 Heisenberg model on the kagome lattice*, Physical Review B **89**, 020408 (2014).

[93] J. Reuther, R. Thomale, and S. Rachel, *Spiral order in the honeycomb iridate* Li_2IrO_3, Physical Review B **90**, 100405 (2014).

[94] I. Rousochatzakis et al., *Phase Diagram and Quantum Order by Disorder in the Kitaev $K_1 - K_2$ Honeycomb Magnet*, Physical Review X **5**, 041035 (2015).

[95] Y. Iqbal et al., *Paramagnetism in the kagome compounds* $(Zn, Mg, Cd)Cu_3(OH)_6Cl_2$, Physical Review B **92**, 220404 (2015).

[96] Y. Iqbal et al., *Spin liquid nature in the Heisenberg $J_1 - J_2$ triangular antiferromagnet*, Physical Review B **93**, 144411 (2016).

[97] Y. Iqbal et al., *Intertwined nematic orders in a frustrated ferromagnet*, Physical Review B **94**, 224403 (2016).

[98] F. L. Buessen and S. Trebst, *Competing magnetic orders and spin liquids in two- and three-dimensional kagome systems: Pseudofermion functional renormalization group perspective*, Physical Review B **94**, 235138 (2016).

[99] M. Laubach, J. Reuther, R. Thomale, and S. Rachel, *Three-band Hubbard model for* Na_2IrO_3*: Topological insulator, zigzag antiferromagnet, and Kitaev-Heisenberg material*, Physical Review B **96**, 121110 (2017).

[100] A. Keles and E. Zhao, *Absence of Long-Range Order in a Triangular Spin System with Dipolar Interactions*, Physical Review Letters **120**, 187202 (2018).

[101] A. Keles and E. Zhao, *Renormalization group analysis of dipolar Heisenberg model on square lattice*, Physical Review B **97**, 245105 (2018).

[102] K. Iida et al., *$q = 0$ long-range magnetic order in centennialite* $CaCu_3(OD)_6Cl_2 \cdot 0.6D_2O$*: A spin-$\frac{1}{2}$ perfect kagome antiferromagnet with $J_1 - J_2 - J_d$*, Physical Review B **101**, 220408 (2020).

[103] N. Astrakhantsev et al., *Pinwheel valence bond crystal ground state of the spin-$\frac{1}{2}$ Heisenberg antiferromagnet on the shuriken lattice*, Physical Review B **104**, 220408 (2021).

[104] C. Balz et al., *Physical realization of a quantum spin liquid based on a complex frustration mechanism*, Nature Physics **12**, 942949 (2016).

[105] Y. Iqbal et al., *Functional renormalization group for three-dimensional quantum magnetism*, Physical Review B **94**, 140408 (2016).

[106] Y. Iqbal et al., *Signatures of a gearwheel quantum spin liquid in a spin-$\frac{1}{2}$ pyrochlore molybdate Heisenberg antiferromagnet*, Physical Review Materials **1**, 071201 (2017).

[107] F. L. Buessen, M. Hering, J. Reuther, and S. Trebst, *Quantum Spin Liquids in Frustrated Spin-1 Diamond Antiferromagnets*, Physical Review Letters **120**, 057201 (2018).

[108] Y. Iqbal et al., *Stability of the spiral spin liquid in* $MnSc_2S_4$, Physical Review B **98**, 064427 (2018).

[109] Y. Iqbal et al., *Quantum and Classical Phases of the Pyrochlore Heisenberg Model with Competing Interactions*, Physical Review X **9**, 011005 (2019).

[110] P. Ghosh et al., *Quantum paramagnetism and helimagnetic orders in the Heisenberg model on the body centered cubic lattice*, Physical Review B **100**, 014420 (2019).

[111] A. Revelli et al., *Spin-orbit entangled $j = \frac{1}{2}$ moments in* Ba_2CeIrO_6*: A frustrated fcc quantum magnet*, Physical Review B **100**, 085139 (2019).

[112] N. Niggemann, M. Hering, and J. Reuther, *Classical spiral spin liquids as a possible route to quantum spin liquids*, Journal of Physics: Condensed Matter **32**, 024001 (2019).

[113] P. Ghosh et al., *Breathing chromium spinels: a showcase for a variety of pyrochlore Heisenberg Hamiltonians*, npj Quantum Materials **4**, 63 (2019).

[114] S. Chillal et al., *Evidence for a three-dimensional quantum spin liquid in* $PbCuTe_2O_6$, Nature Communications **11**, 2348 (2020).

[115] M. Rück and J. Reuther, *Effects of two-loop contributions in the pseudofermion functional renormalization group method for quantum spin systems*, Physical Review B **97**, 144404 (2018).

[116] J. Thoenniss et al., *Multiloop Pseudofermion Functional Renormalization for Quantum Spin Systems: Application to the Spin-$\frac{1}{2}$ Kagome Heisenberg Model*, arXiv:2011.01268 (2020).

[117] F. L. Buessen, V. Noculak, S. Trebst, and J. Reuther, *Functional renormalization group for frustrated magnets with nondiagonal spin interactions*, Physical Review B **100**, 125164 (2019).

[118] N. Wentzell et al., *High-frequency asymptotics of the vertex function: Diagrammatic parametrization and algorithmic implementation*, Physical Review B **102**, 085106 (2020).

[119] P. Anderson, *Resonating valence bonds: A new kind of insulator?*, Materials Research Bulletin **8**, 153160 (1973).

[120] L. Savary and L. Balents, *Quantum spin liquids: a review*, Reports on Progress in Physics **80**, 016502 (2016).

[121] S. Trebst, *Kitaev Materials*, arXiv:1701.07056 (2017).

[122] C. Hickey and S. Trebst, *Emergence of a field-driven U(1) spin liquid in the Kitaev honeycomb model*, Nature Communications **10**, 530 (2019).

[123] C. Hickey et al., *Field-driven gapless spin liquid in the spin-1 Kitaev honeycomb model*, Physical Review Research **2**, 023361 (2020).

[124] C. Hickey, M. Gohlke, C. Berke, and S. Trebst, *Generic field-driven phenomena in Kitaev spin liquids: Canted magnetism and proximate spin liquid physics*, Physical Review B **103**, 064417 (2021).

[125] C. Berke, S. Trebst, and C. Hickey, *Field stability of Majorana spin liquids in antiferromagnetic Kitaev models*, Physical Review B **101**, 214442 (2020).

[126] G. Jackeli and G. Khaliullin, *Mott Insulators in the Strong Spin-Orbit Coupling Limit: From Heisenberg to a Quantum Compass and Kitaev Models*, Physical Review Letters **102**, 017205 (2009).

[127] T. Itou et al., *Quantum spin liquid in the spin-1/2 triangular antiferromagnet* $EtMe_3Sb[Pd(dmit)_2]_2$, Physical Review B **77**, 104413 (2008).

[128] M. P. Shores, E. A. Nytko, B. M. Bartlett, and D. G. Nocera, *A Structurally Perfect $S = 1/2$ Kagomé Antiferromagnet*, Journal of the American Chemical Society **127**, 1346213463 (2005).

[129] M. J. P. Gingras and P. A. McClarty, *Quantum spin ice: a search for gapless quantum spin liquids in pyrochlore magnets*, Reports on Progress in Physics **77**, 056501 (2014).

[130] A. A. Abrikosov et al., *Possibility of Formulation of a Theory of Strongly Interacting Fermions*, Physical Review **111**, 321328 (1958).

[131] D. Roscher et al., *Functional renormalization group approach to $SU(N)$ Heisenberg models: Momentum-space renormalization group for the large-N limit*, Physical Review B **97**, 064416 (2018).

[132] V. Popov and S. Fedotov, *The functional-integration method and diagram technique for spin systems*, JETP **67** (1988).

[133] D. Roscher et al., *Cluster functional renormalization group and absence of a bilinear spin liquid in the J_1-J_2 Heisenberg model*, Physical Review B **100**, 125130 (2019).

[134] G. Li et al., *Efficient implementation of the parquet equations: Role of the reducible vertex function and its kernel approximation*, Physical Review B **93**, 165103 (2016).

[135] J. S. Dai, *Euler-Rodrigues formula variations, quaternion conjugation and intrinsic connections*, Mechanism and Machine Theory **92**, 144152 (2015).

[136] A. Genz and A. Malik, *Remarks on algorithm 006: An adaptive algorithm for numerical integration over an N-dimensional rectangular region*, Journal of Computational and Applied Mathematics **6**, 295302 (1980).

[137] S. M. Winter et al., *Models and materials for generalized Kitaev magnetism*, Journal of Physics: Condensed Matter **29**, 493002 (2017).

[138] S. Hu, W. Zhu, S. Eggert, and Y.-C. He, *Dirac Spin Liquid on the Spin-1/2 Triangular Heisenberg Antiferromagnet*, Physical Review Letters **123**, 207203 (2019).

[139] Z. Zhu and S. R. White, *Spin liquid phase of the $S = \frac{1}{2}$ $J_1 - J_2$ Heisenberg model on the triangular lattice*, Physical Review B **92**, 041105 (2015).

[140] A. Szasz, J. Motruk, M. P. Zaletel, and J. E. Moore, *Chiral Spin Liquid Phase of the Triangular Lattice Hubbard Model: A Density Matrix Renormalization Group Study*, Physical Review X **10**, 021042 (2020).

[141] N. Niggemann, J. Reuther, and B. Sbierski, *Quantitative functional renormalization for three-dimensional quantum Heisenberg models*, SciPost Physics **12**, 156 (2022).

[142] R. Orús, *A practical introduction to tensor networks: Matrix product states and projected entangled pair states*, Annals of Physics **349**, 117158 (2014).

[143] E. Stoudenmire and S. R. White, *Studying Two-Dimensional Systems with the Density Matrix Renormalization Group*, Annual Review of Condensed Matter Physics **3**, 111128 (2012).

[144] K. I. Kugel and D. I. Khomskii, *The Jahn-Teller effect and magnetism: transition metal compounds*, Soviet Physics Uspekhi **25**, 231256 (1982).

[145] T. Mizoguchi, L. D. C. Jaubert, R. Moessner, and M. Udagawa, *Magnetic clustering, half-moons, and shadow pinch points as signals of a proximate Coulomb phase in frustrated Heisenberg magnets*, Physical Review B **98**, 144446 (2018).

[146] X.-Y. Song, C. Wang, A. Vishwanath, and Y.-C. He, *Unifying description of competing orders in two-dimensional quantum magnets*, Nature Communications **10**, 4254 (2019).

[147] M. Hering and J. Reuther, *Functional renormalization group analysis of Dzyaloshinsky-Moriya and Heisenberg spin interactions on the kagome lattice*, Physical Review B **95**, 054418 (2017).

[148] Y. Iqbal et al., *Gutzwiller projected states for the J_1-J_2 Heisenberg model on the kagome lattice: achievements and pitfalls*, Physical Review B **104**, 144406 (2021).

[149] Z. Zeng et al., *Possible Dirac quantum spin liquid in the kagome quantum antiferromagnet* $YCu_3(OH)_6Br_2[Br_x(OH)_{1-x}]$, Physical Review B **105**, 121109 (2022).

[150] A. Revelli et al., *Fingerprints of Kitaev physics in the magnetic excitations of honeycomb iridates*, Physical Review Research **2**, 043094 (2020).

[151] J. W. F. Venderbos and R. M. Fernandes, *Correlations and electronic order in a two-orbital honeycomb lattice model for twisted bilayer graphene*, Physical Review B **98**, 245103 (2018).

[152] W. M. H. Natori, R. Nutakki, R. G. Pereira, and E. C. Andrade, *SU(4) Heisenberg model on the honeycomb lattice with exchange-frustrated perturbations: Implications for twistronics and Mott insulators*, Physical Review B **100**, 205131 (2019).

[153] J. Beyer, J. B. Hauck, and L. Klebl, *Reference results for the momentum space functional renormalization group*, The European Physical Journal B **95**, 65 (2022).

[154] S.-J. O et al., *Effect of exchange interaction on electronic instabilities in the honeycomb lattice: A functional renormalization group study*, Physical Review B **99**, 245140 (2019).

[155] C. Xu and L. Balents, *Topological Superconductivity in Twisted Multilayer Graphene*, Physical Review Letters **121**, 087001 (2018).

[156] N. F. Q. Yuan and L. Fu, *Model for the metal-insulator transition in graphene superlattices and beyond*, Physical Review B **98**, 045103 (2018).

[157] L. Classen, C. Honerkamp, and M. M. Scherer, *Competing phases of interacting electrons on triangular lattices in moiré heterostructures*, Physical Review B **99**, 195120 (2019).

[158] P. Corboz et al., *Spin-Orbital Quantum Liquid on the Honeycomb Lattice*, Physical Review X **2**, 041013 (2012).

[159] W. M. H. Natori, E. C. Andrade, and R. G. Pereira, *SU(4)-symmetric spin-orbital liquids on the hyperhoneycomb lattice*, Physical Review B **98**, 195113 (2018).

[160] F. Krien, A. Valli, and M. Capone, *Single-boson exchange decomposition of the vertex function*, Physical Review B **100**, 155149 (2019).

[161] E. Walter et al., *Multiloop flow equations for single-boson exchange fRG*, arXiv:2201.04878 (2022).

A Appendix

A.1 Frequency structure of pseudofermion vertices

In Sec. 4.4.3, we presented an algorithm to dynamically adjust the frequency grids for the 2PR vertices γ_c during the fRG flow. Since our routine is based on cuts along different bosonic (fermionic) frequency axes, one has to ascertain that these one-dimensional snapshots of the data are representative of the full (three-dimensional) frequency structure. This is further exemplified with Fig. A.1, where we decompose the two-particle vertex, as obtained from a PA calculation with fixed frequency grids for the ferromagnet on the cubic lattice, into its reducible contributions to the spin and density component (see Sec. 4.5.2). For brevity, we fix $\Lambda/J = 0.8$ and $\omega_c = 0$, henceforth. As expected from the discussion in Sec. 4.3.3, the most dominant features in the ν_c-ν_c' plane are indeed found in vicinity of the origin $\nu_c = \nu_c' = 0$. Importantly, γ_c can peak either on the fermionic axis or along the diagonal cut $\nu_c = \nu_c'$, a circumstance which necessitates scans along both directions to faithfully adapt the numerical grids to the frequency structure of the vertices. This is most prominently visible in the t channel (see the second column of Fig. A.1), wherein the density component γ_t^d exhibits a sharp peak at some $\nu_c = \nu_c' > 0$ on the one hand, but, on the other hand, evaluates to zero along the fermionic axis due to symmetry constraints (see Sec. 4.3.4).

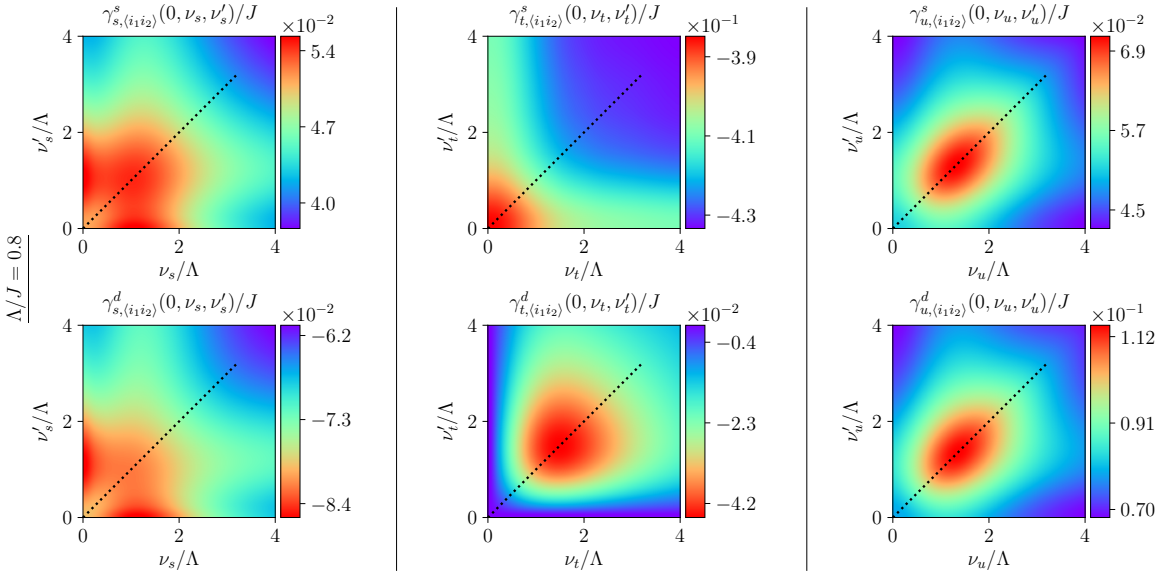

Figure A.1: Decomposition of the two-particle vertex into 2PR channels. We perform parquet calculations at $\Lambda/J = 0.8$ to determine Γ for the cubic ferromagnet, where it can be described in terms of a spin (top row) and density component (bottom row), both of which fall apart into $s/t/u$-reducible diagrams corresponding to the individual columns, respectively. The 2PR vertices exhibit their most dominant features close to the origin, either on the fermionic axis or along the $\nu_c = \nu_c'$ diagonal (dotted line).

A.2 Scaling of pffRG code

The majority of the computing time in pffRG is spent on evaluating the cutoff derivative of the two-particle vertex, that is, the right-hand side of the respective flow equation. To calculate the latter, a Matsubara integral for every component of the 2PR bubbles[1] needs to be determined. These can, however, be calculated independently from one another thus opening up the possibility to exploit parallelization over several computing units. In our code, `PFFRGSolver.jl`, we utilize the built-in multi-threading capabilities of the Julia programming language to speed up the evaluation of $\frac{d}{d\Lambda}\Gamma$. To cope with the adaptive nature of our quadrature, which implies that computing times differ between individual Matsubara integrals, dynamical load balancing is applied.

[1] In Refs. [98, P2] examples for the number of flow equations are given.

To test for the (shared-memory) scalability of our implementation, we measured computing times for single evaluations of the vertex derivative on different processors. Our results are summarized in Fig. A.2. In most cases, the observed speedup is near ideal, the only visible deviations appear for the Intel Xeon Platinum CPU (see [Fig. A.2(b)]), where scaling appears to be suboptimal for more than 16 threads. For this particular processor, however, we simultaneously find the single-thread efficiency to be higher, which could imply that scalability might be impeded by the workloads per thread becoming too trivial.

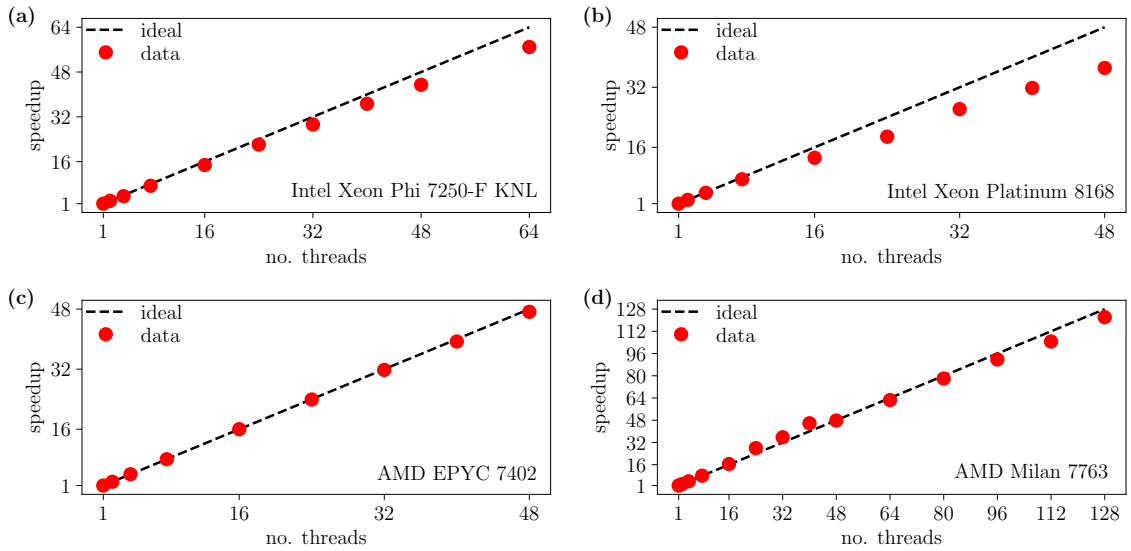

Figure A.2: Scaling of pffRG computing times with multiple threads. We test the performance of the `PFFRGSolver` Julia package on four different CPUs: **(a)** Intel Xeon Phi Knights Landing (JURECA Booster, Forschungszentrum Jülich), **(b)** Intel Xeon Platinum (JUWELS, Forschungszentrum Jülich), **(c)** AMD EPYC (JUWELS Booster, Forschungszentrum Jülich) and **(d)** AMD Milan (NOCTUA-2, Paderborn Center for Parallel Computing). Scaling is near optimal in most cases, attesting to the parallel efficiency of our code.

'There are very few things that can be proved rigorously in condensed matter physics.'

These famous words, brought to us by Nobel laureate Anthony James Leggett in 2003, summarize very well the challenging nature of problems researchers find themselves confronted with when entering the fascinating field of condensed matter physics. The former roots in the inherent many-body character of several quantum mechanical particles with modest to strong interactions between them: their individual properties might be easy to understand, while their collective behavior can be utterly complex. Strongly correlated electron systems, for example, exhibit several captivating phenomena such as superconductivity or spin-charge separation at temperatures far below the energy scale set by their mutual couplings. Moreover, the dimension of the respective Hilbert space grows exponentially, which impedes the exact diagonalization of their Hamiltonians in the thermodynamic limit. For this reason, renormalization group (RG) methods have become one of the most powerful tools of condensed matter research - scales are separated and dealt with iteratively by advancing an RG flow from the microscopic theory into the low-energy regime.

In this thesis, we report on two complementary implementations of the functional renormalization group (fRG) for strongly correlated electrons. Functional RG is based on an exact hierarchy of coupled differential equations, which describe the evolution of one-particle irreducible vertices in terms of an infrared cutoff Λ. To become amenable to numerical solutions, however, this hierarchy needs to be truncated. For sufficiently weak interactions, three-particle and higher-order vertices are irrelevant at the infrared fixed point, justifying their neglect. This one-loop approximation lays the foundation for the N-patch fRG scheme employed within the scope of this work. As an example, we study competing orders of spinless fermions on the triangular lattice, mapping out a rich phase diagram with several charge and pairing instabilities. In the strong-coupling limit, a cutting-edge implementation of the multiloop pseudofermion functional renormalization group (pffRG) for quantum spin systems at zero temperature is presented. Despite the lack of a kinetic term in the microscopic theory, we provide evidence for self-consistency of the method by demonstrating loop convergence of pseudofermion vertices, as well as robustness of susceptibility flows with respect to occupation number fluctuations around half-filling. Finally, an extension of pffRG to Hamiltonians with coupled spin and orbital degrees of freedom is discussed and results for exemplary model studies on strongly correlated electron systems are presented.

University of Cologne

thp Institute for Theoretical Physics University of Cologne

bcgs Bonn-Cologne Graduate School of Physics and Astronomy